

AD-A186 609

DTIC FILE COPY Bulletin 52
(Part 3 of 5 Parts)

2

THE SHOCK AND VIBRATION BULLETIN

Part 3
Environmental Testing and Simulation,
Flight Environments

MAY 1982

A Publication of
THE SHOCK AND VIBRATION
INFORMATION CENTER
Naval Research Laboratory, Washington, D.C.

DTIC
ELECTE
NOV 19 1987
S & D



Office of
The Under Secretary of Defense
for Research and Engineering

Approved for public release; distribution unlimited.

87 10 28 020

**BLANK PAGES
IN THIS
DOCUMENT
WERE NOT
FILMED**

SYMPOSIUM MANAGEMENT

THE SHOCK AND VIBRATION INFORMATION CENTER

Henry C. Pusey, Director

Rudolph H. Volin

J. Gordan Showalter

Jessica Hileman

Elizabeth A. McLaughlin

Bulletin Production

**Publications Branch, Technical Information Division,
Naval Research Laboratory**

Bulletin 52
(Part 3 of 5 Parts)

THE SHOCK AND VIBRATION BULLETIN

MAY 1982

**A Publication of
THE SHOCK AND VIBRATION
INFORMATION CENTER
Naval Research Laboratory, Washington, D.C.**

Accession For	
NTIS CRA&I	<input checked="checked" type="checkbox"/>
DTIC TAB	<input type="checkbox"/>
Unannounced	<input type="checkbox"/>
Justification	
By	
Distribution/	
Availability Codes	
Dist	Avail and/or Special
A-1	

The 52nd Symposium on Shock and Vibration was held at the Monteleone Hotel, New Orleans, LA on October 26-28, 1981. The Defense Nuclear Agency, Washington, D.C. and the U.S. Army Waterways Experiment Station, Vicksburg, MS were Co-Hosts.



**Office of
The Under Secretary of Defense
for Research and Engineering**

CONTENTS

PAPERS APPEARING IN PART 3

Environmental Testing and Simulation

DIGITAL CONTROL OF A SHAKER TO A SPECIFIED SHOCK SPECTRUM ; J. F. Unruh, Southwest Research Institute, San Antonio, TX	1
GUNFIRE VIBRATION SIMULATION ON A DIGITAL VIBRATION CONTROL SYSTEM ; J. Cies, Hewlett-Packard Company, Paramus, NJ	11
MEASUREMENT OF ALL COMPONENTS OF STRAIN BY A 3-D FIBER OPTIC STRAIN GAGE ; S. Edelman and C. M. Davis, Jr., Dynamic Systems, Inc., McLean, VA	19
REGISTRATION OF THREE SOIL STRESS GAGES AT 0 THROUGH 28 MPa (4000 psi) ; C. R. Welch, U.S. Army Engineer Waterways Experiment Station, Corps of Engineers, Vicksburg, MS	25
CABLE PROTECTION FOR GROUND SHOCK INSTRUMENTATION IN SEVERE ENVIRONMENTS — — RESULTS OF AN EVALUATION TEST ; C. R. Welch, U.S. Army Engineer Waterways Experiment Station, Corps of Engineers, Vicksburg, MS	31
STRUCTURAL RESPONSE OF HEPA FILTERS TO SHOCK WAVES ; P. R. Smith, New Mexico State University, Las Cruces, NM and W. S. Gregory, Los Alamos National Laboratory, Los Alamos, NM	43
A TECHNIQUE COMBINING HEATING AND IMPACT FOR TESTING REENTRY VEHICLE IMPACT FUZES AT HIGH VELOCITIES ; R. A. Benham, Sandia National Laboratories, Albuquerque, NM	53
USE OF A DROPPED WEIGHT TO SIMULATE A NUCLEAR SURFACE BURST ; C. R. Welch and S. A. Kiger, U.S. Army Engineer Waterways Experiment Station, Corps of Engineers, Vicksburg, MS	65
ANALYSIS AND TESTING OF A NONLINEAR MISSILE AND CANISTER SYSTEM ; R. G. Benson, A. C. Deerhake and G. C. McKinnis, General Dynamics/Convair Division, San Diego, CA	77
BIO-DYNAMIC RESPONSE OF HUMAN HEAD DURING WHOLE-BODY VIBRATION CONDITIONS ; B. K. N. Rao, Birmingham Polytechnic, Perry Barr, England	89

Flight Environments

YC-15 EXTERNALLY BLOWN FLAP NOISE ; Capt. L. G. Peck, Flight Dynamics Laboratory, Air Force Wright Aeronautical Laboratories, Wright-Patterson AFB, OH	101
DETERMINATION OF THE DYNAMIC ENVIRONMENT OF THE F/FB-111 TAIL POD ASSEMBLY ; J. Chinn and P. Bolds, Air Force Wright Aeronautical Laboratories, Wright-Patterson AFB, OH	115
AN ASSESSMENT OF THE A-10's CAPABILITY TO OPERATE ON ROUGH SURFACES ; T. G. Gerardi and D. L. Morris, Air Force Wright Aeronautical Laboratories, Wright-Patterson AFB, OH	131
SUBCRITICAL FLUTTER TESTING USING THE FEEDBACK SYSTEM APPROACH ; C. D. Turner, North Carolina State University, Raleigh, NC	145
TOMAHAWK CRUISE MISSILE FLIGHT ENVIRONMENTAL MEASUREMENT PROGRAM ; E. S. Rosenbaum and F. L. Gloyna, General Dynamics/Convair Division, San Diego, CA	159
TEST PROGRAM TO DEVELOP VIBROACOUSTICS TEST CRITERIA FOR THE GALILEO BUS ; D. L. Kern and C. D. Hayes, Jet Propulsion Laboratory, California Institute of Technology, Pasadena, CA	229
SLV-3 FLIGHT VIBRATION ENVIRONMENT ; S. A. Palaniwami, G. Muthuraman and P. Balachandran, Aerospace Structures Division, Vikram Sarabhai Space Centre, Trivandrum, India	249

PAPERS APPEARING IN PART 1

Welcome

WELCOME

Colonel Tilford Creel, Commander/Director, U.S. Army Waterways Experiment Station, Vicksburg, MS

Keynote Address

KEYNOTE ADDRESS

Marvin Atkins, Director, Offensive and Space Systems, Office of the Under Secretary of Defense
Research Engineering, Department of Defense, Washington, DC

Invited Papers

EQUIPMENT SURVIVABILITY ON THE INTEGRATED BATTLEFIELD

Charles N. Davidson, Technical Director, U.S. Army Nuclear and Chemical Agency, Springfield, VA

NAVAL OPERATIONS IN A NUCLEAR ENVIRONMENT

Captain Donald Alderson, U.S.N., Acting Chief, Tactical Nuclear Weapons Project Office (PM-23)
Department of the Navy, Washington, DC

SURVIVABILITY REQUIREMENTS FOR FUTURE AIR FORCE SYSTEMS

Henry F. Cooper, Deputy for Strategic and Space Systems, Assistant Secretary of the Air Force
(Research, Development and Logistics), Washington, DC

NUCLEAR HARDNESS VALIDATION TESTING

Edward Conrad, Deputy Director (Science and Technology), Defense Nuclear Agency, Washington, DC

ELIAS KLEIN MEMORIAL LECTURE — THE CHANGING DIMENSIONS OF QUALIFICATION TESTING

H. Norman Abramson, Vice-President, Engineering Sciences, Southwest Research Institute, San Antonio, TX

REQUIRED DEVELOPMENTS IN STRUCTURAL DYNAMICS

Ben K. Wada, Jet Propulsion Laboratory, Pasadena, CA

EFFECT OF SEALS ON ROTOR SYSTEMS

David P. Fleming, NASA, Lewis Research Center, Cleveland, OH

MACHINERY VIBRATION EVALUATION TECHNIQUES

R. L. Eshleman, The Vibration Institute, Clarendon Hills, IL

SHAFT VIBRATION MEASUREMENT AND ANALYSIS TECHNIQUES

Donald E. Bently, President, Bently Nevada Corporation, Minden, NV

Rotor Dynamics and Machinery Vibration

SPIN TEST VIBRATIONS OF PENDULOUSLY SUPPORTED DISC/CYLINDER ROTORS

F. H. Wolff and A. J. Molnar, Westinghouse Research and Development Center, Pittsburgh, PA

MODAL ANALYSIS AS A TOOL IN THE EVALUATION OF A TURBINE WHEEL FAILURE

A. L. Moffa and R. L. Leon, Franklin Research Center, Philadelphia, PA

CONTRIBUTION TO THE DYNAMIC BEHAVIOUR OF FLEXIBLE MECHANISMS

E. Imam, J. Der Hagopian and M. Lalanne, Institut National des Sciences Appliquées, Villeurbanne, France

SELF-EXCITED VIBRATION OF A NONLINEAR SYSTEM WITH RANDOM PARAMETERS

R. A. Ibrahim, Texas Tech University, Lubbock, TX

PAPERS APPEARING IN PART 2

Invited Papers

Space Shuttle Loads and Dynamics

SPACE SHUTTLE MAIN ENGINE (SSME) POGO TESTING AND RESULTS

J. R. Fenwick, Rockwell International, Rocketdyne Division, Canoga Park, CA and
J. H. Jones and R. E. Jewell, NASA, Marshall Space Flight Center, Huntsville, AL

SPACE SHUTTLE SOLID ROCKET BOOSTER WATER ENTRY CAVITY COLLAPSE LOADS

R. T. Keefe and E. A. Rawls, Chrysler Corporation, Slidell, LA and
D. A. Kroas, NASA, Marshall Space Flight Center, Huntsville, AL

**SPACE SHUTTLE SOLID ROCKET BOOSTER REENTRY AND DECELERATOR SYSTEM
LOADS AND DYNAMICS**

R. Moog, Martin Marietta/Denver Division, Denver, CO and D. Kroas, NASA,
Marshall Space Flight Center, Huntsville, AL

**INVESTIGATION OF SIDE FORCE OSCILLATIONS DURING STATIC FIRING OF THE
SPACE SHUTTLE SOLID ROCKET MOTOR**

M. A. Behring, Thiokol Corporation/Wasatch Division, Brigham City, UT

Space Shuttle Data Systems

**DEVELOPMENT OF AN AUTOMATED PROCESSING AND SCREENING SYSTEM FOR THE
SPACE SHUTTLE ORBITER FLIGHT TEST DATA**

D. K. McCutchen, NASA, Johnson Space Center, Houston, TX, J. F. Brose, Lockheed Engineering and
Management Services Company, Inc., Houston, TX and W. E. Palm, McDonnell Douglas Corp., Houston, TX

**DEVELOPMENT OF A VIBROACOUSTIC DATA BASE MANAGEMENT AND
PREDICTION SYSTEM FOR PAYLOADS**

F. J. On, NASA, Goddard Space Flight Center, Greenbelt, MD and
W. Hendricks, Lockheed Missiles and Space Company, Sunnyvale, CA

AUTOMATION OF VIBROACOUSTIC DATA BANK FOR RANDOM VIBRATION CRITERIA DEVELOPMENT

R. C. Ferebee, NASA, Marshall Space Flight Center, Huntsville, AL

**THE DEVELOPMENT AND VERIFICATION OF SHUTTLE ORBITER RANDOM
VIBRATION TEST REQUIREMENTS**

M. C. Coody, NASA, Johnson Space Center, Houston, TX, H. K. Pratt, Rockwell International Corporation,
Downey, CA and D. E. Newbrough, Management and Technical Services Corporation, Houston, TX

SPACE SHUTTLE ORBITER ACOUSTIC FATIGUE CERTIFICATION TESTING

R. A. Stevens, Rockwell International, Downey, CA

Space Shuttle Thermal Protection Systems

STRUCTURAL CHARACTERISTICS OF THE SHUTTLE ORBITER CERAMIC THERMAL PROTECTION SYSTEM

P. A. Cooper, NASA, Langley Research Center, Hampton, VA

SHUTTLE TILE ENVIRONMENTS AND LOADS

R. J. Muraca, NASA, Langley Research Center, Hampton, VA

DYNAMIC AND STATIC MODELING OF THE SHUTTLE ORBITER'S THERMAL PROTECTION SYSTEM

J. M. Housner, G. L. Giles and M. Vallas, NASA, Langley Research Center, Hampton, VA

BUFFET LOADS ON SHUTTLE THERMAL-PROTECTION-SYSTEM TILES

C. F. Coe, NASA, Ames Research Center, Moffett Field, CA

UNSTEADY ENVIRONMENTS AND RESPONSES OF THE SHUTTLE COMBINED LOADS ORBITER TEST

P. H. Schuetz, Rockwell International, Downey, CA and
L. D. Pinson and H. T. Thornton, Jr., NASA, Langley Research Center, Hampton, VA

Space Shuttle Main Engine Dynamics

VIBRATION MATURITY OF THE SPACE SHUTTLE MAIN ENGINES

E. W. Larson and E. Mogil, Rockwell International/Rocketdyne Division, Canoga Park, CA

STRUCTURAL RESPONSE OF THE SSME FUEL FEEDLINE TO UNSTEADY SHOCK OSCILLATIONS

E. W. Larson, G. H. Ratekin and G. M. O'Connor, Rockwell International/Rocketdyne Division, Canoga Park, CA

PAPERS APPEARING IN PART 4

Fatigue and Random Loading

FATIGUE LIFE PREDICTION FOR VARIOUS RANDOM STRESS PEAK DISTRIBUTIONS

R. G. Lambert, General Electric Company, Aircraft Equipment Division, Utica, NY

FATIGUE LIFE EVALUATION, STOCHASTIC LOADING AND MODIFIED LIFE CURVES

M. El Menoufy, H. H. E. Leipholz and T. H. Topper, University of Waterloo, Waterloo, Ontario, Canada

THE EFFECTS OF ENDURANCE LIMIT AND CREST FACTOR ON TIME TO FAILURE UNDER RANDOM LOADING

A. J. Curtis and S. M. Moite, Hughes Aircraft Company, Culver City, CA

SINGLE POINT RANDOM MODAL TEST TECHNOLOGY APPLICATION TO FAILURE DETECTION

W. M. West, Jr., NASA, Johnson Space Center, Houston, TX

FORCED VIBRATIONS OF A LARGE DAMPED MECHANICAL SYSTEM

D. W. Nicholson, Naval Surface Weapons Center, White Oak, Silver Spring, MD

INDIRECT FOURIER TRANSFORM (IFT) AND SHOCK RESPONSE — A DETAILED PRESENTATION OF BASIC THEORY

C. T. Morrow, Encinitas, CA

Control, Isolation and Damping

ACTIVE VIBRATION CONTROL OF LARGE FLEXIBLE STRUCTURES

T. T. Soong and J. C. H. Chang, State University of New York at Buffalo, Buffalo, NY

FORCE OPTIMIZED RECOIL CONTROL SYSTEM

P. E. Townsend, U.S. Army Armament Research and Development Command, Dover, NJ,
R. J. Radkewics, U.S. Army Armament Research and Development Command, Rock Island, IL and
R. F. Gartner, Honeywell, Inc., Edina, MN

PERFORMANCE ANALYSIS OF HIGH-SPEED HYDRAULIC SUSPENSION SYSTEMS IN MULTIPLE WHEELED LAND TRANSPORTERS

P. Woods, Martin Marietta Corporation, Denver, CO

NONLINEAR ANALYSIS OF PNEUMATIC FORCE GENERATORS USED FOR VIBRATION CONTROL

S. Sankar, Concordia University, Montreal, Quebec, Canada, R. R. Guntur, Union College, Schenectady, NY,
and S. G. Kalumber, Electronic Associates, Inc., West Long Branch, NJ

REDUCTION OF HYDRAULIC LINE OSCILLATING PRESSURES INDUCED BY PUMP CAVITATION

G. Druhak, P. Marino and M. Bernstein, Grumman Aerospace Corporation, Bethpage, NY

RUBBER ISOLATORS FOR THE ADATS MISSILE

J. Frottier, Oerlikon-Buehler Werkzeugmaschinenfabrik, Zurich, CH and
C. F. O'Hearne, Martin Marietta Orlando Aerospace, Orlando, FL

TIME AND TEMPERATURE EFFECTS ON CUSHIONS

G. S. Mustin, Naval Sea Systems Command, Washington, DC

EXTRANEIOUS EFFECTS IN DAMPING MEASUREMENT

R. J. Hooker, University of Queensland, Queensland, Australia and
S. Prasertan, Prince of Songkla University, Hat-yai, Thailand

DYNAMIC ANALYSIS OF A LARGE STRUCTURE WITH ARTIFICIAL DAMPING

Q. L. Tian, D. K. Liu, Y. P. Li and D. F. Wang, Institute of Mechanics,
The Chinese Academy of Sciences, Beijing, China

AN EXPERIMENTAL STUDY OF THE NONLINEAR BEHAVIOUR OF A STRANDED CABLE AND DRY FRICTION DAMPER

C. S. Chang and Q. Tian, Institute of Mechanics, The Chinese Academy of Sciences, Beijing, China

RESPONSE OF PNEUMATIC ISOLATOR TO STANDARD PULSE SHAPES

M. S. Hundal, The University of Vermont, Burlington, VT

PAPERS APPEARING IN PART 5

Mathematical Modeling

DAMPED STRUCTURE DESIGN USING FINITE ELEMENT ANALYSIS

M. F. Kluesener and M. L. Drake, University of Dayton Research Institute, Dayton, OH

DETERMINATION OF NORMAL MODES FROM MEASURED COMPLEX MODES

S. R. Ibrahim, Old Dominion University, Norfolk, VA

THE EFFECT OF JOINT PROPERTIES ON THE VIBRATIONS OF TIMOSHENKO FRAMES

I. Yaghai, Sharif University of Technology, Tehran, Iran and

D. A. Frohrib, University of Minnesota, Minneapolis, MN

SOIL STRUCTURE INTERACTION AND SOIL MODELS

J. M. Ferritto, Naval Civil Engineering Laboratory, Port Hueneme, CA

FINITE ELEMENTS FOR INITIAL VALUE PROBLEMS IN DYNAMICS

T. E. Simkins, U.S. Army Armament Research and Development Command, Watervliet, NY

Structural Dynamics

A PROCEDURE FOR DESIGNING OVERDAMPED LUMPED PARAMETER SYSTEMS

D. J. Inman, State University of New York at Buffalo, Buffalo, NY and

A. N. Andry, Jr., Lockheed California Company, Burbank, CA

ON THE OPTIMAL LOCATION OF VIBRATION SUPPORTS

B. P. Wang and W. D. Pilkey, University of Virginia, Charlottesville, VA

DYNAMIC BUCKLING OF PINNED COLUMNS

J. M. Ready, David W. Taylor Naval Ship Research and Development Center, Bethesda, MD

LARGE DEFLECTION RANDOM RESPONSE OF SYMMETRIC LAMINATED COMPOSITE PLATES

K. R. Wentz and D. B. Paul, Air Force Wright Aeronautical Laboratories, Wright-Patterson AFB, OH and

C. Mei, Old Dominion University, Norfolk, VA

DYNAMIC CHARACTERISTICS OF A NON-UNIFORM TORPEDO-LIKE HULL STRUCTURE

A. Harari, Naval Underwater Systems Center, Newport, RI

VIBRATION AND ACOUSTIC RADIATION FROM POINT EXCITED SPHERICAL SHELLS

E. H. Wong, Naval Ocean Systems Center, San Diego, CA and

S. I. Hayek, The Pennsylvania State University, University Park, PA

DAMPING OF SHALLOW-BURIED STRUCTURES DUE TO SOIL-STRUCTURE INTERACTION

F. S. Wong and P. Weidlinger, Weidlinger Associates, Menlo Park, CA and New York, NY

TITLES AND AUTHORS OF PAPERS PRESENTED IN THE SHORT DISCUSSION TOPICS SESSION

NOTE: These papers were only presented at the Symposium. They are not published in the Bulletin and are only listed here as a convenience.

TRANSFER FUNCTION ANALYSIS OF LARGE STRUCTURES

H. J. Weaver, Lawrence Livermore National Laboratory, Livermore, CA

SHOCK HARDENED STRUCTURAL ATTACHMENTS FOR HONEYCOMB BULKHEADS

P. W. Buermann, Gibbs & Cox, Inc., New York, NY

DISCOVERING THE THIRD (AND SECOND) DIMENSION

B. Meeker, Pacific Missile Test Center, Point Mugu, CA

A MICROPROCESSOR BASED ADAPTIVE ISOLATION AND DAMPING OF A VIBRATING STRUCTURE

A. S. R. Murty, Indian Institute of Technology, Kharagpur, India

HARMONIC RESPONSE OF A STRUCTURE INCLUDING A DRY FRICTION DAMPER

J. Der Hagopian and M. LaLanne, Institut National des Sciences Appliquees, Villeurbanne, France

- RATIONALE FOR VIBRATION TESTING IN MIL-STD-810D (DRAFT)**
H. J. Caruso, Westinghouse Electric Corporation, Baltimore, MD
- VIBRATION ISOLATION OF SENSITIVE IUS COMPONENTS REQUIRING THERMAL CONDUCTION**
F. W. Spann, Boeing Aerospace Company, Seattle, WA
- FINITE ELEMENT ANALYSIS OF SHOCK AND VIBRATION FIXTURES**
L. G. Smith, Hughes Aircraft Company, Fullerton, CA
- A UNIQUE METHOD FOR VIBRATION TESTING FAR BELOW THE NORMAL AMBIENT NOISE LEVEL OF ELECTRODYNAMIC SHAKERS**
H. D. Camp, Jr., U.S. Army; ERADCOM, Fort Monmouth, NJ
- BOLTS AND FASTENER TIGHTENING TO BROCHURE IDEALNESS THROUGH VIBRATION SIGNATURES**
A. S. R. Murty, Indian Institute of Technology, Kharagpur, India
- COST EFFECTIVE METHODS OF INCREASING DATA RECORDING CAPACITY**
M. Dowling, Franklin Research Center, Philadelphia, PA
- PIEZOELECTRIC FORCE GAUGE WITH HIGH SENSITIVITY**
R. R. Bouche, Bouche Laboratories, Sun Valley, CA
- PYROTECHNIC SHOCK ENVIRONMENTS MEASURED ON INERTIAL UPPER STAGE (IUS)**
C. J. Beck, Jr., Boeing Aerospace Company, Seattle, WA
- USE OF BAND-SELECTABLE HANNING SMOOTHING TO IMPROVE TRANSIENT WAVEFORM REPRODUCTION ON SHAKERS**
D. O. Smallwood and D. L. Gregory, Sandia National Laboratories, Albuquerque, NM
- SHAKER SHOCK TEST DATA — BASED ON OPTIMIZED PRE AND POST PULSES**
R. T. Fandrich, Harris Corporation, Melbourne, FL
- PROGRESS ON THE EDESS MACHINES**
F. J. Szama, Naval Surface Weapons Center, Silver Spring, MD
- MULTI-AXIS RANDOM VIBRATION TESTER FOR AVIONICS**
D. Everett, Pacific Missile Test Center, Point Mugu, CA and G. Greanias, UCLA, Los Angeles, CA
- ACOUSTIC FACILITY FOR CRUISE MISSILE TESTING**
O. H. Moore, Jr., General Dynamics/Convair, San Diego, CA
- EFFECT OF FRICTION AND MISTUNING ON THE RESPONSE OF A BLADED DISK DISCRETE MODEL**
A. Muszynska, University of Dayton and Bently Nevada Corp., Minden, NV
- CURRENT DEVELOPMENTS IN HUMAN VIBRATION RESEARCH**
J. C. Guignard, Naval Biodynamics Laboratory, New Orleans, LA

ENVIRONMENTAL TESTING AND SIMULATION

DIGITAL CONTROL OF A SHAKER TO A SPECIFIED SHOCK SPECTRUM

James F. Unruh
Southwest Research Institute
San Antonio, Texas

A digital computer based control system was developed for a bi-axial electrohydraulic shaker table used for seismic qualification testing of nuclear power plant components. The system drive signals were developed from a weighted linear sum of 1/6-octave pseudo random noise signals. Preliminary drive signal shaping is accomplished through the use of a series of table mounted dummy mass transfer functions obtained from a previously generated data bank. Adjustments to the drive signal are made by direct comparison of the resulting test response spectrum (TRS) to the required response spectrum (RRS). Drive signal shaping sequences for a 2000 lb electrical equipment control cabinet are presented to demonstrate the effectiveness of the control system for seismic qualification.

NOMENCLATURE

a_i = weighting coefficient
 f = frequency, Hz
 g = gravity units
 i, j = indices
 t_k = discretized time variable
AMIN = lower margin for TRS to RRS match
AMAX = upper margin for TRS to RRS match
ADC = analog to digital conversion
DAC = digital to analog conversion
FFT = Fast Fourier Transform
 $H(f)$ = system transfer function
 $H_T(t)$ = table dummy mass transfer function
NB = number of input 1/6-octave bands
RRS = required response spectrum
 $S(y_R(t))$ = shock response spectrum operator

TRS = test response spectrum
 $W(t_k)$ = build-hold-decay weighting function
 $X(f)$ = input frequency spectrum
 $X_D(t_k)$ = exciter drive signal
 $Y(f)$ = output frequency spectrum
 $Y_R(t_k)$ = table acceleration response
ZPA = zero period acceleration
 θ_j = random phase angle
 π = constant, 3.14159
 ϕ_i = 1/6-octave pseudo random signal

INTRODUCTION

A digital computer based control system was developed for Southwest Research Institute's (SwRI) biaxial electrohydraulic shaker table used for seismic qualification testing of nuclear power plant components. The overall program objective was to reduce costs associated with the design and qualification of nuclear power plant components by decreasing control signal resolution bandwidth to minimize component over-test and by implementing automated procedures to

greatly reduce signal shaping time over that of conventional analog control methods.

The criteria appropriate for the seismic qualification of a majority of nuclear plant components are specified by the plant architect engineers in the form of a base acceleration Required Response Spectrum (RRS). To meet the specified criteria the Test Response Spectrum (TRS) measured at the base of the component must envelope the RRS based on a 1/6 octave resolution. Recall that a shock response spectrum is a plot of peak response of a series of single degree-of-freedom oscillators versus oscillator natural frequency for a given critical damping ratio (see Fig. 1). The corresponding base input earthquake time history is a non-stationary broadband random excitation with energy in the range from 1 to 33 Hz [1]. The duration of the input motion is usually 30 seconds with the non-stationary character often being synthesized by a signal build-hold-decay envelope, 5-15-10 seconds, respectively. The peak acceleration in the input time history is specified by the Zero Period Acceleration (ZPA). The ZPA is the high frequency asymptote of the shock response spectrum. In Fig. 1 the ZPA of the RRS is approximately 0.35 g's while the ZPA of the TRS is stated as 0.546 g's.

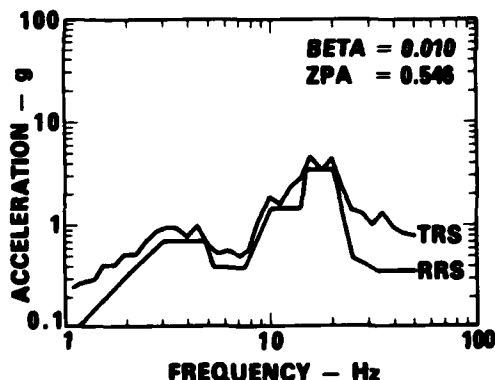


Fig. 1 - Typical response spectra

Typically, analog drive signal generation processes generally consisted of recording multiple band passed random noise signals onto analog tape. The drive signals were then scaled, summed and passed through a build-hold-decay weighting circuit to simulate the non-stationary character of an earthquake event as is shown in Fig. 2. For independent biaxial drive, signal input resolution was limited to one octave when using a single standard 14-channel magnetic tape. Shaping the drive signals required manual adjustment of the summing potentiometers with repeated dummy weight or test item excitation until enveloping of the required response spectra (horizontal and

vertical RRS's) were achieved. The analog signal shaping process often required two working days to obtain acceptable results. A diagram of the analog control process used on SwRI's biaxial shaker table is given in Fig. 3. As schematically shown in Fig. 3 the shaker table has independent vertical and horizontal axis control. The exciters are electrohydraulic with 6-inch 20,000 lb_f and 8-inch 10,000 lb_f capabilities, respectively in the vertical and horizontal axes.

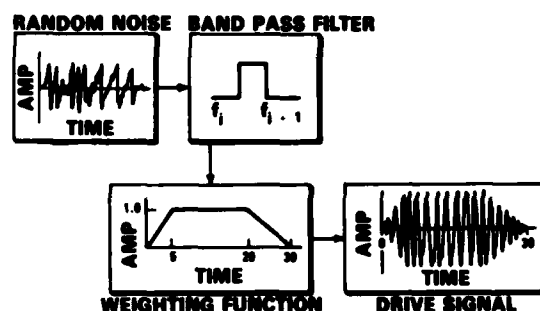


Fig. 2 - Analog drive signal generation process

DIGITAL CONTROL PROCESS

Digital control testing for shock simulation is not a new area of development [2-5]. In fact, several minicomputer-based digital control systems are now readily available which can rapidly and accurately reproduce transient waveform time histories on linear systems by use of the Favour and LeBrun technique [2]. This control technique is a straightforward application of linear transfer function theory wherein the desired output frequency response signal, $Y(f)$, is obtained from the multiplication of the system transfer function, $H(f)$, times the input frequency spectrum, $X(f)$. Thus if a frequency response output spectrum and the system transfer function is known, then an input frequency response function can be obtained directly as $X(f) = Y(f)/H(f)$. With the use of the Fast Fourier Transform (FFT) algorithm the required time history can then be generated. These operations work quite well for electromagnetic exciters which are linear with respect to acceleration control. Due to the nonlinear response of electrohydraulic exciters direct application of the Favour and LeBrun method has not been successful for electrohydraulic exciters. However, several control system methods are presently in use that compensate for the nonlinear effects [3-5]. Kao, et al, [3] used an iterative approach while updating the system transfer function during the qualification test by incrementally increasing the drive level until a full level test was accomplished. Hunter [4] determined the nonlinear gain characteristics

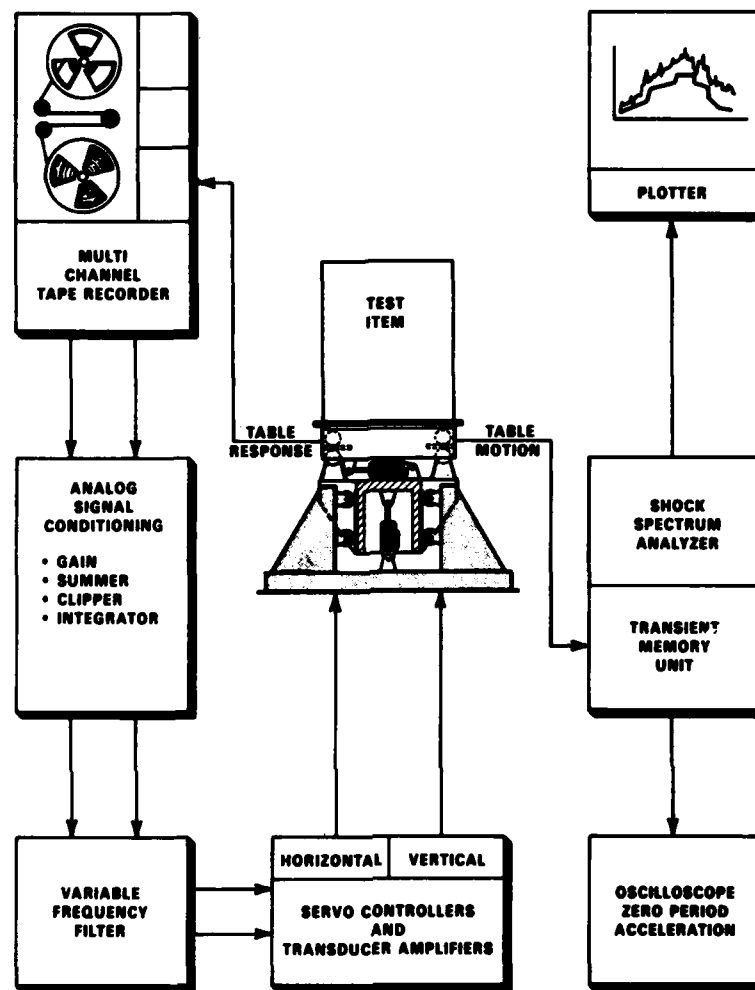


Fig. 3 - Seismic simulator analog control process

of the system prior to item test and used the gain schedule to modify the drive signal. Nichols [5] realized that an electrohydraulic exciter is a displacement controlled device which is quite linear with respect to displacement amplitude and worked directly on control of the displacement drive signal via a required displacement response time history.

It must be realized that there are an infinite number of acceleration response time histories that can produce a given shock response spectrum. The above control procedures operate directly on the time history and therefore indirectly on the corresponding shock response spectrum. A problem therein arises for producing a drive signal with excessive actuator stroke. However, through an iterative process Nichols [5] was able to systematically modify the required acceleration time history,

by random juggling of the phase components, to reduce stroke requirements and thereby still match the RRS. Nevertheless, it is conceivable that no acceptable time history can be found which would lie within the exciter's stroke capability. In such case it is permissible to reduce the low frequency response spectrum requirements so long as the test item does not exhibit resonant response in this low frequency range.

The digital control system on SwRI's seismic simulator is an open loop system with the operator in direct control. The input drive signal is adjusted based directly on the match of TRS to the RRS. The exciter displacement drive signal is generated from the linear sum of a series of 1/6-octave pseudo random noise signals. Each narrow band drive signal is the weighted sum of twenty (20) phase-shifted

cosine functions whose frequencies are uniformly distributed with the 1/6-octave band. The relative phase among the signals has a uniform random distribution in the interval $[0-\pi]$. The build-hold-decay (5-15-10) weighting is imposed on each of the narrow band signals to simulate the nonstationarity of an earthquake event. The signals are generated in the time domain as

$$\phi_i(t_k) = W(t_k) \bar{\phi}_i(t_k) \quad i = 1, 34 \quad (1)$$

where

$$\bar{\phi}_i(t_k) = \sum_{j=1}^{20} \cos [2\pi f_{ij} t + \theta_j], \quad (2)$$

f_{ij} are the uniformly distributed frequencies in the i^{th} 1/6-octave band, θ_j are the uniform random distribution of phases, t_k is a time variable discretized at a fixed sampling rate, and $W(t_k)$ is the build-hold-decay weighting function (5-15-10). For the most part, each of the generated signals appear to be nonstationary narrow band random. Time histories of several of the 1/6-octave band drive signals are given in Fig. 4. Two sets of independent narrow band (1/6-octave) drive signals were generated, one set for each drive axis and stored on disk for repeated use. The drive signal for a single axis is then obtained by a weighted sum of the individual 1/6-octave

band signals,

$$X_D(t_k) = \sum_{i=1}^{NB} a_i \phi_i(t_k) \quad (3)$$

where the a_i 's are the weighting coefficients and NB is the number of bands for which signal energy is to be input. Out of the thirty four (34) 1/6-octave bands only energy input out to the ZPA is required, usually 33 Hz.

In order to obtain an initial estimate of the weighting coefficients for a given drive signal, an estimate of the system transfer function is obtained from a data bank. Table transfer functions for both the horizontal and vertical table axes were obtained for a series of table mounted dummy mass configurations, with variable center of gravity positions, using a moderate level of continuous random excitation. Transfer functions for the two extreme dummy mass configurations are given in Fig. 5. As can be seen by these transfer function data, a significant resonance occurs in the horizontal table for a heavy mass, high c.g. test item. It was important, therefore, that a good estimate of the transfer function be available prior to test item mounted table excitation so that overtest of the item will not occur during drive signal shaping. Through the use of the data bank of transfer functions an initial estimate of the table

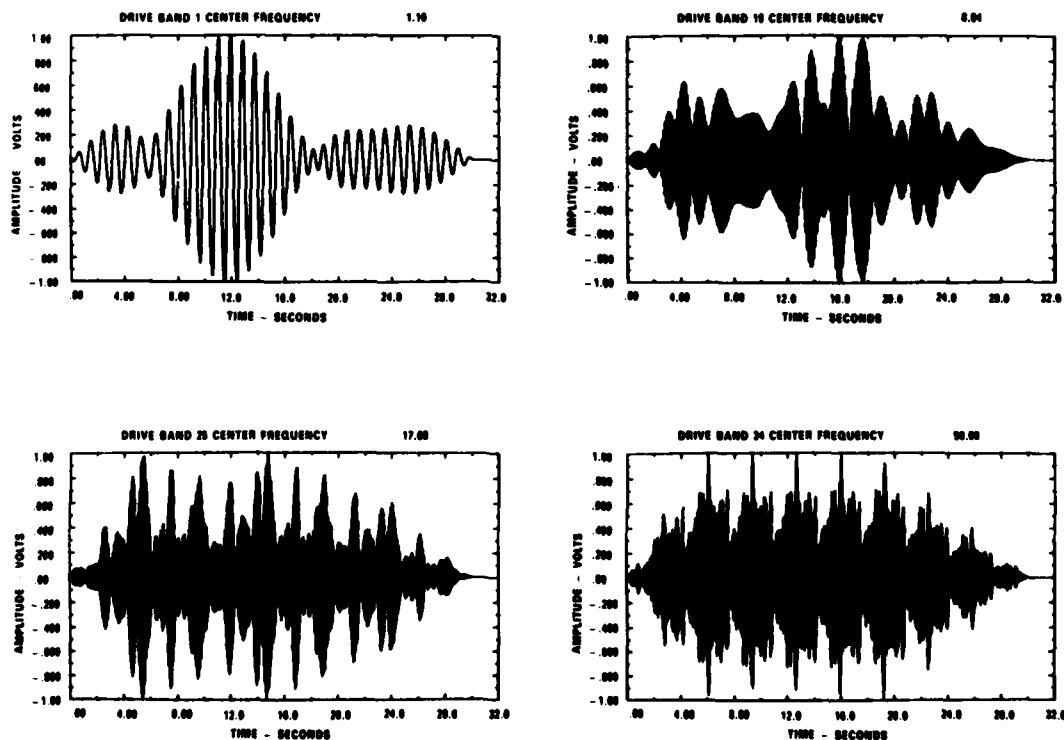


Fig. 4 - Typical 1/6-octave digital drive signals

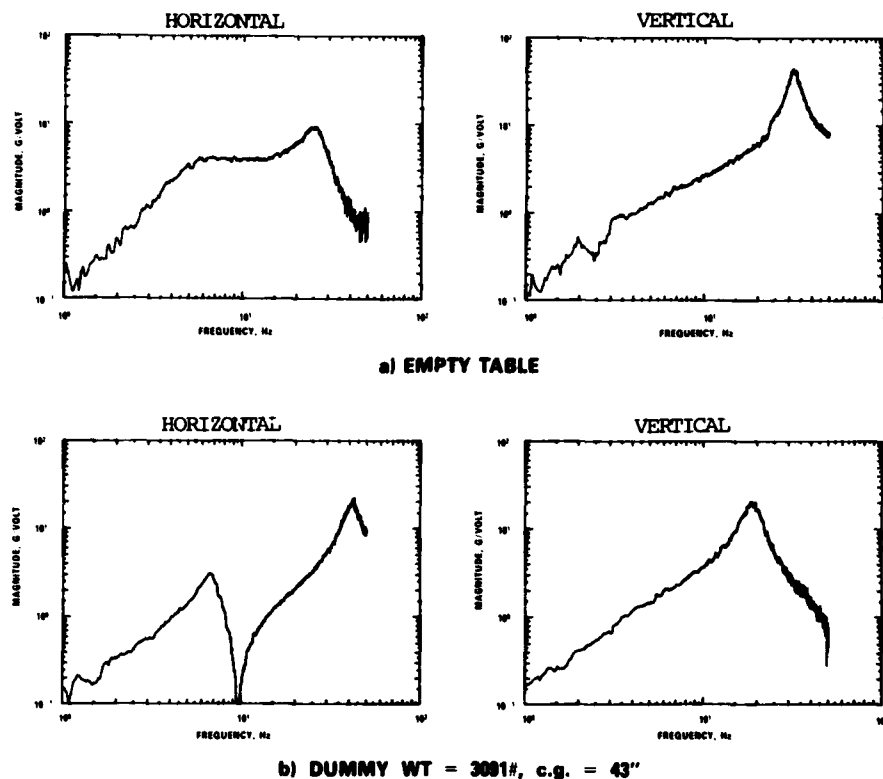


Fig. 5 - Typical dummy mass transfer functions

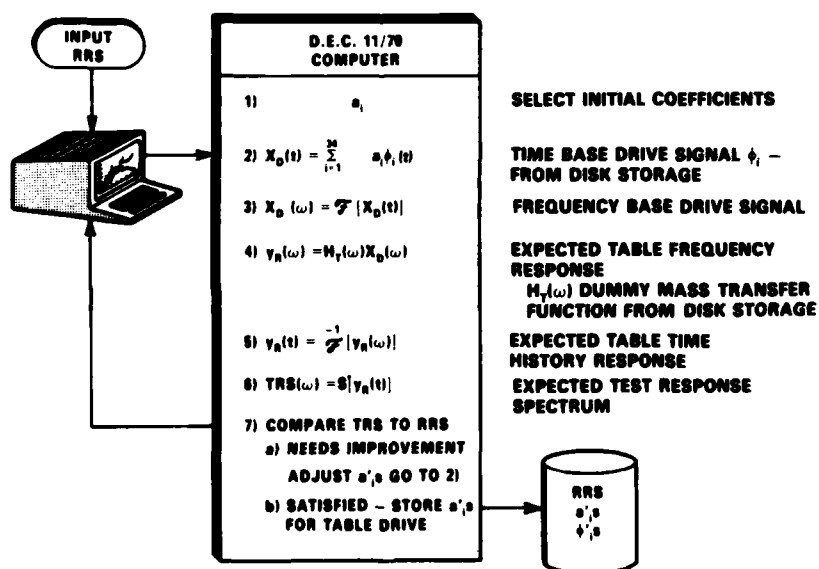


Fig. 6 - Initial table drive signal development

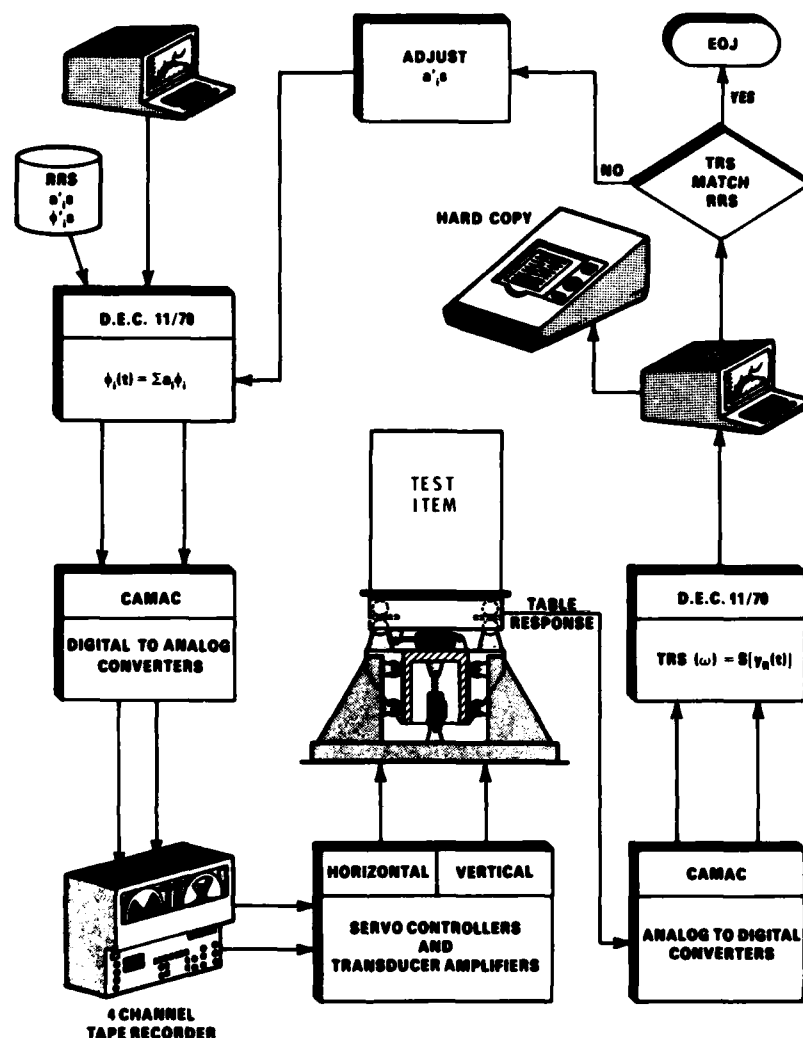


Fig. 7 - Seismic simulator digital control process

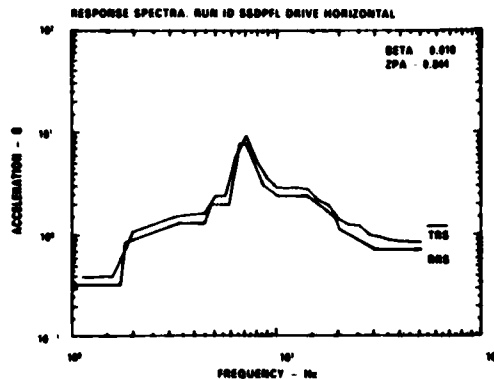
response is made according to the flow chart given in Fig. 6. Initially the "a" coefficients are assigned a value of 1.0 and the individual energy bands are summed to generate the drive signal. A frequency spectrum is then obtained via an FFT of the drive signal. The frequency spectrum of the response is then obtained from the product of a preselected dummy mass transfer function and the input spectrum. The inverse FFT of the frequency response spectrum yields an expected table response time history, and from the response time history an expected TRS is calculated. The TRS is then compared to the RRS and the "a" coefficients are adjusted, and the process repeated until a satisfactory matching is obtained. The a-weighting coefficients are then stored for future use during actual item excitation. A drive signal for the second axis is then independently shaped in an identical manner.

The algorithm for adjusting the a-weighting coefficients is based directly on the match of the TRS to the RRS and is mathematically quite simple. At the onset of the signal shaping operation the test operator selects desirable tolerances by which the TRS must match the RRS. The lower limit (AMIN) usually requires the TRS to exceed the RRS by 10% (AMIN = 1.1) while the upper limit (AMAX) typically is set at 30% (AMAX = 1.3) above the RRS. For the i^{th} 1/6-octave band, if

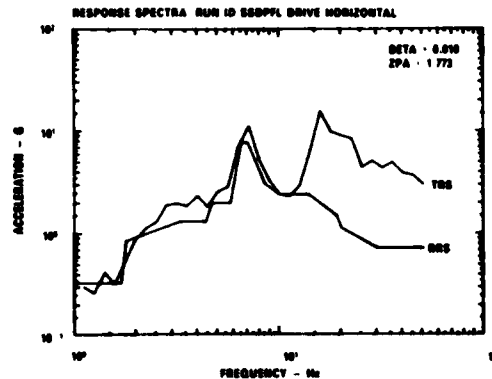
$$RRS_i \cdot AMIN \leq TRS_i \leq RRS_i \cdot AMAX \quad (4)$$

then no adjustment in the corresponding a_i is necessary. However, if Eq. 4 is not satisfied an adjustment of the form

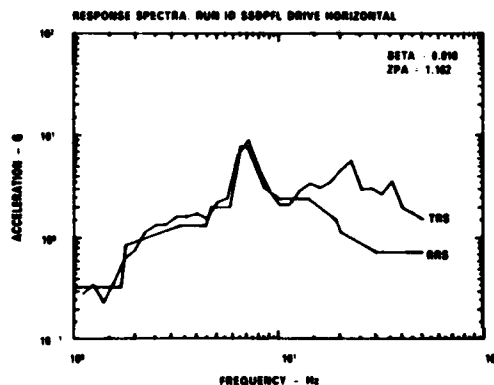
$$\bar{a}_i = ((AMAX+AMIN)/2) \cdot (RRS_i/TRS_i) \cdot a_i \quad (5)$$



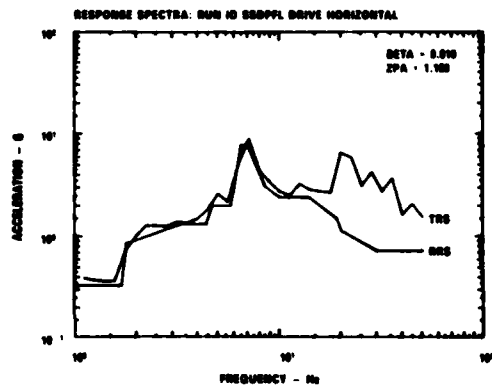
a) INITIAL EXPECTED RESPONSE



b) FIRST TABLE DRIVE



c) SECOND TABLE DRIVE



d) FOURTH TABLE DRIVE

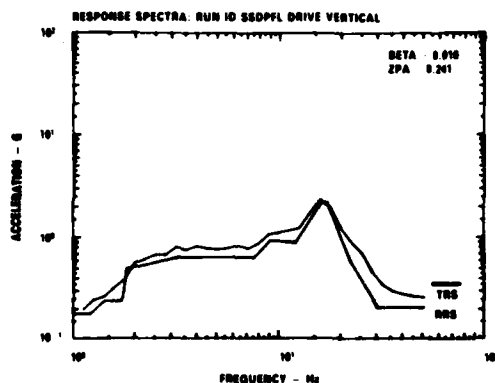
Fig. 8 - Typical horizontal drive sequence

is made to generate \bar{a}_i , a modified weighting coefficient for that band. For those response values far below the required RRS_i an accelerator factor can be used to insure a more rapid convergence. In those cases where the low frequency response requirements exceed the exciter stroke capabilities, adjustment to AMIN and AMAX or direct edit of the a_i coefficients can be made to insure a drive signal within the shaker capabilities.

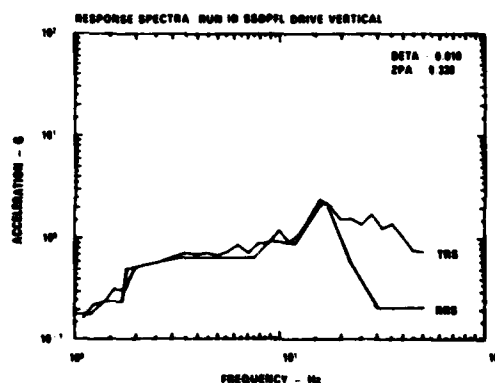
The initial shaping operation is accomplished totally with software resident in a Digital Equipment Corporation PDP 11/70 minicomputer which services various laboratory sites through a CAMAC (Computer Automated Measurement and Control) system. The CAMAC system provides electrical, logical, and mechanical standards for all interface hardware which are controlled through FORTRAN software handlers [6]. The PDP 11/70 operates under RSX-11M, a realtime operating system which will respond to event-driven interrupts from laboratory equipment.

With preliminary signal shaping completed the test item is mounted on the table and ex-

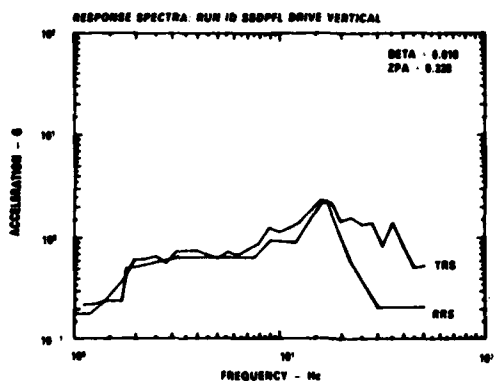
cited with the initial drive signals which may, at the option of the test engineer, be reduced to 1/2 or 1/4 level. In this manner the effects of table axis coupling and item table interaction can be determined without jeopardizing the safety of the test item. A schematic of the seismic simulator digital control process is given in Fig. 7. The digital drive signals are transferred initially to a 4-channel analog tape recorder via a set of digital to analog converters (DAC) housed in a CAMAC crate located in close proximity to the electrohydraulic shaker table. The tape drive is used mainly to preserve the drive signals for repeated runs and to minimize the amount of high priority run time required from the shared PDP 11/70 minicomputer system. During excitation of the test item analog to digital converters (ADC) are used to obtain digitized table response time histories from which the TRS's are generated. A comparison of the match between the TRS's and RRS's is made and appropriate adjustments to the drive signal a-weighting coefficients are made as in the preliminary shaping operation described above. The operation continues until the matching criteria associated with AMIN and AMAX are



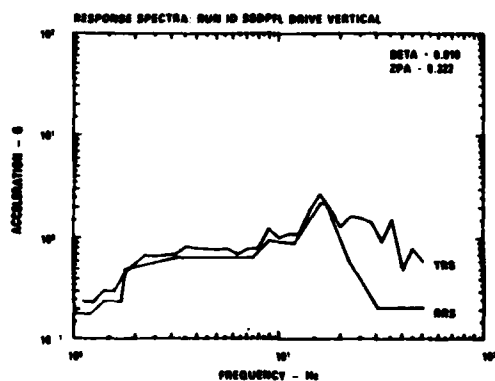
a) INITIAL EXPECTED RESPONSE



b) FIRST TABLE DRIVE



c) SECOND TABLE DRIVE



d) FOURTH TABLE DRIVE

Fig. 9 Typical vertical drive sequence

satisfied. Typically, at most four iterations are necessary to insure sufficient enveloping of the RRS's.

TYPICAL RESULTS

In Fig.'s 8 and 9 typical TRS to RRS matching sequences are given, as taken from a qualification test of a 2000 lb electrical equipment control cabinet. A picture of the cabinet on the seismic simulator is given in Fig. 10. Fig. 8 shows the horizontal drive sequence. The initial expected response from preliminary signal shaping is shown in Fig. 8a and, as can be seen, the expected TRS and RRS match is very close. In the first drive sequence the effects of the generation of higher harmonics in the table, coupling between the two axes, and cabinet high frequency rattling response appears. After three adjustments to the drive signal coefficients the final matching is given in Fig. 8d. For this particular test no drive energy beyond 15 Hz was input, however, due to higher harmonic generation by the mechanical table and

high frequency rattling response of the cabinet, the high frequency spectrum could not be as closely matched as the spectrum below 15 Hz. It should be noted that the TRS is computed at the center frequency of each 1/6-octave band from 1 to 50 Hz. Straight lines are drawn between each computed point which may give the impression that the TRS did not match the RRS at all points below 15 Hz. Close examination of the data will show that this is not the case. The vertical drive sequence corresponding to the horizontal sequence of Fig. 8 is given in Fig. 9. As can be seen by these data the generation of higher harmonic energy is not as pronounced as in the horizontal drive. Again the matching of the TRS to the RRS was accomplished within three iterations.

The time required for preliminary drive signal shaping is highly dependent on the response of the time shared computer system. Typically each axis requires approximately one hour of operator time. Final drive signal shaping during item excitation usually requires two to four hours depending on the scope of

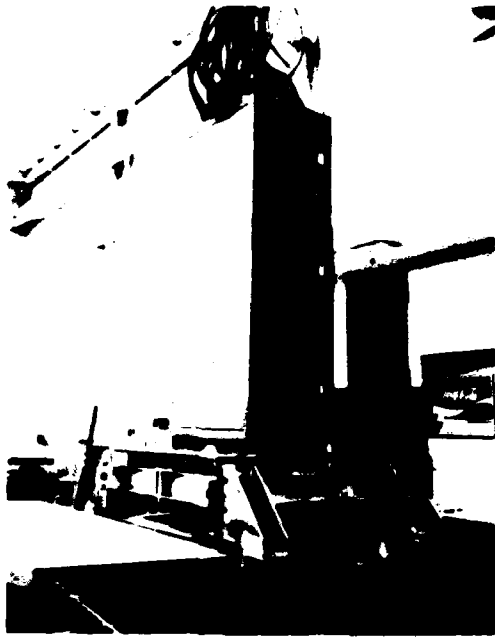


Fig. 10 - Seismic simulator and test specimen

additional signal monitoring required to insure item functionality during seismic excitation. Generally all item functions are monitored during shaping even though fractional input levels are used initially. In this manner, a measure of fragility may be obtained if item failure eventually occurs.

CONCLUSIONS

A digital based control system was developed for SwRI's biaxial seismic simulator with the objective to minimize component overtest and reduce drive signal shaping time. The digital control system, which directly adjusts the shaker input time histories based on the match of the resulting TRS to the RRS, has been in operation for approximately six months. During this time we have found that the objectives of the program were successfully accomplished. The 1/6-octave band drive signal resolution allows for closer matching of the TRS to the RRS than previously obtained with the analog control system thereby minimizing item overtest. Due to the computer automated procedures, signal shaping time was also greatly reduced.

REFERENCES

1. Design Response Spectra for Seismic Design of Nuclear Power Plants, U.S. Nuclear Regulatory Commission, Reg. Guide 1.60, December 1973.
2. J.D. Favour, J.M. LeBrun, and J.P. Young, "Transient Waveform Control of Electromagnetic Test Equipment," Shock and Vibration Bulletin No. 42, Part 2, pp 45-53, January 1972.
3. G.C. Kao, K.Y. Chang, and W.W. Holbrook, "Digital Control Technique for Seismic Simulation," Shock and Vibration Bulletin No. 43, Part 1, pp 109-118, June 1973.
4. N.F. Hunter, "Transient Waveform Reproduction on Hydraulic Actuators Using a Non-Linear Gain Estimation Technique," Proceedings of Environmental Sciences, pp 202-206, 1974.
5. R.S. Nichols, "Seismic Shock Waveform Reproduction and Shock Spectra Synthesis on Hydraulic Actuator," Shock and Vibration Bulletin No. 47, Part 1, pp 133-149, September 1977.
6. C. Weitzman, Distributed Micro/Minicomputer Systems, Prentice-Hall, Inc., pp 187-191, 1980.

GUNFIRE VIBRATION SIMULATION
ON A DIGITAL VIBRATION CONTROL SYSTEM

John Cies
Hewlett-Packard Company
Paramus, New Jersey

This paper describes a method of synthesizing a shaped pulse train required to simulate gunfire vibration. The pulse train yields the desired line spectrum resulting from machine gun firing vibration excitation on a typical military aircraft. The shaped line spectrum comes directly from the specification. The shape is determined by the location on the aircraft and the line spacing depends upon the firing rate of the gun. In addition to giving the line spectrum, some of the current specifications for this vibration environment detail how to set-up the test using analog equipment. However, this technique has some limitations as well as extraneous information when compared to the digital system approach. A comparison of the two methods will be included and the extraneous data of the specification will be discussed as it applies to the digital controller. It is also intended to compare the digital system method to actual recorded acceleration data taken from a test firing of one of these Gatling guns.

Present day digital systems have the ability to acquire field measured data and then duplicate this data on a vibration exciter. Having acquired the actual gunfire response, a comparison will also be made between the duplication of the actual response and the synthesized pulse train. Obviously, the best approach is to use the duplicated field data. However, field data may not be available for every equipment mounting location on every aircraft/Gatling gun type and configuration. When actual data is not available, the next best approach should be used; the synthesized pulse train. In any event, one point should become evident, that digital vibration control systems offer the power and flexibility to handle some of the more "exotic" vibration environments and with an accuracy not available from analog systems.

INTRODUCTION

Based upon the variety of acceptable methods of performing a gunfire vibration test, it does not take long to realize how formidable a problem specifying and performing such a test can be. Replication of the spectral content, particularly the fundamental firing rate and its harmonics as transmitted through the structure to the test package becomes the desired goal. However, it appears that very little data is available to adequately define the environment. As a result, there are presently four known test methods outlined in the military specifications.

1. Swept sine on random.
2. Multiple narrow band swept sine on random.

3. Shaped line spectrum (pulse train).
4. Swept pulse repetition rate shaped line spectrum.

As an alternate to 2, swept narrow band random on random has been used, but it is not known whether this is considered an acceptable alternative. These methods will be described briefly below. However, the focus here is to discuss one method, the shaped line spectrum, in detail, from two aspects: its implementation on a digital vibration control system, and how it compares to actual measured data from a test firing of a Gatling gun.

BACKGROUND

The actual operating environment during a Gatling gun firing is a quite complex combined vibration - pulsed excitation from the gun and structure borne noise from the engine which is considered random in nature. Swept sine on random approximates this combined excitation in a very limited sense in that a discrete component is superimposed over a shaped random spectrum. Two obvious limitations exist for this method:

1. Only one frequency combines with the random as opposed to having the fundamental firing rate and all its harmonics combined with the random at any given instant of time.
2. Sweeping a single frequency over the entire test frequency range results in unnecessary excitation at frequencies in between the firing rate and its harmonics.

The multiple swept narrow band sine on random is a closer approximation to gunfire, however, it only includes the fundamental and the first three harmonics. During the test, four narrow band sine sweeps are synchronously swept over a ten percent bandwidth with the background random excitation. Whether four bands is a limitation cannot be answered in a general sense since it depends on other factors. One definite limitation, however, is that it requires multiple sine controls in a complex interconnection to perform this test. The set-up time alone for this method could be prohibitive, not to mention the equipment cost.

A reasonable alternative to this method is to sweep narrow random bands rather than sine. A plot of the control signal will look identical to the swept narrow band sine on random even though the excitation in the narrow bands is random, not sine. One consideration for this method is that the sweep is discrete; i.e., the higher level random in the narrow bands occurs at discrete frequencies (multiples of Δf). Therefore, some frequencies in the narrow bands may not get excited. However, the advantage to this method is that only one digital control system is required.

The two remaining techniques constitute a significant departure from the rationale behind the previous methods. For the shaped line spectrum, the underlying assumption is that the gunfire excitation has a much greater amplitude or damage potential than the random and, therefore, the random portion can be neglected. This simplifies the test by making it a single excitation environment, but it does not make specifying it any easier. Performing this test with analog equipment can be rather complicated as well. This technique will be described in detail in the next section. The last method is identical to the above in approach, the difference being that the funda-

mental firing rate is swept over a narrow frequency band which in turn sweeps all the harmonics. This method is just a bit more complicated than the fixed pulse rate test since it requires a more sophisticated waveform synthesizer to sweep the pulse rate.

DISCUSSION

The specific gunfire vibration specification to be described herein is for the M-61 machine gun on the A-7 airplane which operates at 6,000 and 4,000 rounds per minute. The technique, however, is applicable to any type of periodic event for which the amplitude spectrum is known.

Before describing the digital system implementation for the shaped line spectrum gunfire, the specification method for doing gunfire vibration will be summarized. In short, it is written around an analog random control console which, upon first glance, can be very misleading, based on the digital approach. The first step is to equalize the spectral shape using a random noise generator (see Figure 1). However, since g pk versus frequency is the desired output, either some modification to the analog console output is required to multiply g^2/Hz by Δf and take the square root, or separate swept filter analysis equipment is required. After the desired shape is achieved, the random noise is replaced with a pulse generator box that will put out square waves of 350 microsecond duration and occur every 10 msec. When this pulse train is fed through the control console to the power amplifier/shaker, the gain is adjusted to get 17 grms. These numbers are for the 6,000 rpm (or 100 Hz pulse repetition rate) spectrum. The misleading part of this approach is the extraneous information put into the specification; this will be explained below. For anyone with experience in a vibration lab, this technique is closer to art than science. Granted it gets the intended test done with minimal additional equipment, but there are several limitations.

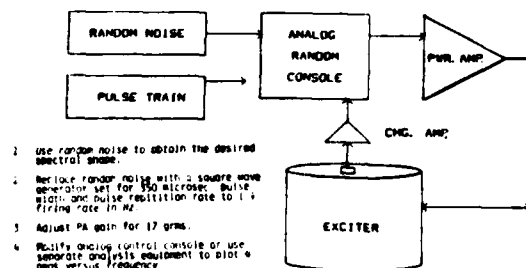


FIGURE 1
ANALOG SCHEME FOR GUNFIRE VIBRATION

1. This laborious set-up and equalization process must be done each time the test is performed.
2. Unless the control accelerometer is band-pass filtered before the rms meter read-out, adjusting the gain for 17 grms could result in an undertest in the defined frequency band.
3. With fixed frequency spacing and large filter bandwidth, the analog system may not achieve a line spectrum for slower gunfire rates because the condition where two spectral lines fall into one filter could be reached.
4. The specification requires the amplitudes between spectral lines must be 30dB down from the reference amplitude, yet this cannot be controlled adequately with the wide spacing of analog filters, and separate analysis with a finer resolution is needed to verify this criteria.

Now for the digital approach. To start, it should be mentioned that taking the specification detailed above to the letter, the digital scheme could be very difficult to sell to the quality control inspector since no pulse generator and no 17 grms tuning are required. The only information required to meet the intent of the specification is the line spectrum (g peak versus frequency). If the phase of the line components is also known, then the desired time domain waveform is totally and uniquely determined. The pulse width and pulse repetition rate are extraneous. The pulse width is required to ensure that the square wave is narrow enough to "ring" the highest frequency filter in the analog console. But, the filters in the digital fast fourier transform (FFT) do not need to be excited. The pulse repetition rate is redundant since it is implicitly specified in the frequency spacing of the line spectrum, i.e., a spectrum with amplitudes spaced every 100 Hz will give a pulse repetition rate of 1/100 Hz or every 10 msec. Therefore, since the desired line spectrum can be synthesized in a digital system and fourier transformed to the time domain, the other information, pulse width, pulse repetition rate and grms are no longer required. The process in the digital system then is to create the desired line spectrum, fourier transform it to the time domain and then use the transient vibration control (TVC) software to control the shaker to the resulting repetitive pulse train. By maintaining control of the exciter to this acceleration waveform, the desired line spectrum is achieved.

It should be pointed out here that the digital system offers some significant advantages:

1. Many more filters in the control and analysis; for the 100 Hz line spectrum the FFT spacing is 5 Hz or 20 "filters" between spectral components.
2. The phase is specifiable and preserved.
3. The set-up process of creating the line spectrum, tailoring the waveform, etc., is done only once because when the desired spectrum is achieved, the test set-up is saved in the digital control system and can be run within minutes after being recalled from the system storage area.
4. The discrete fast fourier transform utilized in the digital system is an exact fit for the discrete line spectrum of the gunfire vibration. The only consideration is the finite portion, or where the fourier series expansion gets truncated. See Appendix A for a mathematical description and Appendix B for a general description of putting the line spectrum into the system.
5. The gunfire pulse train can be generated at one location and passed on to other test facilities by transferring discs with the gunfire set-ups already saved. This could serve to standardize the test and make it repeatable whenever the test is performed.

Some additional considerations regarding the digital approach should also be mentioned.

1. The line spectrum can only be specified at multiples of Δf , in this case 5 Hz. Other choices allowed by TVC are 20, 10, 2, 1, 0.5 and 0.2 Hz. The trade-off for using the other resolution choices becomes the maximum frequency tested to which is $512 \text{ lines} * \Delta f$.
2. TVC only allows one control channel so this method cannot be used for multiple control points.
3. The pulse train cannot be superimposed on background random vibration.

Neither of the above are considered limitations. Gunfire vibration testing is typically performed on black boxes which do not generally require average control from multiple accelerometers. Also varying resolution data blocks may be possible using external sampling techniques to acquire data to pass to TVC. Future work will include trying to use external sampling techniques for gunfire vibration.

Lastly, the test specifications for this type of test do not require superimposing random

vibration on the pulse train so it too does not appear to be a limitation. The real problem in trying to superimpose the two is how to then separate them so that the line spectrum and the random can be controlled separately.

To get a feel for how good the digital system handles the gunfire vibration, source data from a C-150 exciter are included. Figure 2 is the desired line spectrum for the 100 Hz rate. The overall shape is $+3\text{dB/oct}$ to 200 Hz flat to 400 Hz and -3dB/oct to 2 kHz. Each component was given a phase shift of 45° from the previous one. This phase shift was arbitrarily chosen to give a reasonably symmetric pulse shape and to center the pulse train in the data block. The only other case tried was all line components with a zero phase shift. Future work will investigate the effects of varying the phase shift between components.

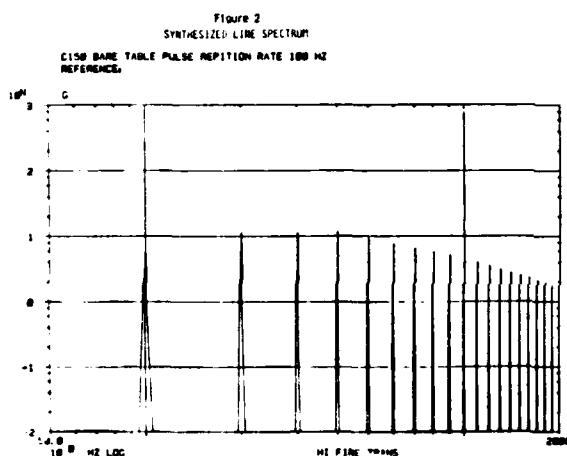
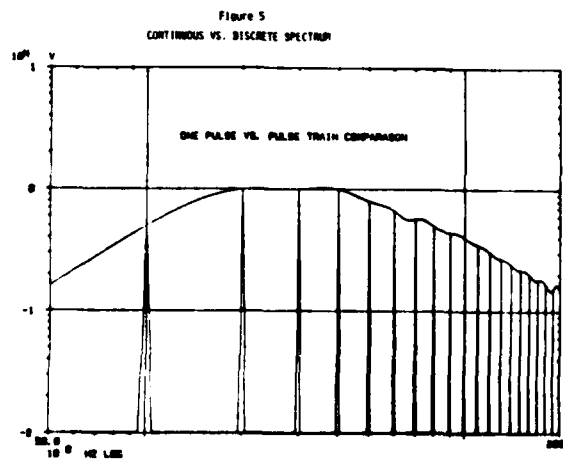
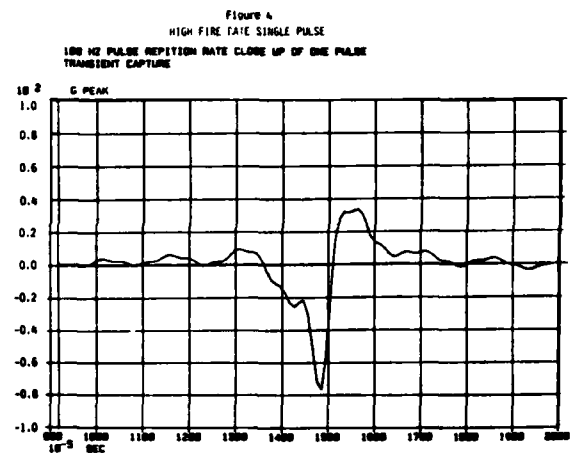
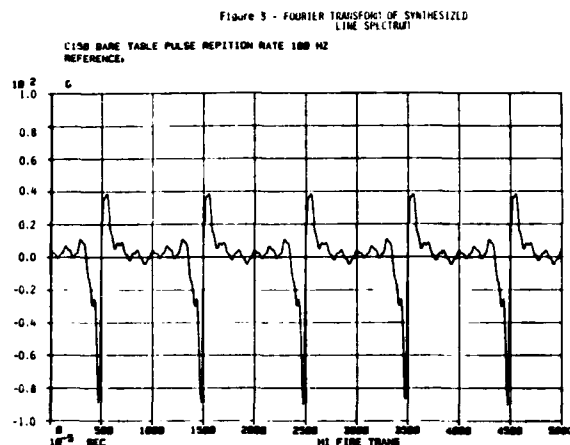
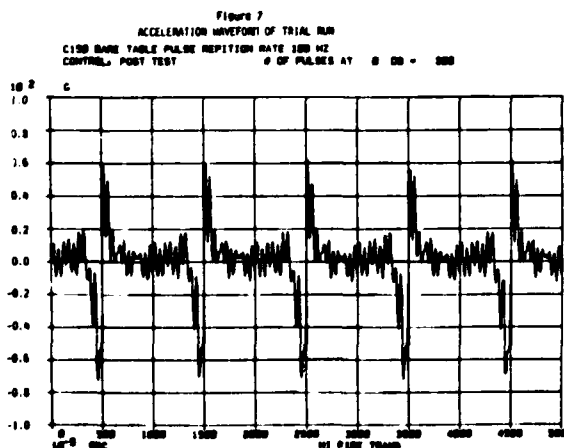
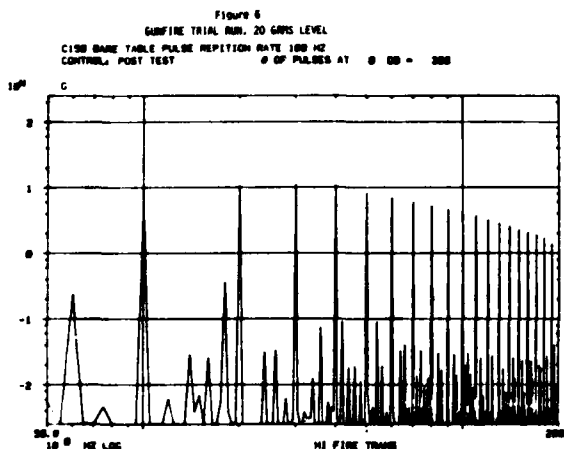


Figure 3 is the fourier transform of the reference spectrum in Figure 2. This is the actual reference waveform used by the transient vibration control software (TVC) to control the exciter. A detail of one pulse is shown in Figure 4. The key to this approach is that the spectral shape mentioned above plus the relative phase uniquely determine the pulse shape in the time domain and by repeating this pulse every 10 msec gives the line spectrum with a spacing of 100 Hz while maintaining the same overall shape. This is verified by the comparison of one pulse versus the pulse train in Figure 5. Notice that even though the continuous spectrum of the single pulse shows some waviness, the amplitudes of both spectra match at the multiples of 100 Hz. The waviness is most likely due to the fact that fourier series expansion for this pulse train only goes to 2 kHz. For the purist, the proper continuous spectrum could be synthesized FFT'd to get a single pulse and then build a pulse train with these pulses spaced every 10 msec. However, with tolerances of $\pm 1.5\text{dB}$ to 1 kHz and $\pm 3\text{dB}$ 1 to 2 kHz the pulse train as created is well within the requirement.



The actual measured spectrum from the control accelerometer is shown in Figure 6. Note that if the 60 and 180 Hz ground loop spikes are excluded, the amplitude between components is greater than 40dB down from the reference amplitude (20dB/decade) or less than 0.1g at the 10g pk area of the spectrum. Figure 7 is the actual time waveform on the shaker head (the FFT of Figure 6). In the ideal case, this pulse train should match exactly the reference pulse train in Figure 3 since the intent is to control the shaker to this acceleration time history. However, the negative peaks are less than the reference and the positive peaks are greater than the reference. It appears, therefore, that the dynamic response of the shaker/amplifier wants to make the peaks equal in magnitude; i.e., make the waveform symmetric. Whether this is due to the low pass filter effect (frequency roll-off) of the shaker system preventing it from tracking the sharp rise and fall of the negative peak or some other limitation in the shaker system is not known. The ground loop noise shows up as well in Figure 7 as the larger oscillations between peaks of the pulse train. Even though some variations in the actual and reference pulse trains appear, the basic shape of each pulse is maintained which keeps the spectral shape well within tolerance.



To summarize, the technique has been more than adequately demonstrated bare table to meet the intent of the specification. Any variation with the test item mounted has to be treated as a fixture/test item dynamics problem and treated accordingly. The actual set-up time for both the 6,000 and 4,000 rpm spectra took approximately four hours from system turn on to running the shaker, after the extraneous information was weeded out.

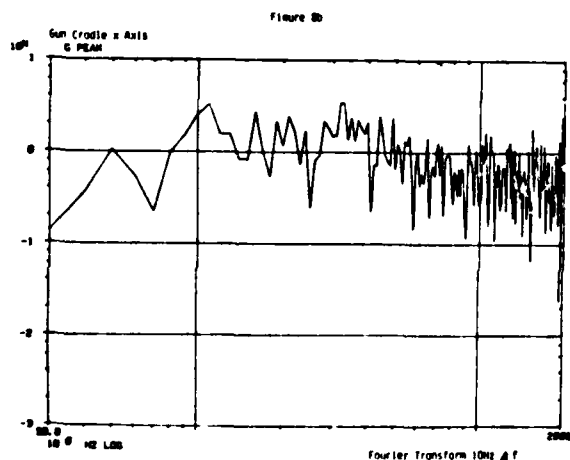
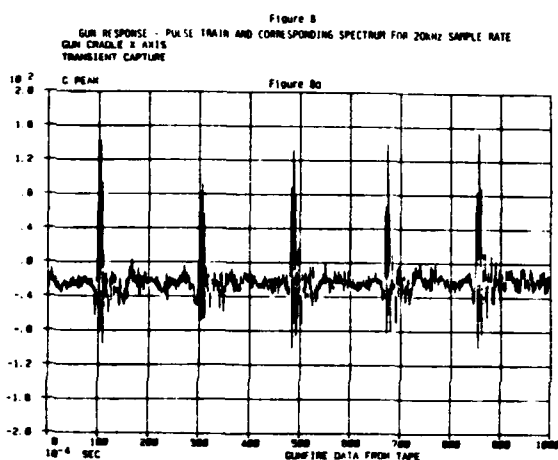
As a final check on the digital gunfire technique, the rms level was computed and found to be 17.0 grms for the reference line spectrum. This should be no surprise since the rms level is just the square root of the sum of the squared values of the rms at each discrete frequency. The actual measured level on the C-150 bare table was 20 grms which also makes sense since this includes the energy in between the line components as shown in Figure 6. This last comparison gives further evidence that the only pertinent information necessary to specify this test is the line spectrum for the digital system approach.

RECORDED GUNFIRE DATA

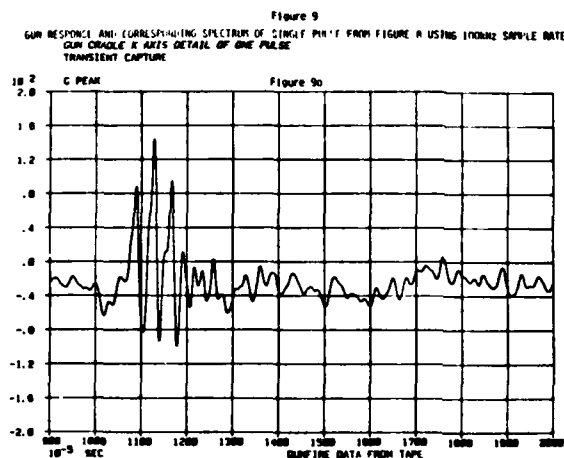
For comparison to the synthesized line spectrum method, acceleration data is included from a test firing of the same gun/plane configuration; the synthesized spectrum represents. The gun was mounted on the airplane using isolators. Data was taken in three directions on the gun cradle and on the isolated side of the mounting structure. Unfortunately, the organization that has allowed me to look at this taped data has requested that I divulge nothing of its source, nor identify the organization. Therefore, there are no figures of the gun mounting configuration, consequently, further description of the test set-up is just not available.

In any event, some insights can be gained from the data that is available. The data presented is for the gunfire only, i.e., no engine or other random excitation, but at a slower firing rate (~ 55 Hz). To start, the acceleration time history (Figure 8a) shows a complex pulse where the peak of each pulse varies, the repetition rate varies and each pulse has several cycles of high acceleration just as expected from a pyrotechnic event. Notice the zero offset of the time response, this is a characteristic of piezoelectric accelerometers and makes integration to get velocity and displacement impossible. The frequency content of the pulse train (Figure 8b) does show peaks at the firing rate and harmonics, but the amplitudes between components is significant, particularly at the higher frequencies. This is due primarily to the fluctuation of the firing rate. Table I summarizes the range of time domain peaks. These values occur simultaneously in all three directions. Figure 9 shows more detail of one pulse for the X cradle response.

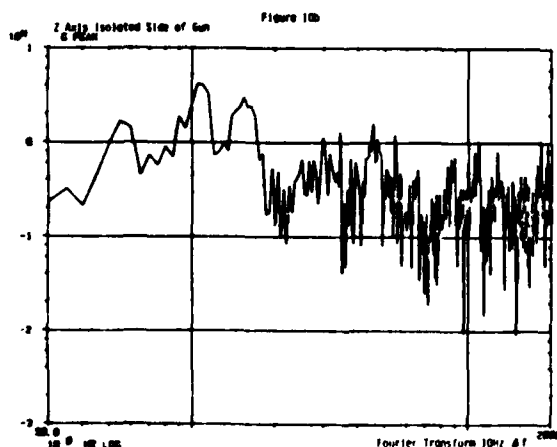
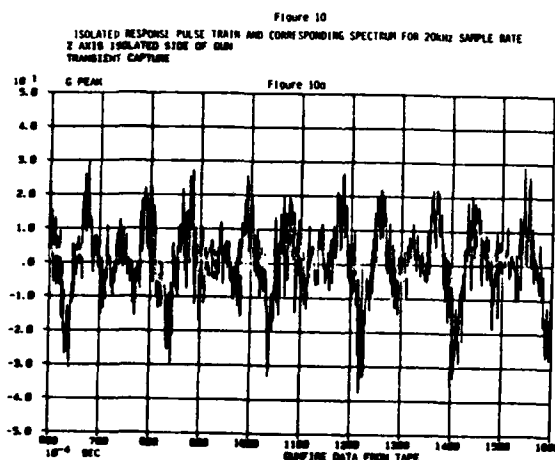
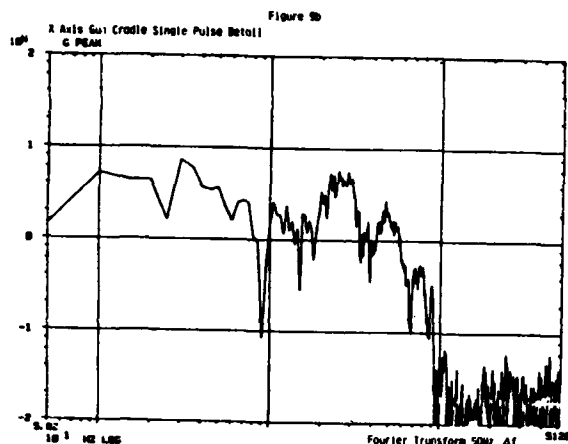
Table 1	
Response Location	Measured Acceleration
X cradle	90 to 145 g peak
Y cradle	150 to 165 g peak
Z cradle	120 to 165 g peak
X isolated	15 to 28 g peak
Y isolated	15 to 35 g peak
Z isolated	15 to 38 g peak



The significant point from this figure is that the response goes to 10 kHz (could possibly be higher since the roll-off could be the tape recorder's maximum frequency). It was not expected to see any response above 5 kHz, consequently the data shown in Figures 8, 9 and 10 have a high probability of being aliased. The amplitude information of the frequency plots, therefore, will be lower than the actual value. Aliasing will also cause the spectrum to deviate from a line spectrum as will the repetition rate variation found in the data. However, to determine how much deviation each causes is not possible from the data as acquired. The frequency content above 10 kHz is most likely the background noise level of the tape recorder; $10\text{mV/g} \times .06\text{g} = .6\text{mV}$. The data was gathered during one afternoon and analyzed at a later date and different location so that access to the data for reanalysis was not possible prior to publication. Figure 10 shows the isolated response on the aircraft. The frequency response below 200 Hz is similar to the cradle response indicating the natural frequency of the isolator is near this frequency. As a general comparison, the grms levels of the taped data are close to the synthesized spectrum on the gun cradle, however, since aliasing is expected, actual values should be even closer to the synthesized value.



To summarize, some light was hopefully shed on performing gunfire vibration and how digital vibration control systems can make this test easier to specify and run with a greater accuracy than analog systems. In closing, I would like to mention that the swept pulse repetition rate gunfire is also possible on the digital vibration control system. However, the technique was not developed in time for publication. A paper is planned describing the details at a later date.



It was intended as part of this effort to duplicate the actual measured gunfire acceleration pulse train on a shaker using the TVC software. However, due to the limitations in the data, the zero offset mentioned above and possibly the aliasing problem as well, duplication of the recorded time waveforms was not possible even at levels much lower than the actual measured peaks. For the next opportunity at measuring gunfire response, the organization that permitted access to this data plans to use piezo-resistive accelerometers which will eliminate the zero offset phenomenon and hopefully allow duplication of the field measured time histories on a shaker head.

REFERENCES

1. Hewlett-Packard 5427 Operating Manual.
2. Fourier Analyzer Training Manual, Application Note 140-0.

APPENDIX A

FOURIER SERIES REVISITED

When computer based FFT analyzers were first introduced, the term DFFT was the buzz word. Many folks thought it represented digital fast fourier transform since it involved a computer when it actually meant discrete fast fourier transform. This term was used specifically to emphasize that the spectrums given by this type of analyzer are discrete, i.e., the only valid data is at the computed frequencies and, therefore, not sure what happens in between.

When plotting then, these DFFT analyzers just "connect the dots" to give the appearance of a continuous spectrum. The discrete nature of these analyzers comes directly from fourier theory. To achieve a continuous spectrum, the fourier integral must be computed from:

$$F(\omega) = \frac{1}{2\pi} \int_{-\infty}^{\infty} f(t)e^{-j\omega t} dt$$

In other words $f(t)$ must be observed (or measured) for all time. The resulting spectrum would have infinitesimal resolution, but who has all this available time? Being pragmatic, the measurement is made for a finite time which gives a finite resolution, e.g., a 0.2 sec measurement or block of data will result in a resolution of 1/.2 or 5 Hz. Measuring for a finite time gives an approximation to the spectral content which is called the fourier series. The pulse train then for the desired line spectrum can be computed by writing the fourier series using the data in the desired line spectrum:

$$x(t) = \sum_{n=1}^{20} A_{100n} \sin(2\pi n 100t + \phi_n)$$

Where $A_{100n} = 5g$; $A_{200n} = 10g$; . . . from Figure 2.

Summing terms to 2000 Hz, the desired maximum frequency. The frequency and amplitude are given in the specification, the phase can be arbitrarily chosen. When the desired line spectrum is entered into the analyzer and Fourier transformed to the time domain, the result is $x(t)$ which is used as the reference waveform to run the shaker. Thus a perfect match, a discrete frequency analyzer for testing to a discrete spectrum.

APPENDIX B

The basic process for the digital method is as follows:

1. Synthesize the desired line spectrum.
2. Fourier transform to the time domain.
3. Center the pulse train in the data block so that beginning and end of the time record are as close to zero as possible.
4. Save this data block in a disc record.
5. Load transient vibration control (TVC) software and specify input as saved disc record from step 4.
6. TVC asks peak g's for time record -- guess for first time.
7. For continuous output answer 1/time record to number transients per second, i.e., for 100 Hz prr, the data block time record = .200 sec, therefore, the number of transients per second = 5.
8. TVC asks number pulses, but test requires total time, so answer for TVC is:

$$\text{Number pulses} = \frac{\text{Total time}}{.2 \text{ sec/pulse}}$$
9. Run test either bare table or system by itself.
10. Compare measured spectrum with desired and edit peak g's from (6) by proper ratio, recheck; if okay, save the set-up. Now, you are ready to run gunfire at any time with just minutes of control console set-up time.

NOTE: The large calculated terminal displacement can be ignored since this time domain data block will be output continuously. It is the opinion of the author that the detailed step by step procedure to run the gunfire should not be a part of this paper. However, anyone interested in performing gunfire vibration on the 5427A or the 5451C Option 350 should contact their local Hewlett-Packard field office.

DISCUSSION

Mr. Zurnaciyan (Northrop Electronics): Is gunfire vibration a forcing function in the time domain or in the frequency domain, or is there a random forcing function?

Mr. Cies: Your output is a time domain signal, an acceleration waveform versus time. That is your specification, and that is what the digital system controls to.

Mr. Zurnaciyan: How would you represent it analytically?

Mr. Cies: It is just the sum of a Fourier series, except you don't have the phase. You may have the five sine wt plus ten sine wt out to however many terms you want to carry it. I only carried it to 20 terms.

Mr. Caustin (GENRAD): Was the spectrum swept in these tests?

Mr. Cies: No. In that particular case, it was not, but it can be. Recently, I found out how to sweep the gunfire, and I hope to do that. Yes, it is possible.

Mr. Smallwood (Sandia National Laboratories): I noticed that you blamed the smearing of the spectrum with the high frequencies primarily on aliasing. How much of it was caused by the jitter and the pulse repetition rate?

Mr. Cies: You can't tell until you get data that are not aliased; that would be the best comparison. There is one other limitation I forgot to mention. My ultimate goal was to get the gunfire tape data and run that on the shaker, but I couldn't because it was aliased, and also, because the piezo-electric accelerometers had an apparent DC off-set. I don't know whether they saturated. I don't know the exact phenomena, but it doesn't allow you to get a good velocity or displacement by integrating the acceleration waveform. Hopefully, the test will be repeated with piezo-resistive accelerometers, and with that kind of data, it should be possible to take the tape data and run it on the shaker.

MEASUREMENT OF ALL COMPONENTS OF STRAIN
BY A 3-D FIBER OPTIC STRAIN GAGE

S. Edelman and C. M. Davis, Jr.
Dynamic Systems, Inc.
McLean, Virginia

This paper describes an instrument which has been designed, but not yet built. A three-dimensional strain gage imbedded in the earth furnishes a complete description of the motions in the neighborhood of the gage. Fiber optic interferometers measure the three axial strains and the three shear strains at a point in terms of half-wavelengths of the laser light used. Arrays of such gages are suitable for geophysical exploration, earthquake studies, and studies of the effect of mechanical shocks on structures. The gage is sufficiently sensitive to monitor the motion of tectonic plates.

INTRODUCTION

A three-dimensional strain gage imbedded in a matrix furnishes a complete description of the motions in the neighborhood of the gage. In this paper we present the mathematical basis and a basic arrangement of a fiber optic three-dimensional strain gage.

Fiber optic sensors currently being developed for a variety of applications (acoustics, magnetics, temperature, pressure, strain, acceleration etc.) promise increased sensitivity, geometric flexibility, EMI/EMP immunity, and decreased cost compared to conventional sensors. The transduction mechanisms employed result in either phase or intensity changes in the light propagating in the core of the optical fiber. The greatest sensitivity is realized for those devices which rely on phase changes.^{1,2,3} The usual matrix will be earth. Obvious applications are:

- geophysical exploration
- earthquake studies
- the effect of explosions and other mechanical shocks on structures

The gage provides the three axial components of strain with more sensitivity and with less trouble and expense than the use of three seismometers. The three shear components are provided simultaneously. Previously, this information about the motion of the earth was not available directly. The outputs can be monitored continuously so that both oscillatory and permanent deformations can be measured.

The technique used to measure the strain allows determination of the time involved. From these data, the rate of change of strain, velocity, and acceleration or force per unit mass can be found easily. Arrays of such instruments can depict the details of the movements of whatever volume of earth is required in a particular investigation. For example, the speed of motion of tectonic plates is given as of the order of one centimeter per year. This is about 3.2×10^{-4} micrometer per second or, for a helium-neon laser using light of the wavelength of 0.6328 micrometers, this is 3.2×10^{-3} radians per second. Phase shifts as small as 10^{-5} radians have been measured at 10Hz using a phase-locked loop technique. Strains corresponding to the motion of tectonic plates could be followed in detail by a strain gage of the kind described here either by using a phase-locked loop technique or by counting several fringes over intervals of about an hour.

In the case of one plate moving parallel to its interface with another, but pinned at the interface, an array of these gages could determine the distortions being developed in all three dimensions and allow an estimate of the strain-energy that would be expended by release of the pinning. Thus, earthquake prediction could be based on much more information than is available now.

DESCRIPTION

The gage consists of six linear strain gages, each forming one edge of a distorted tetrahedron. See Figure 1. The distorted

tetrahedron is formed by a plane cutting off equal distances along the axes from one vertex of a cube. Each linear strain gage consists of an active fiber and a reference fiber-pair within a common sheath. See Figure 2. The sheath consists of two telescoping cylinders with knobbed and roughened projections to couple intimately with the matrix. The active fiber is attached to both parts of the sheath so that the fiber extends and retracts with the motion of the sheath. The projections of the sheath, in turn, follow the motion of the matrix in which they are imbedded.

One fiber of the reference pair is nominally the same length as the active fiber. Departure from exact equality is treated below. The length of the two fibers making up the reference pair differ by a small amount, ideally one-eighth of the wavelength of the light used.

The light from the active fiber is combined with the light from each of the reference fibers to form two interferometers, each of which measures the strain in the active fiber. The count of one interferometer either leads or lags the count of the other depending on the direction of motion of the active fiber. The change from lead to lag or vice versa is used to control the counting that provides a measure of the strain in each direction.^{5,6} Recording of the motion can be done automatically by counters or by a microprocessor using well-known techniques.

Each fiber enters the sheath through the cap of one cylinder, is wrapped several times around a reel consisting of a thin-walled piezoelectric cylinder with a low-friction surface, and then leaves the sheath through another point in the same cylinder cap. All fibers are cemented to the cylinder cap at entrance and exit. Outside the sheath, all of the fibers and the electric leads to the piezoelectric cylinders are fastened together in a bundle for mutual support and so that any strains or temperature changes affect all fibers equally. The reel for the active fiber is fastened to the portion of the telescoping sheath opposite to the entrance and exit cap while the reels for the reference fibers are fastened to the portion of the telescoping sheath that bears the entrance and exit cap. Thus, the active fiber shares the extension and retraction of the sheath, but the reference fibers do not. All of the reels are at least one centimeter in radius since sharper bends cause deterioration of the fiber and loss of light. The knobbed and roughened projections anchor the piezoelectric cylinders and the cap by which the fibers enter the sheath to the matrix.

DETAILS AND CONSTRAINTS

It is expected that the best way to imbed a gage in the field will be worked out in practice. However, we go through the mental

exercise of planting a gage to show how two of the inherent constraints can be handled. If the data from the gage are to be useful, it is necessary to know the orientation of the three axes accurately. We assume that for a particular investigation, a gage is to be placed at a given depth in the ground. A hole of suitable diameter to the proper depth is dug with a posthole digger or earth auger and the bottom leveled. A thin layer of liquid mud allowed to dry without disturbance will provide a flat level floor. The gage, attached by releasable bonds to a thin tubular framework as shown in Figure 3, is properly oriented and lowered to the bottom of the hole while the floor is still tacky. The hole is then backfilled carefully, one thin layer of liquid mud at a time, to minimize settling and disturbance of the position of the gage. After the hole is filled, the positions of the vertical pipes indicate the positions of the corners, O, A, B, C and thus the orientation of the axes. As the pipes are hollow, a borescope can show if they have been bent or twisted during the backfilling. After checking the orientation and the pipes, the gage can be released from the frame.

Another part of the same process occurs because each linear gage must be able to measure displacements that either increase or decrease its length. To allow displacement in either direction, each linear gage is extended a little more than 0.5% of its length before being fastened to the frame for insertion. The total allowable extension of the fiber is 1% of its length. When the gage is released from the frame, the knobs imbedded in the earth tend to hold each linear gage in the extended position. Any partial recovery is monitored by recording changes in the interferometer fringes so that the equilibrium length of the active fiber in position is known.

Fiber optic interferometers are preferable to other kinds of strain gage for the studies contemplated here because their greater sensitivity allows the gages to be smaller and thus, they more closely represent the motion at a point. If a given application entails displacements which might exceed the 1% limit, the effective length of the active fiber can be increased greatly by controlling the length of a portion of the fiber using an electrical signal to change the circumference of the piezoelectric reel in the sheath. This does not obviate the advantage mentioned above since the distance between ends of each linear gage is not changed.

There are a number of ways to use different kinds of piezoelectric motion generators to provide a reservoir of optical fiber. We will consider only a length of fiber wound around the outer surface of a thin-walled piezoelectric cylinder as described above. It has been shown that the change in the circumference of such a cylinder is a precise func-

tion of the voltage applied to the cylinder. Here we assume that a microprocessor has been counting interference fringe passages in both directions as well as keeping a record of the voltage applied to the piezoelectric cylinder so that the current length of the active fiber is always known. If the length of fiber approaches either allowable limit, the microprocessor applies a voltage to the piezoelectric cylinder to reel fiber in or out, as needed, to maintain the tension in the fiber or to prevent the extension from exceeding the limit, respectively. The record of the voltage applied to the piezoelectric cylinder together with the counts of interference fringe passages in each direction furnish the data needed to calculate the current length of the fiber.

Any drift due to temperature can occur only from temperature changes which affect the active fiber and the reference fibers differently. Since all three fibers are enclosed in the cylinder buried in the matrix, in most cases all will experience the same temperature. In unusual cases in which a temperature gradient will occur inside the cylinder, fiber-optic temperature sensors can be used to change the circumference of the piezoelectric reels to compensate.

CALCULATIONS

The phase shift, ϕ , of an optical beam of wave number k , which occurs when the beam propagates through an optical fiber of length L and refractive index n is

$$\phi = knL \quad (1)$$

where the change $\Delta\phi$ is given by

$$\Delta\phi = knL \left(S_{11} + \frac{\Delta n}{n} \right) \quad (2)$$

and $S_{11} = \Delta L/L$ is the axial strain and

$$\frac{\Delta n}{n} = -\frac{n^2}{2} \left[(P_{11} + P_{12}) S_{\perp} + P_{12} S_{11} \right] \quad (3)$$

P_{11} and P_{12} are the Pockels coefficients, S_{\perp} is the strain perpendicular to the axis. For constant volume $S_{\perp} = -1/2 S_{11}$. Substituting $P_{12} = .12$, $P_{11} = .27$ and $n = 1.46$ into Eq. (3) we obtain $\Delta n/n = -0.085 S_{11}$ and Eq. (2) becomes

$$\Delta\phi = 0.92knLS_{11} \quad (4)$$

Optical phase shifts are readily measured by means of an optical interferometer such as the Mach Zehnder configuration shown in Figure 4. Light from a single-mode laser is introduced into a single-mode fiber and divided by a 3 dB coupler⁸ into the arms of the interferometer. The sensor arm is subjected to the strain while the reference arm remains unstrained. The resultant optical phase shift is

converted to an intensity variation by the second 3 dB coupler. Using a homodyne detection scheme in a phase locked loop configuration, phase shifts as small as 10^{-5} radians have been measured at 10 Hz.⁴ For a HeNe laser source, this corresponds to measuring length changes of 10^{-12} m (or 10 Å).

Consider the electric fields E_s and E_r corresponding to light of angular frequency ω in the sensor and reference arms of the interferometer

$$E_s = Ae^{-i(\omega t + \phi)}, E_r = Be^{-i(\omega t)} \quad (5)$$

respectively. The intensity at the output of a 3 dB coupler is given by

$$P = (E_s + E_r)(E_s^* + E_r^*) = A^2 + B^2 + 2AB \cos\phi,$$

Large phase shifts can be determined by simply counting axis crossing and multiplying by π .

The measured strain in the linear gage OA is

$$S_{OA} = \frac{\left[(dx + \frac{\delta u}{\delta x} dx)^2 + (\frac{\delta v}{\delta x} dx)^2 + (\frac{\delta w}{\delta x} dx)^2 \right]^{1/2} - dx}{dx} \quad (7)$$

Terms in which the differentials appear to the second power or higher can be neglected in comparison with differentials to the first power. Accordingly:

$$S_{OA} = \left(1 + 2 \frac{\delta u}{\delta x} \right)^{1/2} - 1 = \frac{\delta u}{\delta x} \quad (8)$$

= ϵ_{xx} , the strain along the x axis

By cyclic permutation:

$$S_{OB} = \epsilon_{yy} \quad (9)$$

$$S_{OC} = \epsilon_{zz} \quad (10)$$

Similarly, the measured strain in the linear gage AB is:

$$S_{AB} = \frac{\left[(dx + \frac{\delta u}{\delta x} dx - \frac{\delta u}{\delta y} dy)^2 + (dy + \frac{\delta v}{\delta y} dy - \frac{\delta v}{\delta x} dx)^2 + (\frac{\delta w}{\delta x} dx - \frac{\delta w}{\delta y} dy)^2 \right]^{1/2} - 1}{AB}$$

$$= \frac{\delta u}{\delta x} \frac{dx^2}{dx^2 + dy^2} + \frac{\delta v}{\delta y} \frac{dy^2}{dx^2 + dy^2} - \left(\frac{\delta u}{\delta y} + \frac{\delta v}{\delta x} \right) \frac{dxdy}{dx^2 + dy^2}$$

since $dx=dy=dz$

$$= \frac{1}{2} \frac{\delta u}{\delta x} + \frac{1}{2} \frac{\delta v}{\delta y} - \frac{1}{2} \left(\frac{\delta u}{\delta y} + \frac{\delta v}{\delta x} \right) \quad (11)$$

$$2S_{AB} = \epsilon_{xx} + \epsilon_{yy} - \epsilon_{xy} \\ \epsilon_{xy} = 2S_{AB} - S_{OA} - S_{OB} \quad (12)$$

by cyclic permutation

$$\epsilon_{zy} = 2S_{BC} - S_{OB} - S_{OC} \quad (13)$$

$$\epsilon_{zx} = 2S_{CA} - S_{OC} - S_{OA} \quad (14)$$

If dx, dy, dz are not exactly equal and if the discrepancies are no more than 1% or so, they do not introduce any serious error. If $dy = dx + e$, then from Eq. (11):

$$\begin{aligned} S_{AB} &= \frac{\delta u}{\delta x} \frac{dx^2}{2(dx^2 + edx)} + \frac{\delta v}{\delta y} \frac{dx^2 + 2e_1 dx}{2(dx^2 + edx)} - \left(\frac{\delta u}{\delta y} + \frac{\delta v}{\delta x} \right) \frac{dx^2 + edx}{2(dx^2 + edx)} \\ &= \frac{1}{2} \frac{\delta u}{\delta x} - \frac{1}{2} \frac{e}{dx+e} \frac{\delta u}{\delta x} + \frac{1}{2} \frac{\delta v}{\delta y} + \frac{1}{2} \frac{e}{dx+e} \frac{\delta v}{\delta y} - \frac{1}{2} \left(\frac{\delta u}{\delta y} + \frac{\delta v}{\delta x} \right) \\ &= \frac{1}{2} \epsilon_{xx} + \frac{1}{2} \epsilon_{yy} - \frac{1}{2} \epsilon_{xy} - \frac{1}{2} \frac{e}{dx+e} \left(\frac{\delta u}{\delta x} - \frac{\delta v}{\delta y} \right) \quad (15) \end{aligned}$$

and it can be seen that the error is of the second order of small quantities.

Our assumption that one of the reference-pair fibers is the same length as the active fiber is also subject to uncertainty. From Eq. (6), the intensity of the combined light is: $A_2 + B_2 + 2AB \cos \phi$. The interference pattern of light and dark fringes is formed as ϕ changes and it can be seen that the greatest contrast between light and dark will occur if $A = B$. Thus, for best sensitivity, the light from the laser should be divided equally between the two fibers and they should be about the same length so that the loss with distance will be about the same. However, for modern low-loss fibers a small discrepancy in length will not cause any serious loss of contrast.

APPLICATIONS

Arrays of these gages could be used to provide information about the details of the deformations of dams, buildings, and other structures, both in response to sudden impulses and over long periods. The creep of masses of earth and of glaciers could be followed.

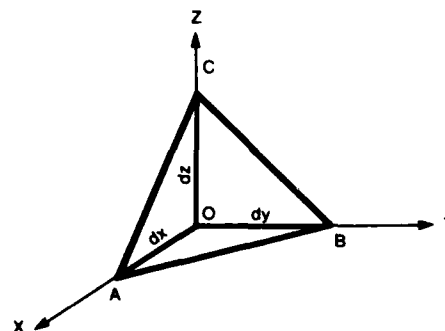
Since each gage provides information about the particle motion at a point, a sufficiently large, closely-spaced array could distinguish between waves of dilatation, distortion, Rayleigh and Love waves if the integrated motion is not too confused.

Similarly, arrays of these gages could be used to furnish the raw data from which the motions of the earth in response to different patterns of explosions could be deduced. This

information could be used to show how stresses are propagated through the earth and exerted on structures.

REFERENCES

1. T. Giallorenzi, Optics and Laser Technology, p. 73 April 1981
2. J. Cole and J. Bucaro, J. Acoust. Soc. Am, **67**, 2108 (1980)
3. A. Dandridge, A. Tveten, G. Sigel, E. West, and T. Giallorenzi, Electron. Lett., **16**, 408 (1980)
4. D. Jackson, A. Dandridge and S. Sheem, Opt. Lett., **5**, 139 (1980)
5. U. S. Patent 2,604,004 granted to Elihu Root, III, July 22, 1952
6. H. D. Cook and L. A. Marzetta, J. Res. Natl. Bur. Stds, **65C2**, 129 (1961)
7. J. Nye, Physical Properties of Crystals, 249 (Oxford, 1978)
8. C. Villarruel and R. Mueller, Electron. Lett., **17**, 243 (1981)



Point	Original Position			Displaced Position		
O	0	0	0	u	v	w
A	dx	0	0	$dx + u + \frac{\delta u}{\delta x} dx$	$v + \frac{\delta v}{\delta x} dx$	$w + \frac{\delta w}{\delta x} dx$
B	0	dy	0	$u + \frac{\delta u}{\delta y} dy$	$dy + v + \frac{\delta v}{\delta y} dy$	$w + \frac{\delta w}{\delta y} dy$
C	0	0	dz	$u + \frac{\delta u}{\delta z} dz$	$v + \frac{\delta v}{\delta z} dz$	$dz + w + \frac{\delta w}{\delta z} dz$

Figure 1
Gage Geometry

Six linear gages are positioned along the edges of the cube corner defined by points O, A, B, C. The original and displaced positions of these points are given in the table.

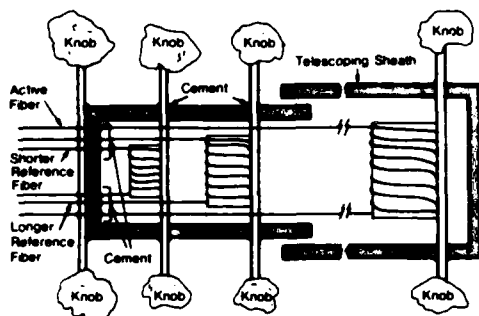


Figure 2
Typical Linear Gage

Knobbed telescoping sheath imbedded in a matrix contains an active fiber which extends and contracts with the sheath and two reference fibers of different length whose lengths are fixed.

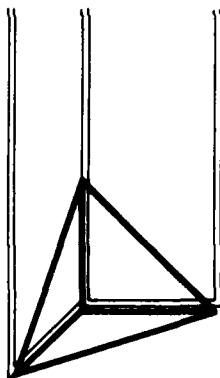


Figure 3
Gage Attached to Tubular Frame
for Insertion and Orientation

Fiber Optic Gage is attached to a frame by releasable bonds during insertion into the ground and backfilling of the hole. The frame shows the orientation of the buried gage.

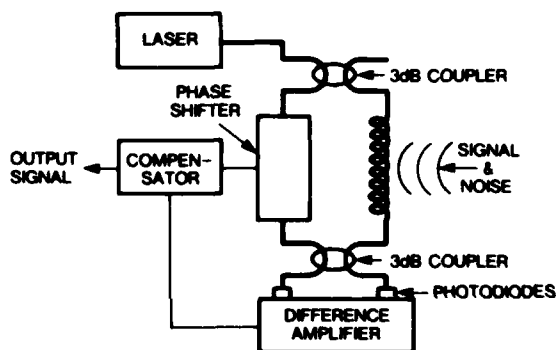


Figure 4
Mach Zehnder Fiber Optic Interferometer

Laser light is transmitted into both a sensor fiber which responds to strain and a reference fiber whose phase can be adjusted. The light is recombined, detected, summed, and amplified.

DISCUSSION

Mr. Favour (Boeing Company): Do you have any predicted frequency response near single elements?

Mr. Edelman: It depends on how long you make the linear gages and how much tension you want to use. I think, practically, you can make the resonance anywhere in the audio range, maybe even up to 20 or 30 kilohertz.

Mr. Smallwood (Sandia National Laboratories): Physically, what kind of dimensions are these?

Mr. Edelman: I was careful not to say that. In working on this, I thought about something like ten centimeters on a side. But there is no inherent reason why you can't make it anywhere from a centimeter up to a half a meter. If you make it too big, this nice deformation that I assume, where you use only the first order derivative, won't fit. But within that limit, you can make it whatever size you like.

REGISTRATION OF THREE SOIL STRESS GAGES AT 0 THROUGH 28 MPa (4000 psi)

Charles R. Welch
U. S. Army Engineer Waterways Experiment Station
Corps of Engineers
Vicksburg, Mississippi

A series of static tests were conducted on three soil stress gages. The gages tested were the currently accepted SE soil stress gage (34 MPa (5000 psi) range), a modified high range SE (HRSE) soil stress gage (138 MPa (20,000 psi) range), and the Waterways Experiment Station Medium Level (WML) stress gage. The tests consisted of multiple static loadings of two different soil types (Reid-Bedford sand and buckshot clay) which contained four HRSE gages, four WML gages, and eight SE gages. The loading range was from 0 to 28 MPa (4000 psi). The test chamber was 1.17 m (46 in.) in diameter by 1.07 m (42 in.) deep. Representative outputs from all three gage types are presented. Of special concern are the recorded outputs from the standard SE gages. These measured the loading of both soil types reasonably well, but consistently over-registered during unloading in the sand. Hysteretic-type behavior was not observed on the other two types of gages. The results imply that for dynamic tests in some soils the standard SE gage will indicate higher impulses than had actually occurred.

INTRODUCTION

Recently the Waterways Experiment Station (WES) was asked to make dynamic soil stress measurements in a 20-MPa (3000-psi) to 70-MPa (10,000-psi) pressure environment. The environment was created by explosively loading wet clay soil with a planar chemical explosive array (i.e., FOAM NEST charge array). Because there were no accepted soil stress gages for use in this pressure range, static laboratory tests were made to examine two experimental gages. The candidate stress gages were the High Range SE (HRSE) soil stress gage and the WES Medium Level (WML) stress gage. These were tested statically in two different soil types: one with significant shear strength (Reid-Bedford sand) and one with negligible shear strength (wet buckshot clay). The tests consisted of hydraulically loading one surface of a soil mass containing the gages. Used as standards for comparison during the tests were SE soil stress gages. The SE soil stress gage has been used for several years to measure dynamic and static soil stresses. Its basic design incorporates the criteria for soil stress gages developed by Peattie and Sparrow [1].

The primary purpose of this paper is to document the hysteretic response observed on standard SE gages and to provide tentative explanations for this response. A secondary

purpose is to describe other experimental gages and their performance.

SE SOIL STRESS GAGE

The SE soil stress gage (Figure 1) is an adaptation from the original design by Ingram [2] and is marketed by Kulite Semiconductor Products, Inc., as their Model No. LQ-080U. It has an overall diameter of 51 mm (2.0 in.) and is 5.8 mm (0.228 in.) thick. This provides an aspect ratio (diameter to thickness ratio) greater than five. It is made of 17-4 PH stainless steel. The gage has a maximum stress range of 35 MPa (5000 psi) and full-scale electrical output of 0.7 v for 10-v excitation. The active portion consists of two opposing diaphragms instrumented with two semiconductor strain gages each. These are connected in a full bridge configuration. The active portion is isolated from lateral loads by a steel edge ring and is connected to this edge ring by a 1.5-mm-(0.05-in.-) thick annulus of silicone rubber. The calculated natural frequency of each diaphragm is about 50 kHz. Overall gage modulus when considering the deflection of the center of the diaphragms is calculated to be 650 MPa (94,000 psi).

HRSE SOIL STRESS GAGE

The HRSE soil stress gage, Model

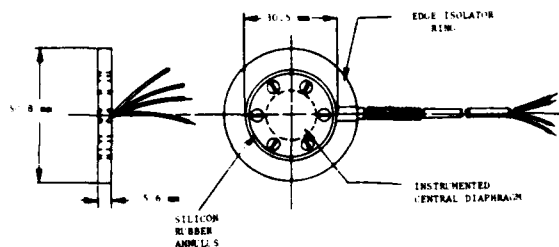


Figure 1 - SE soil stress gage

No. LQV-080-8U (Figure 2), is another Kulite adaptation of the original design by Ingram. The HRSE gage is similar to the SE gage except that the diaphragms are twice as thick making the overall gage thickness 11.5 mm (0.453 in.). The gage is mounted in an aluminum paddle by WES to provide the proper aspect ratio for making soil stress measurements and to isolate it from lateral loads. The paddle also aids in gage placement and in attaching cable protection. The gage has a linear stress range of about 140 MPa (20,000 psi). The calculated natural frequency is 100 kHz. The overall modulus, considering only center diaphragm deflection, is calculated to be 10,350 MPa (1,500,000 psi).

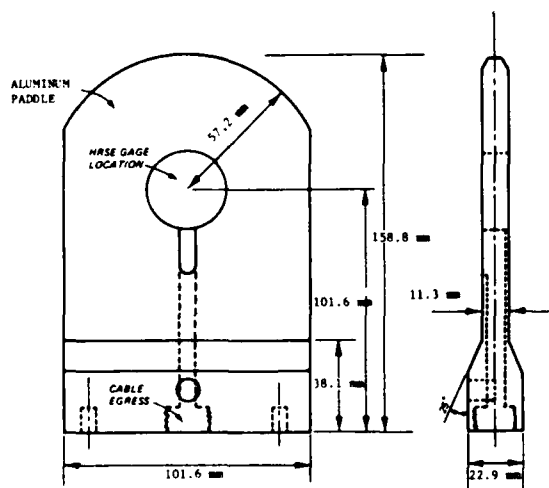


Figure 2 - HRSE soil stress gage in aluminum paddle

WML STRESS GAGE

The WML stress gage (Figure 3) is radically different from the other two stress gages. It was originally designed to make stress measurements in rock. The gage has an outside diameter of 95 mm (3.75 in.) and overall thickness of 19 mm (0.75 in.). It is based on an original design by MAJ Richard

Kanda, U. S. Army Corps of Engineers. The gage consists of a series of concentric rings loaded in compression by two thick plates. The rings are formed by cutting grooves into the bottom plate. The central ring is instrumented with longitudinal and circumferential foil strain gages connected in a full bridge configuration. The material used for the gage is either high strength aluminum (7075-T6 alloy) or a high strength steel, depending on range. For these evaluation tests aluminum was used. The overall gage modulus for the aluminum version is about 18,600 MPa (2,700,000 psi). Its peak stress range is approximately 140 MPa (20,000 psi). Full-scale electrical output is about 70 mv for 8-v excitation.

TEST DESCRIPTION

Prior to the tests, all stress gages were calibrated statically in a hydraulic chamber.

The geometry for the static tests in sand and clay was the same. The tests were conducted in a large chamber (Figure 4). A hydraulic load was applied through a rubber membrane to the soil surface. The outputs of the stress gages were recorded along with the outputs from two pressure gages which monitored the hydraulic pressure.

The soil was placed within 150 mm (6 in.) of the top of the chamber. A double-greased liner of polyethylene was used between the soil and the chamber walls to reduce sidewall friction. To insure uniform soil placement, the soil was rained in place for the Reid-Bedford sand and was hand-compacted in 100-mm (4-in.) lifts for the buckshot clay.

The stress gages were positioned in the soil during placement of the soil as shown in Figure 4. The gages were alternated in the circle to preclude biasing any gage type due to local test bed or soil stress irregularities. In addition, all gages were the same distance from the chamber walls so that the gages in each array would be loaded in the same fashion regardless of sidewall friction effects. Electrical cables from the stress gages exited the bottom of the chamber and were connected via additional cables to the recording station some 20 m (70 ft) away.

For each soil type, the hydraulic load was cycled up and down four times. The peak hydraulic pressure for each cycle was about 28 MPa (4000 psi). The outputs from the soil stress gages and the pressure gages were amplified and recorded on a 32-track FM magnetic tape recorder. All gages were powered by the same power supply. The recorded outputs were digitized for plotting by computer.

TEST RESULTS

Typical gage outputs for the three gage types in the clay and in the sand are shown in Figures 5 and 6. In each figure the hydraulic pressure (vertical axis) versus the stress gage output (horizontal axis) is shown. For the clay tests, all four loading cycles are

presented for each gage type. For the sand only one loading cycle is presented. The vertical fluctuations seen on the records for the sand tests are due to electrical noise on the pressure gage output and not to hydraulic pressure fluctuations. This noise was also seen on the other pressure gage. It did not occur during the clay tests. Its source is unknown.

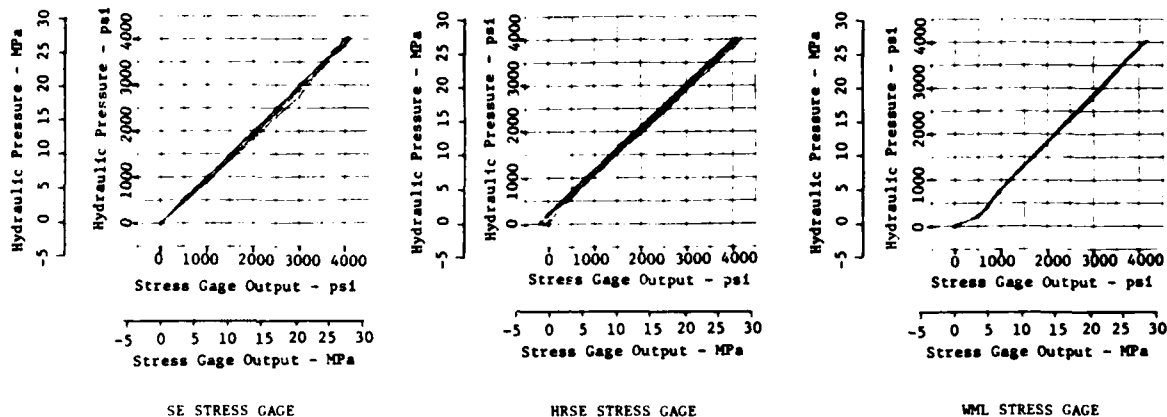


Figure 5 - Hydraulic pressure versus gage output for the SE, HRSE, and WML stress gages during the clay tests

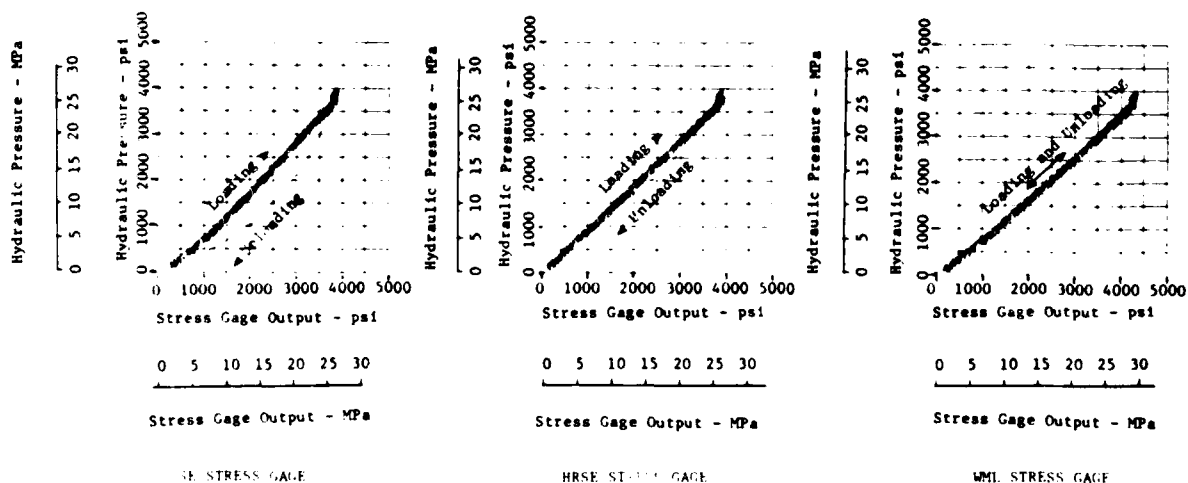


Figure 6- Hydraulic pressure versus gage output for the SE, HRSE, and WML stress gages during the sand tests. (Note: vertical fluctuations are due to electrical noise on the hydraulic pressure transducer channel)

Additional observations are:

1. No significant differences occurred in the measurements in either the sand or the clay due to gage location.
2. No changes occurred in gage response as a result of repeated loadings.
3. In general no appreciable hysteresis and no over- or under-registration of stress was observed for any of the gages in the clay.
4. The WML gages exhibited a non-linearity during the clay test below about 3.5 MPa (500 psi). This nonlinearity occurred during the sand test but the electrical noise on the hydraulic pressure gages prevented its detection.
5. The WML gages tended to over-register approximately 10 percent in sand. Over- or under-registration during loading of the other two gage types in sand was not observed, possibly because of the noise levels on the hydraulic pressure gages.
6. A hysteretic response occurred in the sand test on every SE gage on all four loading cycles. In each case the SE gages followed reasonably well the hydraulic load during loading but over-registered during unloading.
7. Three of the four HRSE gages suffered apparent electrical problems during the sand tests. The remaining gage performed satisfactorily and showed no hysteresis and no over- or under-registration.
8. The WML gages did not exhibit hysteretic behavior in the sand.

Observations 1 and 2 indicated that the stress environment for the different gages was similar and that gages were probably coupled well to the soil (i.e., no void spots above the gages). Observation 3 combined with Observations 5 and 6 suggests that over-registration, under-registration, or hysteretic behavior of the stress gage is dependent on the shear strength of the soil. This contention is supported by the fact that calibration of the gages in hydraulic fluid (which has negligible shear strength) did not produce these three types of behavior. Observation 2, the nonlinearity of the WML gage at the low stress levels, has been observed during the fluid calibration and is caused by all of the supporting rings not making contact with the top loading plate under initial loading.

The electrical problems that the three HRSE gages experienced during the sand tests (Observation 7) is attributed to intermittent breaks and shorts in the electrical cables from the test chamber to the recording

station. The problem did not occur on the clay tests because different cables were used for these same gages. Although the one gage performed satisfactorily in sand, before the HRSE is recommended for use in sand or other soils with significant shear strength, it should undergo additional testing.

Observation 6, the hysteretic behavior of the SE gage, has special significance. The SE gage has typically been used in the past in dynamic tests to measure peak stress and impulse (i.e., area under the stress-time curve). Since the WML and HRSE gages did not exhibit hysteresis (Observations 7 and 8), it is hypothesized that the SE gage hysteresis was not caused by locked-in stresses from frictional effects between the sand and the chamber walls. Since the hysteretic behavior was observed under static conditions, the dynamic response is suspect.

POSSIBLE EXPLANATIONS FOR THE SE GAGE RESPONSE

It is postulated that the diaphragms remained in the partially loaded (i.e., deflected) position due to shear stresses which developed in the sand. These shear stresses were the result of the uneven vertical movement of sand particles which followed the diaphragms during loading. The sand particles moved further at the center of the gage, while at the edges they moved very little. In order for the diaphragms to return to the no-load positions, the reverse must happen, i.e., the diaphragms must push the center sand grains up past the grains at the edges. The resultant shear forces between the sand particles prevented this until the surface load was reduced. It should be noted that the relatively soft SE gages undergo much larger deflections and soil particle motions than the HRSE gages or the WML gages.

The data from the static tests are insufficient to confirm this hypothesis.

CONCLUSIONS

1. The WML, HRSE, and the SE stress gages will perform satisfactorily in clay, although the WML gage is nonlinear below approximately 3.5 MPa (500 psi).
2. The SE soil stress gage shows stress-dependent hysteretic behavior in sand under static conditions. It will probably over-register slightly during loading in sand and may over-register during unloading. On dynamic tests this could cause the gage to over-register impulse.
3. Aside from possible nonlinear behavior at low stress levels the WML gage

performs satisfactorily in sand. It tends to over-register about 10 percent.

4. The HRSE gage appears to perform satisfactorily in sand, without hysteretic behavior and without over- or under-registering. However, this is based on a single gage's performance and should be further verified.

RECOMMENDATIONS FOR FUTURE WORK

The three stress gages tested each need additional work. The limitations on the use of SE gages in high shear strength soils needs to be quantified in terms of both stress level and shear strength.

The linearity of the WML gage needs to be improved. This could be a quality control problem since the degree of nonlinearity varies widely with new gages. Its output also needs to be increased. The WML gage's linearity can be improved by lapping the top and bottom plate together before assembly. Its output can be increased by using semiconductor strain gages in place of the foil strain gages to instrument the central column. This would also require increasing the overall gage stiffness by either decreasing the area of the grooves or by using steel for the gage body.

The HRSE soil stress gage needs further verification in sand. It appeared to perform well. It has both good linearity and high output. In soils with high shear strength

and/or at higher stress levels, it may exhibit the same hysteretic behavior as the SE gage.

ACKNOWLEDGEMENTS

Special thanks is due Leo Ingram and Jim Ingram (of WES) for their editorial comments and Mrs. Modell Holloway and Brenda Young (both of WES) for preparing this manuscript. This work was sponsored by the Defense Nuclear Agency.

REFERENCES

1. Peattie, K. R. and Sparrow, R. R., "The Fundamental Action of Earth Pressure Cells," Journal of the Mechanics and Physics of Solids, London, Vol 2, pp 141-155, 1954.
2. Ingram, James K., "Development of a Free-Field Soil Stress Gage for Static and Dynamic Measurements," Technical Report No. 1-814, 1968, U. S. Army Engineer Waterways Experiment Station, CE, Vicksburg, Miss.
3. Hvorslev, M. Juul, "The Changeable Interaction Between Soils and Pressure Cells; Tests and Reviews at the Waterways Experiment Station," Technical Report No. S-76-7, 1976, U. S. Army Engineer Waterways Experiment Station, CE, Vicksburg, Miss. (Not cited directly.)

CABLE PROTECTION FOR GROUND SHOCK INSTRUMENTATION IN SEVERE
ENVIRONMENTS - RESULTS OF AN EVALUATION TEST

Charles R. Welch
U. S. Army Engineer Waterways Experiment Station
Corps of Engineers
Vicksburg, Mississippi

The results of an explosive test on two candidate cable protection systems for ground shock instrumentation are presented. The protection systems consisted of 1/4-in. stainless steel (304 alloy) tubing and 3/8-in. oil-filled hydraulic hose. The test consisted of a 3.7 m by 3.7 m FOAM HEST with a charge density of 44.4 kg/m³ overlying a wet clay. Fifteen cable protection channels were included. They ranged from 0.3 m to 1.4 m below the charge array and were terminated with passive bridge resistor networks. Stress gages and shock-isolated accelerometers in the test bed indicated peak stresses and particle velocities of 31MPa and 20.3 m/s, respectively. Surface airblast pressures of 69 MPa and surface displacements of 0.8 m were recorded. Despite this, almost all cable protection system channels survived over 100 msec. Many were alive posttest. Noise levels in the hydraulic hose systems during wave engulfment were acceptable. Noise levels generated in the steel tubing systems were almost nonexistent. Both are presented in terms of an anticipated gage's output. Typical data return from several later tests which employed these two systems is then reviewed. The results indicate that cable protection for ground motion transducers, in at least this environment, need no longer be a problem.

INTRODUCTION

The Waterways Experiment Station (WES) was recently charged with making ground motion measurements in an extremely severe ground shock environment produced by explosively loading a wet clay with a high density FOAM High Explosive Simulation Technique (HEST) charge array. The environment produced survival problems, both for the ground motion transducers and the transducer cables. Initial efforts to produce instruments and cable protection systems to make measurements in a similar environment are described in Ref. [1]. These efforts included the use of aluminum tubing and oil-filled hydraulic hose to protect instrument cable and a shock-isolated accelerometer system to measure particle velocity. The work was largely successful but indicated where improvements might be made. This led to an evaluation test on two prospective cable protection systems: (1) a steel tubing system suggested by the earlier work, and (2) an oil-filled hydraulic hose system not tested fully on the previous test. Both of these cable protection systems were designed to act as conduits for a small diameter (3.2 mm) 4-conductor (28 gage conductor) foil-shielded instrument cable. Both were designed to withstand the

primary ground shock environment (typically 20 to 50 msec). The evaluation test was specifically designed to test the cable survivability and the noise generated in the cables protected by these systems.

This paper deals with this evaluation test. In it we will describe the cable protection systems, the evaluation test, and its results. Typical survival rates from two later tests are also provided.

GROUND SHOCK ENVIRONMENT

The ground shock environment of interest was generated by loading a wet clay with a FOAM HEST charge array with an explosive charge density of about 44.4 kg/m³ TNT equivalent. The FOAM HEST explosive array is comprised of lengths of high explosive contained in a polystyrene foam lattice and mounded over with soil for containment. It is used to explosively load large planar areas. Peak airblast from the HEST charge ranged up to about 150 MPa. The resulting ground shock was characterized by the following: peak accelerations from 10 kg to 150 kg, peak particle velocities to 30 m/sec, surface displacements to 0.7 m, and peak soil stresses from 20 MPa to 40 MPa.

HYDRAULIC HOSE CABLE PROTECTION SYSTEM

The protection philosophy behind the oil-filled hydraulic hose system (Figure 1)

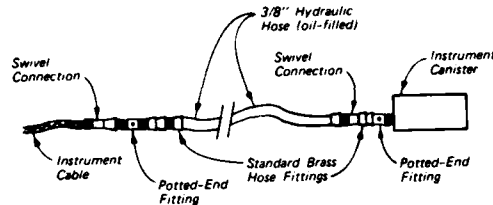


Figure 1 - Hydraulic hose cable protection system

is that the hose acted as a membrane to contain the oil around the transducer cable while the oil actually protects the cable. The hose used is typically used as air hose; it is 3/8 in. in diam and is nonreinforced. A thick machine oil was used inside the hose. Each end of the hose was terminated with machined potted fittings which sealed the oil around the cable. The contained oil allowed only hydrodynamic pressures to be transmitted to the cable; i.e., no localized tensile or shear stresses would occur on the cable. It also cushioned the cable from the surrounding acceleration environment. If the hose should rupture during the explosive event, the oil leaking out of the hose would provide a lubricant between the cable and the soil to minimize localized stretching of the cable. The advantages of the hydraulic hose are: (1) it is flexible and hence has minimum effect on the motion of the instrument it serves, (2) it can be had in lengths up to about 30 m, and (3) it is easy to handle in the field. Its disadvantages are: (1) it offers little shear protection or protection from the pressure environment, (3) while it prevents localized stretching of the cable it does not prevent overall stretching of the cable between the potted-end fittings, and (3) it is moderately expensive (~\$3.28/m).

STEEL TUBING CABLE PROTECTION SYSTEM

The philosophy behind the steel tubing protection system (Figure 2) is straightforward; it completely isolates the cable from the stress environment. This protection system consisted of 1/4-in. stainless steel tubing with an inside diameter of 4.6 mm. When used to service a ground motion instrument, a small slip joint was normally incorporated in the tubing near the transducer. The slip joint allowed the tubing to elongate up to about 130 mm during the explosive event. This helped to minimize the effect of the tubing on the transducer's motion. The stainless steel alloy chosen for the tubing (Stainless 304) had a fairly low-yield strength (240 MPa) with a much higher ultimate tensile strength (550 MPa). It was felt that this property would allow the tubing to strain easily under load without breaking. This was borne out by static laboratory tensile tests in which the tubing would normally undergo about 30 percent strain before failure. Swagelok (commercial name) stainless steel fittings were used to attach the tubing to the ground motion instruments and to make connections between tubes. Through laboratory tests it was found that these fittings produced little, if any, stress concentration in the tubing at the point of engagement, yet they provided a connection which had good tensile strength. Advantages of the steel tubing are: (1) it offers protection for the cable from the normal, shear, and tensile stress, and (2) it is fairly inexpensive (~\$1.28/m for the tubing and \$5.00 each for the fittings). Its disadvantages are: (1) it offers no protection for the cable from the acceleration environment, (2) it is not as easy to handle in the field as the hydraulic hose, and (3) there is a greater chance of it affecting the motion of the instrument it serves than the hydraulic hose.

EVALUATION TEST DESCRIPTION

The evaluation test was conducted on a firing range at Ft. Polk, Louisiana. It consisted of a 3.7-m by 3.7-m clay test bed

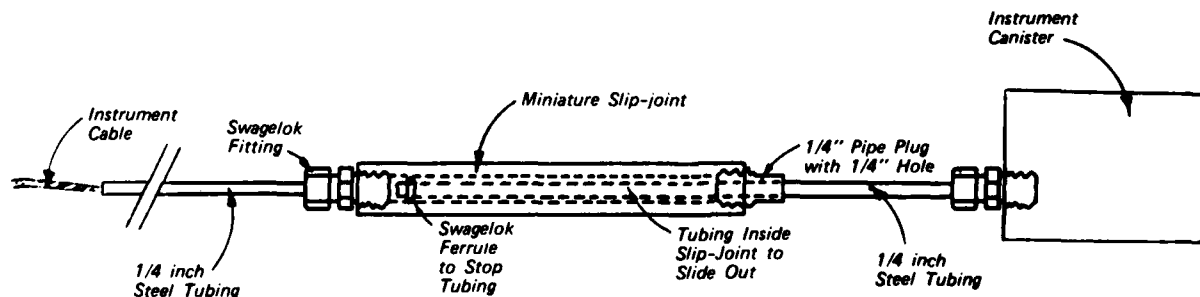


Figure 2 - Steel tubing cable protection system with miniature slip joint

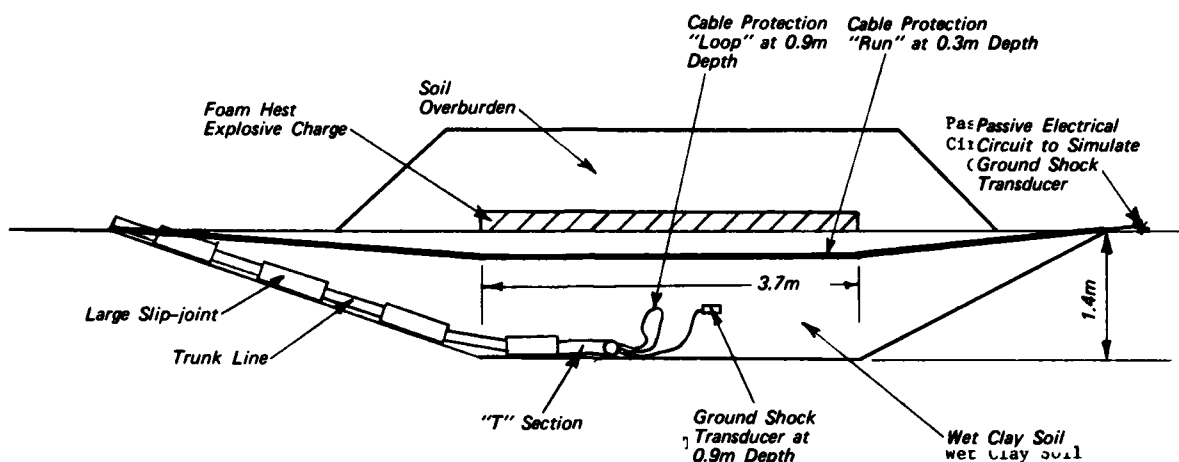


Figure 3 - Schematic of test bed showing different types of cable protection channels, trunk line, and ground shock transducer

(Figure 3) upon which was placed a FOAM HEST explosive charge (also 3.7 m by 3.7 m). The charge was composed of Iremite 60 explosive placed at a charge density of 44.5 kg/m³ TNT equivalent. A 0.76-m thick overburden of sand was placed over the charge to help confine the explosion. In the clay test bed were instruments to record the surface airblast pressures and the ground shock, as well as candidate channels of the cable protection. All were recorded on 32 track FM tape recorders during the event. Minimum throughput frequency response for the recording system,

including signal conditioning circuits, was 12 kHz. The various channels are listed in the experiment matrix in Table 1.

There were fifteen cable protection channels. These were: a Type A stainless steel "run" and a Type B stainless steel "run" and one hydraulic hose "run" each at the 0.3-, 0.9-, and 1.4-m depths, and one stainless steel "loop" and one hydraulic hose "loop" each at the 0.3-, 0.9-, and 1.4-m depths. The cable protection runs were simply lengths of steel tubing or hydraulic hose containing

Table 1
Experiment Matrix

Channel Designation	Type Transducer/Measurement	Depth (m)	Type of Cable Protection	Time of Channel Failure (msec)	Comments
R S1A	Type A Steel Tubing Run	0.3	Steel Tubing	60	2.1-m separation between broken ends
R S3A	"	0.9	"	Did not fail	
R S4.5A	"	1.4	"	Did not fail	
R S1B	Type B Steel Tubing Run	0.3	Steel Tubing, no Small Slip Joint	>100	Cable failed outside test bed and outside steel tubing
R S3B	"	0.9	"	Did not fail	Cable failed outside test bed and outside steel tubing
R S4.5B	"	1.4	"	20	
R H1	Hydraulic Hose Run	0.3	Hydraulic Hose	55	
R H3	"	0.9	"	>100	
R H4.5	"	1.4	"	Did not fail	
L S1	Steel Tubing Loop	0.3	Steel Tubing	Did not fail	
L S3	"	0.9	"	"	
L S4.5	"	1.4	"	"	
L H1	Hydraulic Hose Loop	0.3	Hydraulic Hose	Did not fail	
L H3	"	0.9	"	"	
L H4.5	"	1.4	"	"	
1	Vertical SI Accelerometer*	0.9	Steel Tubing	--	Failed pretest
2	Horizontal SI Accelerometer	0.82	Hydraulic Hose	35	
3	Vertical SI Accelerometer	0.84	Hydraulic Hose	57	
3h	Vertical Hard-Mounted Accelerometer	0.84	Steel Tubing	28	
4	Vertical SI Accelerometer	0.84	Steel Tubing	14	

* SI - Shock-Isolated.

Table 1 (Concluded)

Channel Designation	Type Transducer/ Measurement	Depth (m)	Type of Cable Protection	Time of Channel Failure (msec)	Comments
5	Horizontal SI Accelerometer	0.80	Steel Tubing	Did not fail	
5h	Horizontal Hard-Mounted Accelerometer	0.80	Steel Tubing	4	
6	Horizontal SI Accelerometer	2.06	Hydraulic Hose	60	
6h	Horizontal Hard-Mounted Accelerometer	2.06	Steel Tubing, no Small Slip Joint	Did not fail	
7	Vertical SI Accelerometer	2.13	"	"	
7h	Vertical Hard-Mounted Accelerometer	2.13	"	"	
8	140 MPa SE Soil Stress Gage	0.88	Hydraulic Hose	42	
9	35 MPa SE Soil Stress Gage	0.84	Hydraulic Hose	Did not fail	
10	140 MPa SE Soil Stress Gage	0.87	Hydraulic Hose	52	
11	35 MPa SE Soil Stress Gage	0.88	Steel Tubing	4	
12	WML Stress Gage*	0.89	Steel Tubing	Did not fail	
13	WML Stress Gage	0.88	Steel Tubing	60	
14	Air Blast Gage	0	Steel Pipe	Did not fail	
15	Air Blast Gage	0	"	"	
16	Air Blast Gage	0	"	"	
17	Air Blast Gage	0	"	"	
18	Tourmaline Crystal Pressure Gage	0.86	None	>20	Difficult to determine time of failure from records
19	Tourmaline Crystal Pressure Gage	0.86	None	>20	"

* WML - WES Medium Level.

instrument cable that ran into the test bed and out the other side at the desired test depth. The steel tubing runs were made of two 6.1-m sections connected by small slip joints for the A runs and by a Swagelok tube-to-tube unions for the B runs. The hydraulic hose runs were made from 15.2-m lengths of hydraulic hose terminated at either end with the potted end fittings mentioned previously.

The cable protection loop channels were continuous loops of cable protection. Their purpose was to provide a test of the cable protection system exposed only to the stress environment beneath the explosive charge. For these the cables were brought into and out of the test bed via a steel trunk line that occurred at the 1.4-m depth and terminated in the test bed in a "T" section (Figure 4). The loops of cable protection left the T section, went up to the desired test depth, and then went back down into the T section and out of the test bed. The trunk line was composed of 2-in. schedule 80 pipe sections connected together by large slip joints (Figure 5) made from 3-in. schedule 80 pipe. Its purpose was to carry the cable through the severe lateral displacement region which occurs at the edge of the test bed during the explosion. The purpose of the T section was to provide an exit point for the loop cable protection channels which would remain stationary relative to the soil immediately around it. This would prevent the cable from being sheared off at the exit point. The smaller cable protection was attached to the T section via the potted

fittings for the hydraulic hose and by Swagelok tube-to-male pipe fittings for the steel tubing.

All fifteen cable protection channels were terminated outside the test bed with passive circuits designed to simulate electrically typical ground shock transducers. These passive circuits consisted of four 350 ohm resistors connected in a full bridge configuration. Because these circuits were passive, and because they were located outside the test bed, any signals which were recorded on these channels were strictly the result of the shock environment on the cables.

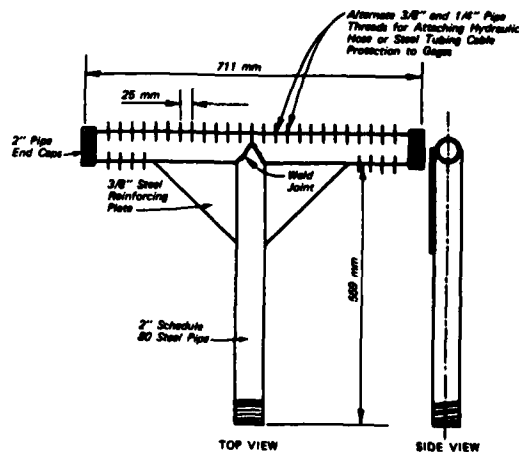


Figure 4 - "T" section used to terminate main trunk line in test bed

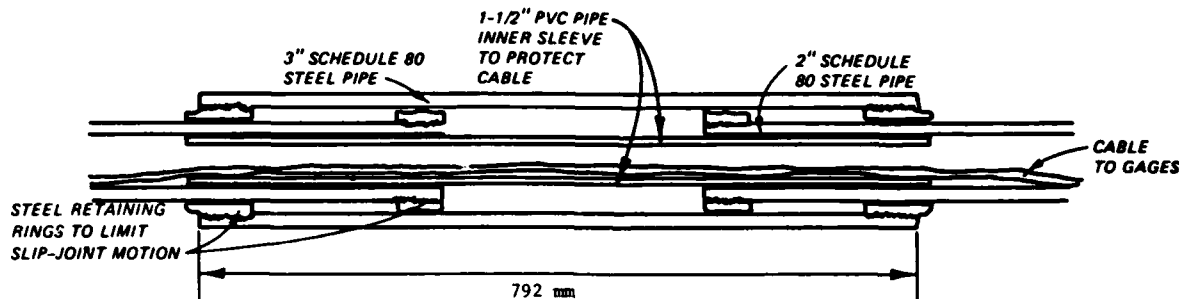


Figure 5 - Cross section of large slip joint used in the main trunk line

All amplifier gain settings were set alike for these channels and were made to mimic the gain settings for a WES Medium Level (WML) stress gage. This gage has a fairly low output (70 mv maximum or 0.4 mv/MPa for 8-v excitation) and it was felt that these gain settings would represent a worst case condition.

Twenty-three instruments were placed in the test bed to measure the shock environment. Beginning at the test bed surface were four airblast gages to measure the explosive cavity pressure. These were contained in mounts designed by the Air Force Weapons Laboratory and designated as "8-hole debris shields." At the 0.19-m depth was a vertically oriented shock-isolated (SI) accelerometer to measure particle velocity. A description of this transducer can be found in Ref [2]. This particular gage failed posttest. Additional SI accelerometers were located at the 0.9-m depth (two oriented horizontally and two oriented vertically) and at the 2.1-m depth (one horizontal and one vertical). Hard-mounted accelerometers to measure the acceleration were located at the 0.9-m depth (one horizontal, one vertical) and at the 2.1-m depth (one horizontal, one vertical). The hard-mounted accelerometers, like the SI accelerometers, were housed in aluminum canisters to protect them from the pressure environment. Soil pressure and soil stress measurements were made using eight gages, all at the 0.9-m depth. These were: two 35 MPa range SE soil stress gages (Kulite Model LQ-080UH), two 140 MPa range SE soil stress gages (Kulite Model LQV-080-8U), two WML stress gages, and two tourmaline crystal (PE) pressure gages. Ref. [3] provides a description of the 35-MPa SE stress gage. All the other pressure and stress gages are described in Ref. [2]. The PE pressure gages were housed in oil-filled 0.3-m sections of 1-in.-diam Tygon tubing. The oil provided coupling between the PE pressure gages and the soil stress.

The cables to all of the transducers, except the airblast gages and the PE gages, were protected by one of the two cable

protection systems. This was necessary, not only for channel survival but also to test the interface between the cable protection systems and the gages or canisters. The cables to these gages entered the test bed through the steel trunk line, left the trunk line at the T section and entered the smaller cable protection, which in turn carried these up to the associated gages.

The airblast gages had their cables protected inside 1-in. schedule 80 steel pipe that extended out beyond the test bed. The PE gages, which utilized low-noise (i.e., shock-resistant) coaxial cable, did not have any cable protection.

TEST RESULTS

The test bed surface was displaced downward by the explosion about 0.8 m. Peak airblast measured at the surface ranged from 52 MPa to 150 MPa. A typical airblast and airblast-impulse (i.e., area under the airblast curve) wave form is shown in Figure 6. In the figure "zero time" is the time at which the detonation of the explosive charge was initiated. Peak accelerations throughout the test bed were in the kg range with 20,000 g vertical acceleration being recorded at the 0.9-m depth (Figure 7) and 10,000 g horizontal acceleration being recorded at the 2.1-m depth (Figure 8) being typical.

Measured peak horizontal particle velocities were less than 9 msec. The velocity wave form derived from the hard-mounted accelerometer at the 2.1-m depth is shown in Figure 9. Vertical particle velocities ranged from 16.5 msec at the 0.9-m depth to 12.7 msec at the 2.1-m depth. A sample of the velocity wave forms derived from the SI accelerometers is shown in Figure 10. Recorded peak soil stresses, all from the 0.9-m depth, ranged up to 103 MPa, although the more believable records indicate peak soil stresses and pressures of about 31 MPa (Figure 11). The disparity between these peak values may be the result of the acceleration effects on some of the stress gages.

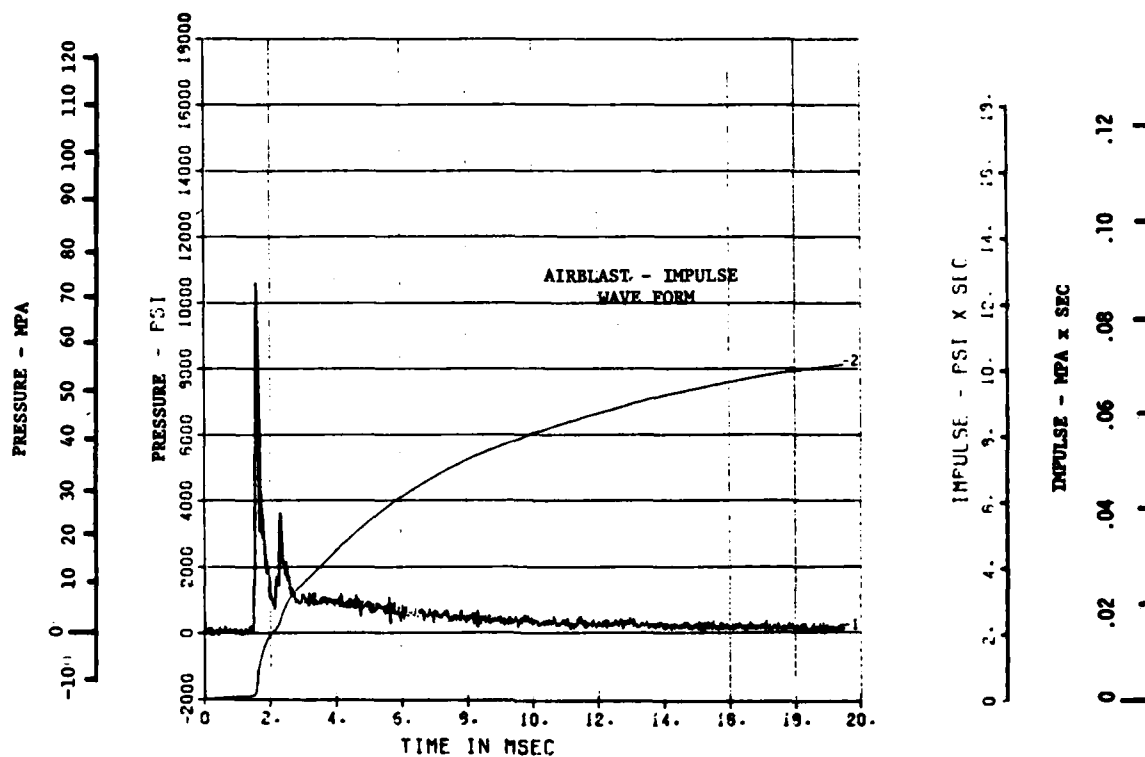


Figure 6 - Typical airblast and airblast-impulse wave form recorded at test bed surface

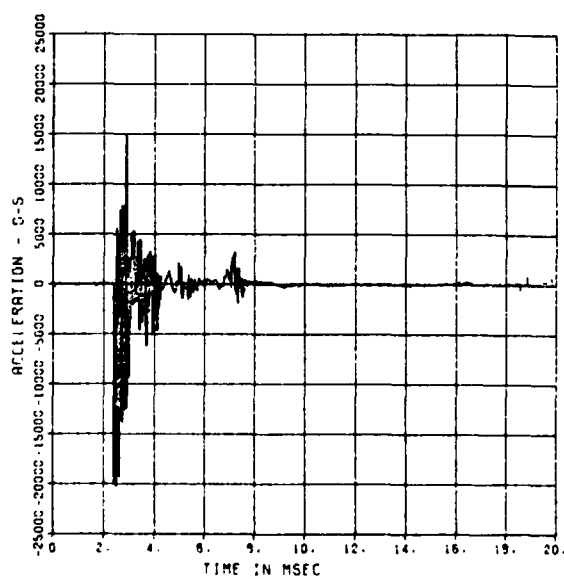


Figure 7 - Vertical acceleration recorded at the 0.9-m depth

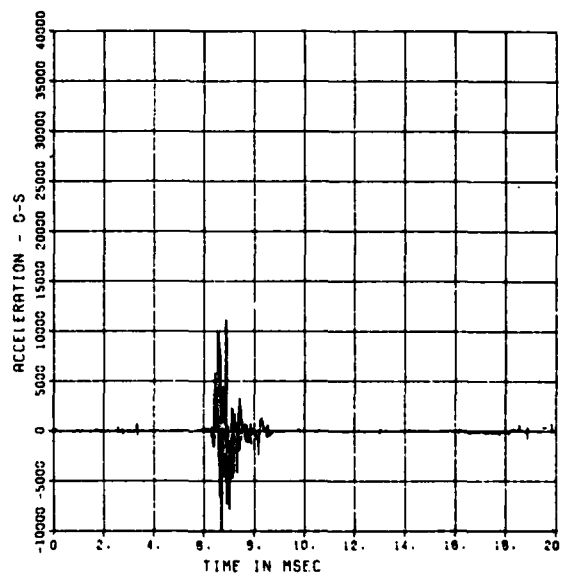


Figure 8 - Horizontal acceleration measured at the 2.1-m depth

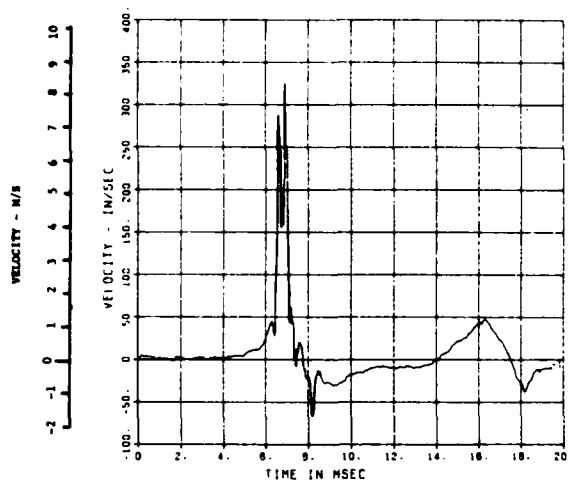


Figure 9 - Horizontal particle velocity derived from the hard-mounted accelerometer at the 2.1-m depth

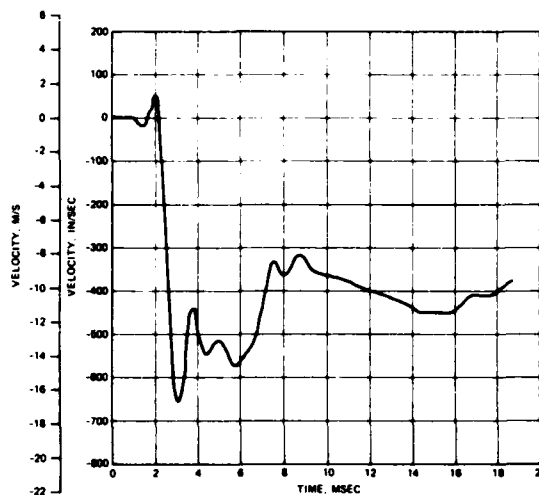


Figure 10 - Vertical particle velocity wave forms derived from the SI accelerometer at the 0.9-m depth

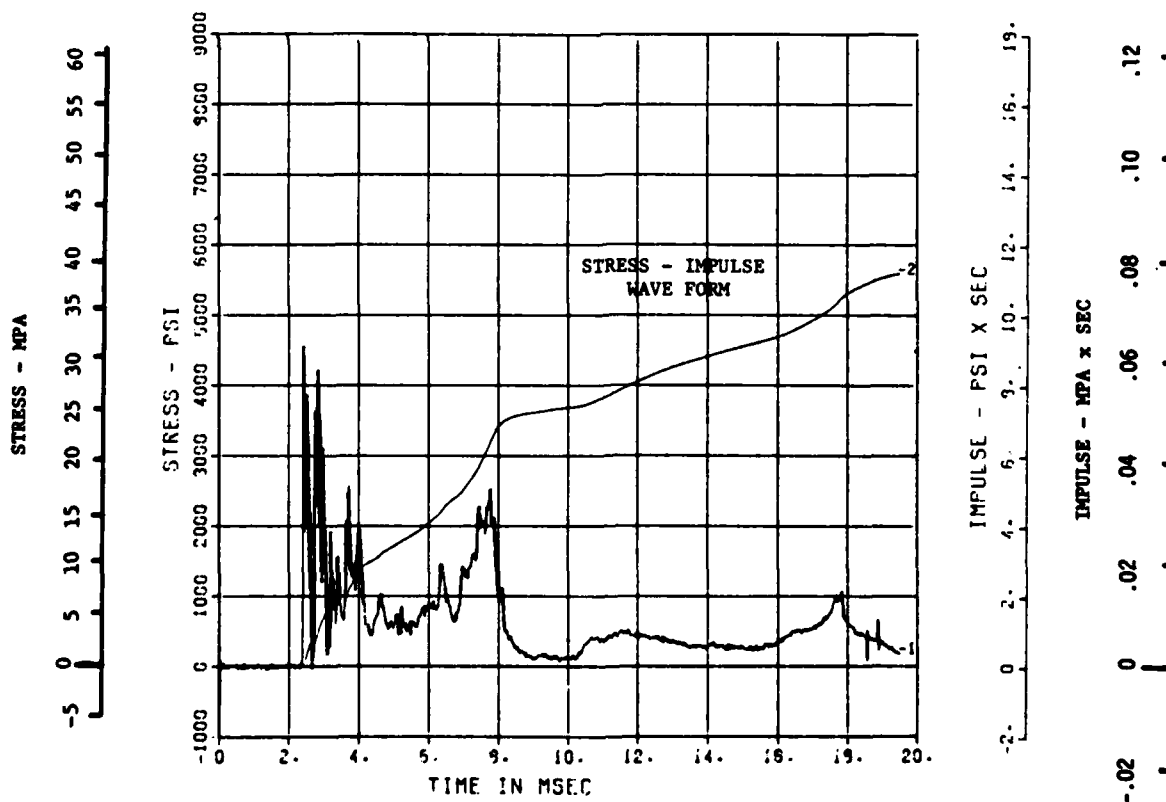


Figure 11 - Vertical stress and vertical stress-impulse wave forms measured at the 0.9-m depth

CHANNEL SURVIVAL RATES

The survival times for the different channels are shown in Table 1. While the survival rates for both the ground shock transducer channels and the cable protection channels were good, the cable protection channels survived better. All fifteen of these survived the primary ground motion (for this experiment, until about 20 msec past zero time). Only three of the cable protection channels failed before 100 msec. These were two steel tubing runs and a hydraulic hose run. The first channel to fail was the Type B steel tubing run at 1.4-m depth. The cable on this channel failed at 20 msec past zero time, outside of the test bed and outside of the steel tubing, apparently as a result of the soil being "squeezed" out from underneath the charge. The second channel to fail was the hydraulic hose run at 0.3-m depth. It failed at 55 msec past zero time and at several places in the test bed, all in tension. The third channel to fail was the Type A steel tubing run at the 0.3-m depth. It failed at 60 msec past zero time at the miniature slip joint near the test bed center. As a measure of the lateral soil displacement that occurred in the test, it is noted that the tubing ends were found 2.1 m apart posttest. (This was the only steel tubing channel whose exterior, i.e., tubing, tubing joints, and miniature slip joints, were not found intact posttest.) Of the remaining twelve cable protection channels, ten survived the complete test.

Three of the ground shock transducer channels (all with steel tubing cable protection) failed before 20 msec. Seven other channels (five with hydraulic hose, two with steel tubing) failed from 20 msec to 60 msec past zero time. The remaining six channels (five steel tubing, one hydraulic hose) survived the test. (Note: the steel tubing channel that failed pretest is not considered in these tabulations.)

All the failures that occurred on the steel tubing transducer channels were caused by tensile failure of the cable inside the tubing. This always occurred at the gage or gage canister. These failures are believed the result of the extension of the miniature slip joint augmented by the travel of the large slip joints on the trunk line. This contention is supported by the fact that the three transducer channels (measurements 6h, 7, and 7h), for which the miniature slip joints had not been used, all survived the test. Discussions with personnel posttest revealed that the cable may have been placed taut in the large trunk line pretest. The failures that occurred in the hydraulic hose also appeared to be tensile in nature. These occurred within 0.6 m of the gage or gage canister. On some channels additional cable failures were observed at other places

in the hydraulic hose. The hydraulic hose was also found to have failed in several places.

All four of the airblast gages survived the test. The two PE pressure gages did not. These six channels were not part of the cable protection study.

INDUCED CABLE NOISE

The noise generated in the cable protection channels by the shock environment for the first 10 msec is shown in Figures 12 through 16. The noise is displayed in all cases as if from the WML stress gage (gage output of about 0.4 mv/MPa). To aid in evaluating these plots, the approximate time of ground shock wave arrival at the various depths are given as: 0.3-m depth - 1.5 msec, 0.9-m depth - 2.3 msec, and 1.4-m depth - 3.3 msec. Hence all cables were engulfed by the ground shock during the displayed 10-msec time frame. Based on this noise data, the following observations are drawn:

1. The hydraulic hose channels (both loops and runs) were noisier than the steel tubing channels. The noise on the hydraulic hose channels was also lower in frequency content.
2. For a given protection system, the runs of cable protection were noisier than the loops of cable protection.

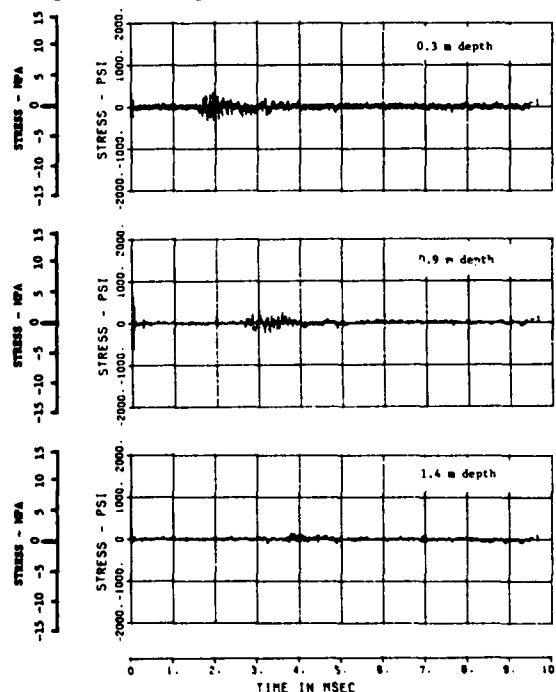


Figure 12 - Noise generated in the steel tubing "A" runs of cable protection at various depths in terms of a WML stress gage's output (0.4 mV/MPa)

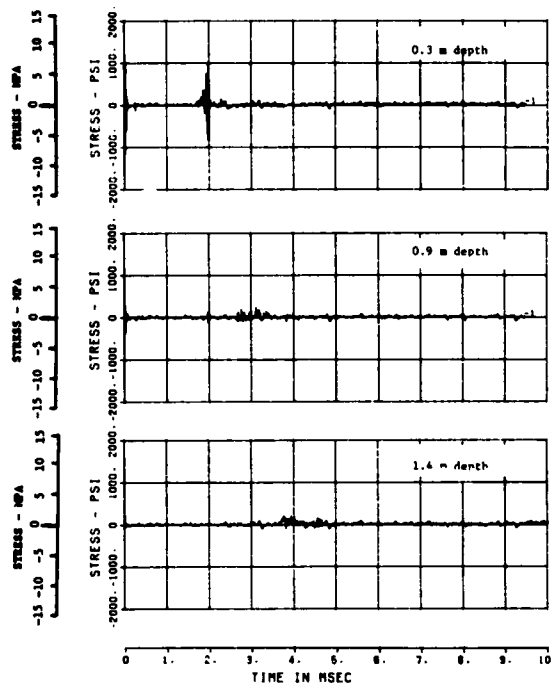


Figure 13 - Noise generated in the steel tubing "B" runs of cable protection at various depths in terms of a WML stress gage's output (0.4 mV/MPa)

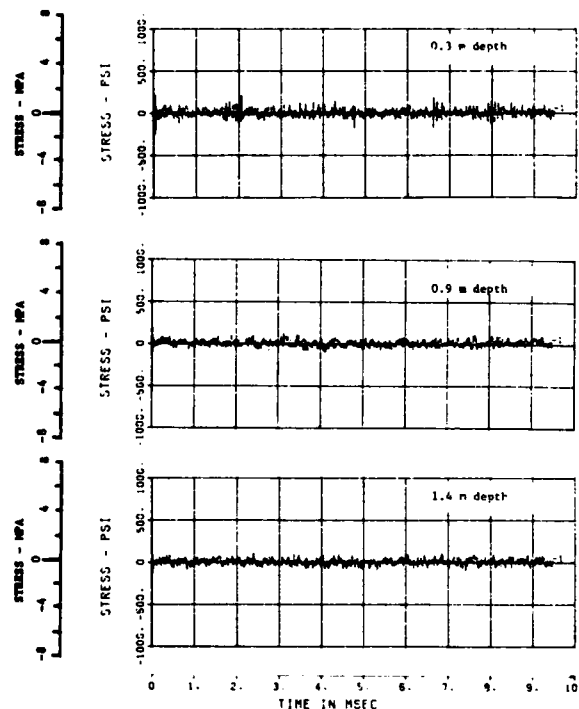


Figure 14 - Noise generated in the steel tubing loops of cable protection at various depths in terms of a WML stress gage's output (0.4 mV/MPa)

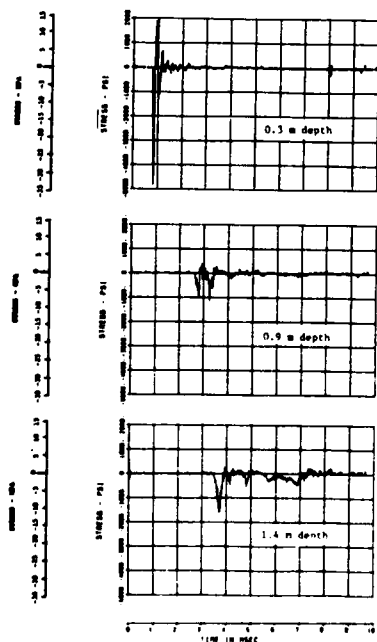


Figure 15 - Noise generated in the hydraulic hose runs of cable protection at various depths in terms of a WML stress gage's output (0.4 mV/MPa)

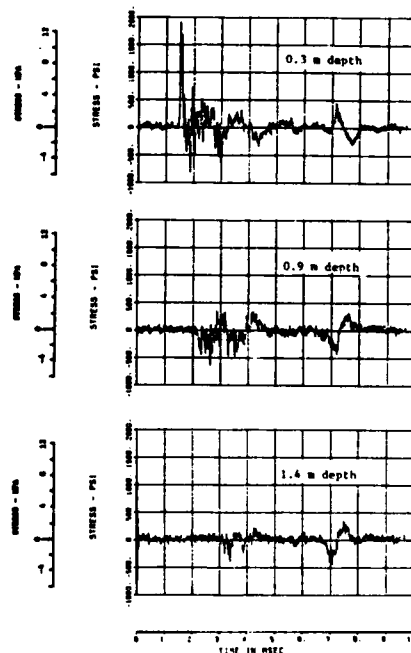


Figure 16 - Noise generated in hydraulic hose loops of cable protection at various depths in terms of a WML stress gage's output (0.4 mV/MPa)

3. Differences in noise levels generated in the Type A and Type B steel tubing runs were within data scatter.

Observation 1 indicates that the instrument cable is more sensitive to the pressure environment than the acceleration environment. Observation 2 indicates that the steel trunk line mitigated the noise generated in the cables in the severe lateral displacement regions at the test bed edges. Observation 3 states that while the miniature slip joints may decrease channel survival rates slightly, they do not significantly increase the noise levels induced on these channels.

If 10 percent of the expected peak signal level is used as the maximum acceptable noise level, then the cable protection channels that produced acceptable noise levels for the simulated WML stress gages were (this assumes the 31 MPa soil stress mentioned previously): the Type A and B steel tubing runs at 0.9-m and 1.4-m depth, all three steel tubing loops, and the hydraulic hose loops at the 0.9-m and 1.4-m depths. These cable protection systems should work better (i.e., have less noise compared to the peak signal) for other ground shock transducers because other ground shock transducers in general produce more output at the gage.

A prominent feature of the records was the noise pulse that occurred simultaneously on the three hydraulic hose loops at about 6 to 8 msec. This pulse is attributed to a reflected stress wave from below the test bed engulfing the T section of the main trunk line. This reflected stress wave is also seen on the stress measurement at the 0.9-m depth at about 7 to 8 msec (Figure 15).

RESULTS FROM LATER TESTS

These cable protection systems, augmented with steel trunk lines to cross the test bed boundaries, were used on two later FOAM HEST tests. These tests were conducted in wet clay and had a ground shock environment similar to that of the evaluation test. The steel tubing was used for ground motion transducers that were less than the 1.4-m depth. The hydraulic hose was used for all deeper gages.

The first test had 29 channels. On this test no cable failures occurred during the primary ground motion. Five channels failed between 62 msec and 110 msec after zero time. All others survived. The cable failures were again tensile in nature. The failures inevitably occurred at the gage or gage canister and inside of the associated cable protection system. (The external portions of all cable protection systems were intact posttest.) The failures are attributed to stretching of the hydraulic hose and

to elongation of the small slip joints on the steel tubing channels.

The second test involved 58 channels. All but four channels were alive posttest. The four that died presumably died in the same manner as in the earlier tests.

CONCLUSIONS

Both the hydraulic hose protection system and the steel tubing protection system produced good survivability in ground shock transducer cables during the primary ground motions under the tested ground shock environment. This ground shock environment was produced by a high density (44.5 kg/m³) HEST charge loading wet clay and is characterized by accelerations greater than 10,000 g, 30 MPa soil stresses, and surface displacements to 0.8 m.

Ground shock induced noises were higher in amplitude and lower in frequency content for instrument cables protected by hydraulic hoses than those protected by steel tubing. In both cases the noise levels were reduced by bringing the cables into the test bed via a larger trunk line.

Even for ground shock transducers that have a low electrical output (70 mv maximum) the hydraulic hose system, augmented with the trunk line, will provide acceptable noise levels when used at depths of 0.9 m and deeper; the steel tubing, augmented with the trunk line, will perform satisfactorily at depths of 0.3 m and deeper; and the steel tubing without the trunk line will perform satisfactorily at depths of 0.9 m and deeper.

RECOMMENDATIONS

In regions of more severe stress and displacement it will either not be possible to make the instrument cables survive, or the cable protection systems will become so massive as to affect the measurements adversely. A possible solution is to avoid instrument cables and use self-recording (self-contained) measuring systems. The technology for such systems has been demonstrated. This approach needs to be broadened. In the interim, the cable protection systems described or variations thereof tailored to specific conditions should be used in severe shock environments.

ACKNOWLEDGEMENTS

I wish to thank Lee Piper and Dr. Rey Shunk (both of Electro-Mechanical Systems, Inc.) and Messrs. John Stout, Jim Hossley, Steve Shore, Leo Ingram, and Dr. Jim Balsara (all of WES) for their help and suggestions during the program. I would also like to especially thank Mrs. Modell Holloway and Mrs. B. A. Young for their careful preparation of this manuscript.

REFERENCES

1. Welch, Charles R., "Measurement of Ground Shock in Severe Environments," presented to the 26th International Instrumentation Symposium, May 1980.
2. Ingram, James K., "Development of a Free-Field Soil Stress Gage for Static and Dynamic Measurements," TR No. 1-814, U. S. Army Engineer Waterways Experiment Station, CE, Vicksburg, Miss., 1968.
3. Welch, Charles R., "Silo Test Program II Instrumentation and Evaluation," U. S. Army Engineer Waterways Experiment Station, CE, Vicksburg, Miss., May 1981.

DISCUSSION

Mr. Keller (DNA): Do you think then, that the pressure protection is more important than the cable slap as far as the noise generated in the cables is concerned?

Mr. Welch: Yes, it is. We felt that was exactly the case, especially considering the high acceleration environments that we were in. The steel tubing is small enough so that it would move with that acceleration environment.

Mr. Keller: What was the total displacement of the gages?

Mr. Welch: It varied. It was about 30 inches at the surface in the evaluation test that I cited. To give you an indication of what the displacements were in the test bed; one of the steel tubes failed in the evaluation test, and it failed after 20 plus milliseconds. It was one foot below a 12 by 12 charge. We found the ends after the test. It broke in the center, and the ends were displaced seven feet. So there was a great deal of soil displacement.

STRUCTURAL RESPONSE OF HEPA FILTERS TO SHOCK WAVES

P.R. Smith
New Mexico State University
Las Cruces, NM

W.S. Gregory
Los Alamos National Laboratory
Los Alamos, NM

Shock waves were produced in a shock tube one meter in diameter and 49 meters in length. The driver of the shock tube was of variable length so that both peak pressure and impulse behind the wave could be controlled. Structural behavior of the HEPA filters as shock waves impacted upon them was recorded by a high speed motion picture camera. Various pressure and temperature transducers recorded the characteristics of the shock wave on a high speed recorder. Impulse per unit area needed to break a given brand of filter was found to be constant for long driver lengths. However, for short driver lengths the high velocity air flow behind the shock wave was apparently responsible for filter failure, rather than shock impulse.

INTRODUCTION

However remote, the possibility exists that within nuclear facilities conditions might arise from which explosions could occur. These might be gas explosions, dust explosions, or chemical explosions. A knowledge of how the explosively driven shock wave from such an event will affect the ventilation system of the facility is necessary in order to evaluate the probability of release of radioactive particulate to the atmosphere. High efficiency particulate aerosol (HEPA) filters, common to nuclear facility ventilation systems, under normal operating conditions prevent radioactive particulates from being exhausted to the atmosphere at the facility boundaries. Typically these filters have efficiencies of 99.97% or better. However, little is known about their efficiency or their structural response when these filters are struck by explosively driven shock waves. Measurement of filter efficiency during the transient of the shock wave passage is difficult, but our studies (1) indicate that efficiency is only slightly reduced during the transient, if the HEPA filter does not fail structurally. However, if filter failure occurs, i.e. if the filter medium breaks, then efficiency falls dramatically and large amounts of radioactive particulate could be released during and after the transient. Therefore, the current study of shock effects on the structural response of HEPA filters provides critical information for safety analysis of nuclear facilities.

The Los Alamos National Laboratory/New Mexico State University .91 meter (36 inch) diameter shock tube has a variable length driver which allows control of both shock over-pressure and shock impulse. Thus, explosive shock waves can be simulated both as to magnitude and distance from the source of the explosion. Eight types of HEPA filters from six different manufacturers were tested. These included both standard and special HEPA filters (e.g. V-Type, separatorless), fabricated by both domestic and foreign manufacturers. A total of 35 tests were made to determine the structural response of the filters to impinging shock waves of various overpressures and impulses.

DESCRIPTION OF TEST APPARATUS

Figure 1 is a reduction of the construction blue-print of the overall shock tube which is located on the New Mexico State University campus in Las Cruces, New Mexico. The total length of the shock tube is approximately 48.77 meters (160 feet). The tube consists of three sections, all made of 0.91 meters (3 feet) inside diameter steel pipe, namely: 1) a driver or high pressure section 11.76 meters (38 feet 7 inches) long, 2) an interstage or double diaphragm section 0.43 meters (17 inches) long, and 3) a driven or low pressure section 36.58 meters (120 feet) long. These sections appear from left to right, respectively, in the drawing of Figure 1.

The driver section can be pressurized to a maximum of about 2413.25 Kpa (350 psig) by a

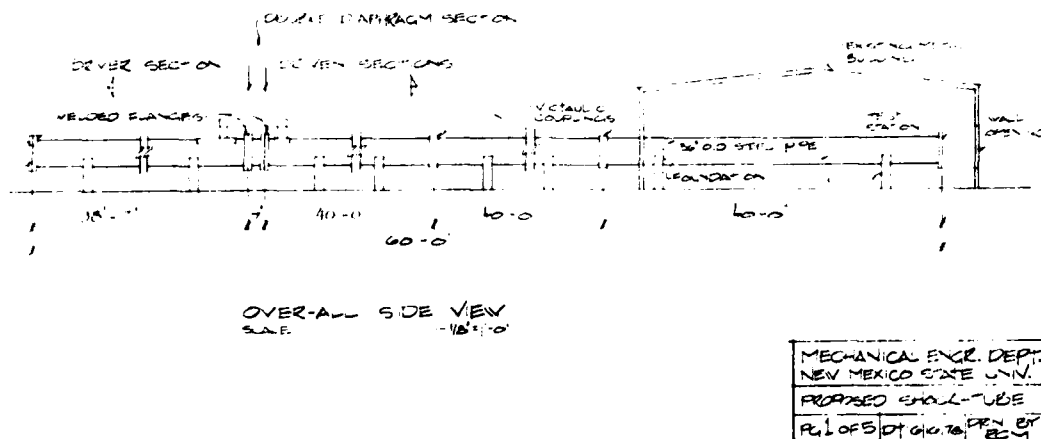


Figure 1 Reduced Copy of Construction Blueprint of the Overall Shock Tube

large diesel driven compressor. Peak pressure differences across the generated shock wave, therefore, will have a maximum of approximately 344.75 Kpa (50 psi). Dwell time of the pressure rise behind the shock wave can be varied from a few milliseconds to approximately 50 milliseconds.

The dwell time of the pressure rise, and therefore the impulse, is controlled by varying the length of the driver (high pressure) section. A movable wall achieves this. The movable wall is sealed by a pneumatically expanded rubber tube around its rim. A system of movable steel carts (i.e. load carrying spacers) transfer the huge axial forces (as high as 1,583,488 N (356,000 lb)) to the rear support flange, and puts the pipe in tension.

The shock tube is fired to generate its simulated explosive wave by rupturing metal or plastic diaphragms separating the driver (high pressure) section from the driven (low pressure) section. A short 0.43 meter length of 0.91 meter tubing is placed between the driver section and the driven section. A thin diaphragm of diameter equal to the flange diameter is placed on both ends of the interstage (double diaphragm) section. Both the interstage and the driver sections are movable. After the diaphragms are in place, a pneumatic piston slides the driver forward until it clamps the interstage against the driven section. Final pressure sealing is obtained by bolting the flanges of the sections together with 0.0508 meter (2 inch) diameter bolts.

METHOD OF TESTING

Size 5 (0.61 meter x 0.61 meter x 0.30 meter) HEPA filters were subjected to shock waves by placing them at the open end of the shock tube as shown in Figure 2. A high speed motion picture camera was placed downstream of

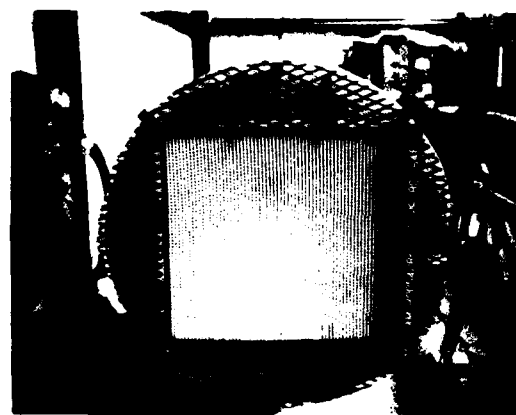


Figure 2 Size 5 HEPA Filter Ready for Testing at Exhaust End of the 0.91 meters Diameter Shock Tube

the filter and focused on the face of the filter during the test. Ten feet upstream of the filter a Kulite model XTH-1-190-10G pressure transducer with a frequency response of 10,000 Hz recorded the pressure of the passing shock wave. The value of the pressure was recorded on a Honey-Well visacorder, model no. 2106. Timing marks on the high speed film and the visacorder were synchronized through a Redlake Corporation timing light generator, model no. 13-0001, thus allowing the time and pressure at the instant of filter failure to be determined. Structural failure of the filter was defined as a visible rupture, however small, of the filter medium on the downstream face of the filter. Several thermocouples in the driver and driven sections of the shock tube recorded static air temperatures prior to firing, thus allowing determination of wave velocities.

Testing proceeded by subjecting a single type of filter to progressively lower shock over-pressures (at a given driver length) until an over-pressure was reached for which the filter did not fail structurally. No filter was subjected to more than one test. Each filter was new and unused. Filters ranged in price from \$150 to \$500 each. Therefore, in order to keep expenses down, most of the tests were conducted at a 9.75 meter driver length. Selected tests were then run for a 5.44 meter and a 1.68 meter driver length. Subsequent to data reduction, four additional tests were found to be necessary at the 5.44 meter driver length.

RESULTS

Table I presents a summary of the results of the first 51 tests which were run. The first column indicates the filter manufacturer and the sequence number of the test. The driver length, L_{DR} , appears in the second column and the shock over-pressure, P_{max} , appears in the third column. The fourth column indicates whether or not the filter failed structurally during the test (yes or no). The integral of the pressure over time, $\int p \Delta t$, up to the point of filter failure is listed in the fifth column and is equivalent to impulse per unit area. The time from the instant the shock wave strikes the filter until the filter fails, Δt , is in the last column. Notice that the tests are listed in order by filter manufacturer, driver length, and shock over-pressures.

The method for determining the shock over-pressures just needed to cause a filter to fail is summarized in Table II. Again, the first column is the filter manufacturer and test sequence number, the second column is driver length, the third column is the shock over-pressure, and the fourth column indicates if failure occurred. Notice for each type of filter, for each driver length, two tests are listed: one for which no failure occurred and one for which failure barely occurred. The shock over-pressure just needed to fail the filter, P_{BRK} , was assumed to be the average of the shock over-pressures of these two tests. The uncertainty in P_{BRK} is taken to be one-half the difference between the shock over-pressures of the two tests. The remaining column of Table II gives the impulse per unit area, $\int p \Delta t$, up to the point of filter failure on the second tests.

Hence, from Table II we find that a standard domestic filter (A) will fail at a shock over-pressure of $7.17 \pm 1.10 \text{ KPa}$ ($1.04 \pm 0.16 \text{ psi}$), a domestic separatorless filter (E) at $5.38 \pm 1.52 \text{ KPa}$ ($0.78 \pm 0.22 \text{ psi}$), both for 9.75 meter (32 feet) driver lengths. However, we find that an E filter will fail at a shock over-pressure of $10.0 \pm .34 \text{ KPa}$ ($1.45 \pm 0.05 \text{ psi}$) if the driver length is 1.68 meters (5.5 feet). As a matter of fact, for all filters tested at various driver lengths, we see from the table that the shock over-pressure for which failure occurs increases with decreasing driver length.

This fact is summarized in Figure 3 in which P_{BRK} is plotted as a function of driver length, L_{DR} .

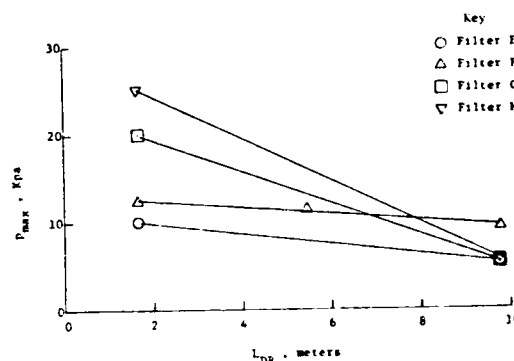


Figure 3 Shock Over-Pressure Needed to Just Break HEPA Filters

The failure over-pressures found in these current tests for 9.75 meters (32 feet) driver lengths (47ms dwell) are all lower than those reported in the literature for similar testing. Anderson and Anderson (2) found that $(0.61 \times 0.61 \times 0.30)$ HEPA filters failed at over-pressures of about $21.96 \pm 0.45 \text{ KPa}$ ($3.185 \pm 0.065 \text{ psi}$). The dwell time behind their shock waves was approximately 50ms. The manufacturers of the filters used in their test were not revealed. The results of the current study certainly show that the breaking point of the filters due to shock over-pressure is very dependent upon manufacturers.

As the driver length is decreased, the time of dwell of the shock over-pressure decreases. Compare Figure 4 to Figure 5. The first is a trace of the pressure for a long (9.75 meters) driver and the latter, a trace of the pressure for a short (1.68 meters) driver. The dwell behind the shock wave in the long driver case is about 47ms and in the short driver case about 5ms. Our previous studies have shown that the reflected wave from the rim of the filter case which appears at the pressure transducer location about 20ms after shock passage is not experienced on the face of the filter nor interior to the filter (1). The results summarized in Figure 3 would appear justified since less impulse per unit area (i.e. the integrated area under the pressure pulses shown in Figures 4 and 5) is available at short driver lengths compared to long driver lengths for the same peak pressure. However, this logic presupposes that it is impulse that causes filter failure. To examine this presupposition, we consider Figure 6, a plot of the impulse per unit area, $I/A = \int p \Delta t$, as a function of driver length, L_{DR} , taken from Table II. If impulse due to the shock over-pressure is the cause of failure, then the lines in Figure 6 should be horizontal, i.e. impulse should not be a function of driver length. Obviously, this

Table I
Summary of Experimental Data

Filter Mnf*/Test No.	LDR meters	P _{max} Kpa	Break?	$\frac{I}{A} = \int p \Delta t$ (Kpa)msec	Δt ms
A#18	9.75	6.07	No	---	---
A#17	9.75	8.27	Yes	229.6	28
A#8	9.75	15.03	Yes	166.17	11
A#7	9.75	16.55	Yes	66.74	4
B#2	9.75	16.55	No	---	---
B#10	9.75	17.93	Yes	609.52	34
B#1	9.75	20.0	Yes	491.61	31
C#16	9.75	8.62	No	---	---
C#15	9.75	10.34	Yes	375.09	37
C#11	9.75	15.17	Yes	428.87	28
C#4	9.75	16.55	Yes	314.41	19
C#9	9.75	18.62	Yes	477.34	28
C#3	9.75	20.00	Yes	377.29	19
D#5	9.75	16.55	No	---	---
D#46	9.75	17.25	No	---	---
D#30	9.75	17.65	Yes	353.02	18
D#47	9.75	17.93	Yes	535.74	30
D#6	9.75	20.00	Yes	539.88	29
E#28	9.75	3.86	No	---	---
E#27	9.75	6.90	Yes	213.75	31
E#38	1.68	9.65	No	---	---
E#37	1.68	10.34	Yes	107.56	30
E#36	1.68	12.41	Yes	103.43	12
F#19	9.75	7.58	No	---	---
F#20	9.75	8.62	No	---	---
F#48	9.75	9.86	Yes	345.44	35
F#29	9.75	10.34	Yes	Film Lost	
F#13	9.75	17.24	Yes	Film Lost	
F#49	9.75	17.24	Yes	485.41	28
F#12	9.75	19.31	Yes	405.43	21
F#51	5.44	10.34	No	---	---
F#50	5.44	12.41	Yes	335.10	27
F#34	1.68	10.34	No	---	---
F#35	1.68	12.07	No	---	---
F#33	1.68	12.76	Yes	120.66	34
F#31	1.68	13.45	No	---	---
F#32	1.68	14.82	Yes	136.52	212
G#23	9.75	3.86	No	---	---
G#22	9.75	6.90	Yes	262.01	38
G#21	9.75	11.03	Yes	222.71	20
G#14	9.75	15.86	Yes	222.02	14
G#39	1.68	17.93	No	---	---
G#40	1.68	19.31	No	---	---
G#41	1.68	20.89	Yes	182.03	15
H#26	9.75	3.65	No	---	---
H#45	9.75	4.83	No	---	---
H#25	9.75	6.90	Yes	206.85	30
H#24	9.75	10.76	Yes	333.72	31
H#42	1.68	24.82	No	---	---
H#43	1.68	25.51	Yes	151.00	7

*Key to Manufacturer Code: A = Standard Domestic, B = Standard Domestic, C = Standard Domestic, D = Standard Domestic, E = Separatorless Domestic, F = V-type Foreign, G = V-type Foreign, H = V-type Domestic. Note: Letters are not related to actual manufacturer's names.

Table II

Shock Over-Pressure to Break Filters

Filter Mnf./Test No.	LDR meters	P _{max} Kpa	Break?	P _{BRK} Kpa	$\frac{I}{A} = \int p \Delta t$ Kpa-msec
A#18	9.75	6.07	No		
A#17	9.75	8.27	Yes	7.17±1.10	229.6
B#2	9.75	16.55	No		
B#10	9.75	17.93	Yes	17.24±0.69	609.52
C#16	9.75	8.62	No		
C#15	9.75	10.34	Yes	9.52±0.90	375.09
D#46	9.75	17.24	No		
D#47	9.75	17.65	Yes	17.44±0.21	535.74
E#28	9.75	3.86	No		
E#27	9.75	6.90	Yes	5.38±1.52	213.72
E#38	1.68	9.65	No		
E#37	1.68	10.34	Yes	10.0±0.34	107.56
F#20	9.75	8.62	No		
F#48	9.75	9.86	Yes	9.24±0.62	345.44
F#51	5.44	10.34	No		
F#50	5.44	12.41	Yes	11.38±1.03	335.1
F#35	1.68	12.07	No		
F#33	1.68	12.76	Yes	12.41±0.34	120.66
G#23	9.75	3.86	No		
G#22	9.75	6.90	Yes	5.38±1.52	262.01
G#40	1.68	19.31	No		
G#41	1.68	20.69	Yes	20.0±0.69	192.37
H#45	9.75	4.83	No		
H#25	9.75	6.90	Yes	5.86±1.03	206.85
H#42	1.68	24.82	No		
H#43	1.68	25.51	Yes	25.17±0.34	151.0

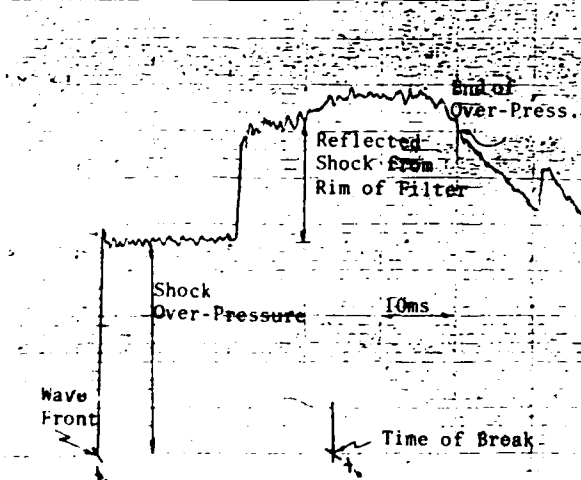


Figure 4 Typical Pressure Trace of Shock Over-Pressure for a 9.75 meter Driver Length (Pressure Transducer Located 3.05 meters Upstream of Filter)

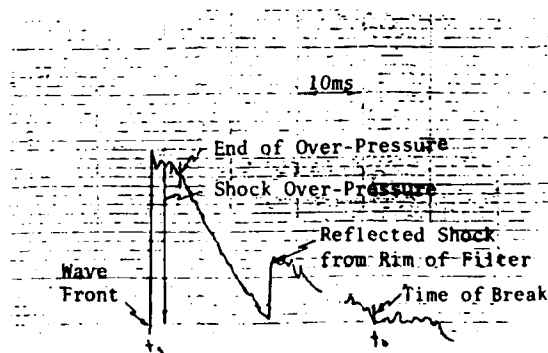


Figure 5 Typical Pressure Trace of Shock Over-Pressure for a 1.68 meter Driver Length (Pressure Transducer Located 3.05 meters Upstream of Filter)

is not true.

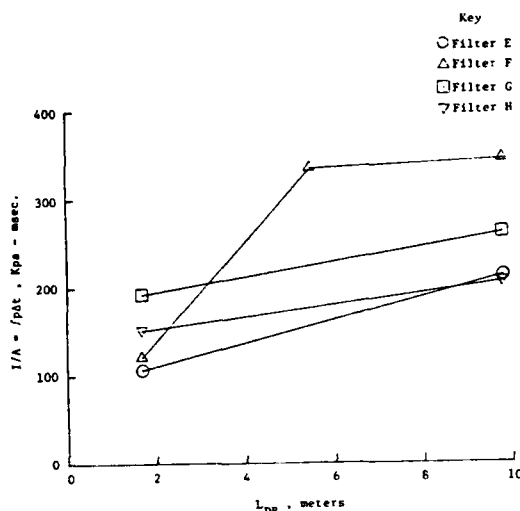


Figure 6 Shock Impulse Needed to Just Break HEPA Filters

Careful examination of the pressure records reveal that, for all the 1.68 meters (5.5 feet) long driver tests, filter failure occurred after the shock impulse had passed through (or more probably, had been absorbed by) the filter. In fact, in one case (F#32) failure did not occur until 212ms after the shock struck the filter. For the remainder of the cases, however, the failure occurred within 7 to 34ms after shock impingement. This would seem to imply that some other mechanism contributes to the failure of the filters at the short 1.68 meters (5.5 feet) driver length. The culprit could be air flow rate. The passage of the shock wave through the air of the tube causes the air to move in the same direction as the shock wave. The trailing expansion wave does not change the direction of this air movement (3).

Notice from Figure 3 the lowest PBRK at a 1.68 meter (5.5 feet) driver length was 10Kpa (1.45 psi) for the E filter. The air velocity behind a shock wave with this over-pressure is 28.17 m/sec. (94.39 ft/sec), or a flow rate through the filter of 641.41 m³/min (22,654 CFM). For the G filter, PBRK at a 1.68 meter (5.5 feet) driver length was 20.0Kpa (2.9 psi). The air velocity behind the shock wave with this over-pressure would be 52.18 m/sec. (171.1 ft/sec), or a flow rate through the filter of 1162.63 m³/min. (41,058 CFM). Our previous tornado testing of filters (4) showed that the flow rates through the filters reached a maximum value of 622.97 m³/min. (22,000 CFM) and that most filter failures occurred at flow rates below this value. Hence, because high residual air flow rates still persist after the passage of the shock impulse, it is probably this high flow rate with its attendant high stagnation pressure that causes failure of the filters.

The odd point on the F curve in Figure 6 may now be explainable. The value of I/A at LDR = 5.44 meters (17.83 feet) is the same as the value of I/A at LDR = 9.75 meters (32 feet) within the limits of error of the measurement ($\pm 37.26 \text{ Kpa-ms}$). That is, for long driver lengths it appears that the impulse needed to cause a filter to fail is constant for this type of filter. It would have been dangerous to generalize this statement to all types of HEPA filters from the small amount of data available for F filters. Therefore, four more tests were run, one each for filter types E, F, G and H, all at a driver length of 5.44 meters (17.83 feet). The shock over-pressures were selected from Figure 3, assuming a linear variation of the over-pressure just needed to break the filters with driver length. Table III summarizes the results of these runs.

If the data of Tables II and III are used to construct another plot of impulse per unit area, $I/A = \int p dt$, as a function of driver length LDR, then Figure 7 results. Notice that for filter types E, F and G, I/A is essentially the same for driver lengths 5.44 and 9.75 meters, supporting our hypothesis that for long driver lengths the shock impulse needed to just cause filter failure is constant for a particular type of filter. However, type H does not appear to support this statement. By examination of the expected error bands in Appendix A, we find for test H#54 the value of I/A is 179.88 Kpa-msec with an error band of approximately $\pm 82.42 \text{ Kpa-msec}$. The value of I/A at driver length 9.75 meters for H#25 is 206.85 Kpa-msec with an expected error of approximately $\pm 23.49 \text{ Kpa-msec}$. Thus, within the limits of accuracy of the experiments, H#54 and H#25 give the same results for I/A. There is, therefore, a strong probability that at long driver lengths the shock impulse needed to fail a particular type of filter is constant.

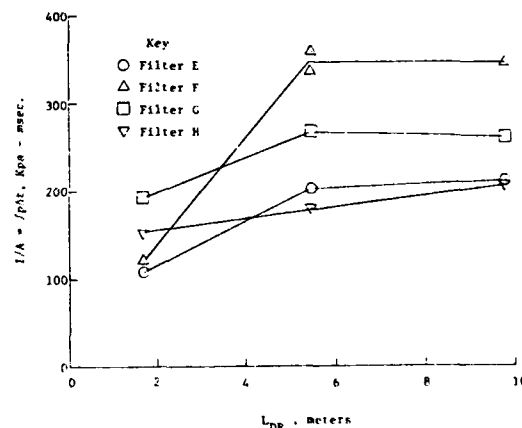


Figure 7 Shock Impulse Needed to Just Break HEPA Filters after Four Additional Tests at LDR = 5.44 m.

*The appendix presents the expected error of the experimental results.

Table III
Supplementary Test Data

Filter Mnf./Test No.	L _{DR} meters	P _{max} Kpa	Break?	$\frac{I}{A} = \int p \Delta t$ Kpa-msec.	Δt msec.
E#55	5.44	8.99	Yes	204.72	23
F#52	5.44	11.59	Yes	359.35	31
G#53	5.44	13.46	Yes	269.1	20
H#54	5.44	16.35	Yes	179.88	11

Thus, both shock impulse per unit area and air flow rate must be considered when designing filtration systems. If expected shock impulse per unit area at a location exceeds the maximum value (~350Kpa-msec) for long driver lengths given in Figure 7, then a filter at that location can be expected to fail structurally. If the shock impulse per unit area is below this value, then the flow rate of the air behind the shock wave should next be considered. If this flow rate exceeds 622.97 m³/min (22,000 CFM), then the filter can again be expected to fail structurally. Notice that these values of shock impulse per unit area and flow rate are maximums, i.e. only certain brands of HEPA filters were found capable of withstanding these imposed conditions. For example, from Figure 7 we see that the long driver length impulse per unit area for filter H was only about 200Kpa-msec. Hence, it would appear that a safety factor of at least two should be applied to the maximum shock impulse per unit area given by Figure 7.

CONCLUSIONS

1. In general, the shock over-pressure needed to cause structural failure of HEPA filters increases as the value of the driver length decreases.
2. At short driver lengths, failure occurs after the shock impulse has passed through or been absorbed by the filter. At long driver lengths, failure occurs during the shock impulse.
3. For short driver lengths there is some evidence that the high residual flow rate of air behind the shock wave might cause the failure of the filters, rather than the shock impulse. Further investigation of this point is strongly suggested since it will enter significantly into computer code predictions of ventilation system behavior during explosions.
4. A high probability exists that shock impulse needed to cause filter failure is constant for each type of filter at long driver lengths.
5. Filter manufacturer was a variable which

had significant effect upon filter failure.

Acknowledgements

The authors gratefully acknowledge Heidi Grothus, Paul Ricketts, Richard Lidh, Craig Ricketts, John Corkran and Kathy Ziehl for their efforts in operating the test facility, reducing data, and typing the manuscript.

REFERENCES

1. W. S. Gregory and P. R. Smith, "Response of Standard and High-Capacity HEPA Filters to Simulated Tornado and Explosive Transients", Los Alamos National Laboratory Report, LA-9210-MS, March 1982
2. W. L. Anderson and T. Anderson, "Effects of Shock Overpressures on High Efficiency Filter Units", 9th AEC Air Cleaning Conference, Vol. 1, Sept. 1966
3. Alan J. Chapman and William F. Walker, Introductory Gas Dynamics, Holt, Rinehart and Winston, New York, 1971
4. C. I. Ricketts, "Tornado-Model Testing of HEPA Filters", Master's Thesis, New Mexico State University, Dec. 1980

Appendix

Table of Expected Experimental Errors

Filter Mnf Test No.	$\int p \Delta t \pm \text{error}$ (msec. Kpa)		
B#1	491.61	+ 60.61,	- 59.37
C#3	377.29	+ 60.61,	- 59.37
C#4	314.41	+ 50.26,	- 49.02
D#6	583.87	+ 60.61,	- 59.37
A#7	66.74	+ 50.26,	- 49.02
A#8	166.17	+ 45.58,	- 44.47
C#9	521.26	+ 56.47,	- 55.23
B#10	609.52	+ 54.50,	- 53.16
C#11	428.87	+ 92.26,	- 89.77
F#12	405.43	+ 58.54,	- 57.30

Table of Expected Errors (con.)

Filter Mnf Test No.	$f_p \Delta t \pm \text{error}$ (msec . Kpa)		
G#14	222.01	+ 48.20,	- 46.95
C#15	375.01	+ 31.65,	- 30.41
A#17	229.6	+ 25.44,	- 24.20
G#21	222.71	+ 33.72,	- 32.48
G#22	362.01	+ 26.89,	- 20.06
H#24	333.72	+ 32.89,	- 31.65
H#25	206.85	+ 26.89,	- 20.06
E#27	213.75	+ 26.89,	- 20.06
D#30	317.86	+ 53.57,	- 52.33
F#32	136.52	+ 1.379,	- 2.07
F#33	120.66	+ 2.07,	- 2.07
E#36	103.43	+ 2.07,	- 13.79
E#37	107.56	+ 2.07,	- 2.07
G#41	192.37	+ 9.65,	- 41.37
H#43	151.0	+ 44.47,	- 59.16
D#47	535.74	+ 54.40,	- 53.16
F#48	345.44	+ 30.20,	- 28.96
F#50	335.10	+ 37.85,	- 36.61
F#52	358.54	+ 51.37,	- 59.99
G#53	268.91	+ 69.43,	- 68.40
H#54	179.75	+ 82.88,	- 81.84
E#55	204.57	+ 46.47,	- 45.44
Time: ± 3 msec			
Pressure:	0.207 Kpa	tests #1	- #30
	0.172 Kpa	tests #31	- #37
	0.103 Kpa	tests #38	- #40, #44, #46
	0.140 Kpa	tests #41	- #43
	0.040 Kpa	tests #45	
	0.124 Kpa	tests #47,	#49
	0.110 Kpa	tests #48	
	0.090 Kpa	tests #50	- #55

DISCUSSION

Voice: Is it an end line driver?

Mr. Smith: Yes, it is. It is a movable wall. It can be moved to within six inches of the diaphragm and back as far as about 40 feet away from the diaphragm. It is pneumatically sealed around the edge, and when we go up to very high pressure in the shock tube, you would never be able to hold that wall. So we have a set of spacers on wheels that we put in behind the wall, and all the forces transfer to the back of the tube. For instance, at our highest pressure possible, which is 400 psi in the driver, there is a half a million pounds of force that has to be put into that tube in tension. It is a lot of force. I don't think that this particular type of device, at least at this diameter, would be very feasible for much higher pressures than we can stand in this one, 400 psi.

A TECHNIQUE COMBINING HEATING AND IMPACT FOR
TESTING REENTRY VEHICLE IMPACT FUZES AT HIGH VELOCITIES

R. A. Benham
Sandia National Laboratories
Albuquerque, New Mexico

A laboratory testing technique has been developed for simulating the combined reentry aerothermal heating and high velocity impact effects on a ballistic missile warhead contact fuze system. This method consists of subjecting a stationary, instrumented nose tip to the flame of an aluminum powder-liquid oxygen torch system just prior to impact by an explosively propelled aluminum flyer plate target. This turnaround technique (the target moves to strike the stationary nose tip) has been used in the development of several advanced fuzing system designs. This paper describes the testing method and presents results from recent tests.

INTRODUCTION

Impact fuze sensors for reentry vehicle weapon systems are continually being developed. New performance and/or packaging requirements come with each new generation of weapon system. Methods of testing these new fuze designs have been developed that are used to understand the fuze operation. Rocket driven sleds can produce nose-tip velocities of up to 2.44 mm/ μ s (8000 ft/s) for impact into various targets. Explosively driven flyer plates can produce impacts of a target material onto a stationary nose tip at velocities of 1.83 to 4.20 mm/ μ s (6000 to 13800 ft/s). Plasma jets provide tests for investigating aerothermal heating, while underground nuclear tests and various other laboratory methods allow testing the effects of radiation on the fuze systems. Rocket flight tests provide a combination of environments experienced by the fuze system along the reentry vehicle trajectory.

Underground and flight tests give the most realistic environments but

they are very expensive, costing millions of dollars for each test. The laboratory methods have generally addressed only one environment at a time. Recently we have developed a laboratory technique which reasonably simulates the combined aerothermal heating and impact effects. This method is capable of providing impact velocities of 1.83 to 4.20 mm/ μ s and heating, on the order of 13×10^6 W/m². This combined technique has been used for the evaluation of several contact fuze systems allowing the recording of fuze functioning parameters after the fuze hardware has been subjected to the critical effects of aerodynamic heating. The test results obtained are timely, of reasonable cost (about \$50,000 for a test) in comparison to flight tests, and are capable of being repeated.

The new combined heating and impact simulation technique consists of subjecting an instrumented nose tip to the flame of an aluminum powder-liquid oxygen torch system for 15 s. With the torch still burning, a metallic flyer plate, which has been

accelerated by a barrel-confined explosive system, impacts the nose tip, thus simulating conditions when an aerothermally heated reentry vehicle strikes a hard, ground target. The timing and flame conditions are selected to approximate the temperature profile along the nosetip axis at the time of impact in a real reentry vehicle. The flyer is designed to rotate end over end as it travels along its trajectory, permitting impacts on the nose tip at any desired angle (between 30° and 90°) of the flyer plate face with respect to the nose-tip axis.

This report describes the combined test method presenting data from two tests that have been conducted. Temperature profiles recorded from embedded thermocouples adjacent to the nose-tip axis is presented along with flash x-ray data of flyer plate impact conditions. Impact velocities of 3.05 and 4.21 mm/ μ s (10,000 and 13,800 ft/s) have been attempted. Sacrificial barriers required to house the 45.4-kg and 90.8-kg (100-lb and 200-lb) explosive charges also are briefly described.

NOSE-TIP HEATING

During the reentry phase of a ballistic missile trajectory, the nose-tip experiences rapid aerothermal heating. The majority of heating occurs during the last few tens of seconds before impact and generates temperatures high enough to cause surface material ablation. The nose tip may experience heat fluxes of several ten millions of W/m^2 (several thousand $Btu/ft^2/s$) with peak fluxes occurring at altitudes above a few tens of thousands of meters (several hundreds of thousands of feet). The rapid heating generates extreme temperature gradients from the surface into the nose-tip material. The temperature experienced along the nose-tip axis of a particular reentry vehicle is dependent on the design and material properties of the nose tip, the ballistic parameters of the flight path, along with many other variables. Past flight test data and analysis lead to estimates of the temperature profile on a new system. The temperature profile along the axis and the shape of the ablated nose tip at impact are the specific conditions that would be reproduced in an adequate laboratory simulation of aerothermal heating. The nose tips to be impacted in our tests are

machined to a calculated or empirically determined ablated shape. We do not attempt to match the heat flux history experienced by a reentering nose tip.

An aluminum powder-liquid oxygen torch system was used to provide the simulated aerothermal heating effect for the combined heating/impact tests. The torch system (schematic shown in Figure 1) was purchased from Science Applications Incorporated by Sandia National Laboratories; the nozzle design is changed to meet Sandia needs. The details of the torch operation are documented in a Sandia internal memoranda [1]. The torch operates by burning 3- μ m to 40- μ m atomized aluminum powder in oxygen producing a theoretical maximum flame temperature of 3900 K (6560 F).

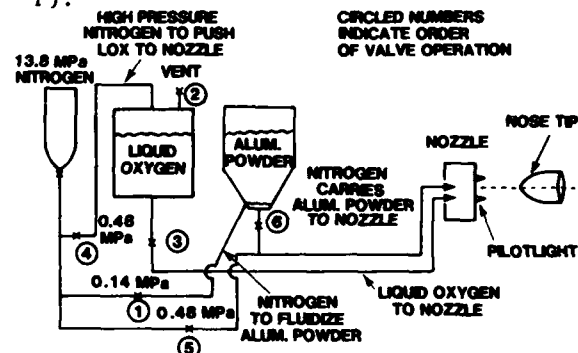


Fig 1 - Schematic of the Aluminum-Oxygen Torch System

The torch performance was measured during several preliminary tests to obtain approximate heat flux input levels to the carbon nose-tip material. Figure 2 shows the torch in operation for one of these tests. A flat carbon slab, instrumented with embedded thermocouples, was used as a

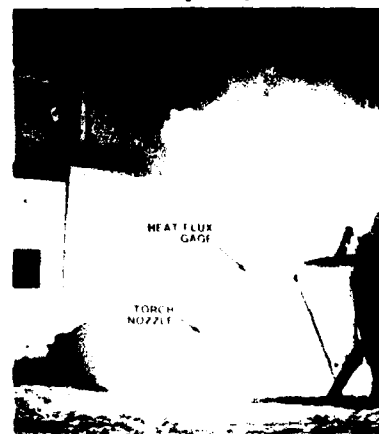


Fig 2 - Aluminum-Oxygen Torch

heat-flux gage. Measured temperatures along with thermal properties of the carbon material allowed estimates of the flux that would cause the observed temperature gradients. A flux level of $5.67 \times 10^6 \text{ W/m}^2$ (500 Btu/ft²/s) was determined from these tests. This heat flux, when applied to a simple, semi-infinite carbon, plane model, showed that a 15-s burn would give a reasonable approximation to the temperature profile experienced in a real reentry situation.

The torch system used in the combined heating/impact test consisted of two nozzles separated by 0.50 m (19.8 in) to allow the flyer plate to pass between them on its trajectory to impact. Figure 3 shows the orientation of the torch heads and nose tip for these tests. Further details of these tests can be found in Sandia test reports [2,3].

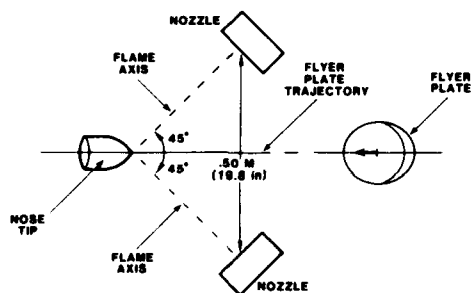


Fig 3 - Plan View of Torch Nozzle Setup

The axis of each nozzle was oriented at 45° to the flyer plate trajectory with the nose tip placed at the intersection of the nozzle axes and flyer plate trajectory. The two nozzles aimed at the nose tip produced an axial flow of combustion products over the nose tip causing nearly axisymmetric heating to be generated. Figure 4 shows a photograph of the nozzle setup for the combined test.

NOSE TIP THERMAL INSTRUMENTATION

The nose tip for the combined test consisted of a graphite cone with a spherical 76.2-mm (3-in) diameter tip. The geometry and material were chosen to be like reentry nose tips, but do not represent any particular system. Three thermocouples were imbedded in the carbon using carefully machined carbon plugs. All voids were filled with carbon cement to minimize the effect

of the installation on the heat flow within the carbon nose tip. After the thermocouples were installed the junction location (from the surface) was precisely measured using an x-ray picture of the nose tip. Figure 5 shows the x-ray of the thermocouples within the carbon material. The thermocouples used were tungsten-tungsten 26% rhenium with a tantalum sheath. The junction is at the end of the sheath tube. These thermocouples are very small (0.203 mm (0.008 in) diameter) and are capable of monitoring temperatures up to 3000 K (5000 F)*

The thermocouples were used in two ways. The first was to obtain data to define the temperature profile down the nose-tip axis at various times. In a test of an actual reentry vehicle nose tip, this data would be compared to expected profiles. The second was to use the temperature histories, at the known positions, in an inverse heat transfer computer code [4] to calculate the surface temperature and heat flux histories at the nose-tip surface. The calculated surface temperature was used with the thermocouple data to complete the temperature profile data.

EXPLOSIVE FLYER PLATE SYSTEM

The barrel tamped explosive flyer plate system for launching rotating metallic flyer plates has been described in several previous papers [5,6,7]. Essentially a heavy metallic barrel houses the Composition C-4 explosive and flyer plate. The barrel confines the detonation gases long enough to drive the plate to the desired velocity while retarding the lateral gas expansion that contribute to flyer plate break-up. A single-point initiation is used to drive a spherically expanding detonation front toward the flyer plate location.

A recent change in the barrel design consists of a steel-jacketed lead barrel instead of cast iron or steel barrels used in the past. The lead barrel system provides nearly the same degree of confinement as the cast iron barrels recently used. The cost of the lead system, as well as the procurement lead time, are

*Paul Beckman Co., 944 Hendretta Ave., Huntingdon Valley, PA 19006; Bulletin CA-1, "Carbon/Ablator In-depth Thermal Sensors"

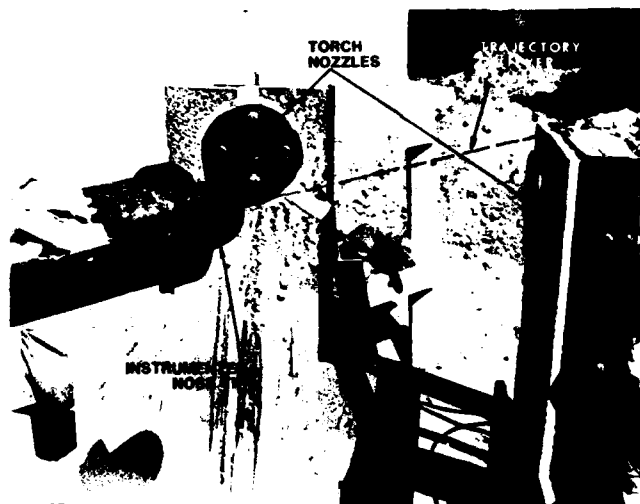


Fig 4 - Nozzle Setup for Combined Test

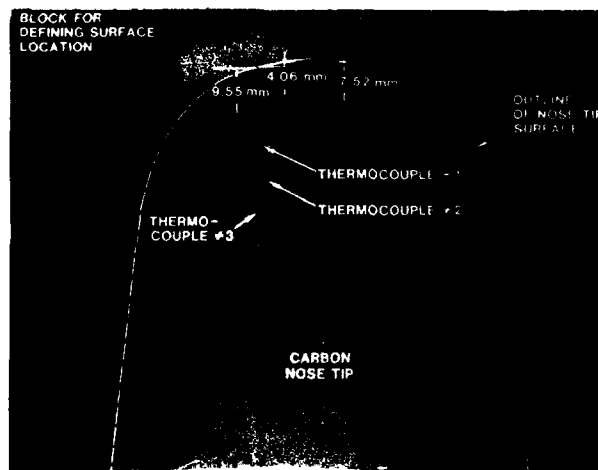


Fig 5 - X-Ray of Thermocouples Within Carbon Nose Tip

significantly less than for the cast iron. Several small scale models of this new lead barrel system were tested [8,9] to demonstrate that even at velocities of $4.63 \text{ mm}/\mu\text{s}$ ($15,200 \text{ ft/s}$) (an extension of the flyer plate velocity capability), the design performed properly. Figure 6 shows a flash x-ray exposure taken during the 1/4-scale model tests for the $4.20 \text{ mm}/\mu\text{s}$ ($13,800 \text{ ft/s}$) test where the high velocity was achieved and the predictions of flyer performance were accurate.

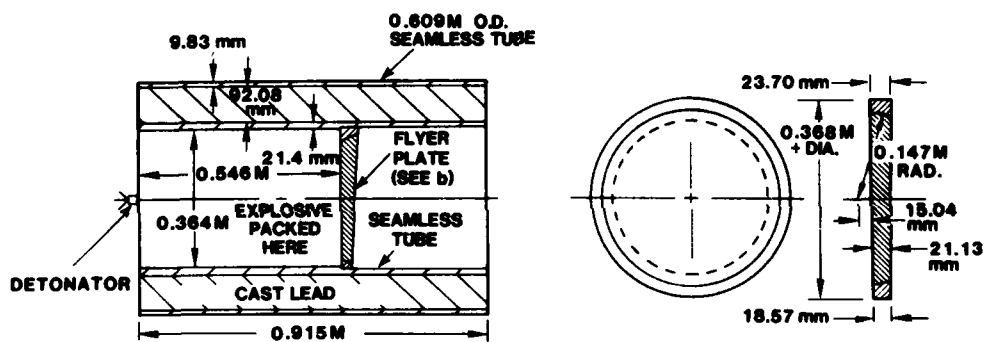
Figure 7 shows a sketch and Figure 8 is a photograph of the explosive barrel system for the 90.812-kg (200 lb) explosive charge used for the combined heating/impact tests. The barrel weighed 1816 kg (4000 lb). The flyer plate was 0.368 m (14.5 in) in diameter and

weighed 5.90 kg (13 lb) for the $4.20 \text{ mm}/\mu\text{s}$ ($13,800 \text{ ft/s}$) impact test. The cushion, which in previous designs was placed between the explosive and flyer plate, was removed in order to achieve higher terminal velocity.

A new method for calculating the launch time and excess rotation angle during launch has been developed [10]. These parameters are used to calculate the motion of the flyer plate. As the flyer plate travels through air, its velocity and rotation rate during the first 90° of rotation are reduced significantly by the effects of air drag. Since impact occurs within the first 90° of rotation, this effect is important. Figure 9 shows the shock wave which rides on the leading edge of the plate as it travels through air. The

ALUMINUM
FLYER PLATE

Fig 6 - Flash X-Ray of 4.20 mm/ μ s Flyer Plate



a) BARREL

b) FLYER

Fig 7 - Sketch of Explosive System

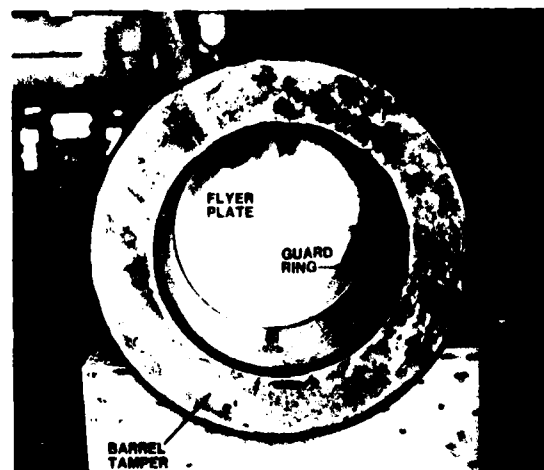


Fig 8 - 90.8 Kg Explosive Flyer Plate System

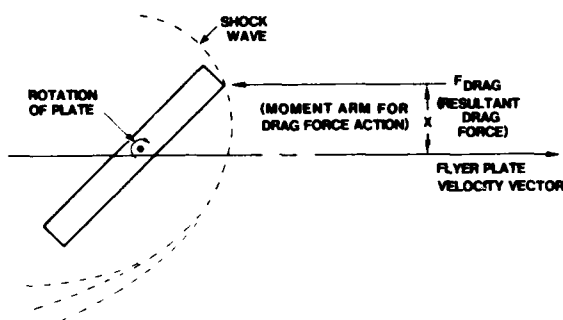


Fig 9 - Drag Forces on Rotating, High Velocity Flyer Plate

drag forces, F_D , are applied to the plate through the center of pressure which approaches the leading edge of the plate as the plate rotates. The moment $F_D \times X$ works to decrease the rotation rate while the force F_D reduces the average plate velocity. Full analysis of these effects have not been accomplished since the introduction of a helium atmosphere around the trajectory essentially eliminates these forces and is easy to accomplish. Results of the scale tests [8], where a helium atmosphere was used, show excellent agreement between the measured and calculated velocity and rotation rate. A mylar tube helium envelope was, therefore, used for the full-scale tests.

PROTECTIVE BARRIER

The explosive charge contains a large amount of metal which turns into intermediate velocity shrapnel (0.61 to 0.91 mm/ μ s (2000 to 3000 ft/s)). A protective barrier was provided to reduce shrapnel hazard to the surrounding area. Figure 10 shows the front of the barrier. A 1.52-m (5-ft) diameter and 2.13-m (7-ft) long corrugated culvert section provided the inside walls for the structure. The explosive barrel assembly was positioned inside the culvert. The barrel and culvert axes were parallel. The end walls were made of 19 mm (3/4 in) thick plywood boards and were held together with wire rope. The volume between the end walls was filled with sand. The minimum depth of sand around the culvert wall was 1.83 m (6 ft). The back end of the tubular opening was vented but plugged with a dirt-filled box. The front end contained an aperture to allow the flyer plate to exit (0.46 x 0.46 m (18 x 18 in)). The remainder of the debris traveling in the general direction of the flyer plate was retarded by a 0.46-m

(18-in) thick layer of sand. The shrapnel hazard distance was calculated by first estimating the shrapnel terminal velocity from the explosive system using Gurney equations. Conservation of momentum was used to obtain the particle exit velocity from the sand. Air drag trajectory calculations then predict the hazard range. The hazard range for this configuration was 650 m (2000 ft).

COMBINED TEST

For the high-velocity, combined heating/impact test the nozzles of the aluminum-oxygen torch were positioned on either side of the flyer plate trajectory so that the nozzle axes intersected at the impact location on the nose tip (see Figure 3). The nose tip was positioned in front of the barriered, explosive flyer plate system at a distance which allowed the plate to rotate to a 35° angle at impact. The plate velocity was 4.20 mm/ μ s (13,800 ft/s); the rotation rate was 900 rps and the transit distance was 4.57 m (15 ft). Figure 11 shows a diagram of the relative positions of the barrier, torch nozzles, and nose tip. Figure 12 shows a photograph of the test setup. A helium filled mylar cylinder provided the low drag atmosphere. The helium tube, however, could not enclose the flame and was, therefore, terminated 0.30 m (1 ft) in front of the line joining the two nozzles. Figure 13 shows a photo of the helium tube in place.

The end closure of the tube was specially designed to withstand the tremendous heat of the torch but not to interfere with the flyer motion. Six layers of commercial aluminum foil separated by air gaps were positioned at the same angle, with respect to the trajectory, that the flyer plate would have at that location. The layers melted sequentially through the 15-s burn time until only two sheets were left at explosive initiation. The flyer uniformly impacted the remaining sheets with no measurable effect on its motion. The last 2 ft of flyer motion was in air and torch products.

Three flash x-ray exposures were obtained to verify plate condition and orientation. The setup and laser alignment methods for this test were as described in past experiments [5,6,8,9].

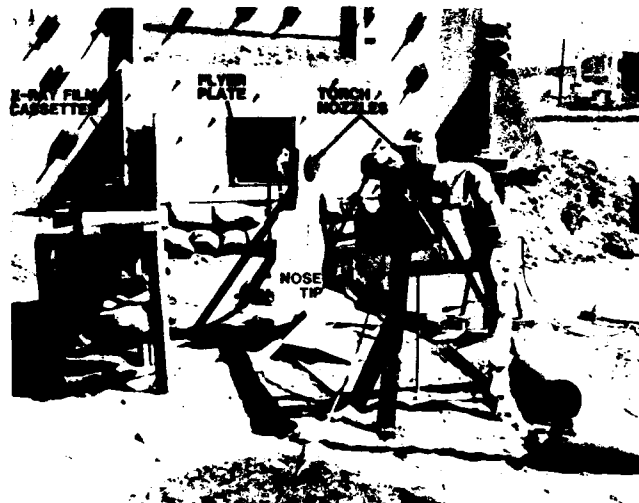


Fig 10 - Front View of Protective Barrier

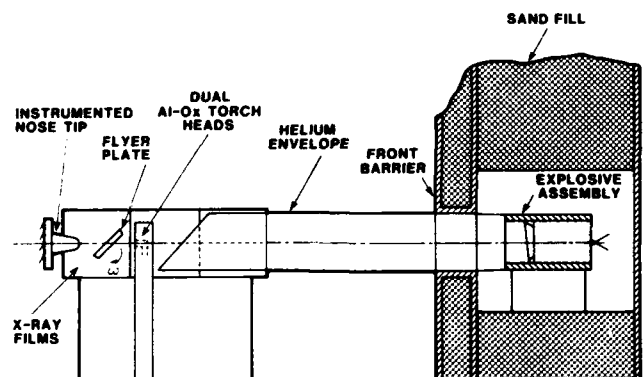


Fig 11 - Impact Fuze Test Setup

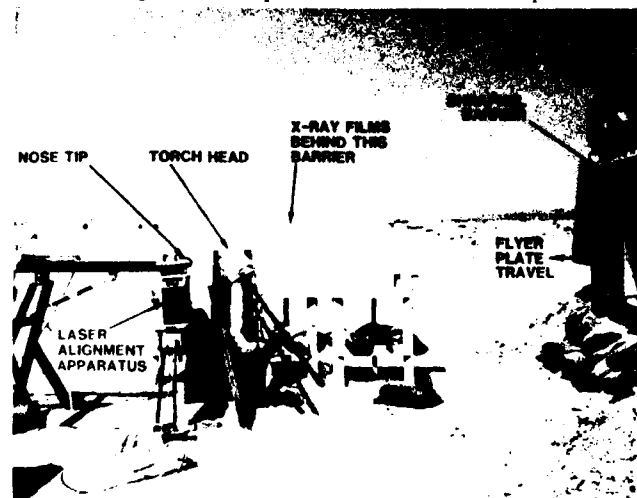


Fig 12 - Test Setup Without Helium Envelope

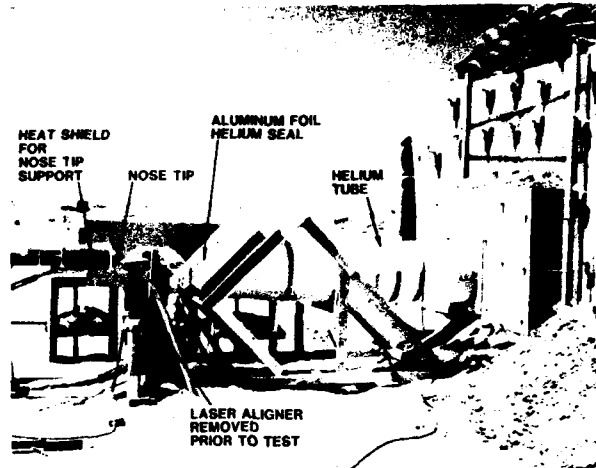


Fig 13 - Test Setup With Helium Tube in Place

RESULTS

Two tests have been conducted: one with an impact velocity of 3.05 mm/ μ s (10,000 ft/s) and impact orientation of 90°, and the other with an impact velocity of 4.20 mm/ μ s (13,800 ft/s) and an impact angle of 35°. The heating data was nearly the same for both tests. Figure 14 shows the temperature histories for the three thermocouples located as shown in Figure 5. Figure 15 shows the temperature profile at two different times. Figure 16 shows the calculated surface temperature using the inverse heat transfer calculations mentioned above. Figure 17 shows the calculated heat flux at the surface from the same set of calculations.

Figure 18 shows an x-ray of the flyer plate just before impact, while

in the torch area (10,000 ft/s 90° test).

CONCLUSIONS

To date, two combined heating/impact tests have been conducted on various contact fuze systems. Through these tests we have demonstrated for the first time the ability to accomplish a dual test simulating both reentry heating and impact shock effects on a reentry fuze system. The heating to a specific nose tip has been quantified and is of sufficient magnitude to be of interest to system designers. Future tests are being considered to qualify different contact fuze systems.

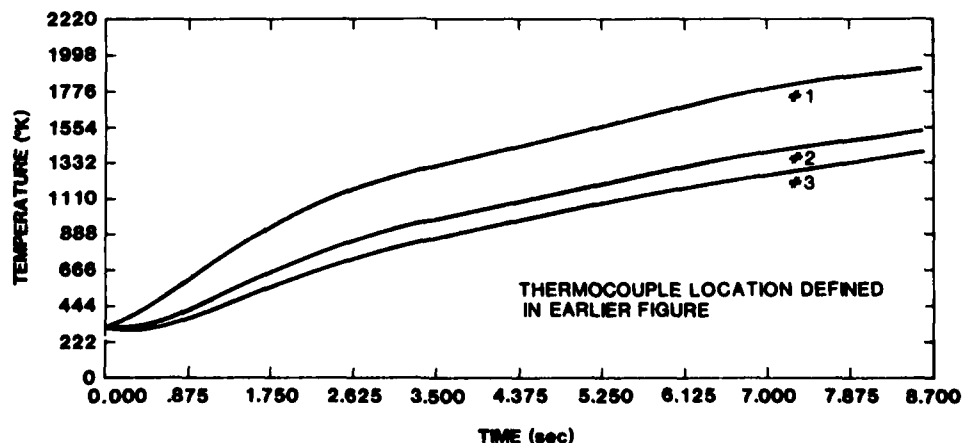


Fig 14 - Imbedded Thermocouple Data

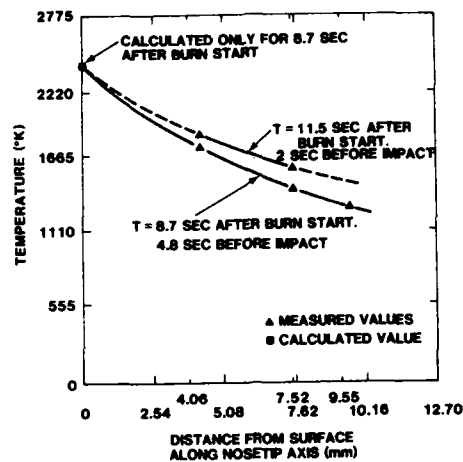


Fig 15 - In-Depth Temperature Profiles Before Impact

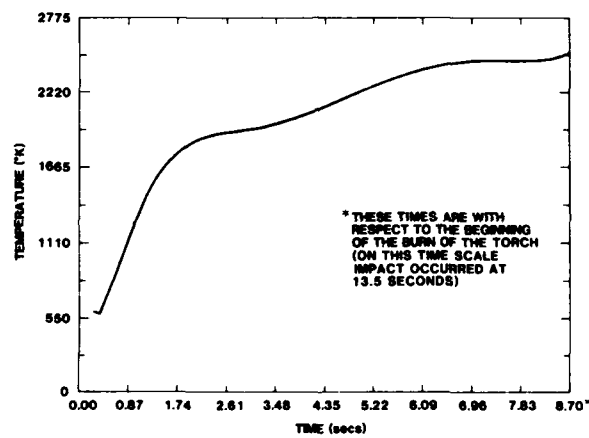


Fig 16 - Nose Tip Surface Temperature History, Calculated From Thermocouple Data

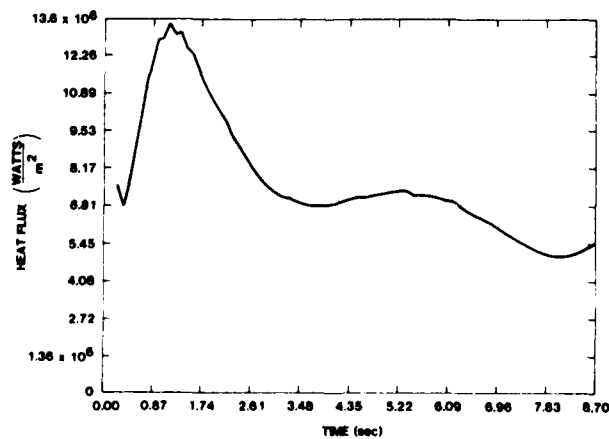


Fig 17 - Heat Flux to Nose Tip, Calculated From Thermocouple Data

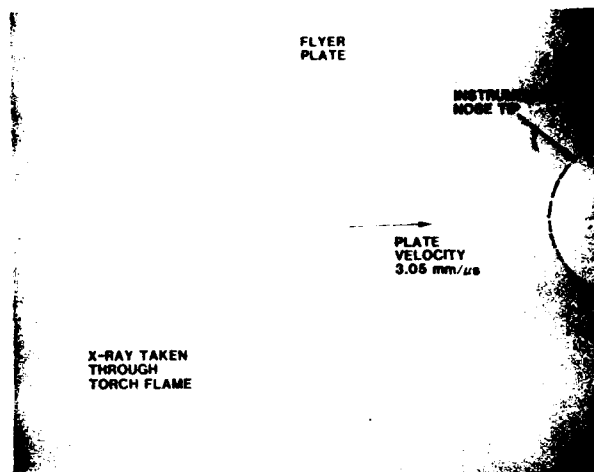


Fig 18 - Flash X-Ray Exposure of Flyer Plate Prior Impacting Nose Tip

ACKNOWLEDGMENTS

The author expresses appreciation to fellow Sandia National Laboratories employees who made these tests possible: Walt Gill, Russ Acton, and Jim Beck (Michigan State University) for providing the direction required in obtaining the heating calculations; to Glenn Perdue for providing site preparation and test

operation; to Dave Shirey for providing the torch operation; to Ben Duggins for test instrumentation and assistance in making the heating calculations; and to Jeana Pineau for her patience and support in preparing the paper. Walt Gill was also instrumental in obtaining the torch system and in characterization of its performance.

REFERENCES

1. D. L. Shirey, "An Aluminum Powder/Liquid Oxygen Torch for Reentry Simulation Heating," Sandia National Laboratories internal memorandum of record, May 26, 1981
2. R. A. Benham, "Combined Heating/Impact Test of a Simulated Reentry Vehicle Nose Tip, Test 10-DFT-90-10,000," Sandia National Laboratories internal letter report to Electro-Optics Division, Dec. 10, 1980
3. R. A. Benham, "Combined Heating/Impact Test of a Simulated Reentry Vehicle Nose Tip, Test 11-T-35-14,000," Sandia National Laboratories internal letter report to Electro-Optics Division, Aug. 1981
4. James V. Beck, "Nonlinear Estimation Applied to the Nonlinear Inverse Heat Conduction Problem," International Journal of Heat Conduction and Mass Transfer, Vol 13, pp. 703-715, 1970
5. F. H. Mathews and B. W. Duggin, "Barrel-Tamped, Explosively Propelled Plates for Oblique Impact Experiments," Shock and Vibration Bulletin, No. 46, Part 2, pp. 145-154, Aug. 1976
6. F. H. Mathews and B. W. Duggin, "Barrel-Tamped Explosively Propelled Rotating Plastic Plates," Shock and Vibration Bulletin, No. 47, Part 1, pp. 113-119, Sept. 1977
7. R. A. Benham, "Terminal Velocity and Rotation Rate of a Flyer Plate Propelled by a Tube-Confined Explosive Charge," Shock and Vibration Bulletin, No. 49, Part 2, pp. 193-201, Sept. 1979
8. R. A. Benham, "1/4 Scale Test of 200 Pound Cast Lead Barrel Explosive Flyer Plate System," Sandia National Laboratories internal letter report to Electro-Optics Division, July 7, 1981
9. D. H. Hill, "1/6 Scale Explosive Flyer Plate Tests" Sandia National Laboratories internal letter report to R. A. Benham, Sept. 2, 1980.
10. R. A. Benham, "Method of Calculating Launch Time and Excess Rotation Angle during the Launch of Rotating Flyer Plates," Sandia National Laboratories memorandum of record, Jan. 12, 1982.

USE OF A DROPPED WEIGHT TO SIMULATE A NUCLEAR SURFACE BURST

Charles R. Welch and Sam A. Kiger
U. S. Army Engineer Waterways Experiment Station
Corps of Engineers
Vicksburg, Mississippi

This paper investigates analytically and experimentally the use of a dropped weight for the simulation of the airblast generated ground shock from a nuclear surface burst. A one-dimensional elastic analytical model of the weight impacting the soil is presented. It indicates that the peak stress induced in the soil is a function of the square root of the drop height and the ratio of acoustic impedances of the dropped weight and soil. Also the impulse generated in the soil is dependent on the thickness and density of the slab and the square root of the drop height. Relations are then developed between the one-dimensional elastic solution and empirical curves for the peak airblast pressure and impulse from a nuclear surface burst. It is found that the peak pressure and impulse can be simulated simultaneously for weapons in the kiloton range to about 1000 psi overpressure. Measured stress and particle velocity wave forms from a series of dropped-weight tests are presented along with the calculated stress wave forms. The tests consisted of dropping two concrete slabs, 12 and 19.5 in. thick by 50 in. in diameter, onto a sand test bed from drop heights of 2-1/2 and 10 ft. It is found that differences between the measured and calculated stress wave forms were due primarily to the nonplanarity of impact of the dropped weight. Limitations and difficulties associated with the dropped-weight simulation technique are discussed as well as problems with displacement boundary conditions, impact planarity requirements, and the smallness of the test bed. Applications of the drop-weight technique to the testing of model underground structures are discussed.

INTRODUCTION

The Limited Nuclear Test Ban Treaty of 1963 prohibited detonation of nuclear devices in the atmosphere. Since then various schemes have been developed to simulate different characteristics of the airblast from nuclear explosions. These include: (1) the Dynamic Airblast Simulator (DABS) described by Martens and Bradshaw [1] which simulates the dynamic drag forces associated with nuclear airblasts; (2) the High Explosive Simulation Technique (HEST) described by Wampler, et al. [2] which simulates the overpressure generated by a nuclear airblast; and, (3) the Direct Induced High Explosive Simulation Technique (DIHEST) which is described by Schlater [3] and is intended to simulate the directly induced horizontal ground shock near the nuclear detonation.

These simulation techniques use large high explosive charges as their energy source; therefore, the test must be performed at remote sites. The energy produced by high explosives and the rate of deposition of that

energy can vary from test to test depending on the type of detonation (high or low order) and the containment of the explosive. Conversely, using a disc-shaped slab dropped onto the soil surface as an energy source has the advantage of being useful in the laboratory. The use of dropped weights to produce ground shock is not new. In 1973, Wallace and Fowler [4] used dropped spheres of various sizes and densities to simulate the far-field seismic motions generated by explosions. In 1976, Ford [5] made correlations between the near-surface vertical velocity wave forms produced by dropping a steel wrecking ball onto sandstone and those wave forms induced by a surface tangent spherical explosive charge.

This paper investigates the use of the flat-dropped weight to simulate ground shock generated by a nuclear surface burst. Some of this material is extracted from an M.S. thesis written by Welch [6]. A one-dimensional elastic wave treatment of the impact problem is presented. Correlations are made between this solution and nuclear airblast predictions by Crawford, et al. [7].

These correlations lead to analytical expressions which relate the parameters of a dropped weight (i.e., density, thickness, drop-height, etc.) to a given yield of nuclear weapon at a given pressure range. The ground motion data from a series of eight dropped-weight tests are then presented and compared to the results of the one-dimensional elastic wave treatment. Limitations of the dropped-weight simulation technique are discussed.

ONE-DIMENSIONAL ELASTIC SOLUTION

The following solution to the drop weight is from Drake [8]. Another solution, obtained without using transforms, is by Welch [6]. Port [9] also obtained the same solution. Gutzwiller [10] developed a solution in terms of harmonic modes.

In the dropped-weight problem shown in Figure 1 a slab of dilatational velocity c_1 ,

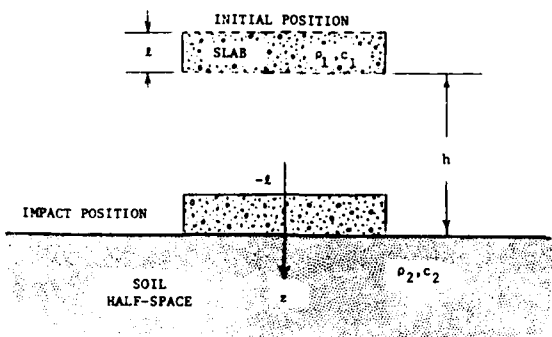


Figure 1 - Schematic of the dropped-weight problem

density ρ_1 , and thickness x , falls through a height, h , onto a soil half space of dilatational velocity c_2 and density ρ_2 . The velocity at impact, v_0 , is:

$$v_0 = \sqrt{2gh} \quad (1)$$

where g is the acceleration due to gravity. The following are assumed:

1. The slab has velocity components only in the vertical direction (i.e., there are no rotational or shear components).
2. The face of the slab and the soil surface are parallel at the time of impact.
3. The soil and the slab are considered linear and elastic.
4. Displacement occurs only in the z direction and is a function only of z (i.e., there are no edge effects).
5. The soil is considered to be a

half space; there are no reflections from a back surface.

6. The slab and soil are always in perfect contact (i.e., no bouncing occurs).

7. $\rho_1 c_1 > \rho_2 c_2$ (This is assured by Assumption 6.) We will let $u_1(z, t)$ be the displacement in the slab and $u_2(z, t)$ be the displacement in the soil. As a result of Assumptions 1 through 4 the equation of motion becomes

$$u_{1tt} = c_1^2 u_{1zz} \quad (2)$$

$$u_{2tt} = c_2^2 u_{2zz} \quad (3)$$

where differentiation with respect to a variable is indicated by a subscript (i.e., $\partial u_1 / \partial z = u_{1z}$). The initial conditions for the slab and soil are

$$u_1(z, 0) = 0 \quad (4)$$

$$u_{1t}(z, 0) = v_0 \quad (5)$$

$$u_2(z, 0) = 0 \quad (6)$$

$$u_{2t}(z, 0) = 0 \quad (7)$$

Boundary conditions at the slab/soil interface (i.e., at $z = 0$) also assume that the back surface of the slab is free of stress. For the one-dimensional case, the stresses in the two media σ_1, σ_2 are given by $\sigma_1 = c_1^2 \rho_1 u_{1z}$ and $\sigma_2 = c_2^2 \rho_2 u_{2z}$. The boundary conditions are written as:

$$c_1^2 \rho_1 u_{1t}(0, t) = c_2^2 \rho_2 u_{2z}(0, t) \quad (8)$$

$$c_1^2 \rho_1 u_{1t}(-l, t) = 0 \quad (9)$$

$$u_1(0, t) = u_2(0, t) \quad (10)$$

The assumption of the soil being a half space leads to the final constraint on the problem; that the displacements in the soil remain finite as z tends to infinity, i.e.,

$$\lim_{z \rightarrow \infty} u_2(z, t) \text{ is finite} \quad (11)$$

Using a bar over a variable to designate the Laplace transform of that variable, the Laplace transforms, with respect to time, of Equations 2 and 3 are written as:

$$s^2 \bar{u}_1(z, s) - s u_1(z, 0) - u_{1t}(z, 0) = c_1^2 \bar{u}_{1zz}(z, s) \quad (12)$$

$$s^2 \bar{u}_2(z, s) - s u_2(z, 0) - u_{2t}(z, 0) = c_2^2 \bar{u}_{2zz}(z, s) \quad (13)$$

Using Equations 4 through 7 in Equations 12 and 13 produces

$$\bar{u}_{1zz}(z, s) - \frac{s^2}{c_1^2} \bar{u}_1(z, s) = -v_0 \left(\frac{1}{c_1^2} \right) \quad (14)$$

$$\bar{u}_{2zz}(z, s) - \frac{s^2}{c_2^2} \bar{u}_2(z, s) = 0 \quad (15)$$

The general solutions to Equations 14 and 15 are

$$\bar{u}_1(z, s) = A_1 \exp\left(-\frac{s}{c_1} z\right) + B_1 \exp\left(\frac{s}{c_1} z\right) + \frac{1}{s^2} v_0 \quad (16)$$

$$\bar{u}_2(z, s) = A_2 \exp\left(-\frac{s}{c_2} z\right) + B_2 \exp\left(\frac{s}{c_2} z\right) \quad (17)$$

Taking the Laplace transform of the boundary conditions 8, 9, and 10, and the radiation condition 11, produces

$$c_1^2 \bar{u}_{1z}(0, s) = c_2^2 \bar{u}_{2z}(0, s) \quad (18)$$

$$c_1^2 \bar{u}_{1z}(-\ell, s) = 0 \quad (19)$$

$$\bar{u}_1(0, s) = \bar{u}_2(0, s) \quad (20)$$

$$\lim_{z \rightarrow \infty} \bar{u}_2(z, s) \text{ is finite} \quad (21)$$

Using Equation 21 in 17 gives

$$B_2 = 0 \quad (22)$$

From Equations 19 and 16

$$A_1 = B_1 \exp\left(-\frac{s}{c_1} 2\ell\right) \quad (23)$$

And from Equations 23 and 16

$$u_1(z, s) = B_1 \left[\exp\left(-\frac{s}{c_1} (2\ell + z)\right) + \exp\left(\frac{s}{c_1} z\right) \right] + \frac{1}{s^2} v_0 \quad (24)$$

Employing the displacement boundary condition (Equation 20) along with Equations 17, 22, and 24 produces

$$B_1 \left[\exp\left(-\frac{s}{c_1} 2\ell\right) + 1 \right] + \frac{1}{s^2} v_0 = A_2 \quad (25)$$

Using the stress boundary condition (Equation 18) along with Equations 24, 17, and 22 gives

$$c_1^2 B_1 \left[\left(-\frac{s}{c_1}\right) \exp\left(-\frac{s}{c_1} 2\ell\right) + \frac{s}{c_1} \right] = c_2^2 A_2 \left(-\frac{s}{c_2}\right)$$

Employing Equation 25 in the above, along with some algebra, produces

$$B_1 = \frac{-\frac{1}{s^2} v_0}{K \left[1 - \exp\left(-\frac{s}{c_1} 2\ell\right) \right] + \left[1 + \exp\left(-\frac{s}{c_1} 2\ell\right) \right]} \quad (26)$$

where

$$K = \frac{c_1^2 \rho_1}{c_2^2 \rho_2} \quad (27)$$

Using Equations 22, 25, and 26 in Equation 17 gives

$$\bar{u}_2(z, s) + \frac{1}{s^2} v_0 \frac{K}{(1+K) + (1-K) \exp\left(-\frac{s}{c_1} 2\ell\right)} \exp\left(-\frac{s}{c_2} z\right) \quad (28)$$

Dividing numerator and denominator of the above by $(1+K)$, and letting $R = (1-K)/(1+K)$, we have

$$\bar{u}_2(z, s) = \frac{K}{(1+K)} \frac{v_0}{s^2} \left[\frac{\exp\left(-\frac{s}{c_2} z\right) - \exp\left(-\frac{s}{c_1} 2\ell - \frac{s}{c_2} z\right)}{1 + R \exp\left(-\frac{s}{c_1} 2\ell\right)} \right] \quad (29)$$

Since $R \exp\left[-(s)/(c_1) 2\ell\right]$ is less than 1, we have (see Selby [11])

$$\frac{1}{1 + R \exp\left(-\frac{s}{c_1} 2\ell\right)} = \sum_{n=0}^{\infty} (-R)^n \exp\left(-\frac{s}{c_1} 2\ell n\right) \quad (30)$$

From Equations 30 and 29

$$\bar{u}_2(z, s) = \frac{K}{(1+K)} \frac{v_0}{s^2} \sum_{n=0}^{\infty} (-R)^n \left[\exp\left(-s \left(\frac{2\ell n}{c_1} + \frac{z}{c_2}\right)\right) - \exp\left(-s \left(\frac{(n+1)2\ell}{c_1} + \frac{z}{c_2}\right)\right) \right] \quad (31)$$

Taking the inverse Laplace transform of the above (see Churchill [12]) we have for the displacement in the soil

$$u_2(z, t) = \frac{K}{(1+K)} v_0 \sum_{n=0}^{\infty} (-R)^n \left[H_1 \left(t - \frac{2\ell n}{c_1} + \frac{z}{c_2} \right) - H_1 \left(t - \frac{(n+1)2\ell}{c_1} + \frac{z}{c_2} \right) \right] \quad (32)$$

where H_1 is the ramp function defined by

$$H_1(t - m) = t - m \quad \text{for } t - m \geq 0 \quad (33)$$

$$= 0 \quad \text{otherwise}$$

While Equation 32 provides the displacements in the soil due to the dropped weight, we are more interested in the generated soil stresses. Thus differentiating Equation 32 with respect to z and multiplying by $c_2^2 \rho_2$ produces

$$\sigma_2(z, t) = \frac{c_2^2 \rho_2 K}{(1+K)} v_0 \left(\frac{1}{c_2} \right) \sum_{n=0}^{\infty} (-R)^n \left[H \left(t - \frac{2\ell n}{c_1} + \frac{z}{c_2} \right) - H \left(t - \frac{(n+1)2\ell}{c_1} + \frac{z}{c_2} \right) \right] \quad (34)$$

where H is the heavyside step function defined by

$$H(t - m) = 1 \quad \text{for } (t - m) \geq 0$$

$$= 0 \quad \text{otherwise}$$

In deriving Equation 34 we utilized the fact that

$$H_{1z} \left(n + \frac{z}{a} \right) = \frac{1}{a} H \left(n + \frac{z}{a} \right)$$

Focusing our attention on the stress in the soil at the interface (at $z = 0$) and recalling that the usual acoustic transmission coefficient, T , is given by

$$T = \frac{2c_2 \rho_2}{c_2 \rho_2 + c_1 \rho_1}$$

Equation 34 becomes

$$\sigma_2(t) = \frac{v_0}{2} \rho_1 c_1 T Z \quad (35)$$

where

$$Z = \sum_{n=0}^{\infty} (-R)^n \left[H \left(t - \frac{2\ell n}{c_1} \right) - H \left(t - \frac{(n+1)2\ell}{c_1} \right) \right] \quad (36)$$

Because of Assumption 7, R is strictly negative, hence $-R$ is strictly positive, and the terms of the series in Equation 36 are all positive. A plot of Z versus time is shown in Figure 2. It is seen that it is equally well represented by

$$Z = (-R)^{\text{int} \left[\frac{c_1 t}{2\ell} \right]} \quad (37)$$

where $\text{int} \left[\frac{c_1 t}{2\ell} \right]$ is defined as the largest positive integer $n \leq \frac{c_1 t}{2\ell}$.

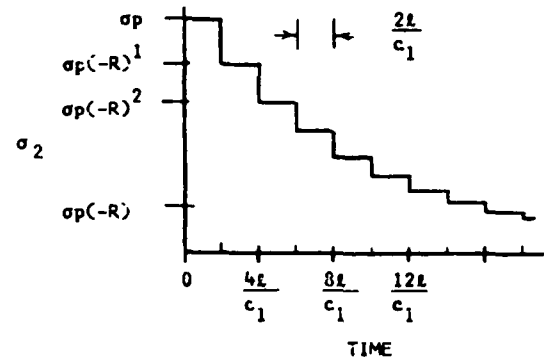


Figure 2 - Predicted normal stress versus time generated in a soil half space by a dropped weight of thickness ℓ and dilatational wave velocity c_1

Placing Equation 37 into Equation 35 produces the final expression for the stress in the soil

$$\sigma_2(t) = \frac{v_0}{2} \rho_1 c_1 T (-R)^{\text{int} \left[\frac{c_1 t}{2\ell} \right]} \quad (38)$$

IMPULSE PRODUCED FROM A DROPPED WEIGHT

In this section an expression for the impulse (i.e., area under the stress-time curve) produced in the soil from a dropped weight will be derived. This expression will involve the peak stress generated in the soil and other parameters of the dropped weight. In the next section the expression will be correlated to the peak stress and impulse from a nuclear surface burst.

The stress generated in the soil from a dropped weight (Equation 38) is shown plotted in Figure 2 where the peak soil stress, σ_p , is defined as:

$$\sigma_p \equiv \frac{v_0}{2} \rho_1 c_1 T \quad (39)$$

From Figure 2, the impulse, I , from a dropped weight is given by:

$$I = \frac{2\ell}{c_1} \sigma_p (-R)^0 + \frac{2\ell}{c_1} \sigma_p (-R)^1 + \dots + \frac{2\ell}{c_1} \sigma_p (-R)^n \quad (40)$$

$$= \frac{2\ell}{c_1} \sigma_p \sum_{n=0}^{\infty} (-R)^n$$

Since $0 < -R < 1$ the sum, I_n , of the first n terms are given by (see Tierney, [13])

$$I_n = \frac{2\ell}{c_1} \sigma_p \left[\frac{1}{1+R} - \frac{(-R)^n}{1+R} \right] \quad (41)$$

Letting $n \rightarrow \infty$ in this expression produces

$$I = \frac{2\ell}{c_1} \sigma_p \frac{1}{T} \quad (42)$$

in which the result $R + 1 = T$ has been used. To show that Equation 42 is what one would expect from a falling weight, we observe from Equations 1 and 39 that

$$I = \frac{2\ell}{c_1} \left(\frac{v_0}{2} \right) \rho_1 c_1 T \left(\frac{1}{T} \right) \\ = \ell \rho_1 \sqrt{2gh}$$

CORRELATION TO A NUCLEAR SURFACE BURST

From Equations 39 and 1, it is seen that for drop heights of 40 ft or less the maximum stress that can be generated in the soil by the dropped weight is around 1000 psi. This assumes a soil dilatational wave velocity of 1000 ft/sec and density of 100 lb/ft³. Hence we will focus our attention on the pressure range of 1000 psi or less.

A plot of impulse and duration versus peak overpressure for a 1-Mt nuclear surface burst is taken from Crawford, et al. [7] and is shown in Figure 3. The impulse produced from an

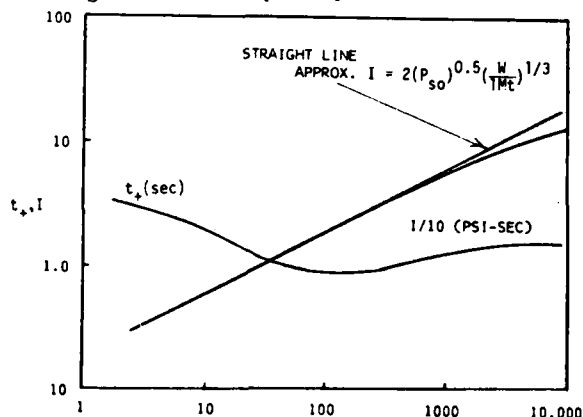


Figure 3 Duration and impulse versus peak overpressure from a 1-Mt nuclear surface burst (from Crawford, et al. [7])

explosion scales as the cube root of the charge weight (see Baker, Westine, and Dodge [14]); for peak overpressures up to 1000 psi the impulse can be represented by

$$I_w = 2(P_{so})^{0.5} \left(\frac{W}{1Mt} \right)^{1/3} \quad (43)$$

where

I_w = in psi-sec
 P_{so} = peak overpressure at the surface (psi)
 W = charge yield in TNT equivalent in Mt

Since P_{so} is the peak overpressure at the surface, it corresponds to σ_p in Equation 42. To correlate the dropped-weight induced soil stress to that induced from the overpressure from a nuclear surface, we set the impulse from the two (Equations 42 and 43) equal and let $P_{so} = \sigma_p$. This produces

$$\frac{2\ell}{c_1} \sigma_p \left(\frac{1}{T} \right) = 2(\sigma_p)^{0.5} \left(\frac{1}{1Mt} \right)^{1/3}$$

or,

$$W = 1Mt \left(\frac{1}{T} \right)^3 \left(\frac{\ell}{c_1} \right)^3 \sigma_p^{1.50} \quad (44)$$

Similar expressions that relate the dropped-weight parameters to triangular-shaped representations (as defined by Crawford, et al. [7] of the nuclear overpressure-time curve are contained in Welch [6].

DURATION DISCREPANCY BETWEEN THE DROPPED WEIGHT AND THE SURFACE BURST

Equation 44 equates a charge yield in megatons from a nuclear surface burst to the parameters of a drop test by requiring that each has the same duration. From Figure 2, for a 1-Mt surface burst between 30 and 1000 psi, the overpressure time duration, t_+ , is fairly constant and is about 1 sec. Since t_+ is also cube root scalable (see Baker, Westine, and Dodge [14]), it can be represented as a function of charge yield as

$$t_+ = \left(\frac{W}{1Mt} \right)^{1/3} (1 \text{ sec}) \quad (45)$$

Using Equations 37 and 39, and considering the period, t_s , of the stress wave produced by the dropped slab to be the time it takes for the stress wave to decay to some fraction γ of the peak value produces

$$\gamma = \frac{\sigma_2(t)}{\sigma_p} = (-R) \int \left[\frac{c_1 t_s}{2\ell} \right] = (-R) \left[\frac{c_1 t_s}{2\ell} \right]$$

Therefore

$$t_s = \frac{2\ell}{c_1} \left[\frac{\ell n \gamma}{\ell n (-R)} \right] (1 \text{ sec}) \quad (46)$$

Solving for γ/c_1 from Equation 44 and placing the results into Equation 46 gives

$$t_s = \frac{T}{\ln(-R)} (2 \ln \gamma) \sigma_p^{-0.5} \left(\frac{W}{1 \text{ Mt}} \right)^{1/3} \quad (47)$$

Recognizing that $(-R) = (1 - T)$ and assuming small values of T produces (see Selby, [11])

$$\ln(-R) = \ln(1 - T) = -T - \frac{1}{2} T^2 - \frac{1}{3} T^3 - \dots \quad \text{for } -1 \leq T < 1 \quad (48)$$

$$= -T \quad \text{for small } T$$

Placing this result into Equation 47 gives

$$t_s = -2 (\ln \gamma) \sigma_p^{-0.5} \left(\frac{W}{1 \text{ Mt}} \right)^{1/3} (1 \text{ sec}) \quad (49)$$

Equation 49 gives the duration of the dropped-weight induced stress pulse that simulates a nuclear weapon of yield, W , in megatons and at an overpressure equal to σ_p . This pulse is considered to have terminated when the stress level has reached a fraction, γ , of the peak stress. The equality in impulse of the dropped weight and the nuclear surface burst has been assured by Equation 44. When t_+ and t_s are equal, the duration of the two wave forms are also equal. Because of the

difference in the form of their defining Equations 45 and 49, this will occur at only one simulated stress level. Assuming a value of γ of 0.01 (i.e., assuming the pulse from the dropped weight has terminated when the stress levels have reached 1 percent of the peak stress) and setting Equation 45 equal to Equation 49 gives

$$\left(\frac{W}{1 \text{ Mt}} \right)^{1/3} (1 \text{ sec}) = -2 \ln(0.01) \sigma_p^{-0.5} \left(\frac{W}{1 \text{ Mt}} \right)^{1/3} (1 \text{ sec})$$

or

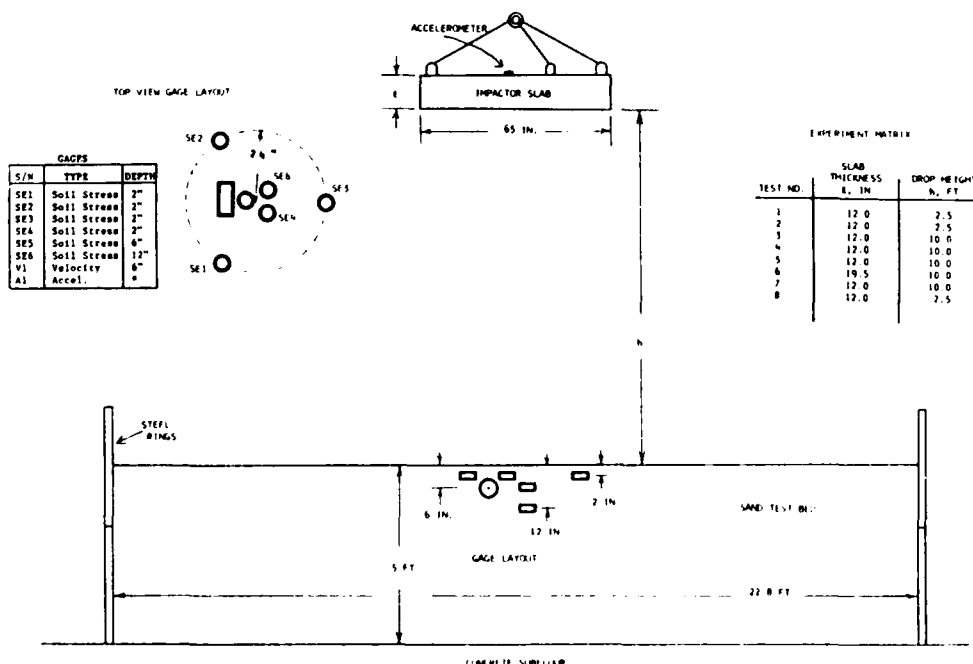
$$\sigma_p = 85 \text{ psi}$$

Thus at 85 psi the dropped weight can simulate the peak stress, impulse, and duration of a nuclear surface burst. Since t_s and t_+ have the same dependence on charge yield, this will be true regardless of the size of the nuclear weapon simulated.

Because of the inverse dependence of t_s on the peak simulated stress (Equation 49), at higher simulated overpressures, t_s will be smaller than t_+ . At the maximum overpressure that the dropped weight can practically simulate (1000 psi), t_s will be about $1/3 t_+$.

DESCRIPTION OF DROPPED-WEIGHT TESTS

The tests consisted of dropping large concrete slabs onto a sand test bed in which were located soil-stress gages and a velocity gage (Figure 4). All tests except Test 6 employed a 65-in.-diam by 12-in.-thick circular



concrete slab as the drop weight. In Test 6 a 19.5-in.-thick by 65-in.-diam concrete slab was used. These slabs weighed 3580 and 5809 lb, respectively.

The test bed was formed from two 3.3-ft-high by 22.8-ft-diam steel rings. These were stacked on one another and filled with Reid-Bedford sand to a depth of 5 ft. The sand was vibrated as it was placed in the rings to ensure uniform density. The test bed was underlain by an approximately 2-ft-thick concrete floor.

Six 5000-psi range SE soil-stress gages (Kulite Model No. 20-080U) and one Sandia Model DX velocity gage were placed in the test bed below the drop weight. The SE gages are instrumented-diaphragm-type, soil-stress gages and are adaptations of an original design developed at WES (Ingram [15]). The DX velocity gage (see Perret, et al. [16]) consists of a free-swinging pendulum which moves through a viscous fluid and whose motion is detected by a variable reluctance circuit. The velocity gage was contained in an approximately 4-in.-diam by 8-in.-long aluminum canister.

Three of the stress gages were placed 120 deg apart at a radius of 2 ft from the test bed center and at a depth of 2 in. The other three gages were placed near the center of the test bed at depths of 2, 6, and 12 in. Each of these was offset slightly so that the gage would not shadow any gages below it. The velocity gage was placed near the test bed center at a 6-in. depth.

All transducer signals were amplified and then recorded on a 32-track FM magnetic tape recorder. Throughput electronic system response was about 20 kHz.

Additional comments concerning each test are as follows:

1. Test 1 -- Conducted on a fresh test bed. The 3580-lb slab was dropped from 2.5 ft. SE gage No. 1 at a 2-in. depth was broken.
2. Test 2 -- Test bed was not resurfaced following Test 1. The 3580-lb slab was dropped from 2.5 ft.
3. Test 3 -- Test bed was not resurfaced. The 3580-lb slab was dropped from 10 ft. SE gage No. 6 at a 12-in. depth was broken.
4. Test 4 -- Test bed was not resurfaced. The 3580-lb slab was dropped from 10.0 ft. SE gage No. 3 broke.
5. Test 5 -- Test bed was not resurfaced. The 3580-lb slab was dropped from 10 ft.
6. Test 6 -- Test bed was resurfaced.

This consisted of removing the SE gages at the 2-in. depth, adding sand to the small crater created by the slab during the first five tests, compacting it, and reinstalling the SE gages at the 2-in. depth. The slab was then lowered slowly onto the test bed to assure the slab and test bed were parallel. The 5809-lb slab was dropped from 10 ft.

7. Test 7 -- Test bed was resurfaced. The 3580-lb slab was dropped from 10 ft.

8. Test 8 -- Test bed was resurfaced. The 3580-lb slab was dropped from 2.5 ft.

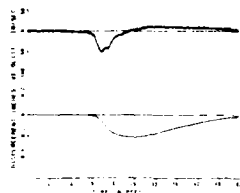
TEST RESULTS AND ANALYSIS

The recorded velocity wave forms are presented in Figures 5 and 6. The recorded stress wave forms along with the stress wave forms predicted by Equation 38 are presented in Figures 7 and 8. In deriving the predicted wave forms, the density and wave speed of the sand was assumed to be 96 lb/ft³ and 1,000 ft/sec and that of the concrete slab to be 155 lb/ft³ and 10,000 ft/sec. These are typical values for these two materials.

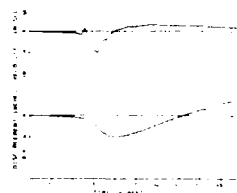
Zero time on the displayed wave forms was chosen arbitrarily for each test. Thus relative differences in shock wave arrival times as detected on different gages on a single test are correct; absolute arrival times are not.

The following seven observations are made based on the stress and velocity data:

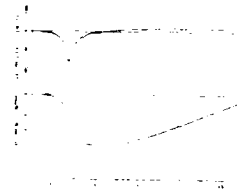
1. The rise times of the stress and velocity pulses tended to decrease from Tests 1 through 3, to increase from Test 4 to 5, and were significantly decreased on Tests 6 through 8.
2. Differences in wave arrival times between stress gages at the same depth were larger for tests with large rise times than for tests with short rise times.
3. The relative magnitudes of the peak stresses on a given test were primarily gage-dependent and not depth-dependent.
4. The highest stress recorded on the 2-1/2-ft drop tests and on the 10-ft drop tests tended toward the predicted values. This tendency increased as the rise time of the wave forms decreased.
5. The pulse durations from both the 19.5-in.-thick slab (Test 6) and the 12-in.-thick slab (all other tests) for the measured stress pulses of shortest duration tended toward the predicted values. Again this tendency increased as the rise time of the wave form decreased.
6. A second and smaller pulse was observed on the stress wave forms on many of the



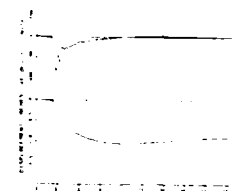
Test 1--2.5-ft-drop,
12-in.-thick slab



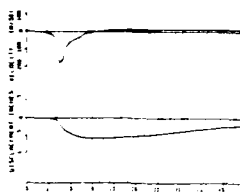
Test 2--2.5-ft-drop,
12-in.-thick slab



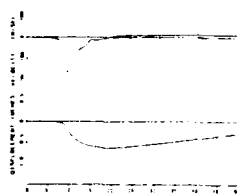
Test 5--10-ft-drop,
12-in.-thick slab



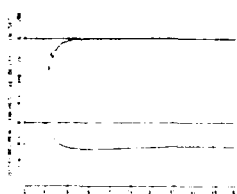
Test 6--10-ft-drop,
19.5-in.-thick slab



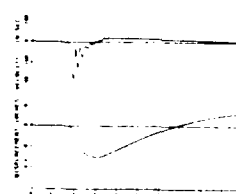
Test 3--10-ft-drop,
12-in.-thick slab



Test 4--10-ft-drop,
12-in.-thick slab



Test 7--10-ft-drop,
12-in.-thick slab



Test 8--2.5-ft-drop,
12-in.-thick slab

Figure 5 - Particle velocity histories and
displacements from Tests 1 through 4

Figure 6 - Particle velocity histories and
displacements from Tests 5 through 8

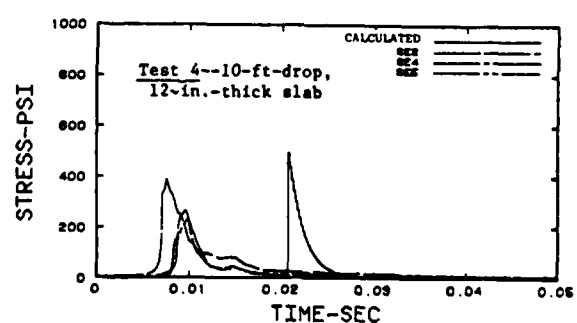
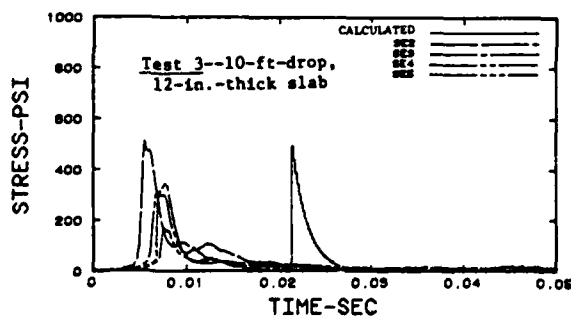
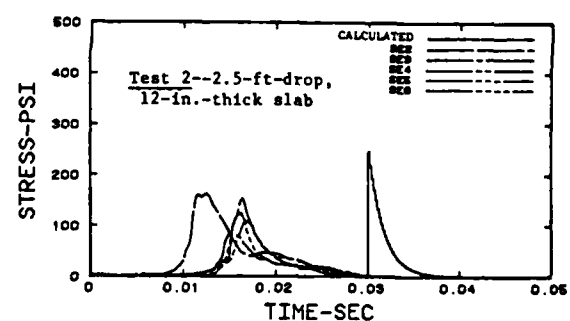
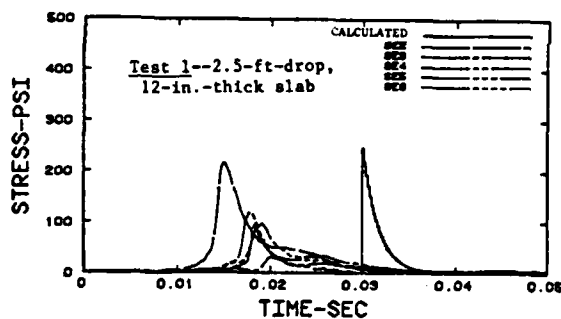


Figure 7 - Measured and calculated stress wave forms for Tests 1 through 4. (Note: Calculated wave forms are displaced to the right of the measured values for clarity)

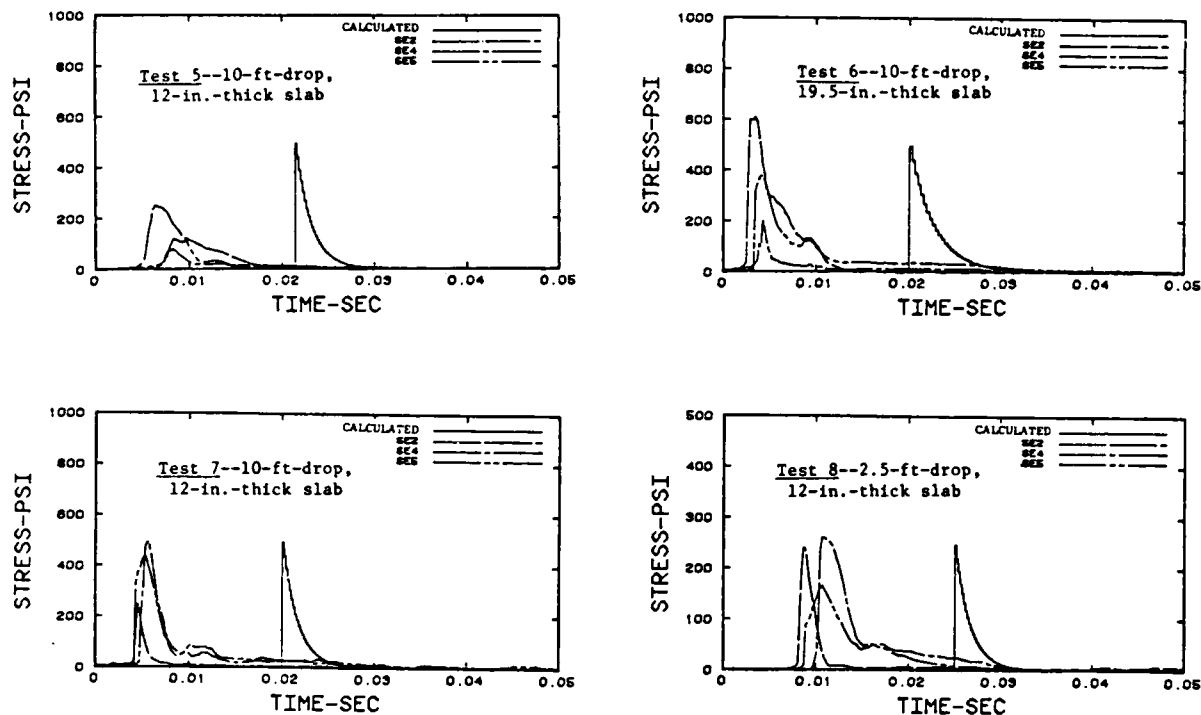


Figure 8 - Measured and calculated stress wave forms for Tests 5 through 8. (Note: Calculated wave forms are displaced to the right of the measured values for clarity)

tests. On those for which the second pulse was not observed, the first pulse was broad enough to have obscured it.

7. A slight positive phase was observed on most of the velocity wave forms.

The following three additional observations were made while the tests were being conducted:

8. The slab did not bounce after impact.

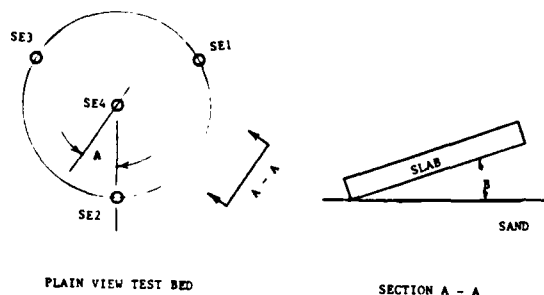
9. On Tests 1 through 5, there was a gradual growth of cracks and crevices (similar to a dry creek bed) in the upper layer of sand directly below the slab. The area affected was about 2-1/2 ft in diameter and was off-set slightly (about 6 in.) from the center of the shallow depression left by the slab. (Note: The test bed was resurfaced after Test 5.)

10. The density of the sand in the affected area mentioned in 9 decreased from pretest conditions (from ~98 lb/ft³ to ~92 lb/ft³).

Observation 1 indicates that the increase or decrease of the wave form's rise times was not caused by material properties (they are not stress-magnitude dependent nor are they constant) but is also due to the nonplanarity of impact of the slab.

Observations 2 and 3 further suggest non-planarity of impact. Accordingly a triangulation method, based on the stress wave arrival times and/or the occurrence of peak stress, was used to determine the degree of impact nonplanarity. The results are shown in Figure 9. For Tests 1 through 3 it was possible to determine both the initial point of impact (as defined by the Angle A) and the tilt of the slab at impact (Angle B). This initial point of contact was always near stress gage SE2. With the loss of SE3 on Test 4, it was possible to define only a minimum value of the tilt angle for the remaining tests. Because the tilt of the slab was not dependent on the drop height and because the initial point of impact remained fairly constant, it is surmised that the slab did not rotate during free fall but was not parallel to the sand bed at its release. Because the tilt angles for Tests 2 and 3 were similar while their associated rise times were quite different, it is surmised that for larger drop heights (hence, higher impact velocities) nonplanarity of impact matters less. And finally because the wave forms from Tests 6, 7, and 8 show much shorter rise times (hence, much better planarity between the slab and the test bed), it is surmised that impact nonplanarity can be reduced significantly with only a moderate amount of effort.

Observations 3, 4, and 5 indicate that the linear elastic model presented is a good approximate solution to the dropped-weight



TEST #	HORIZONTAL ANGLE A (DEGREES)	TILT ANGLE B (DEGREES)	DROP HEIGHT (h)
1	6.1	1.3	2.5
2	41.4	2.3	2.5
3	48.9	2.1	10.0
4	--	1.45*	10.0
5	--	1.27*	10.0
6	--	0.67*	10.0
7	--	0.69*	10.0
8	--	0.21*	2.5

* Minimum vertical angle.

Figure 9 - Horizontal and vertical tilt of slab at the time of impact as determined from the data

problem, at least for near-field regions in the sand. Differences between this solution and the data appeared to have been caused by the impact nonplanarity discussed above and the occurrence of a reflected stress pulse to be discussed below.

Observations 6, 7, 9, and 10 indicate that the input stress wave was reflected at the sand/concrete interface at the bottom of the test bed and arrived back at the surface. Here it would attempt to spall the sand as the weight of the slab was overcome. The fact that the affected area was offset from center about 6 in. (Observation 9) indicates that the tilt of the slab at impact was about 3 deg. This is in agreement with tilt angles cited earlier. The disturbance of the sand in the vicinity of the stress and velocity gages by the reflected stress wave is also believed partially responsible for the stress data scatter seen in Test 5.

Two other phenomena not mentioned were observed on the velocity and stress wave forms. While not necessary for an understanding of the physics of the tests, they are cited and explained now for completeness. These are:

1. Beginning in Test 6, a 900-Hz "ringing" was observed on the velocity traces.

2. Also beginning in Test 6, SE4 consistently indicated a wave arrival time later than SE5, despite the fact that SE5 is supposed to be 4 in. directly below SE4.

Observation 1 is due to resonance in the

DX velocity gage or its mount and has been observed on other field tests. It did not occur in Tests 1 through 5 because the impact particle velocities did not contain frequency components high enough and of sufficient magnitude to excite it. Observation 2 is believed caused by the mislocation of SE4 when the test bed was resurfaced. It is suspected that SE4 was moved to either the location of SE1 or SE3 at this time.

For another analysis of the data the reader is referred to Robert Port's analysis which appears in the report by Baum and Lodde [17].

LIMITATIONS AND PROBLEMS OF THE DROPPED-WEIGHT SIMULATION TECHNIQUE

The principal difficulty with the use of a dropped-weight simulator is assuring the planarity of impact of the dropped weight onto the test bed surface. The falling slab has a much slower velocity (~25 ft/sec for a 10-ft drop) compared to the dilatational wave speeds of most soils (1000 ft/sec to 6000 ft/sec). When one portion of the slab strikes the soil, a precursor stress wave is generated. This precursor destroys the one-dimensionality of the geometry and leads to the long rise times and mitigated peaks observed during the tests. To prevent serious degradation of the simulation environment requires impact planarity between the soil and dropped weight of less than 1 deg, depending on the slab impact velocity and the soil dilatational wave speed.

Other limitations include: (1) maximum peak stress, (2) size of the dropped weight, and (3) test geometries for which the dropped weight can be used. The limitation on peak stress is a result of the low impact velocity that can be produced for practical drop heights. This limits the peak-simulated overpressure to about 1000 psi for most dry soils.

The size limitations of the drop weight are a result of the requirement that the drop weight must be lifted and held and it must not break up on impact. This limits the size of the area that can be loaded and the maximum weapon that can be simulated.

If one assumes a 50-ton lifting and holding capability and a 2-ft-thick concrete slab, the diameters of the slab and loaded area become about 20 ft. If such a slab were dropped 40 ft onto a sand test bed, then (from Equation 44) it would simulate a nuclear weapon of about 180-ton TNT equivalent at about the 1000-psi pressure range. This scales up to 1.4-kt, 9.2-kt, and 5.9-Mt TNT equivalents for model testing of 1/2, 1/8, and 1/32 scales, respectively. Such a test environment, even with its small size, would prove useful for many applications.

The last limitation is caused by the boundary conditions imposed by the slab onto

the soil. This prevents the dropped-weight simulation technique from being useful for testing buried structures at very shallow depths, particularly in soft soils. The dropped weight imposes continuity of stress and displacement conditions on the soil surface. Since the bottom surface of the slab is planar and remains so after impact, it forces the soil into a planar displacement boundary condition. If a relatively hard spot exists in the soil (e.g., a shallow buried, stiff structure) then local stress concentrations will occur above the structure as a result. If the same buried structure were loaded through the soil by the overpressure from a nuclear airblast, such would not occur. Because of this the following should be taken as a rule-of-thumb. If for a simulation test one would expect the loading from the nuclear overpressure to cause the loaded area to displace at the surface unevenly, then the dropped weight probably should not be used as the energy source.

CONCLUSIONS

1. The dropped-weight technique is a valuable tool for simulating ground shock generated by nuclear airblast. It can be especially useful in a laboratory environment in small-scale experiments where high explosives cannot be used and repeatability is important.

2. As is seen in Figures 7 and 8, the one-dimensional elastic solution for soil stress agrees reasonably well with the experimental data.

3. Due to limitations on practical drop heights, the maximum peak overpressure that can be simulated by a dropped weight is about 1000 psi.

4. The amount of weight that can be picked up limits the size of the loaded area and yield that can be simulated by the dropped weight. A 2-ft-thick, 20-ft-diam, 50-ton weight dropped 40 ft onto a sand test bed will simulate the peak overpressure and impulse from a 180-ton TNT equivalent nuclear surface burst at the 1000-psi level. For 1/2-, 1/8-, and 1/32-scale models, the 180-ton yield scales up to 1.4-kt, 9.2-kt, and 5.9-Mt simulated yields, respectively, on a prototype structure.

5. The duration of the stress pulse produced by the dropped weight is generally less than the duration from simulated nuclear overpressure. At 80 psi the duration is about the same. At 1000 psi the dropped-weight duration is about 1/3 that of the simulated nuclear surface burst.

6. The displacement boundary conditions imposed by the dropped weight on the soil surface cause it to be unsuitable for testing rigid buried structures at shallow depths in soft soil.

RECOMMENDATIONS FOR FUTURE WORK

Because the dropped weight appears to be a useful tool for nuclear simulations, further development of the technique is warranted. This development should focus on five areas: (1) developing an adequate mechanism to detect time of impact; (2) developing methods to ensure planar impact of the dropped weight (an in-flight self-leveling mechanism would be ideal); (3) developing methods to shape the input stress wave form by employing drop weights of different materials and cross section; (4) developing additional driving mechanisms (besides just free fall) to increase the impact velocity; and (5) developing methods to better simulate the boundary conditions imposed on the soil surface.

Other possible uses for the dropped weight need to be explored. These areas include in situ dynamic soil property testing and calibration of development of ground motion instruments.

ACKNOWLEDGEMENTS

This research was jointly funded by the Defense Nuclear Agency and Office, Chief of Engineers.

We thank Mr. Paul Eagles (of WES) who supervised the dropped-weight tests; Mr. Robert Port (R&D Associates) who suggested the tests; Dr. Martin H. Sadd (University of Rhode Island) and Dr. Walter R. Carnes (Mississippi State University) who guided the thesis; and Mr. James L. Drake (of WES) who supplied the elastic solution based on Laplace transforms. In addition we thank Mrs. M. H. Holloway, Ms. E. K. Klein, and Mrs. B. A. Young (all of WES) for preparing this manuscript and Mr. Leo Ingram (of WES) for his thoughtful review and editing of the text.

REFERENCES

1. Martens, D. P., and Bradshaw, J. C. 1976. "Dynamic Airblast Simulator Parametric Test Series, Events I-A, I-B, I-C, I-D, and I-E Data Report," AFWL-TR-76-018, Air Force Weapons Laboratory, Kirtland Air Force Base, N. Mex.
2. Wampler, H. W., Leigh, G. G., and Furbee, M. E. 1978. "A Status and Capability Report on Nuclear Airblast Simulation Using HEST," Proceedings of the Nuclear Blast and Shock Simulation Symposium, 28-30 November 1978, Vol. 1, General Electric-TEMPCO, Santa Barbara, Calif.
3. Schlater, D. R. 1974. "DIHEST Improvement Program TEST DIP IIIA," AFWL-TR-74-16, Air Force Weapons Laboratory, Kirtland Air Force Base, N. Mex.

4. Wallace, J. G., and Fowler, J. 1973. "Fundamental Experiments in Ground Shock Phenomenology," Miscellaneous Paper N-73-2, U. S. Army Engineer Waterways Experiment Station, CE, Vicksburg, Miss.
5. Ford, Max B. 1976. "Correlation of Impact and Explosively Created Ground Shock Phenomena," Miscellaneous Paper N-76-10, U. S. Army Engineer Waterways Experiment Station, CE, Vicksburg, Miss.
6. Welch, Charles R. 1981. "Dropped-Weight Simulation of Nuclear Surface Burst Induced Ground Shock - A Feasibility Study," M.S. Thesis, Mississippi State University, Starkville, Miss.
7. Crawford, R. E., Higgins, C. J., and Bultmann, E. H. 1974. "The Air Force Manual for Design and Analysis of Hardened Structures," AFWL-TR-74-102, Air Force Weapons Laboratory, Kirtland Air Force Base, N. Mex.
8. Drake, James L. 1981. Personal communication. U. S. Army Engineer Waterways Experiment Station, CE, Vicksburg, Miss.
9. Port, Robert. 1976. Unpublished intra-office memoranda from R&D Associates, P. O. Box 9695, Marina del Ray, California, dated December 13, 1976.
10. Gutzwiller, M. C. 1962. "The Impact of a Rigid Circular Cylinder on an Elastic Solid," Royal Society of London, Philosophical Transactions, Series A, Vol. 255, No. 1053, pp 153-191.
11. Selby, S. M. (ed.) 1972. "Standard Mathematical Tables," Chemical Rubber Co., 20th Edition, p 456.
12. Churchill, Ruel V. 1958. "Operational Mathematics," McGraw-Hill Book Company, Inc., New York, NY.
13. Tierney, John A. 1968. "Calculus and Analytic Geometry," Allyn and Bacon, Inc., 470 Atlantic Avenue, Boston, Mass., p 519.
14. Baker, E. W., Westine, P. S., and Dodge, F. T. 1973. Similarity Methods in Engineering Dynamics: Theory and Practice of Scale Modeling, Hayden Book Company, Rochelle Park, N. J.
15. Ingram, James K. 1968. "Development of a Free-Field Soil Stress Gage for Static and Dynamic Measurements," Technical Report No. 1-814, U. S. Army Engineer Waterways Experiment Station, CE, Vicksburg, Miss.
16. Perret, W. R., et al. 1965. "Four Papers Concerning Recent Work on Ground Motion Measurements," Report No. SC-R-65-905, Sandia Corporation, Albuquerque, N. Mex.

NOTATION

A_1, A_2, B_1, B_2	Constants
c_1	Slab dilatational wave velocity
c_2	Soil dilatational wave velocity
g	Acceleration of gravity
h	Slab drop height
H	Heavyside step function
H_1	Ramp function
I	Impulse from dropped weight
I_w	Impulse from nuclear surface burst
K	Impedance ratio, $\rho_1 c_1 / \rho_2 c_2$
x	Slab thickness
P_{so}	Peak blast overpressure on the surface
R	$1 - K / (1 + K)$
s	Laplace transform
t_s	Period of soil stress wave
t_+	Blast wave positive phase duration
T	Acoustic transmission coefficient
u_1	Displacement in slab
u_2	Displacement in soil
u	Laplace transform of u
v_o	Slab impact velocity
w	Explosive yield
z	Vertical direction
γ	Ratio of stress amplitude to peak stress, $= \sigma_2(t) / \sigma_p$
ρ_1	Slab density
ρ_2	Soil density
σ_1	Stress in slab
σ_2	Stress in soil
σ_p	Peak soil stress

ANALYSIS AND TESTING OF A NONLINEAR MISSILE AND CANISTER SYSTEM

R.G. Benson, A.C. Deerhake, and G.C. McKinnis
General Dynamics Convair Division
San Diego, California

Analyses and tests were performed to evaluate the nonlinear vibration response of a missile in its protective canister. A diametric rattle space exists between the missile and the canister liner, an elastomer with load deflection properties that are approximately exponential. Simplified MSC/NASTRAN transient response analyses predict the response to be a series of repeated shocks with peak amplitudes that exceed some component allowables. A full-scale vibration test of this configuration showed that the predicted response character is correct but that the amplitude is conservative.

INTRODUCTION

The original Tomahawk Cruise Missile System was designed for torpedo tube launch from 688 Class Submarines. Two significant design considerations were the MIL-S-901C near-miss shock and MIL-STD-167 shipboard-vibration requirements. Both are imposed while the missile is stowed in the submarine storage rack. The Tomahawk-capsule assembly is moved from the storage rack to the torpedo tube immediately before launch. The design which evolved to meet these requirements consists of a close-tolerance steel capsule with a thin elastomeric liner into which Tomahawk is inserted. Aboard the submarine, the capsule is lashed to the storage rack with sufficient force to elastically deform

the capsule onto the missile, closing the diametric gap (rattle space) between the two. This design successfully protects the missile against damage when subjected to the aforementioned shock and vibration environments.

In the last few years, Tomahawk launch platforms have expanded to include a mobile ground launcher and two surface ship launchers. Unlike the submarine version, the surface-launched vehicles are launched from the storage location. For these vehicles the booster is ignited in the canister. Sufficient clearance must be provided between liner and missile to accommodate both missile and canister dimensional variances and booster radial expansion. A schematic of the system is shown in Fig. 1. In an attempt to avoid using an active system to eliminate the rattle space during storage and to release

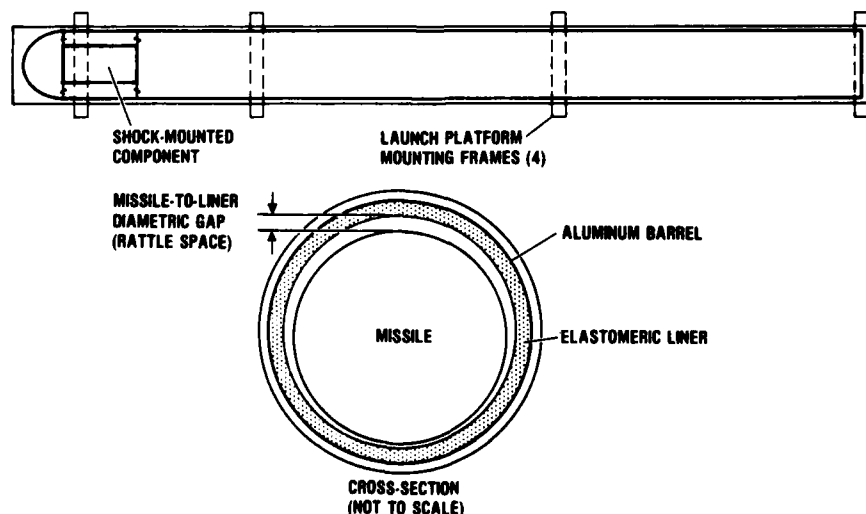


Fig. 1 — Schematic of missile in canister

at launch, an evaluation of the effect of allowing rattle space during shipboard and ground launched use was undertaken. This paper presents the results of a full-scale development test to investigate rattle space-induced effects on vibration response. These test results are compared to the pretest analytical predictions.

ANALYSIS

Missile response analyses were performed using a modified modal transient solution. The nonlinearities were included using techniques developed for the shock analysis presented by Dreyer, et al., and Martin[1,2] to predict the Tomahawk missile response to near-miss shock excitation. The analysis is nonlinear for two reasons: the rattle space creates a dead zone and the elastomer which lines the canister inner diameter has a nearly exponential force deflection curve (Fig. 2).

Normal modes were developed under the assumption of a zero gap and a linear spring constant for the

liner (dashed line in Fig. 2). Selection of the linear spring magnitude was premised on minimizing the nonlinear perturbations within the range of anticipated liner deflections. The equations to be solved are shown in Fig. 3. Differences between the actual spring force and that resulting from the assumed linear formulation are treated by superimposing a displacement-dependent force in the modal transient response analysis. The MSC-NASTRAN code was used to perform these analyses. Important simplifying assumptions were that the rattle space was uniform over the length of the missile and that the canister and missile were straight and parallel. Tests of the liner material have shown that there is a significant amount of hysteresis in the force-deflection characteristics, not addressed in these analyses. Fig. 4 lists the calculated modal frequencies.

Enforced accelerations at selected frequencies from the MIL-STD-167 sinusoidal vibration test specification (Fig. 5) were used as canister forcing functions. Fig. 6 shows that the calculated missile response

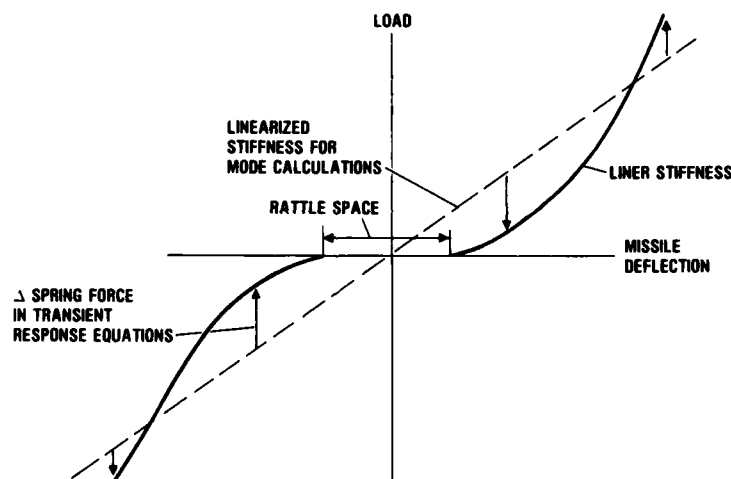


Fig. 2 — Elastomeric canister liner-load vs deflection

SOLUTION IN GENERALIZED (MODAL) COORDINATES:

$$\{x\} = \Phi \{q\}$$

MODAL EQUATION OF MOTION:

$$\{\ddot{q}\} + [2\zeta\omega] \{\dot{q}\} + [\omega^2] \{q\} = [M]^{-1} [\Phi]^T \{F(t) + \bar{F}\}$$

WHERE MODAL PARAMETERS ω , M , Φ ARE CALCULATED USING LINEARIZED LINER/RATTLE SPACE STIFFNESS

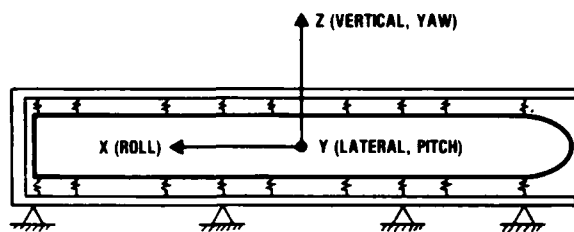
AND \bar{F} IS DELTA NONLINEAR FORCE FROM ACTUAL LINER/RATTLE SPACE SPRING AND DAMPING CHARACTERISTICS

DELTA NONLINEAR FORCE:

$$\bar{F}_i = \bar{P}(x_i - x_j) + \bar{C}(x_i - x_j) \cdot (\dot{x}_i - \dot{x}_j)$$

WHERE i & j ARE POINTS ON EACH SIDE OF LINER/RATTLE SPACE SPRING

Fig. 3 — Transient response equations



Mode	Frequency (Hz)	Mode Shape
1	19.20	Missile lateral translation
2	19.23	Missile vertical translation
3	21.43	Missile yaw
4	21.43	Missile pitch
5	30.35	Missile first lateral bending
6	30.97	Missile first vertical bending
7	49.16	Missile second lateral bending
8	49.62	Missile second vertical bending
9	86.01	Missile third lateral bending
10	87.62	Missile third vertical bending

Fig. 4 — AUR finite-element model modal data

to a 1.27 g input at 25 Hz is a series of repeated shocks that peaked at approximately 18 g for a rattle space of 0.07 inch. This response level is far in excess (factors of 5 to 10) of the defined sinusoidal allowables of some of the vibration-sensitive missile components. Comparing a repeated spike loading environment to a sinusoidal allowable is not strictly correct. This was a major reason for using actual component hardware during the design development testing.

To reduce this predicted response, a set of "shock pads" were added to the canister liner, reducing the rattle space to zero at a critical component mounting station (Fig. 7). Fig. 8 compares the calculated responses to shock and vibration excitation for the vary-

ing liner configurations. The results indicated that a canister with the "shock pads" would meet the vibration and shock limitations for all components and the production drawings reflect this design. However, it was found that there were producibility problems inherent in this design. Tolerances on the canister liner could not be held within the required specifications. The consequence was that the nominal rattle space had to be increased from 0.070 ± 0.050 to 0.135 ± 0.050 inches, to ensure that adverse tolerance buildup would not inhibit launch. Additionally, it had been found that the "shock pads" were generally damaged or dislodged as the missile was loaded into the canister. This made it imperative to modify the liner design to eliminate them. Although the missile response analyses for this new liner configuration were thought to be conservative because of the simplifying assumptions, the predicted responses were of a sufficient magnitude to justify a development test. It was decided the factors such as liner thickness variation, hysteresis, and damping could be evaluated only through a test program.

TEST SETUP AND TEST PROCEDURE

A full-scale vibration test was conducted to measure the response characteristics of the missile in a canister with varying rattle space conditions. The test specimen consisted of an inert cruise missile test vehicle (Launcher Test Inert Vehicle — LTIV) with actual hardware for the vibration-sensitive components. The selected canister had the maximum internal diameter available and resulted in an average missile-to-liner diametric rattle space of 0.10 inch. Testing was conducted at the Naval Ocean Systems Center on a mechanical vibration table designed to test large

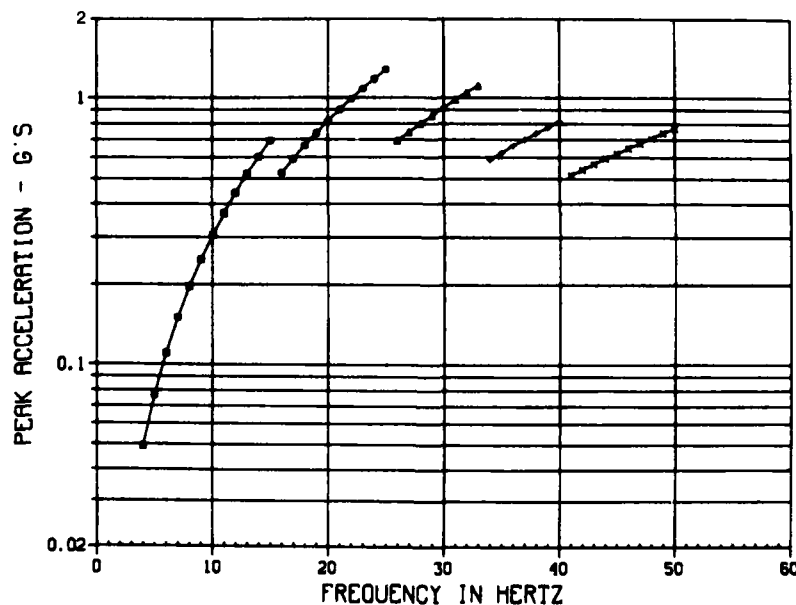


Fig. 5 — MIL-STD-167 sinusoidal vibration input levels

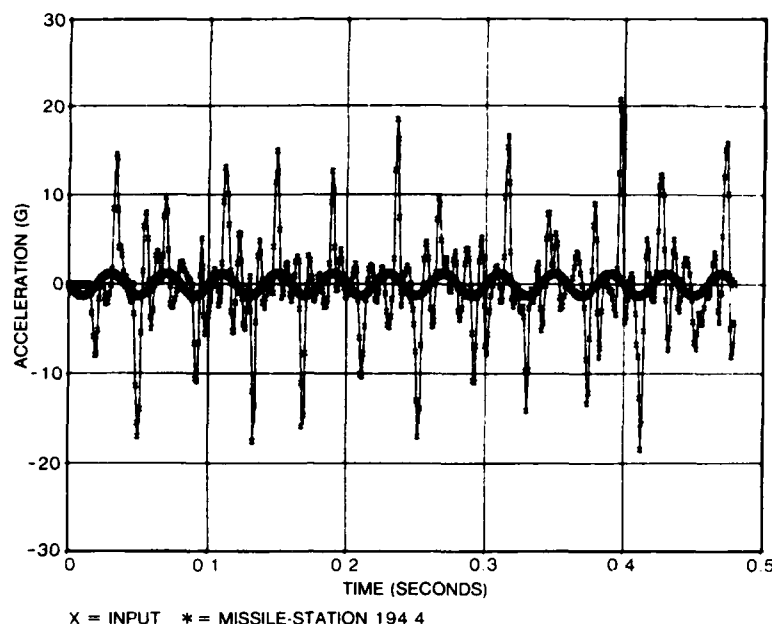


Fig. 6 — Missile time history response — analytical excitation = 1.27g at 25 Hz

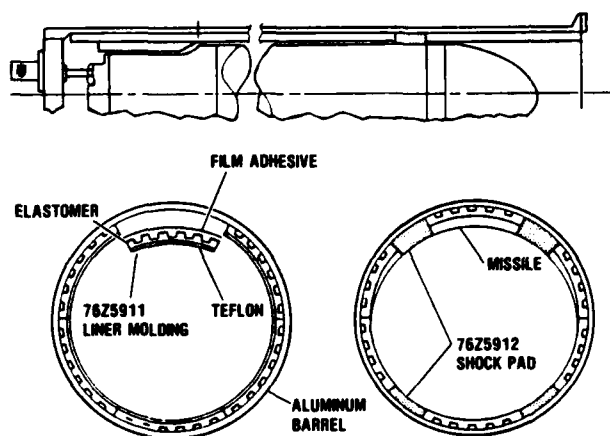


Fig. 7 — Canister liner

	LINER GAP (IN.)	GUIDANCE GAP (IN.)	LINER ELASTOMER (K/KVTON)	GUIDANCE ELASTOMER (K/KVTON)	MIL-S-901			MIL-STD-167		
					PEAK SHOCK RESPONSE (g)			PEAK VIB RESPONSE (g)		
					GUIDANCE	ENGINE	BOOSTER	GUIDANCE	ENGINE	BOOSTER
SUB	0	0	1	1	185	187	206	3.5	1.9	1.8
	0	0	1	1	87	172	118	1.5	1.7	1.4
ABL	0.07	0.07	1	1	327	292	180	19.2	7.7	3.8
	0.07	0	1/8	5	192	220	131	6.2	9.5	4.9
	0.07	0	1	5	83	94	81	3.4	5.4	8.0

ZERO GUIDANCE GAP RESULTS FROM SHOCK PAD INSTALLATION
ASSUMPTION: 5% CRITICAL DAMPING
VIBRATION INPUT OF 1.27G AT 25 HZ

Fig. 8 — Calculated Tomahawk ship launch shock/vibration response

specimens to MIL-STD-167 requirements. Fig. 9 is a schematic of the test setup and Figs. 10 and 11 are photographs of the two configurations tested. Both horizontal and vertical missile orientations were tested to establish the effect of gravity on missile response. Excitation was applied in the canister and missile vertical axes (Fig. 9). The horizontal orientation corresponds to the shipboard Armored Box Launcher (ABL) and the Trailer-Erector-Launcher (TEL) used in the Ground Launched Cruise Missile (GLCM) program.

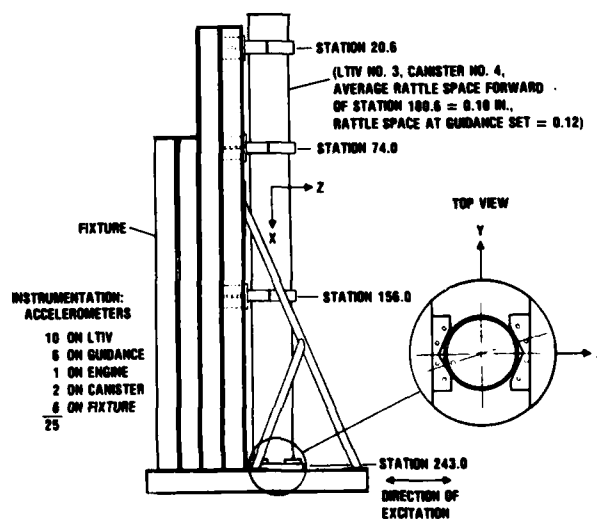


Fig. 9 — Test configuration for vertical orientation

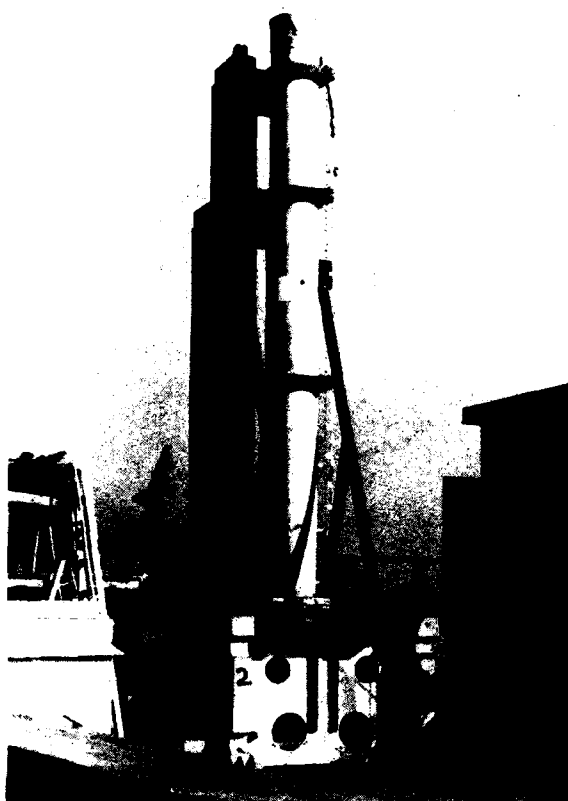


Fig. 10 — Vibration test fixture (vertical orientation)



Fig. 11 — Vibration test fixture (horizontal orientation)

Vertical orientation of the test specimens represents a portion of the surface ship vertical launch system (VLS) configuration. The four mounting frames shown in Figs. 8 through 10 correspond to canister support frame locations which are common to these launch platforms.

Total weight of the LTIV, canister, and test fixture exceeded 20,000 lb in the vertical orientation and 12,000 lb in the horizontal. The shaker used was a mechanically driven device with no feedback control system. It is designed to operate as a constant amplitude device that

is controlled by the prerun positioning of eccentric rotating weights. Weights and c.g. locations of the test specimen extended the test facility to its functional limits, particularly for the vertical missile orientation. However, the facility was inexpensive and available, and it was felt that any full-scale test data would be valuable in both quantifying rattle space effects on missile response and in validation and tuning of the analytical model.

Testing for both the horizontal and vertical orientations was conducted for three constraint configurations:

- No shimming — missile-to-liner rattle space was unconstrained along the missile length.
- One shim location — shims placed at station 20.6 between the support frame and the canister closed the missile-to-liner rattle space to zero at this station.
- Three shim locations — shims were placed between the support frames and the canister at stations 20.6, 74.0, and 156.0 to close the missile-to-liner rattle space to zero at these stations.

Tables 1 and 2 show the matrix of test conditions. The matrices were developed to explore the sensitivity of missile response to excitation amplitude and frequency within the capabilities of the test equipment.

DATA REDUCTION AND TEST RESULTS

The vertical orientation was tested and, as predicted by prior analysis, a fixture resonance occurred at 12 Hz. This was in the range of interest, as shown in Figure 12a, which is an example of response curves as measured by the NOSC real-time analyzer and shows both the missile response and the support frame response at station 20.3. To maintain the test level in some cases, a resonance of this type will require a driving force beyond the shaker capability. However, the system did not isolate and the shaker had sufficient force to maintain the approximate test level above 12 Hz. Since the input at the four frames was not uniform, it was decided to define the missile-to-canister transmissibility to be the ratio of the response on the missile, adjacent to a frame, to the acceleration on the frame, at that station. In the horizontal case, fixture flexibility was not a problem, and the excitation was nearly uniform at the four frame stations.

As predicted by analyses, the missile response was frequently characterized as a series of repeated impact shocks, as illustrated in Fig. 12b. Response levels were significantly lower (factors of 2 to 3) than had been predicted. Figs. 12a and 12b also illustrate a pitfall that must be avoided in this type of testing. The curves in Fig. 12a were made from the NOSC analyzer. In comparing these data with the data of Figure 11b (Brush recorder strip charts) at 30 Hz, obtained from the same magnetic tapes, it is obvious that the analyzer introduced an apparent filter on the data, with the result that the repeated spike loadings were smoothed and not recorded.

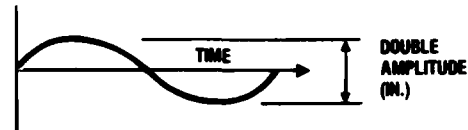
The NOSC analyzer converted the oscillatory signal to a DC level by means of a rectifier. General Dynamics

TABLE 1 — Vibration-vertical orientation test matrix

Run Number — Vertical Orientation Lateral Excitation			Set Table Double Amp. inches	Frequency Range (Hz)				
0.10 In. Avg Rattle Space	Zero Rattle Space Station 18.3 0.10 In. Avg at others	Zero Rattle Space Sta. 18.3, 74, 156		4-15	16-25	26-33	34-40	41-50
7	8	14	0.006					X
3	11	15	0.010				X	
4	12	16	0.020			X		
5	13	17	0.040	X				

X MIL-STD-167A LEVEL

Note: double amplitude (in.) = $\frac{19.56 \cdot G}{(f_{\text{hertz}})^2}$



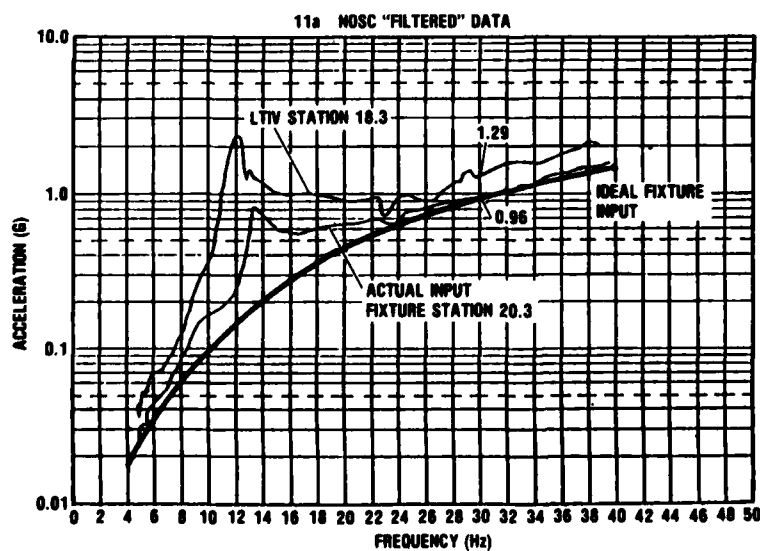
Example: 0.04 inch double amplitude excitation at 25 Hertz gives a peak G value of 1.28

TABLE 2 — Vibration-horizontal orientation test matrix

Run Number — Vertical Orientation Lateral Excitation			Set Table Double Amp. inches	Frequency Range (Hz)				
0.10 In. Avg Rattle Space	Zero Rattle Space Station 18.3 0.10 In. Avg at others	Zero Rattle Space Sta. 18.3, 74, 156		4-15	16-25	26-33	34-40	41-60*
2	13	14	0.016					
3	12	15	0.026					
4	11	16	0.046					
5	10	17	0.081					
6	9	18	0.153	X	X			
7	8	19	0.195	X				
22	21	20	0.003					

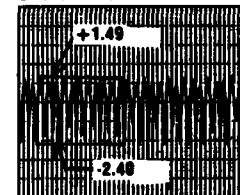
* 60 HZ OR HIGHEST OBTAINABLE

X GLCM POINT



11b CONVAIR BRUSH DATA
AT 30 Hz EXCITATION

LTV: STA. 18.3



FIXTURE (CANISTER): STA. 20.6



Fig. 12 — Typical data samples

experience with this type of system shows that it will produce a DC record that is exact for a sinusoidal input signal but will be 1 to 2 dB low for a purely random input. Fig. 12b shows that the response is not sinusoidal and has a random amplitude.

All the response data presented herein were based on the Brush recordings. In no case was the response symmetric when spiking was observed; the responses being biased in one direction. This suggests that a larger gap would not aggravate missile response for the vibration levels tested.

Although transmissibility in the strictest sense is a linear concept, it is used herein as the ratio of the peak missile response to the corresponding frame input level. Data shown in Fig. 13 illustrates the observed dependency of transmissibility on amplitude and frequency of the excitation. As expected, transmissibilities were reduced when shimming was introduced. Figs. 14 through 19 are from Reference 3 and show the maximum measured transmissibilities at two missile stations for each of the shimming arrangements and missile orientations. Figs. 14 and 17 show that the maximum transmissibility for the unshimmed case generally occurred for the horizontal orientations. Contrary to expectations, the gravity force did not reduce the response.

An unexpected result was that response of a shock-isolated component was lower for the no shimming case (Fig. 20). The reason for this is thought to be that when the rattle space is eliminated, the system is nearly linear, especially for small amplitudes. Thus the time history response (Fig. 21) is nearly sinusoidal, resulting in a component resonance response at 48 Hz. For the case with rattle space, the response is not sinusoidal, rather it is a series of shocks that excite a number of harmonics, diffusing the input to many frequencies. Therefore, not all of the input energy goes into driving the component

at the input excitation frequency when it coincides with the component suspension frequency.

CONCLUSIONS

The test results show that the analysis is conservative and needs to be modified to correlate with the test results. The analysis did correctly predict that shimming at a single station would be effective in reducing overall missile response levels. Use of the transmissibilities in Figs. 14 through 19 to predict missile response to the im-

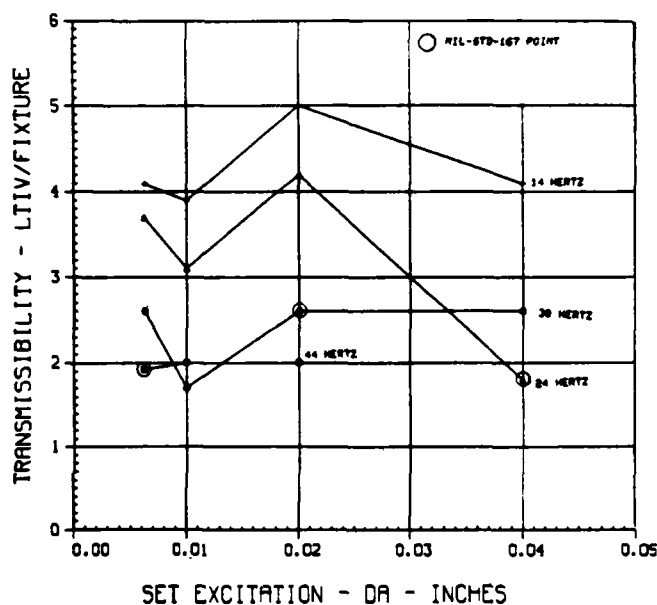


Fig. 13 — Nonlinear relationship between transmissibility and amplitude

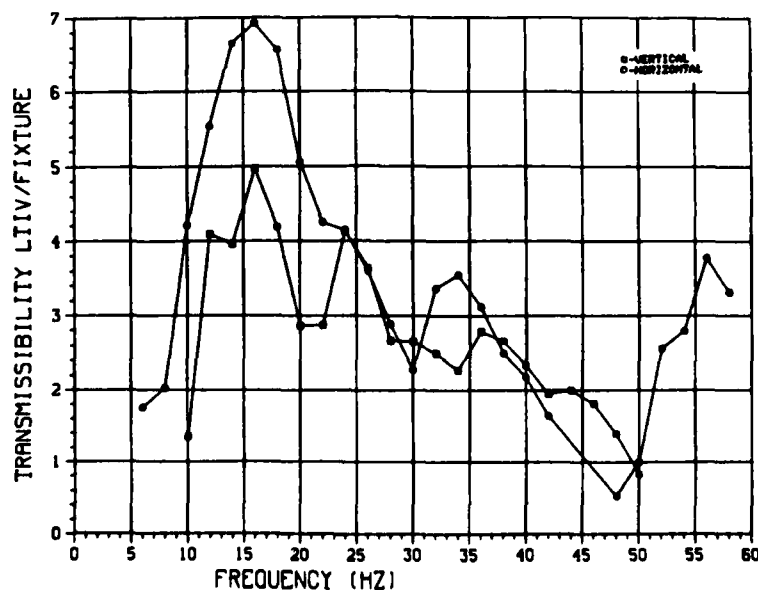


Fig. 14 — T envelopes, horizontal and vertical, station 18.3, no shims

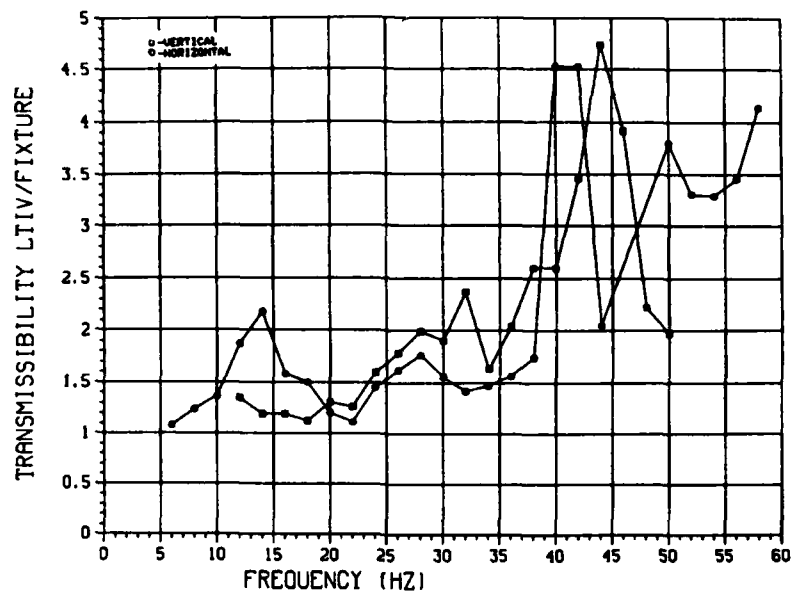


Fig. 15 — T envelopes, horizontal and vertical, station 18.3, one shim

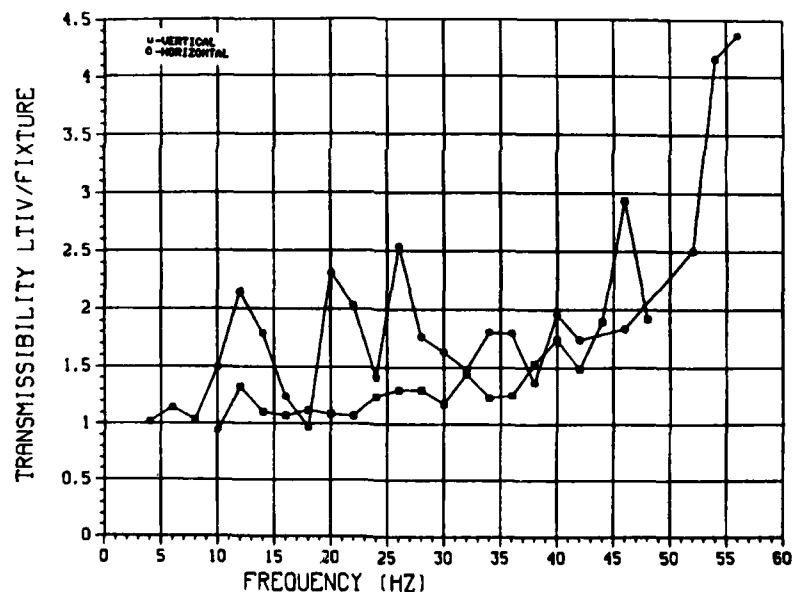


Fig. 16 — T envelopes, horizontal and vertical, station 18.3, three shims

posed vibration environments showed that for the unshimmed case, the two critical component allowables would be marginally exceeded for some frequency ranges of the imposed vibration. During post-test inspection, both of the vibration-sensitive components were found to be functional, except for damage caused by bolts backing out. Although the tests were imperfect because of lack of feedback control and fixture resonances, the results were encouraging and have shown that a design with rattle space is feasible. This design concept is being pursued.

In the coming year a prequalification test of a Tomahawk missile in a production canister with rattle space will be performed. The test will be performed with servo-controlled electrodynamic shakers, using the horizontal missile orientation. This was the worst case observed in the recent test and has the advantage of minimizing fixture flexibility effects. Testing will be performed in all three missile axes. The mathematical model will also be modified to correlate with these test results. This calibrated analytical model is needed to evaluate various rattle space distributions as well as to

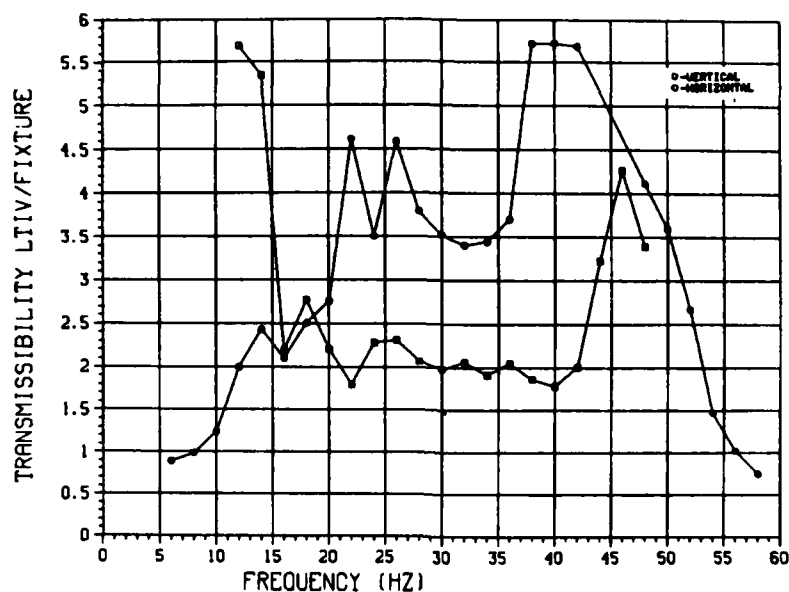


Fig. 17 — T envelopes, horizontal and vertical, station 192.5, no shims

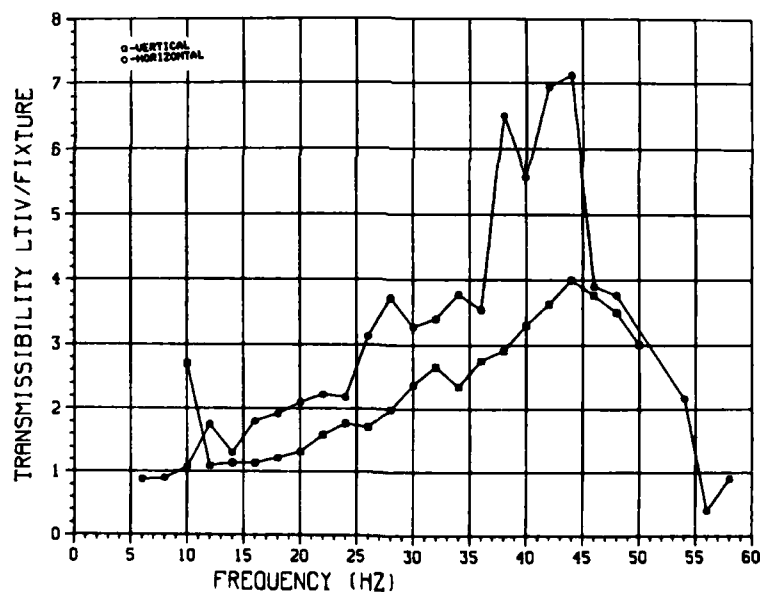


Fig. 18 — T envelopes, horizontal and vertical, station 192.5, one shim

predict missile response to shock inputs such as transportation, handling, and the MIL-S-901C near-miss shock environment.

REFERENCES

1. W.M. Dreyer, R.E. Martin, R.G. Huntington, "Development and Validation of Prelaunch Shock Capability for the Navy Tomahawk Cruise Missile", DoD 48th Shock and Vibration Symposium, Oct. 18-20, 1977.
2. R.E. Martin, Presentation to AFDC, "Correlation of Nonlinear Response Calculations with Floating Shock Platform Tests of the Tomahawk Cruise Missile", April 21, 1977.
3. R.G. Benson, A.C. Deerkake, "All-up Round Vibration Test Results in Support of Canister Redesign," December 19, 1980 — February 5, 1981, General Dynamics Convair Division Report D-81-30-CM.

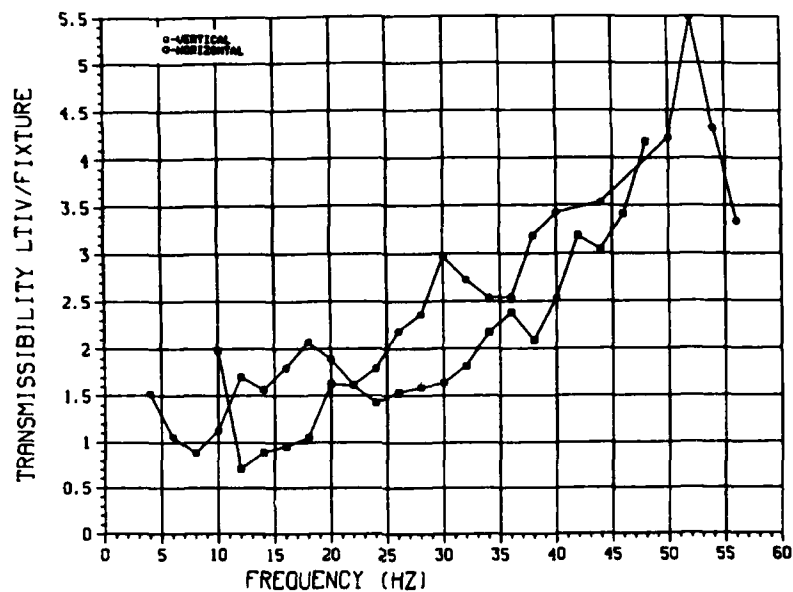


Fig. 19 — T envelopes, horizontal and vertical, station 192.5, three shims

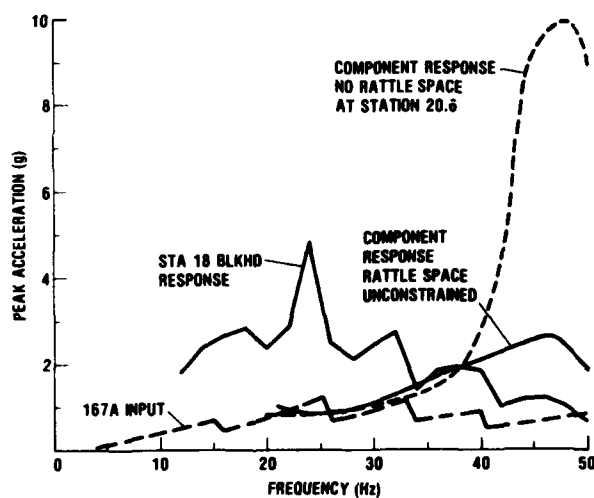


Fig. 20 — Response to MIL-STD-167A vibration input

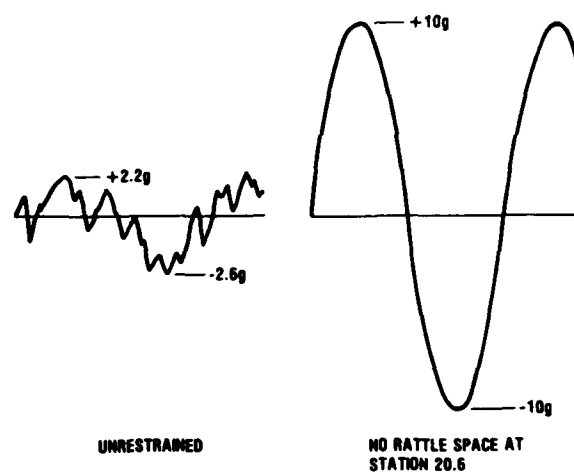


Fig. 21 — Component response time history to 0.7g, 48 Hz sinusoidal input

DISCUSSION

Voice: In your analysis did you assume the missile was translating from the canister?

Mr. McKinnis: Yes, we assumed it was translating.

Voice: In the test did you make any provisions to ensure that it would translate uniformly, or did you want it to pitch?

Mr. McKinnis: In the horizontal configuration the whole canister translated almost uniformly. We did have it tied down at the back with tie-down bolts. They allow it to rotate some. So it is probably not a good assumption to let it do that.

BIO-DYNAMIC RESPONSE OF HUMAN HEAD DURING WHOLE-BODY VIBRATION

CONDITIONS

B.K.N.RAO

Department of Mechanical & Production Engineering,
Birmingham Polytechnic, Perry Barr, England

SUMMARY

Studies have shown that many commercial and military vehicles transmit high acceleration levels to the occupants in the frequency regions of 1 to 30 Hz, wherein lies the major body resonances. These bodily resonances influence the performance and psychology of drivers and passengers in various ways depending upon the magnitude of vibration input, posture, nature of task, attitude, etc. In the vehicle ride application area, it is now realised that the transmission of these vibrations to the head of occupants may significantly effect their dynamic visual acuity, resulting in 'tunneling' and/or 'blurring' of vision. Very few studies have been cited in the literature concerning the transmission of vibration from feet-to-head, or/and from seat-to-head. Owing to a limited number of subjects employed, limited postures, different facilities and experimental techniques, the results of these studies have been interpreted in different ways. Also, most of the data refers to military personnel and its application to civilian population raises some doubts. Clearly, a need exists for accurate information on the head transmissibility characteristic of the human head, by exposing subjects from the civilian population to low frequency sinusoidal and random vibrations in the frequency range of 1 to 30 Hz. This paper covers the results obtained for various postures and different conditions.

A LITERATURE SURVEY

Some attempts have been made in the past to study the transmission of vertical vibration to the human head from the feet and the seat in various postures. Coermann (1) in 1938 compared the motion of the head of ten male subjects standing on a vibrating platform (driven by electric motor) with that of the platform itself, in the frequency range of 20 to 140 Hz, and demonstrated a resonance in the region of 20 Hz. Von Békésy (2), Müller (3) and Lockle (4) made measurements at lower frequencies and showed head resonance in the 8-12 Hz range. Investigations carried out by Latham (5) and Dieckmann (6,7) showed the same general trends but differed in detail due to differences in recording methods, and differences in the mechanical behaviour of subjects. Dieckmann's results, which are based on one subject exhibit two resonances, one in the region of 20-30 Hz. Radke (8) conducted investigations into the vibration transmission behaviour of the head of standing and sitting subjects and the results show that in the sitting posture, the head resonates in the frequency range of 2-4 Hz. Although the position of the accelerometer is shown, the method of mounting is not given. Guignard and Irwing (9) studied the head transmissibility of ten male seated subjects, by using a

mechanical shake table. The seated erect posture was standardised and the head response obtained by strapping an accelerometer to the subject's head. The results exhibit two resonances, one in the region of 2-2.4 Hz and the other at 4.8 Hz and the authors observed that the head in a non-linear fashion. Non-linearities have also been noted by Edwards and Lange (10), Vogt, et al (11), and Wittman and Philips (12), whereas, Lange and Edwards (13) and Lee and King (14) have claimed that the head response is linear. Using improved techniques, Coermann (15) studies the vibration transmission from feet to head and seat to head of one subject, in the frequency range of 1-20 Hz. He showed multi-resonances for an erect seated posture, with peaks at approximately 2.5, 5, 11 and 15 Hz, while for the standing erect posture only two resonances have been observed, one in the region of 5 Hz and the other in the region of 12-13 Hz. To obtain the data, light weight accelerometers were mounted on the top of the head with an elastic bandage. Although, the results obtained from these studies provide some basic useful information on the response of the head, they suffer from the following drawbacks: (a) the vibrators employed in majority of the studies were of electro-mechanical types, which might have significantly distorted the fundamental waveform thus contaminating the data, (b) in some

cases, only one or two subjects have been employed, (c) it appears that, in most cases, very few civilians were employed, (d) there exists wide variations in experimental methodologies and measurement techniques, and (e) in some cases, no details have been given about methods of securing accelerometers.

Other reported studies have employed better facilities and better experimental techniques, to evaluate the dynamic response of human head to vibrations. Pradko, et al (16) employed transfer function techniques to investigate the transmissibility of the head acceleration to the input acceleration of a total of fortyone seated erect subjects (all military personnel). They employed both random and sinusoidal vibrations in the range of 1-60 Hz. Random vibrations employed were of a white noise type, filtered through 2 Hz and 10 Hz band pass filters. Results, in general, showed strong linearities between head acceleration and input acceleration. The mean transmissibility of the head acceleration to input acceleration shows two resonant peaks, one at around 4 Hz and the other at around 20 Hz. During the investigation, the accelerometer was taped to a flexible brass plate to facilitate mounting and a wide band adhesive tape was used to restrain the accelerometer from independent movement relative to the head. Rowlands (17) employed a swept sine technique to determine the frequency response of the human body, in the frequency range of 1-30 Hz and presented acceleration amplitude ratio and phase angle plots of head and shoulder for eight various seated postures and limb positions. He employed six male subjects and three acceleration levels. The investigation was carried out by using a multi-axis electrohydraulic vibrator which was designed to produce low acceleration waveform distortions not exceeding 15%. The results of the head/seat response for an average subject, for all the conditions and levels, showed two peaks, one at 3.5 Hz with an amplitude ratio of 1.25 and the second at 13.5 Hz, with an amplitude ratio of 1.83. In between, the curves formed a dip at 8 Hz with an amplitude ratio of 0.3. He also found that the head/seat response was slightly non-linear, and that body posture had considerable influence on the vibration transmitted to the head. A specially designed head harness which could be adjusted to individual requirements was used. The accelerometer was secured onto the harness. Using a man carrying electrodynamic vibrator, Griffin (18) conducted an experiment with 12 seated civilian subjects and six levels of vibration, at 12 frequencies ranging from 7-75 Hz. The principal finding was that body posture had considerable effect on the vibration transmitted to the head. Transmissibility

was calculated in terms of head to seat acceleration ratio. Slight non-linearities were noted in the head response at frequencies below 25 Hz. He employed a 'bite-bar' consisting of a thin steel tube 15 cms in length covered with nylon tubular sleeving and a 14 cms rod attached to one end, and at the other end of which an accelerometer was secured to a magnesium block. This was placed in the mouth of the subject who was asked to bite firmly on the nylon tube and to ensure that the bar remained approximately horizontal. Gary and Ross (19) made head/table transmissibility measurements of 12 male and female civilian standing subjects, in the frequency range of 1-50 Hz. The test table was driven by a hydraulic vibrator. Transmissibility results have been presented in terms of displacement ratio at the head and feet with various acceleration levels being employed. The results show resonant peaks in the neighbourhood of 2,6,20 and 40 Hz, and the authors have claimed good linearity in the head response. Measurements were made by bolting the accelerometer to a plexiglass frame, which was strapped to subject's head. In this study, an attempt has been made to accurately determine head to feet and head to seat transmissibility ratios VS frequency responses of eight civilian male subjects, standing and sitting in various postures. This has been made possible by utilising digital spectrum analysers. All acceleration measurements from the head have been made by employing a light weight miniature accelerometer, which was carefully positioned in subjects' mouth and firmly gripped with their front teeth.

EXPERIMENTAL METHOD

A total of eight healthy male subjects, representing students, academicians, and technicians volunteered to participate in a series of experiments which will be described at a later stage. Table 1 gives the subject details. The following eight typical postures have been considered: (a) Subjects standing straight (P1), (b) Subjects standing straight with arms stretched as in a typical reading situation (P2), (c) Subjects sitting erect with palm on knees (unrestrained and not leaning against the backrest) (P3), (d) Subjects sitting erect with palms on knees (unrestrained but leaning against the backrest) (P4), (e) Subjects sitting erect with arms stretched as in a typical reading situation (unrestrained and not leaning against the backrest) (P5), (f) Subjects sitting erect with arms stretched as before (unrestrained and leaning against the backrest) (P6), (g) Subjects sitting erect with palms on knees (leaning and restrained against the backrest) (P7), (h) Subjects sitting erect with arms stretched as before (leaning and restrained against the backrest) (P8). While adopting the above postures, subjects were asked to completely relax and

TABLE 1							
Subject No.	Age (years)	Weight (kg)	Height (m)	Subject No.	Age	Weight	Height
1	26	67	1.72	5	24	55	1.70
2	35	68	1.70	6	26	75	1.84
3	26	63	1.74	7	39	69	1.80
4	30	65	1.83	8	21	83	1.85

to keep their head as straight as possible, and to avoid all unnecessary body movements. While standing, they were asked to keep their heels together and feet spread at an included angle of approximately 45°, and to keep their body weight distributed equally on both feet. In the arms stretched posture, subjects were asked to hold an A4 size clipping board, weighing approximately 410 grams, so that its center marked by 'X' was at their eye level, and at a distance of approximately 35 cms from their eyes. While sitting, the subjects' feet were kept flat on the vibrator foot rest and the upper & lower legs were maintained perpendicular to each other. While adopting restrained postures, subjects sat on the seat as far back as possible, supported against the backrest in a normal way, without applying extra force at any point. A car seat belt was used to study the effects of the restraint system on the subjects during vibration. Subjects were asked to tighten the seat belt in a snug-fit fashion. In the unrestrained leaning posture, same procedures as described above were followed. Throughout the investigation, constant checks ensured the maintenance of the adopted postures.

The stimulus details are shown in Table 2. A specially designed electrohydraulic vibrator which could be used for human factors work was employed (20). The acceleration waveform distortion produced by the vibrator was in the range of 15-20%. Four levels of 'constant velocity' type of random vibration inputs were employed, details of which are given in Table 3. All random vibration studies were carried out by employing some Ride Simulator vibrators, as described by Ashley (21).

the input and at the head. The input accelerometer was used to monitor the acceleration levels at subject's feet and seat. Measurement of head acceleration was made after orienting the accelerometer in its balanced position and gripping its horizontal flat surfaces by the front teeth in the balanced position. The end of the cable carrying the accelerometer was not allowed to fall abruptly from subject's mouth, instead, the end of the cable was gently lifted up and held in level with the head accelerometer by another subject, or the experimenter who also kept a close watch on the positioning of the head accelerometer and on the attitude of subject's head during vibration conditions. Since the electrohydraulic vibrators employed in this study produced high percentage of acceleration distortion on the fundamentals, it was considered necessary to separate the fundamentals from the harmonics. This was achieved by carrying out spectral analysis on the acceleration signals which was passed through a digital spectrum analyser (Ubiquitous Model UA6 & 1510/UA-500A) which could perform the Fourier Transform at a very high rate and in real time, and calculating the head/table acceleration amplitude ratios of the fundamentals. By this method it was possible to accurately determine the head response at any chosen frequency. Because of the limited capabilities of spectral analysers, it was not possible to extract phase information. Amplitude information on the fundamental vibration was obtained after averaging the spectral information 16 times.

EXPERIMENTAL PROCEDURE

The experimental procedure consisted of exposing each subject in a given posture

Frequency(Hz)	2.5	4	6	8	10	13.5	15	17.5	20	25	30
P.V.S. acceleration level at feet/vibrator	Low Input(L)				Medium Input(M)				High Input(H)		
subject/seat interface (ms ⁻²)	0.64				1.32				2.0		

Oscillator used:- Precision Oscillator made by Prossor Scientific Limited.

TABLE 3		
Input Levels	Mean r.m.s. acceleration (ms ⁻²)	Facilities used
I1	0.3	(a)Pseudorandom signal generator
I2	0.64	(b)'Constant Velocity Filter'
I3	1.32	
I4	2.4	

Two accelerometers (Endevco 2265-20) were used to measure the acceleration levels at

to each of the above points. Starting from the

a duration of approximately a minute, during which time the shaker table input and head response acceleration signals were spectrally analysed. By using the cursor or the calibrated X-Y plotter, r.m.s. acceleration amplitudes of the two signals at a given frequency were accurately determined. The exposure duration of one minute was chosen in order to provide sufficient time for the subjects to stabilize their given posture and to obtain an ensemble average of 16 spectra under steady state conditions. The averaging process was carried out to improve the signal-to-noise ratio and hence the accuracy of the results. The input level was gradually raised to the next higher level and maintained over a duration of one minute during which time the two signals (input and head response) were spectrally analysed and the amplitude ratio calculated. The input level was raised gradually to the next higher level and the whole procedure repeated. After a brief rest, the subject was exposed to another frequency selected at random, and the whole procedure repeated, until all frequencies were covered.

In order to decide on the number of measurements to be made, some limited spectral measurements were repeated four times on one subject at several frequencies & the acceleration amplitude ratios calculated. The results showed repeatability of results within narrow limits of $\pm 10\%$. It was therefore decided to make one spectral analysis at each instant and to make a single amplitude measurement on the fundamental frequency. Similar procedures to that described above were applied to evaluate the transmissibility characteristics of the head to random vibrations. The r.m.s. acceleration levels at subject's input and output (head) were monitored by passing the acceleration signals through low-pass (0-30 Hz) filters (Krohn-Hite) & measuring the filtered signals with a time-domain analyser (JM1860). The head transmissibility spectrum for each subject and posture was obtained after subtracting the input spectrum from the head spectrum at various frequencies. A general layout of the experimental arrangements to evaluate the transmissibility characteristics of the head to sinusoidal & random vibrations is shown in Figure 1. Since the object of this study was to explore the vibration levels present at the head with respect to a specified input level, rather than the dynamic load that the subject imposes on the system, i.e. impedance, the frequency response approach has been preferred to the more usual impedance approach.

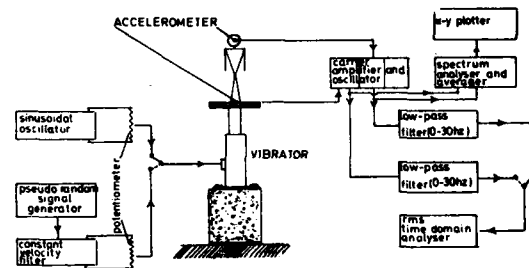


FIGURE 1
GENERAL LAYOUT OF EXPERIMENTAL ARRANGEMENTS TO EVALUATE THE BIO-DYNAMIC RESPONSE OF HUMAN HEAD TO SINUSOIDAL AND RANDOM VIBRATIONS

RESULTS AND DISCUSSIONS

SINUSOIDAL STUDIES

The r.m.s. acceleration data collected from each posture, at various levels and frequencies were converted to acceleration ratios, by dividing the r.m.s. head acceleration by the respective r.m.s. input acceleration. From the pooled ratios of all the individuals, mean and standard deviation values corresponding to each frequency and level were calculated. The results of all the postures were collated from which graphs showing mean acceleration ratio versus frequency have been plotted and are shown in Figures 2 to 5.

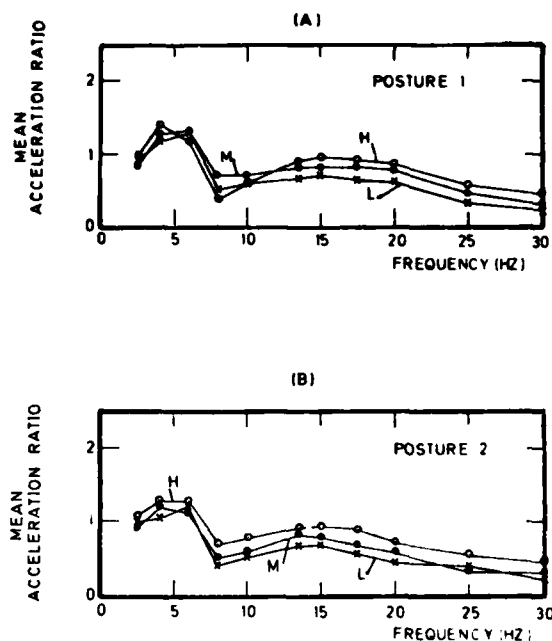


FIGURE 2. HEAD RESPONSE OF STANDING SUBJECTS. (A) Ss STANDING STRAIGHT (B) Ss STANDING STRAIGHT WITH ARMS STRETCHED (L=LOW INPUT; M=MEDIUM INPUT; H=HIGH INPUT)

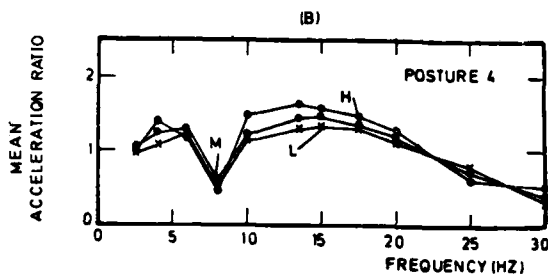
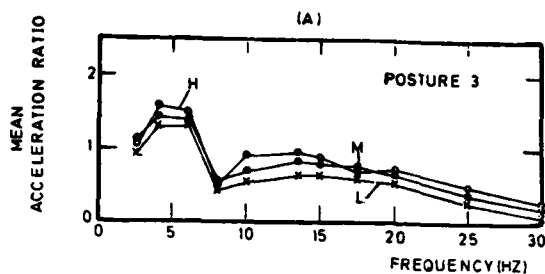


FIGURE 3. HEAD RESPONSE OF SEATED SUBJECTS (A) Ss SITTING STRAIGHT (UNRESTRAINED AND NOT LEANING AGAINST THE BACKREST) (B) Ss SITTING STRAIGHT (UNRESTRAINED AND LEANING AGAINST THE BACKREST)

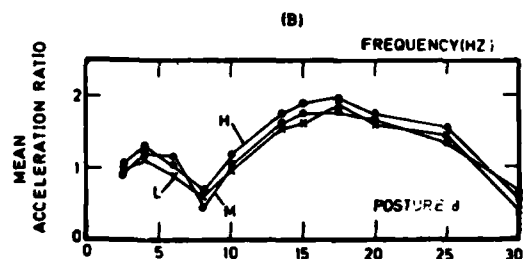
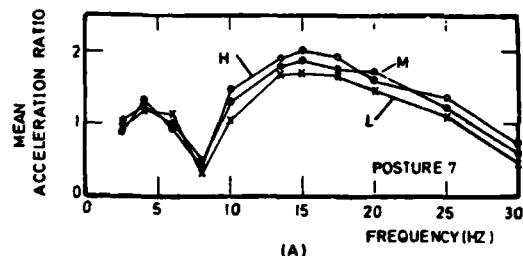


FIGURE 4. HEAD RESPONSE OF SEATED SUBJECTS (A) Ss SITTING STRAIGHT (LEANING AND RESTRAINED AGAINST THE BACKREST) (B) Ss SITTING STRAIGHT (AS IN (A) AND WITH THEIR ARMS STRETCHED)

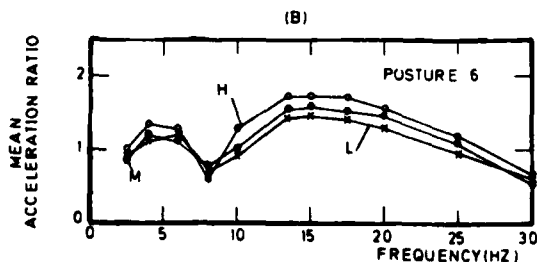
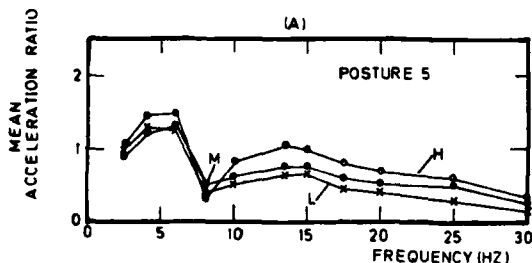


FIGURE 4. HEAD RESPONSE OF SEATED SUBJECTS (A) Ss SITTING STRAIGHT WITH ARMS STRETCHED (UNRESTRAINED AND NOT LEANING AGAINST THE BACKREST) (B) Ss SITTING STRAIGHT WITH ARMS STRETCHED (UNRESTRAINED AND LEANING AGAINST THE BACKREST)

As is seen from these figures, the mean data points are connected by a smooth curve to reveal the shapes of transmissibility characteristics. From the pooled mean data, information on the first resonant frequency, the mean amplitude ratio of the fundamental peaks, mean damping factor, second resonant frequency, mean amplitude ratio at the second resonance, mean damping factor, frequency of the dip together with the mean amplitude ratio, are presented in Table 4. The damping factor, γ , was calculated by using the formula (22),

$$\gamma = \frac{1}{2Q} \quad \text{where } Q = \frac{f_n}{f_2 - f_1}$$

where, f_1 and f_2 are side band frequencies. These points are also referred to as the half-power points (at -3 db). f_n is the resonant frequency (Hz), and Q refers to the sharpness of resonance. It must be realised, that the values of γ are only approximate, as the values of f_n are extrapolated from the curves.

From the analysis, the following general conclusions emerge:-

(a) Within the range of 2.5 to 30 Hz, all the curves exhibit the characteristics of two-degree-of-freedom system, with the first peak occurring in the range of 4 to 6 Hz (mean peak amplitude ratio ranging from 0.82 to 1.87). In between the two peaks, the curves show a dip in the frequency region of 8 Hz with the mean amplitude ratio ranging from 0.41 to 0.68.

TABLE 4

Mean Head Response of Subjects Exposed to Sinusoidal Vibrations

Response	Level Average	Posture 1 (P1)	Posture 2 (P2)	Posture 3 (P3)	Posture 4 (P4)	Posture 5 (P5)	Posture 6 (P6)	Posture 7 (P7)	Posture 8 (P8)
1st Resonant Frequency (Hz)									
L	5	5	5	5	5	5	5	5	5
M	5	5	5	5	5	5	5	5	5
H	5	5	5	5	5	5	5	5	5
Mean	5.3	5.3	5.3	5.3	5.3	5.3	5.3	5.3	5.3
1st Resonant Amplitude Ratio or Resonance									
L	1.2	1.2	1.2	1.2	1.2	1.2	1.2	1.2	1.2
M	1.39	1.12	1.41	1.39	1.32	1.39	1.32	1.39	1.39
H	1.45	1.38	1.47	1.39	1.49	1.38	1.38	1.38	1.38
Mean	1.34	1.25	1.42	1.35	1.36	1.35	1.35	1.35	1.35
2nd Resonant Frequency (Hz)									
L	15	15.5	15	15	15.5	15	15	15	15.5
M	16.2	16.7	15.3	16.7	15.9	15	15	15.3	17.3
H	17	17	15.5	15.5	15.5	15.5	15	15	17.5
Mean	16.4	16.4	15.2	16.4	15.6	15.2	15	15.2	17.3
2nd Resonant Amplitude Ratio or Resonance									
L	0.7	0.66	0.66	1.39	0.69	1.09	1.25	1.09	1.39
M	0.88	0.79	0.89	1.46	0.81	1.36	1.36	1.36	1.39
H	0.95	0.95	0.97	1.49	1.05	1.71	1.67	1.67	1.67
Mean	0.93	0.83	0.87	1.45	0.85	1.39	1.43	1.43	1.45
Mean Frequency of the Dip									
L	0	0	0	0	0	0	0	0	0
M	0	0	0	0	0	0	0	0	0
H	0	0	0	0	0	0	0	0	0
Mean	0	0	0	0	0	0	0	0	0

Response	Level Average	Posture 1 (P1)	Posture 2 (P2)	Posture 3 (P3)	Posture 4 (P4)	Posture 5 (P5)	Posture 6 (P6)	Posture 7 (P7)	Posture 8 (P8)
Mean Amplitude Ratio of the 1st Resonant Peak									
L	0.69	0.42	0.42	0.39	0.43	0.73	0.52	0.61	
M	0.71	0.39	0.41	0.49	0.39	0.73	0.49	0.47	
H	0.39	0.49	0.33	0.47	0.36	0.69	0.43	0.47	
Mean	0.53	0.36	0.32	0.32	0.42	0.69	0.41	0.39	
Mean Damping Factor of the 2nd Resonant Peak									
L	0.39	0.36	0.36	0.37	0.40	0.43	0.43	0.37	
M	0.41	0.31	0.37	0.40	0.46	0.40	0.37	0.36	
H	0.31	0.37	0.33	0.33	0.43	0.37	0.44	0.37	
Mean	0.44	0.47	0.40	0.42	0.46	0.39	0.35	0.36	
Mean Damping Factor of the 1st Resonant Peak									
L	0.43	0.39	0.46	0.43	0.36	0.47	0.43	0.40	
M	0.40	0.36	0.46	0.46	0.39	0.47	0.47	0.41	
H	0.43	0.40	0.42	0.46	0.39	0.36	0.49	0.43	
Mean	0.42	0.36	0.46	0.46	0.39	0.39	0.46	0.41	

An examination of the curve shapes reveals that the first peaks are much sharper than the second peaks. The mean rate of fall-off of the second peaks have been found to be between 9 to 12 dB/octave. Approximate calculations of γ (damping factor) from the two peaks reveal that the first is slightly heavily damped (mean γ ranging from 0.43 to 0.56) than the second (mean γ ranging from 0.33 to 0.5). Comparison of resonant frequency results obtained from this study with that of Dieckmann(7), Rowlands(17) and Gary & Ross(19), in general, shows good agreement. Comparison of acceleration amplitude ratios obtained from the current findings with that of Dieckmann(7) shows good agreement. Whereas that obtained from Rowlands(17) showed first mean amplitude ratios in the range of 1.12 to 1.62 and second mean amplitude ratios in the range of 0.85 to 1.88. The mean amplitude ratio at the dip was found to lie in the range of 0.2 to 0.63. The first peak showed a damping factor of 0.72, followed by a very lightly damped second system. From a phase lag point of view, Rowlands showed the existence of two sub-systems for the first peak, both heavily damped followed by a further two lightly damped systems for the higher peak. To correctly define the number of degree-of-freedom involved in a multiple system such as the human body, information on amplitude ratio and phase at various closely spaced frequencies are needed. Since the number of data points presented

in this paper are very limited and cover no phase information, it must be realised that the conclusion arrived at defining the order of the system is only tentative. Results gathered from various tests, in general, showed large standard deviation values in the frequency region of 2.5 to 17.5 Hz, whereas above 17.5 Hz the variations gradually diminished. The causes for the large variations in the low frequency range may be attributed to (a) subject variability, (b) involuntary postural variations under dynamic conditions, and (c) rotational and transverse movements of the head. At high frequencies, these effects appear to have little influence on the vibration transmission behaviour of the head. Existence of rotational and transverse movements of head subjects were exposed to vertical vibrations have been reported by Walsh(23), Simic(24), and Rance(25). The results have also shown that stretching the arms in various postures do not significantly influence the vibration transmission to the head.

(b) From the results gathered, some postures have shown slight non-linear trends. Out of these some showed a decrease in resonant frequency associated with an increase in amplitude ratio and others have shown increase in resonant frequency with an increase in amplitude ratio as the input level increase. These observations are, however, only approximate as they are based on a limited number of distantly spaced frequency points. By applying the swept sine technique, Rowlands(17) has observed an increase in the maximum amplitude ratio and its associated resonant frequency, as the input level decreased. Griffin(18) has also noticed slight non-linearities in the head response in the frequency range of 7 to 25 Hz.

(c) The dynamic response of the head has been found to vary with different postures. A frequency shift from 4 to 5.3 Hz has been noticed in the first resonance peak. The associated average shift in the amplitude ratio has been found to vary from 1.21 to 1.42. A frequency shift from 14 to 17.5 Hz has been noticed in the second resonance peak. Average amplitude ratios at the second peak varied from 0.82 to 1.87, with no shift in frequency noticeable at the dip. However, the average amplitude ratio at the dip varied from 0.41 to 0.68.

Some basic differences between various postures and conditions were found and these are discussed below:-

A. STANDING SUBJECTS:- Two postures (P1 & P2) were adopted by subjects. Of these, posture P2 showed slight downward shift in the resonant frequencies at the first and second peaks. Whereas the shift in resonant frequency at the first peak was accompanied by a downward shift in the mean amplitude ratio, the shift in resonant frequency at the second peak was associated with a slight upward shift in the mean amplitude

ratio. This means that posture P2 reduces the low frequency transmission and slightly increases the high frequency transmission to the head.

B. SITTING SUBJECTS (POSTURES P3 & P4): Posture P3 reduced high frequency transmission and slightly increased low frequency transmission to the head. Posture P4 had the opposite effect, namely, reduced low frequency transmission and increased high frequency transmission to the head. These findings are in good agreement with those of Rowlands(17).

C. SITTING SUBJECTS (POSTURES P5 & P6): Similar trends as those observed above were noticed.

D. SITTING SUBJECTS (POSTURES P7 & P8): The two postures showed very little difference in its vibration transmission behaviour to the head at low and high frequencies.

Even though different postures produced slight shifts in the first resonant peaks, the differences were not statistically significant at $p=0.05$ level. However, significant shifts in second resonance peaks ($p=0.01$) were observed. Also, significant changes ($p=0.001$) in the maximum amplitude ratios at the two peaks were shown to exist. Tests on statistical significance between posture variables (at different level conditions) were carried out by applying the Friedman Two-Way Analysis of Variance test(26).

ANALYSIS & INTERPRETATION OF RAW DATA

Some detailed into the variations in vibration transmission behaviour of the head due to postural changes have been made and the data on minimum/maximum resonant frequencies and minimum/maximum amplitude ratios observed at the two peaks & dip have been gathered and presented in Table 5. These parameters are selected for discussion because they are regarded as important factors of the transmissibility curves. From the table the following can be observed:-

- For each posture and for each level, there exists minimum & maximum resonant frequencies & amplitude ratios at the peaks and dip.
- Examining the data corresponding to the resonant peak, it is seen that some subjects exhibit resonances in the region of 2.5, 4 and 6 Hz & amplitude ratios in the range of 0.88 to 1.87 have been observed. The occurrence of head resonance in the region of 2.5 Hz has also been observed by Radke(8), Guignard & Irving(9), Coermann(15), Rowlands(17), & Garg & Ross(19). The cause for this resonance is still not clearly understood, and is presumed to be due to the response of the spine. Resonances in the region of 4 to 6 Hz are mainly attributed to the masses of various internal organs located in the thoracic cavity and the mass of the upper body on the stiffness of the spine. The

TABLE 5

Minimum/Maximum Resonant Frequencies and Amplitude Ratios of the Peaks and Troughs (Values are only approximate)

Parameters	Amplitude Ratio	P1	P2	P3	P4	P5	P6	P7	P8
First Resonant Peak:-									
Minimum Resonant Frequency (Hz)	L	2.5	2.5	4	2.5	4	4	2.5	4
	M	4	2.5	2.5	4	4	4	2.5	4
	H	5	2.5	2.5	4	4	4	2.5	4
Amplitude Ratio (Minimum values)	L	1.10	0.90	1.10	1.00	1.21	0.90	0.90	0.90
	M	1.10	0.90	1.32	1.10	1.19	0.90	0.90	1.10
	H	1.10	1.10	1.00	1.10	1.01	1.01	1.10	1.10
Minimum Resonant Frequency (Hz)	L	0	0	0	0	0	0	0	0
	M	0	0	0	0	0	0	0	0
	H	0	0	0	0	0	0	0	0
Amplitude Ratio (Maximum values)	L	1.00	1.41	1.40	1.07	1.40	1.00	1.00	1.01
	M	1.00	1.40	1.01	1.00	1.00	1.00	1.00	1.40
	H	1.00	1.00	1.07	1.10	1.00	1.00	1.00	1.00
Second Resonant Peak:-									
Minimum Resonant Frequency (Hz)	L	10	10	10	10.5	10	10	10.5	10
	M	10	10	10	10.5	10.5	10.5	10.5	10.5
	H	10.5	10	10.5	10.5	10.5	10.5	10.5	10.5

Parameters	Amplitude Ratio	P1	P2	P3	P4	P5	P6	P7	P8
Amplitude Ratio									
Minimum Amplitude Ratio	L	0.60	0.60	0.57	1.30	0.50	1.30	1.44	1.40
	M	0.70	0.60	0.60	1.30	0.50	1.30	1.30	1.30
	H	0.67	0.60	0.60	1.40	0.50	1.44	1.30	1.40
Maximum Amplitude Ratio	L	10	10	10	17.5	10	10	17.5	17.5
	M	10	10	17.5	10	10	10	17.5	17.5
	H	17.5	17.5	10	17.5	10	17.5	17.5	17.5
Amplitude Ratio (Minimum values)	L	0.50	1.10	0.70	1.00	0.70	1.00	1.10	1.40
	M	1.00	1.00	1.00	1.10	1.10	1.00	1.40	1.40
	H	1.00	1.10	1.10	1.07	1.40	1.00	1.40	1.40
Amplitude Ratio (Maximum values)	L	0	0	0	0	0	0	0	0
	M	0	0	0	0	0	0	0	0
	H	0	0	0	0	0	0	0	0
Amplitude Ratio (Minimum values)	L	0.50	0.50	0.50	0.50	0.50	0.50	0.50	0.50
	M	0.50	0.50	0.50	0.50	0.50	0.50	0.50	0.50
	H	0.50	0.50	0.50	0.50	0.50	0.50	0.50	0.50

Parameters	Amplitude Ratio	P1	P2	P3	P4	P5	P6	P7	P8
Amplitude Ratio									
Minimum Amplitude Ratio	L	10	10	0	0	10	10	0	0
	M	0	10	0	0	0	0	0	0
	H	0	10	0	0	0	0	0	0
Maximum Amplitude Ratio	L	0.50	0.50	0.50	0.71	0.50	1.00	0.50	0.50
	M	0.50	0.70	0.70	0.67	0.70	0.91	0.70	0.50
	H	0.50	0.50	0.70	0.60	0.50	0.91	0.50	0.50

existence of these resonances has been confirmed by Dieckmann(7), Radke(8), Guignard & Irving(9), Schmitz, et al(27), Coermann(15), Pradko et al(16), Rowlands(17), & Garg & Ross(19).

(c) Data corresponding to the second resonant peak shows resonances at 10, 13.5, 15, 17.5 and 20 Hz. Due to the fact that the secondary resonances are spread over a wide range of frequencies, the shapes of the mean transmissibility curves in this region are not sharply defined. Amplitude ratios in the range of 0.54 to 2.88 have been recorded. The existence of these secondary resonances of the head have been demonstrated by the above authors and these are attributed to the mass of the whole body on the stiffness of the legs, axial compression of the torso controlled by the elastic properties of the spine column and its supporting musculature, resonant oscillation of the head with respect to the trunk, and numerous minor resonances of superficial structures in the head. Subjective comments during vibration exposures confirmed some of the above attributes.

(d) Dips in the transmissibility curves have been found to occur in the frequency region of 8 to 10 Hz, with amplitude ratios ranging from 0.2 to 1.09. The occurrence of

dips in this range have been reported by some of the above authors. Of these, Rowlands(17) demonstrates frequency dips extending below 8 Hz, well into the region of 6 Hz. The study has shown the existence of frequency and amplitude ratio variations at the peaks and dips, between postures and within postures. Also, response differences between subjects for each posture and at each input level have been noticed. A Wilcoxon test was carried out to find any significant differences between the levels at various frequencies, for each posture and the results showed no significant differences at $p = 0.05$ level. Similar tests were carried out to determine significant differences between various postures and the results are shown in Table 6.

TABLE 6

RESULTS OF WILCOXON TEST BETWEEN VARIOUS POSTURES												
(a) Between Standing straight(P1) and Sitting straight(P3) postures												
Frequency (Hz)	2.5	4	6	8	10	13.5	15	17.5	20	25	30	
Levels												
L	NS	NS	NS	NS	NS	NS	NS	NS	NS	NS	NS	0.02
M	0.02	NS	NS	NS	NS	NS	NS	NS	NS	NS	NS	0.01
H	NS	NS	0.05NS	0.05	NS	NS	NS	NS	NS	NS	NS	NS
(b) Between Sitting straight(P3) & Sitting leaning(P4) postures												
Frequency (Hz)	2.5	4	6	8	10	13.5	15	17.5	20	25	30	
Levels												
L	NS	NS	NS	NS	.02	.01	.01	.01	.01	.01	.02	
M	NS	.02	NS	NS	.02	.01	.01	.01	.01	.01	.02	
H	NS	NS	.02	NS	.01	.01	.01	.01	.01	.01	.05	
(c) Between Sitting straight(P3) & Sitting restrained(P7) postures												
Frequency (Hz)	2.5	4	6	8	10	13.5	15	17.5	20	25	30	
Levels												
L	NS	NS	NS	.05	.01	.01	.01	.01	.01	.01	.01	
M	NS	.01	.01	NS	.01	.01	.01	.01	.01	.01	.01	
H	NS	.02	.01	NS	.01	.01	.01	.01	.01	.01	.01	
(d) Between Sitting leaning(P4) & Sitting restrained(P7) postures												
Frequency (Hz)	2.5	4	6	8	10	13.5	15	17.5	20	25	30	
Levels												
L	NS	NS	NS	NS	NS	.01	.02	.02	.02	.02	NS	
M	NS	NS	.05	NS	NS	.02	.02	.02	.02	.02	NS	
H	NS	NS	.01	NS	NS	.02	.01	NS	.02	.01	NS	
(e) Between Standing straight(P1) & Standing with arms stretched(P2) postures												
Frequency (Hz)	2.5	4	6	8	10	13.5	15	17.5	20	25	30	
Levels												
L	NS	NS	NS	NS	NS	NS	NS	NS	.05	NS	NS	
M	NS	NS	NS	NS	NS	NS	NS	NS	.05	.02	.01	
H	NS	NS	NS	.01	NS	NS	NS	NS	NS	NS	.02	
(f) Between Sitting straight(P3) & Sitting straight with arm stretched(P5) postures												
Frequency (Hz)	2.5	4	6	8	10	13.5	15	17.5	20	25	30	
Levels												
L	NS	NS	NS	NS	NS	NS	NS	.01	.01	NS	NS	
M	NS	.01	NS	NS	NS	NS	NS	NS	.05	NS	NS	
H	NS	NS	NS	.01	NS	NS	NS	NS	NS	NS	NS	
(g) Between Sitting leaning(P4) & Sitting leaning with arm stretched(P6) postures												
Frequency (Hz)	2.5	4	6	8	10	13.5	15	17.5	20	25	30	
Levels												
L	NS	NS	NS	.02	NS	NS	NS	NS	NS	NS	NS	
M	NS	NS	.05	NS	.01	NS	NS	NS	.05	.01	NS	
H	NS	NS	NS	.05	.02	NS	NS	NS	NS	.05	.01	
(h) Between Sitting restrained(P7) & Sitting restrained with arm stretched(P8) postures												
Frequency (Hz)	2.5	4	6	8	10	13.5	15	17.5	20	25	30	
Levels												
L	NS	NS	.01	.02	NS	NS	NS	NS	NS	.02	NS	
M	NS	NS	.05	NS	NS	NS	NS	NS	NS	NS	NS	
H	NS	NS	NS	.05	NS	NS	NS	NS	NS	NS	.02	

NS = Not significant

RANDOM VIBRATION STUDIES SPECTRAL ANALYSIS

Some investigations into the response of the head to vertical random vibration input, of subjects standing straight(P1) & standing with knees bent(P1A) postures were made by Rao(28). The main findings of this study are summarised below:-
(a) Mean head transmissibility curves for the standing straight posture showed two resonant peaks, one in the region of 3.5 to 5.5 Hz and the other in the region of 12 to 15 Hz, thus exhibiting the characteristics of a two-degree-of-freedom system. At higher frequencies the response attenuated at a rate of approximately 12 dB per octave. The dips were found to lie in the region of 6 to 10 Hz. The results also showed that the response of the head was dependent upon the level of the input. The level of damping increased with the intensity of input vibration.
(b) In the knees bent posture, mean transmissibility spectra showed the first resonant peak in the region of 2 to 3 Hz with a lower level of damping than the corresponding mode in the standing straight posture. Adoption of this posture also revealed considerable isolation at frequencies above 6 Hz. A slight degree of non-linearities in the response of the head were also noticed. Mean head transmissibility spectra for postures 2 & 3 are shown in Figures 6 & 7. Since the ordinates of the transmissibility curves were not calibrated, the scales are only arbitrary in nature.

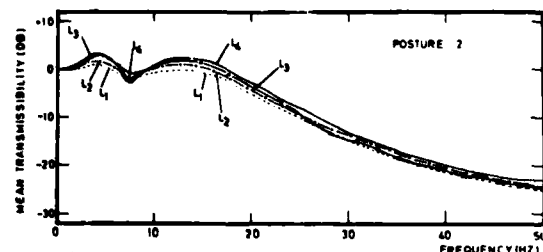


FIGURE 6 HEAD RESPONSE OF STANDING SUBJECTS TO RANDOM VIBRATIONS (IN STANDING STRAIGHT WITH THEIR ARMS STRETCHED)

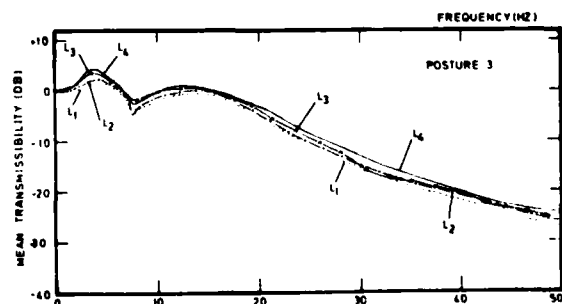


FIGURE 7 HEAD RESPONSE OF SEATED SUBJECTS TO RANDOM VIBRATIONS (IN SITTING UNRESTRAINED AND NOT LEANING AGAINST THE BACKREST)

The curves, in general, reveal the following:-

(a) All the curves exhibit the characteristics of a two-degree-of-freedom system.
(b) Posture 3 has shown a reduction in high frequency transmission and a slight increase in low frequency transmission to the head, whereas, posture 4 has shown the opposite effect. Similar observations have been made under sinusoidal vibration conditions.

(c) Slight non-linear trends in each posture have been shown to exist. The direction of non-linearity for different postures are dissimilar. Similar trends have been observed under sinusoidal conditions.

(d) At higher frequencies the response of all the transmissibility curves attenuates at the rate of approximately 12 dB/octave. Within the frequency range of 1 to 30 Hz, the results of both sinusoidal and random vibration studies have shown good agreement in terms of overall response curve shapes, resonance frequencies, and non-linear trends.

ANALYSIS OF WEIGHTED ACCELERATION LEVELS

In each posture, a set of six weighted r.m.s. acceleration measurements were taken over the exposure duration of one minute, on each subject and at each input level. These results were converted to percentage transmissibility figures. The overall mean and standard deviation data on the head transmissibility of subjects in various postures are presented in Table 7. The results reveal the following:-

TABLE 7

Mean and Standard Deviation Data on Head Transmissibility (%) of Subjects Exposed to Constant-Velocity Type of Random Vibration

Levels	Posture 1 (P1)	Posture 1A (P1A)	Posture 2 (P2)	Posture 3 (P3)	Posture 4 (P4)	Posture 5 (P5)	Posture 6 (P6)	Posture 7 (P7)	Posture 8 (P8)
1	MEAN 98	56	98	92	12.4	99.3	127.6	112.3	100.9
	SD 39	21	22	22	22	22.3	22.9	21	19
2	MEAN 86	45	88	88	114	86.1	116.4	114.3	107.5
	SD 15	20	9	20	26	16.3	22.2	20	19
3	MEAN 77	36	75	71	98	76.3	106.1	106.8	100.8
	SD 10	22	7	15	19	14.3	18.4	14	17
4	MEAN 73	20	72	66	91	66.2	98.6	98.9	95.3
	SD 19	18	11	6	6	9	17	17	21

ing:-

(a) All postures show a decrease in percentage transmissibility with an increase in input level. This may be attributed to the general dislike of subjects to random vibrations resulting in complaints of discomfort sensations relating to the head region. Because of this, subjects knowingly or unknowingly may well have adjusted their postures in such a way as to attenuate vibrations transmitted to the head.

(b) The results also show that leaning against the backrest increases the level of vibration transmission to the head.

(c) The straight legs in posture 1 merely act as a vibration transmitting columns. If the knees are allowed to bend, as in posture 1A, the lower limbs can be effectively used as very efficient vibration isolators. This fact has also been demonstrated by Radke(29) and Hornick(30) using sinusoidal vibrations. The current study has also shown no significant variations in head transmissibility of standing subjects (postures 1 & 1A) over an exposure duration of one minute. This observation contradicts the findings of Hornick(29) who reported that human legs lost some of their isolation properties within a two minute period.

(d) Stretching arms in various postures has very little influence on the amount of vibration transmitted to subjects' head. Results of Wilcoxon test applied between various postures are shown in Table 8.

TABLE 8

RESULTS OF WILCOXON TEST BETWEEN VARIOUS POSTURES

RANDOM VIBRATION INPUT

Postures	Level 1 (L1)	Level 2 (L2)	Level 3 (L3)	Level 4 (L4)
P1 - P3	NS	NS	NS	NS
P3 - P4	<0.05	0.05	<0.05	0.05
P3 - P7	NS	<0.05	<0.05	0.05
P4 - P7	NS	NS	NS	NS
P1 - P2	NS	NS	NS	NS
P1 - P1A	<0.05	<0.05	<0.05	<0.05
P2 - P5	NS	NS	NS	NS
P4 - P6	NS	NS	NS	NS
P7 - P8	NS	NS	NS	NS

NS = Not Significant

The results, in general, reveal the following:-

(a) Significant differences ($p \leq 0.05$) between sitting straight (P3) and sitting leaning (P4) postures, between sitting straight (P3) and sitting restrained (P7) postures, and between standing straight (P1) and standing with knees bent (P1A) postures have been found.

(b) No significant differences were noticed between any other postures.

SOME STUDIES ON THE MEASUREMENT OF HEAD & SHOULDER VIBRATION DURING WALKING

An attempt was made to investigate the vibration characteristics of head and shoulder of twenty nine civilian male subjects during walking by Rao(31). The main relevant findings of this study are:-

(a) The normal walking frequencies lie in the range of 1.2 to 2 Hz, with the mean at 1.45 Hz. High r.m.s. acceleration levels at head and shoulder have been observed. The mean levels found are within 25 mins. and 1 hour ISO FDP boundaries.

(b) The frequency response of the head

during walking show the existence of three resonances and the two dips. The first peak occurring in the frequency region of 1.2 to 2 Hz, the second peak in the frequency region of 3.7 to 6 Hz, and the third resonance in the region of 13 to 24 Hz. The first dip has been found in the region of 2.2 Hz and the second dip in the frequency region of 7.5 to 10 Hz approximately. As it was not possible to evaluate the transmissibility characteristics of the head at that time, it would be difficult to predict precisely, the number of degrees-of-freedom that the head possess during walking.

(c) Comparison of the results obtained from the walking studies with those of sinusoidal studies have shown good agreement in terms of resonant frequencies in the region of 2.5 to 30 Hz.

GENERAL CONCLUSION

In this paper, attempts have been made to accurately determine the transmission of sinusoidal and random vibrations from feet and seat to the heads of standing and sitting subjects in various postures. It is realised, of course, that this study will not solve most of the problems faced by previous investigators. However, it is a step forward and does not solve some other major instrumentation problems.

In the case of sinusoidal studies, amplitude ratio vs frequency information covering various postures have been presented and the results discussed both individually and collectively.

Results of random vibration experiments covering some limited postures have been presented in terms of mean transmissibility spectra, percentage transmissibility vs time, percentage transmissibility vs input levels and the results discussed.

Also, some investigations into the vibrational characteristics of head and shoulder during walking have been made and the results discussed.

Results gathered from sinusoidal and random vibration studies have shown the following common features:-

- (a) The head behaves like a two-degree-of-freedom, visco-elastic system, the first peak lying in the region of 2.5 to 6 Hz, the second peak occurring in the frequency region of 10 to 24 Hz, and the dip appearing in the region of 8 to 10 Hz.
- (b) The first peak has been found to be much sharper than the second peak.
- (c) Both studies have shown non-linear tendencies, but the direction of non-linearities have not been the same throughout.
- (d) Both studies have revealed that leaning against the backrest increases the high frequency transmission and decreases the low frequency transmission to the head

whereas, opposite trends are indicated where the backrest is not used.

(e) Stretching of arms in various postures have brought slight but insignificant changes in the vibration transmission behaviour of the head.

(f) Changes in the vibrational behaviour of head between sitting unrestrained and sitting restrained have been noticed. Such changes are occasionally significant.

(g) Slight but insignificant changes in the vibrational characteristics of head have been noticed between standing and sitting postures.

Studies conducted on walking subjects have revealed high vibrational levels at the head and shoulder. Barton & Hefner(32) have similarly showed that the statistical measures of whole-body vibration from ambulation to be higher than those from operation of earth moving machinery and significantly higher than the published guidelines for human exposure to whole-body vibration.

It was also found that when some subjects in the standing straight posture, were exposed to whole-body sinusoidal vibrations corresponding to the resonant frequencies of the head in such a way that the input r.m.s. acceleration levels at the foot-vibrator interface were adjusted to give corresponding r.m.s. acceleration levels at the head, the sensation of some subjects ranged from being 'neutral' to 'very uncomfortable'. Some others complained total discomfort sensations well before the desired levels were reached. It, therefore, appears that during walking, some filtering process is generated within the body so as to reduce excessive vibration levels from reaching the sensitive parts of the human body. It would be interesting to explore in some depth the mechanics of this filtering process. It is also interesting to note that the results of walking studies showed head resonances in the same frequency range as those observed during sinusoidal & random vibration studies.

The ISO(33) while publishing their specification on Guide to Human Response to Whole-body Vibration, have recognised maximum sensitivities in the frequency region of 4 to 8 Hz. This paper has clearly shown that resonances of the head in the frequency region of 2 Hz and 10 to 25 Hz are equally important from the view point of human comfort, performance and quite possibly health.

ACKNOWLEDGEMENT

The author is grateful to the SERC for their financial support and to the Head of the Mechanical Engineering Department, The University of Birmingham, England for providing the necessary facilities to carry out the investigations.

REFERENCES

1. Coermann, R.R. (1938). Jahrb. deut. Luftfahrtforschung. 3. 111.
2. von Békésy, G. (1939). Akust. Z. 4. 360.
3. Mullen, E.A. (1939). Die wirkung sinusförmiger vertikaler schwingungen auf den sitzenden menschen. Arbeitphysiologie. 10. 464-476.
4. Lockle, W.E. (1944). Arbeitphysiologie. 13. 79.
5. Latham, F. (1957). A study of body ballistics: Seat ejection. Proc. Royal. Soc. B. 147. 121-139.
6. Dieckmann, D. (1957). Einfluss vertikaler mechanischer schwingungen auf den menschen. Intern. A. angew. Physiol. 16. 519-564.
7. Dieckmann, D. (1958). A study of the influence of vibration on man. Ergonomics. 1(4). 347-355.
8. Radke, A.O. (1957). Vehicle vibration. Man's new environment. Paper 57454. Presented at ASME meeting. New York.
9. Guignard, J.C. & Irwing, A. (1960). Effects of low frequency vibration on man. Engineering. 9.
10. Edward, R.G. & Lange, K.O. (1964). A mechanical impedance investigation of human response to vibration. AMRL-TR-64-91. Wright-Patterson Air Force Base.
11. Vogt, H.L., Coermann, R.R. & Fust, H.D. (1968). Aerospace Medicine. 39(7). 675-679.
12. Witman, T.G. & Phillips, N.S. (1969). Journal of Biomechanics. 2. 281-288.
13. Lange, K.O. & Edwards, E.G. (1970). Aerospace Medicine. 41(5). 538-543.
14. Lee, R.A. & King, A.I. (1971). Journal of Applied Physiology. 30(2). 281-286.
15. Coermann, R.R. (1962). The mechanical impedance of the human body in sitting & standing position at low frequencies. Human Factors. Vol. 4. No. 3.
16. Pradko, F., Orr, T.R. & Lee, R.A. (1965). Human vibration analysis. SAE paper 650426.
17. Rowlands, G.F. (1974). The transmission of vibration by the human body with special reference to the problem of measurement and analysis. Ph.D. Thesis. Loughborough University of Technology.
18. Griffin, M.J. (1975). Aviat. Space Environ. Med. 46. 269-276.
19. Gary, D.P. & Ross, M.A. (1976). Vertical mode human body vibration transmissibility IEEE Transactions on Systems, Man & Cybernetics. Vol. SMC-6. No. 2. 102-112.
20. Rao, B.K.N. (1978). Some studies on human response to low frequency whole-body vibrations. Ph.D. Thesis. University of Birmingham.
21. Ashley, C. (1972). The constant velocity approach to vehicle ride testing in the laboratory. Belgrade International Automobile Engineering Symposium. Paper H4.
22. Thomson, W.T. (1969). Vibration theory & applications. George Allen & Unwin Ltd. London.
23. Walsh, E.G. (1966). Head movements during rail travel. Bio-Medical Engng. 402-407.
24. Simic, D. (1971). Physiologische Grundlagen des schwingungskomforts. Automobile Industrie. Roma. May-June.
25. Rance, B. (1975). Angular head motion produced by linear vertical (G_z) vibration of seated human subjects. Paper to the U.K. Informal Group Meeting on Human Response to Vibration. University of Southampton. September.
26. Siegel, S. (1956). Nonparametric statistics for the behavioral sciences. McGraw-Hill Book Co. Inc. New York.
27. Schmitz, M.A., Simons, A.K. & Boettcher, C. (1960). The effect of low frequency, high amplitude, whole-body vertical vibration on human performance. Report 130. Bostram Research Labs. Milwaukee. Wisconsin.
28. Rao, B.K.N., Ashley, C., Jones, B. (1975). Effects of postural changes on the head response of standing subjects subjected to low frequency constant velocity spectral inputs. Journal of the Society of Environmental Engineers. March.
29. Radke, A.O. (1958). Mech. Engng. N.Y. 80(7). cited by Guignard, J.C. in 'A textbook of aviation physiology', Edited by Gillies, J.A. Oxford: Pergamon. Chapter 29. 1965.
30. Hornick, R.J. (1962). Vibration isolation in the human leg. Human Factors. 4. 301-303.
31. Rao, B.K.N. & Jones, B. (1975). Some studies on the measurement of head & shoulder vibration during walking. Ergonomics. No. 5. 555-566.
32. Barton, J.C. & Hefner, R.E. (1976). Whole-body vibration levels: a realistic baseline for standards. Society of Automotive Engrs. Paper No. 760415.
33. The International Standardisation Organisation. ISO. 2631. Guide to Human Response to Whole-Body Vibration. Geneva.

FLIGHT ENVIRONMENTS

YC-15 EXTERNALLY BLOWN FLAP NOISE

Capt. Lyle G. Peck
Flight Dynamics Laboratory
Air Force Wright Aeronautical Laboratories
Wright-Patterson AFB, Ohio

The purpose of this project is to determine the acoustic environment on the wing/flap region of the McDonnell-Douglas YC-15 Short Takeoff and Landing cargo aircraft. The YC-15 is designed for augmented lift through the use of externally blown flaps deflecting the jet exhaust thereby turning the flow and increasing lift. This process creates an intense acoustic environment on the wing/flap region. Ten transducers on the right inboard wing/flap were selected for data analysis. Test conditions included takeoff, landing, taxi, cruise and ground static over the full range of operating conditions. Results of the test are in the form of narrowband and one-third octave plots, comparing the affects of engine pressure ratio, flap angle, microphone location, and forward speed on the acoustic environment in the wing/flap region.

INTRODUCTION

The purpose of this paper is to present the results of an analysis of the acoustic environment on the wing and flap region of the YC-15 aircraft. The four engine aircraft employs an Under-the-Wing (UTW), Externally Blown Flap (EBF) system to provide the additional lift necessary for short takeoff and landing capability. The engine exhaust impinges on the wing and double flap system, creating an intense acoustic environment conducive to the acoustic fatigue of structural components.

While considerable acoustic data exist from model tests of EBF systems, data from full-scale operational systems are quite limited. The objective of this program is to determine the effect of a number of flight parameters (engine pressure ratio, flap angle, transducer location and forward speed) on the acoustic environment in the near field of the engine, wing and flap.

While the complete YC-15 EBF acoustic test program included 22 thermocouples, 10 accelerometers, 22 static pressure transducers, 22 fluctuating pressure transducers, 2 flap internal

pressure, and 4 total pressure transducers (Kiel probes), this paper is concerned with only those fluctuating pressure transducers (FPT) in the immediate vicinity of the #3 inboard engine. This includes 5 FPT's located on the underside of the wing/flap structure on the centerline extending aft from the engine. One FPT was located on the top of the front flap and three additional FPT's were located off the centerline, two inboard and one outboard. In addition to the 9 FPT's, 1 accelerometer, located on the second flap, was selected to provide sample vibration data. The intent was to provide a fairly complete survey of the engine near field acoustic environment yet maintain a manageable amount of data.

Tests were performed for a variety of conditions during both ground and flight operations. Engine pressure ratio varied from 1.0 at idle to 2.2 at takeoff power. Noise data were recorded at flap angles of 0°, 22°, and 46°, which covers the entire range of flap motion, for forward velocities from 0 ft/sec at ground static condition to 326 knots (550 ft/sec) during flight. Noise

data were reduced in the form of 1/3 octave and narrowband plots.

AIRPLANE DESCRIPTION

The YC-15 is a full-scale prototype of a Short Takeoff and Landing (STOL) cargo plane designed by McDonnell-Douglas for the USAF Advanced Medium STOL Transport program. A description of the YC-15 is given in Reference 1 and is included here.



Fig. 1 - YC-15 Aircraft

The YC-15 (Figure 1) is a wide-bodied, high-wing, T-tailed military transport airplane. Four Pratt & Whitney JT8D-17 engines, rated at 16,000 pounds (71,168 N) thrust at sea level under static conditions, are mounted in a forward position under the wing. The unswept wing embodies supercritical airfoil technology enabling the YC-15 to achieve modern jet transport speeds. The high-lift system of the YC-15 consists of large chord two-segment flaps, and full-span leading-edge devices. The flaps are designed to penetrate the engine exhaust even at small deflection angles and to deflect the engine efflux downward at approximately the same angle as the flap deflection. This is accomplished by a double four-bar linkage which lowers the flap initially, and then progressively deflects and separates the two almost equal chord segments of the flap. The spoilers ahead of the flaps are drooped as a function of flap motion, to maintain an effective slot between the forward flap and the wing upper lip (spoiler trailing edge). The high lift system relies to a degree on the underlying principle of the jet flap; therefore, the required lift is achieved both from the

deflected thrust and the increased wing circulation.

Further details of the YC-15 airplane and test program can be found in the flight test plan [2]. The YC-15 systems that directly pertain to this paper are described below.

The engines are installed in nacelles (no acoustic treatment) that are supported by a wing pylon, positioning the engine exhaust nozzles forward of and just below the wing leading edge. The general arrangement of the propulsion system is illustrated in Figure 2.

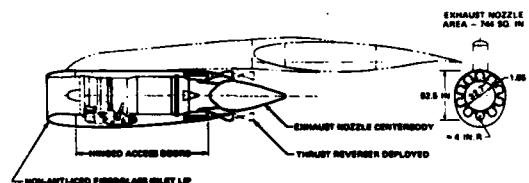


Fig. 2 - Propulsion System

The external mixer nozzle arrangement promotes good mixing of fan and primary exhaust air with freestream air to produce rapid temperature and velocity reduction and to spread the exhaust wake over a large span of the flap.

The centerlines of the inboard and outboard engines are at fuselage station $Z = 34.3$, $X = +206.0$ and $Z = 33.5$, $X = +331.0$, respectively, and the jet exit planes are at $Y = 693.5$ and 706.0 , respectively. The flap linkage system is shown in Figure 3 [1].

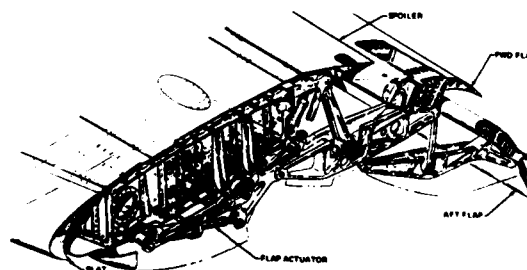


Fig. 3 - Wing/Flap System

TEST DATA ACQUISITION, AND DATA REDUCTION

Testing took place on 5 and 7 May 1976 at Edwards Air Force Base, California. The aircraft used during the test was designated aircraft No. 1. Table I gives the aircraft operational conditions for the two flights analyzed.

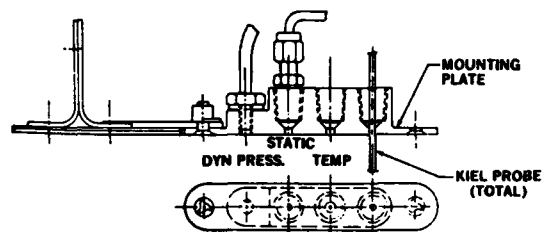


Fig. 4 - Transducer Mounting Plate

TABLE I
Aircraft Operational Condition [3]

Weight Data	Flight 71	Flight 72
Zero Fuel Weight, lbs (kgs)	117,400 (53,364)	117,400 (53,354)
Ramp Gross Weight, lbs (kgs)	171,400 (77,909)	140,600 (63,909)
C.G. (% MAC)	32.5	31.4

This report is concerned with the fluctuating pressure transducers and one accelerometer near the #3 engine.

The FPT's are flush mounted through the wing/flap skins as shown in Figure 4. The location of the transducers is shown in Figure 5 with their exact positions denoted in Table II.

TABLE II
Transducer Location 3

TRANSDUCERS	LOCATION OF FLAP INSTRUMENTATION (INCHES)								
	$\alpha=0$ DEG			$\alpha=22$ DEG			$\alpha=46$ DEG		
	X	Y	Z	X	Y	Z	X	Y	Z
MIC 01	206.00	179.77	-7.20	206.00	179.77	- 7.20	206.00	179.77	- 7.20
MIC 10	189.85	199.50	-4.42	101.31	218.10	-14.29	192.54	228.03	-21.17
MIC 14	203.00	198.80	-4.42	204.44	217.08	-14.06	205.65	226.85	-20.76
MIC 17	203.00	199.50	8.75	204.49	221.11	- 1.46	205.90	233.98	- 9.67
MIC 20	202.80	209.92	-2.75	204.54	228.26	-15.27	205.93	237.33	-24.82
MIC 24	282.05	196.75	-4.05	284.01	213.12	-12.81	285.15	221.79	-18.99
MIC 46	189.85	221.32	-0.43	193.78	254.20	-25.41	196.88	266.76	-46.54
ACC 49	201.10	219.00	-1.25	204.90	251.22	-25.14	207.91	263.70	-45.27
MIC 50	201.50	228.10	-0.20	205.74	259.93	-27.88	208.94	270.71	-51.08
MIC 56	201.20	238.16	0.55	205.91	259.42	-31.28	209.33	278.22	-57.80

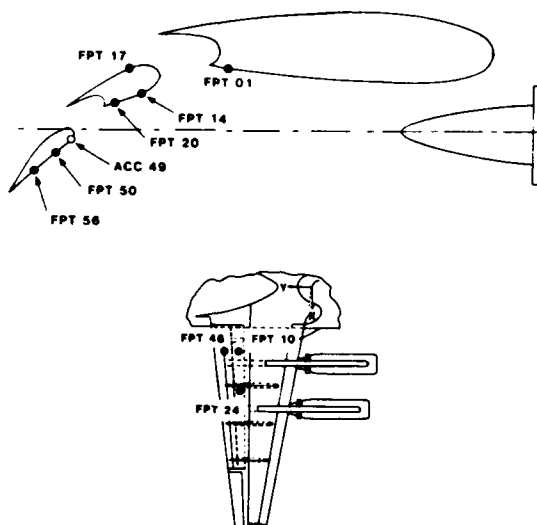


Fig. 5 - Transducer Location on Engine #3 Centerline

A complete description of the equipment calibration, data collection and preliminary data reduction can be found in Reference 1.

Tables III and IV list the conditions at which data for this paper were taken.

The data, which were stored on analog magnetic tape, were reduced to 1/3 octave and narrowband plots. One-third octave plots for all transducers at all the test conditions in Tables III and IV were produced in frequencies from 0 to 10K Hertz. Narrowband plots were made from the output of FPT 01 and accelerometer 49, for the frequency range 3HZ - 10KHZ. In some instances the transducers are denoted by the last two digits of their four digit designation. (e.g. 14 is transducer 2614)

DISCUSSION AND RESULTS

The sources of jet noise associated with conventional aircraft are clearly present in the YC-15. The noise associated with high velocity, high temperature exhaust flow is present, as in standard cargo aircraft. In addition, sources unique to STOL aircraft add to the noise environment. The exhaust jet impinges on and is deflected by the wing/flap system creating "scrubbing" noise. Trailing edge noise and high speed air flowing around and between the flaps intensify the fluctuating pressure at certain frequencies. The combination of these sources produces an intense acoustic environment conducive to fatigue of aircraft structure. This environment is extremely complex, and only rudimentary techniques to predict the near field acoustic levels are currently available.

TABLE III
Ground Tests

Condition	Altitude	Flaps	Velocity	Engines
Ground Static	2275	0°	0	1,2,3,4 @ IDLE
Ground Static	2275	0°	0	2,3 @ 1.55, 1,4 @ IDLE
Ground Static	2275	0°	0	2,3 @ 1.85, 1,4 @ IDLE
Ground Static	2275	0°	0	2,3 @ 2.21, 1,4 @ IDLE
Ground Static	2275	22°	0	1,2,3,4 @ IDLE
Ground Static	2275	22°	0	2,3 @ 1.55, 1,4 @ IDLE
Ground Static	2275	22°	0	2,3 @ 1.85, 1,4 @ IDLE
Ground Static	2275	22°	0	2,3 @ 2.21, 1,4 @ IDLE
Ground Static	2275	46°	0	1,2,3,4 @ IDLE
Ground Static	2275	46°	0	2,3 @ 1.55, 1,4 @ IDLE

TABLE IV
Flight Tests

Condition	Altitude	Flaps	Velocity (Kts)	Engines
Level Flight	18,069	0°	192	1,2,3,4 @ 1.42
Level Flight	18,069	0°	245	1,2,3,4 @ 1.6
Level Flight	17,998	0°	287	1,2,3,4 @ 1.68
Level Flight	18,028	0°	325	1,2,3,4 @ 1.9
Level Flight	29,777	0°	238	1,2,3,4 @ 2.01
Takeoff and Climbout	2275+	24°	100	1,2,3,4 @ 2.23
Approach	2275+	46°	85	1,2,3,4 @ 1.40

In addition to the environment noted above, additional problems associated with the physical conditions under which data were collected may introduce greater complexity in evaluating the results. A few preliminary comments address these phenomena.

The presence of the ground plane affects the SPL. References 4-7 address the problem of ground reflection of jet exhaust suggesting up to 10 dB variation in SPL at frequency dependent locations. For a microphone over a perfect reflector, the difference in overall sound pressure level (OASPL) is estimated to be, on an average, 3 dB above the free-field value, with non-perfect surfaces [5]. An acoustic wave reflected from the ground would not be expected to have a significant effect on the locations in the jet flow because of the overwhelming effect of localized pressure fluctuations.

Taking measurements in the jet flow presents other difficulties when interpreting the results since the transducers are excited by combined jet noise and surface flow-generated noise. For this study, no attempt was made to separate these two noise sources and the data are reported in terms of sound pressure level (SPL). The major interest was in the acoustic fatigue environment seen by the wing/flap structure, and both the acoustics and fluid flow contribute to the structural excitation.

These physical constraints should be considered if the data presented here is compared with other STOL data

taken under different physical conditions.

ENGINE PRESSURE RATIO

Engine Pressure Ratio (EPR) is used in this paper only as a reference for engine thrust setting. The EPR varies from 1.0 at idle to 2.2 at full throttle (takeoff thrust). Figure 6 depicts the jet Mach number and percent thrust as a function of EPR for the range of static and flight conditions as tabulated in Reference 1.

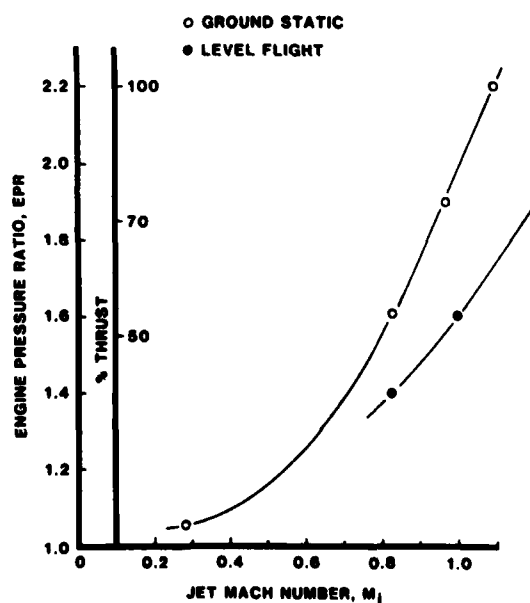


Fig. 6 - Jet Mach Number vs. EPR and Thrust

Figure 7 illustrates typical effects of increasing the engine pressure ratio for the FPT's on the lower surface of the wing/flap system on the engine centerline. The test condition for Figure 7 is with flaps at 0°, engine 1 and 4 at idle and engines 2 and 3 varying from idle to takeoff condition in four steps.

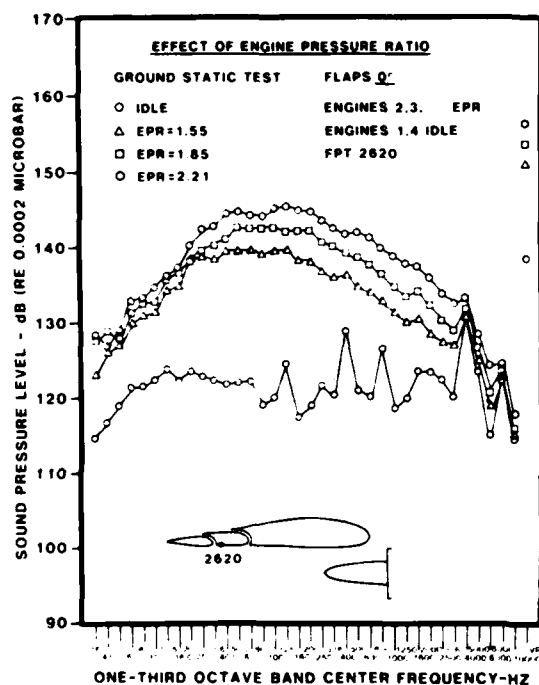


Fig 7 - Effect of Engine Pressure Ratio, Ground Static

The shape of the noise spectra is the familiar "haystack" typical of jet noise from conventional aircraft. The sound pressure level increases with frequency up to a fairly wideband peak in the range of 30-400 Hz for the ground static tests, and then decreases in SPL with increasing frequency.

For all FPT's the spectra for the idle condition do not display the noted trends and are generally flat with the exception of peaks, due to rotational sources in the engine at low EPR's. Overall sound pressure levels increase 12-15 dB as EPR is increased from 1.0 (idle) to 1.42. Further increases in OASPL of 2 to 3 dB are noted for EPR increases to 1.85 and 2.2.

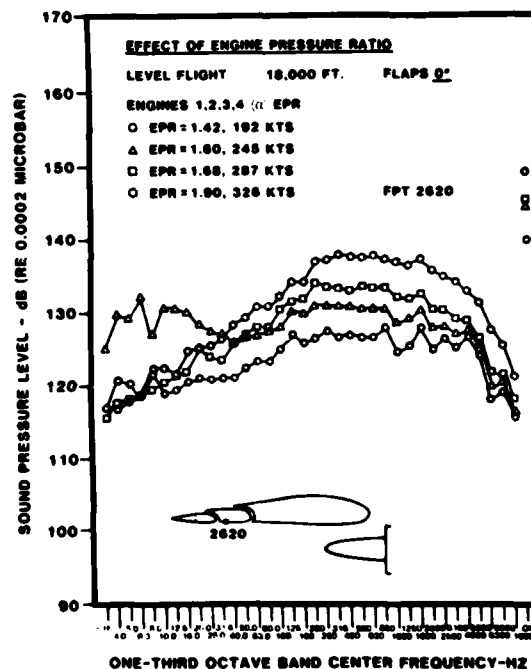


Fig. 8 - Effect of Engine Pressure Ratio, Level Flight

The effect of engine pressure ratio on noise was also evaluated during level flight conditions. Figure 8 illustrates a set of typical spectra, these being for the microphone on the aft portion of the first flap. Notable changes in spectrum shape are seen with forward velocity and will be discussed in a subsequent section. Approximately a 10 dB increase in OASPL is seen with an increase in EPR from 1.42 to 1.90. A significant disparity is seen for the EPR = 1.60 case; below approximately 40 Hz the spectrum is 5 to 10 dB above the level for the other three cases. The spectrum becomes consistent with the other EPR's above 40 Hz. This effect is also seen on the FPT on top of the flap, where little or no EPR effect was seen. The cause of this anomaly is not readily apparent since no other parameter changes were reported for this test condition.

FLAP ANGLE EFFECTS

The YC-15 flaps are continuously variable from 0° to 46°. Three test conditions were selected to simulate STOL takeoff (22°), STOL landing (46°), and cruise (0°). For the test conditions of 0° and 22°, EPR's varied from

1.0 to 2.2. However, for the 46 flap deflection the highest EPR was approximately 1.55 due to operational restrictions. A comparison of SPL's for the three flap angles is shown in Figure 9 for the 1.55 EPR condition.

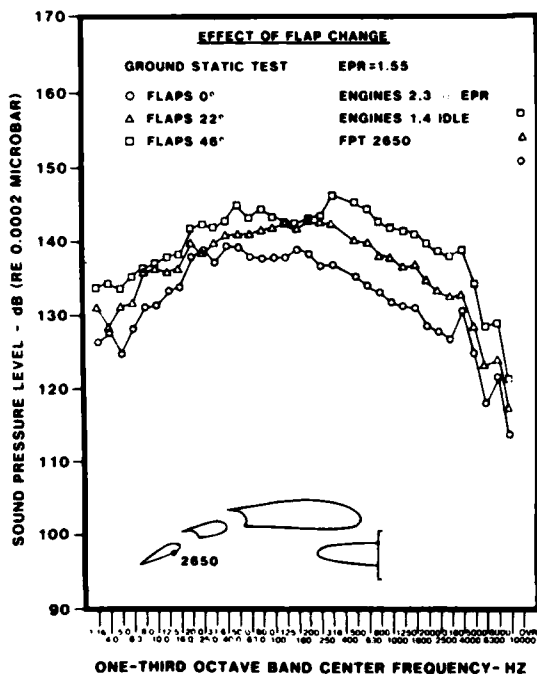


Fig. 9 - Effect Flap Angle Change

This figure typifies the effect of changing flap angle for the underside of the wing/flap structure. The effect due to the flap angle change is most apparent on the forward FPT of the aft flap (2650). An increase in flap angle from 0° to 22° or from 22° to 46° corresponds to an increase of 3 dB overall for each change, for a total increase in OASPL of approximately 6 dB. The spectra display a roughly continuous 5 dB SPL difference in the 316 to 10,000 Hz range. FPT 2650 registered the highest OASPL for any condition, with an overall level of approximately 161 dB. In contrast, FPT 2601 on the rear of the wing structure shows very little difference in spectrum shape or OASPL as flap angle is changed. The OASPL only increases from 150 dB to 151 dB with a flap change from 0° to 46°. This is as expected, since the relative location of the FPT with respect to the exhaust flow does not vary with flap angle. Consequently, any change in SPL is dependent on feedback and flow perturbations caused by interaction of the

efflux and flaps downstream of the transducer.

FLUCTUATING PRESSURE TRANSDUCER LOCATION

The effect of location has already been touched upon for the underside of the wing/flap structure on the engine centerline. Figure 10 compares the spectra of the two FPT's inboard and outboard of the engine centerline on the underside of the leading flap.

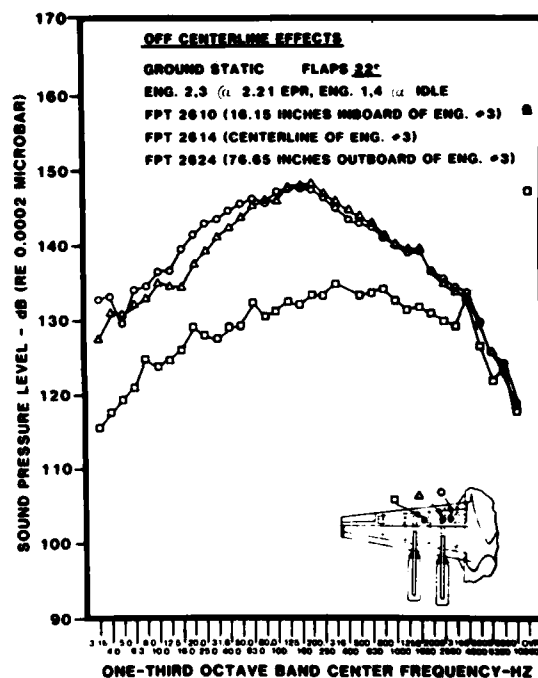


Fig. 10 - Transducer Inboard and Outboard of Engine #3 Centerline

FPT 2610 is 16.15 inches inboard of FPT 2614 which is on the centerline. FPT 2624 is 76.65 inches outboard of the centerline. The spectra for 2610 and 2614 are very similar since both FPT's are in the exhaust flow. At frequencies up to approximately 80 Hz the inboard FPT exhibits a level up to 5 dB above the centerline FPT. Above that frequency, they compare very closely. The OASPL's compare within + 1 dB. FPT 2624, which is not in the exhaust flow, shows an approximately 10-12 dB lower OASPL but also a significant frequency shift to a broad peak in the 300-800 Hz range. Low frequency levels are approximately 10 dB below the levels

for the two FPT's in the exhaust. The difference increases to about 15-18 dB at midrange and then tends to converge at higher frequencies. A similar trend is noted on the rear flap where FPT 2646, which is 13.15 inches inboard of the centerline, shows a higher SPL, up to about 100 Hz. At higher frequencies 2650 shows up to 6 dB higher SPL's. Overall levels consequently only differ by 2 dB.

FPT 2617, which is on the upper surface of the leading flap, is in a different environment than FPT 2614 which is on the lower surface. The effect of shielding by aircraft structure is clearly shown in Figure 11.

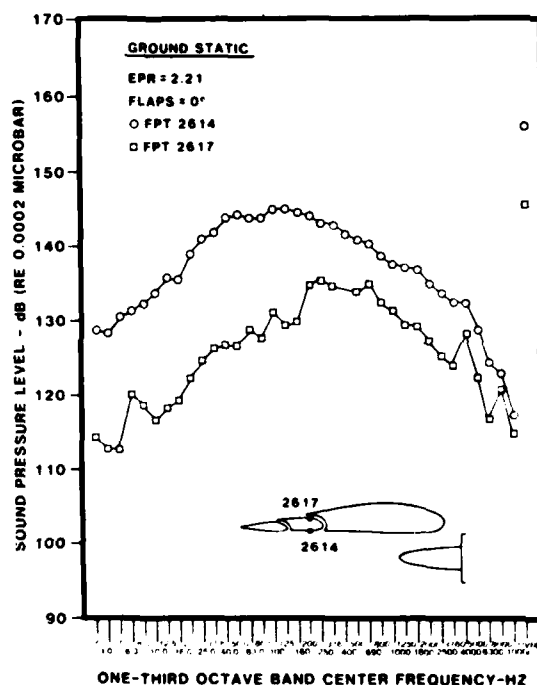


Fig. 11 - Effect of Structural Shielding

In this case with 0 flap deflection, no exhaust flow impinges the upper surface. In addition, the spoiler on the upper surface (Figure 3) also protects the FPT since the leading flap slides up underneath the spoiler at small flap deflection angles. Consequently, the majority of the acoustic energy must be transmitted through or around the wing/flap structure or from other locations in the distributed jet noise source. The spectrum of FPT 2617 is significantly below the spectrum of FPT 2614, with the differences as high as 18 dB at frequencies up to 160 Hz. Beyond this frequency the SPL remains approxi-

mately 5-8 dB below the level seen by FPT 2614. On the upper surface the peak level is in the frequency range of 200-630 Hz, with an OASPL roughly 10-12 dB below that of the undersurface.

As the flaps are extended some of the exhaust flow is channeled to the upper surface so that the upper surface is no longer shielded. Impingement by the flow normal to the FPT is not as likely as on the lower surface, but the environment shows similarities to that of the lower surface. In fact, at takeoff condition, FPT 2617 shows an OASPL 3 dB higher than FPT 2614, which is not as one might expect. Figure 12 illustrates the effect of flap deflection for the extended flap conditions. Only a small change in spectrum is seen by the upper surface as compared to the lower surface. The spectrum peak frequency decreases slightly, with a decrease in OASPL of 2-3 dB. The spectra at frequencies above 500 Hz are very comparable.

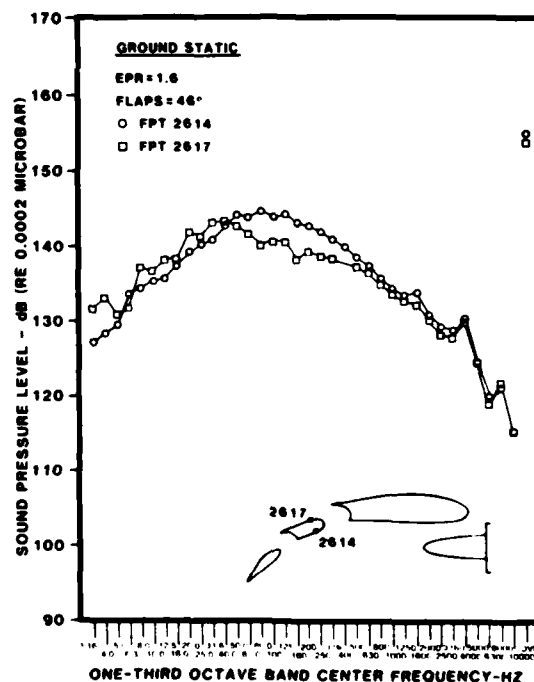


Fig. 12 - Effect of Flap Deflection on Upper Surface

FORWARD VELOCITY

The effect of forward velocity on the acoustic spectrum is significant both in frequency shift and in SPL. Comparison of typical spectra is made in Figure 13.

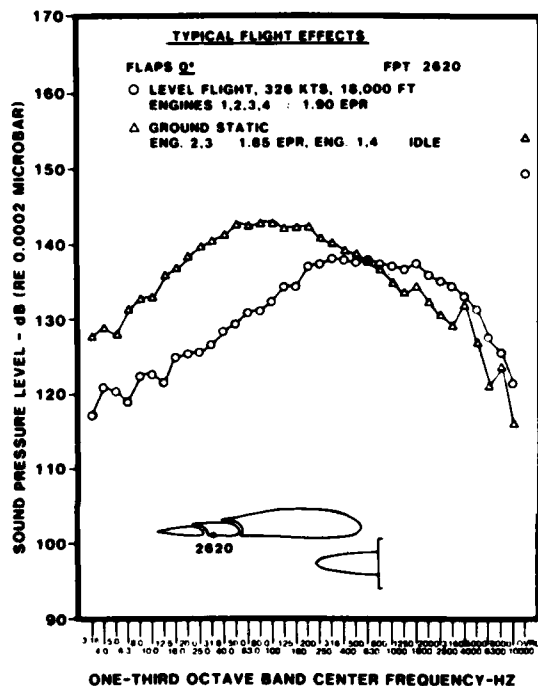


Fig. 13 - Level Flight vs. Ground Static

The peak frequency shifts from approximately 100 Hz at ground static to approximately 600 Hz at level flight condition. Additionally the OASPL decreases by approximately 5 dB. Similar effects are seen from all FPT's in the exhaust flow.

In Figure 14 a comparison is made of the OASPL's for FPT 2614 at ground static and level flight using jet Mach number M_j as the independent parameter. M_j is obtained from propulsion system performance related parameters in Reference 1. In both cases sound pressure level shows a direct relationship to the jet Mach number. The OASPL is typically 10-14 dB higher in the ground static case than in the level flight case for similar conditions. However, references 4, 8, and 9 all suggest an expected forward velocity noise reduction in the range of 1 to 3 dB depend-

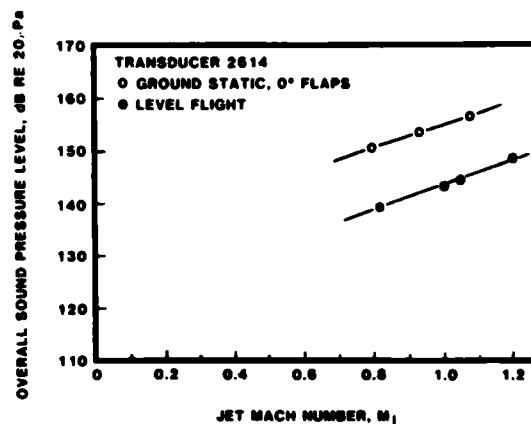


Fig. 14 - OASPL vs. Jet Mach Number

ing on flap setting, forward velocity, etc. These predictions are predominantly designed for far field but a degree of comparison is expected. To determine a possible explanation for this difference a comparison was made with the FPT outside of the jet flow. Figure 15 compares the OASPL's of FPT 2614 in the jet flow versus FPT 2624. Note that going from ground static to level flight corresponds to a 10-12 dB decrease in level for FPT 2614, while FPT 2624 shows only a 2-3 dB decrease. This 2-3 dB decrease corresponds to that predicted in the literature. Apparently, the flow due to forward velocity reduces the flow impingement by compressing the exhaust plume, thus preventing attachment of the exhaust flow. The amount of noise reduction appears to be independent of forward velocity in the range of speeds for the

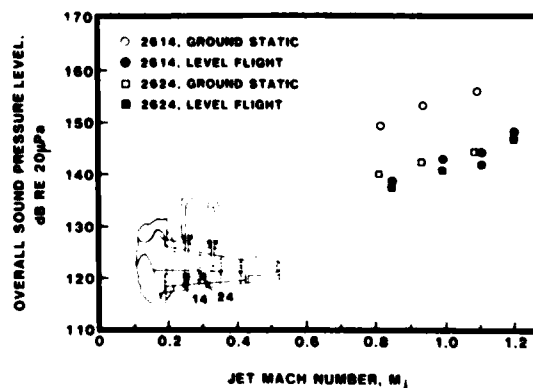


Fig. 15 - OASPL vs. Jet Mach Number

TABLE V
OASPL At Test Conditions

Condition					Transducer Number								
Test Condition	Engine (EPR)	Flaps	Altitude (FT)	Velocity (KTS)	01	14	20	50	56	10	17	24	46
Ground Static	Idle	0°	2275	0	137	138	138	140	138	137	138	139	138
"	"	22°	"	"	138	139	138	140	138	138	139	139	140
"	"	46°	"	"	137	140	139	140	137	138	138	139	140
"	1.55	0°	"	"	150	150	151	152	151	151	140	143	151
"	"	22°	"	"	150	153	152	154	153	153	152	143	154
"	"	46°	"	"	151	155	155	157	155	156	154	145	155
"	1.85	0°	"	"	153	153	154	154	154	154	143	144	153
"	"	22°	"	"	154	156	156	158	157	156	154	143	157
"	2.2	0°	"	"	156	156	157	157	157	156	145	146	156
"	"	22°	"	"	157	158	158	161	160	158	156	147	159
Takeoff	2.2	24°	2275	100	153	154	154	155	154	154	157	150	155
Level Flight	1.42	0°	18,069	192	139	139	140	144	138	138	135	140	137
"	1.60	"	18,069	245	142	144	145	146	142	142	140	144	142
"	1.68	"	17,998	287	142	145	145	145	143	143	138	143	141
"	1.90	"	18,028	325	150	149	149	148	147	147	138	147	145
"	2.01	"	29,777	238	142	144	144	147	142	142	134	142	141
Approach	1.42	46°	2275	85	145	148	148	154	150	151	147	145	150

level flight test, 192-325 kts, since the slope of the OASPL VS M_j line is approximately parallel with the ground static data.

As flaps are deflected the influence of forward velocity becomes smaller but is still apparent. At takeoff condition, with a forward velocity of 100 kts and 22° of flaps, the OASPL is approximately 4 dB below the ground static case. At an approach velocity of 85 kts with 46° flaps, the difference in OASPL is approximately 7 dB, still significantly below the ground static case. In both cases the transducers outside the flow shows only a 2-3 dB decrease with forward velocity.

SUMMARY

A summary of the OASPL for each test condition is shown in Table V. In addition, a graphical representation of the range of OASPL's for the respective test conditions is shown in Figure 16.

The range of the fluctuating pressure levels at the 1/3 octave band frequencies in the jet flow under the wing/flaps, is shown in Figure 17. The spectra are normalized to the SPL at the peak frequency. The 1/3 octave band levels are most consistent for the ground static test conditions. The maximum range of SPL's is approximately 15 dB at the low frequency end, decreasing to 6-8 dB at higher frequencies.

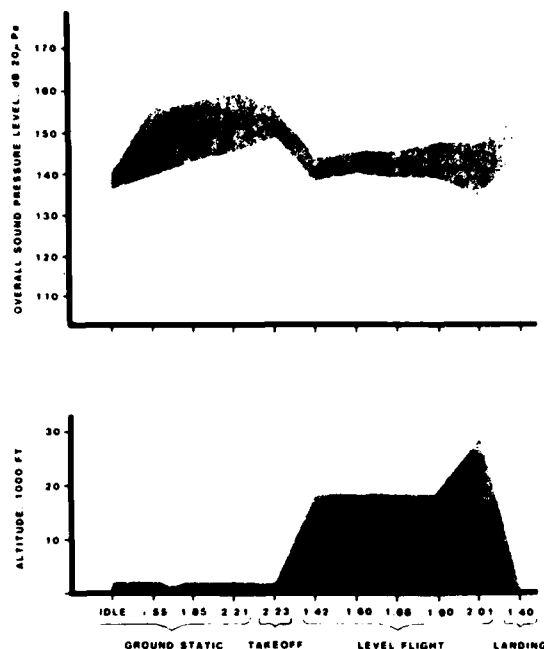


Fig. 16 - OASPL and Altitude vs. Test Condition

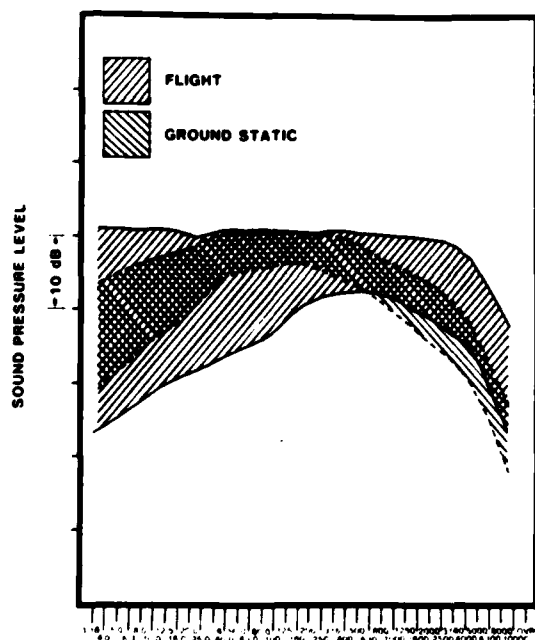


Fig. 17 - Range of Spectrum Shape for Ground Static and Flight Conditions

The spectra for the flight conditions, which include "takeoff" and "approach" have a much wider range. At low frequencies, variations as high as 30 dB are seen. Again the difference decreases with increasing frequency to 10-15 dB at the high end of the spectrum.

CONCLUSIONS

Based on the results shown in the previous sections, the following conclusions are drawn:

(1) The highest sound pressure levels are obtained for large flap deflection and high engine pressure ratios. SPL's as high as 161 dB occur on the second flap.

(2) The effect of engine pressure ratio is relatively consistent for all transducers. Idle spectra are fairly level which is typical for jet engine noise. Increasing the EPR from 1.55 to 1.85 and 2.2 corresponds to an approximate OASPL increase of 2-3 dB for each change. Little change is seen in spectrum shape.

(3) The effect of flap change is sensitive to location. Only a 1-2 dB increase is seen with a flap angle increase from 0° to 46° for the aft portion of the wing and outside the exhaust flow. For other locations the OASPL's increase by up to 8 dB.

(4) The location of the transducers proved the most significant parameter. Overall levels varied by as much as 14 dB for the same test condition when comparing measured levels in the flow as opposed to outside the flow. FPT's in the flow showed a variation of approximately 5-6 dB with levels increasing from front to rear reaching a maximum on the forward portion of the aft flap.

(5) Forward speed effects were most evident in FPT's in the exhaust flow. Going from ground static to level flight resulted in a decrease in OASPL of 10-14 dB and a significant shift in spectrum toward higher frequencies. With increasing flap angles the overall difference becomes smaller with an OASPL change approximately 4-7 dB. Outside the exhaust flow, only a 2-3 dB decrease occurs with forward velocity.

(6) The spectra display significant levels of low frequency excitation in the range of 130-140 dB. This level of excitation is conducive to acoustic fatigue in improperly designed aircraft structures. Consequently, the detrimental effects of high level noise should be considered when designing aircraft employing the type of engine/flap configuration similar to the YC-15.

REFERENCES

1. Warnix, J. L. and Hines, D. E., "YC-15 Interior Noise Measurements-Technical Discussion," AFFDL-TR-76-140, Dec. 1976.
2. "Flight Test Plans--YC-15 Ground and Flight Data Acquisition for NASA and AFFDL: Interior Noise, EBF Aero-Acoustic Loads and Thermal Environment, and Engine Inlet Acoustics," Douglas Aircraft Company Report No. MDC-J6055, April 1976.
3. "YC-15 EBF Aero-Acoustic Loads and Thermal Environment Measurements," Douglas Aircraft Company Report No. MDC-J7190, Feb. 1977.
4. Ungar, E. E., et al, "A Guide for Estimation of Aeroacoustic Loads on Flight Vehicle Surfaces," AFFDL-TR-76-91, Vol. 1, Feb. 1977.
5. Howes, W. L., "Ground Reflection of Jet Noise," NASA-TR-R-35, 1959.
6. Hermes, P. H. and Smith, D. L., "Measurement and Analysis of the J57-P21 Noise Field," AFFDL-TR-66-147, Nov. 1966.
7. Sutherland, L. C. and Brown, D., "Prediction Methods for Near Field Noise Environments of V/TOL Aircraft," AFFDL-TR-71-180, May 1972.
8. Fink, M. R., "A Method for Calculating Externally Blown Flap Noise," NASA-CR-2954, Mar. 1973.
9. Goodykoontz, J., et al, "Forward Velocity Effects in Under-the-Wing Externally Blown Flaps," AIAA Paper 75-476, 1975.

DISCUSSION

Mr. Moore (Convair-San Diego): Was any attempt made to shield the transducers from dynamic wind noise, or was this taken into consideration when you reduced your data?

Mr. Peck: No, we didn't consider that in this phase of the test. We didn't know whether we would be able to do it, or what its exact value would be.

DETERMINATION OF THE DYNAMIC ENVIRONMENT OF THE F/FB-111 TAIL POD ASSEMBLY

Janice Chinn and Phyllis Bolds
Air Force Wright Aeronautical Laboratories
Wright-Patterson Air Force Base, Ohio

A comprehensive dynamic study was conducted on the F/FB-111 aircraft by Air Force Wright Aeronautical Laboratories. The vibration and acoustic data were needed to define the environment of the tail pod assembly in order to mount sensitive electronic equipments within. These data were compared with predicted F-111 Tail Warning Systems Specification ASD/ENAM-78-1 and Military Standard Environment Test Methods, 810-C. From the analysis of the data presented in this study, vibration data in the 300 to 500 Hz range exceeded the specification and does not allow a sufficient cushion for endurance testing for many of the transient conditions.

INTRODUCTION

Existing vibration prediction technology is insufficient to meet many Air Force engineering requirements that occur during the development phase of new weapons systems. Recent research efforts under two Air Force contracts have produced methods for predicting forced vibration of skin-stiffened structures. To complement these efforts, a data base is needed for verifying how vibration induced at the aircraft skin is transmitted to critical components and equipment items mounted on and within. An F-111E vibration and acoustic in-flight test was conducted in support of the Fighter Aircraft Vibration Prediction (FAVP) study being conducted by the Structural Vibration Branch of the Air Force Wright Aeronautical Laboratories, Wright-Patterson Air Force Base, Ohio.

This organization measured, recorded, and reduced acoustic and vibration data to describe the dynamic environment on the vertical stabilizer of the F-111E aircraft. The in-flight test was conducted at Eglin AFB, Florida, during the period October 1979 to September 1980.

The test was a part of a comprehensive in-house program, "Dynamic Environment on Current and Future Air Force Flight Vehicles". The acoustic and vibration data was used to develop the specification for the F/FB-111 tail pod assembly. These data, taken during turns and pull-ups, provided hard evidence of potential integration problems, i.e., mechanical chatter. The early identification of this condition enabled the development of a more realistic dynamic specification for the Infrared Tail Warning System.

The objective of this paper is to illustrate the need for measured dynamics data to:

- (1) solve operational problems in a timely manner;
- (2) update specifications;
- (3) improve system reliability;
- (4) improve combat readiness;
- (5) increase flight safety.

MEASUREMENT AND ANALYSIS

Test Vehicle Description. The F-111E aircraft is a two-place, all weather, high or low altitude, supersonic, tactical fighter/bomber, (Figure 1). The aircraft has dual controls and requires a crew of two seated side-by-side. It provides the pilot with the in-flight capability to select any angle of wing sweep between .28 and 1.265 radians (16 and 72.5 degrees, respectively). The aircraft has double slotted trailing edge flaps, full-span fowler action and is powered by two jet after-burning engines internally mounted in the fuselage. The aircraft has a conventional tricycle gear with the main gear as a single assembly. It has a large vertical stabilizer and a conventional rudder plus ventral strikes located on the lower portion of the engine access doors approximately .5236 radians (30°) from the vertical.

Test Instrumentation. In the airborne data acquisition system, 104 accelerometers and 29 microphones were used for measuring the vibration and acoustic environment of the aircraft. The three accelerometers and one microphone germane to this paper were located on the tail pod at the top of the vertical stabilizer, (Figure 2). The signal conditioning and recording instrumentation consisted of (1) 12 position switch box, (2) a tape recorder, (3) a portable data acquisition system, (4) a time code generator, (5) voice from the aircraft intercom system, (6) two six-channel automatic gain changing amplifier boxes, (7) an in-house fabricated programmable transfer box, (8) a pair



Fig. 1 - F-111 Aircraft with External Stores

- E11A - TIP AFT OF VERTICAL STAB.
ON STRUCTURE, VERTICAL
- E12A - NORMAL TO SPIN HEAD TOP
VERTICAL STABILIZER
- E12B - TIP AFT OF VERTICAL STAB.
ON STRUCTURE, LATERAL
- B12M - FLUSH MOUNTED TOP VERTICAL
STABILIZER

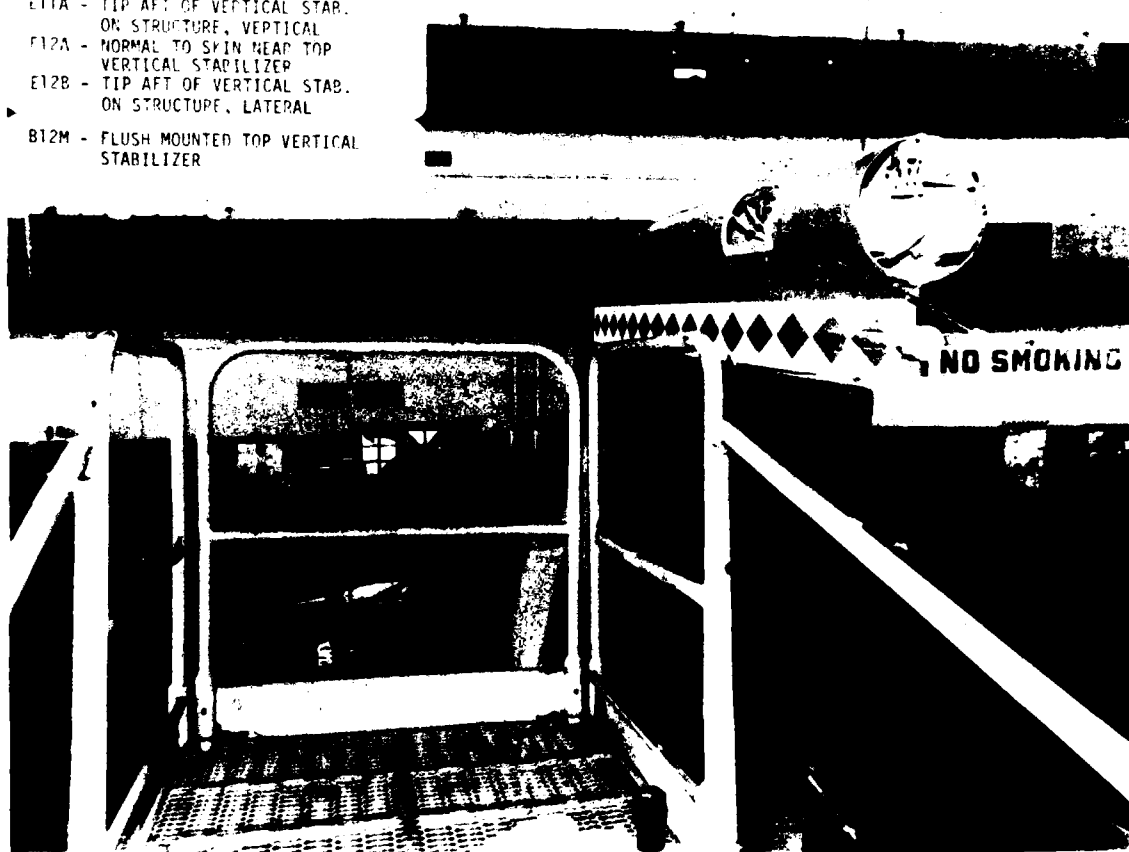


Fig. 2 - Transducer Location in the Tail Pod of the F-111 Aircraft

of frequency multiplexers each consisting of two voltage control oscillators and one mixer amplifier. Figure 3 is a block diagram of the data acquisition instrumentation.

Data Acquisition. Dynamics data were recorded for test conditions which included ground runup, takeoff, climb, level acceleration and deceleration runs, sideslip, turns, stabilized flight, gunfiring passes, takeoff and landing, and standard maneuvers. A complete listing of these test conditions including Mach number and altitude is given in Reference (1).

Test data were recorded during preplanned conditions for 3 to 5 minutes. Twelve transducers that were grouped together on one switch position were recorded simultaneously. The switch was then advanced to the next position and data were recorded for the second set of twelve transducers while the pilot maintained the same stabilized flight condition. This procedure continued until the switch had been sequenced through twelve positions, and

data had been recorded for all 133 accelerometers and microphones. These data were recorded utilizing 0.762 mps (30 ips) tape speed and 54 KHz center frequency FM record amplifiers. All transducers were calibrated in the laboratory using the same cables, connections and mounting brackets used during flight measurements. The accuracy limitations of the flight measurement systems are a summation of errors contributed by transducers, signal conditioning equipment and tape recorder. The maximum error of any one of these elements is unlikely to exceed 5% of full scale output. A reasonable estimate of the maximum overall error is the root-mean-square of the errors of the three contributors of $\pm 8.7\%$ of full scale output.

Data Analysis. Analog tapes recorded during the flight test were analyzed in the Vibration and Aeroelastic Facility located at WPAFB, Ohio. Figure 4 shows the block diagram of the analysis system. Using the results of a quick-look digital RMS program, the proper amplifier gain factor and the matching transducer sensitivity for each data sample produced an RMS

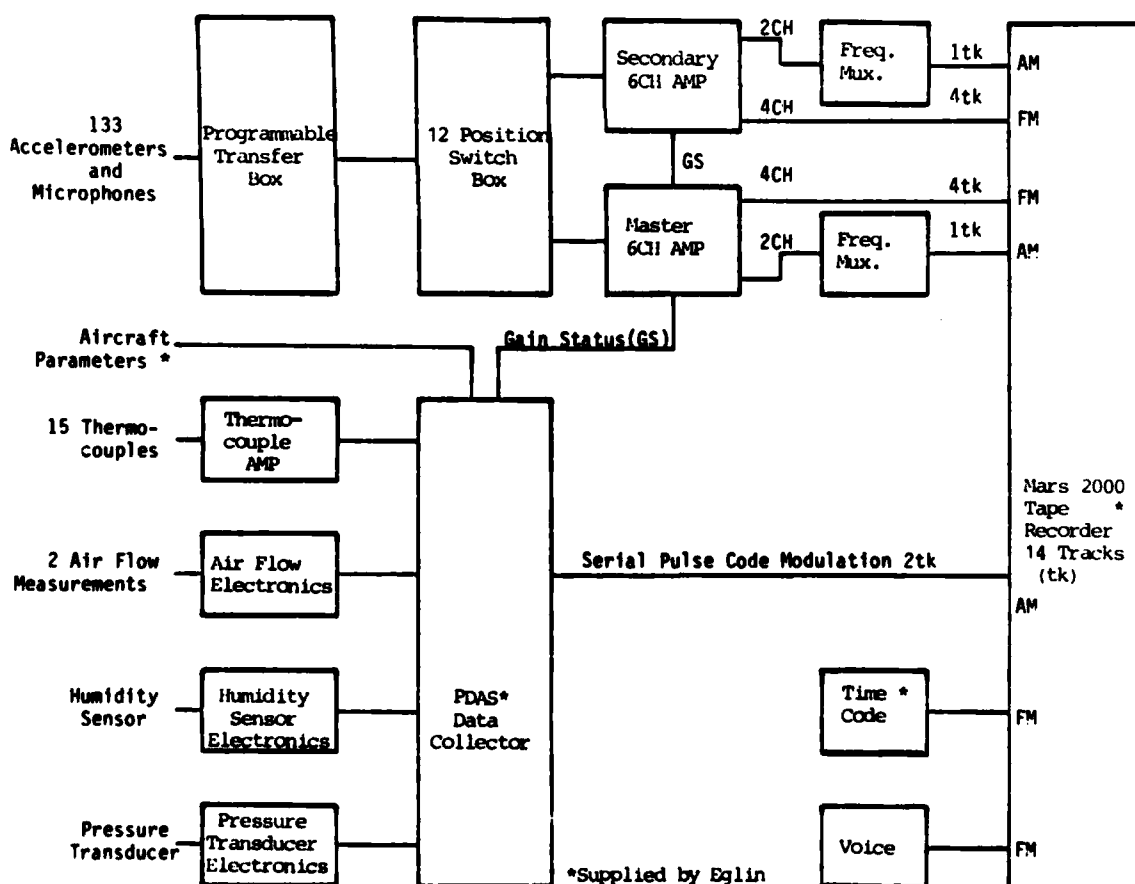


Figure 3. Data Acquisition System

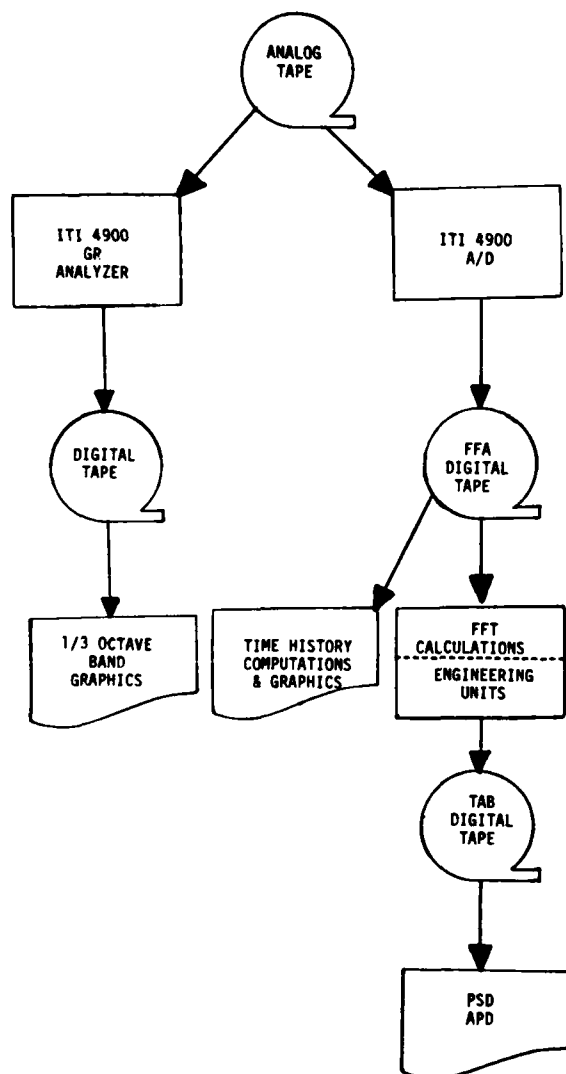


Figure 4. Analysis System

time history curve in engineering units of g RMS for accelerometers and dB-sound pressure level (re .00002 Pa) for microphone data. The RMS time histories indicated whether these data were reasonable and stationary.

The digitizing parameters used in the analysis of the Power Spectral Density, Amplitude Probability Density, and Time Histories, of the vibration data are contained in Table I.

Data Presentation. The vibration and acoustic data selected for presentation in this paper are shown in Figures 5 through 30 and were obtained during the conditions in Table II. Figures 5 through 22 show the power spectral density (PSD) of these data. The PSD is computed using standard Fast Fourier Transform (FFT) techniques and is presented as g^2/Hz .

These data are compared with the predicted levels for the tail warning system contained in the tail pod of the F-111 aircraft, ASD/ENAM-78-1 report (2).

TABLE 1
Digitizing Parameters

Cutoff Frequency	2000 Hz
Digitizing Time	3.2767 Seconds
Delta Frequency	4.8828 Hz
Number of Transforms	16
Transform Size	1024

Figure 23 is the Amplitude Probability Density (APD) of the normal (or Gaussian) Probability Density. A comparison was made of this figure with the APDs presented in Figures 24 to 26 of the actual data during the speed brake out flight condition. The APD, assuming the data is stationary, is given by:

$$p(F/\sigma) = (1/\sqrt{2\pi}) e^{-\frac{1}{2}(F/\sigma)^2} \quad (1)$$

where σ is the standard deviation or RMS magnitude of the variable (F) and $(-3 < F < +3)$. The normal probability distribution has been found to describe suitably the statistical distribution of the instantaneous magnitude of random vibration.

The acoustic data recorded from the microphone located at the top of the tail pod of the F-111 aircraft is shown in Figure 30. The amplitude is the Sound Pressure Level (SPL) and f is the broad (constant percentage 0.70 f_i) bandwidth for the i th band under consideration

$$\text{SPL} = 20 \log \left(\frac{P}{r_p} \right) \quad (2)$$

where P is the measured pressure and r_p is the reference pressure (0.00002 Pa).

RESULTS

The results of this study consist of a discussion of the figures and tables referenced in the Data Presentation Section of this paper. Figures 5 through 22 illustrate the Power Spectral Densities of the data that were measured on top of the vertical stabilizer and they are compared with reference (2) for each of the flight conditions treated in this paper. During these flight conditions, the highest overall level occurred in the lateral direction, Table III. Since the Speed-Brakes-Out flight condition was the most severe, additional analysis of the three accelerometers was performed.

TABLE II
Selected Flight Conditions

<u>CONDITION</u>	<u>ALTITUDE</u>	<u>AIRSPPEED</u>
<u>VIBRATION DATA</u>		
Stabilized Level Flight	4572 m (15K ft)	1.2 Mach
Weapons Drop	3657.6m (12K ft)	1.1 Mach
Level Turn Constant g	914.4m (3K ft)	0.85 Mach
Level Turn Max g	914.4m (3K ft)	0.85 Mach
Speed Brakes Out	914.4m (3K ft)	0.85 Mach
Steady Heading Side Slip	914.4m (3K ft)	0.85 Mach
<u>ACOUSTIC DATA</u>		
Stabilized Level Flight	914.4m (3K ft)	0.5 Mach
Stabilized Level Flight	914.4m (3K ft)	0.7 Mach
Stabilized Level Flight	914.4m (3K ft)	0.8 Mach
Stabilized Level Flight	914.4m (3K ft)	0.9 Mach

TABLE III
RMS Values - 10 to 2000 Hz

<u>CONDITION</u>	<u>VERTICAL</u>	<u>ATTITUDE LATERAL</u>	<u>FORE & AFT</u>
1.2N @4572M	7.27 g	9.70g	4.89g
Weapons Drop	3.83	5.05	4.02
Turns Cons. g	5.43	7.54	6.20
Turn Max g	6.32	10.81	8.27
Speed Brakes Out	<u>7.90</u>	<u>14.77</u>	<u>9.35</u>
Side Slip	5.96	8.14	6.44

Figures 5 through 7 show the vibration data measured during stabilized level flight exceeded the specifications in reference (2) at frequencies below 400 Hz, for the three directions. The RMS levels for the stabilized level flight, as expected, are the lowest.

Figures 8 through 10 show the PSD levels measured during the weapons drop condition. The RMS levels are higher than the specification curve, however, this is a transient condition and will only be experienced for short durations and the frequencies that exceed it are below 400 Hz.

During the constant g turn condition, the RMS levels are slightly higher than the stabilized level flight, (Figures 11-13). Again, the specification is exceeded in the frequency range below 400 Hz. In some cases, it is greater than two orders of magnitude. This condition will be experienced somewhat more than the transient condition, but a great deal less than the stabilized level flight condition.

The maximum g turn condition (Figures 14 through 16), exceeds the specification in the region below 400 Hz by an order of magnitude. In the lateral direction, the specification curve is much higher than the data in the

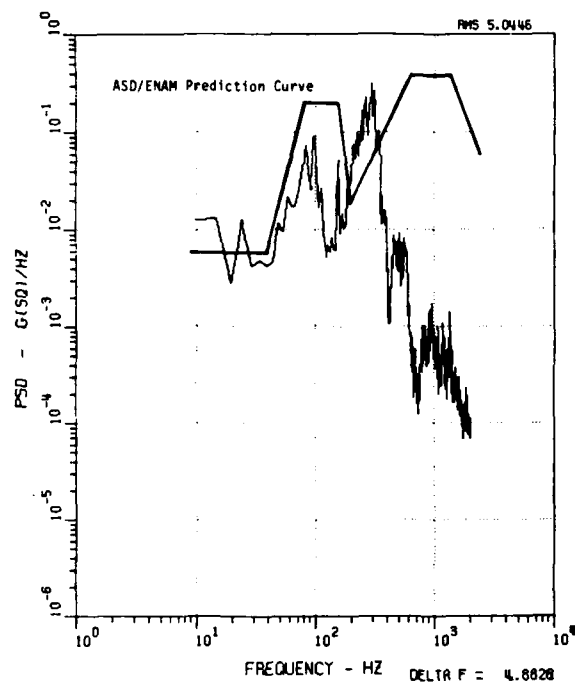


Fig. 5 - Stabilized Level Flight LAT

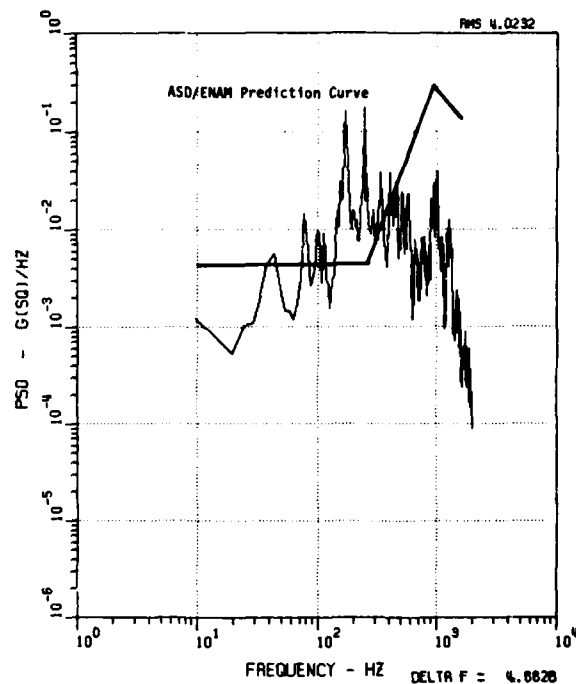


Fig. 7 - Normal to Skin NEAR TOP of Vert
STABILIZER-Stabilized Level Flight

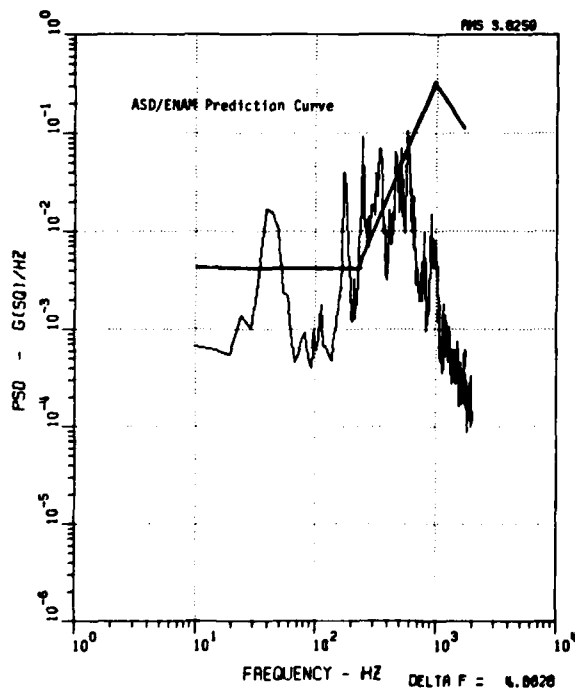


Fig. 6 - VERT-Stabilized Level Flight

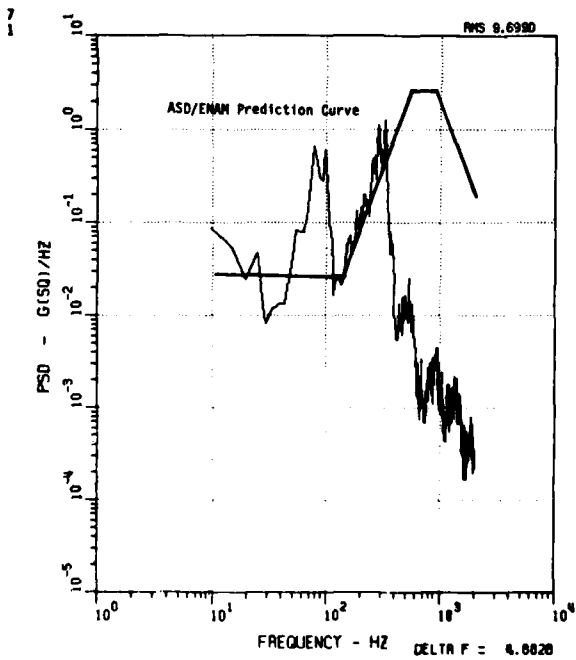


Fig. 8-LAT-Weapons Drop

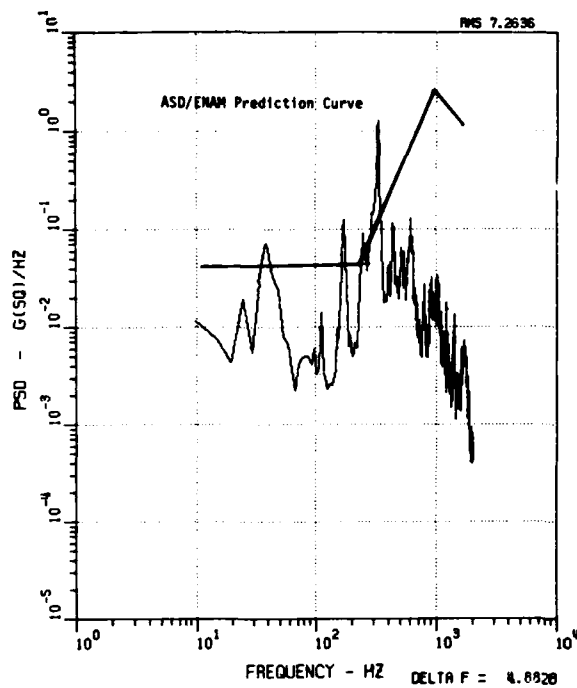


Fig. 9 - VERT-Weapons Drop

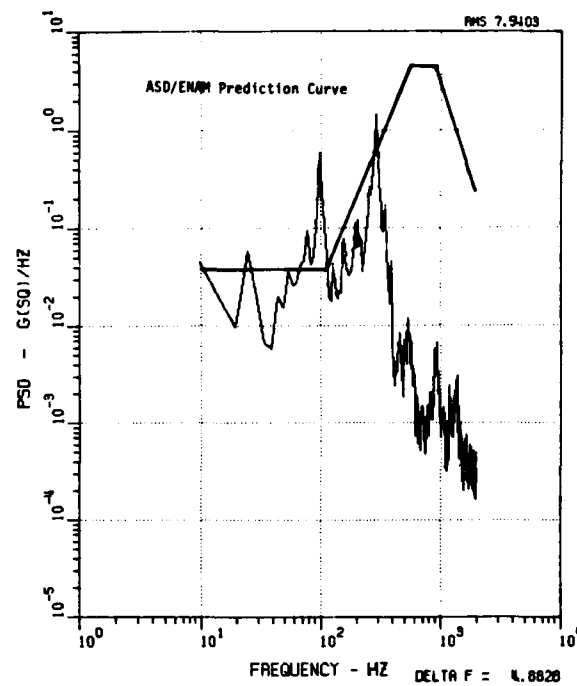


Fig. 11 - LAT-Level Turn Constant G

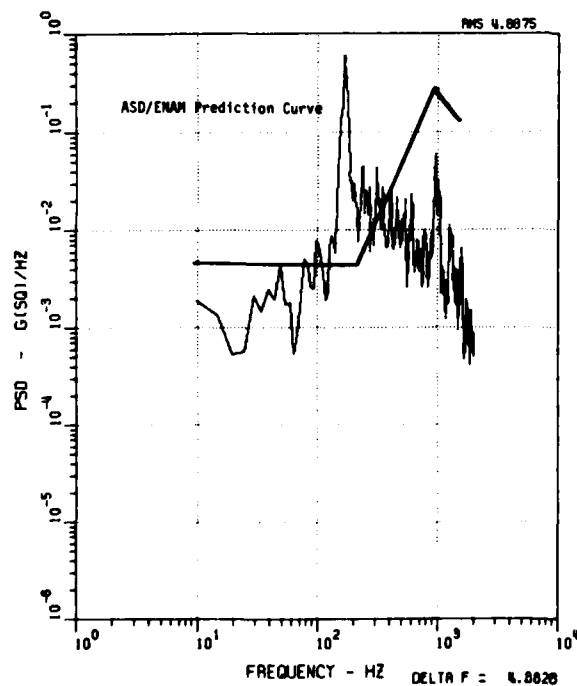


Fig. 10 - Normal to Skin Near Top
VERT STAB-Weapons Drop

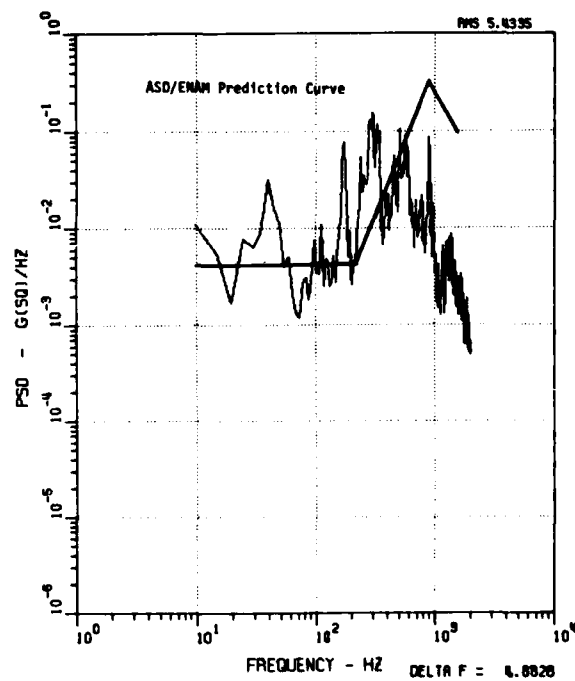


Fig. 12 - VERT-Level Turns Constant G

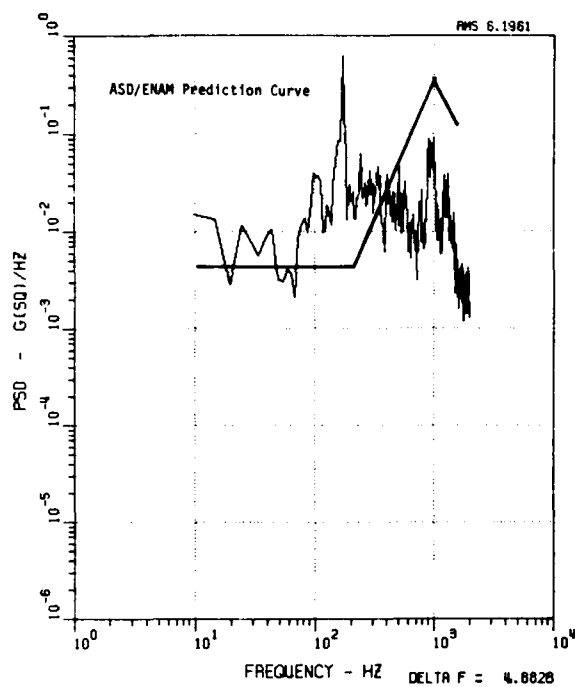


Fig. 13 - Normal to Skin TOP VERT STABILIZER-Level Turn Constant G

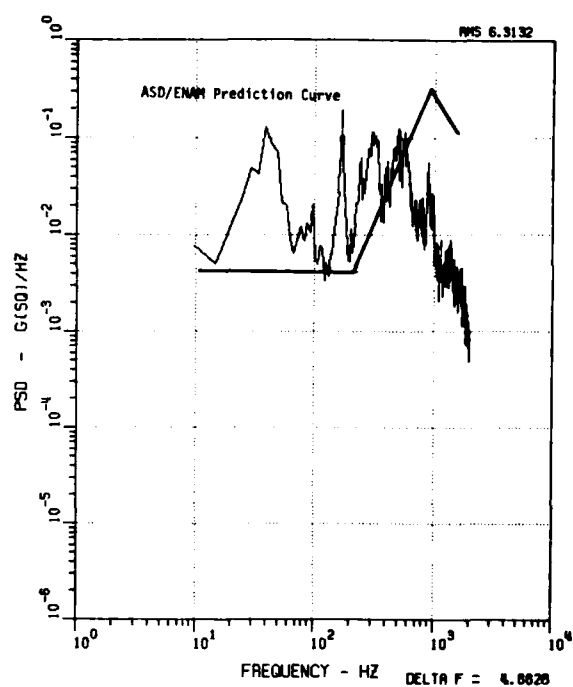


Fig. 15 - VERT-Level Turn Maximum G

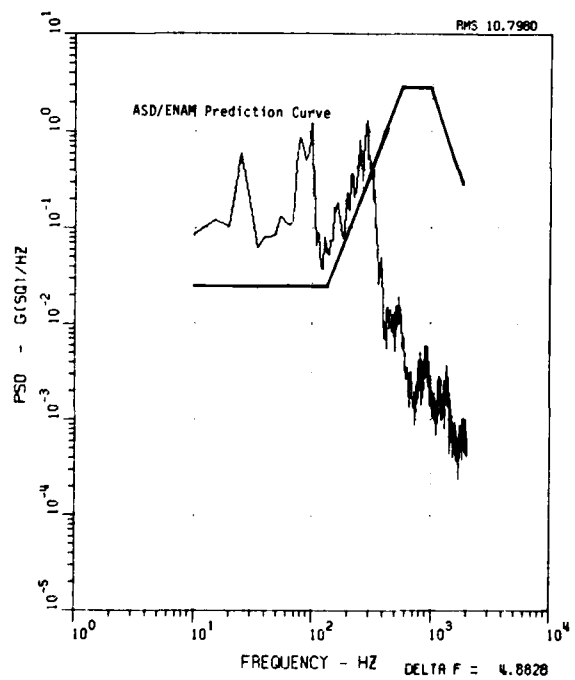


Fig. 14 - LAT-Level Turn Maximum G

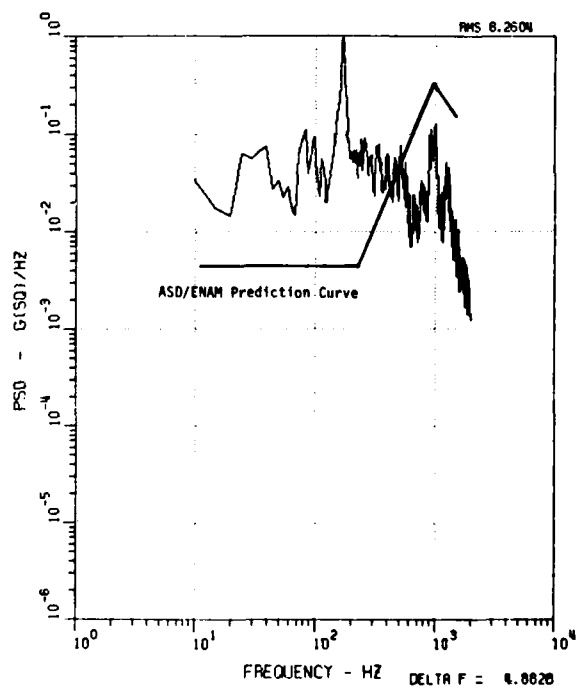


Fig. 16 - Normal to Skin NEAR TOP VERT STABILIZER-Level Turn Maximum G

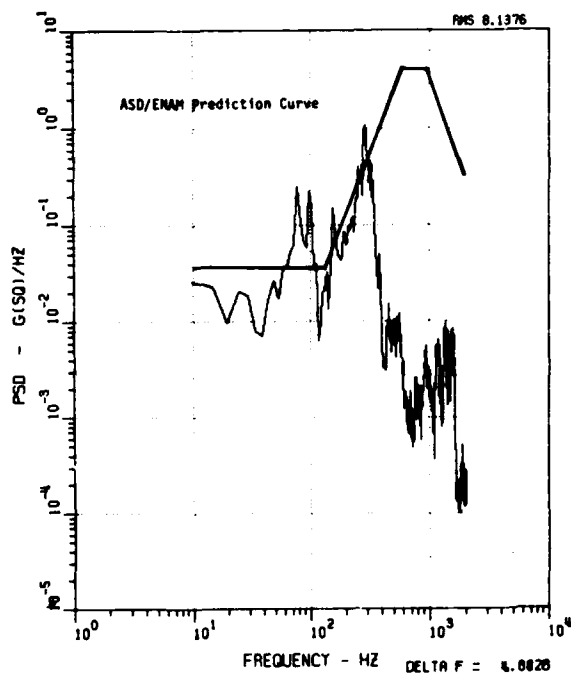


Fig. 17 - LAT-Side Slip

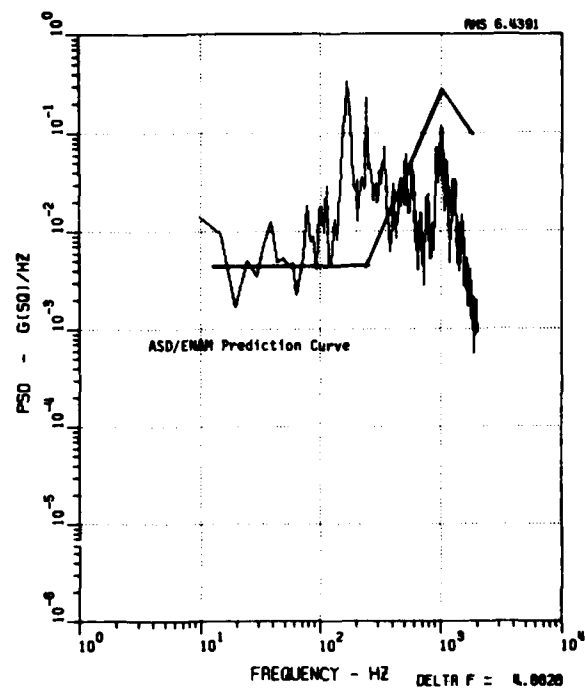


Fig. 19 - NORMAL TO SKIN NEAR TOP OF
VERT STABILIZER-Side Slip

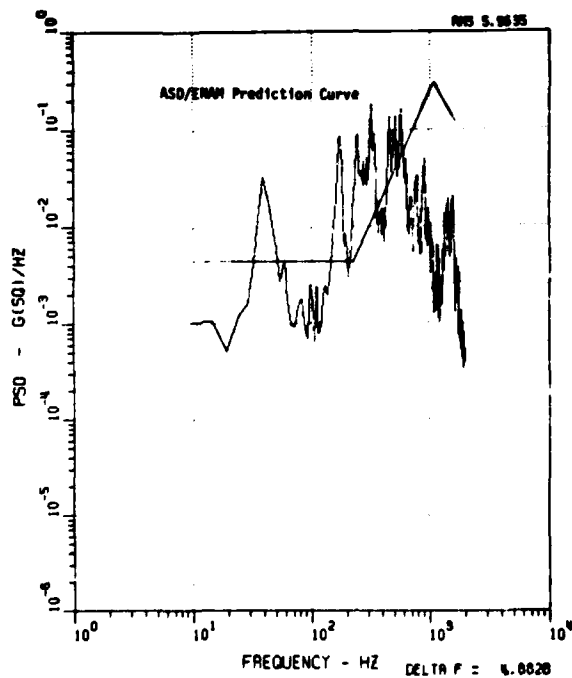


Fig. 18 - VERT-Side Slip

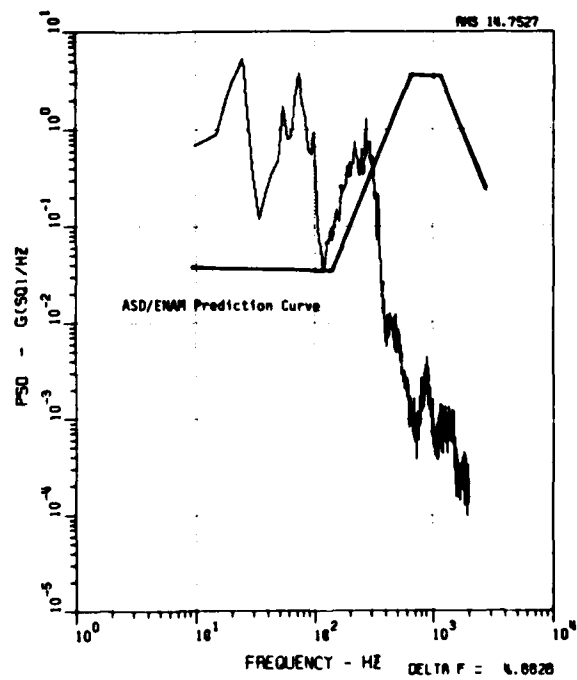


Fig. 20 - LAT-Speed Brakes Out

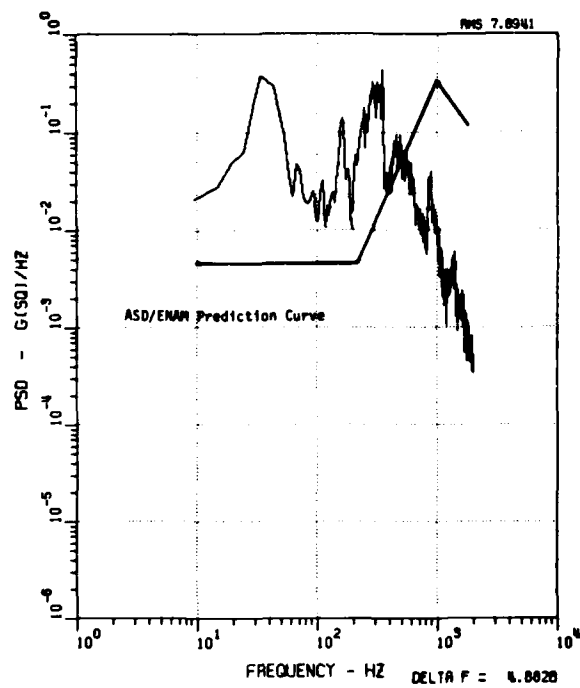


Fig. 21 - VERT-Speed Brakes Out

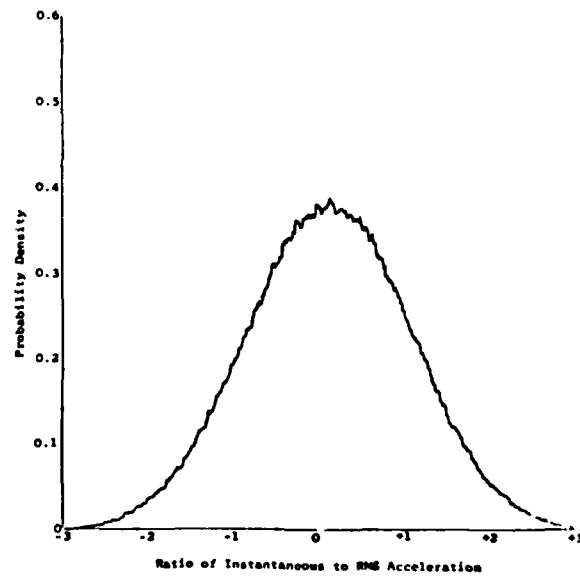


Fig. 23 - Random Gaussian Input

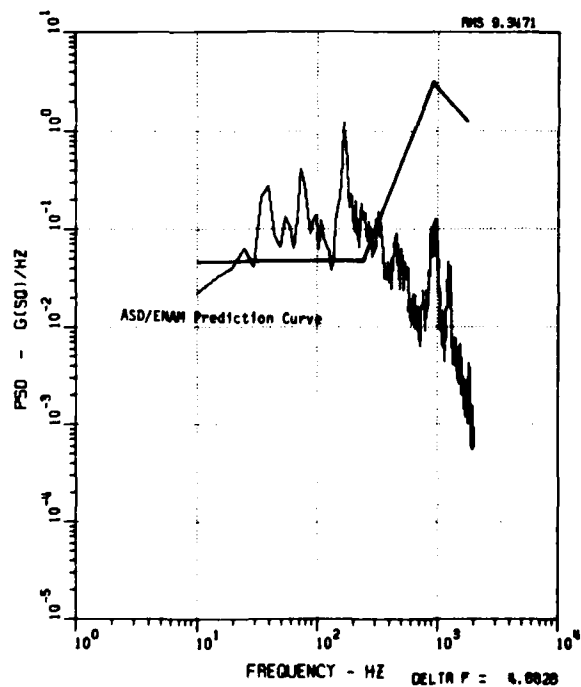


Fig. 22 - NORMAL TO SKIN NEAR TOP VERT STABILIZER-Speed Brakes Out

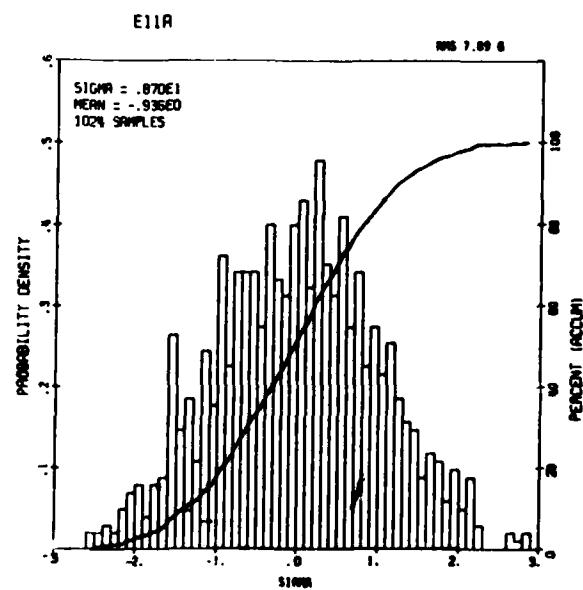


Fig. 24 - FORE & AFT-Speed Brake

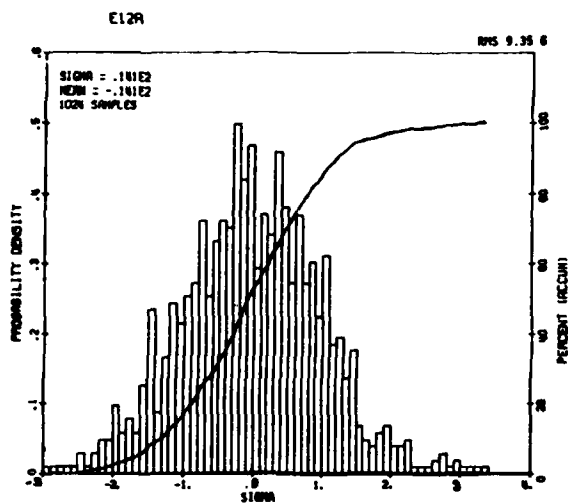


Fig. 25 - VERT-Speed Brake

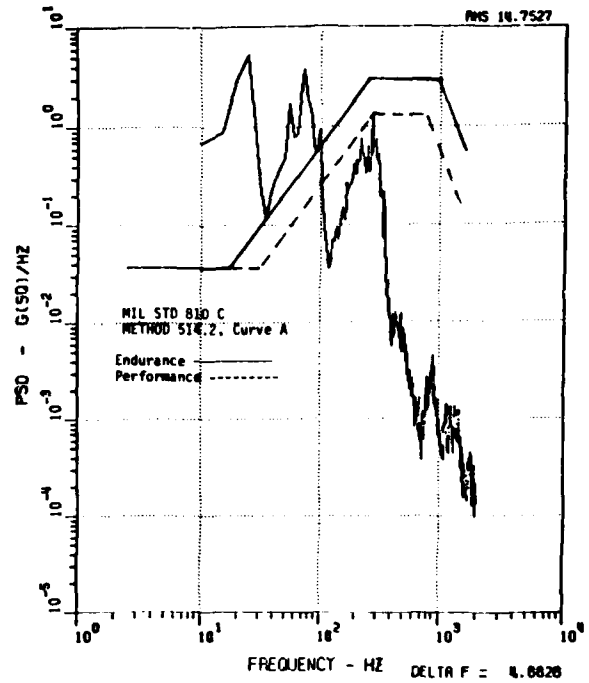


Fig. 27 - LAT-Speed Brakes Out

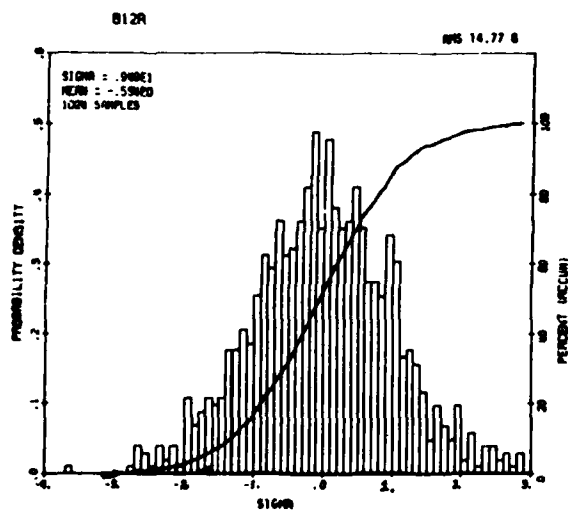


Fig. 26 - LAT-Speed Brake

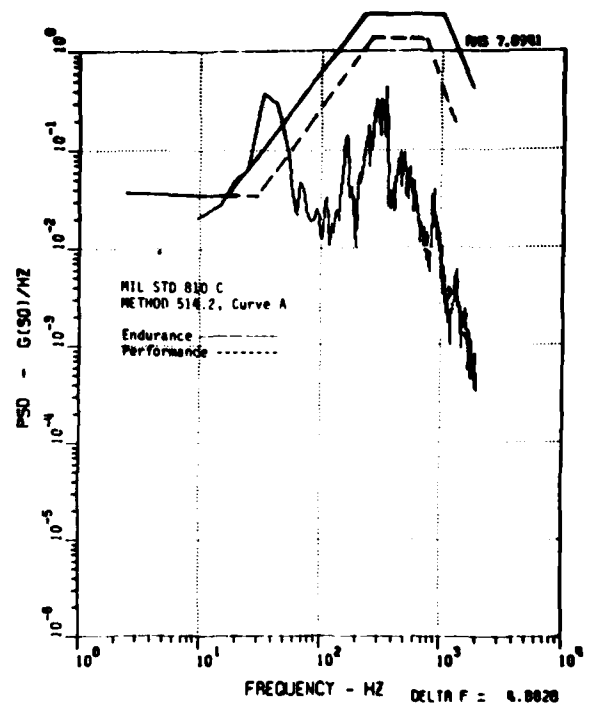


Fig. 28 - VERT-Speed Brakes Out

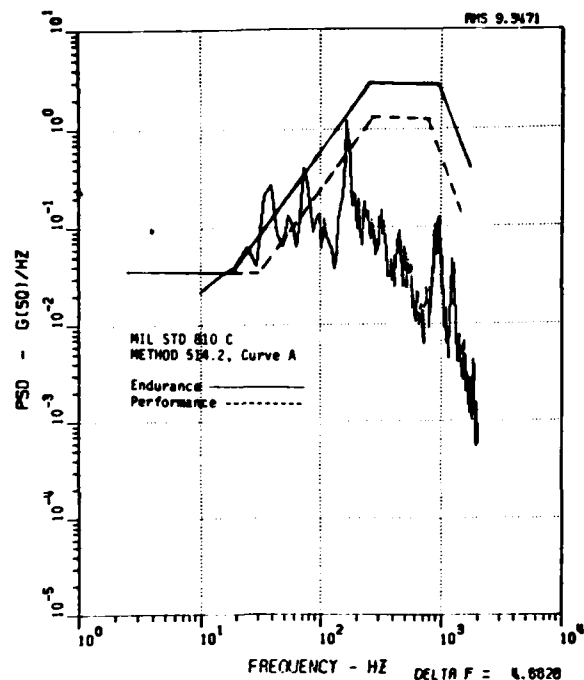


Fig. 29 - NORMAL TO SKIN NEAR TOP VERT STABILIZER-Speed Brakes Out

frequency range above 400 Hz. The aircraft often experiences this condition in the fighter mode during maneuvers.

Figures 17 through 19 show the side slip condition; again the data exceeds the specification in the lower frequency range. In the vertical and fore and aft directions, normal to skin, the levels exceed the proposed specification curve by more than an order of magnitude. This condition is for a very small portion of the overall life of the aircraft.

The speed-brakes out condition is by far the most severe. Figures 20 through 22 indicate that levels in the region below 400 Hz are much greater than the proposed specification curve. Table III shows that in each direction the RMS value is the largest for the speed brake out condition. Additional analyses were conducted using these data. An amplitude probability density analysis was made of the data measured in each direction. The data (Figures 24-26), measured over the frequency range of 10 to 2000 Hz showed a near normal distribution from -3σ to $+3\sigma$ indicating wide band random vibration. A comparison of these measured PSD levels was made (Figures 27-29) with the MIL STD 810C curve for jet aircraft, method 514.2 curve A, (Ref 3) for both endurance and performance. Again, the data exceeded the curve in the lower frequencies.

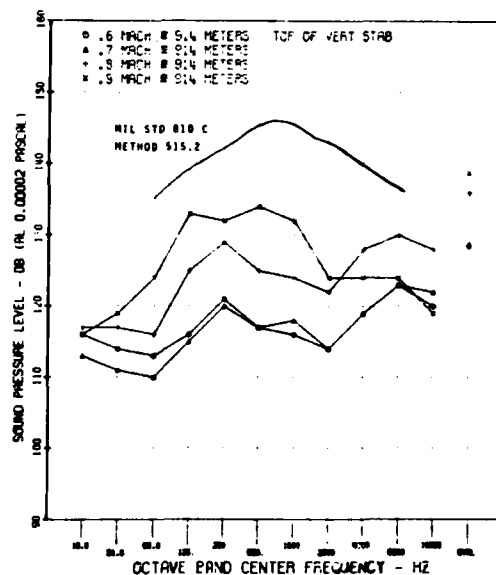


Fig. 30 - Aerodynamic Acoustic Data

The acoustic data (Figure 30), shows the SPL associated with the different altitudes and Mach values during stabilized level flight. The acoustic data curve (Ref 3) for external noise levels at the top of the vertical stabilizer is well above the noise level measured during level flight.

CONCLUSIONS

From the analysis of the data presented in this study, the following conclusions are reached.

(1) Vibration data in the 300 to 500 Hz range does exceed the specification and does not allow a sufficient cushion for endurance testing for many of the transient flight conditions.

(2) To prevent mechanical linkage chatter, a knowledge of the low frequency spectrum, below 300 Hz, is required.

(3) These data are required to determine critical modes in order to design the proper shock mounts for electronic equipments for:

- (a) increased safety
- (b) combat readiness
- (c) updated specifications
- (d) improved system reliability

RECOMMENDATION

It is recommended that current and future aircraft be made available for comprehensive dynamic measurement programs so that problems such as the one described herein can be solved in a timely manner.

REFERENCES

1. Ach, J. et al, "F-111E Flight Vibration and Acoustics Test Program," AFWAL-TR-81-3162, (November 1981).
2. F-111 Tail Warning System Specification, ASD/ENAM-78-1.
3. Military Standard Environmental Test Methods, MIL-STD-810C (March 1975).

ACKNOWLEDGMENT

The authors would like to thank those of the Structural Vibration Branch, Messrs. Dansen Brown, John Ach, Lowell Vaughn, Richard Talmadge, Charles Willhite and J. Edward Huffman for conducting the measurement and analysis and for their contribution to the success of this effort; Mr. T. Campbell of ASD/ENAMD for his technical assistance and special acknowledgment to Mrs. Diana Howdyshehl for typing this manuscript.

DISCUSSION

Mr. Caruso (Westinghouse Electric Corporation):
The worst case that you observed was when the speed brakes were out. How many times does that condition occur, and how long does it last during a typical mission? I assume it is a transient condition.

Mrs. Bolds: According to our measurements that condition represents a very small portion of the overall life of the aircraft.

Mr. Silver (Westinghouse Electric Corporation):
We have some problems with this low frequency phenomenon when we locate equipment in the tail cap. We are getting very severe definitions of that environment for long periods of time; enveloping those major low frequency modes and putting them in test specifications gives us a great deal of difficulty. If we have to run those high level tests for long durations, we will get extreme heating of the isolators which is not realistic. It is important that these high test levels be realistic; we can't afford to envelope to extremes. It is also important for the test durations to be realistic. I wonder if these are really transient events that are possibly being described as continuous events.

Mrs. Bolds: I would think testing should be conducted for short durations because they are accelerated to begin with. You would only have this condition for a short amount of time compared to the overall life cycle of the

airplane; that also depends on the mode of use of the airplane, fighter, bomber or other.

Mr. Wafford (Aeronautical Systems Division):
Let me help you answer Mr. Silver's question since our organization is responsible for specifications. Any time you have unusual heating conditions that are not realistic, due to testing for long durations, you can either use artificial cooling, or you can test for short durations and accumulate the test time over the expected life of the equipment.

Mr. Volin (SVIC): Do you plan to include separate test requirements in MIL-STD-810D for equipment located in the tails of aircraft?

Mr. Wafford: At the present time there are no good techniques available for predicting the tail vibration environment. We have extremely high vibration levels in the tails of many of our aircraft, F-15, F-111, which are not accounted for in the prediction techniques in MIL-STD-810; so it is sort of a unique condition. Data of the kind that are available from the F-15 and F-111 aircraft can and should be used to develop environmental test requirements for equipment in this area.

Mr. Caruso (Westinghouse Electric Corporation):
We didn't consider the vibration environment in the tail area of the aircraft because most of the equipment is located elsewhere in the aircraft. It is mostly a special case, but it should be considered.

AN ASSESSMENT OF THE A-10'S CAPABILITY TO OPERATE ON ROUGH SURFACES

Tony G. Gerardi and David L. Morris
Air Force Wright Aeronautical Laboratories
Wright-Patterson Air Force Base, Ohio

A study has been conducted on the A-10's capability to operate on rough surfaces; specifically rapidly repaired bomb damaged runways and taxiways. Emphasis was placed on a European combat configured takeoff gross weight of 40,755 pounds and a typical landing configuration weight of 30,300 pounds. Five types of bomb damage repairs were considered, specifically A through E category repairs. Results of the study indicate that the A-10 tends to respond to rough surfaces in its rigid body pitch mode thus making the nose landing gear (NLG) the critical component. An analytical study shows that by increasing the NLG strut precharge pressure from 179 psi to 250 psi, peak NLG loads are reduced by 20%. In addition, application of aft stick will unload the NLG and reduce NLG loads.

INTRODUCTION

At the 51st Shock & Vibration Symposium, a paper entitled, "Aircraft Response to Operations on Rapidly Repaired Battle Damaged Runways and Taxiways" was presented. It described the US Air Force project HAVE BOUNCE and the approach being taken to develop Rapid Runway Repair (RRR) criteria for a given aircraft. This paper presents the results when the HAVE BOUNCE approach was applied to the A-10 aircraft.

The A-10 is a single-place, close-air support aircraft (Figure 1) manufactured by Fairchild Republic Company. The tricycle forward retracting landing gear is equipped with an antiskid system and a steerable nosewheel. The nose gear is installed to the right of the centerline to permit near centerline gunfire.

A close-air support mission usually requires forward basing of the aircraft. In the European theater, air-basis and particularly forward airbases will be prime targets during a conflict. In order to respond quickly following such an attack, rapid repair will be made to the runways, taxiways, and parking ramps. These rapid repairs will result in rougher than normal surfaces due to upheaved pavement, crater

settlement and the height of the AM-2* repair mat. Generally, the faster that the repair is made, then the rougher the repair quality will be. In order to know how smooth the repairs must be, it is necessary to know the surface roughness capabilities of each aircraft. The purpose of this study then was to determine the roughness capability of the A-10 aircraft and to evidence ways of improving its roughness capability if required.

PROCEDURE

The procedure used to evaluate the A-10's rough runway capabilities was typical for all aircraft under the HAVE BOUNCE (HB) project. HAVE BOUNCE is an Air Force project managed by ASD/TAAMF to determine the roughness characteristics of most aircraft in the US Air Force inventory. The approach is to:

- Develop a computer program capable of simulating the aircraft traversing uneven surfaces during taxi, takeoff, landing, and braking.
- Validate that computer program with measured test data.

*(Extruded Aluminum 54' x 78' x 1.5")

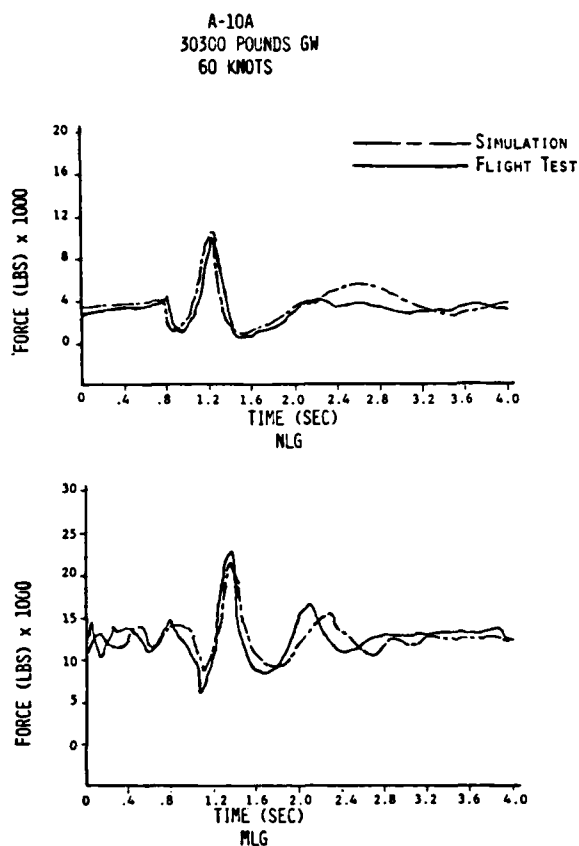


FIGURE 2. LIGHTWEIGHT 60 KNOT TEST DATA

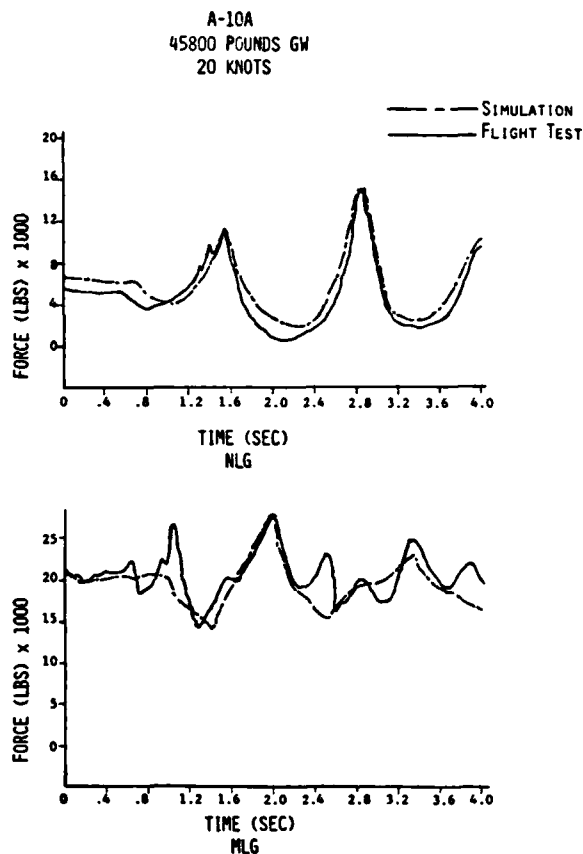


FIGURE 3. HEAVYWEIGHT 20 KNOT TEST DATA

dip at Edwards AFB. The dip has a 50 foot wavelength with a 5-inch amplitude. Several speed/aircraft conditions were simulated and compared to similar test runs. Two are contained in this paper

GROSS WEIGHT #	SPEED KTS	FIGURE
30,300	40	-
30,300	60	2
30,300	80	-
45,800	20	3
45,800	40	-

Generally, magnitudes of the peak values for the nose and main landing gears compared favorably to the measured data. In addition, the frequency simulated matches the measured test data. Correlation was good enough to consider the program "validated" for constant speed runs.

Using the validated simulation program, a large number of computer runs (velocity plots) were made over single and multiple A through E category repairs which are defined in Figure 4.

"Velocity Plots" are plots of peak loads and accelerations for all velocities from 20 feet per second to take-off speed in 5-foot per second increments. They are obtained by executing a "do" loop around a normal TAXI time history run (see Figure 5). Table I contains a summary of the peak loads predicted for all the velocity analysis simulations made. Those with an asterik exceeded the NLG tire bottoming load. MLG loads were within limits for all conditions simulated. Figure 6 is a typical velocity analysis and shows the results when a class "C" repair is traversed. Note the resonance at 25 knots.

Figure 7 is a plot of the A-10's velocity as it rolls down the runway for

REPAIRED RUNWAY PROFILES

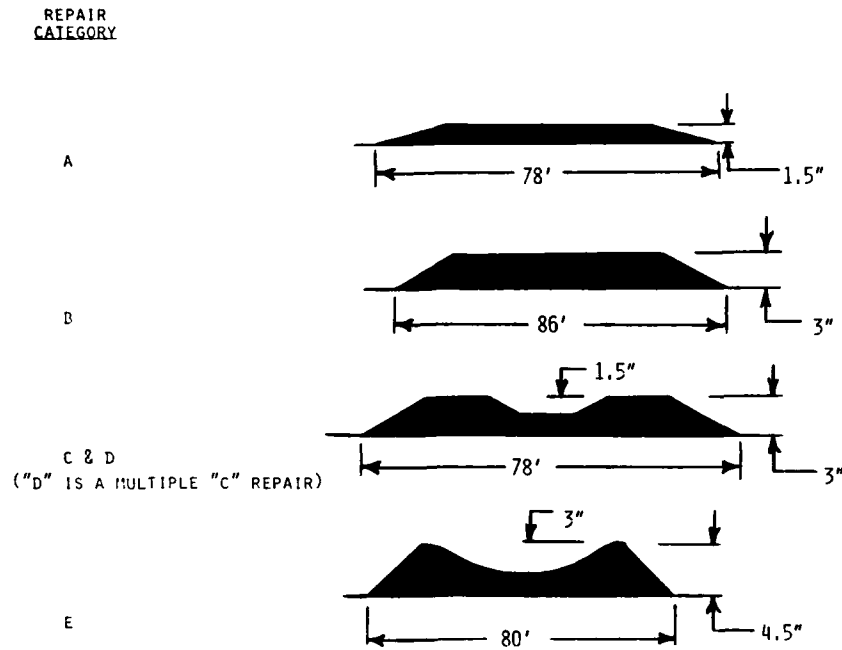


FIGURE 4. "A" THROUGH "E" CATEGORY REPAIRS

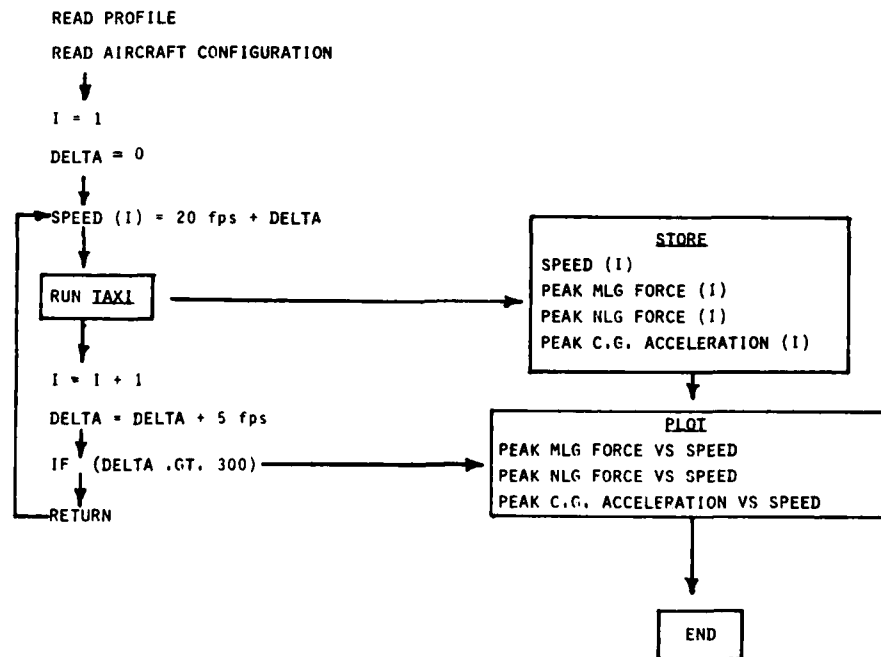


FIGURE 5. TAXI WITH A "DO" LOOP DESIGNED TO PRODUCE VELOCITY PLOTS

	REPAIR CATEGORY	TAKEOFF CONFIGURATION 40,755 LBS		LANDING CONFIGURATION (BRAKING) 30,300 LBS	
		STANDARD STRUT	HIGH PRESSURE STRUT	STANDARD STRUT	HIGH PRESSURE STRUT
ONE AM-2 MAT	A	12,200	---	12,400	---
TWO AM-2 MATS, 70 FEET APART	A	16,000	---	15,230	---
ONE AM-2 MAT, 3" HIGH	B	16,500	---	15,380	---
TWO AM-2 MATS, 3" HIGH, 74 FEET APART	B	28,180*	23,325	25,680*	22,560
ONE AM-2 MAT, 3" HIGH, 1.5" SAG	C	22,025	---	18,800	---
TWO AM-2 MATS, 3" HIGH, 1.5" SAG, 80 FEET APART	D	25,475*	21,200	22,360	---
ONE AM-2 MAT, 4.5" HIGH, 3" SAG	E	27,000*	22,040	22,025	---
TWO AM-2 MATS, 4.5" HIGH, 3" SAG, 80 FEET APART	E	34,700*	29,130*	34,180*	29,620*

* INDICATES TIRE BOTTOMING LOAD (24,000 #) WAS EXCEEDED

NOTE: MAIN LANDING GEAR LOADS WERE WITHIN TIRE BOTTOMING
LIMITS FOR ALL CONDITIONS SIMULATED.

TABLE I. SUMMARY OF PEAK NOSE LANDING GEAR LOADS

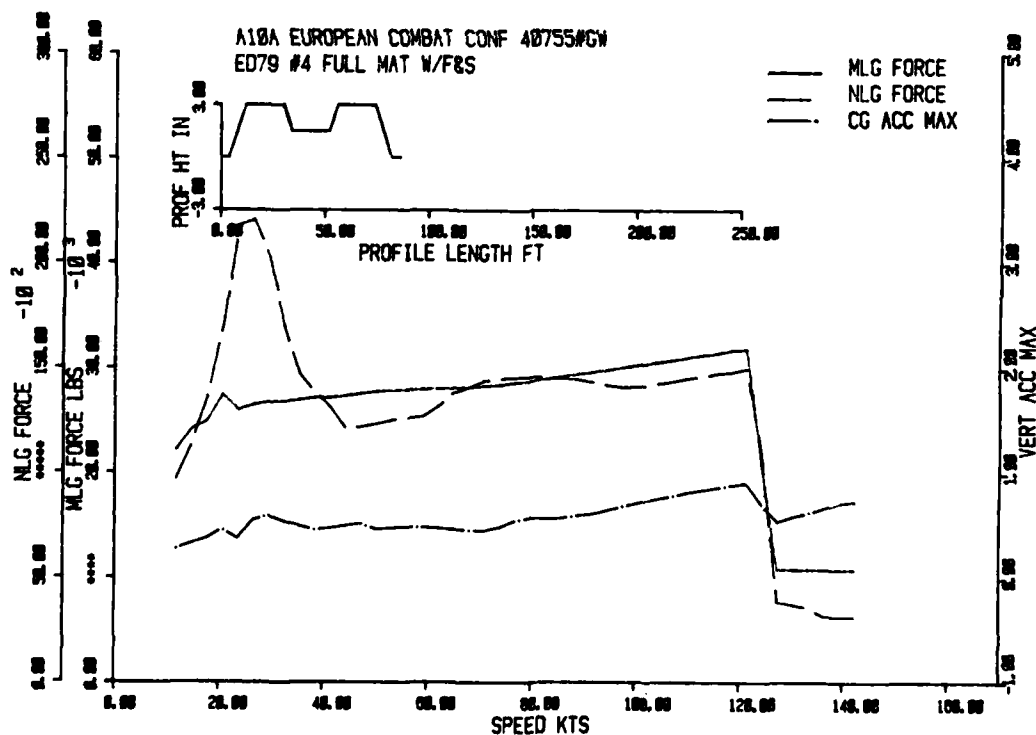


FIGURE 6. TYPICAL VELOCITY ANALYSIS OF A 40,755 POUND
A-10 TRAVERSING A CLASS "C" REPAIR

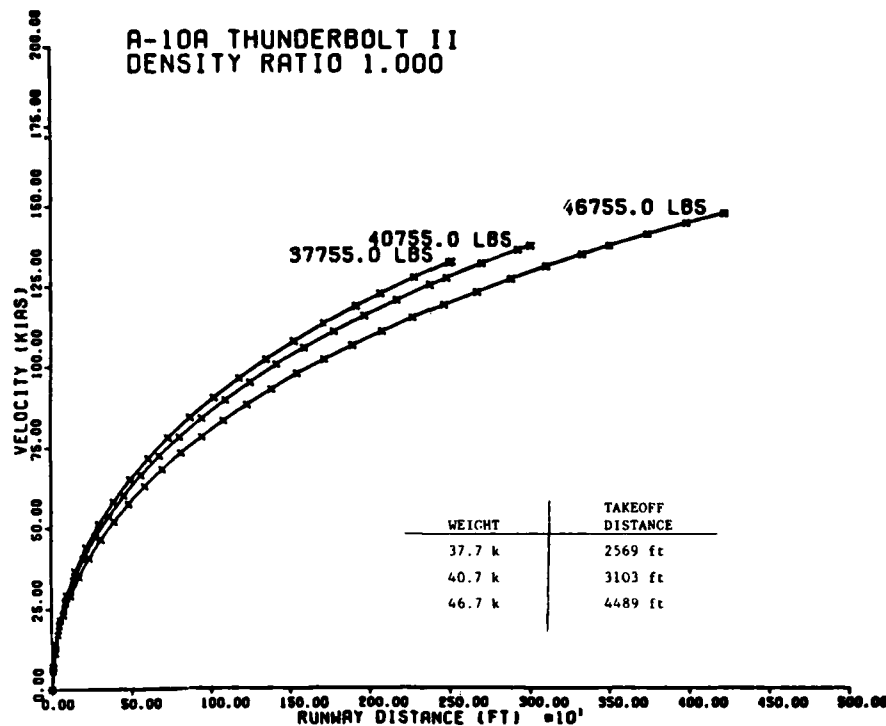


FIGURE 7. PLOT OF A-10 VELOCITY VS DISTANCE DOWN THE RUNWAY

takeoff. The "X's" on the curves denote one second intervals and can be used for repair spacing criteria. A velocity plot for each aircraft/bump configuration used in conjunction with a takeoff velocity profile as shown in Figure 7 will enable repair teams to determine the quality of repair required at a particular location or a minimum operating strip (MOS).

Generally, the A-10 responds primarily in the pitch mode and the vulnerable component is the NLG. This loading up of the NLG is aggravated during takeoff roll when full thrust is applied because the thrust vector centerline is significantly higher than the waterline of the center of gravity thus producing a nose down moment as illustrated in Figure 8. In an effort to determine the magnitude of the thrust moment on peak NLG loads, a velocity analysis was run with and without the thrust moment included. The velocity analysis shown in Figure 9 contains the results and shows that for a class "C" repair, peak loads can increase by 17 percent.

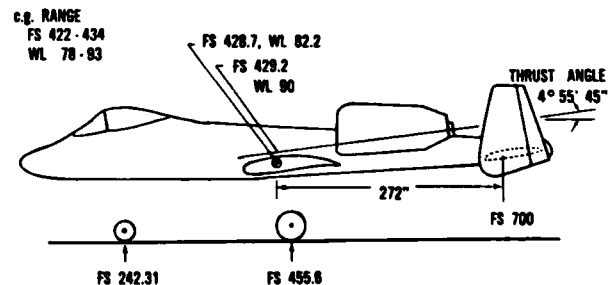


FIGURE 8. THRUST LINE RELATIVE TO C.G. AND FUSELAGE STATION AND WATERLINE LOCATIONS

Application of full aft stick (35° of elevator) will unload the NLG as forward velocity increases. Figure 10 shows that the tail moment will exceed the thrust moment at 90 knots. Figure 7 shows that 90 knots is exceeded 1100 feet down the runway for a 40,700 pound A-10. It should be noted that an aft stick takeoff will increase the ground roll distance and is not recommended procedure at this time.

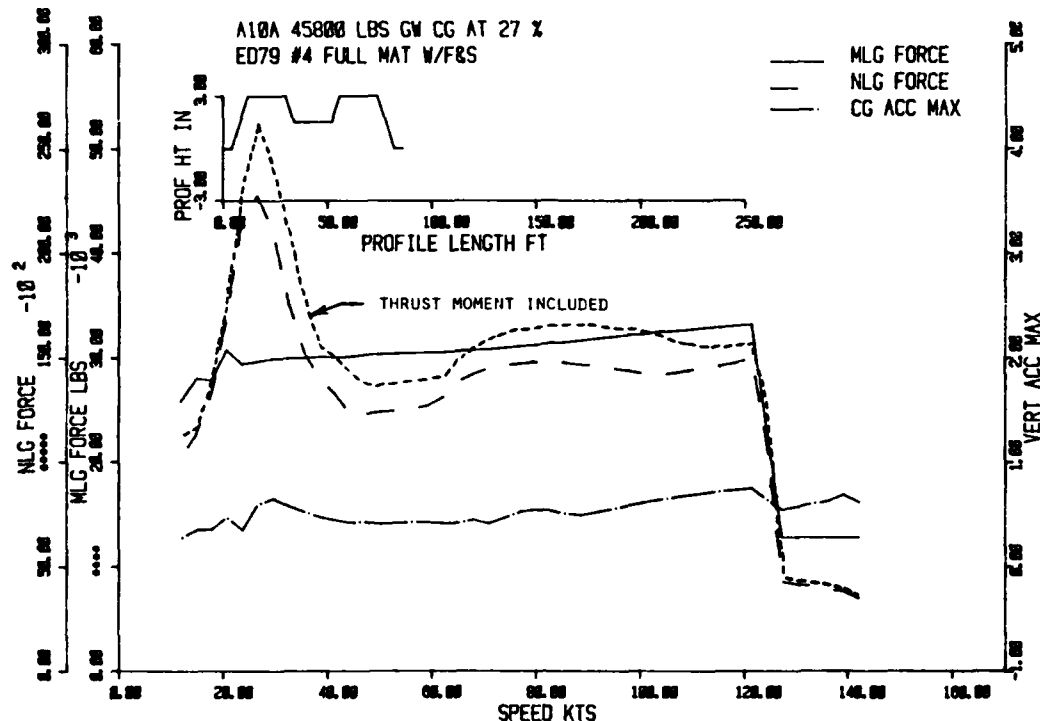


FIGURE 9. VELOCITY ANALYSIS SHOWING THE EFFECT OF THRUST MOMENT

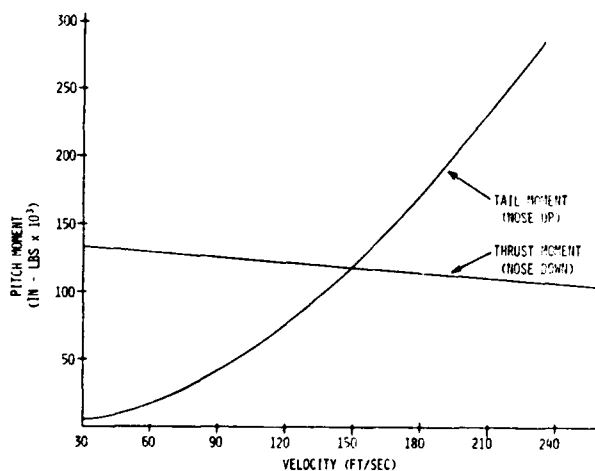


FIGURE 10. A-10 PITCH MOMENT

Examination of all of the velocity plots made indicated that for the single A through E category repairs, the slower speeds (less than 40 knots) produce the higher loads. Again from Figure 7 it can be seen that 40 knots is exceeded 250 feet down the runway.

Therefore, any single repair (A - E) encountered past the 250 foot mark will not produce loads over the limit. When multiple repairs are encountered, however, a second peak will occur on the velocity analysis as can be seen in Figure 11. This second resonant peak is produced when the NLG, after rebounding from the first bump, encounters the second bump. In order to determine the effect of bump spacing on peak loads, a wavelength analysis was performed. The wavelength analysis was a parametric study in which the spacing between two "E" category repairs was varied from 40 to 300 feet. The plotted results of that study are shown in Figure 12. For all spacings (λ), a peak occurs around 20 knots. This corresponds to impacting the first class "E" repair. A second family of peaks occurs for λ of 40 to 100 feet. This family of peaks is due to the first rebound of the NLG. A third family of peaks occurs for λ of 120 to 280 feet and corresponds to the second rebound of the NLG. Finally, a fourth family of peaks begins to appear for $\lambda = 200$ to 300 plus. These peaks correspond to the third NLG strut rebound. It can be seen that considerable damping is achieved after each rebound. In fact for $\lambda = 120$ to

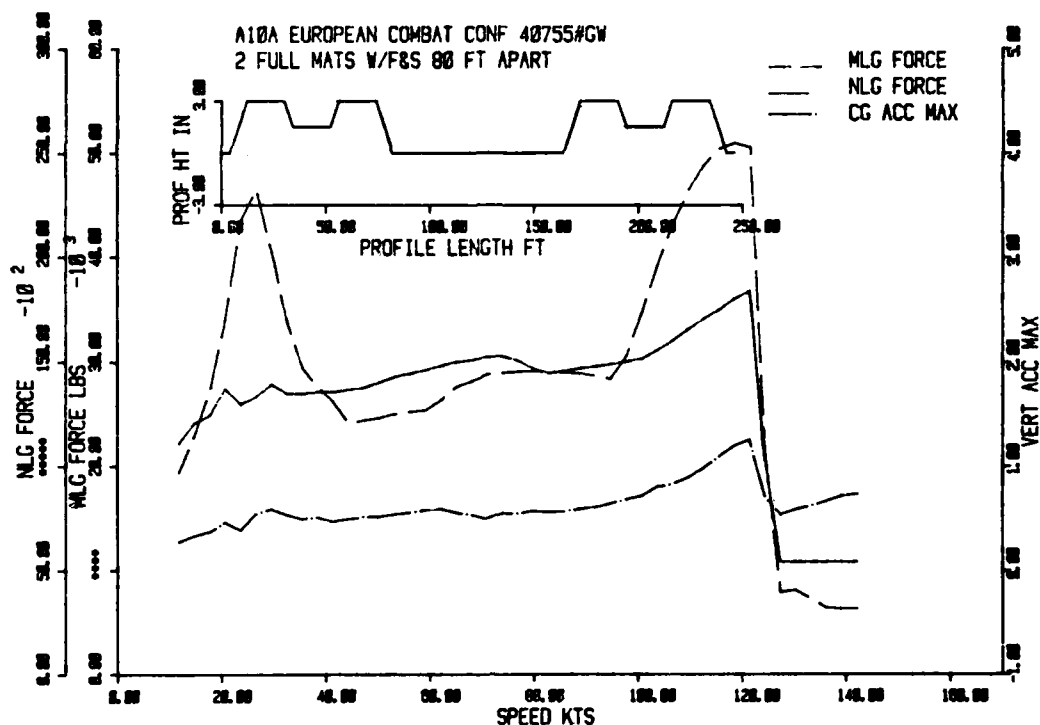


FIGURE 11. VELOCITY ANALYSIS OF AN A-10 TRAVERSING 2 CLASS "C" REPAIRS

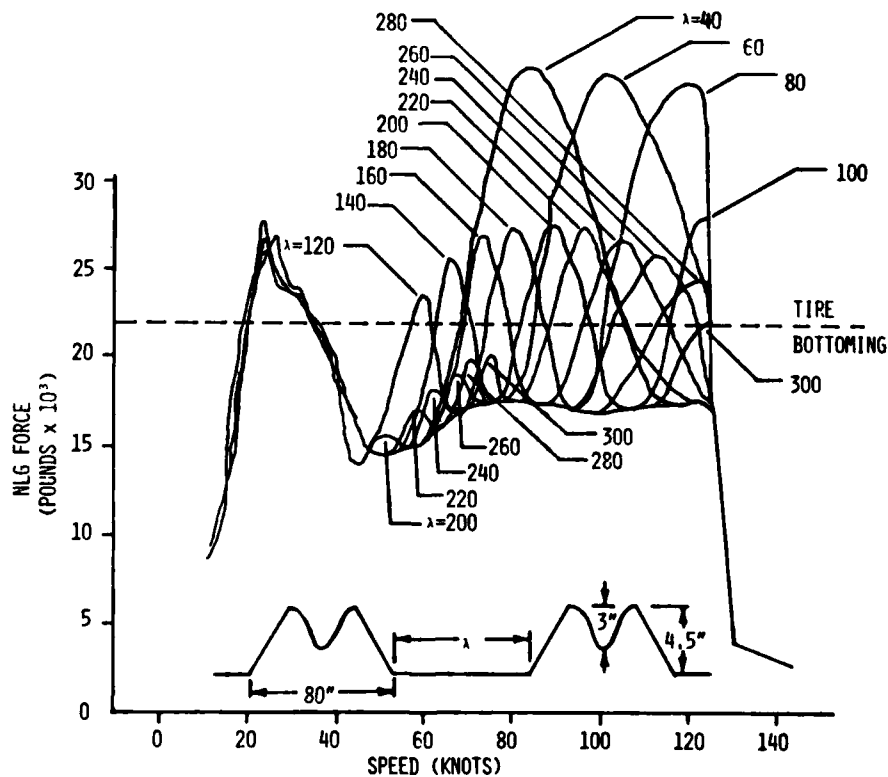


FIGURE 12. MAT SPACING ANALYSIS, A-10 EUROPEAN COMBAT CONFIGURATION 40,755 POUNDS GROSS WEIGHT, 2 CLASS E BUMPS

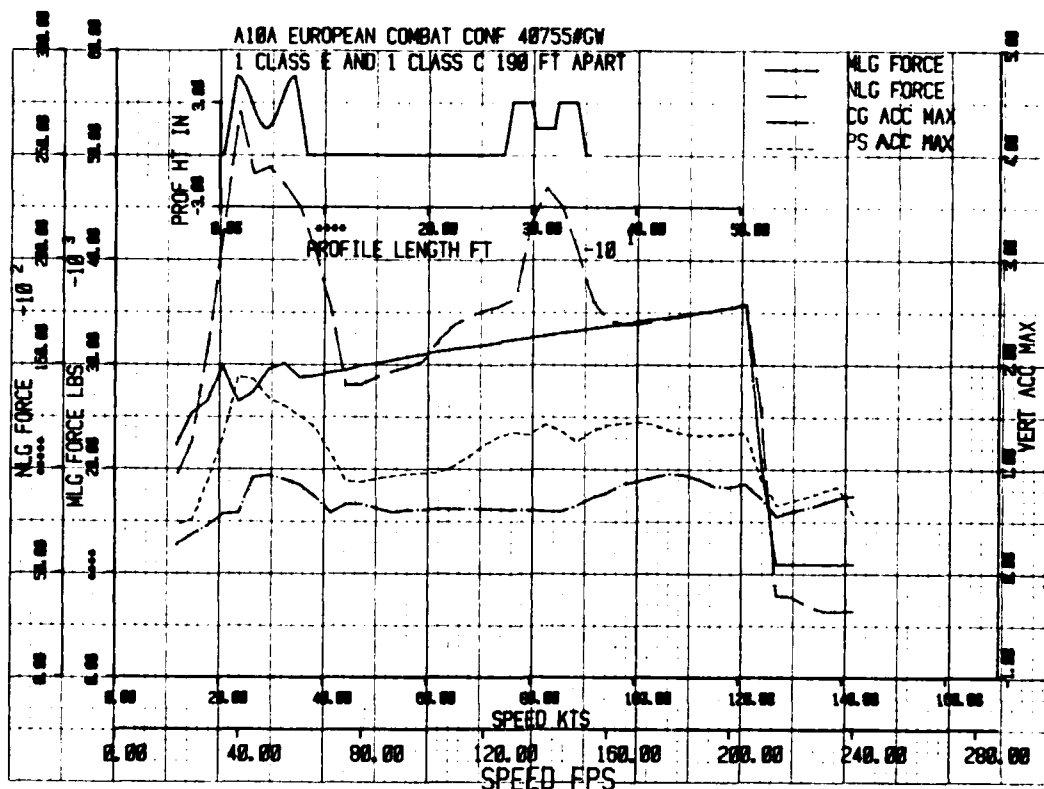


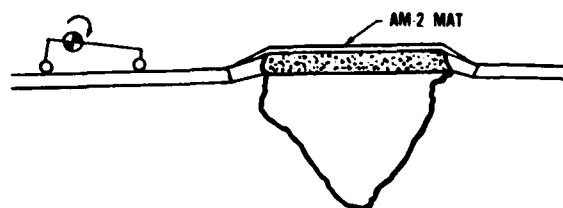
FIGURE 13. A-10 RESPONSE TO AN "E" REPAIR FOLLOWED BY A "C" REPAIR

280 feet, the second repair can be treated as a single repair encounter.

Several important facts can be deduced from the results shown in Figures 12 and 13:

- Single "E" repairs (or better) are satisfactory beyond 40 knots.
- Multiple "E" repairs (or better) are satisfactory when spaced 300 or more feet apart.
- An "E" repair followed by a "C" repair is satisfactory when spaced 120 feet or more apart.

Simulations were also made of the A-10 in a hard braking condition as in landing rollout (see Figure 14). Even though the aircraft weight is down to 30,300 pounds (which reduced gear loads), high NLG loads can be produced over closely spaced "E" repairs when the brakes are applied at the main landing gear (MLG) and a subsequent pitch down moment is produced.



SIMULATION DIFFICULTIES

- BRAKING COEFFICIENT
- PILOT INFLUENCE
- ANTISKID INPUT
- SURFACE CONDITIONS (FRICTION)

FIGURE 14. BRAKING OVER REPAIRS

Since the A-10 responds primarily in pitch, a parametric study was performed to see how higher NLG strut preload pressures would affect its performance. Figure 15 shows a plot of peak NLG loads for various preload

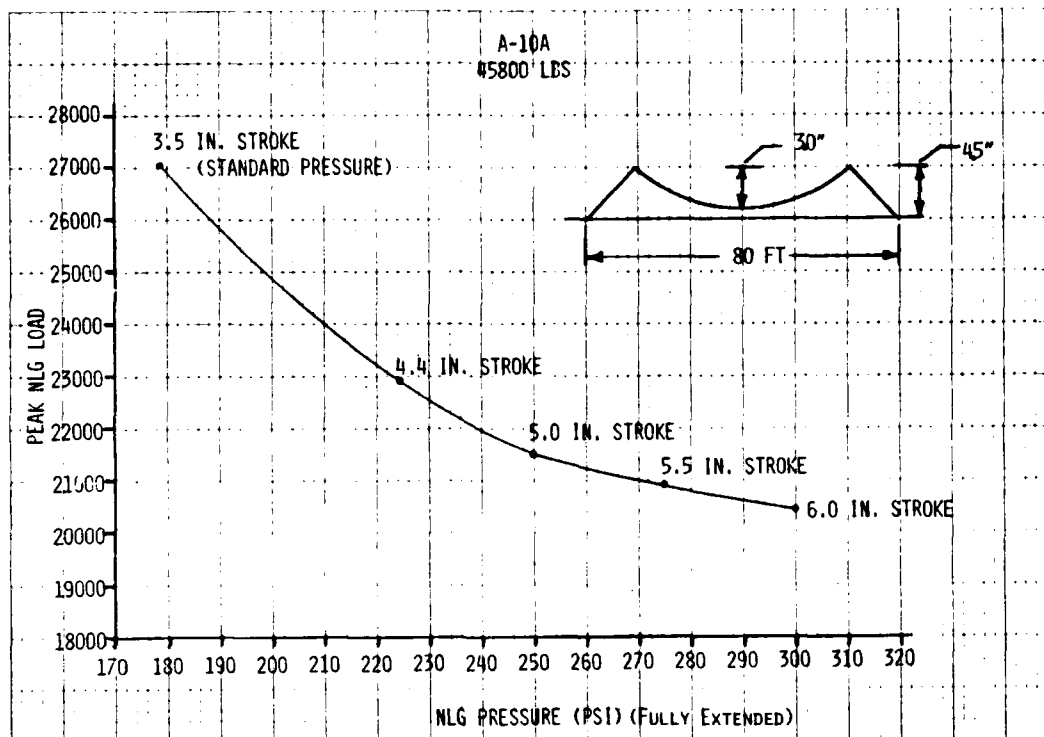


FIGURE 15. EFFECT OF NLG PRELOAD PRESSURE ON MAXIMUM NLG FORCE

pressures from the standard 179 psi up to 300 psi. From this chart, a value of 250 psi was selected to the rest of the parametric study. This increase in preload pressure is equivalent to a 1.5 inch increase in strut stroke remaining.

Velocity analyses with 250 psi NLG strut were run for all repair categories where the NLG force with the standard strut exceeded the tire bottoming load. Figure 16 is typical of the results of these simulations. Generally speaking, the increase in preload pressure resulted in a 20 percent reduction in peak loads on the NLG. There was very little change in MLG response.

Landing in areas where there are repairs may produce excessive landing gear loads because of the increase in effective sink speed. Figure 17 illustrates the point that the positive slope in pavement can produce an effective sink speed greater than the design limit of 10 fps. This effective sink speed is of short duration, however. Simulations of landing and

nose gear slapdown on repairs were not made.

DEFINITION OF A MINIMUM OPERATING STRIP (MOS)

Using all of the velocity charts produced and the data contained in Figures 12 and 13, a preliminary minimum operating strip (MOS) for the European combat configured A-10 has been defined for taxi and takeoff.

Since the A-10's ability to land in the repair zone is unknown, the uni-directional MOS shown in Figure 18 indicates that "A" quality repairs must be made in the first 500 feet.

- Multiple "E" quality repairs must be spaced 300 feet apart.
- An "E" quality repair may be followed by a "C" quality repair providing they are spaced 120 feet or more apart.

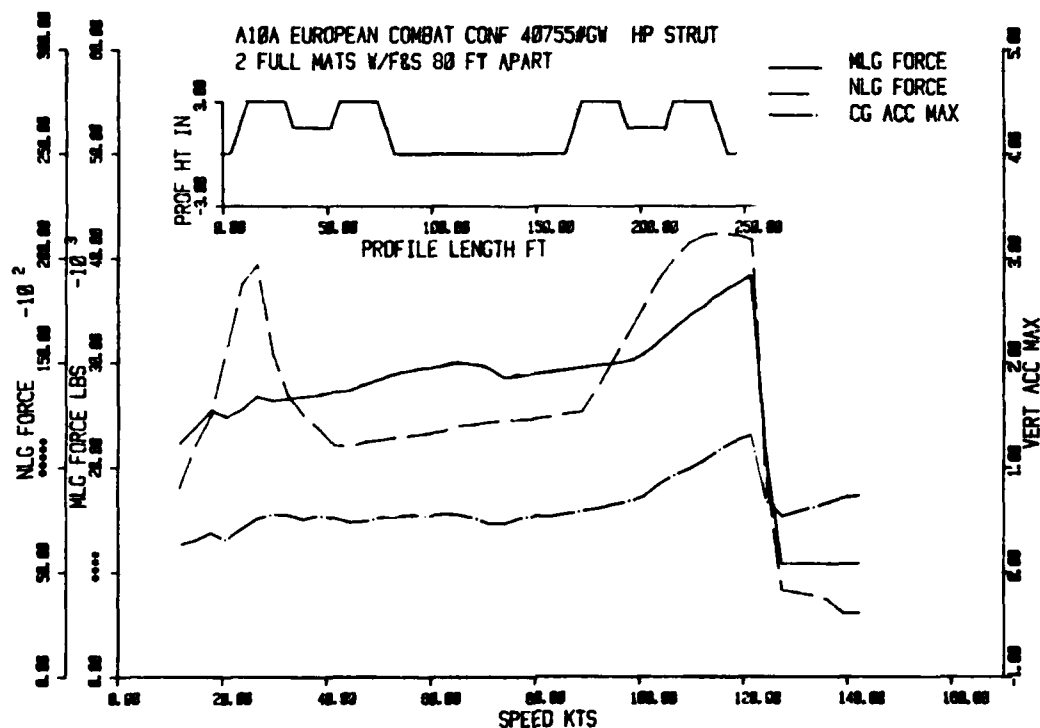
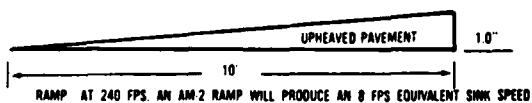


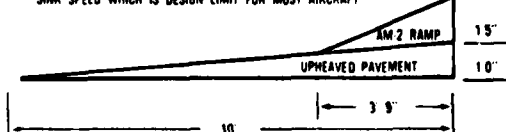
FIGURE 16. A-10 RESPONSE OVER 2 "C" REPAIRS WITH INCREASED NLG STRUT PRELOAD PRESSURE

VERTICAL LOADS:

UPHEAVAL AT 240 FPS (142 KTS) UPHEAVAL IN 10 FEET WILL PRODUCE A 2 FPS EQUIVALENT SINK SPEED



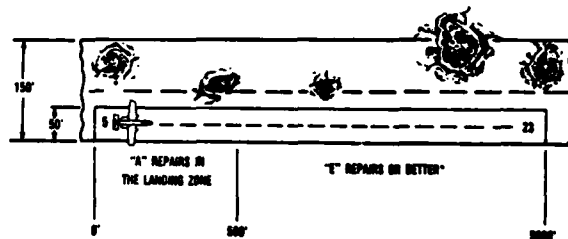
AN AM 2 RAMP ON 1' OF UPHEAVAL (IN 10') WILL PRODUCE AN EQUIVALENT 10 FPS SINK SPEED WHICH IS DESIGN LIMIT FOR MOST AIRCRAFT



THEREFORE A TOUCHDOWN SINK SPEED OR A DYNAMIC LOAD COUPLED WITH THE ABOVE COULD PRODUCE EXCESSIVE VERTICAL LOADS

DRAW LOADS: SIMILARLY DRAW LOADS WILL BE INCREASED IN PROPORTION TO THE ANGLE OF THE RAMP OR UPHEAVAL PAVEMENT

FIGURE 17. EFFECTS OF UPHEAVAL



- "A" QUALITY REPAIRS ARE REQUIRED IN FIRST 500 FEET (LANDING ZONE)
- MULTIPLE "E" QUALITY REPAIRS MUST BE SPACED 300 FEET APART
- AN "E" REPAIR FOLLOWED BY A "C" REPAIR CAN BE SPACED 120 OR MORE FEET APART
- MULTIPLE REPAIRS CLOSER THAN 120 FEET APART SHOULD BE MADE AS A SINGLE REPAIR
- TAXIWAY REPAIRS MAY USE "E" QUALITY REPAIRS TAXI SPEEDS OVER "E" REPAIRS SHOULD BE LIMITED TO 15 KNOTS

FIGURE 18. A-10 UNIDIRECTIONAL MINIMUM OPERATING STRIP (MOS)

SUMMARY

An analysis has been made to assess the A-10's ability to operate on rapidly repaired bomb damaged surfaces. Based on this analysis, a preliminary minimum operating strip (MOS) has been defined.

The A-10 can takeoff (40,755 pounds or less) and land (30,300 pounds or less) on a 50 foot by 5,000 foot MOS (Figure 18) providing that:

- "A" quality repairs are made in first 500 feet (landing zone).
- Multiple "E" quality repairs are spaced 300 feet apart.
- An "E" repair followed by a "C" repair must be spaced 120 feet apart.
- Where multiple repairs are closer than 120 feet apart, those crater repairs should be made as a single repair.
- Taxiway repairs may use "E" quality repairs. Taxi speeds over "E" repairs should be limited to 15 knots.

Increasing the precharge pressure from 179 psi to 250 psi will improve the A-10's ability to operate on rough surfaces by approximately 20 percent.

Employing an aft stick takeoff procedure will make significant improvements in the A-10's rough surface capability. The takeoff distance will be increased, however, therefore an aft stick takeoff is not recommended at this time.

Reducing the A-10's gross weight will result in increasing its rough surface operational capability.

The minimum operating strip (MOS) defined in this report for safe A-10 operations is based on main and nose landing gear vertical loads only. Pylon, store, aircraft structure, avionics and etc failures were not considered. Additional testing should be accomplished so that simulation programs can be validated for response at the wings, pylons, aircraft structure, etc.

In addition, A-10 testing over AM-2 mats with hard brakes applied should be accomplished so that more realistic values for strut bearing friction can be defined.

A-10 operations over unrepaired spalls (small craters) were not simulated. Testing and simulations over spalls should be conducted.

Finally, testing an A-10 landing in the repaired zone should be accomplished.

REFERENCES

1. Gerardi, Tony and Caldwell, R., "Aircraft Response to Operations on Rapidly Repaired Battle Damaged Runways and Taxiways", 51st Shock and Vibration Bulletin, May 1981.
2. Gerardi, Tony G., "Digital Simulation of Flexible Aircraft Responses to Symmetrical and Asymmetrical Runway Roughness", AFFDL-TR-77-37, Air Force Flight Dynamics Laboratory, Wright-Patterson AFB OH 45433, August 1977.

DISCUSSION

Voice: I noticed, in your plot of landing gear force versus speed for different values of λ (bump spacings), that your second peak kept getting smaller and smaller. I would think there would be some value of λ where the second peak would be equal to the first peak. What is that value? You got up to about 300 feet on your bump spacing, and your second peak is much smaller than your first peak. I would think there would be a point where your second peak should be equal to your first peak; essentially zero initial conditions.

Mr. Gerardi: After the second rebound, the strut has cycled twice, and you have taken out much of the energy by allowing the strut to damp and so forth.

Voice: There must be some bump spacing where you are starting off from almost as if you were going over the first bump again.

Mr. Volin (SVIC): I realize you are mostly concerned with the landing gear. What effects would operation over roughly repaired runways have on the equipment in the aircraft, or on the capability of the pilot to keep the aircraft under control during take-off or landing?

Mr. Gerardi: That is a good question. We anticipated problems on the F-4 aircraft when we tested it. We anticipated problems with the external stores, and, in fact, we predicted problems with our computer analysis, but they did not occur. We really aren't concerned with secondary structure, hydraulic lines and the like. We are looking at pilot acceleration; we went through the test, we got some pilot comments, and we found nothing that would hamper the operation of the aircraft. The primary concern seems to be nose landing gear, particularly on this aircraft. We have done the same thing on the C-130 and the C-141 aircraft. We did have some fairly high load factors out on the engine pylons on both of those aircraft.

Voice: In one particular aircraft, passing over a very specialized runway profile, we managed to drive the acceleration to the point where the pilot couldn't function very well. That is the only case I am aware of where the pilot's performance was a limiting factor.

Mr. Gerardi: Some analytical studies of avionics show that their higher frequency response isn't really affected that much by the type of runway unevenness that we are looking at.

SUBCRITICAL FLUTTER TESTING USING THE FEEDBACK SYSTEM APPROACH

C. D. Turner
Assistant Professor
Mechanical and Aerospace Engineering Department
North Carolina State University
P. O. Box 5246
Raleigh, NC 27650

Current experimental flutter data analysis techniques assume an open-loop system for the aerodynamic and structural model. Frequency, damping, and modal energy are obtained from the experimentally obtained open-loop transfer function. These quantities are used directly or with other analytical methods to predict the critical flutter speed, or for use in subcritical analytical/experimental data comparisons. History has shown that the various techniques and methods are not always reliable. This paper presents an additional technique that represents the aerodynamic and structural model as a closed-loop or feedback system. The feedback system approach is compatible with most current techniques, with the only additional data requirement being the zero air speed transfer function which is obtained during the ground vibration test. In using this approach, two additional parameters are obtained for use in the prediction of the critical flutter speed or for subcritical data comparison, these are the aerodynamic transfer function and the product of the aerodynamic transfer function with the zero air speed transfer function. The development of the feedback system approach and its application to a simple and complex model are presented.

INTRODUCTION

Due to the limitations of aeroelastic analysis, flight flutter testing is performed with models and drones to validate analyses and with prototype aircraft to demonstrate freedom from flutter. As has been demonstrated in the past on many aircraft flight test and model tunnel test programs, flutter has been encountered without warning resulting in the loss or damage of the aircraft or wind tunnel model. In an effort to prevent these unpredicted occurrence, various subcritical flutter testing techniques have been developed. These methods serve two purposes. First they allow for the extrapolation of test data to determine the critical flutter speed, thus in theory preventing an unpredicted flutter occurrence. Second, they allow for analytical/experimental data comparison throughout the flight envelope instead of just at the critical flutter speed.

The earliest method used pulses of the aircraft control surfaces along with a strip chart recordings of the resulting motion. By using logarithmic decrement one could obtain the damping for a given airspeed, and in this manner damping versus airspeed could be plotted.

The major limitation of this method was the maximum frequency that could be excited was only eight to ten Hertz. With the advent of powered controls the maximum was raised to about fifteen Hertz. Therefore, subcritical flutter testing could only be used for critical modes occurring below the eight to fifteen Hertz range. Due to the low frequency range that could be excited, improvements were made in the methods of exciting the aircraft. These included inertia shakers [1] harmonically operated aerodynamic surfaces [2,3], pyrotechnics [4,5], and later the use of atmospheric, wind tunnel, and aircraft generated turbulence [6,7]. Similar improvements have been made in the area of data acquisition and data reduction methods [8-11], thus having made on line data analysis possible. These various methods are similar in that they treat the structure and aerodynamic model as an open-loop system, but differ in the technique that is used to obtain the frequency and damping data or how this data is used. Each of these techniques obtains frequency and damping or a set of transfer functions as a function of air speed.

The critical flutter speed can then be obtained from plots of damping [8], flutter margin [2,12], modal energy [10,13], or differential equation coefficients [8] versus air speed. Parallel efforts also have been made in the generation of analytical flutter data that can be compared directly to wind tunnel and flight test data [14-17]. Even with these improvements no one method can consistently be relied on to give valid results for all aircraft and model test. For this reason several methods are normally applied to the test data. In an effort to circumvent some of the problems in the currently used techniques, the feedback system approach has been developed. As presented in the next section, the feedback system approach allows the calculation of the aerodynamic transfer function. This function can be used to predict the critical flutter speed or it can be used along with the zero air speed transfer function to predict the critical flutter speed.

FEEDBACK SYSTEM APPROACH TO SUBCRITICAL FLUTTER TESTING

As indicated above present experimental flight flutter test methods assume an open-loop model for the aerodynamic and structural model, Figure 1. The techniques that use this approach are seeking to determine the effect of the aerodynamics on the structure as a change in the total system response to some form of excitation that is measured or where the form can be assumed. This approach may allow some useful information to be lost. If the aerodynamic force over some frequency range is of the same magnitude and and directly opposed to the exciting force at a given air speed then the mode at this frequency would be considered highly damped and little information would be contained in total system transfer function for this particular mode, but the data obtained from a ground test would indicate the presents of this mode. Jennings, Olsen, and Walter [11] discussed the possibility of using the zero air speed transfer function with the data obtained during flight test to describe the aerodynamic transfer function. To obtain the aerodynamic transfer function, a feedback representation of the aerodynamic and structural model is needed, Figure 2. The use of the feedback system is not new to aviation, it has been used for both load alleviation and flutter suppression. For active flutter suppression the total system response is measured and an aerodynamic surface is used to generate an aerodynamic force which counteracts the naturally generated aerodynamic force- the aerodynamic transfer function.

The open-loop transfer function $H(\omega)$ and the feedback system transfer functions are related by [18]:

$$H(\omega) = \frac{H_1(\omega)}{1 + H_1(\omega) H_2(\omega)}$$

The transfer function $H(\omega)$ is obtained from flight test data as is currently being done. The transfer function $H_1(\omega)$ is obtained from ground vibration test data which is available. Thus $H_2(\omega)$ can be found,

$$H_2(\omega) = \frac{H_1(\omega) - H(\omega)}{H_1(\omega) H(\omega)}$$

Once $H_2(\omega)$ is found then either $H_2(\omega)$ or the product $H_1(\omega) H_2(\omega)$ may be used to predict the critical flutter speed or be used in the comparison of analytical and experimental data. Before either of the above transfer functions are used for this purpose their behavior as a function of air speed would need to be considered.

The aerodynamic transfer function for a two degree of freedom flutter model (Figure 3) is given for three air speeds in Figure 4. Transfer functions for the product $H_1(\omega)H_2(\omega)$ are given in Figures 5 and 6. The aerodynamic transfer function for a five degree of freedom flutter model (Figure 7) is given for three air speeds in Figure 8. Either of the transfer functions, $H_2(\omega)$ or $H_1(\omega) H_2(\omega)$, can be used to predict the critical flutter speed. Examples of the use of the transfer functions to predict the critical flutter speed are given in the next section.

USE OF $H_2(\omega)$ IN PREDICTING THE CRITICAL FLUTTER SPEED

As indicated in the plots given in the last section the maximum magnitude and phase shift occur at an almost constant frequency for the various air speeds. Therefore, the aerodynamic transfer $H_2(\omega)$ or the transfer function $H_1(\omega) H_2(\omega)$ can be used to predict the critical flutter speed. The method currently being used to estimate the critical flutter speed is to obtain $H_2(\omega)$ as a function of air speed, then calculate the transfer functions $H_1(\omega) H_2(\omega)$ and $H(\omega)$ for various air speeds. Each new experimentally obtained total system transfer function $H(\omega)$ can be compared to the previously calculated transfer function, then the procedure is repeated each time more data becomes available. During each phase of calculation the critical flutter speed is updated. In using the transfer function $H_1(\omega) H_2(\omega)$ the feedback instability

$$H_1(\omega) H_2(\omega) = -1$$

is used to determine the critical flutter speed.

For the two mode examples the use of either damping or modal energy, Figures 3 and 9, as a predictor of critical flutter speed would be unsafe due to the sudden change in slope of the curves as the critical flutter speed is approached. In this case the flutter margin technique or the use of the transfer function $H_2(\omega)$ or $H_1(\omega) H_2(\omega)$, Figure 9, would yield much better results. For the five mode examples the use of damping, Figure 7, modal energy, Figure 10 or the

transfer functions $H_1(\omega)$, $H_2(\omega)$ and $H_3(\omega)$, Figure 10, would yield safe predictions of the critical flutter speed, with the transfer function $H_1(\omega)$, $H_2(\omega)$ being the most conservative.

CONCLUSIONS

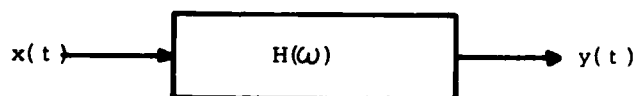
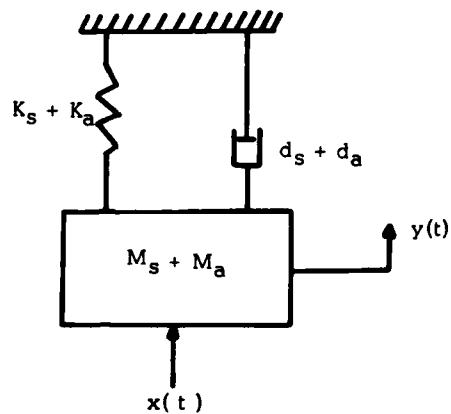
In using the feedback system approach the aerodynamic transfer function can be calculated using both the currently obtained flight flutter test data and the available ground vibration test data. The characteristics of this function make it extremely useful in both predicting the critical flutter speed and for use in subcritical data analysis. Since this method requires little change from methods currently being used, it can easily be implemented.

This approach will complement the methods currently being used in that the aerodynamics are being treated as a force instead of a change in the overall system, thus allowing two additional methods for predicting the critical flutter speed. These methods also allow information to be obtained on the more heavily damped modes. The use of this method also has a disadvantage, the prediction of the critical flutter speed and subcritical data comparison involves complex functions instead of the simple scalar numbers generated by the current techniques.

The feedback technique is now being refined. A wind tunnel test program is being planned at this time and should be completed by early 1982. Additional efforts are being made in the use of the feedback technique in analytical flutter calculations.

REFERENCES

1. M. Dublin and R. Peller, "Flight Flutter Testing of Supersonic Interceptors", NASA SP-385, 1958.
2. S. R. Hurley, "The Application of Digital Computers to Near-Real-Time Processing of Flutter Test Data," NASA SP-415, 1975.
3. H. Katz, F. G. Foppe, and D. T. Grossman, "F-15 Flight Test Program", NASA SP-415, 1975.
4. R. H. Stringham and E. J. Lenk, "Flight Flutter Testing Using Pulse Techniques," NASA SP-385, 1958.
5. C. E. Tammadge, "Excitation by Rockets", NASA SP-385, 1958.
6. C. E. Hammond and R. V. Doggett, "Determination of Subcritical Damping by Moving-Block/Randomdec Applications," NASA SP-415, 1975.
7. M. A. Alba, "The Application of Recent Techniques in Flight Flutter Testing," NASA SP-415, 1975.
8. J. C. Houbolt, "On Identifying Frequencies and Damping in Subcritical Flutter Testing," NASA SP-415, 1975.
9. R. W. Lenz and B. McKeever, "Time Series Analysis in Flight Flutter Testing at the Air Force Flight Test Center: Concept and Results," NASA SP-415, 1975.
10. L. Enochson, "The GenRad Laplace Transform Applied to Flight Flutter Data Analysis," GenRad Application Note, August 21, 1980.
11. W. P. Jennings, N. L. Olsen, and M. J. Walter, "Transient Excitation and Data Processing Techniques Employing the Fast Fourier Transform for Aeroelastic Testing," NASA SP-415, 1975.
12. N. H. Zimmerman and J. T. Weissenburger, "Prediction of Flutter Onset Speed Based on Flight Flutter Testing at Subcritical Speeds," Journal of Aircraft, Vol. 1, No. 4, 1964.
13. H. J. Perangelo and F. W. Milordi, "Flight Flutter Testing Technology at Grumman," NASA SP-415, 1975.
14. R. Rosenbaum and R. H. Scanlan, "A Note on Flight Flutter Testing," Journal of the Aeronautical Sciences, June 1948.
15. F. J. Fruch and J. M. Miller, "Prediction of Dynamic Response from Flutter Analysis Solutions, Air Force Office of Scientific Research, SR-65-0952 June, 1965.
16. W. P. Rodden and B. Stahl, "A Strip Method for Prediction of Damping in Subsonic Wind Tunnel and Flight Flutter Tests," Journal of Aircraft, Jan.-Feb. 1969.
17. H. J. Hassig, "An Approximate True Damping Solution of the Flutter Equation by Determining Iteration," Journal of Aircraft, November 1971.
18. J. S. Bendat and A. G. Piersol, Engineering Applications of Correlation and Spectral Analysis, John Wiley & Sons, New York, 1980.



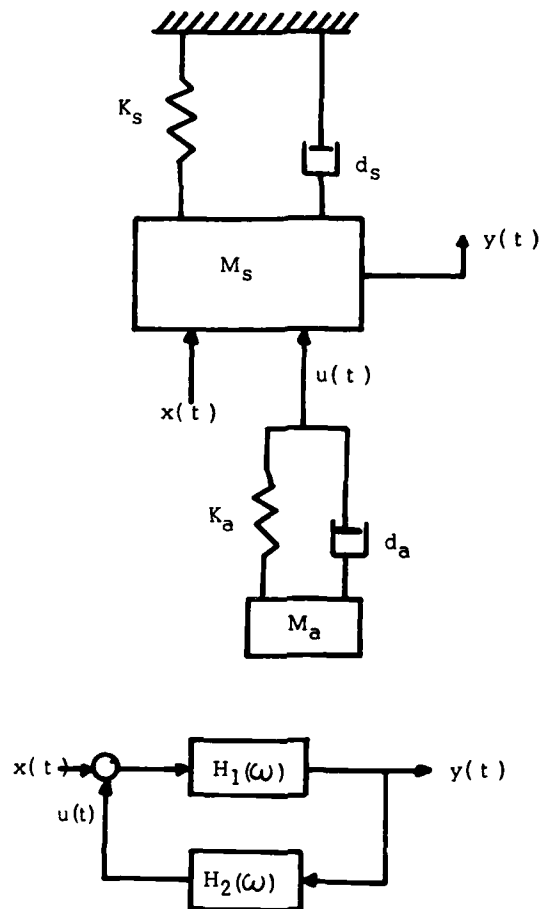
Symbols

$H(\omega)$ - system transfer function
 K - stiffness
 d - damping
 M - mass

Subscripts

s - structural parameters
 a - aerodynamic parameters

Figure 1. Open-loop model.



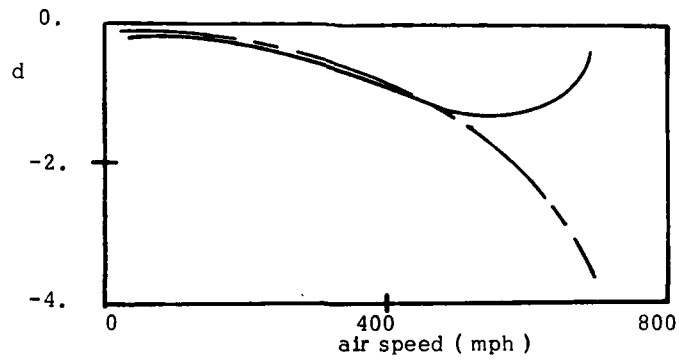
Symbols

$H_1(\omega)$ - structural transfer function
 $H_2(\omega)$ - aerodynamic transfer function
 K - stiffness
 d - damping
 M - mass

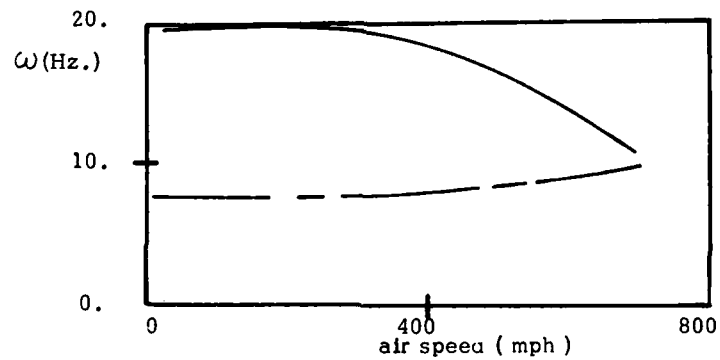
Subscripts

s - structural parameters
 a - aerodynamic parameters

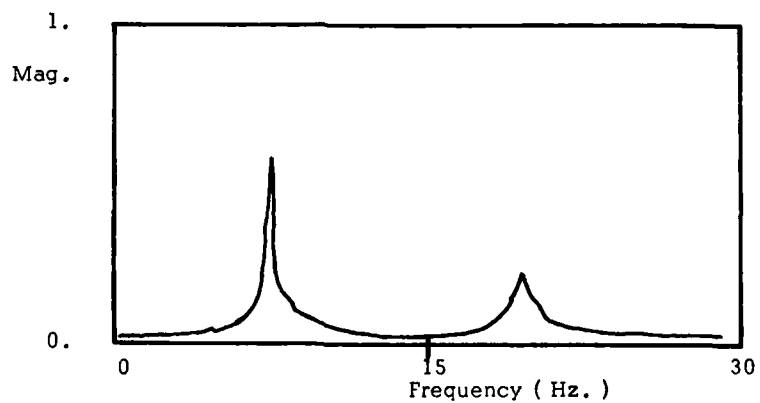
Figure 2. Feedback model.



a. Damping versus air speed.

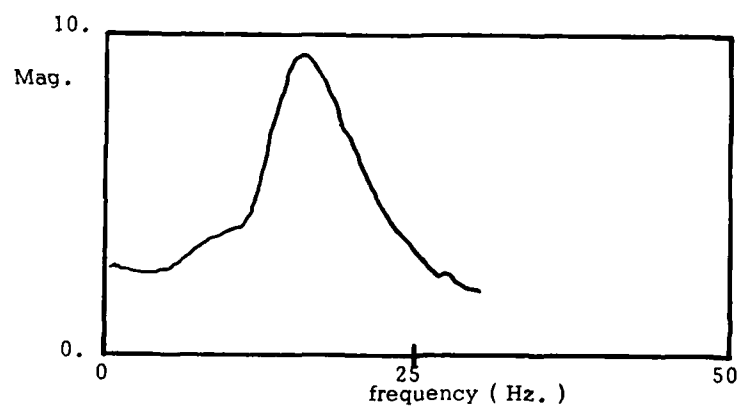


b. Frequency versus air speed.

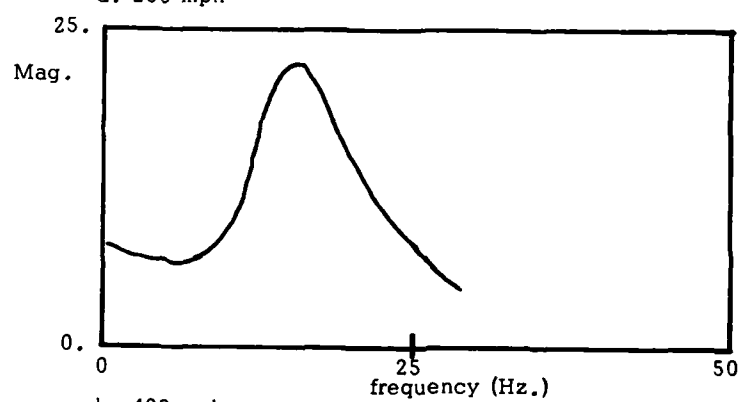


c. Magnitude versus frequency for zero air speed.

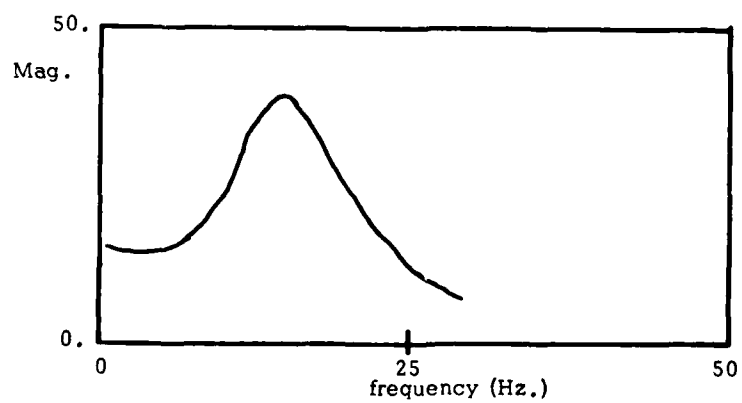
Figure 3. Two degree of freedom flutter model.



a. 200 mph



b. 400 mph



c. 600 mph

Figure 4. Aerodynamic transfer function.

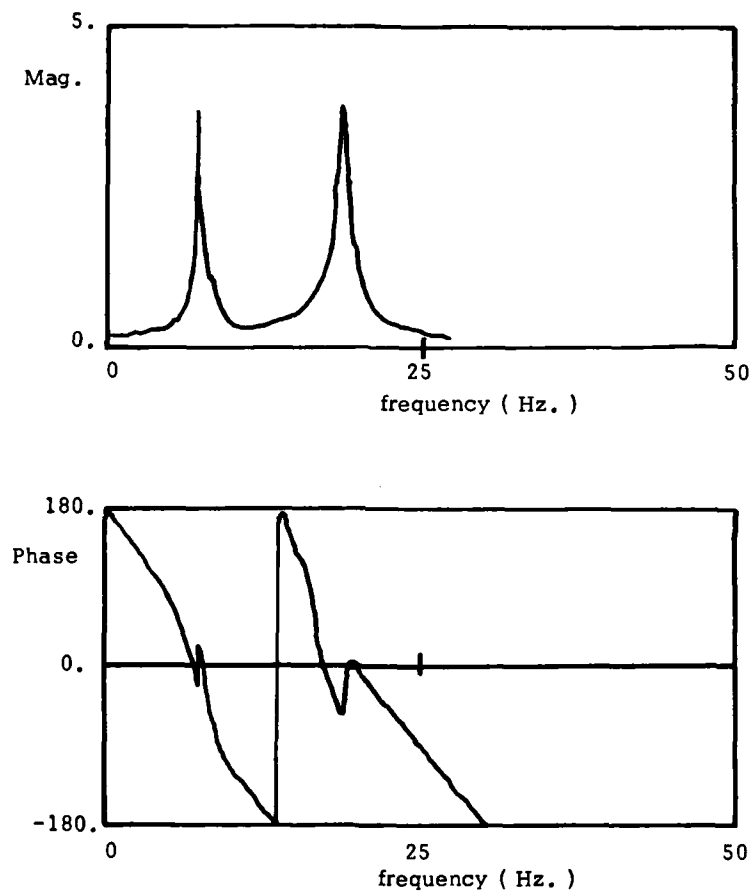


Figure 5. $H_1(\omega) H_2(\omega)$ frequency response function
for 400 mph.

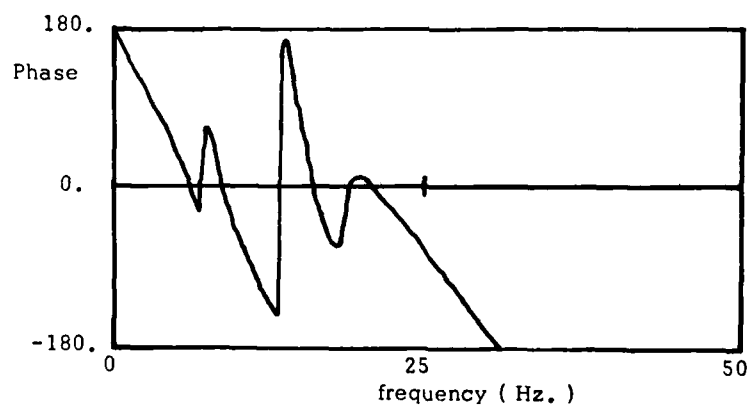
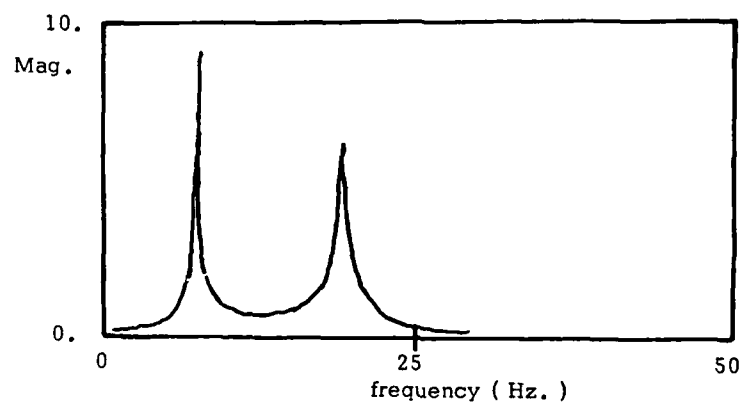
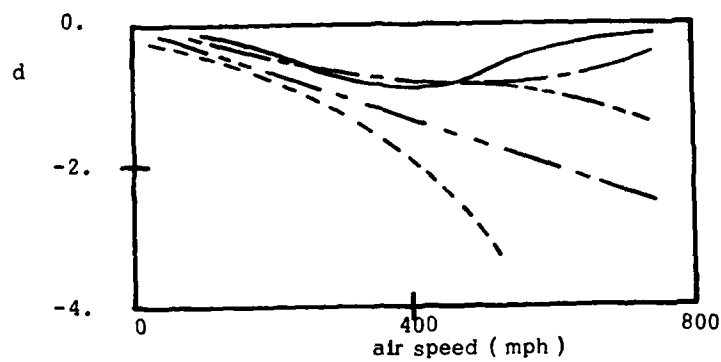
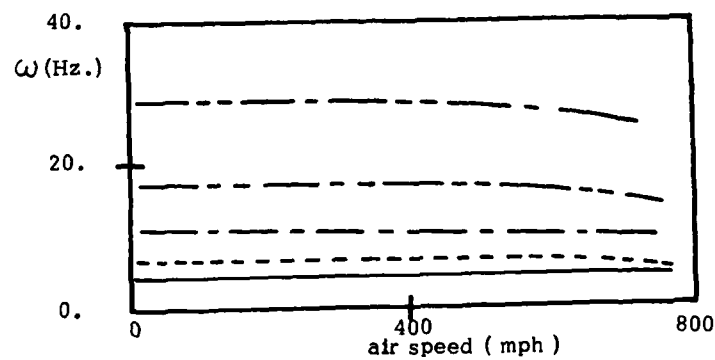


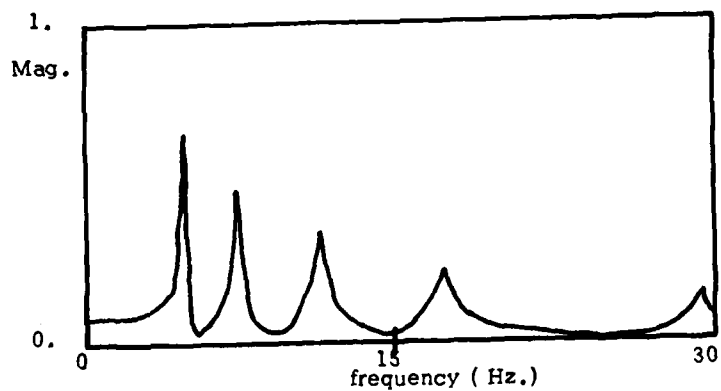
Figure 6. $H_1(\omega) H_2(\omega)$ frequency response function
for 600 mph.



a. Damping versus air speed.

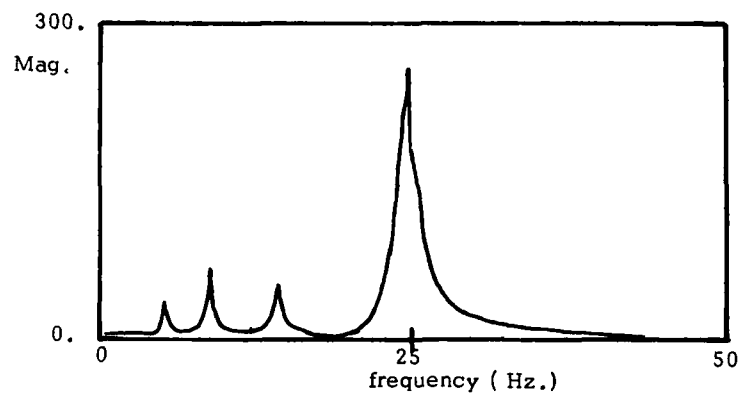


b. Frequency versus air speed.

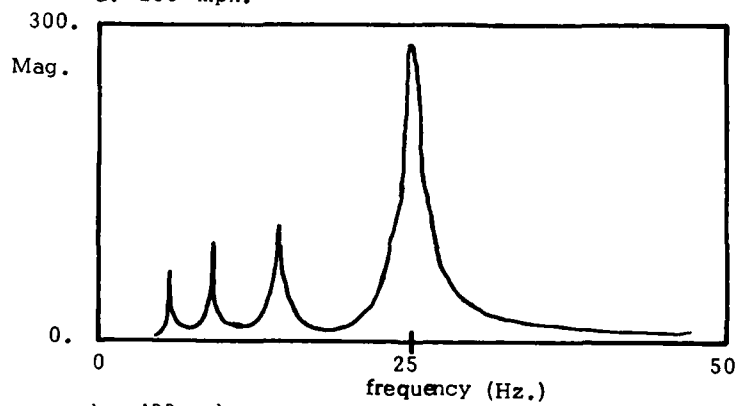


c. Magnitude versus frequency for zero air speed.

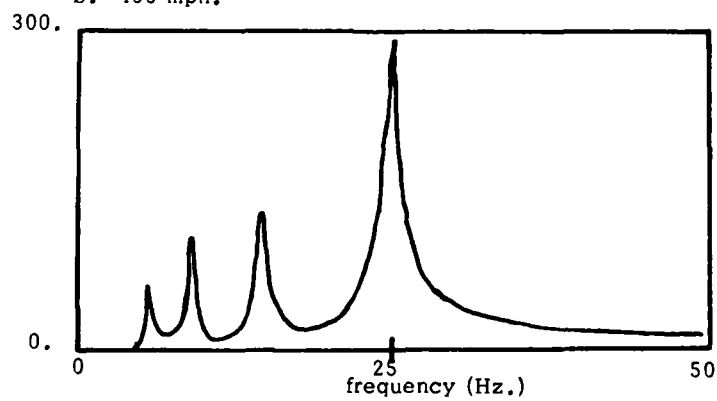
Figure 7. Five degree of freedom flutter model.



a. 200 mph.

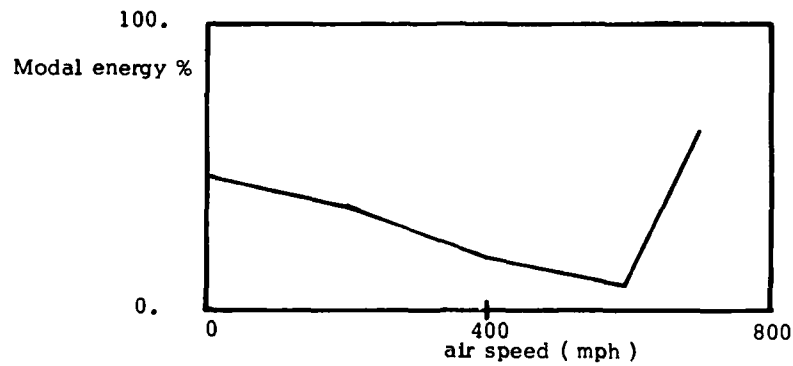


b. 400 mph.

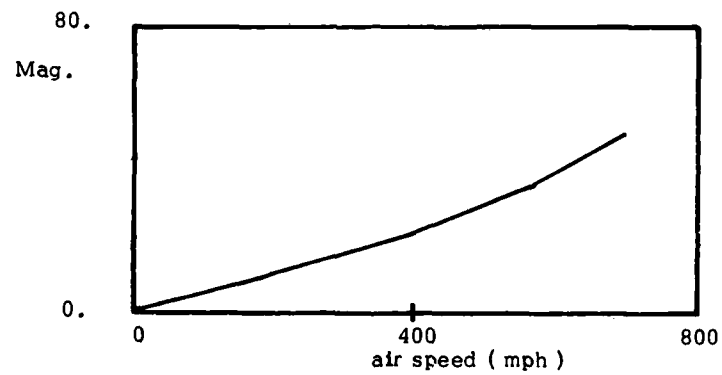


c. 600 mph.

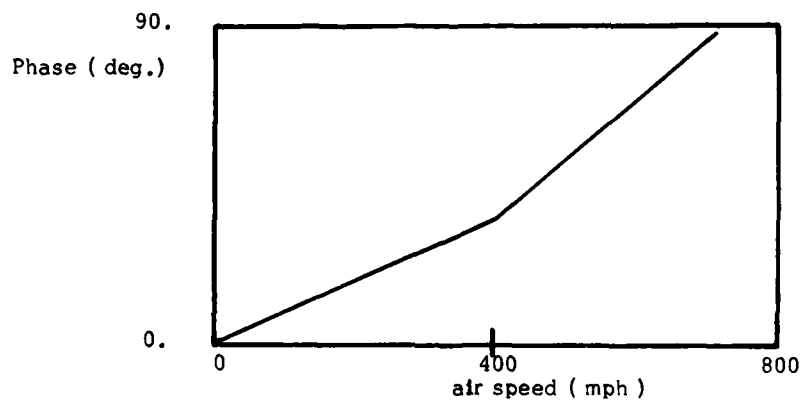
Figure 8. Aerodynamic transfer function.



a. Modal energy versus air speed.

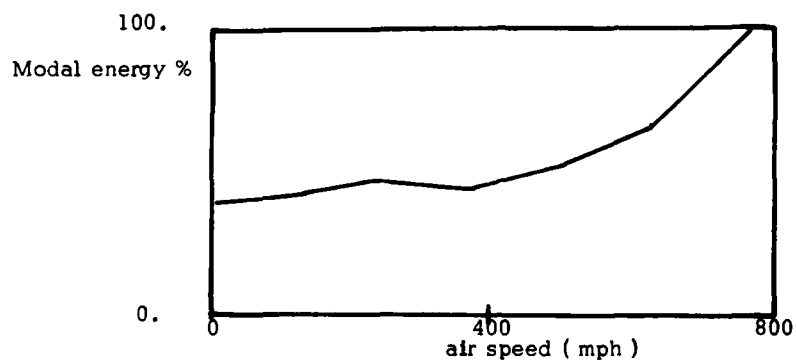


b. Magnitude of critical mode versus air speed.

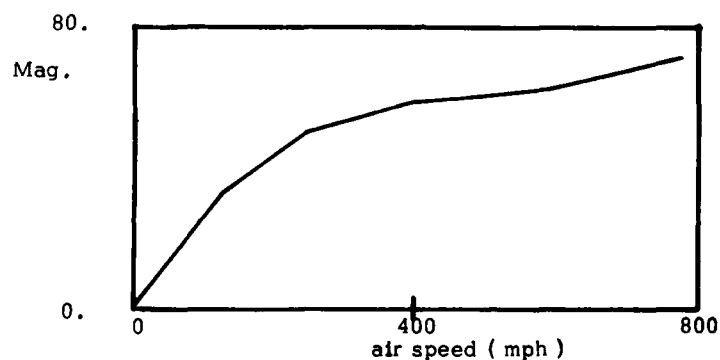


c. Phase of critical mode versus air speed.

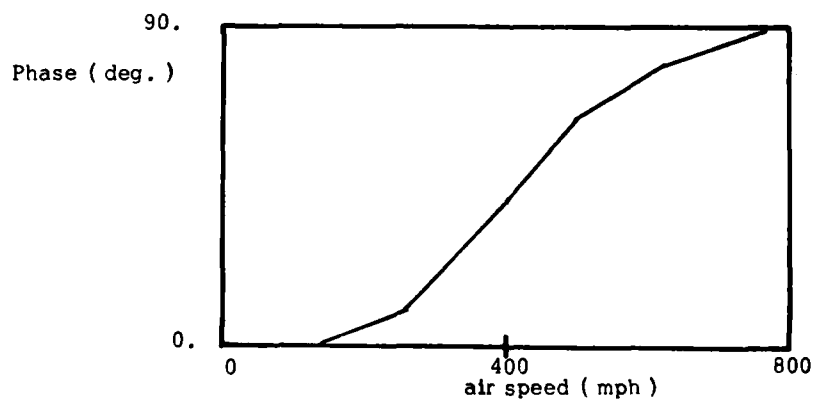
Figure 9. Two degree of freedom flutter model.



a. Modal energy versus air speed.



b. Magnitude of critical mode versus air speed.



c. Phase of critical mode versus air speed.

Figure 10. Five degree of freedom flutter model.

TOMAHAWK CRUISE MISSILE FLIGHT ENVIRONMENTAL MEASUREMENT PROGRAM

E.S. Rosenbaum, F.L. Gloyna
Convair Division of General Dynamics Corporation

This paper presents a summary of vibration measurements made during the Systems Integration and Design Validation Phases of the Tomahawk Cruise Missile Program. Data is also presented for the Ground Launched (GLCM), Sea Launched (SLCM) and Air Launched (ALCM) variants, in both power spectral density and shock spectra formats.

INTRODUCTION

The Tomahawk cruise missile has been designed as a highly efficient flying machine to meet its basic mission goal of long-range, low-altitude flight. General Dynamics chose to use an encapsulation system for both the GLCM and SLCM (ship) versions. This provides a means of separating the in-flight performance requirements from the peculiar requirements of the launch platform. In addition, the Tomahawk may be launched from various aircraft such as the A-6, A-7, B-52 and F-16. The main features of the Tomahawk cruise missile are presented in Figure 1.

During the development phase of the Tomahawk program, the Convair Division of General Dynamics Corporation implemented a basic inflight-dynamics data-measurement program. The purposes of this program were, essentially, threefold:

1. Verify environmental predictions.
2. Determine environmental levels at specific locations.
3. Provide a means for investigating failure analysis.

In this regard, we used the data presented by Messrs. Noonan, Gubser and Harmening (Reference 1) to develop the vibration instrumentation plan. Note that virtually no acoustic measurements were made except during the ALCM proposal effort and one measurement late in the Tomahawk program. Essentially, this was done because there were no known acoustically sensitive components in areas that might be predicted to have a relatively high acoustic environment; say 150dB (Ref). In addition, the design of the structure and mission profile were such that sonic fatigue was not considered a problem. There were three unsuccessful attempts to measure the underwater boost environment with an on-board, recoverable, tape recorder.

The Vibration Data Bank Code (Reference 2) developed by Convair Division and presented at the

1977 Shock and Vibration Symposium by G.E. Wadleigh of Convair Division, was used to store, retrieve, and analyze the shock and vibration data obtained during this program.

It is the purpose of this paper to summarize the flight test data from the various Convair Division cruise missile programs and to show how a vibration data bank may be utilized as an effective tool for analyzing these data.

DATA MEASUREMENT SYSTEMS

All vehicle flight vibration measurements were made with piezoelectric-type sensors. The test vehicles were equipped with an S-band telemetry system and transmitted at a frequency of 2,260.5 MHz. Flight data was transmitted to telemetry ground stations directly, or by utilizing available microwave relay links. In addition, data was transmitted to a Navy A-6 aircraft equipped with an Ampex AR1700 wideband multi-channel recorder designed for airborne applications. Up to 14 channels of record electronics were available using 1-inch tape on 14-inch precision reels. Vehicle vibration data were measured continuously utilizing IRIG channels 15 through 20; for the most part only three channels were used on any one flight. IRIG-B time code and voice annotations were recorded on tape along with the telemetry test data.

SPECTRAL ANALYSIS

All flight data were recorded on magnetic tape. Typically, the flight data were limited to a 10-2,000 Hz bandwidth; essentially dictated by the telemetry system. Accelerometer time histories were first obtained by playback on a low-speed oscillograph, one ips, to select the general times of interest, and then again at 10 ips or 40 ips to select more specific times for analysis. In some cases, RMS plots were made of the raw data to assist in

determining flight times of interest. The resulting time histories were analyzed for either stationary or nonstationary trends. Stationary data were analyzed by the use of power spectral density techniques and transient, nonstationary, data by the use of shock spectra.

In general, one second of flight data was sampled for the power spectral density analysis; a 2,100 Hz low-pass output filter (LPOF) and 20 Hz bandwidth were used. Spectral densities and auto-correlation functions were obtained using the "Blackman-Tukey" (Reference 3) method of computing the power spectral density. This standard method is based on computing the power spectral density function via its Fourier transform relation to the auto-correlation function. Although the "Cooley-Tukey" method of computing the power spectral density directly via a finite range fast Fourier transform (FFT) of the original data is more efficient, from a computational standpoint, our computer codes are set up for the former. Sinusoidal amplitudes may be estimated from the auto-correlation function using the relationship:

$$A(\text{sine-rms}) = (2 \times \text{Auto-covariance amplitude})^{.5}$$

The frequency of the sinusoid may be estimated from the relationship:

$$f(\text{sine-Hz}) = \text{Sampling rate}/(\text{no. of lags/cycle}).$$

The duration of transient data that was analyzed varied from 20 ms to 60 ms. These data were filtered with a 2,100 Hz LPOF and digitized at a rate of either 6,000 samples/second or 10,000 samples/second. The digitized data was then analyzed using a shock spectra computer code; 5% critical damping was used.

VEHICLE VIBRATION MEASUREMENTS

As in most programs, everyone wants to know about shock and vibration environments in order to design structure and components, but no one wants to pay for it. Once the data is obtained and preliminary analyses indicate levels within predictions, no one wants to pay to complete the data reduction. At Convair Division, however, we have reached a reasonable balance between the quantity of data that could be obtained at reasonable cost; data that could be reduced, again at reasonable cost; and data that was required to prove the present design. The flight data presented in this paper is a representation of approximately 71 flights from all the Convair Division cruise missile programs. For all practical purposes, all the cruise missile variants are of similar design; structural variations, in general, did not result in significant response differences due to either aerodynamic or mechanical flight-vibration stimuli.

To keep this paper to some reasonable length, we will not delve into the history of the Convair Division cruise missile programs, nor into the specific structural differences of the cruise missile variants, although this may be seen to some degree in Figure 1. However, to better correlate the vibration data, and to reference the vibration levels to the stimuli, a typical SLCM (sub) mission profile is presented (Figure 2).

The SLCM is ejected from the submarine launch platform via pneumatic pressure and, once clear, the booster is ignited. After surface broach, a number of discrete flight events occur such as jettison of the shroud, inlet covers, and wing doors, and deployment of the wings and fins. Approaching the end of the boost phase, the vehicle is flying at approximately Mach 0.52. At this point, the booster is jettisoned and the cruise engine started. It should be noted that the mission profile presented is a typical one, the parameters are neither maximums nor minimums.

The mission profile for both the SLCM (ship) and GLCM are similar, but differ from the SLCM (sub) in the ejection technique from the launch platform. For the SLCM (ship) and GLCM, the booster is ignited in the launch tube and the vehicle ejected at about the same velocity the SLCM (sub) achieves at underwater broach. Unlike the SLCM or GLCM cruise missiles, the Air Launched Cruise Missile (ALCM) does not require a booster; the launch platform provides the initial velocities required for stable cruise engine start and flight. Once any of the cruise missile variants achieve cruise flight, the vibration environments are essentially the same. A summary of the vehicle vibration data is presented in Table 1. The location of the accelerometers are better defined in Figure 3.

As stated in Reference 1, the vibration levels measured in the forward portion of the vehicle were, typically, less than 0.5 g (rms) overall. Low-level sinusoids, generally associated with engine operating frequencies, less than 0.25 g (rms) are evident in the data. The vibration levels were low enough not to warrant further investigation. The highest vibration levels were measured in the tail section, primarily from the cruise engine. For the turbojet engine, a sinusoid is noted at about 670 Hz, which represents the engine operating frequency (Figures 46 through 57). This is verified by the data presented in Reference 1; the Harpoon missile uses the same turbojet engine for the cruise propulsion system. The sinusoid at 1,330 Hz also appears to be engine induced. Of particular interest from a component design viewpoint is the rather high, wide-band random environment, 9.0 g (rms), measured at the fin actuators (Figures 48 and 49). Vibration levels for the turbofan engine, characteristically, included sinusoids at the shaft operating frequencies of 560 Hz and 1,060 Hz (Figures 58 through 73). It is interesting to note the background wide-band random vibration levels on the vehicle structure, in both the forward and aft sections of the vehicle, were less than 0.5 g (rms) overall, regardless of flight phase.

After the first few launches of each cruise missile variant, standard accelerometers (A462, A456, or A476, and A474) were used to monitor the vibration environment. In fact, the A474 pickup (WRC turbofan engine) was monitored in real time over an audio system. Thus, one could listen to the flight in real time to ensure proper engine operation. This technique was implemented by Convair Division and the Williams Research Corp.

early in the Tomahawk program after an engine threw a turbine blade; audio analysis in conjunction with standard mechanical analysis enabled us to identify the failure mode.

B52 captive-carry data were obtained during the ALCM competition. As expected, the maximum vibration levels were obtained at takeoff. The variation in vibration levels along the mission were dependent on the location within the missile (Figures 4 through 10). External and internal acoustic levels, for correlation with the vehicle vibration, are presented in Figures 9 and 10. In general, the duration of these levels was less than 60 seconds (total) for each mission. Once the B52 was airborne, the missile vibration levels decreased to an overall of less than one g (rms), Figures 11 through 17. This compares favorably with the A-6 captive-carry environment, Figures 18 through 24. Throughout the Tomahawk program, cruise missiles have been launched from A-6 aircraft to prove out the basic airframe, propulsion, and guidance systems designs prior to launch from the sub, ship, or ground launch platforms.

SLCM (ship) and GLCM launch vibration levels, with the vehicle emerging from the launch tube, were lower than expected. Vibration levels at the guidance were about the same as measured during the A-6 captive-carry or cruise portion of flight. Approximately two g (rms) overall random was measured at the aft section of the missile. These data are presented in Figures 25 through 30; the 100 Hz sinusoid evident in the data represents the first vehicle axial mode.

The boost-phase data are presented in Figures 31 through 45. Of particular interest are the measurements made on the air-data package (ADP). Ground tests in the Convair Division reverberant acoustic chamber predicted higher vibration levels with the inlet in the up position rather than with the inlet in the deployed position; Figures 39 and 40 indicate otherwise. We have concluded from reviews of both the ground acoustic test and flight-test data that the testing in the reverberant acoustic chamber was overly conservative, even though we reproduced the expected flight external acoustic levels. As expected, the vibration levels at the end of the boost phase were higher than at the start of the boost phase. This is a measure of increased aerodynamic effect on the vehicle internal vibration levels.

VEHICLE SHOCK

The shock environment, except for aircraft ejection and launch-tube ignition, is generated by numerous pyrotechnic devices within the vehicle (Figure 74). The most significant of these shocks are due to the 25-grains/foot shaped charges at Missile Station 190, used for the shroud jettison, and at Missile Station 219, booster jettison. Although the flight measurement system was not designed with measurement of these transients in mind, nevertheless, valid and useful data were obtained.

In summary, the highest shocks at the aft section of the missile were measured at shroud and booster jetti-

sion. However, the shock levels dissipated rapidly within the vehicle and were less than ten-g at the forward end (guidance section) of the missile. The highest shock levels measured at the guidance section were generated from the recovery system. All test vehicles incorporated a recovery exercise module (REM), which deploys a parachute. The production vehicles do not incorporate a REM.

Figures 75 through 96 depict the shock transients measured at Missile Station 182; pickup A462. We were fortunate in the location of this pickup in that this measurement was able to discriminate virtually all discrete missile events. These data were significant in accurately determining missile events that could be used in performance and failure analyses; electrical data identifying the missile discretes were recorded on a pulse-coded modulation system (PCM), which was only accurate to within 20 milliseconds.

Figures 97 through 116 present the significant shock environments measured at the forward section of the missile guidance section. In addition to the REM pyrotechnic events, the shroud jettison event seems to have excited a 100 Hz lateral mode, probably the second vehicle bending mode (Figure 99). To complete the shock spectrum analyses, Figures 117 through 124 present the shock levels measured on the WRC turbofan engine. The location of this measurement and the mass of the engine tended to make it relatively insensitive to the pyrotechnic environment.

DATA MANAGEMENT

A computer management program was developed to organize large quantities of x-y arrays representing vibration and shock measurements from both flight and ground test. Called the Environmental Vibration Data Base Management System, and operating in either batch or interactive modes on the Control Data Corporation Cyber series computer system, the program provides for storage, maintenance, retrieval, and algebraic manipulation of the data arrays. In the present context, the data arrays are both power-spectral densities and shock spectra.

When an x-y function is entered into the data base, it is accompanied by a measurement descriptor in the form of text, and stored under keyword control. The data are organized using an hierarchy of seven keywords, ranging from very general to very specific description of the measurement. Typical keywords include such descriptors as vehicle number, measurement number, time of flight, and measurement location.

The random access structure of the stored data, both text and arrays, is such that the keywords are used to identify and isolate subpopulations. These data may be plotted directly or manipulated in some algebraic fashion, such as MAX-MIN, 3-SIGMA, or enveloping. In addition, text information may be sorted by vehicle number, flight number, or measurement number, and printed in the form of a report. Under keyword control, hierarchy of detailed information is possible in these

reports. Thus, the program functions as a home, if you will, for the data of diverse origins.

Because of the presupposed sensitivity of the guidance set to the flight vibration levels, measurements at Missile Station 18, interface with the land attack guidance set, were of particular interest. Vibration measurements in both the lateral and longitudinal directions are presented in Figures 125 and 126, respectively. The maximum vibration during five flights are enveloped in these figures, and are compared without regard to cruise speed or time of flight. The vibration peaks occurring at approximately 600 Hz are induced by the cruise engine, as described previously.

Envelopes of the maximum vibration measurements, without regard to direction or flight time, are shown in Figure 127. The curves are representative maximum vibration levels for Station 18, guidance, during boost flight, cruise, and A-6 captive carry. To demonstrate further the use of this powerful tool, Figure 128 was developed. This figure presents a comparison of vibration levels measured at three different locations on the same Tomahawk flight, T12-3. The data presented are for the cruise engine, Station 182, and Station 40 (guidance) locations.

SUMMARY

The cruise missile environmental measurement program has provided significant and useful shock and

vibration data. These data will be used to define environmental specifications for components and, if necessary, to support design changes. The Tomahawk missile vibration data provides information for sub, ship, ground- and air-launched variants. In addition, data is correlated with respect to the flight profile and location within the missile for both the turbojet and turbofan engines. The shock data provides measure of the attenuation throughout the vehicle to high-frequency transients from pyrotechnic events. It is hoped that these data will be used by the appropriate agencies, and vibration community in general, to update standard military specifications for future use.

REFERENCES

1. V.S. Noonan, J.L. Gubser, R.D. Harmening, "Harpoon Missile Flight Environmental measurement Program." The Shock and Vibration Bulletin, No. 44, August 1974.
2. G.E. Wadleigh, "Environmental Vibration Data Base Management System — P5856," Convair Division of General Dynamics Corp. dated 1 September 1977.
3. R.B. Blackman, J.W. Tukey, "The Measurement of Power Spectra," Dover Publications, New York, 1958.

DISCUSSION

Mr. Zurnaciyan (Northrop Electronics): What are the worst case environments in the guidance bay, including shock?

Mr. Rosenbaum: The worst case environment in the guidance bay was the B-52 take-off which lasted for about 15 or 20 seconds. Vibration-wise, that was up around one and a half or two G's RMS random. The worst case of shock occurred from blowing the parachute covers from this recovery package. The booster jettison and shroud jettison shocks were very low up at the front. We saw levels on the order of 5 or 6 G's on a plus or minus 15-G accelerometer, whereas we saw levels up around 25 G's on the recovery package. Remember, this was only about a 2,100 or 2,500 Hz accelerometer, so things could be happening at the higher frequencies. We did think, however, that the data that we would see in the low frequencies, up to 2,500 Hz would be indicative of the things that occurred at somewhat higher frequencies.

Mr. Anderson (Rosemont, Inc.): Were the vibrations that occurred when you boosted your recovery package off included in the qualification specifications?

Mr. Rosenbaum: Yes. They did not affect things in the back at all.

Mr. Anderson: I know. We didn't have a problem with that one.

Mr. Volin (SVIC): Did pyro-shock affect the

functioning of your on-board systems?

Mr. Rosenbaum: It turns out we have a package in the back called Mission Control Module which has lots and lots of relays in it, and that was a serious problem early in the program. We were using two or three hundred G relays, standard relays, and they were running drop tests on the relays and failing them like mad. So we developed a hammer test (typical of things that we talked about in our pyro-technic-shock meeting the other day) and found that two or three hundred G relays were really good for two, three or four thousand G's if the test is proper. In some cases we had to shock isolate the relays, and we leaned heavily on the Goddard-Martin Pyrotechnic Shock data. I hope to add to that data with some test data that we have from the Tomahawk program. And I would also like to see Mil Standard 810 updated with this data because I think we have a vehicle that is different; it is a different kind of thing than you see in this standard now.

Mr. Mitchell (Naval Air Systems Command): Did you have a flight flutter test program to validate the flutter margins of the control surfaces?

Mr. Rosenbaum: Yes, there was one. There were some flight test data on Tomahawk early in the program; weren't some flutter test data also obtained on the ALCM, Craig?

Mr. McKinnis (General Dynamics/Convair Division): Yes.

TOMAHAWK GENERAL ARRANGEMENT

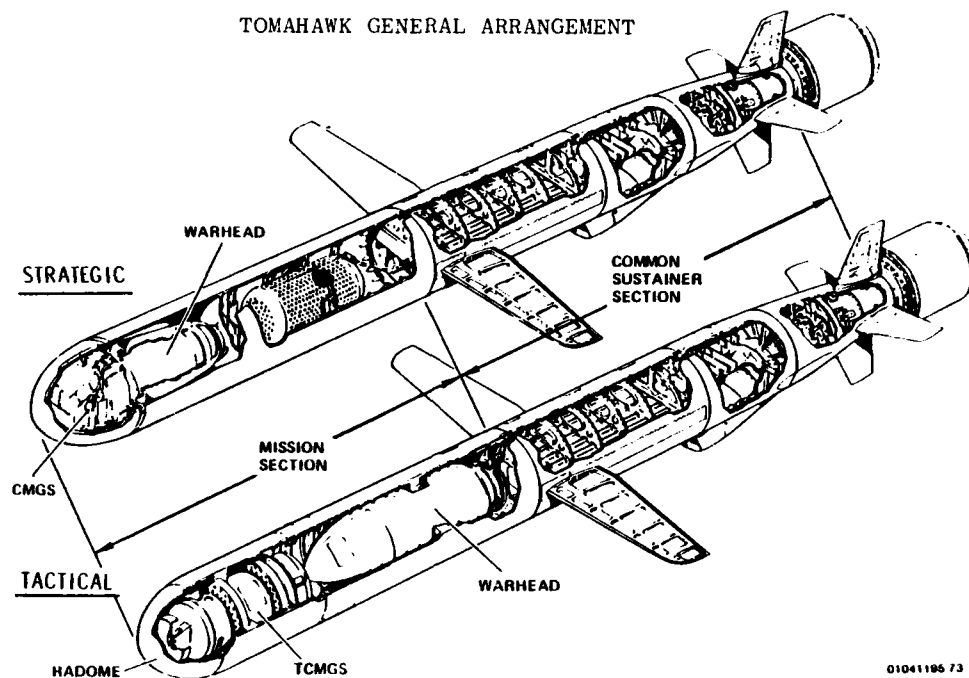
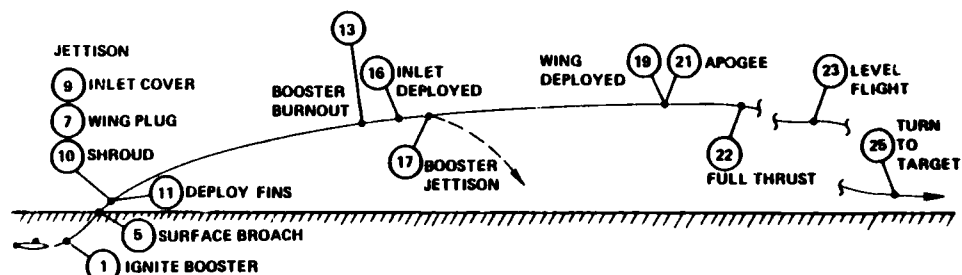


FIGURE 1

01041195 73

LAUNCH PROFILE



MAJOR EVENT	TIME (SEC.)	VELOCITY (FPS)	ALTITUDE (FT.)
1 IGNITE BOOSTER	2.6	30	
5 SURFACE BROACH	6.6	115	0
7 JETTISON INLET COVER	7.1	144	47
9 JETTISON WING PLUG	7.1	144	47
10 JETTISON SHROUD	7.2	150	60
11 DEPLOY FINS	7.2	150	60
13 BOOSTER BURNOUT	14.8	587	1,308
16 INLET DEPLOYED	15.5	583	1,355
17 BOOSTER JETTISONED	15.6	581	1,366
19 WING DEPLOYED	19.1	566	1,547
21 APOGEE	19.1	566	1,547
22 FULL THRUST	22.1	671	1,476
23 LEVEL FLIGHT (2.8 N.M.I.)	38.6	619	908
25 TURN TO TARGET (6.3 N.M.I.)	70	781	200

FIGURE 2

01041195 81

Meas No.	Location Sta-Dir ²	Event ¹										
		A	B	C	D	E	F	G	H	I	J	K
A88	10-V		2.46	0.81								
A102	190-O		2.39	0.86								
A103	190-V		3.04	0.89								
A120	8-V		1.43	0.88								
A456	18-O	0.61			0.54	0.22	0.47	0.35	0.30	0.65	0.75	
A460	18-A	0.45								0.45	0.52	
A461	182-V	0.34										
A462	182-O	0.92			2.11	0.13	0.14			2.92	0.94	1.36
A463	182-A	0.66										
A464	182-V	0.74										
A474	192-A		1.43	0.87	1.36	0.16				6.89	2.97	4.42
A476	40-A						0.18			0.26	0.26	0.30
A489	100-O					0.48		3.77	0.84			
A490	207-O				1.27	0.63	1.37	4.69	2.24			
A491	207-R						2.21	8.97	8.45			
A493	155-O				1.83	0.65	1.90	6.87	1.67	0		

Notes:

- A. A6 captive carry B. B52 takeoff C. B52 captive carry

D. Launch tube E. Early boost F. Late boost

G. Turbojet - start H. Turbojet - cruise I. Turbofan - start

J. Turbofan - early cruise K. Turbofan - end cruise
- O = Longitudinal V = Vertical A = Lateral R = Radial
- Overall acceleration levels (G-rms) include sinusoidal as well as narrow band & wide band random

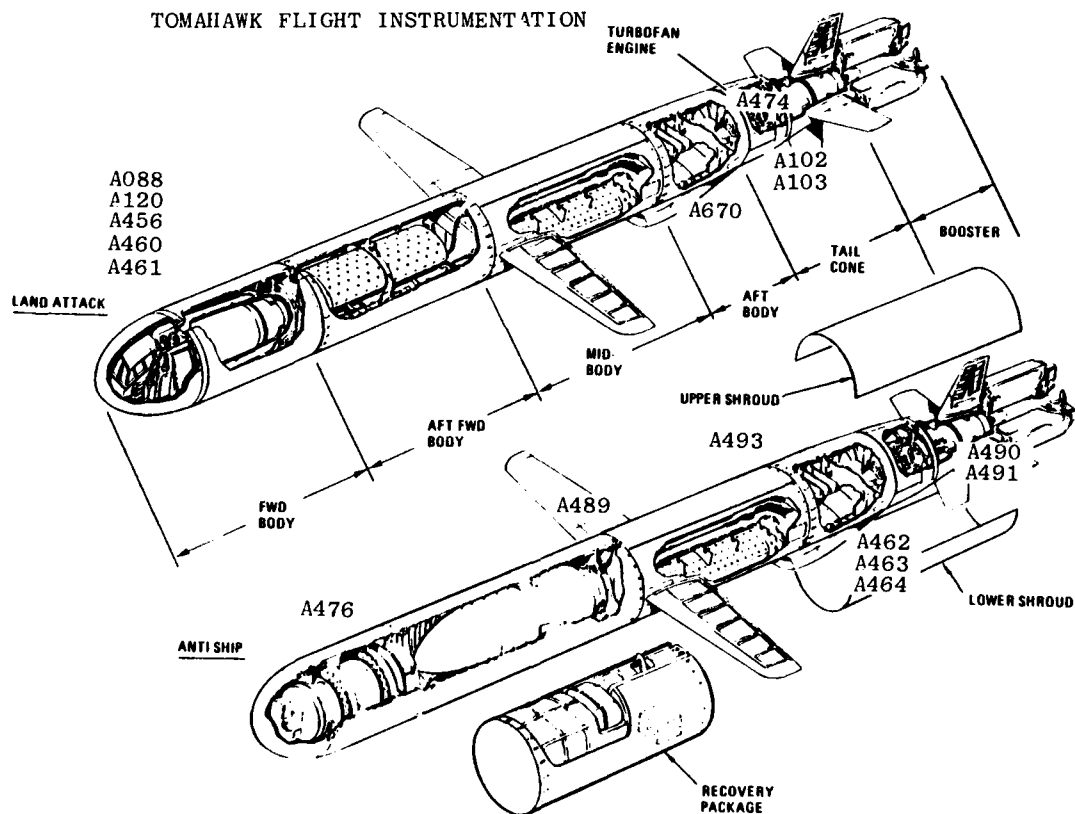
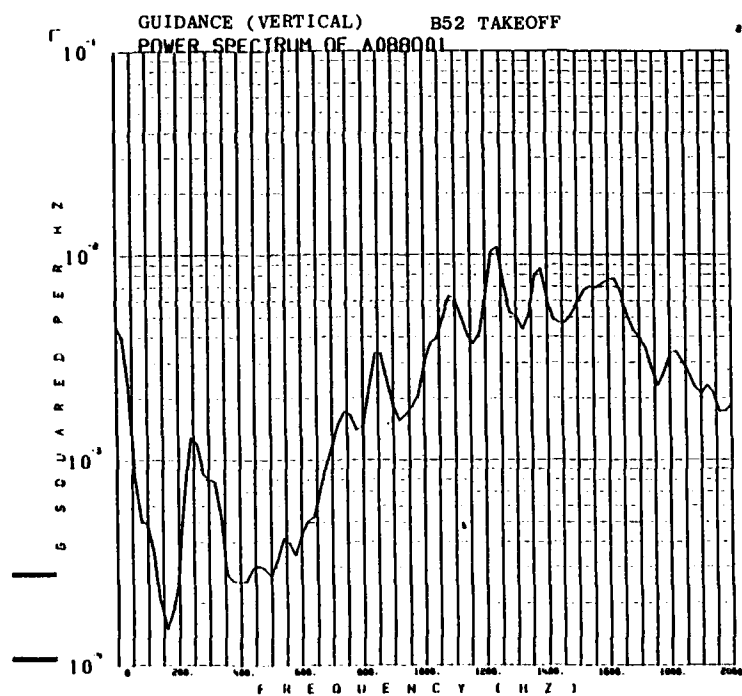
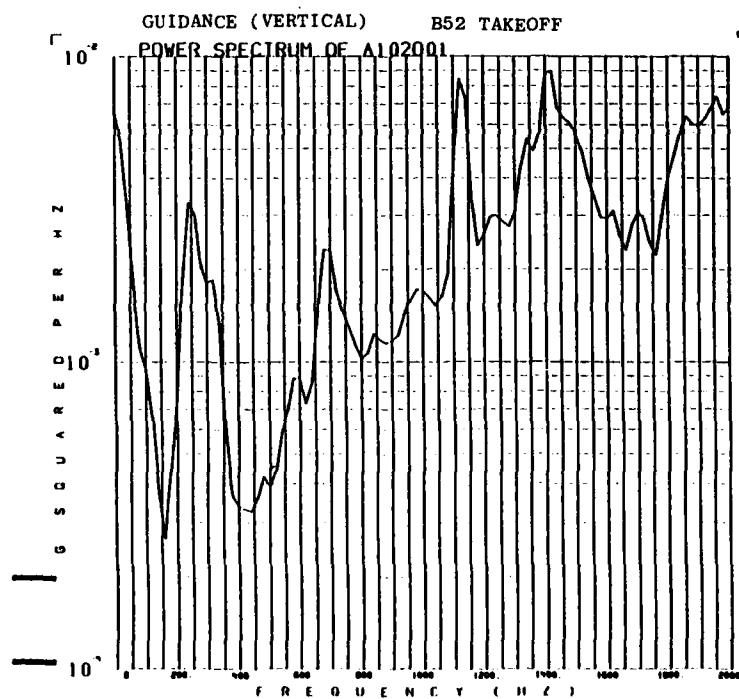


FIGURE 3



DF = 00 BW = 2.000E+01 RMS = 2.463E+00
AL-5 FLIGHT 1 10-00-30 10 10-00-31 LPOF=2100

FIGURE 4



DF = 00 BW = 2.000E+01 RMS = 2.391E+00
AL-5 FLIGHT 1 10-00-30 10 10-00-31 LPOF=2100

FIGURE 5

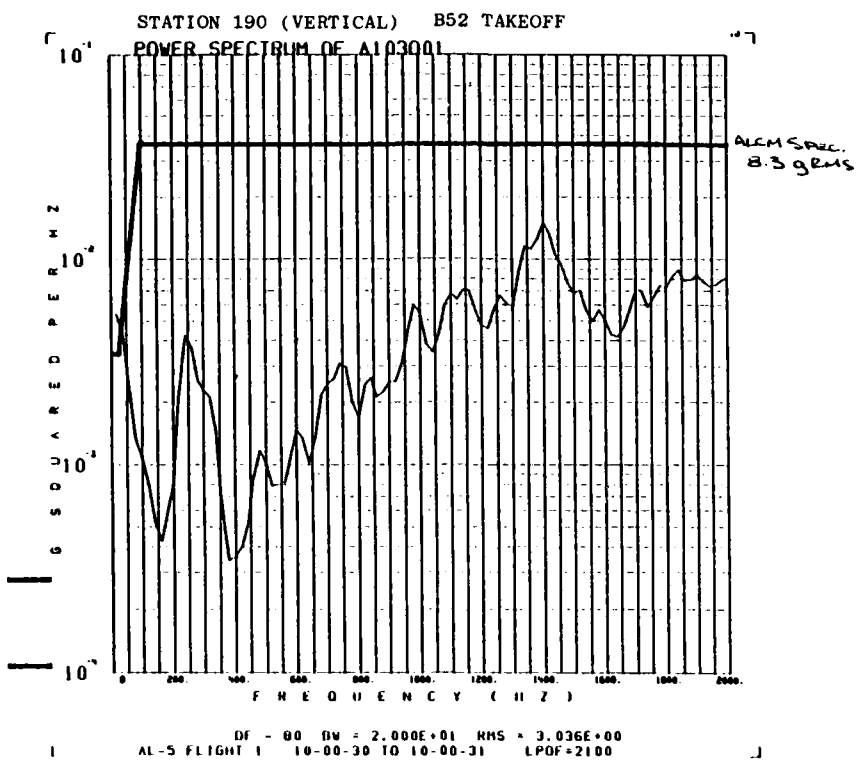


FIGURE 6

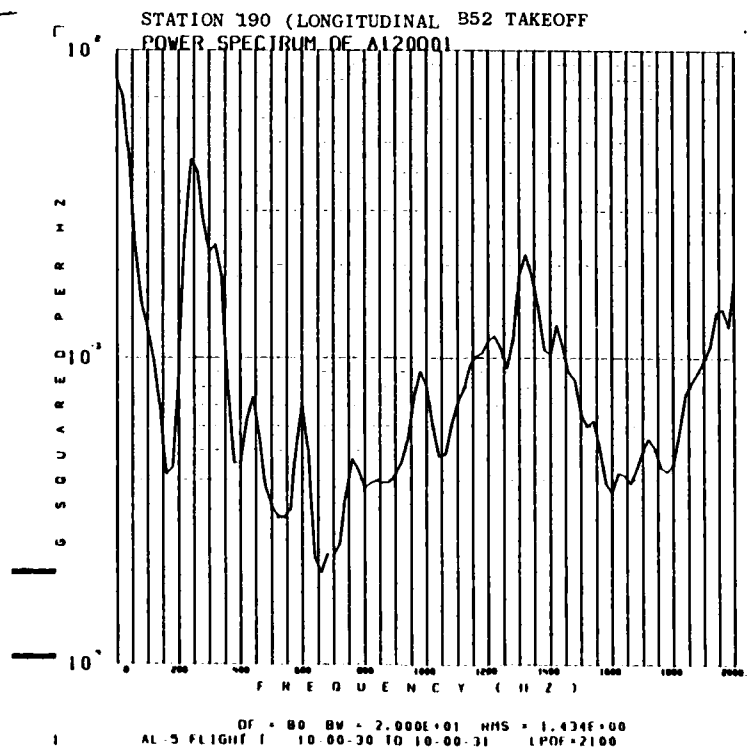


FIGURE 7

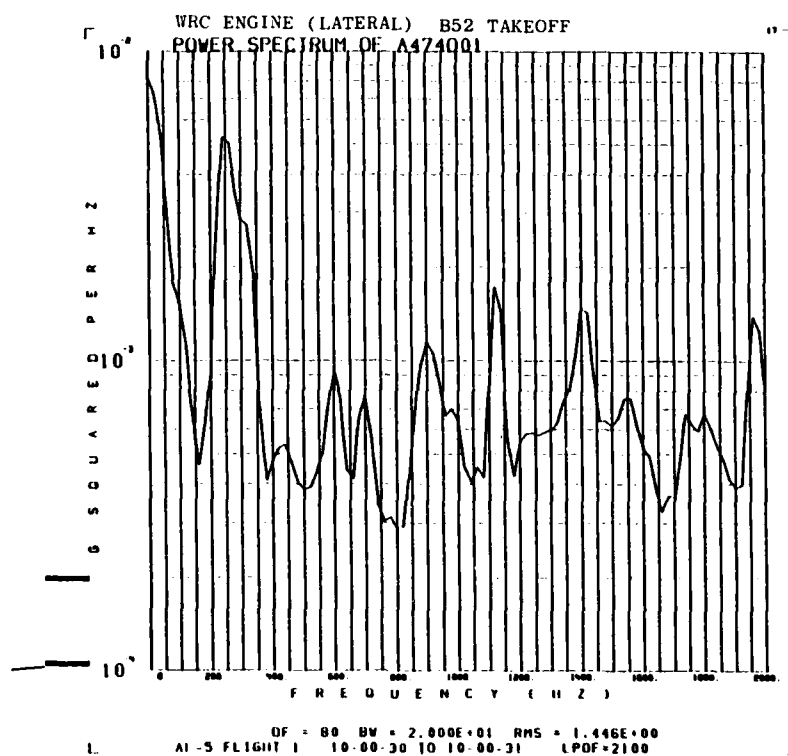
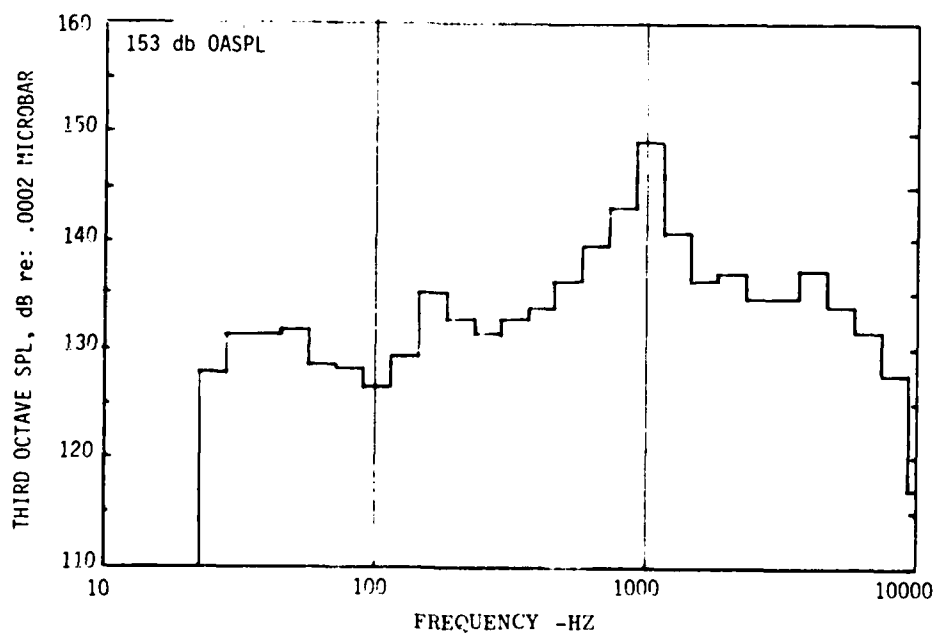
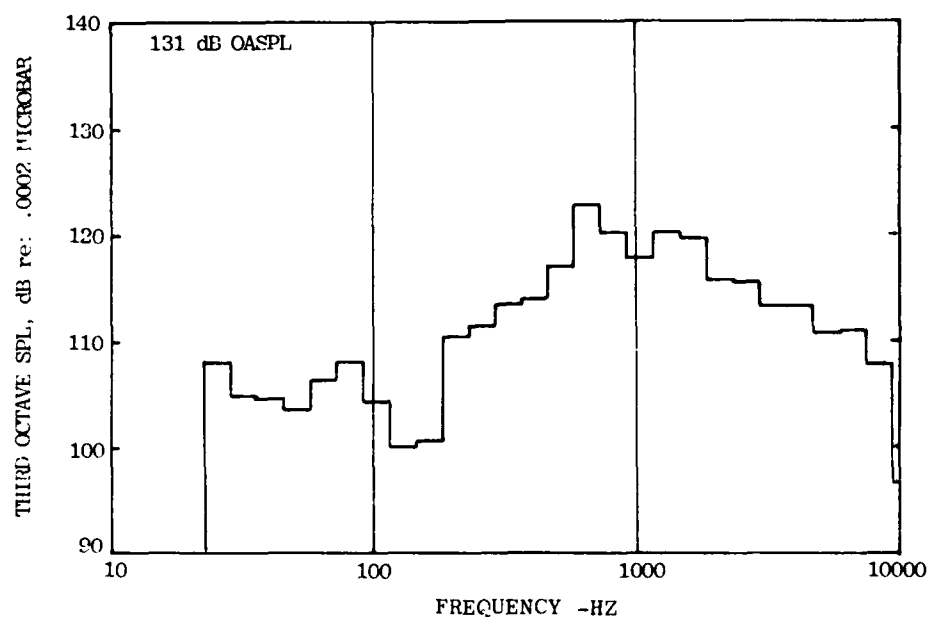


FIGURE 8



EXTERNAL ACOUSTIC SPECTRUM - B52 TAKEOFF FIGURE 9

FIGURE 9



INTERNAL ACOUSTIC SPECTRUM - B52 TAKEOFF

FIGURE 10

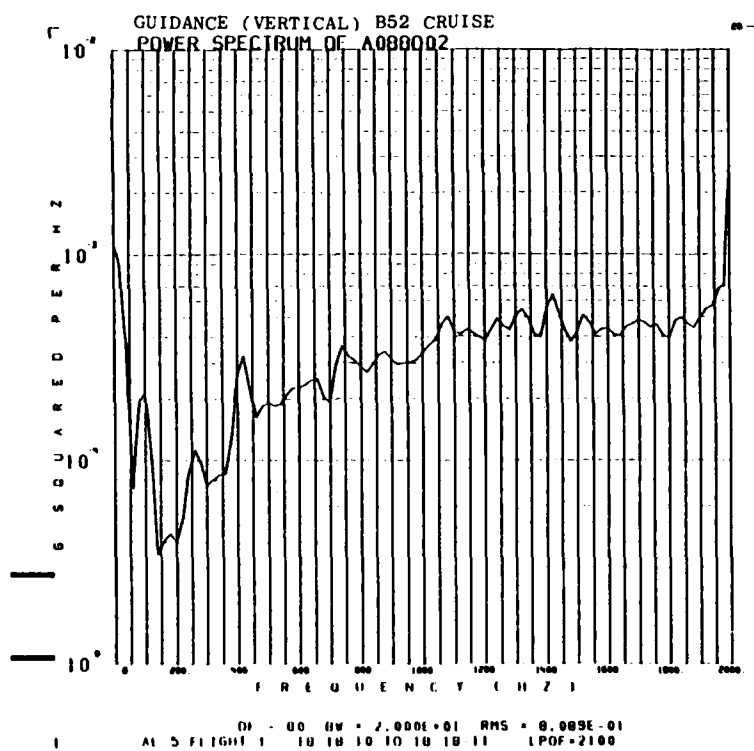
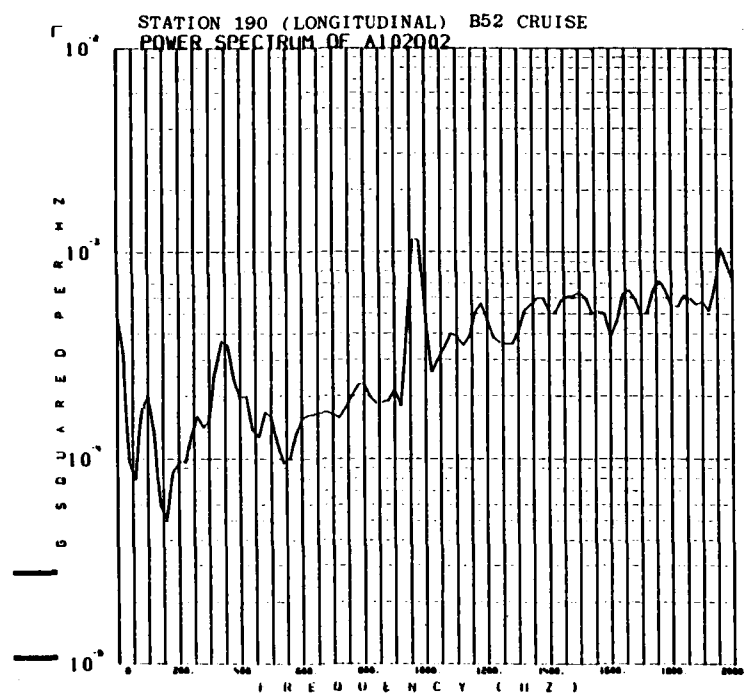
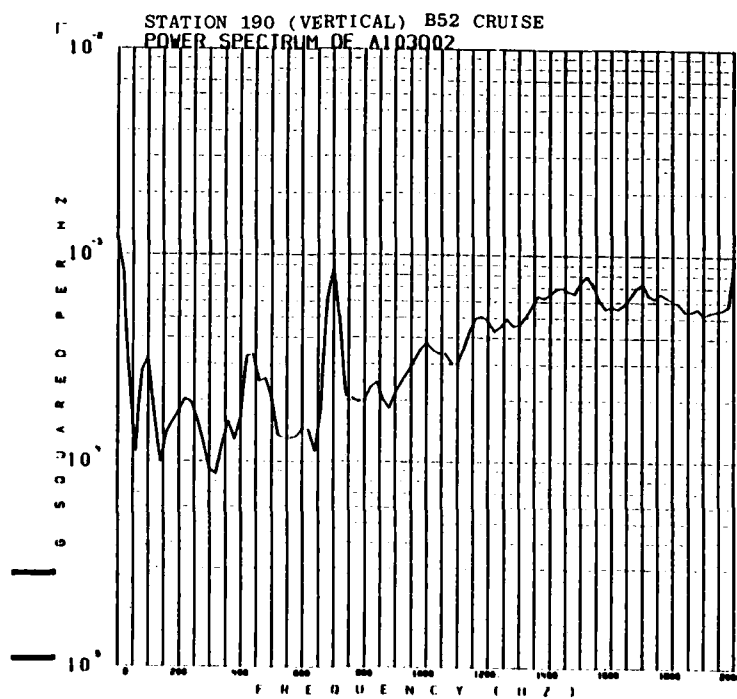


FIGURE 11



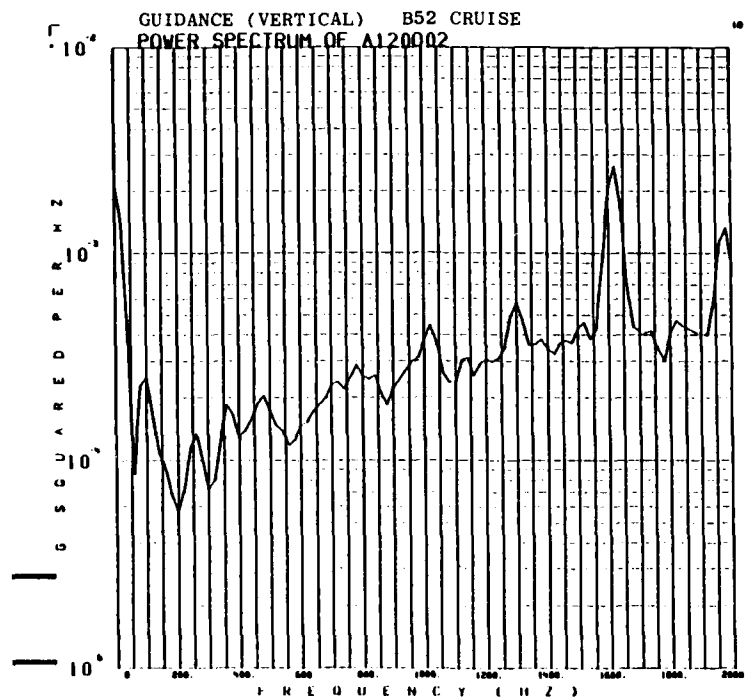
DF = 00 UV = 2.000E+01 RMS = 0.647E-01
AL-5 FLIGHT 1 10-10-10 TO 10-10-11 LPOF=2100

FIGURE 12



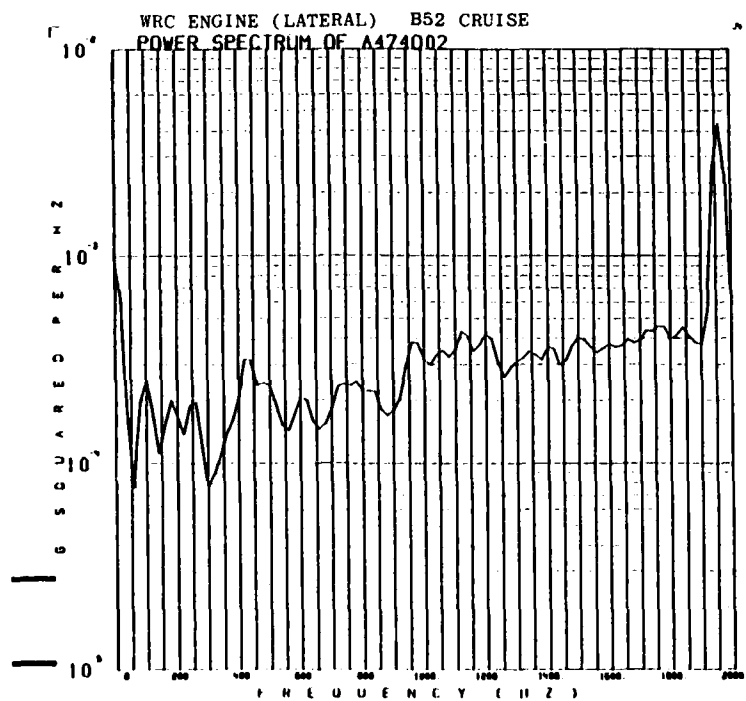
DF = 00 UV = 2.000E+01 RMS = 0.928E-01
AL-5 FLIGHT 1 10-10-10 TO 10-10-11 LPOF=2100

FIGURE 13



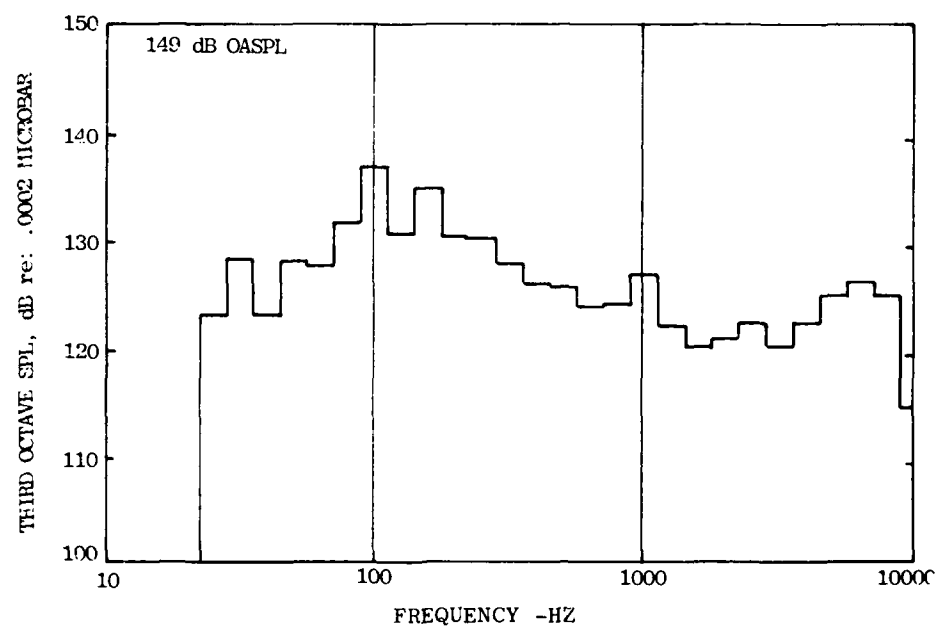
DF = 80 DW = 2.000E+01 RMS = 0.820E-01
AL 5 FLIGHT 1 10-10-10 TO 10-10-11 LPOF=2100

FIGURE 14



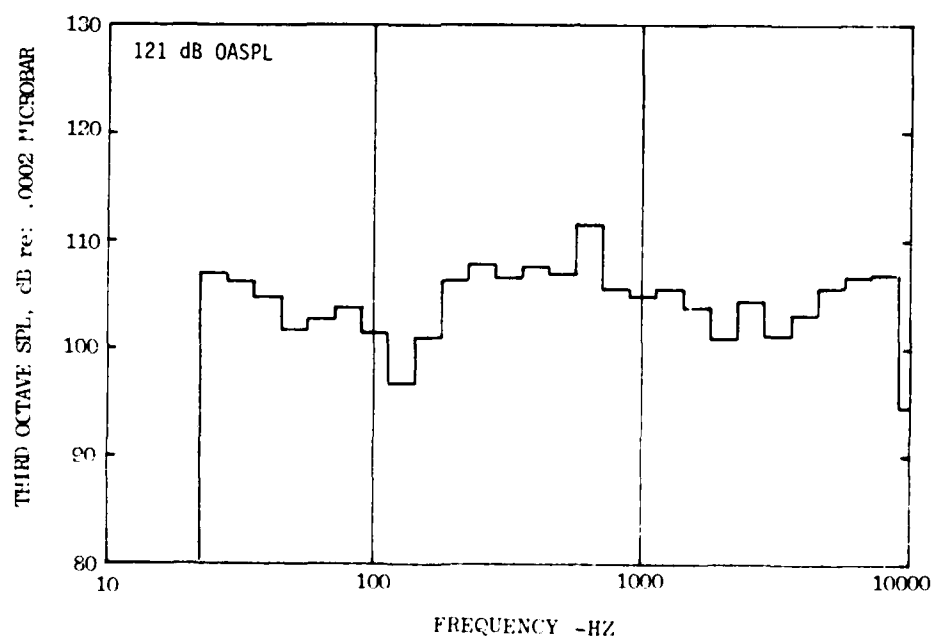
DF = 80 DW = 2.000E+01 RMS = 0.670E-01
AL 5 FLIGHT 1 10-10-10 TO 10-10-11 LPOF=2100

FIGURE 15



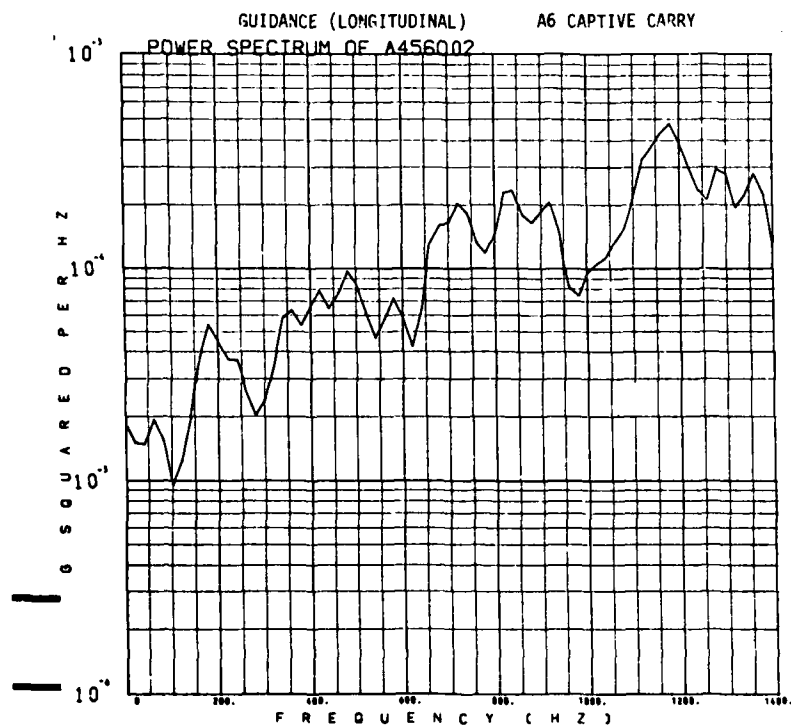
EXTERNAL ACOUSTIC SPECTRUM - B52 CRUISE, $M=.6$

FIGURE 16



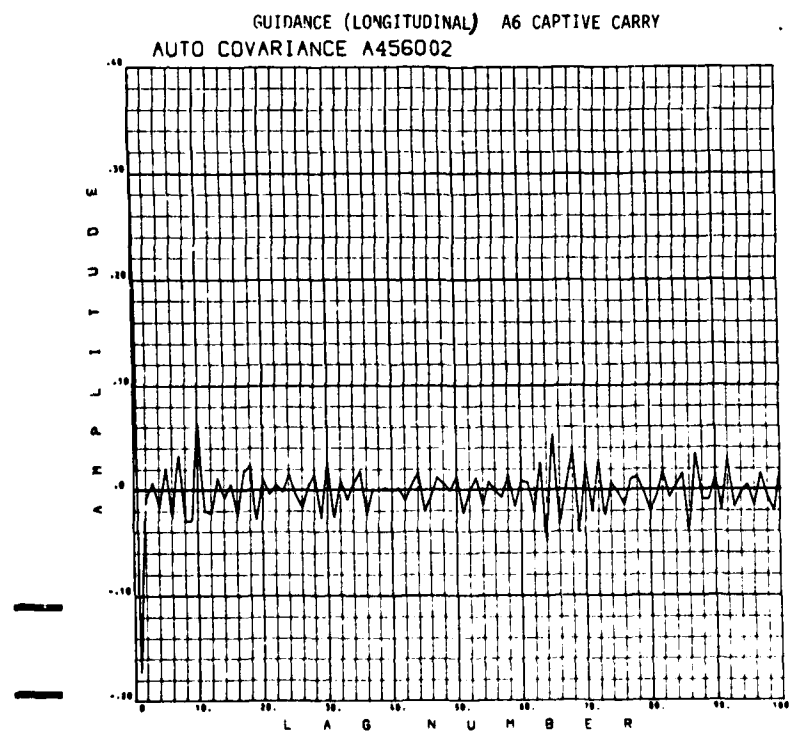
INTERNAL ACOUSTIC SPECTRUM - B52 CRUISE, $M=.6$

FIGURE 17



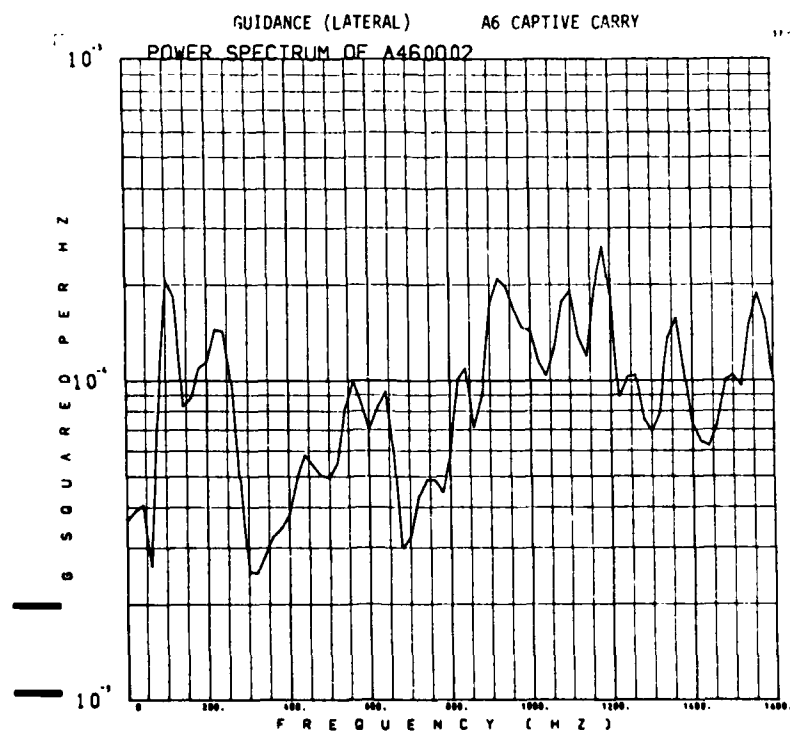
DF.=2.00000E+01 RMS=4.33550E-01
TOMAHAWK 9-1 *02* LPCF=1400

FIGURE 19



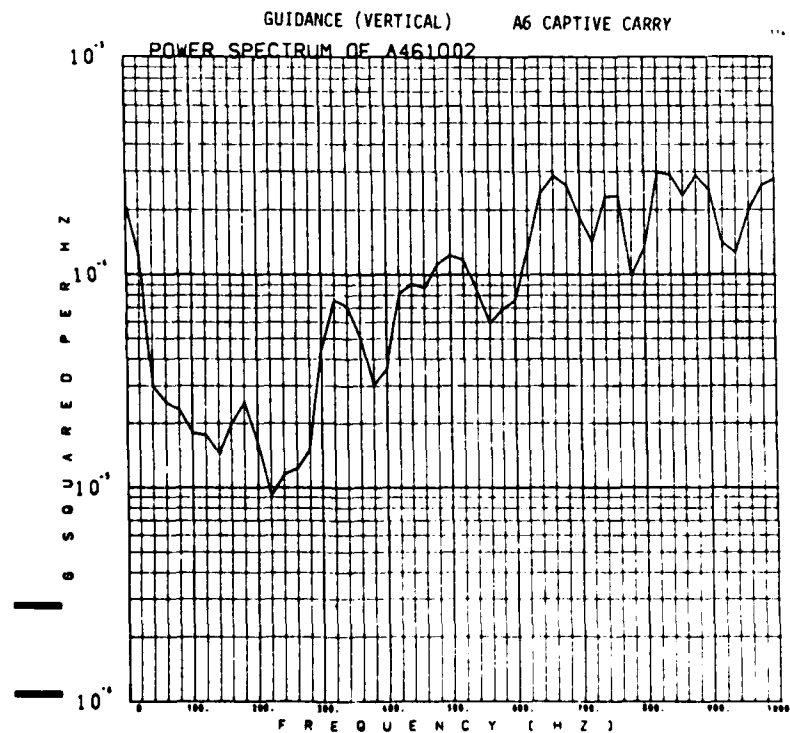
TOMAHAWK 9-1 *02* LPCF=1400

FIGURE 19



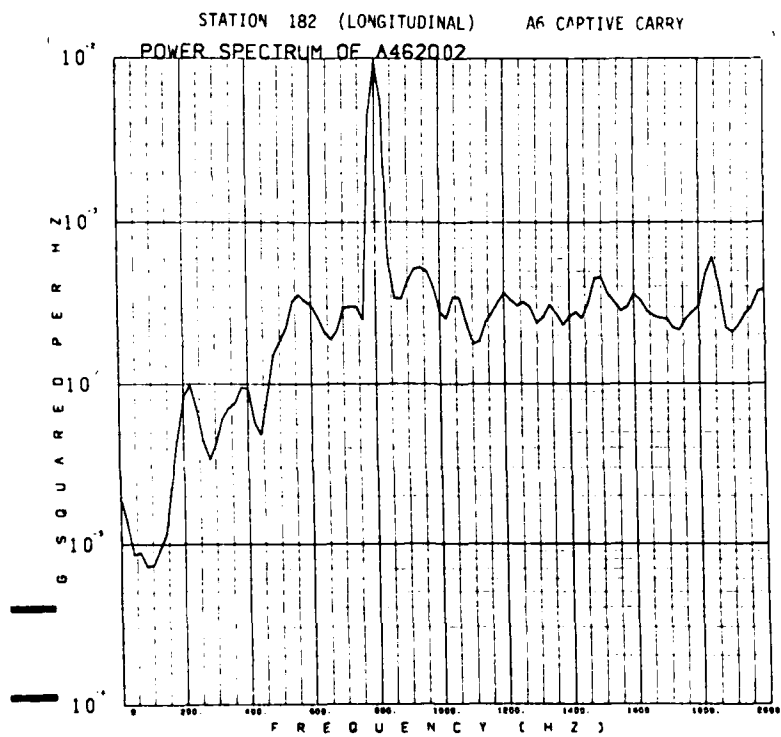
DF.=2.00000E+01 RMS=3.97598E-01
TOMAHAWK 9-1 *02* LPOF=1600

FIGURE 20



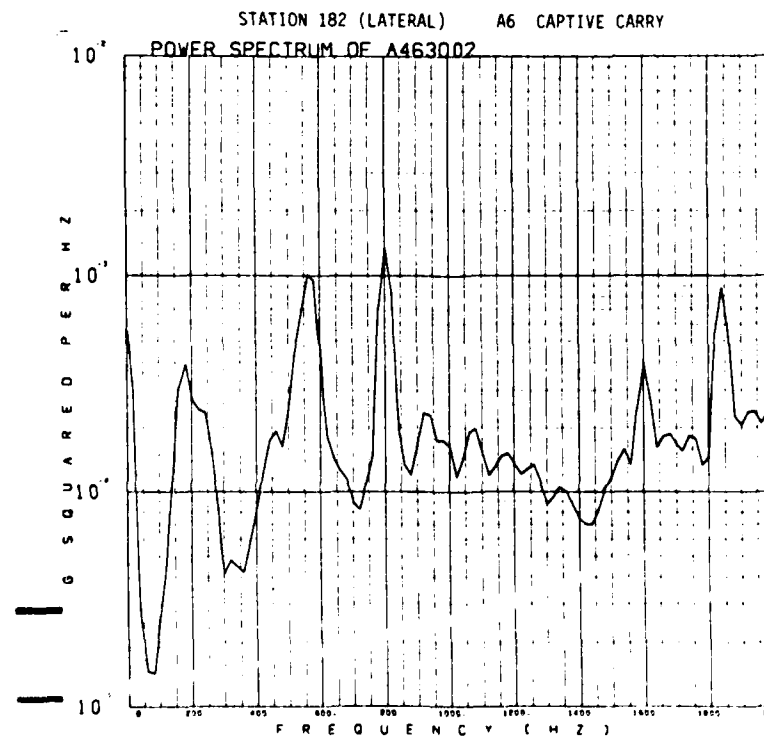
DF.=2.00000E+01 RMS=3.42154E-01
TOMAHAWK 9-1 *02* LPOF=1050

FIGURE 21



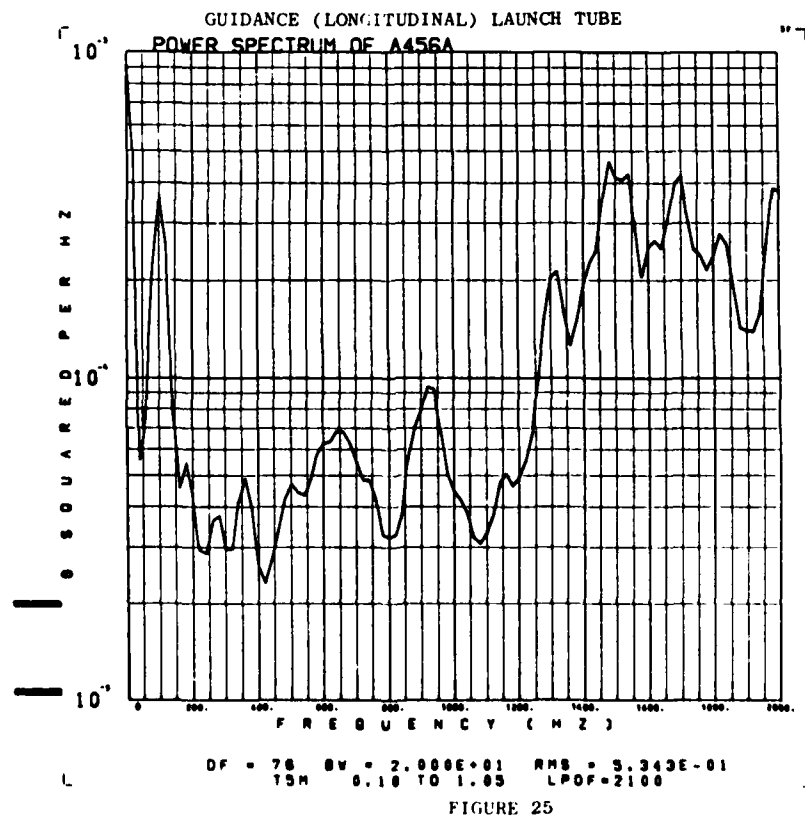
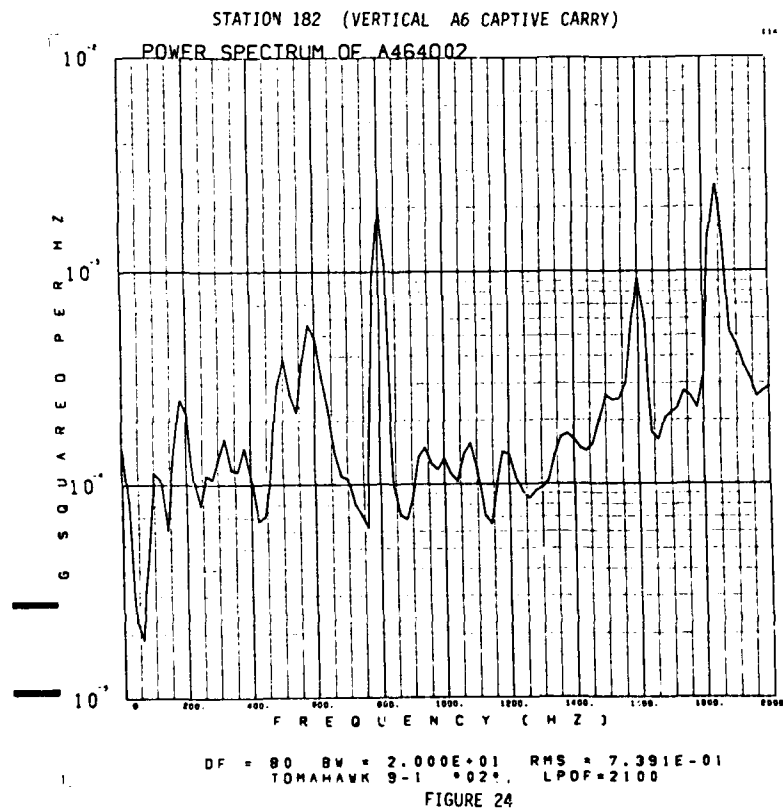
DF = 80 BW = 2.000E+01 RMS = 9.269E-01
TOMAHAWK 9-1 *02* LPOF=2100

FIGURE 22



DF = 80 BW = 2.000E+01 RMS = 8.617E-01
TOMAHAWK 9-1 *02* LPOF=2100

FIGURE 23



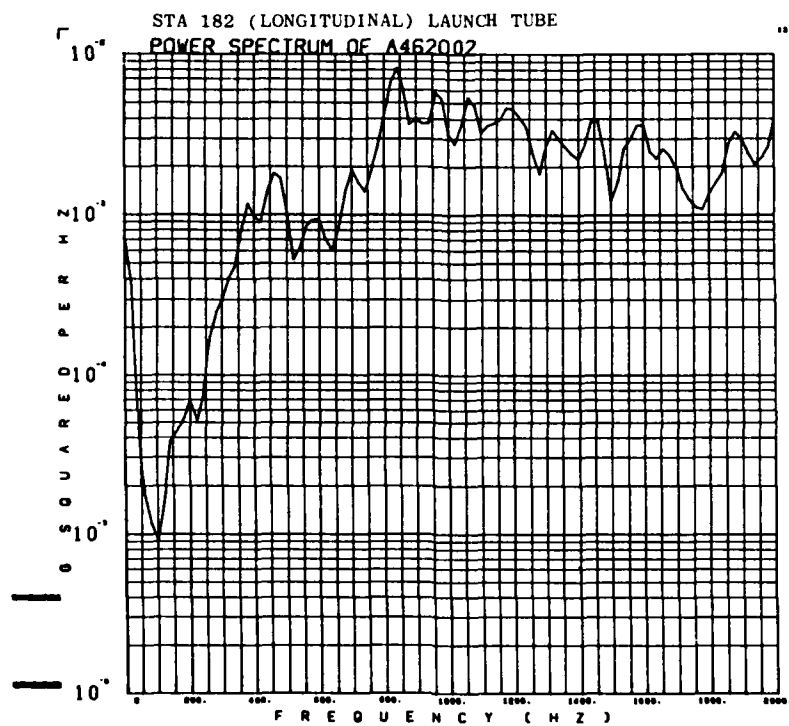


FIGURE 26

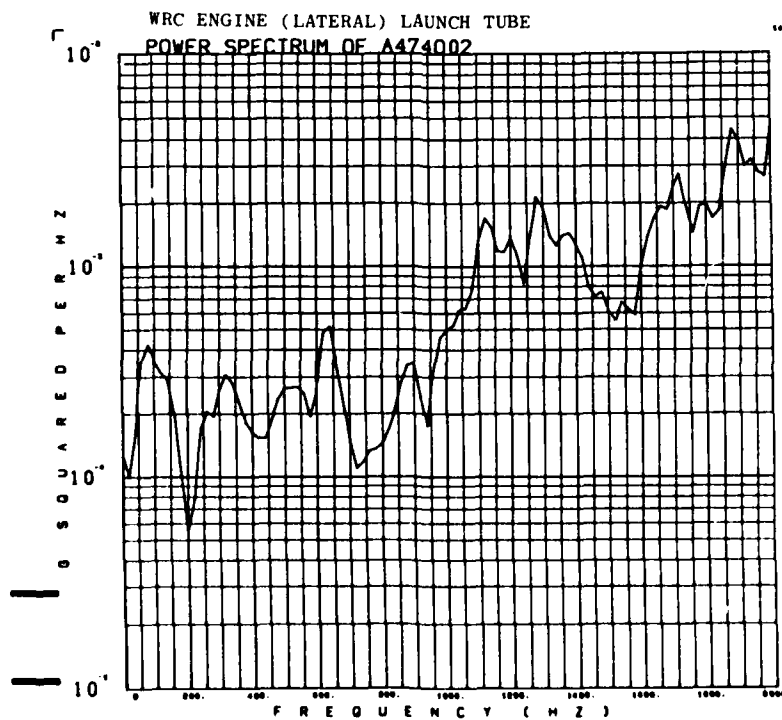
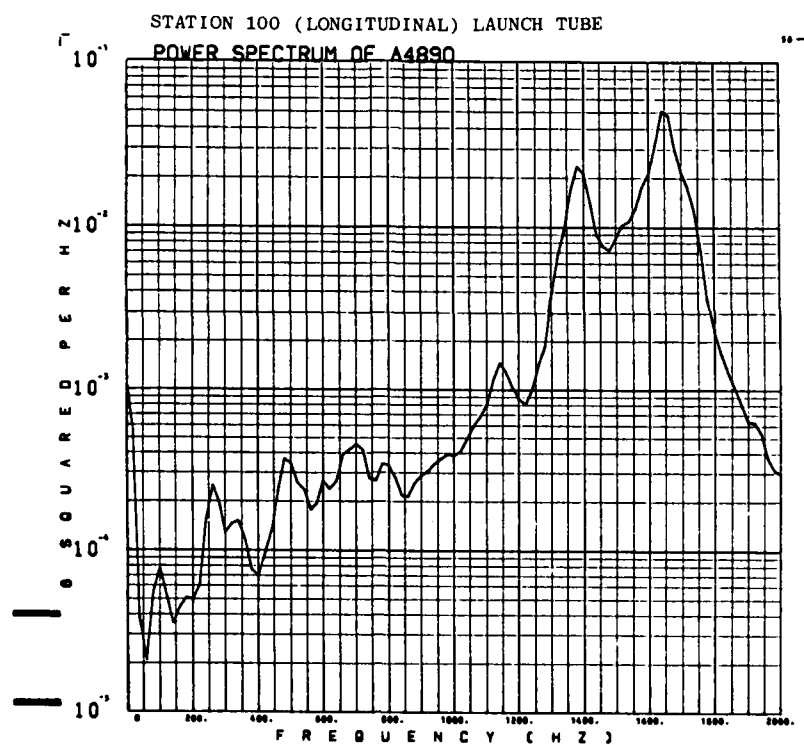
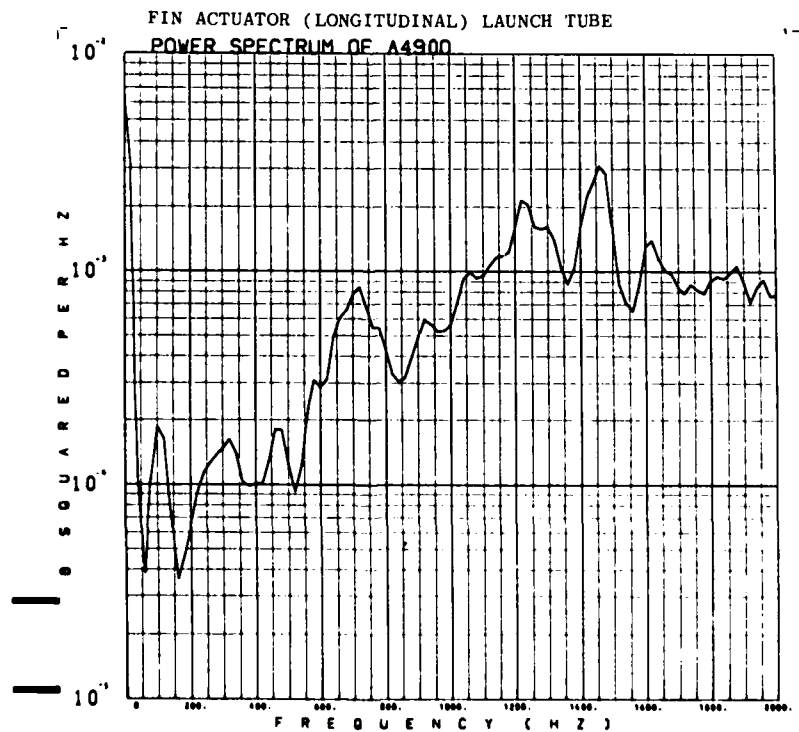


FIGURE 27



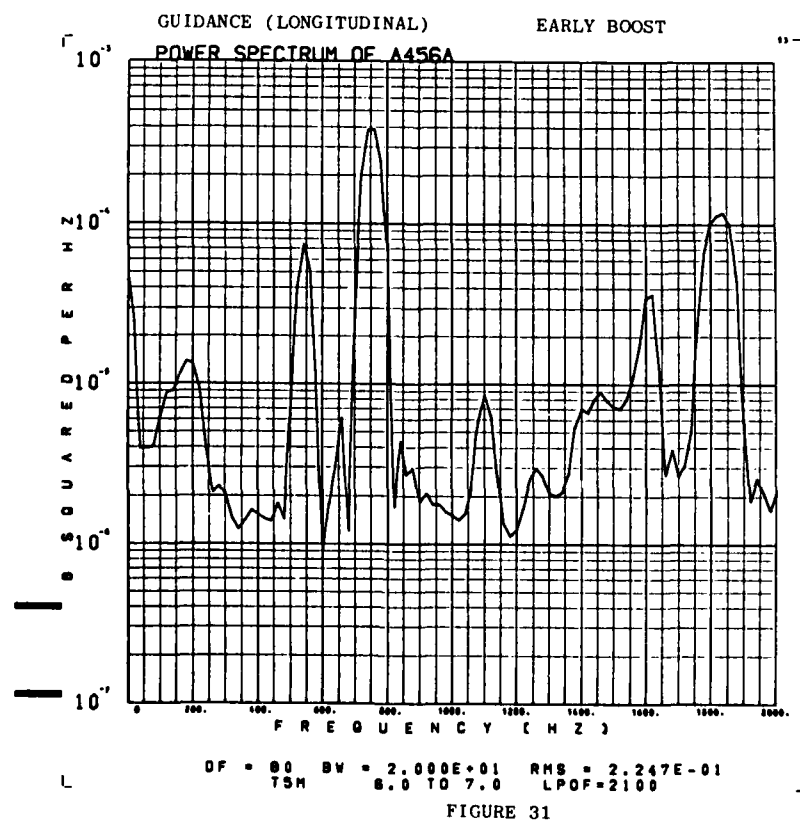
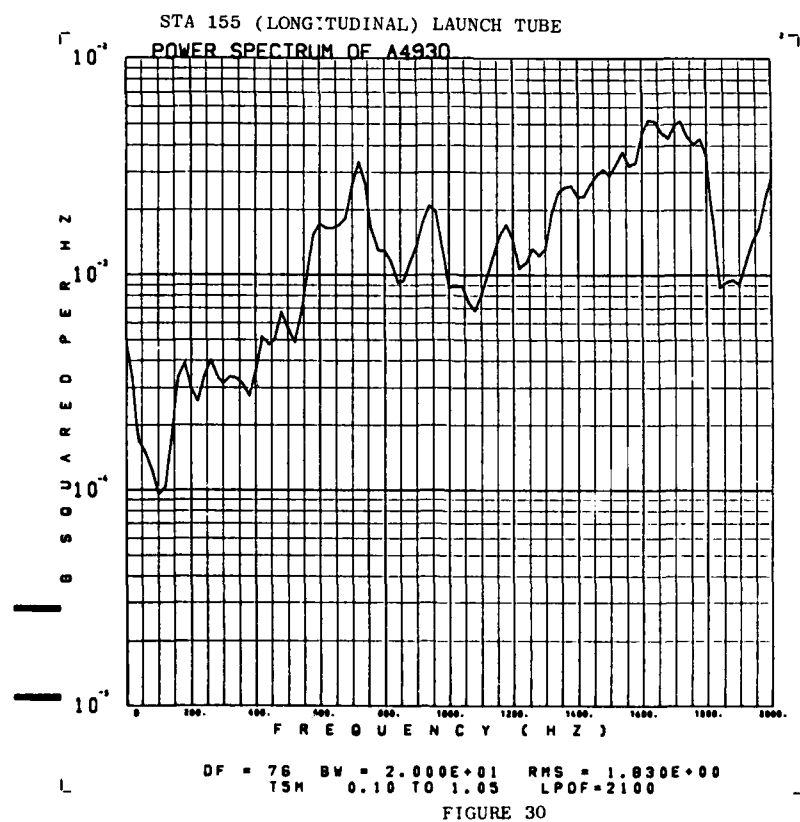
DF = 76 BV = 2.000E+01 RMS = 3.040E+00
TSM 0.10 TO 1.05 LPOF=2100

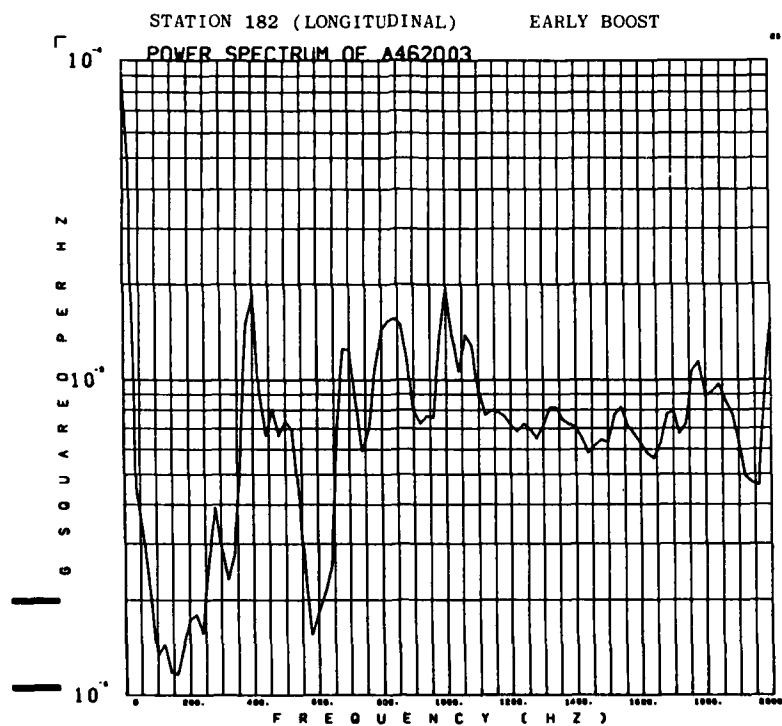
FIGURE 28



DF = 76 BV = 2.000E+01 RMS = 1.272E+00
TSM 0.10 TO 1.05 LPOF=2100

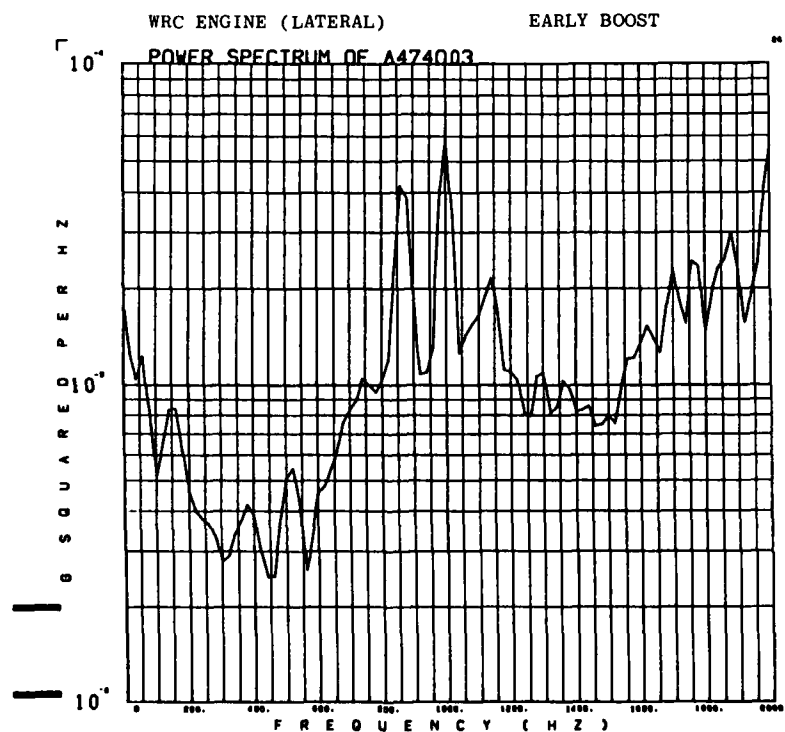
FIGURE 29





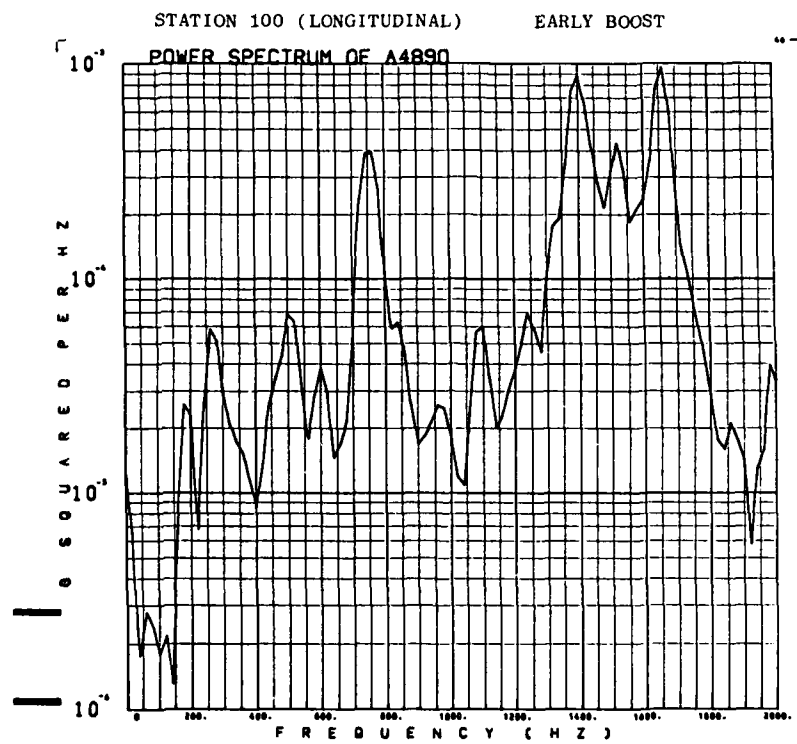
DF = 80 BW = 2.000E+01 RMS = 1.276E-01
TOM 20-1 19-00-01.50 TO 19-00-02.50 LPOF=2100

FIGURE 32



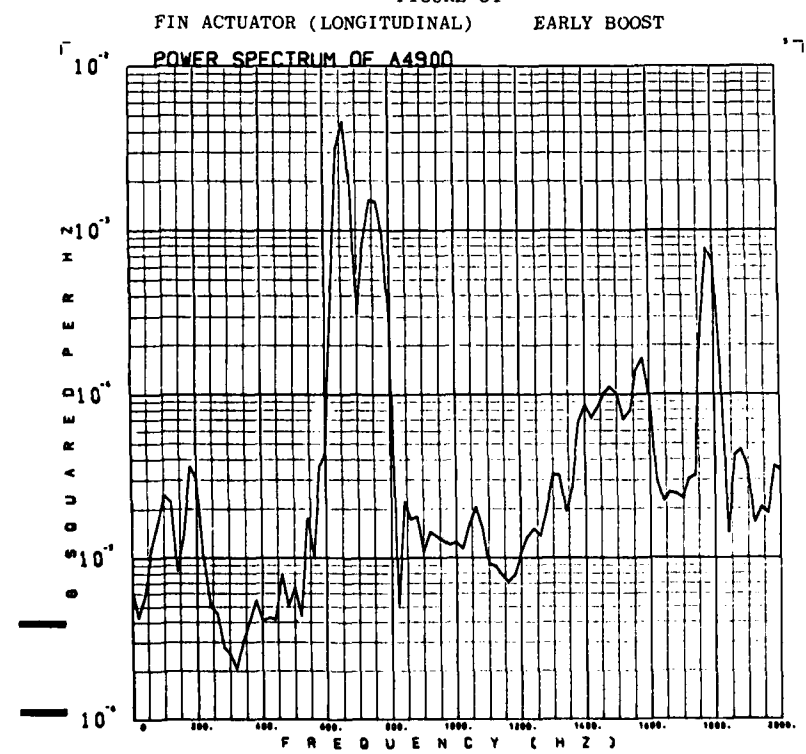
DF = 80 BW = 2.000E+01 RMS = 1.617E-01
TOM 20-1 19-00-01.50 TO 19-00-02.50 LPOF=2100

FIGURE 33



DF = 80 BV = 2.000E+01 RMS = 4.782E-01
TSM 6.0 TO 7.0 LPOF=2100

FIGURE 34



DF = 80 BV = 2.000E+01 RMS = 6.253E-01
TSM 6.0 TO 7.0 LPOF=2100

FIGURE 35

STATION 155 (LONGITUDINAL) EARLY BOOST

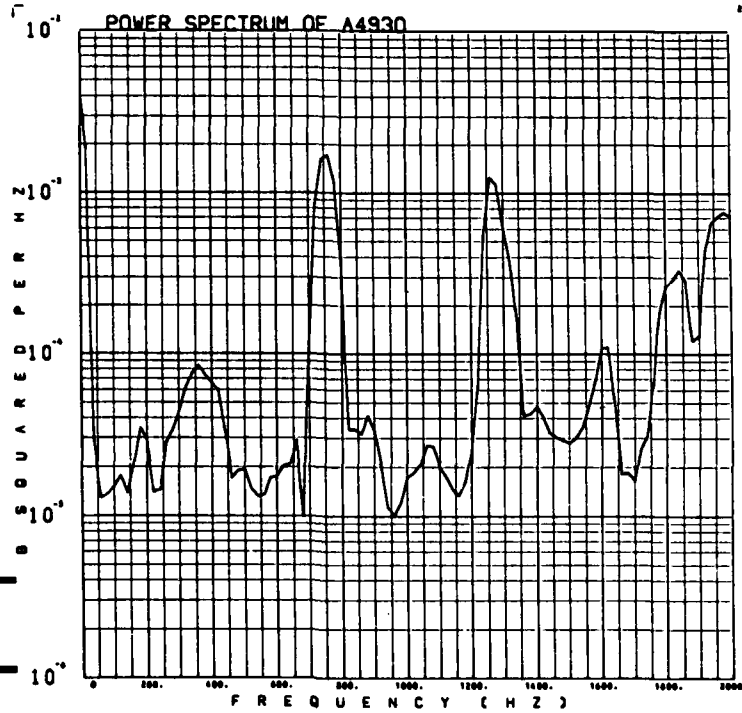


FIGURE 36

GUIDANCE (LATERAL) LATE BOOST

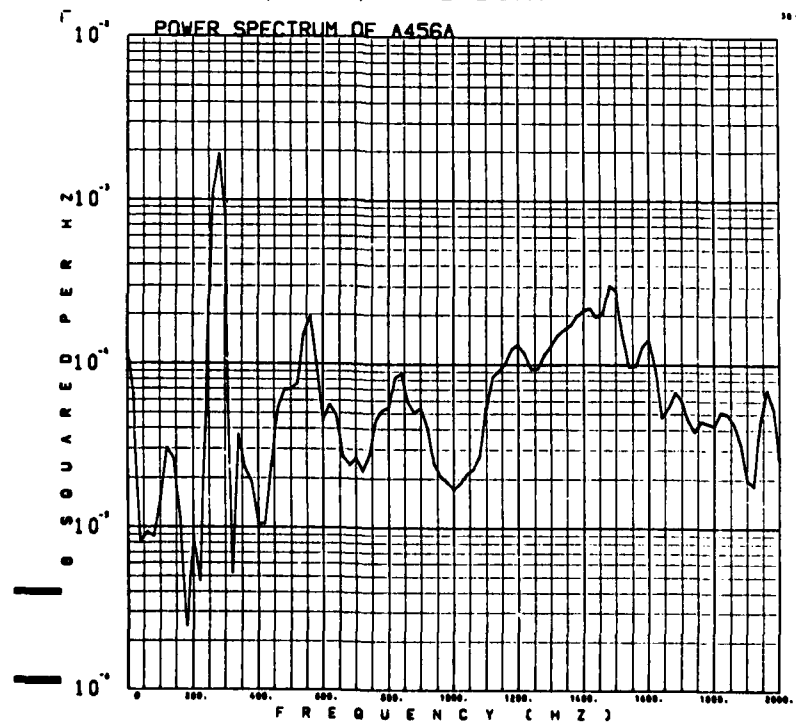
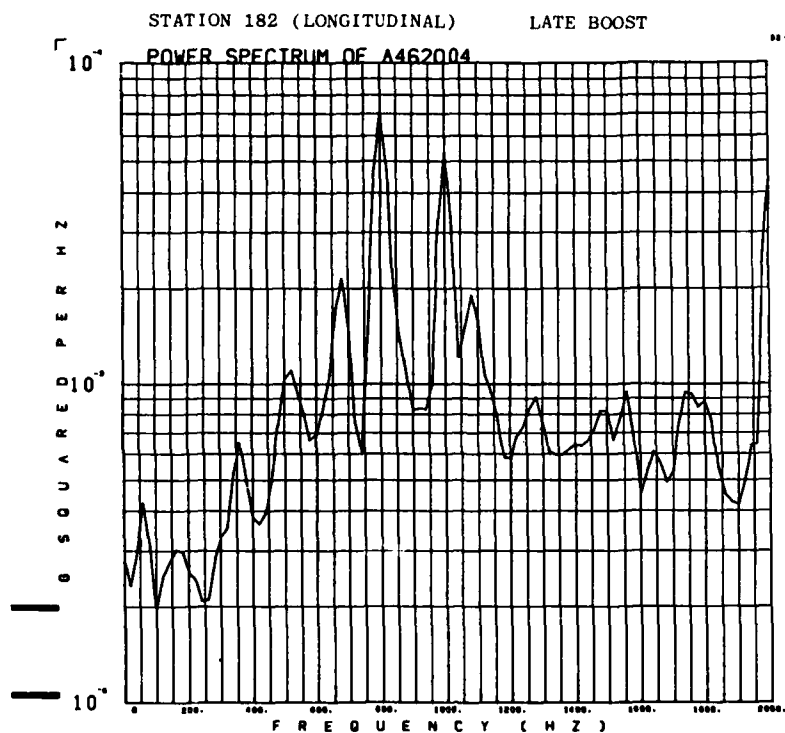
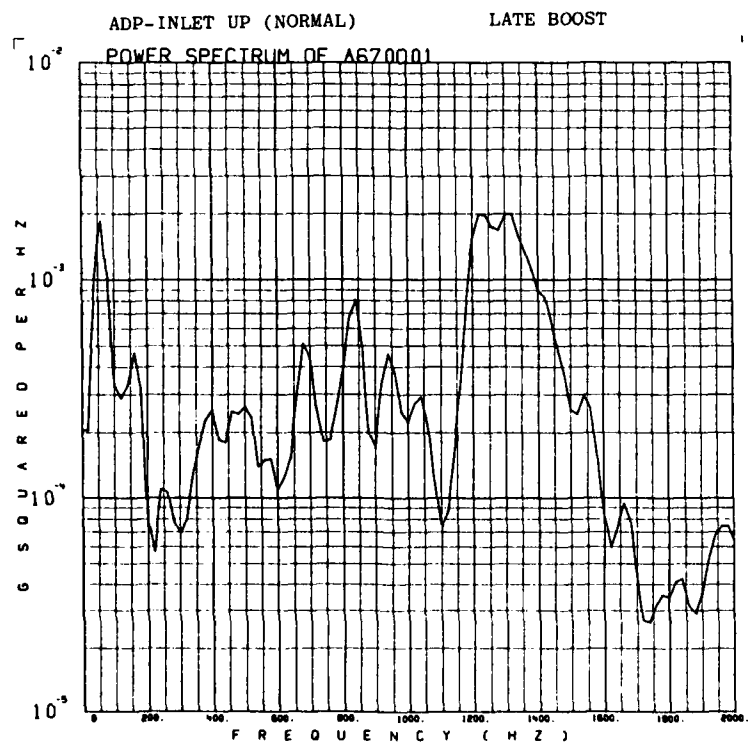


FIGURE 37



DF = 80 BW = 2.000E+01 RMS = 1.427E-01
 TOM 20-1 19-00-09.00 TO 19-00-10.00 LPDF=2100

FIGURE 38



DF = 80 BW = 2.000E+01 RMS = 9.042E-01
 TOM 17-3 PSOS 20-02-10.0 TO 20-02-11.0 LPDF=2100

FIGURE 39

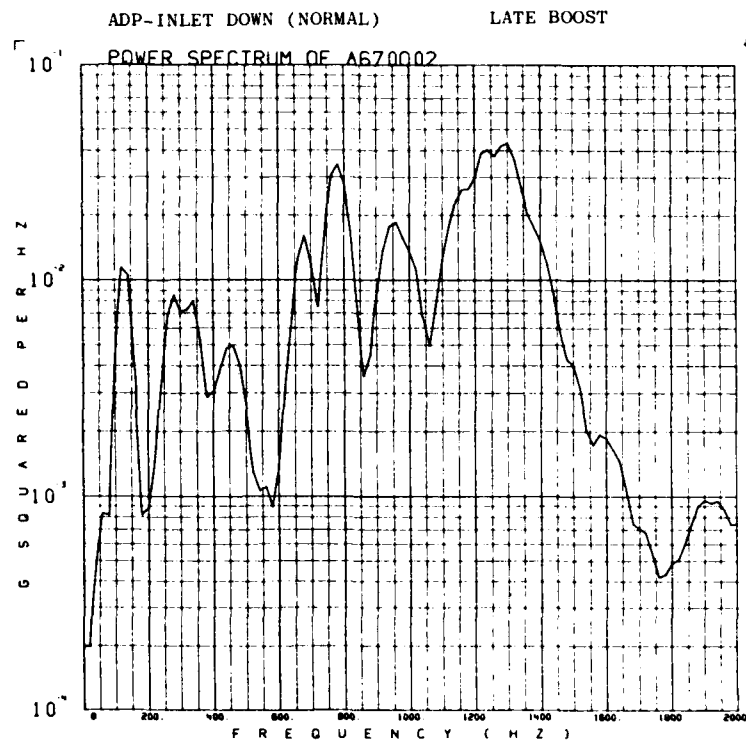


FIGURE 40

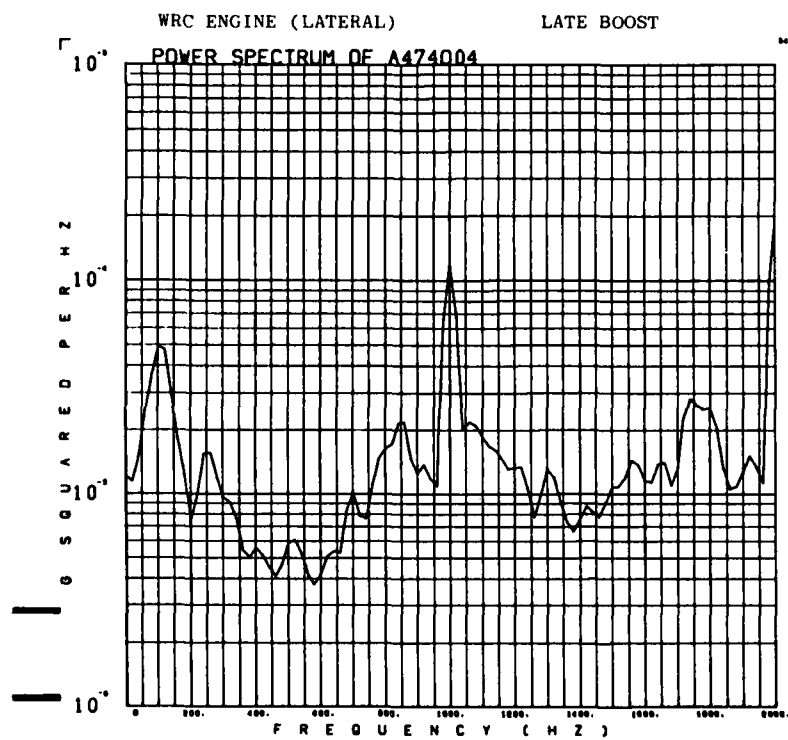
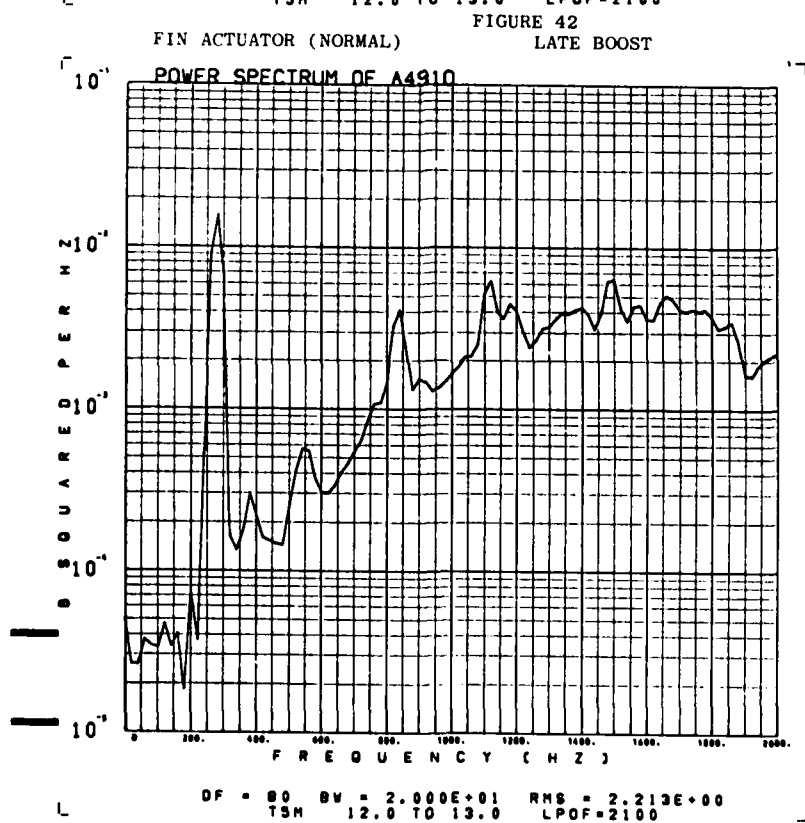
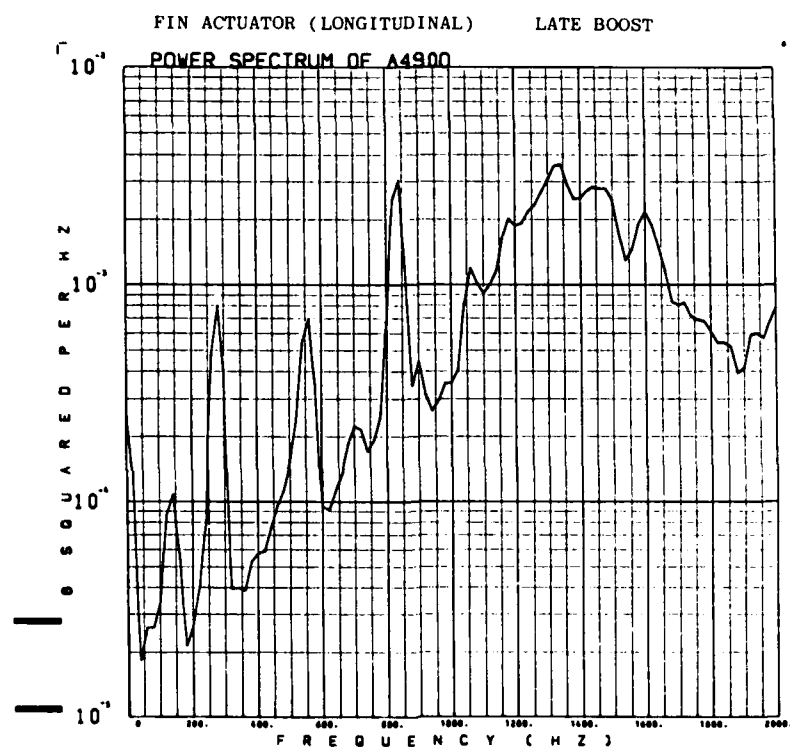
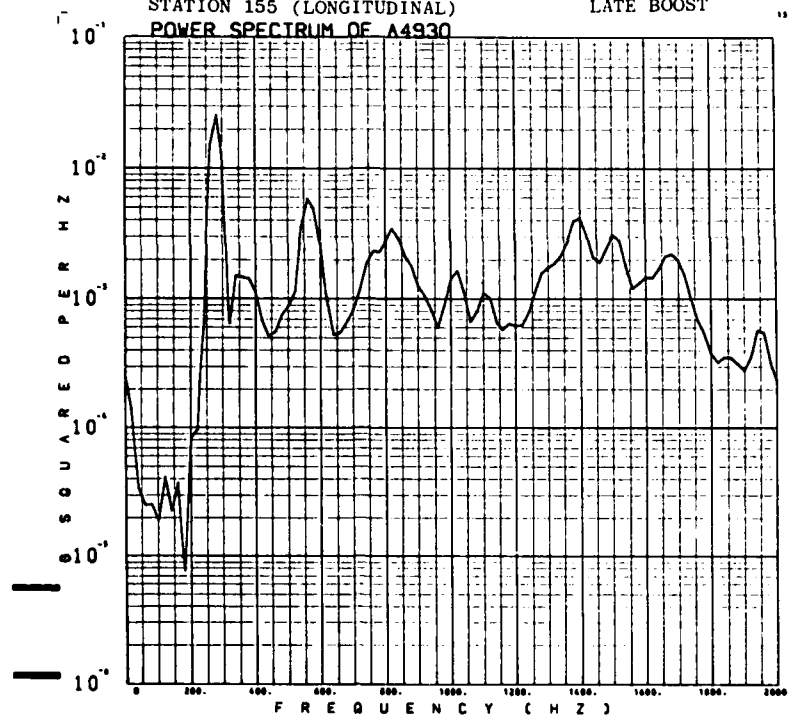


FIGURE 41



STATION 155 (LONGITUDINAL)
POWER SPECTRUM OF A4930

LATE BOOST



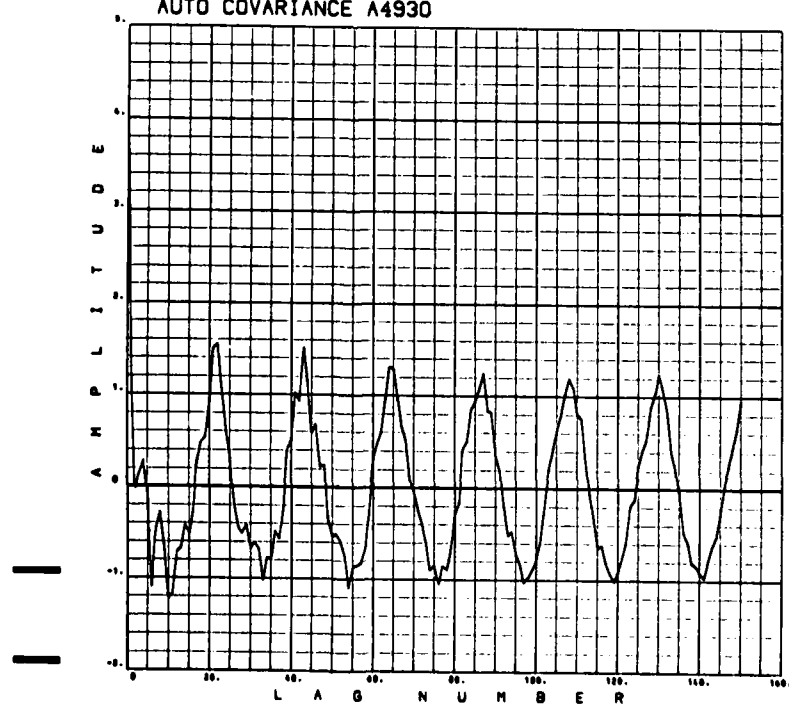
DF = 80 BW = 2.000E+01 RMS = 1.898E+00
TSM 12.0 TO 13.0 LPOF=2100

FIGURE 44

STATION 155 (LONGITUDINAL)

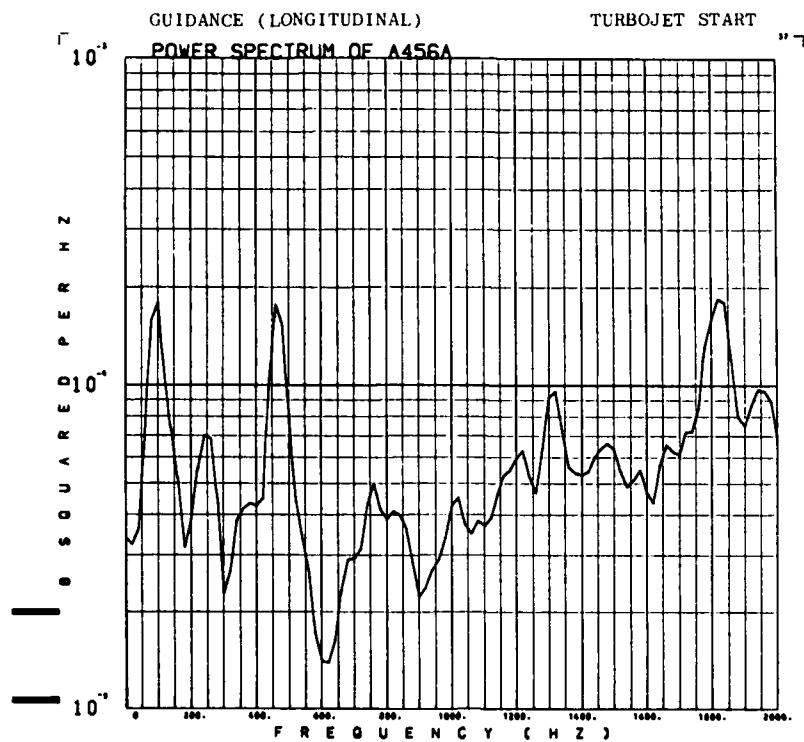
LATE BOOST

AUTO COVARIANCE A4930



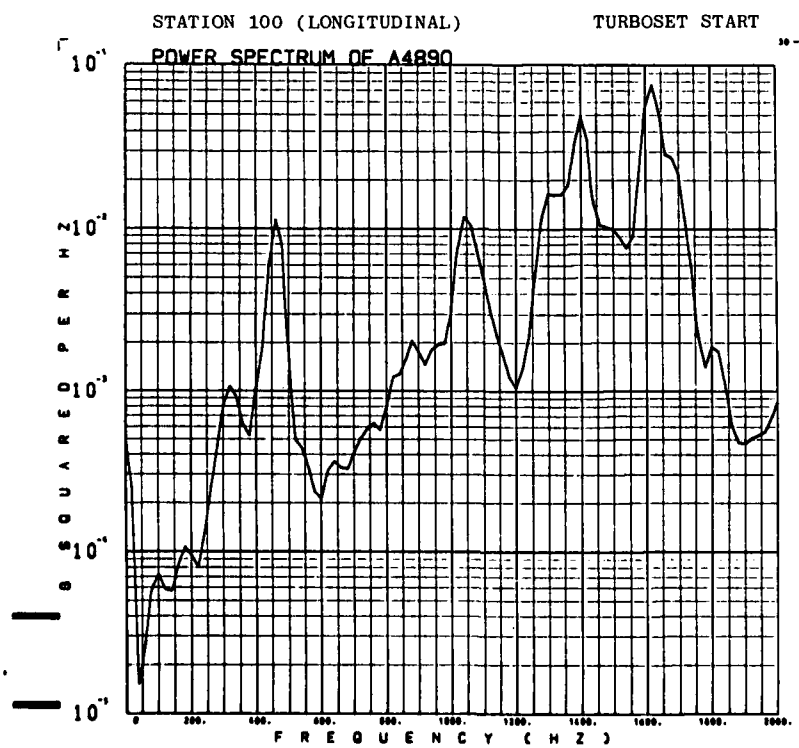
TSM 12.0 TO 13.0 LPOF=2100

FIGURE 45



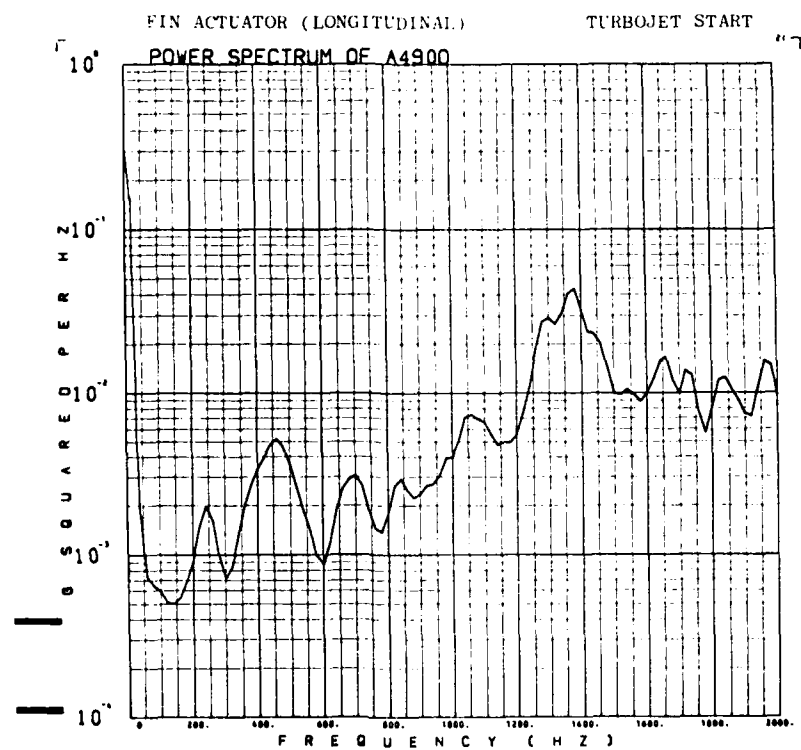
DF = 80 BW = 2.000E+01 RMS = 3.485E-01
TSM 14.5 TO 15.5 LPOF=2100

FIGURE 46



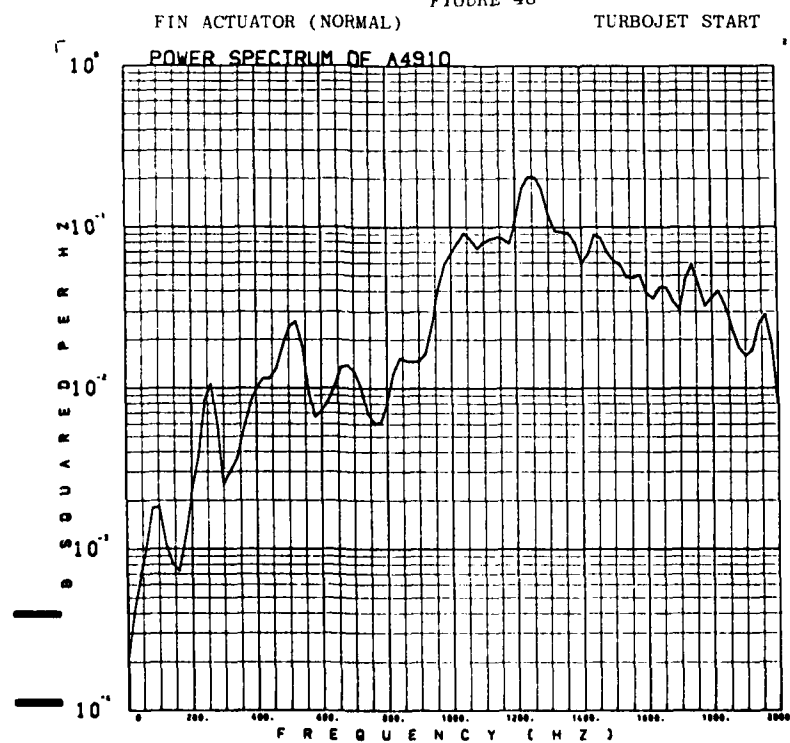
DF = 80 BW = 2.000E+01 RMS = 3.768E+00
TSM 14.5 TO 15.5 LPOF=2100

FIGURE 47



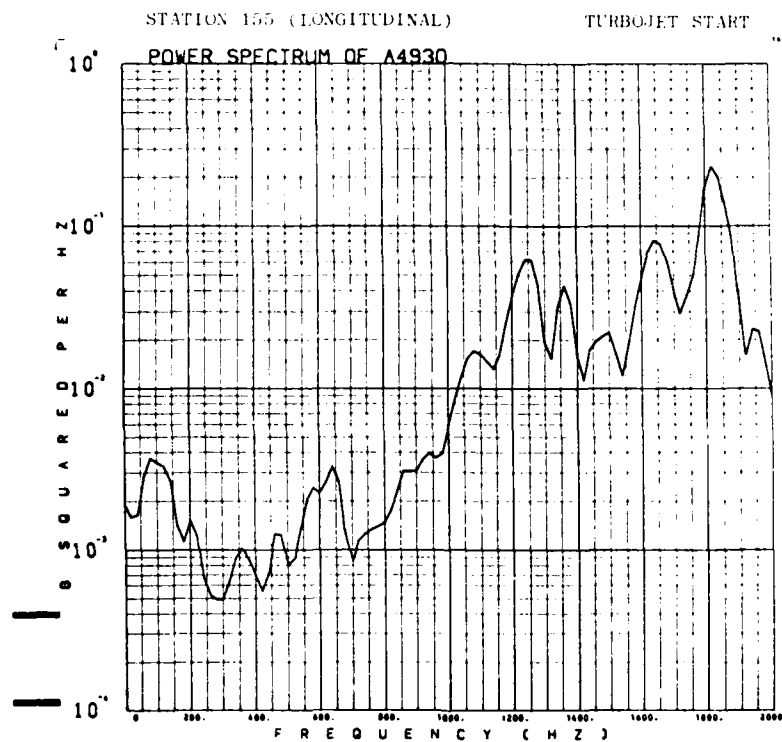
DF = 80 BW = 2.000E+01 RMS = 4.690E+00
TSM 14.5 TO 15.5 LPDF=2100

FIGURE 48



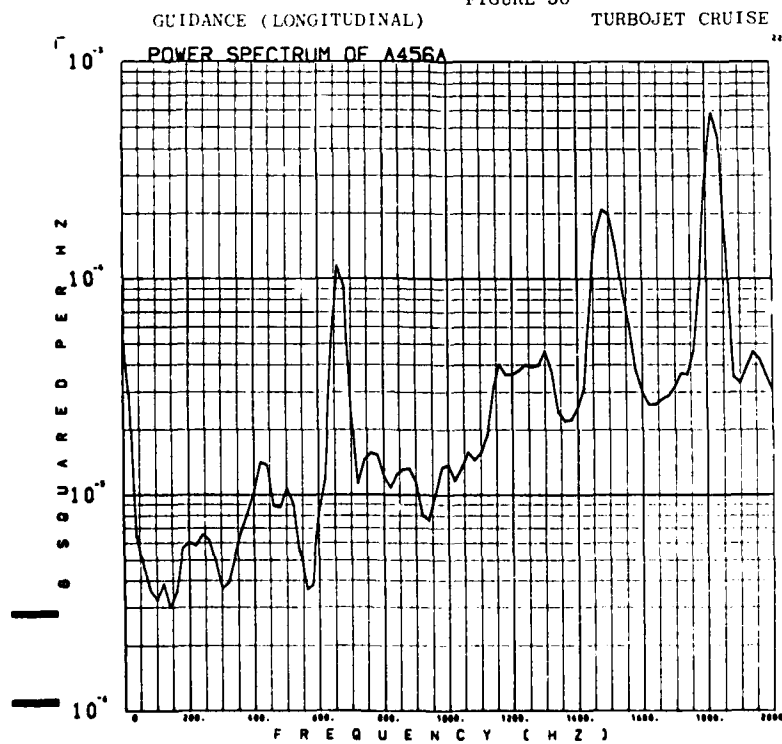
DF = 80 BW = 2.000E+01 RMS = 8.966E+00
TSM 14.5 TO 15.5 LPDF=2100

FIGURE 49



OF = 80 BV = 2.000E+01 RMS = 6.866E+00
TSM 14.5 TO 15.5 LPOF=2100

FIGURE 50



OF = 80 BV = 2.000E+01 RMS = 2.979E-01
TSM 21.0 TO 22.0 LPOF=2100

FIGURE 51

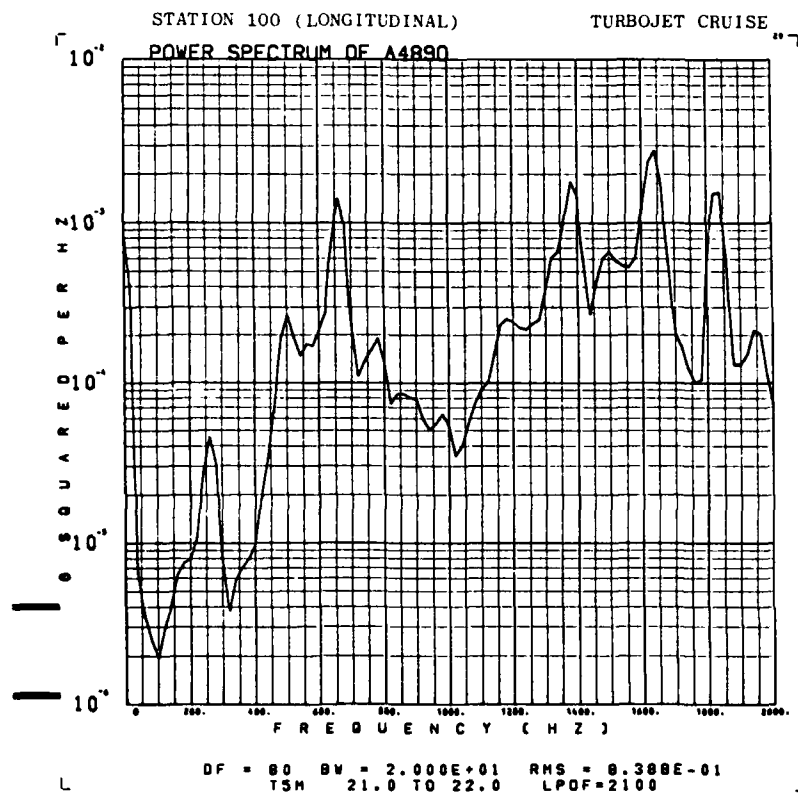


FIGURE 52

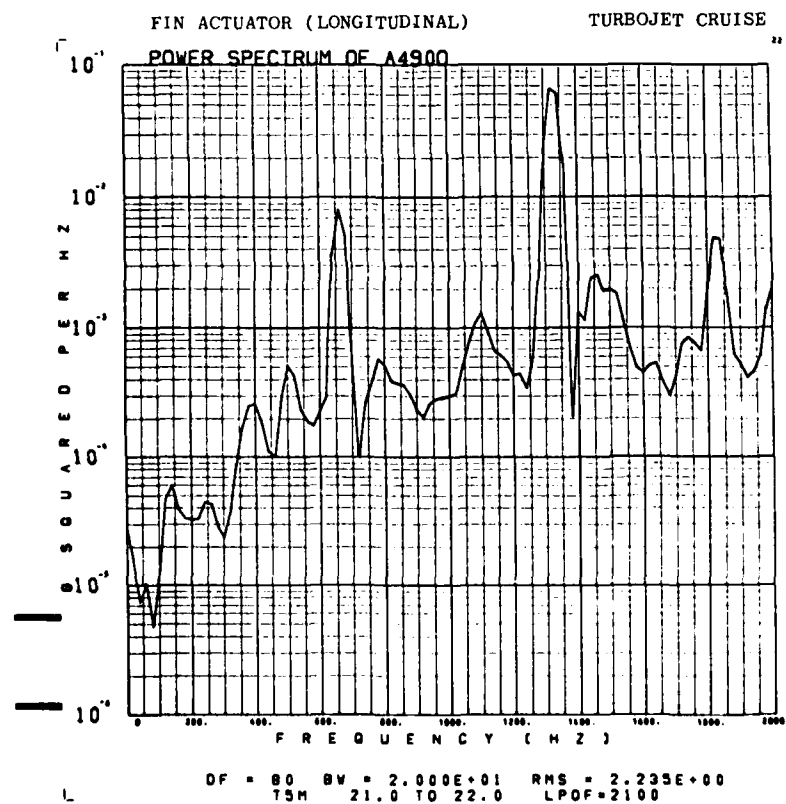
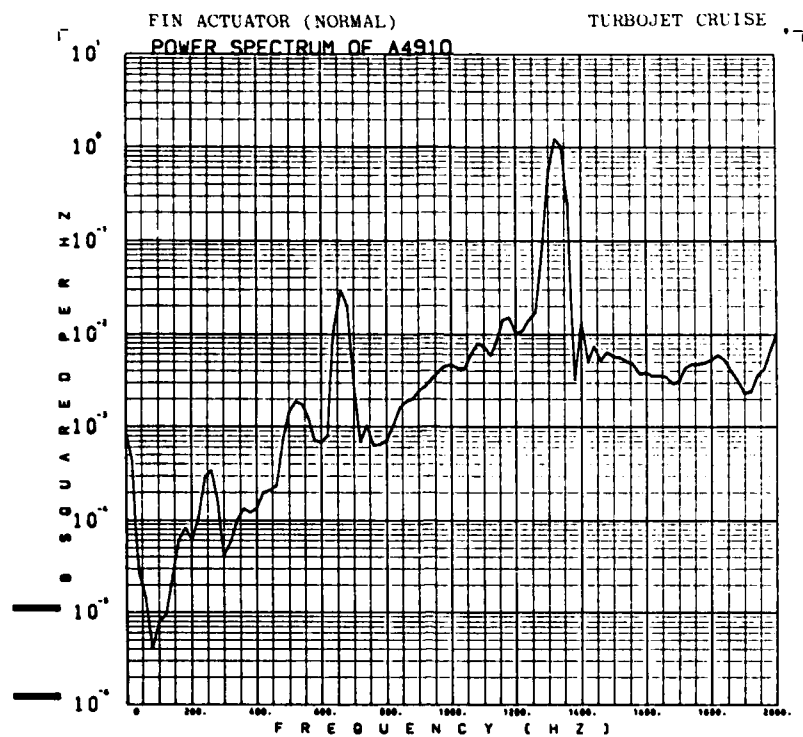
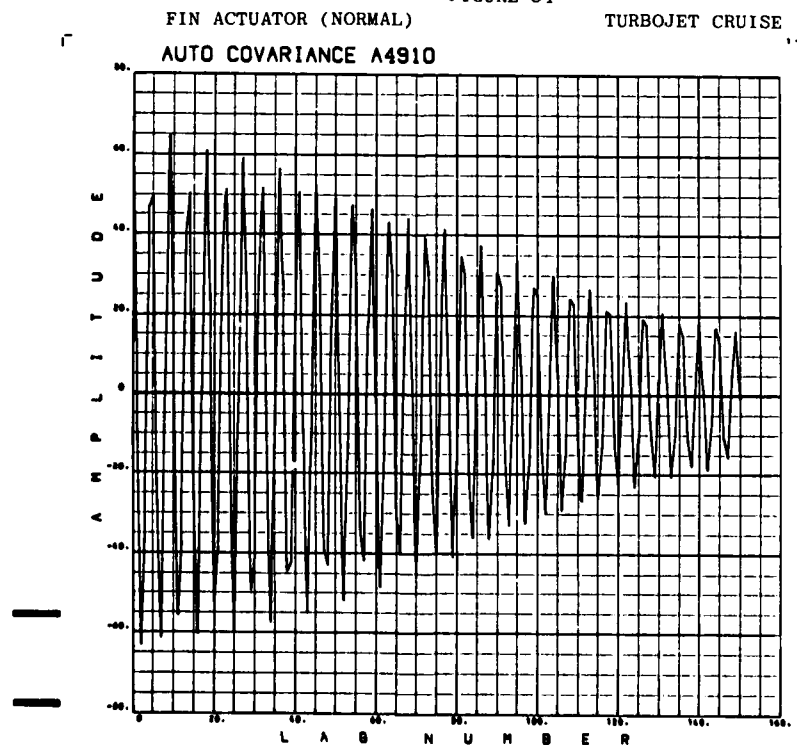


FIGURE 53



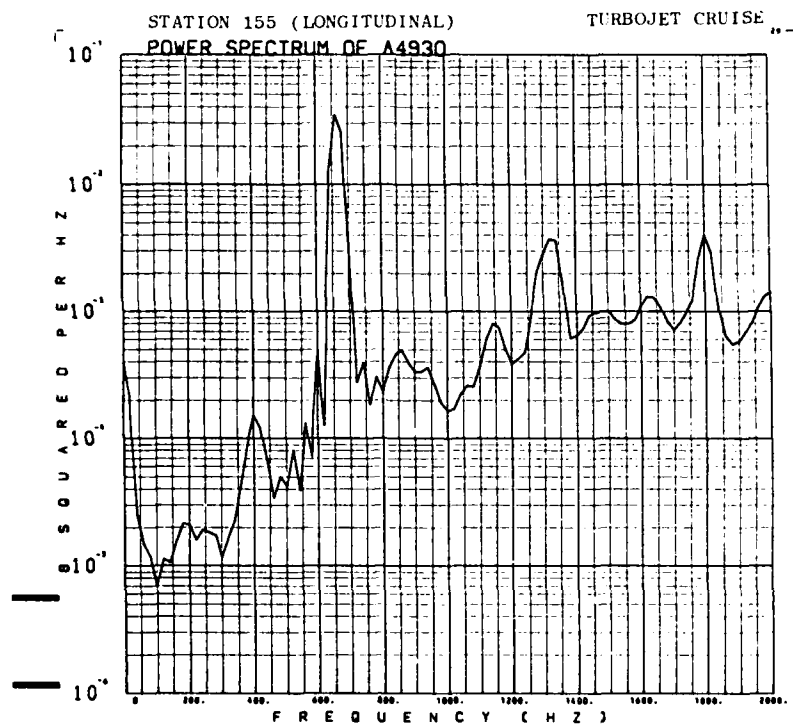
DF = 80 BV = 2.000E+01 RMS = 8.450E+00
TSM 21.0 TO 22.0 LPOF=2100

FIGURE 54



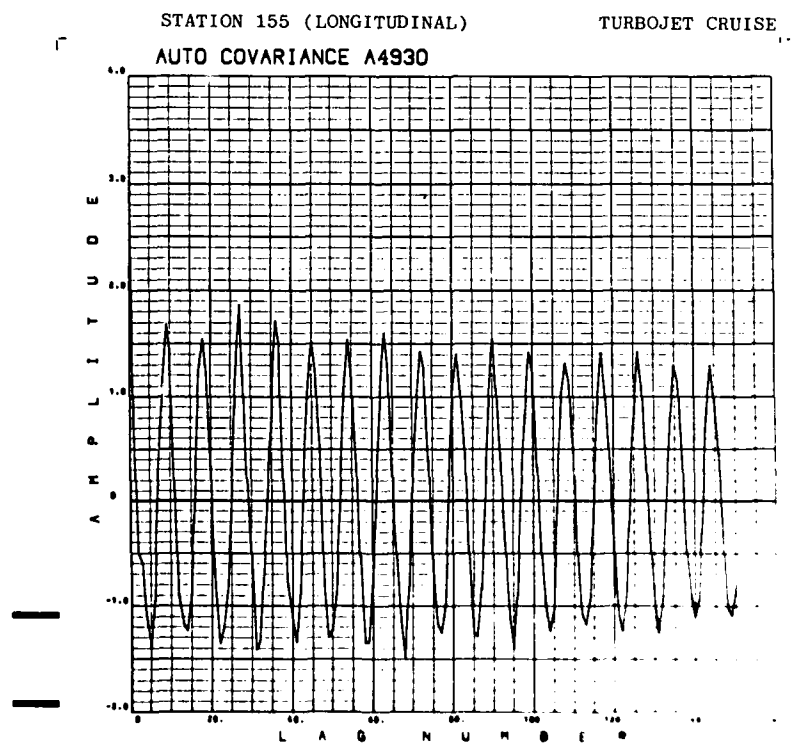
TSM 21.0 TO 22.0 LPOF=2100

FIGURE 55



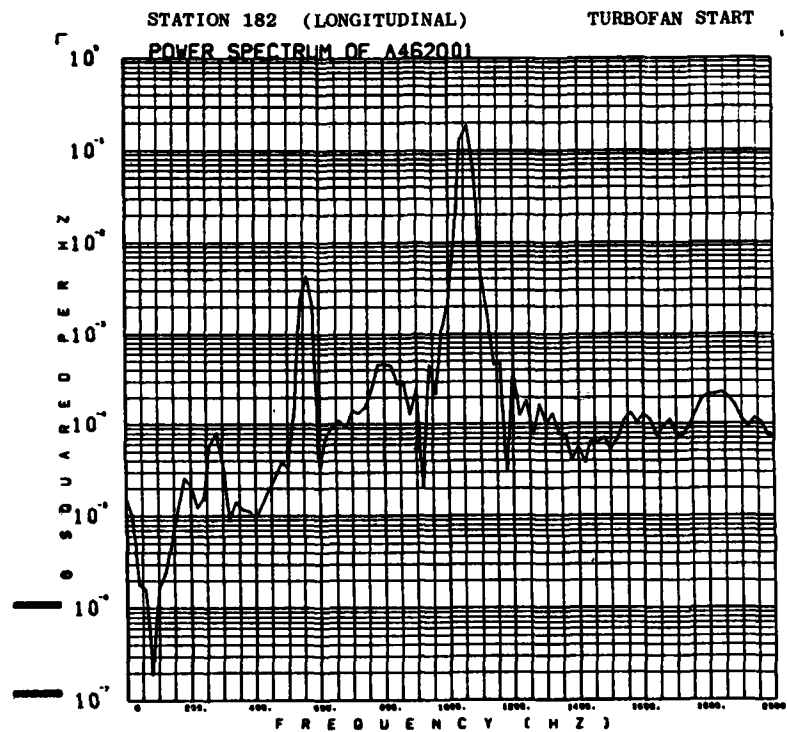
DF = 80 BW = 2.000E+01 RMS = 1.670E+00
TSM 21.0 TO 22.0 LPOF=2100

FIGURE 56

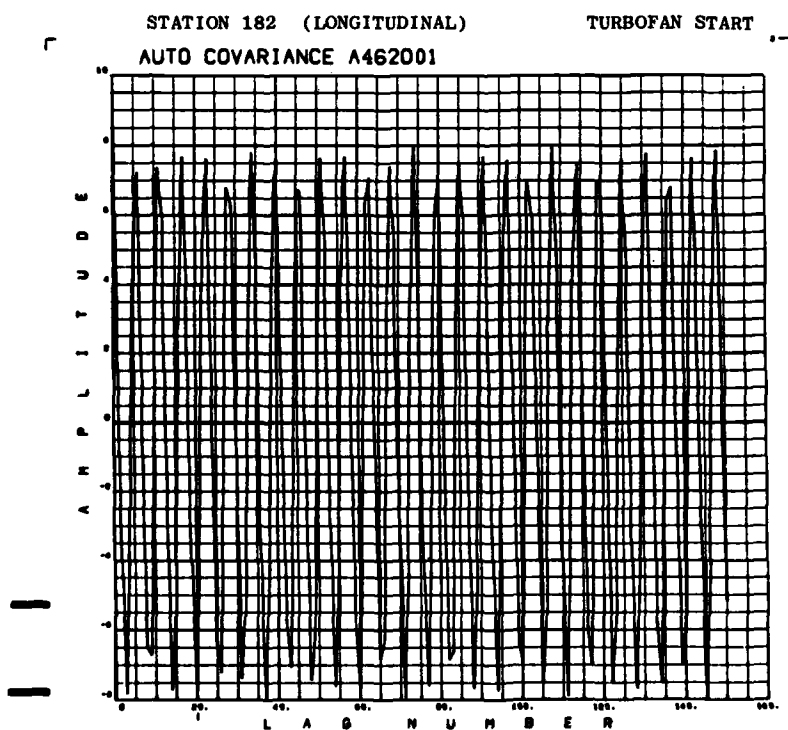


TSM 21.0 TO 22.0 LPOF=2100

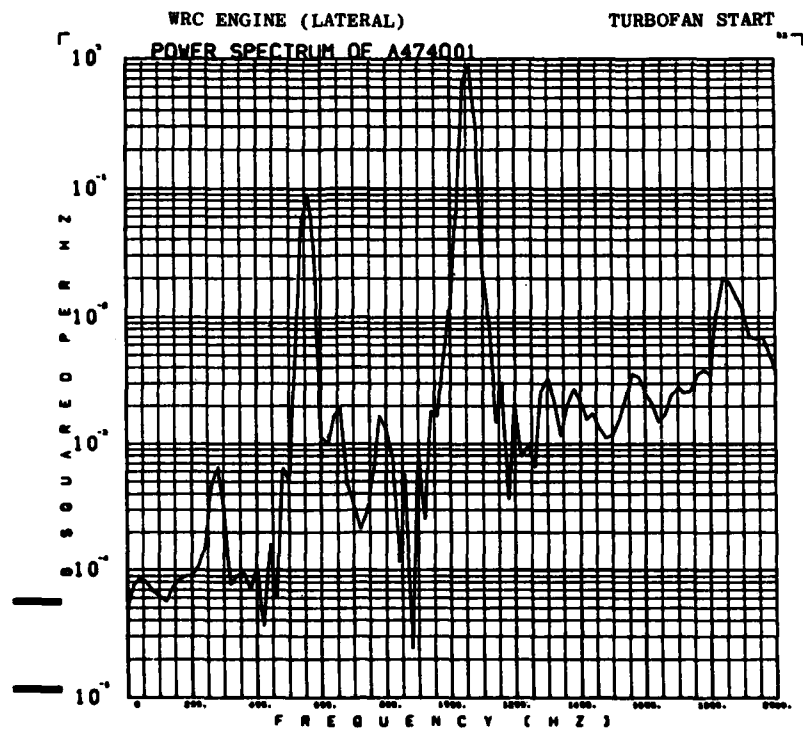
FIGURE 57



OF = 80 BV = 2.000E+01 RMS = 2.922E+00
TOM 24-1 19-00-23.00 TO 19-00-24.00 LPDF=2100
FIGURE 58

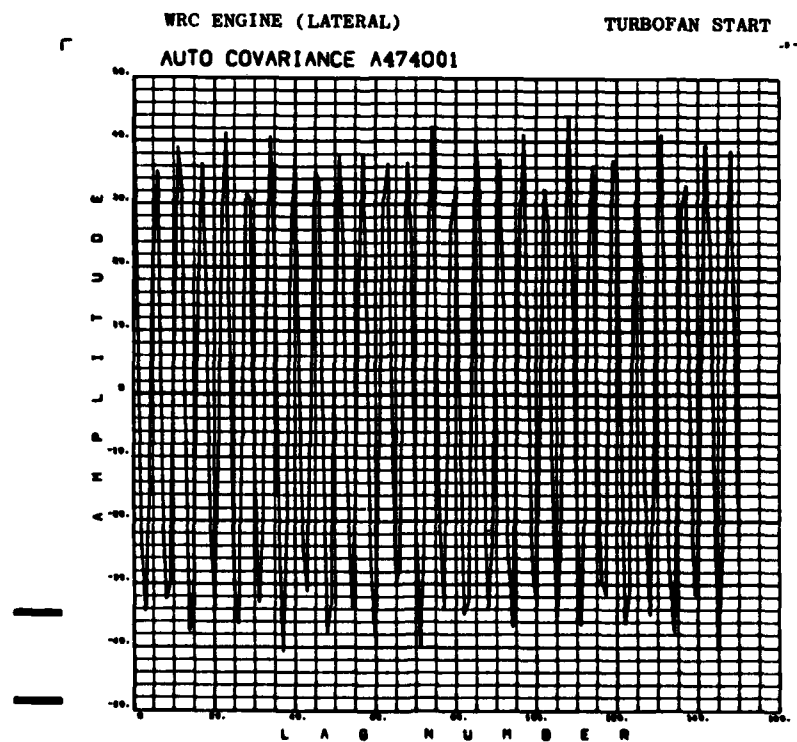


TOM 24-1 19-00-23.00 TO 19-00-24.00 LPDF=2100
FIGURE 59



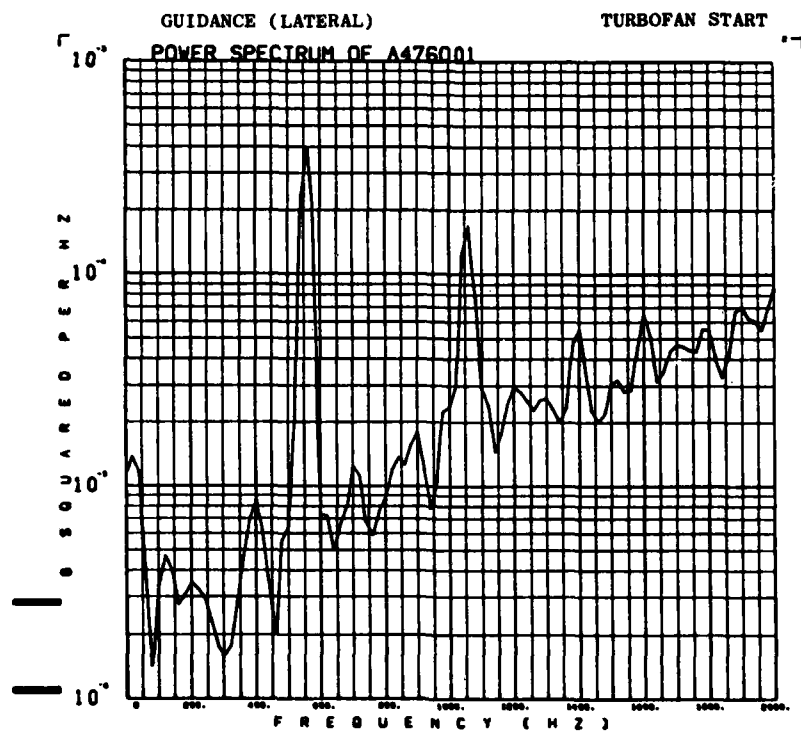
DF = 80.00 BY = 2.000E+01 RMS = 8.093E+00
 TOM 24-1 19-00-23.00 TO 19-00-24.00 LPOF=2100

FIGURE 60



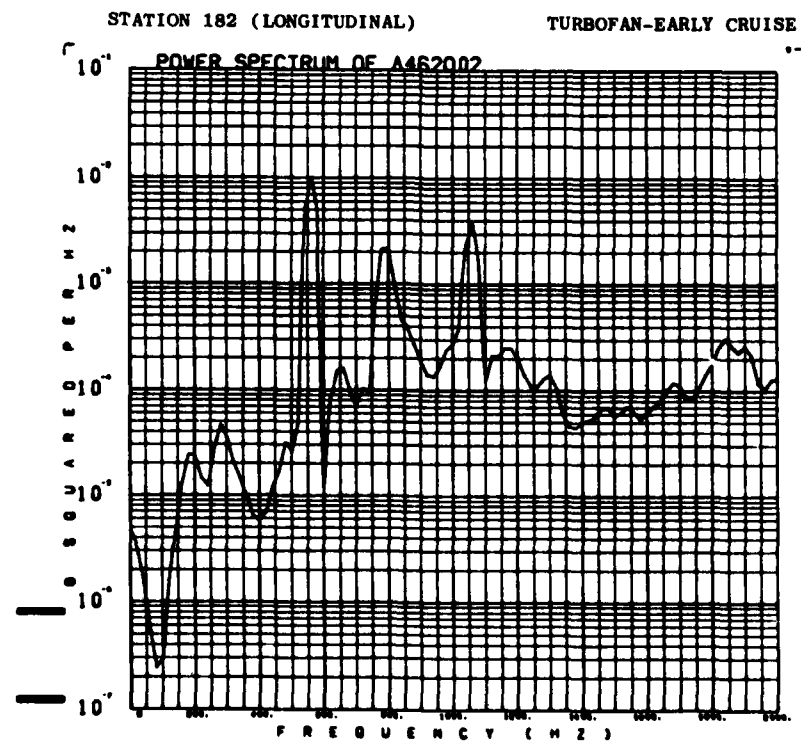
TOM 24-1 19-00-23.00 TO 19-00-24.00 LPOF=2100

FIGURE 61



OF = 00 BV = 2.000E-01 RMS = 2.502E-01
 TOM 24-1 19-00-23.00 TO 19-00-24.00 LPDF=2100

FIGURE 62

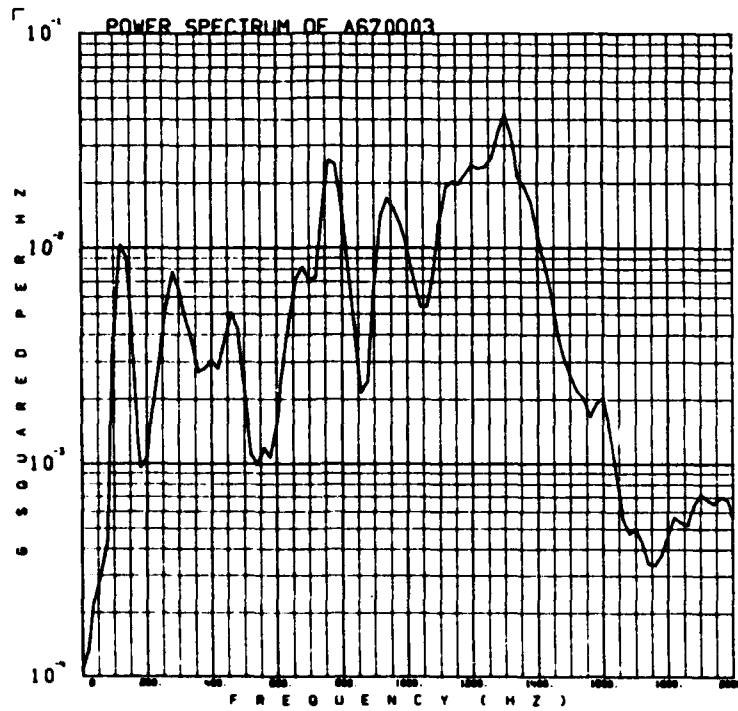


OF = 00 BV = 2.000E-01 RMS = 9.301E-01
 TOM 24-1 19-00-41.00 TO 19-00-42.00 LPDF=2100

FIGURE 63

AIR DATA PACKAGE (NORMAL)

TURBOFAN - EARLY CRUISE

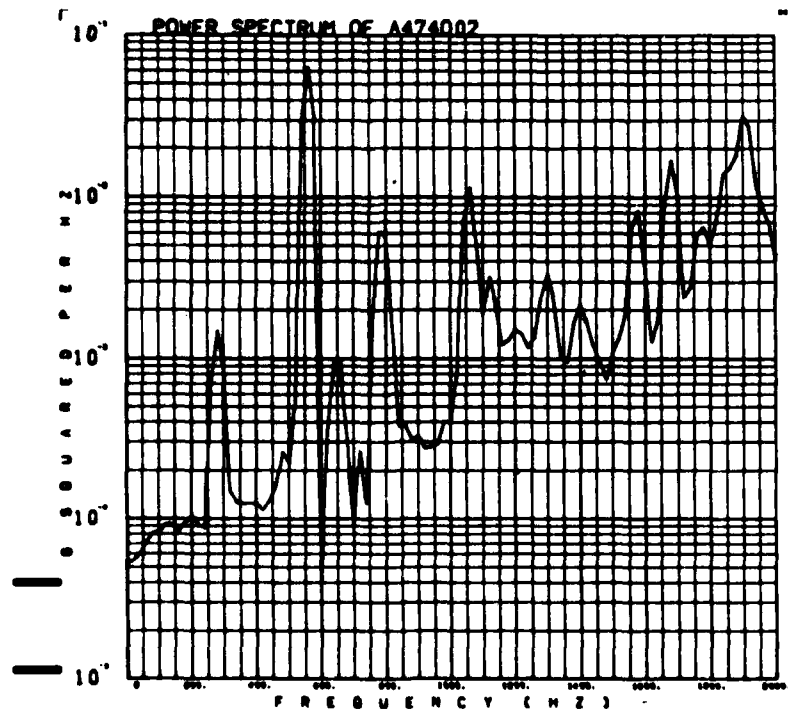


DF = 80 BW = 2.000E+01 RMS = 3.873E+00
TOM 17-3 PSDS 20-02-33.0 TO 20-02-34.0 LPOF=2100

FIGURE 64

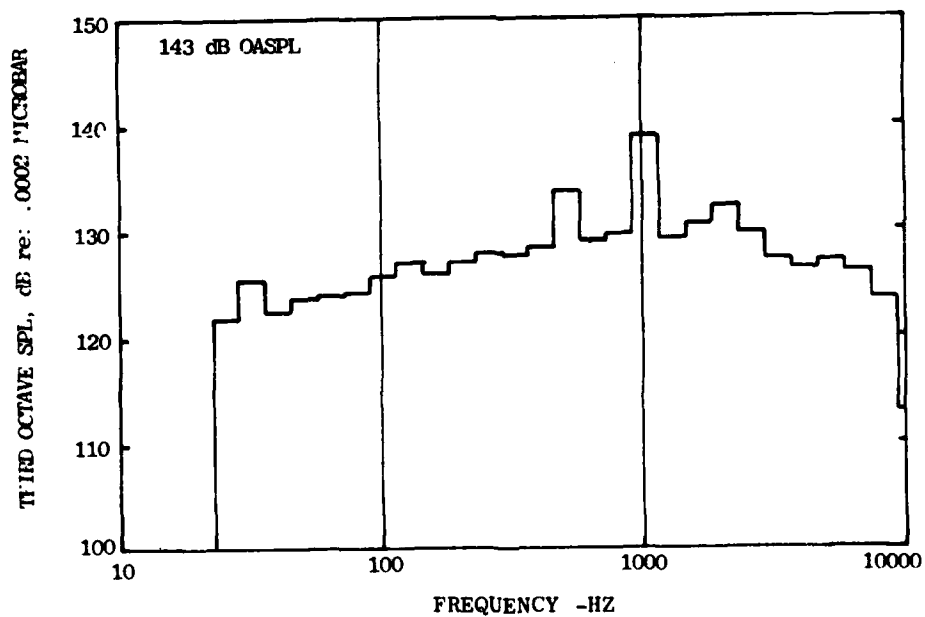
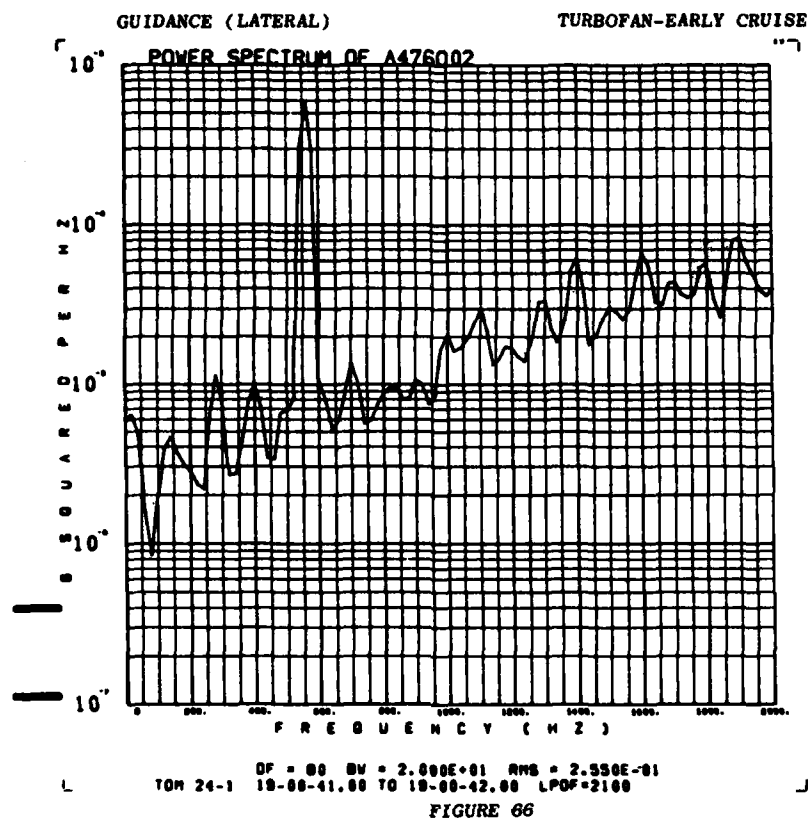
VRC ENGINE (LATERAL)

TURBOFAN - EARLY CRUISE



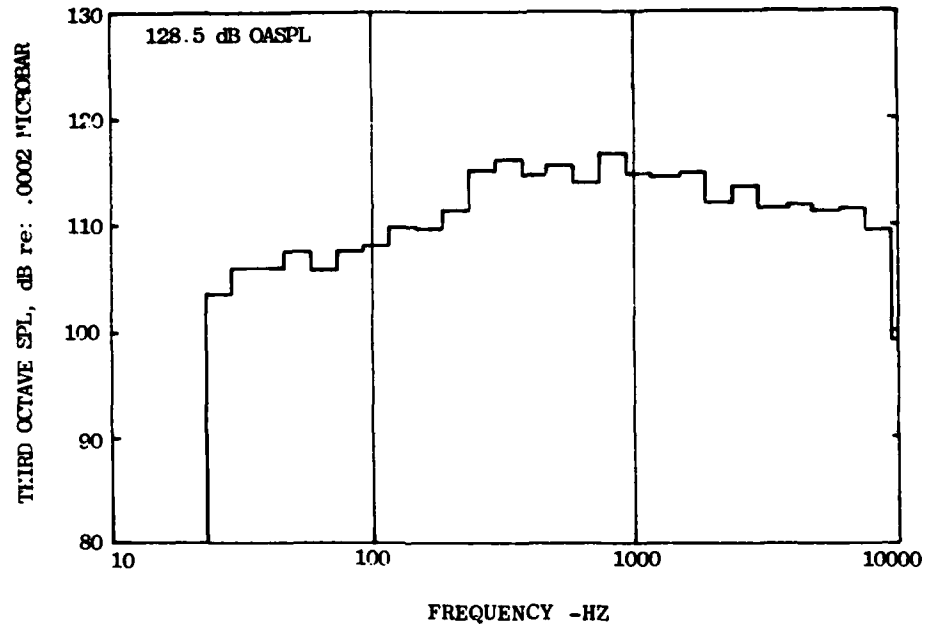
DF = 80 BW = 2.000E+01 RMS = 2.974E+00
TOM 24-1 19-00-41.00 TO 19-00-42.00 LPOF=2100

FIGURE 65



EXTERNAL ACOUSTIC SPECTRUM - CRUISE FLIGHT, $M=0.8$

FIGURE 67



INTERNAL ACOUSTIC SPECTRUM - CRUISE FLIGHT, $M=0.8$

FIGURE 68

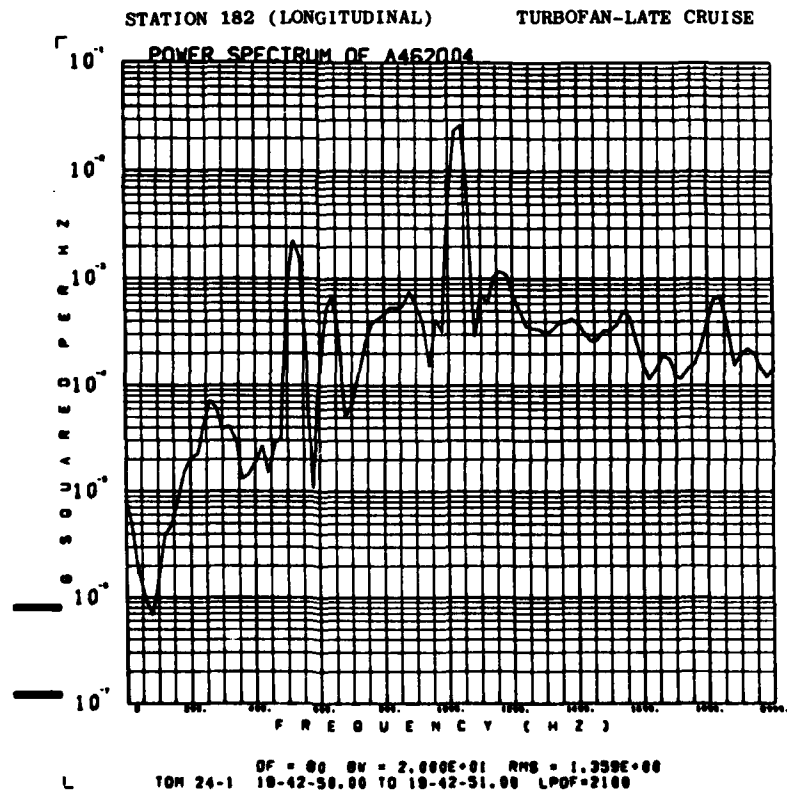
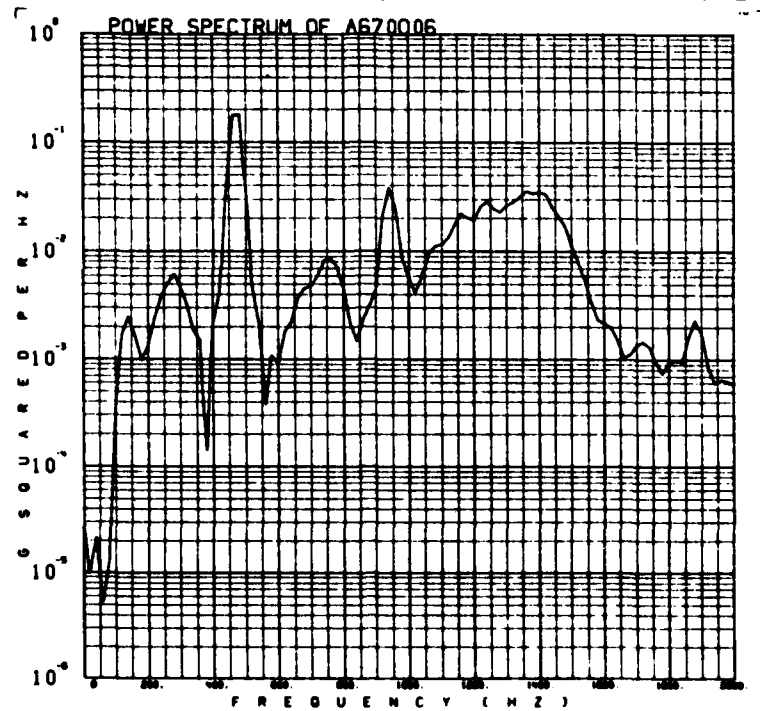


FIGURE 69

AIR DATA PACKAGE (NORMAL)

TURBOFAN - LATE CRUISE

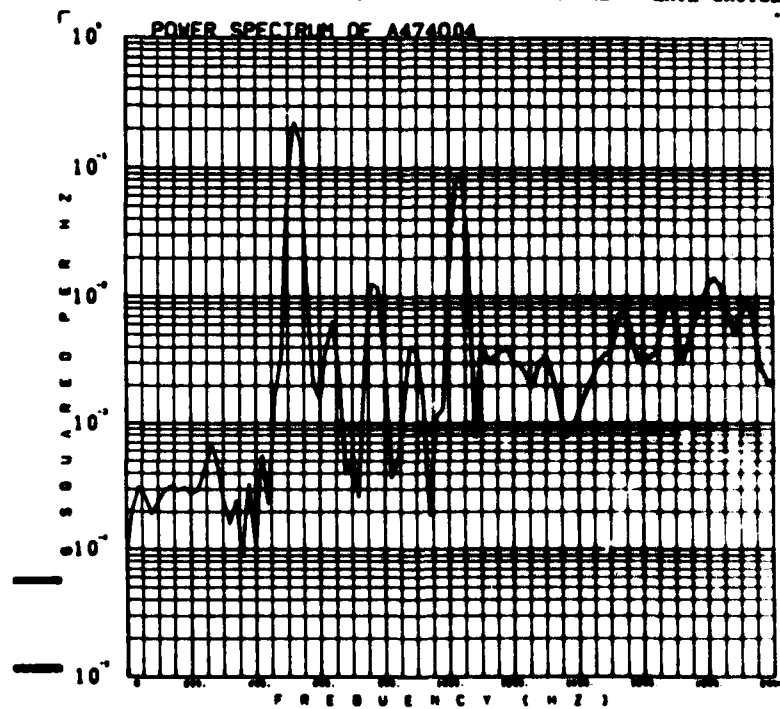


DF = 80 BV = 2.000E+01 RMS = 4.951E+00
TOM 17-3 PSDS 20-14-22.0 TO 20-14-23.0 LPOF=2100

FIGURE 70

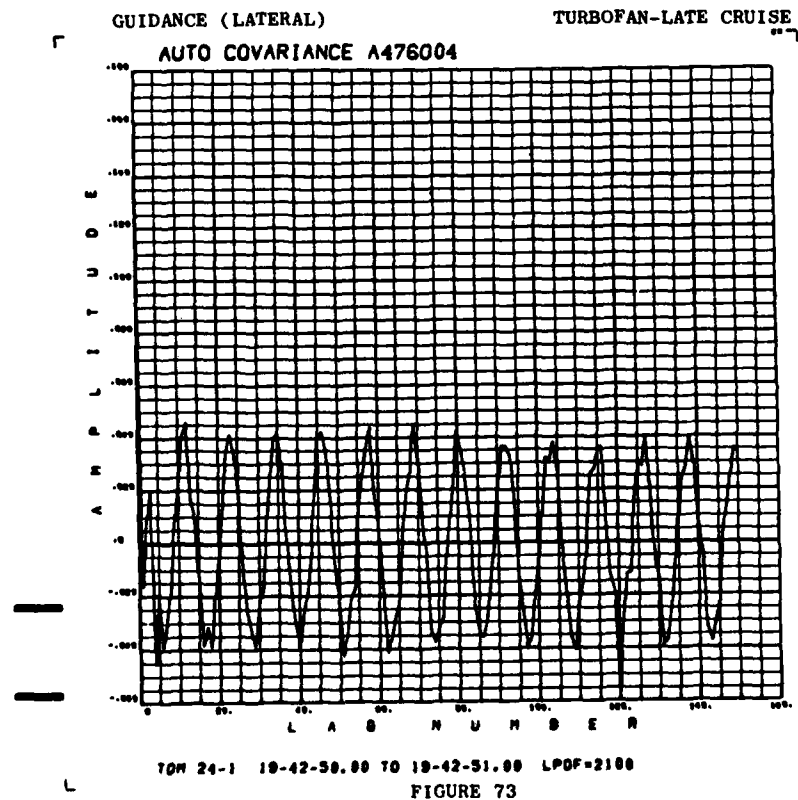
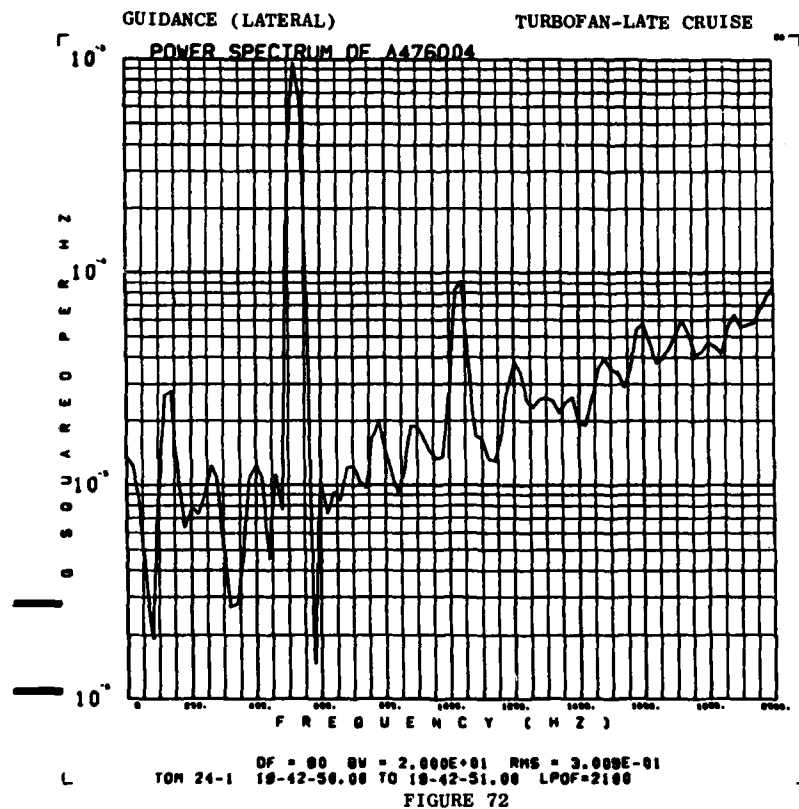
WRC ENGINE (LATERAL)

TURBOFAN - LATE CRUISE



DF = 80 BV = 2.000E+01 RMS = 4.410E+00
TOM 24-1 10-42-50.00 TO 10-42-51.00 LPOF=2100

FIGURE 71



PYROTECHNIC SYSTEMS

ITEM	DEVICE	ITEM	DEVICE
1	Booster safe/arm device	9	TVC GN ₂ release valve (normally closed — NC)
2	Booster separation	11	Pneumatic power system GN ₂ release valve (NC)
3	Thrust termination assembly	12	Wing deploy valve (NC)
4	Cable cutter	13	Wing slot door-close valve (NC)
5	Shroud separation assembly	14	Warhead air valves (2)
6	Inlet cover separation assembly	15	Thermal batteries
7	Wing slot plug assemblies (2)		
8	Turbofan start cartridge		

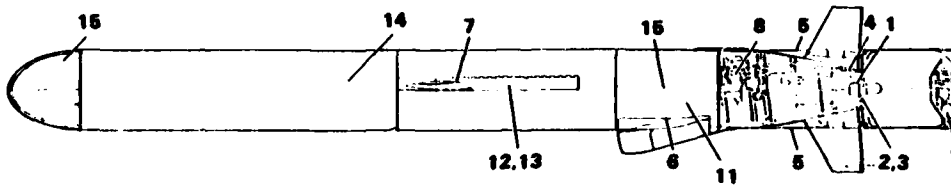


FIGURE 74

01041195 76

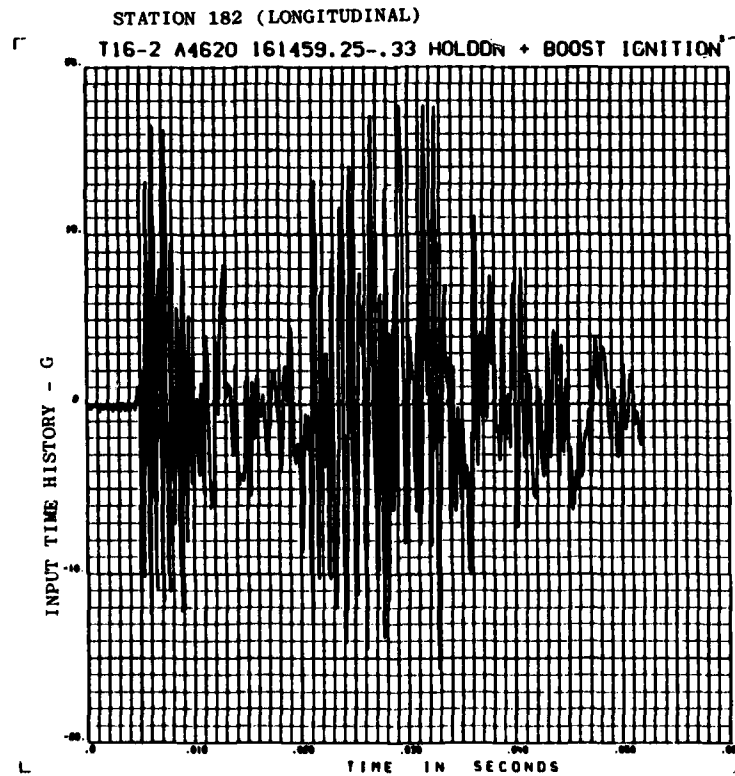


FIGURE 75

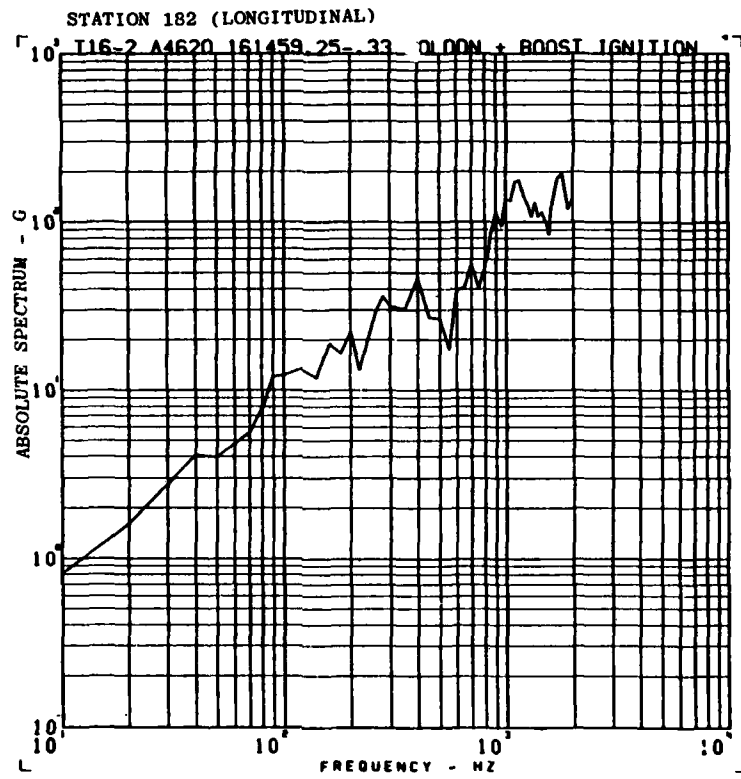


FIGURE 76

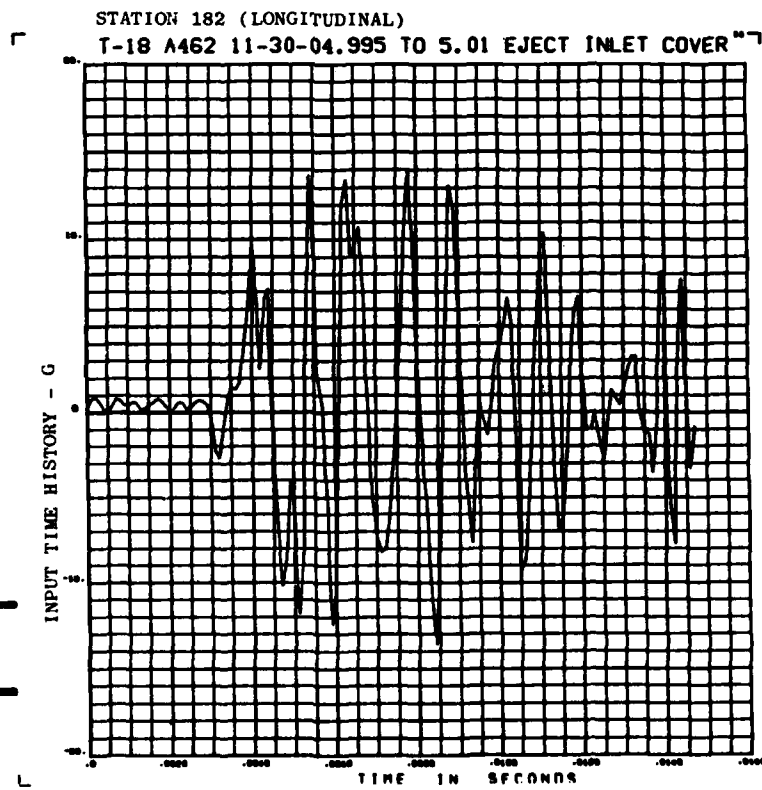
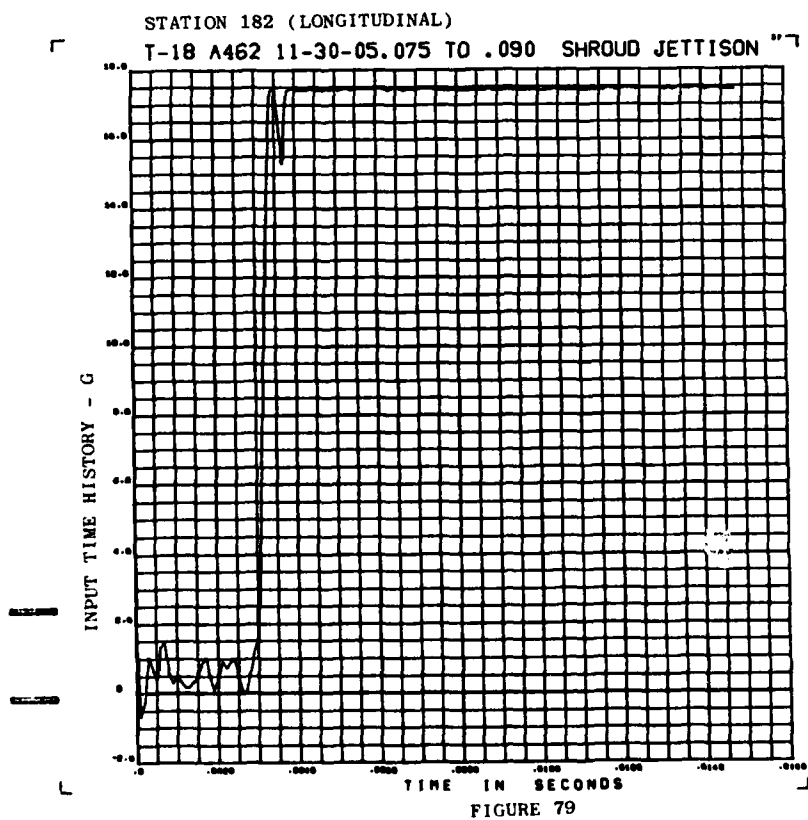
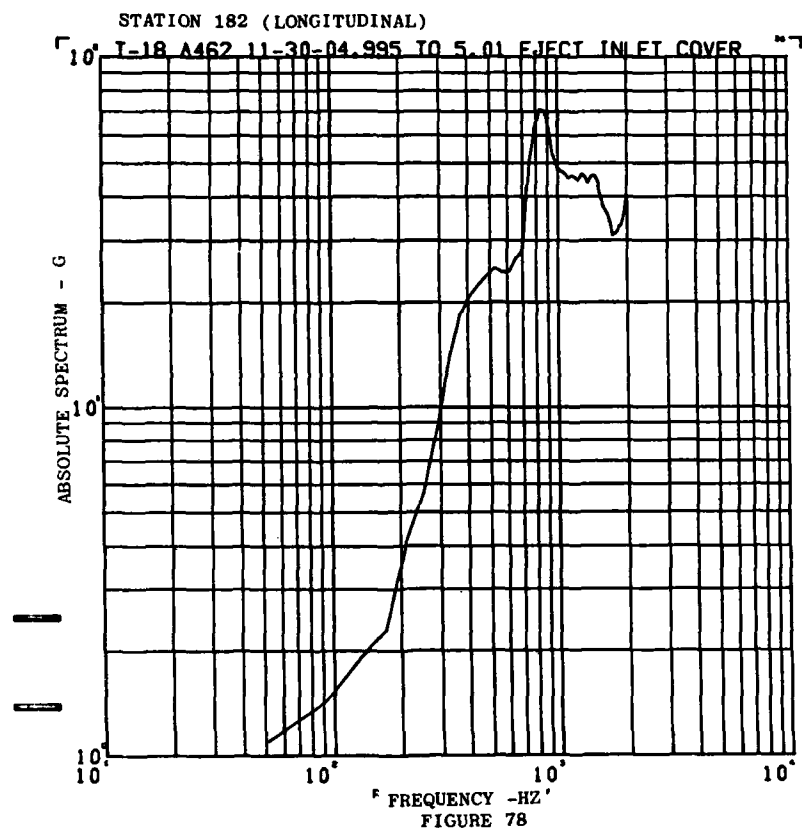
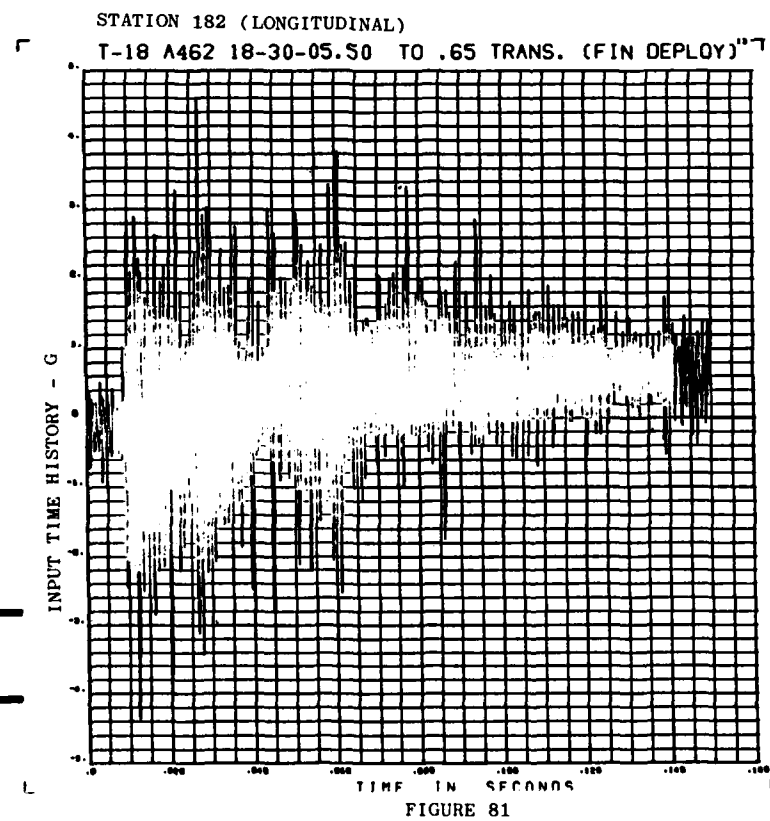
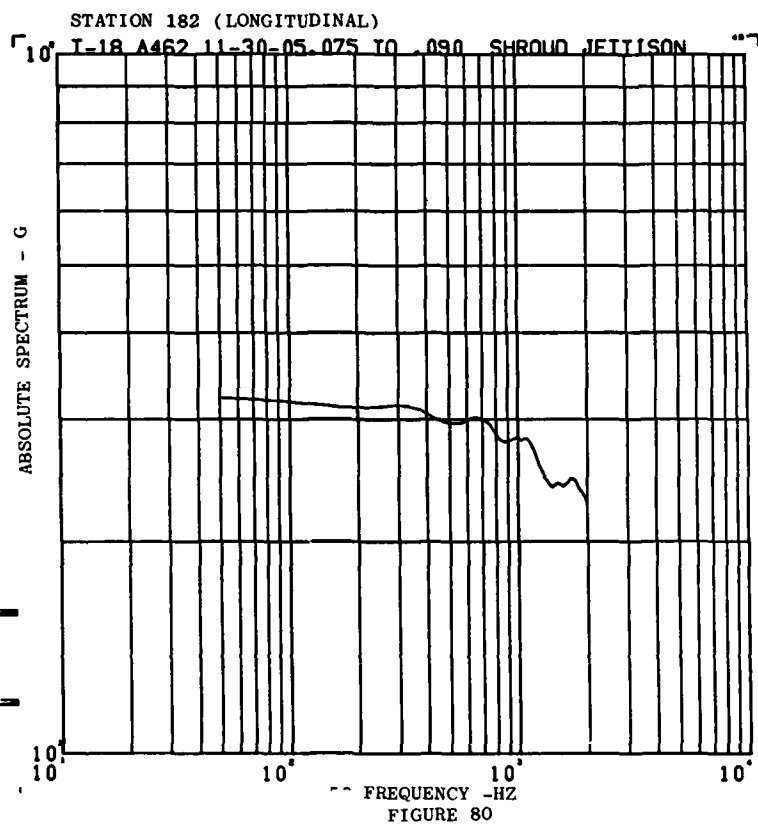
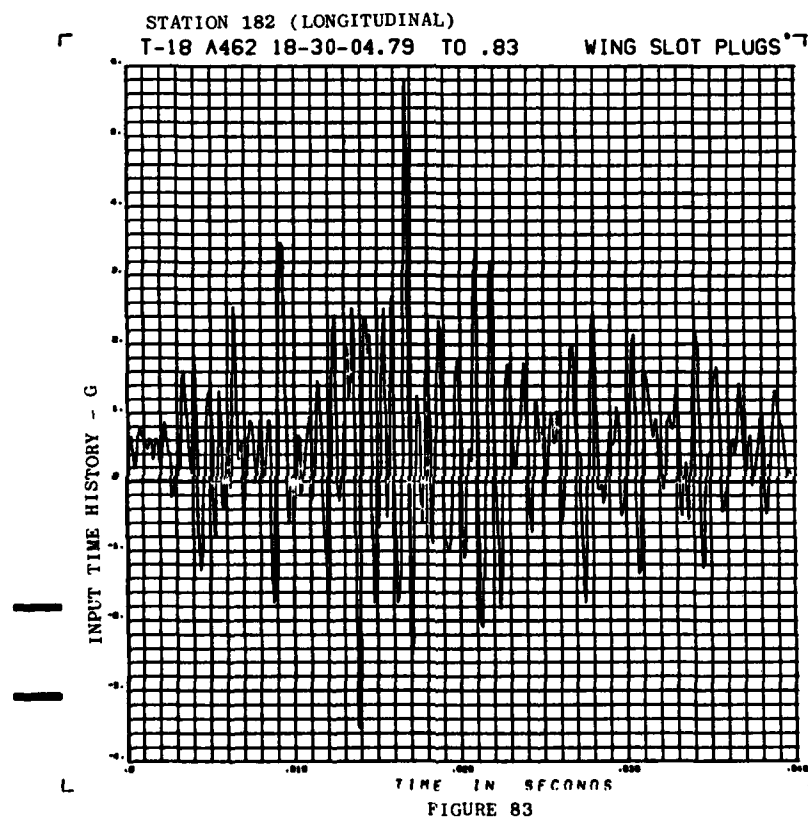
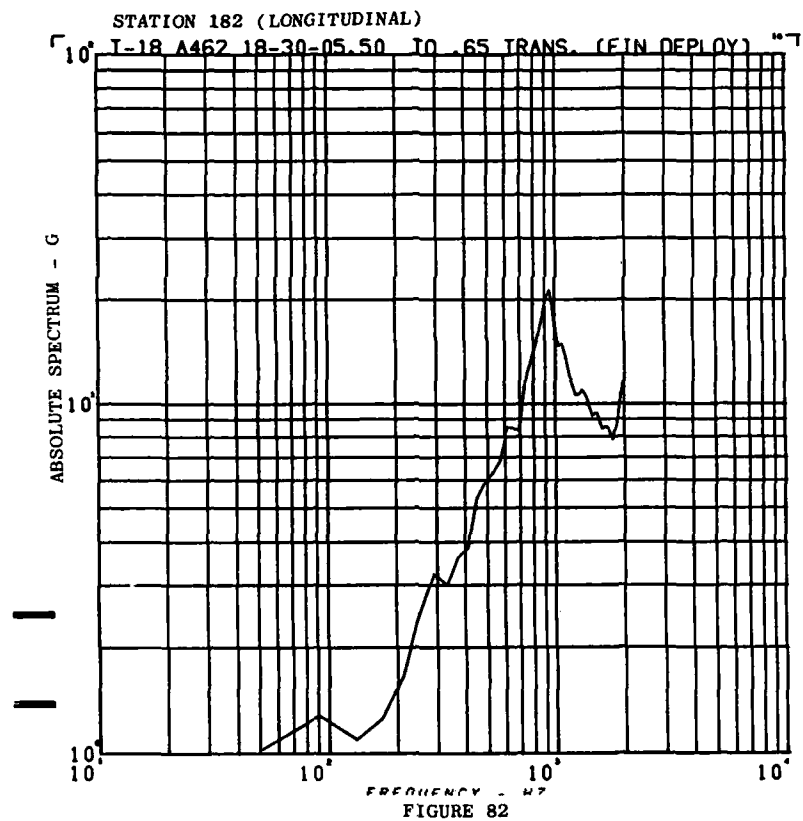


FIGURE 77







STATION 182 (LONGITUDINAL)

T-18 A462 18-30-04.79 TO .83 WING SLOT PLUGS "7"

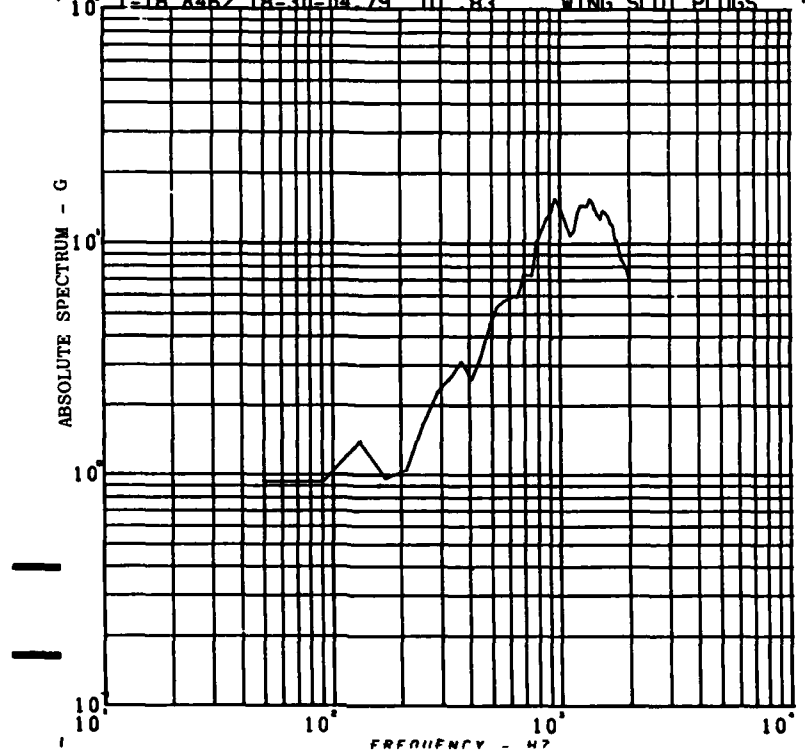


FIGURE 84

STATION 182 (LONGITUDINAL)

T-18 A462 11-30-13.475 TO .490 DEPLOY INLET "7"

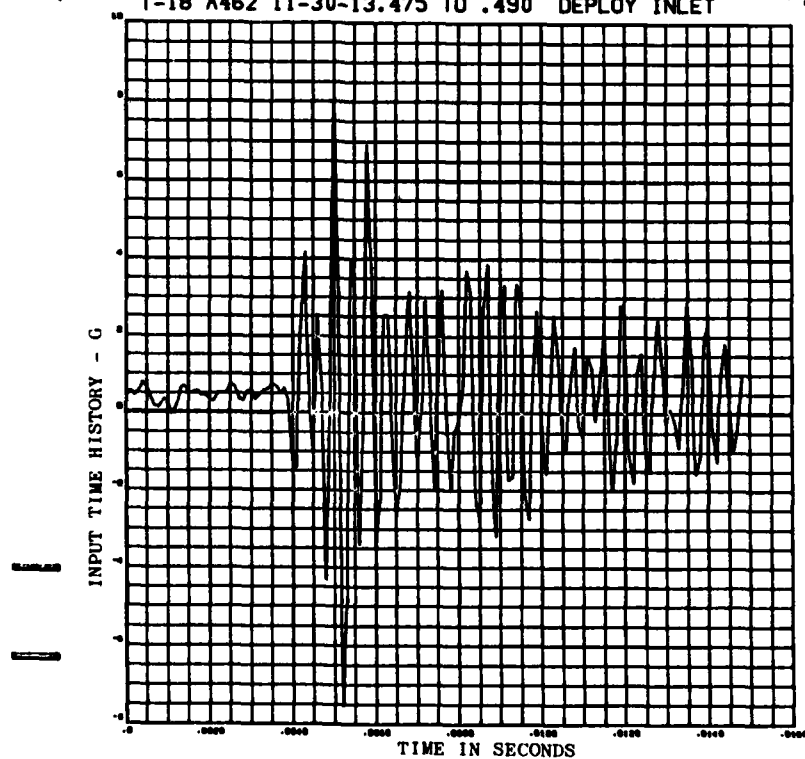
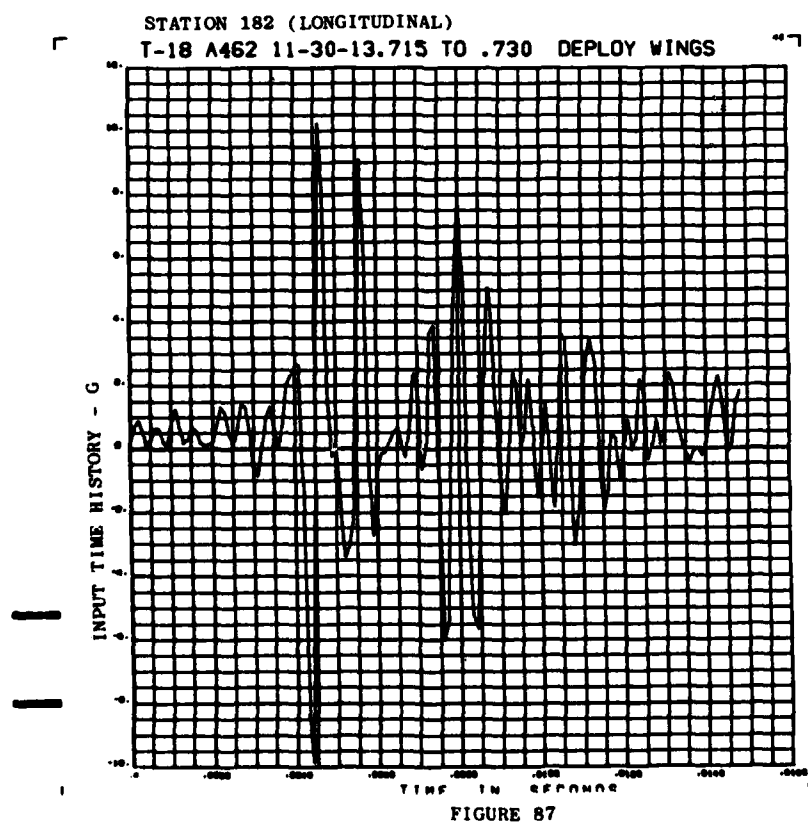
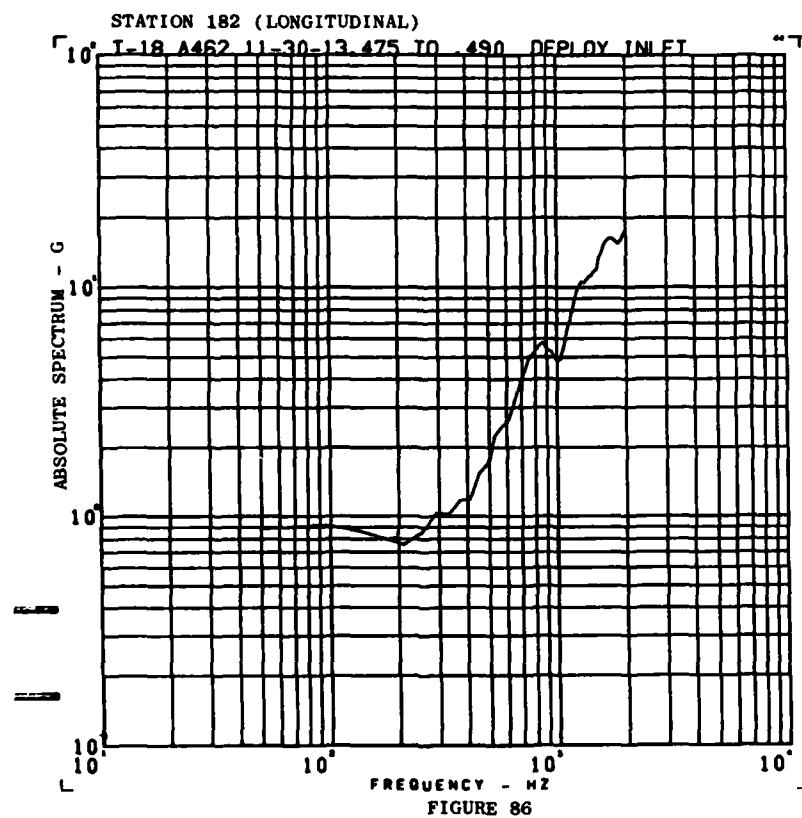
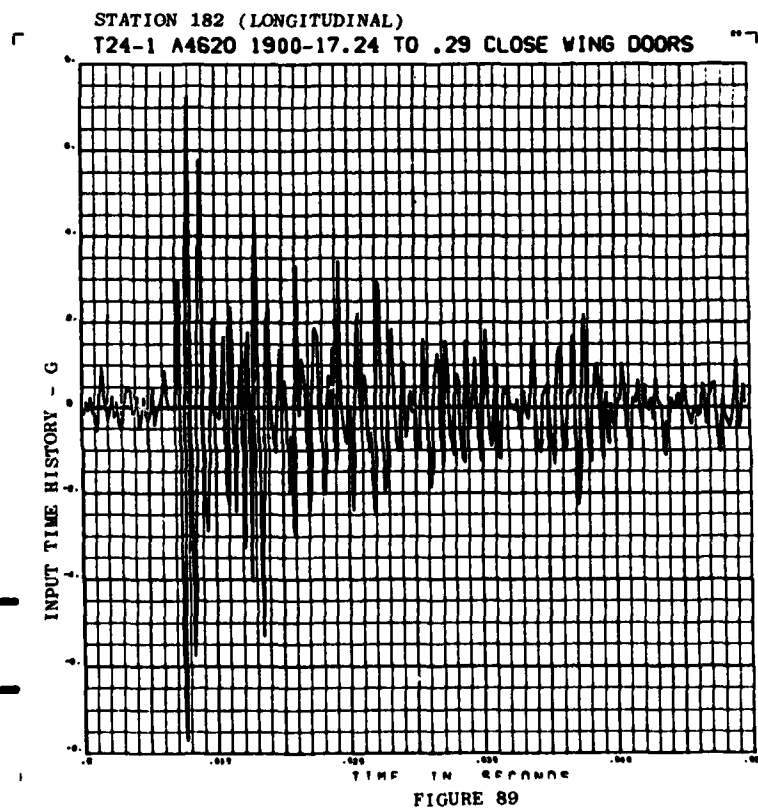
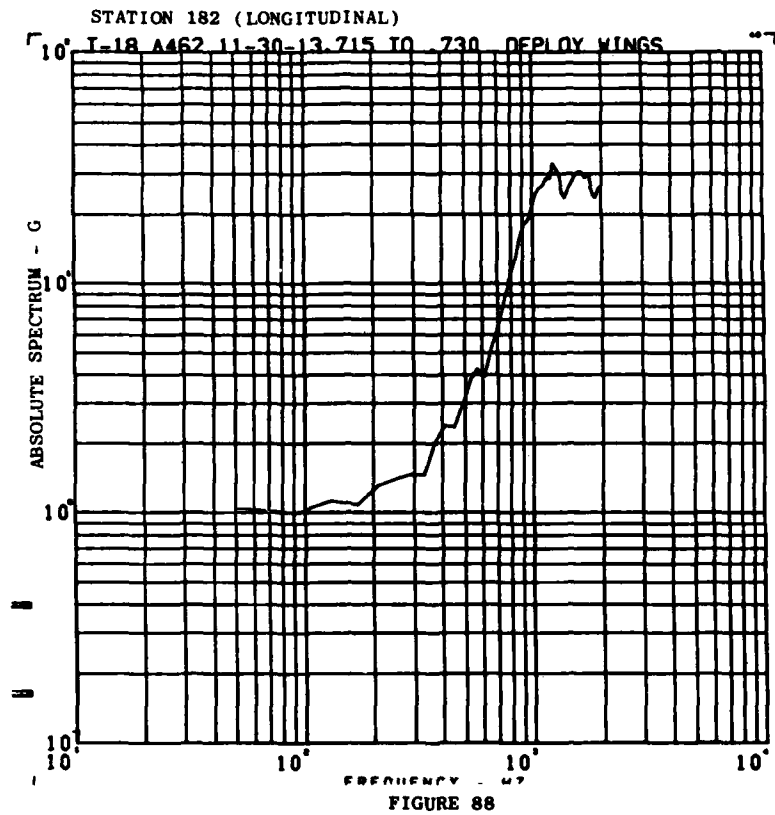
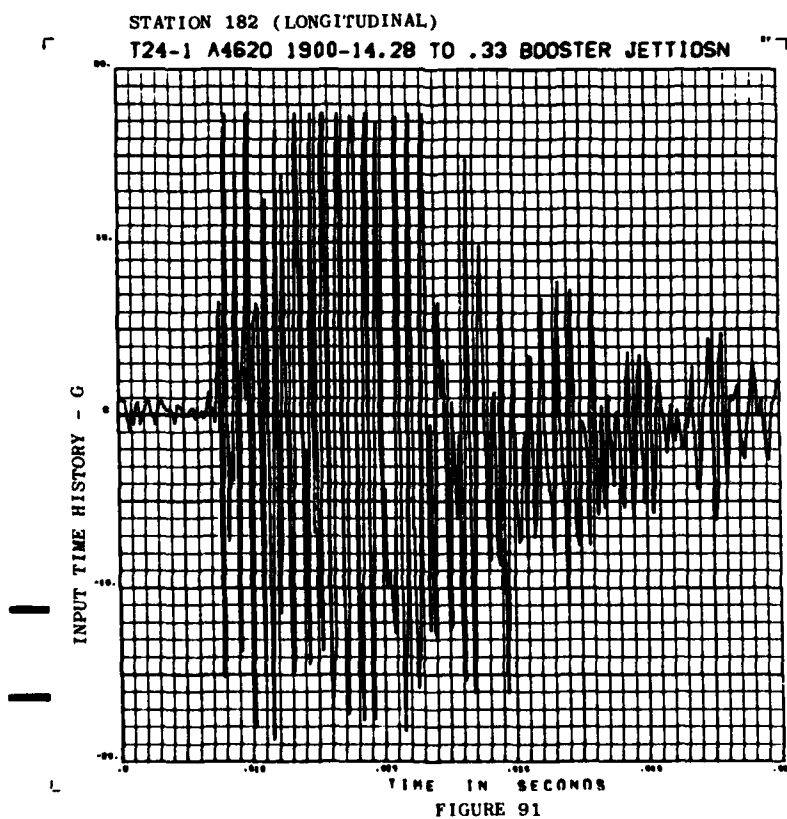
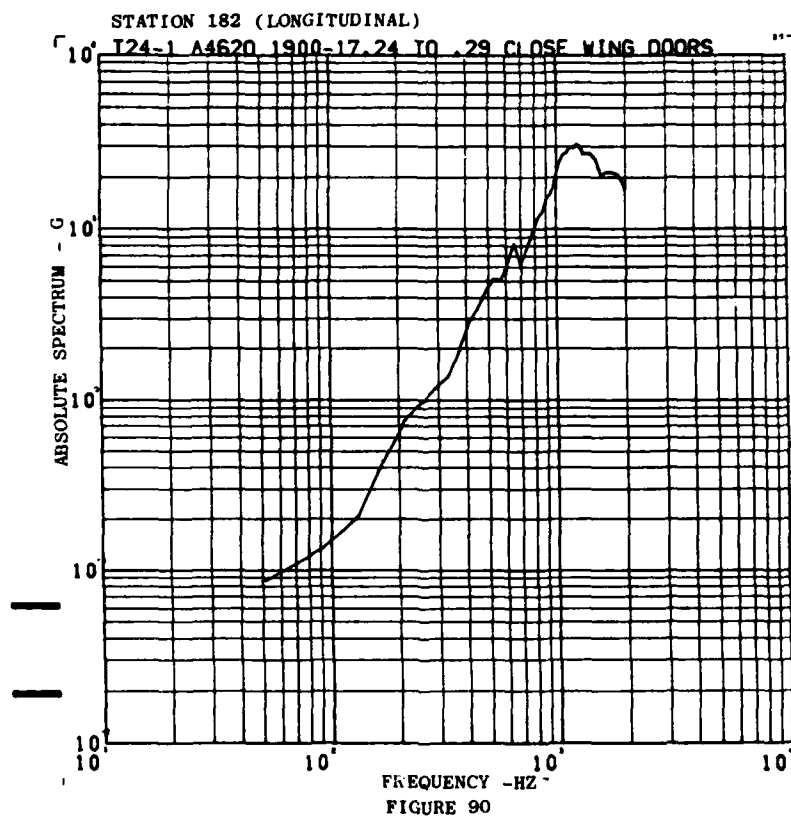


FIGURE 85







STATION 182 (LONGITUDINAL)

T24-1 A4620 1900-14.28 TO .33 BOOSTER JETTISON

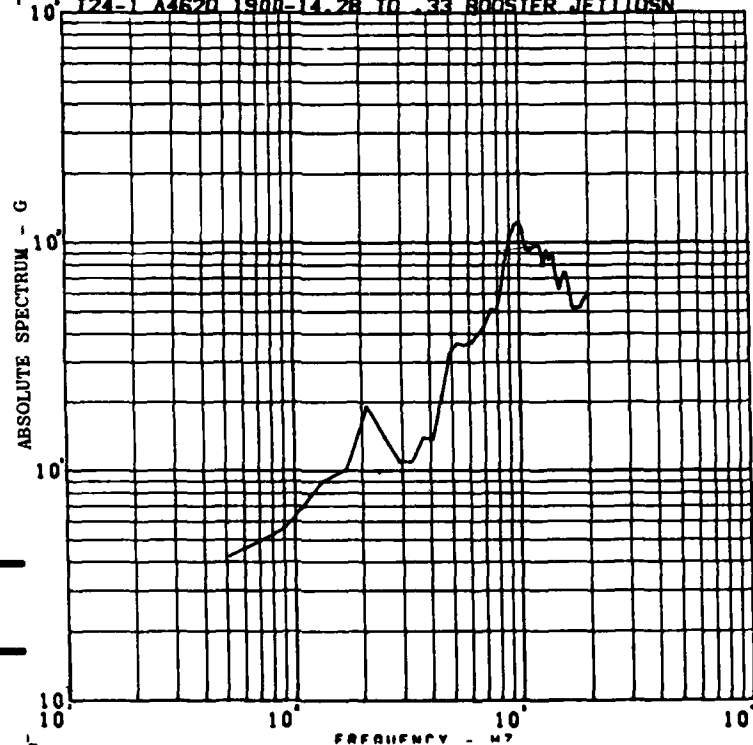


FIGURE 92

STATION 182 (LONGITUDINAL)

T24-1 A4620 1943-51.20 TO .30 REL. DRAG CHUTE

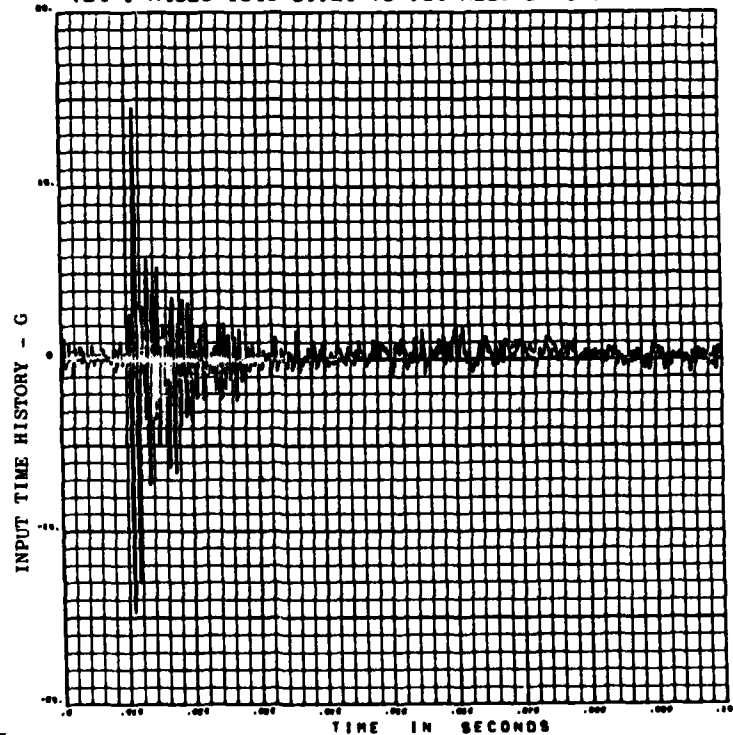


FIGURE 93

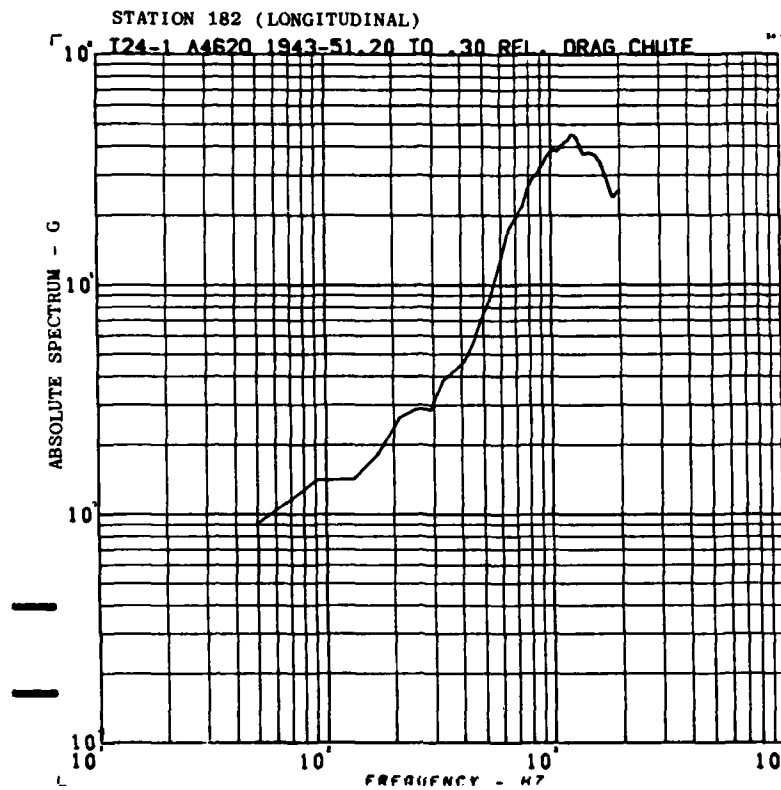


FIGURE 94

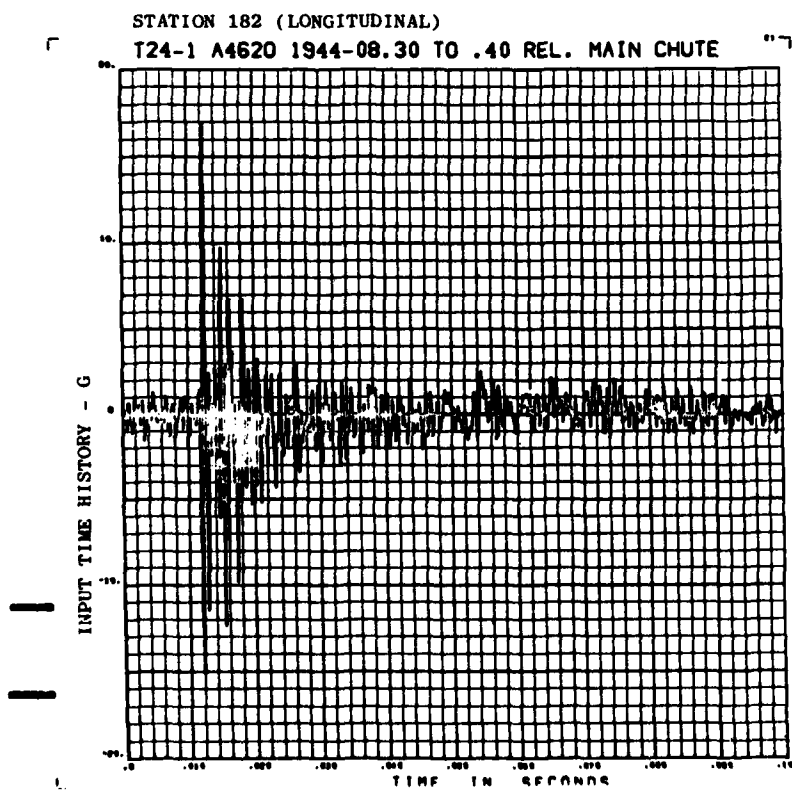


FIGURE 95

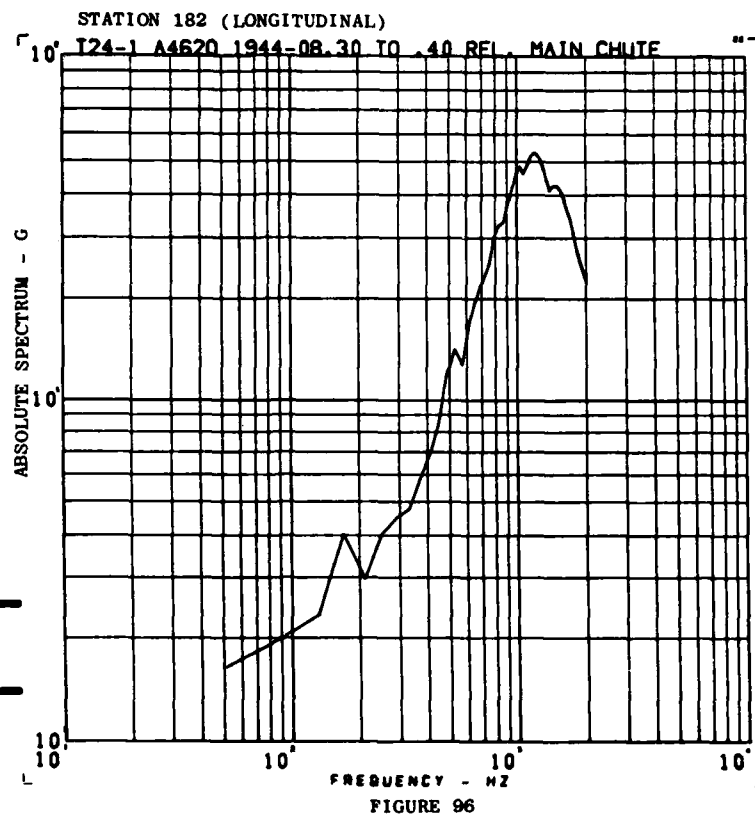


FIGURE 96

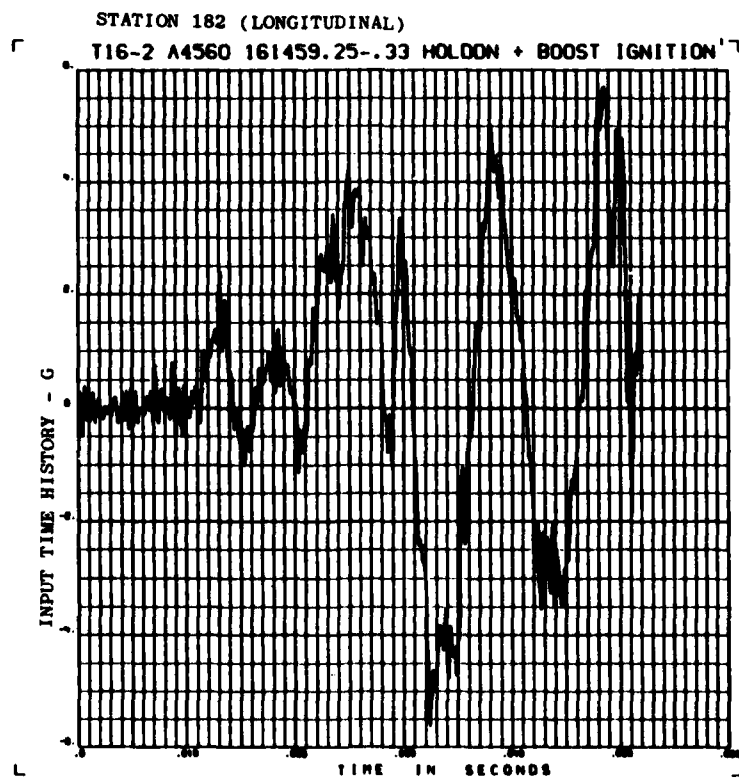


FIGURE 97

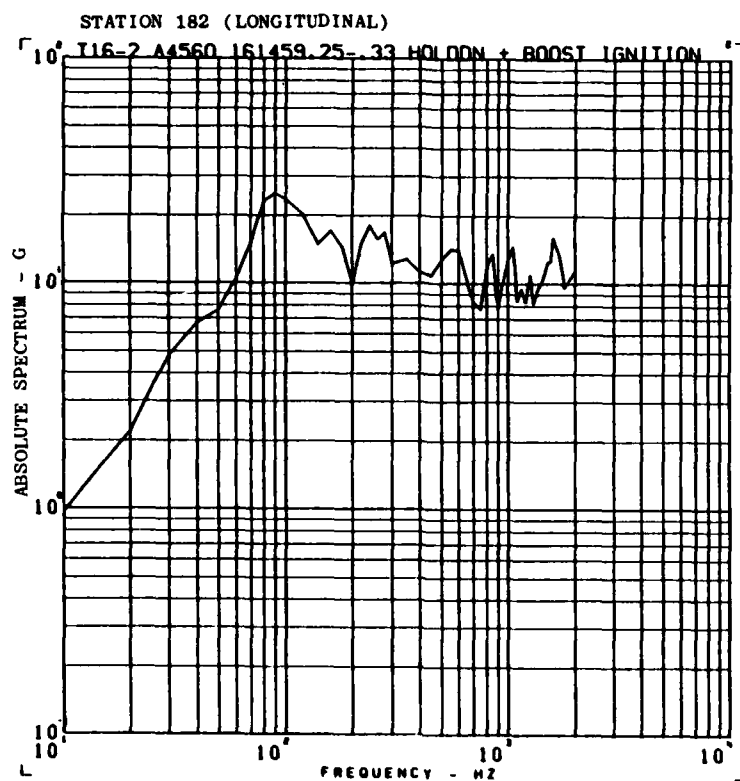


FIGURE 98

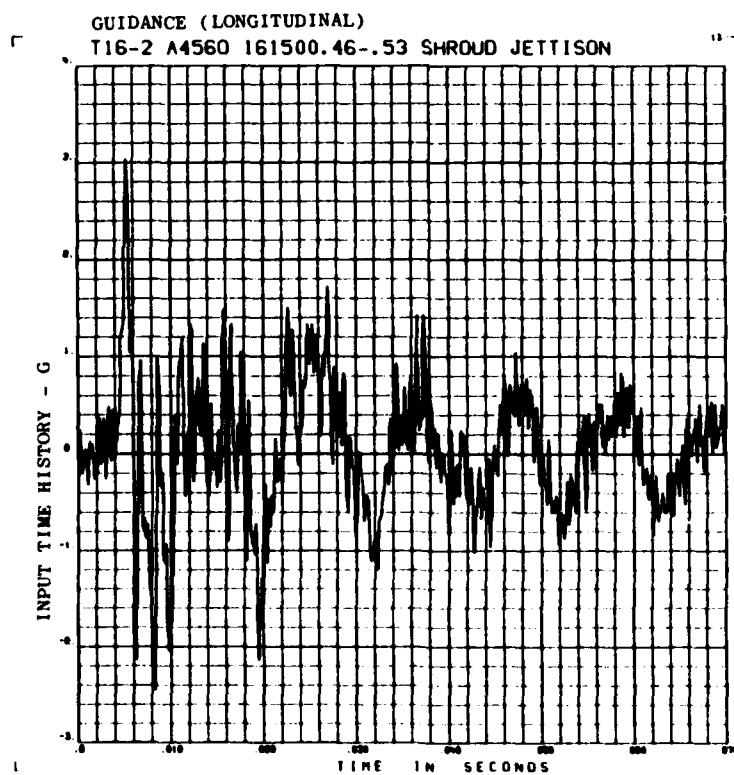


FIGURE 99

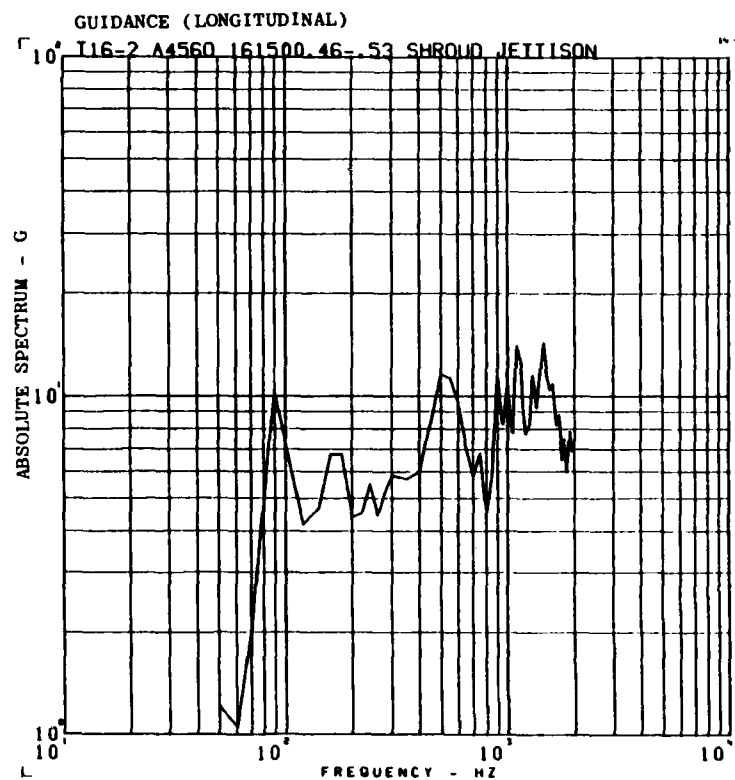


FIGURE 100

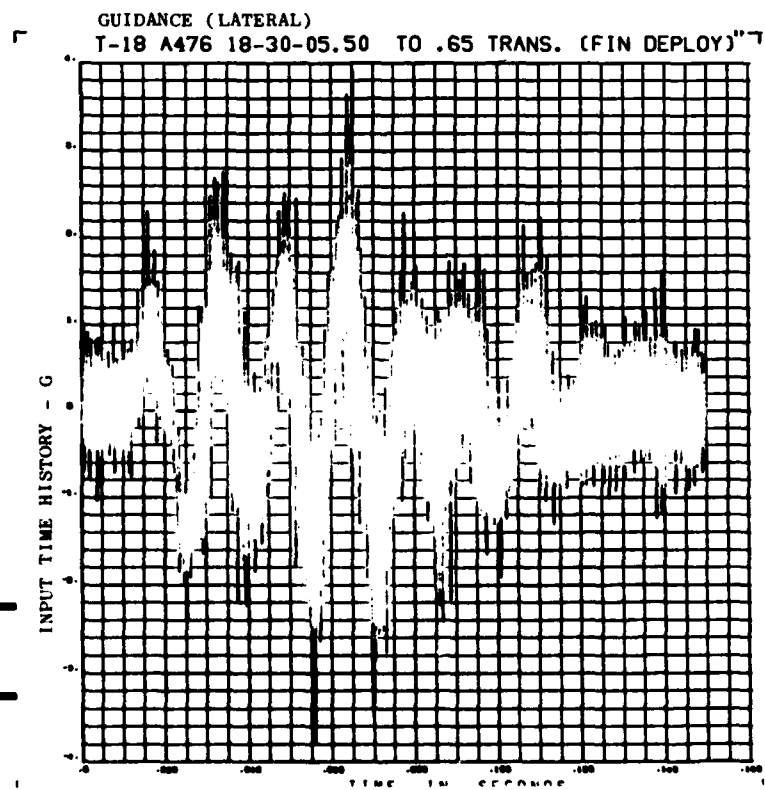
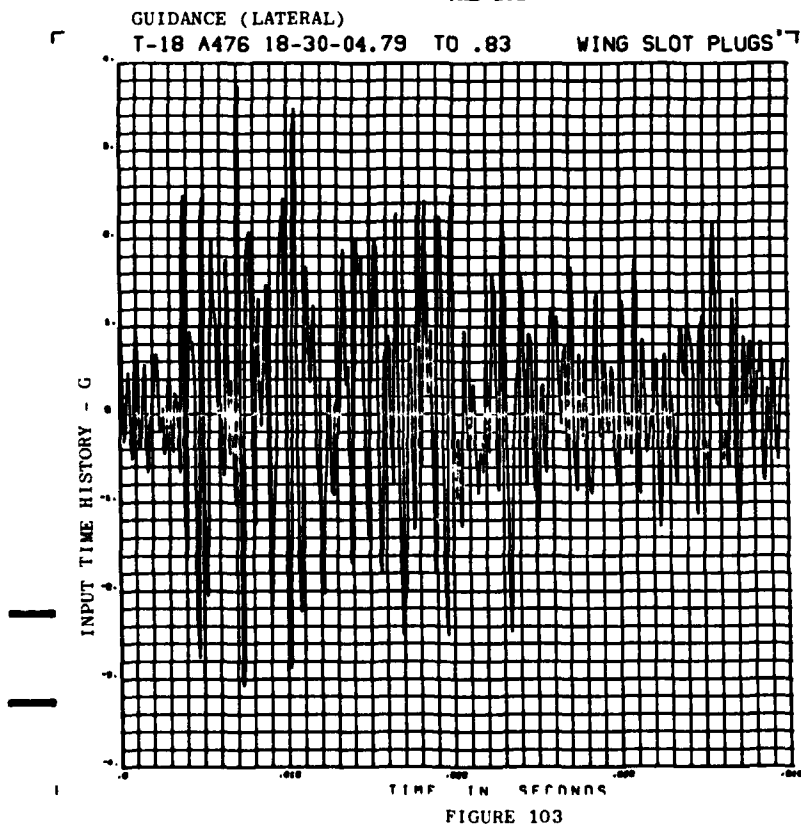
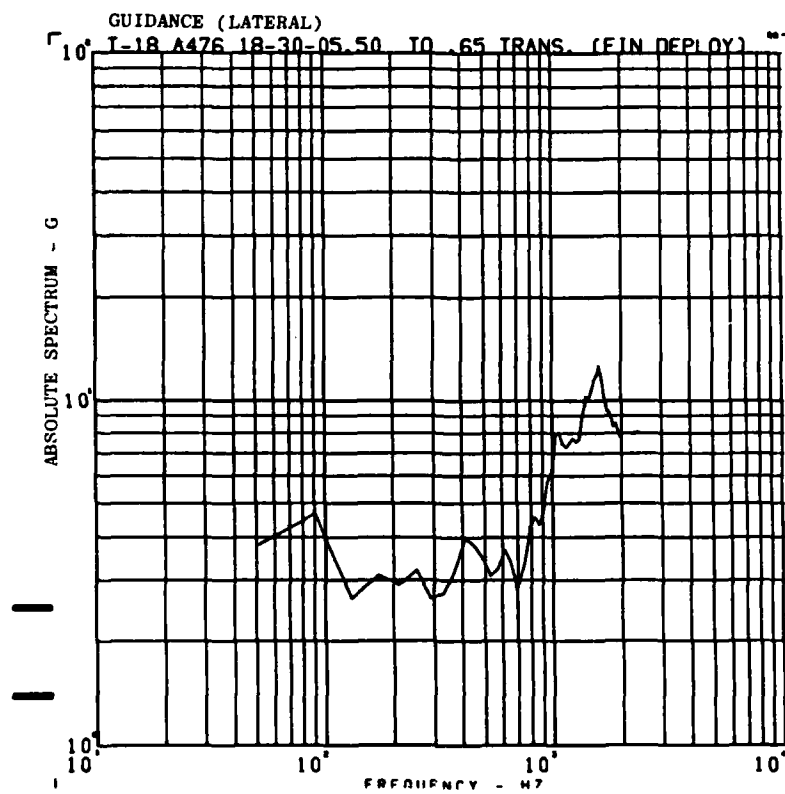


FIGURE 101



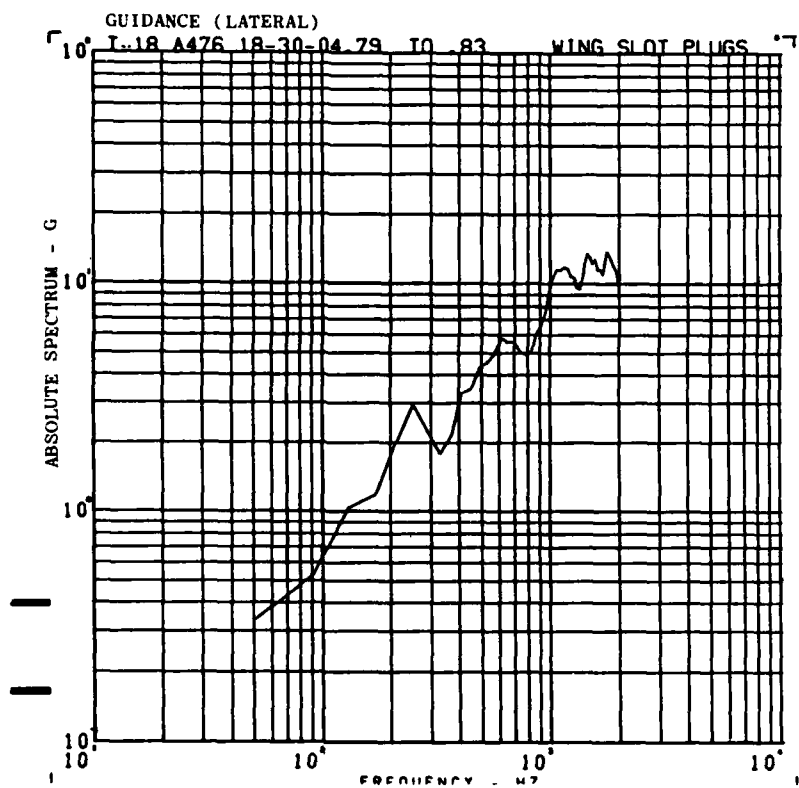


FIGURE 104

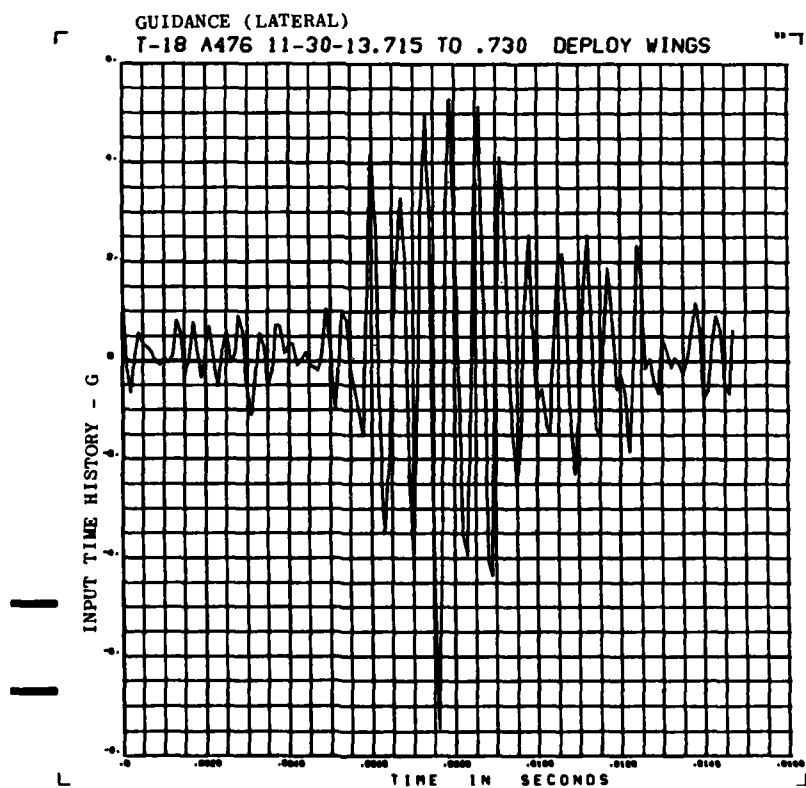


FIGURE 105

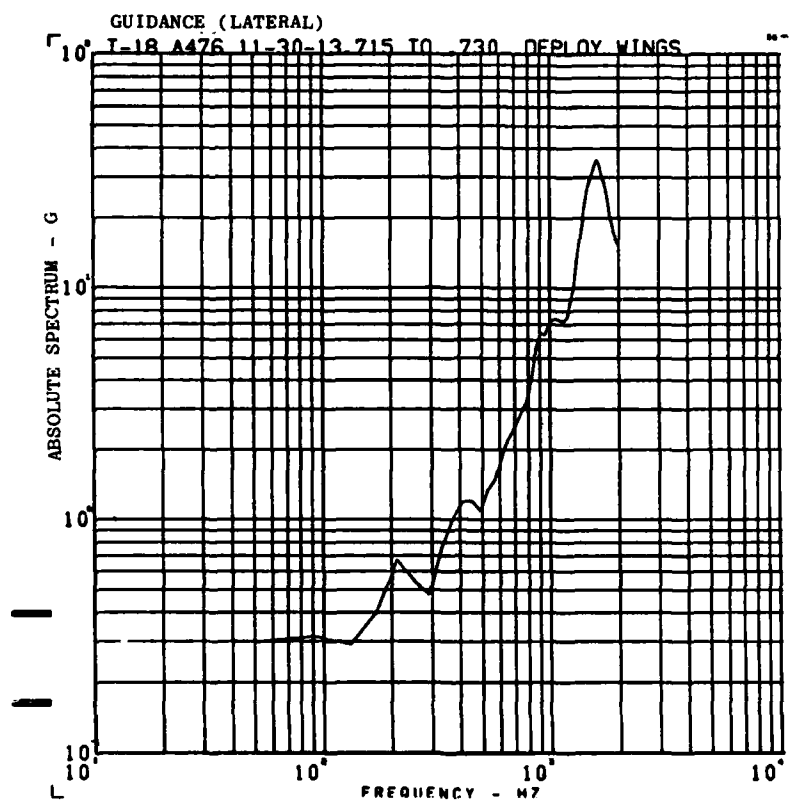


FIGURE 106

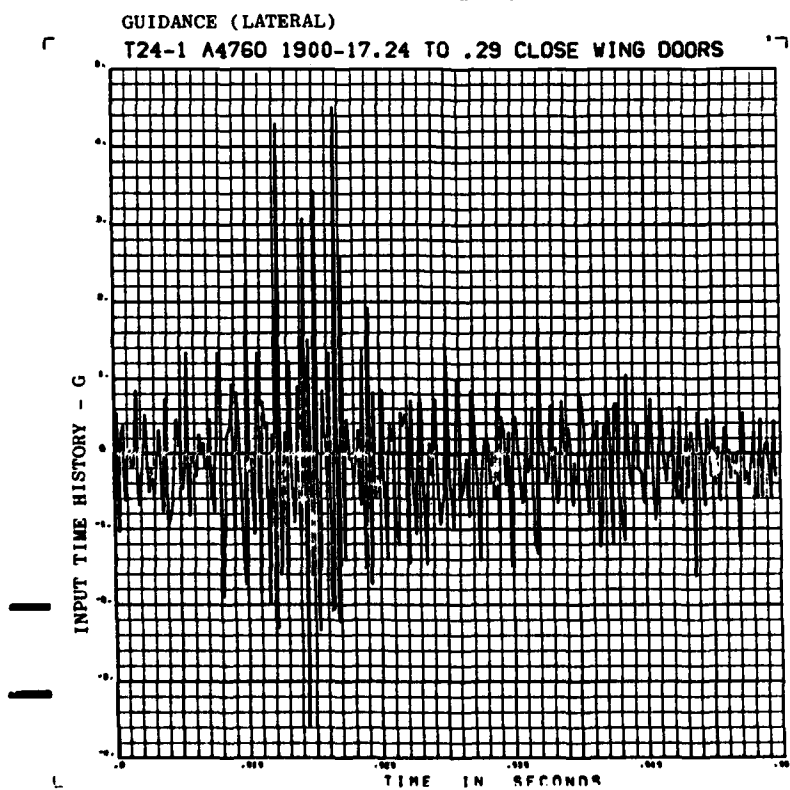


FIGURE 107

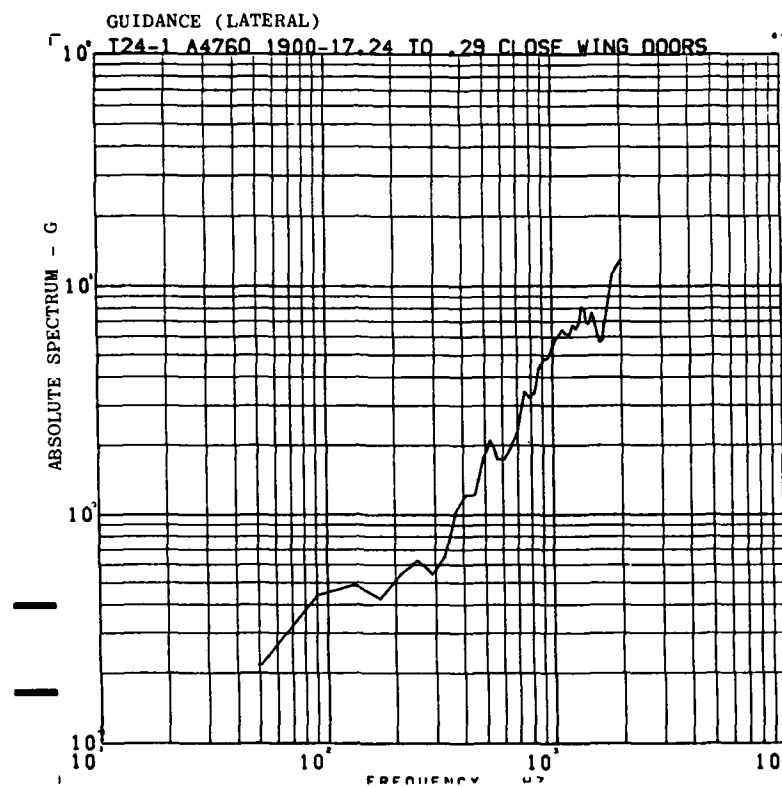


FIGURE 108

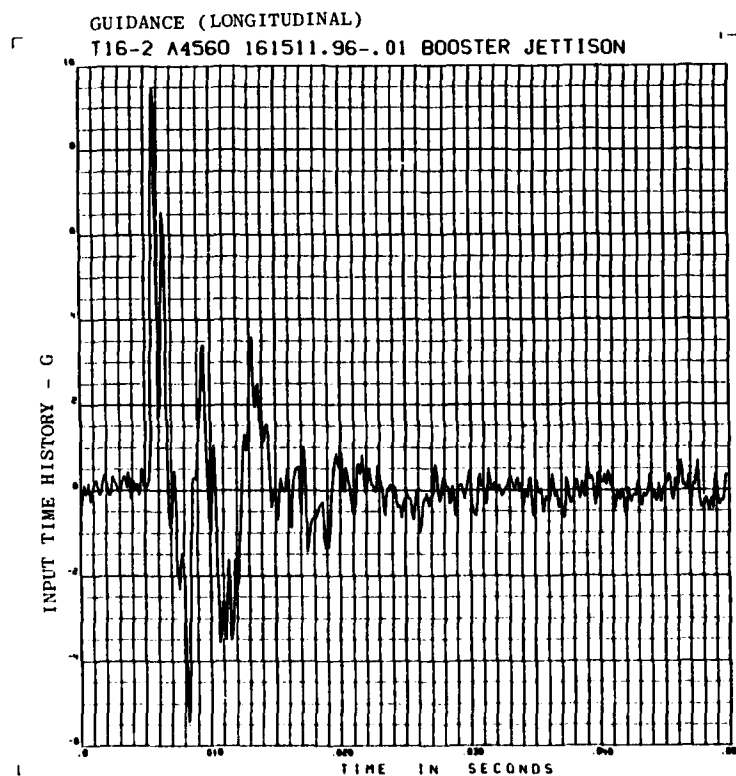
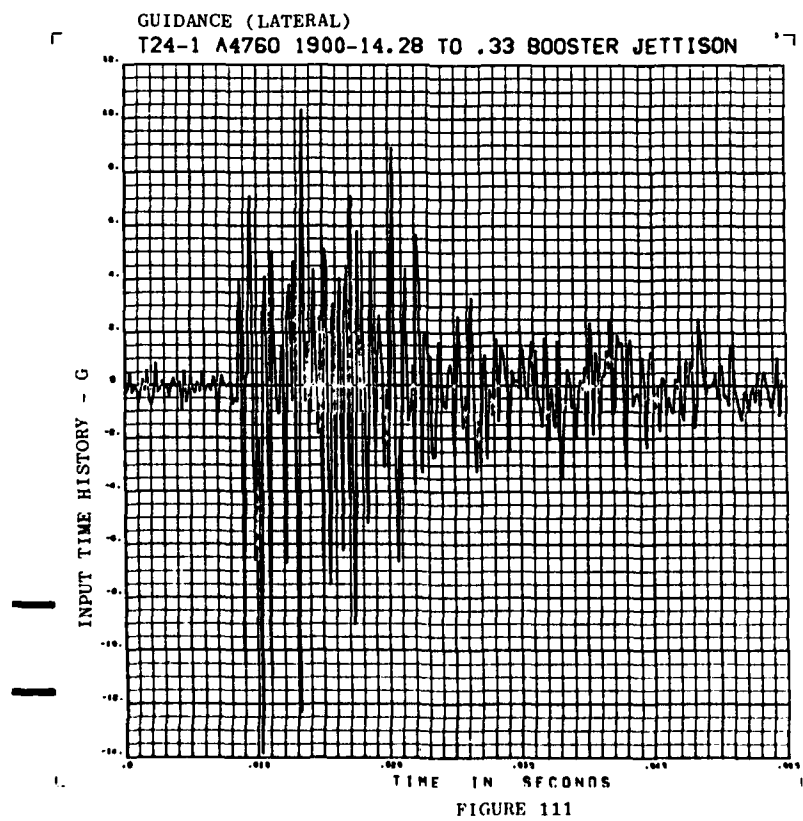
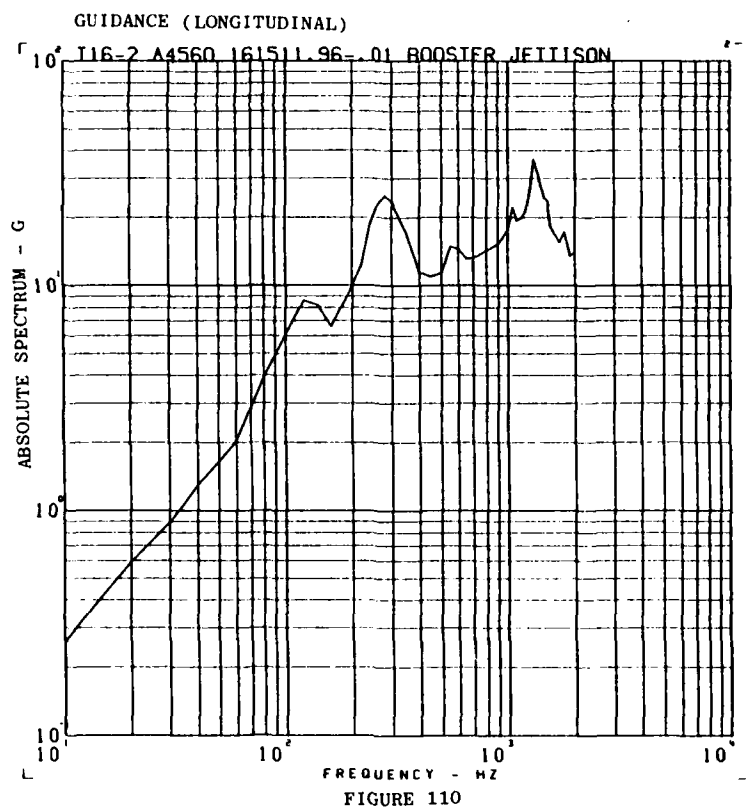


FIGURE 109



GUIDANCE (LATERAL)

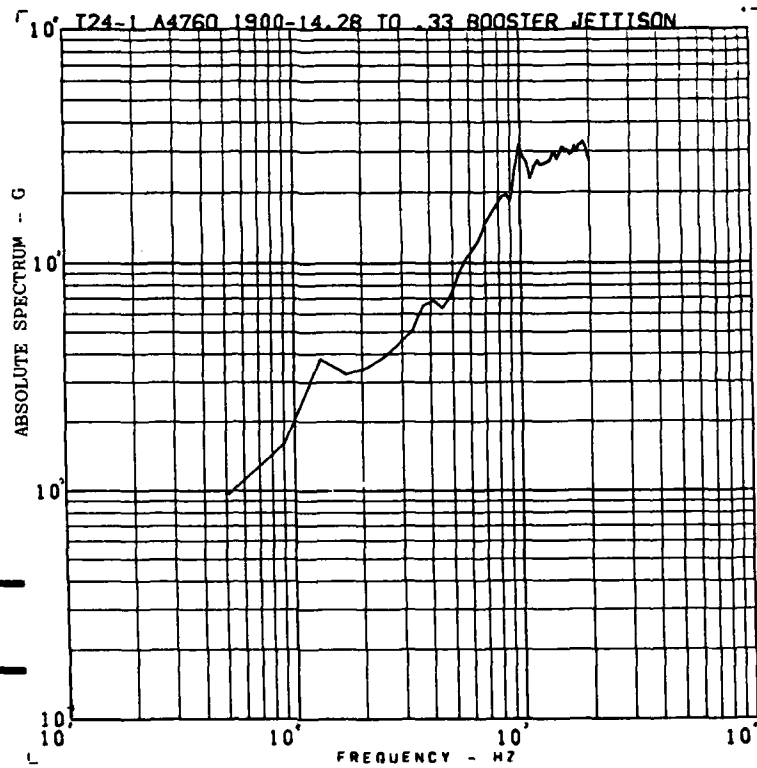


FIGURE 112

GUIDANCE (LATERAL)

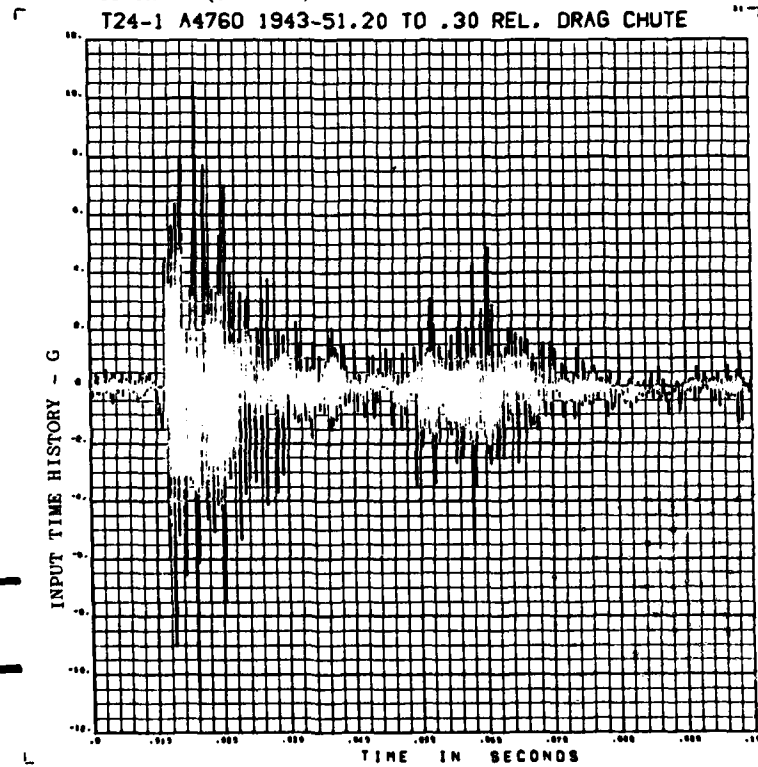
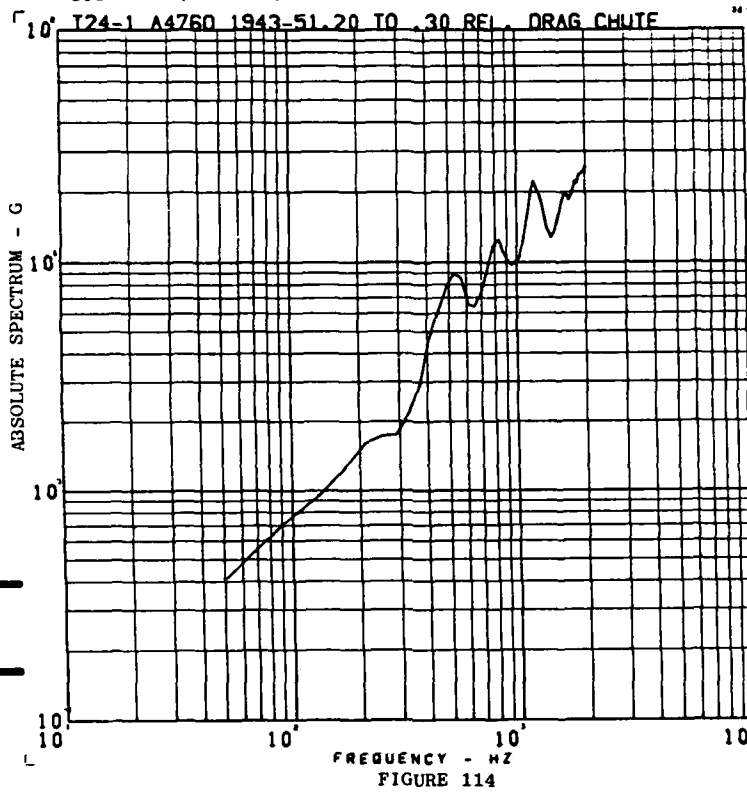
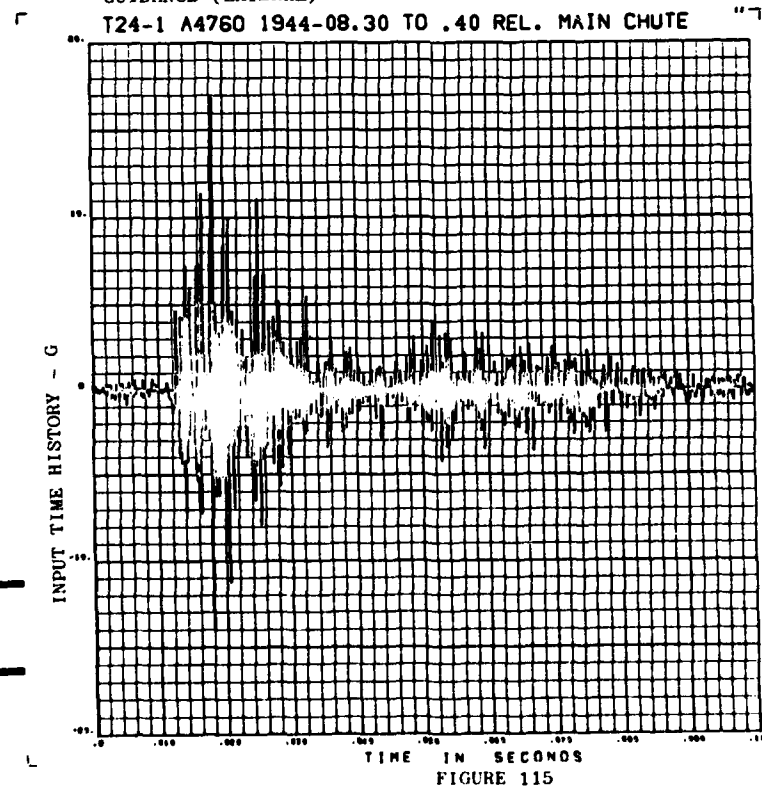


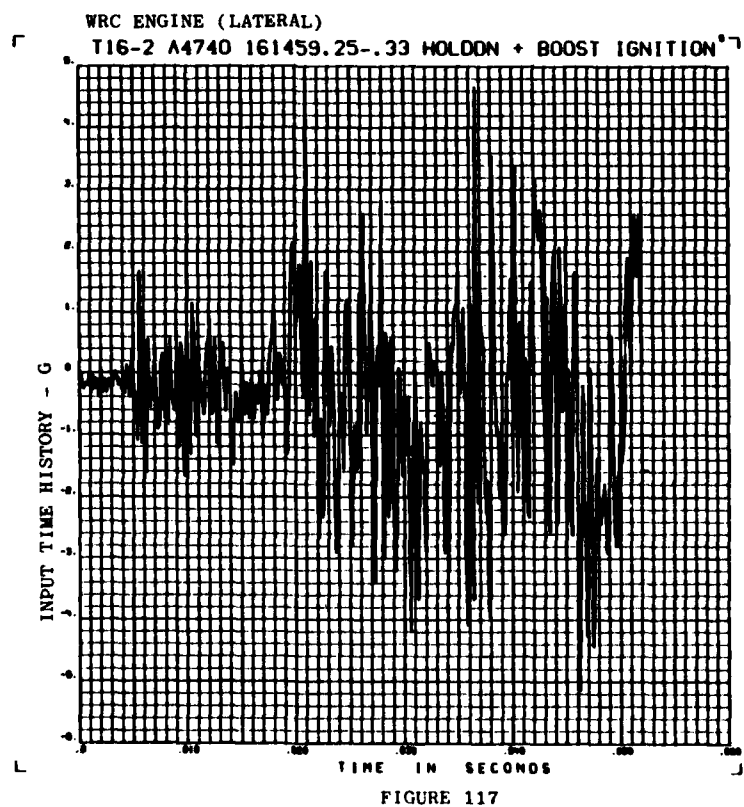
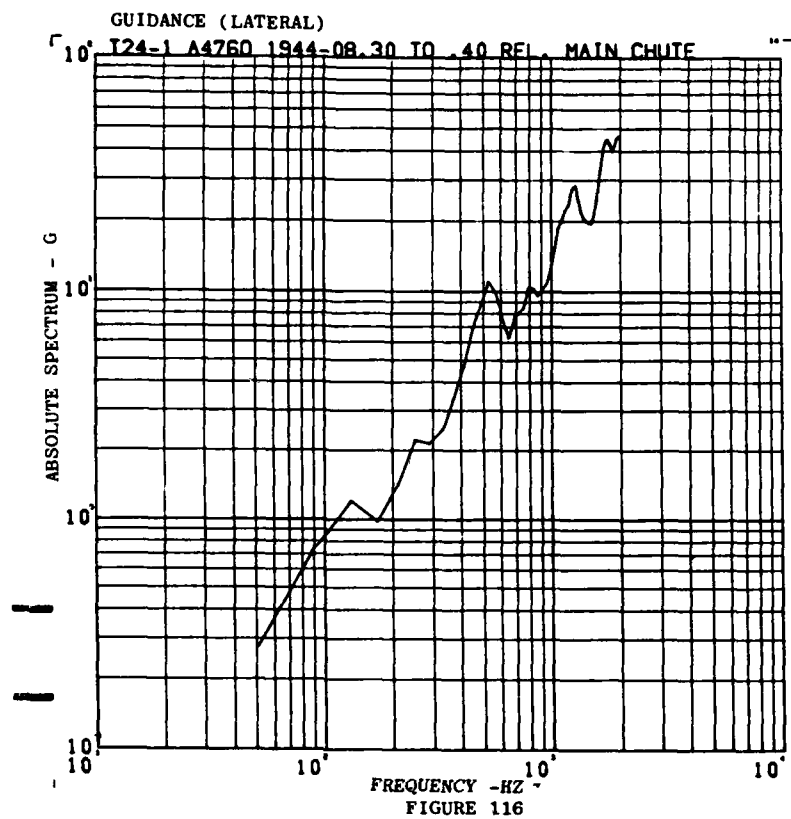
FIGURE 113

GUIDANCE (LATERAL)



GUIDANCE (LATERAL)





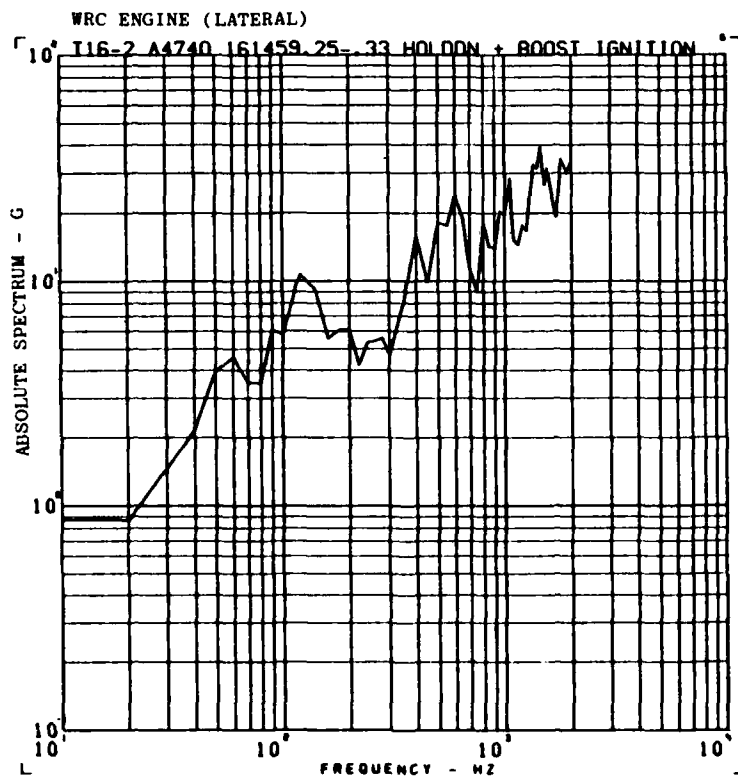


FIGURE 118

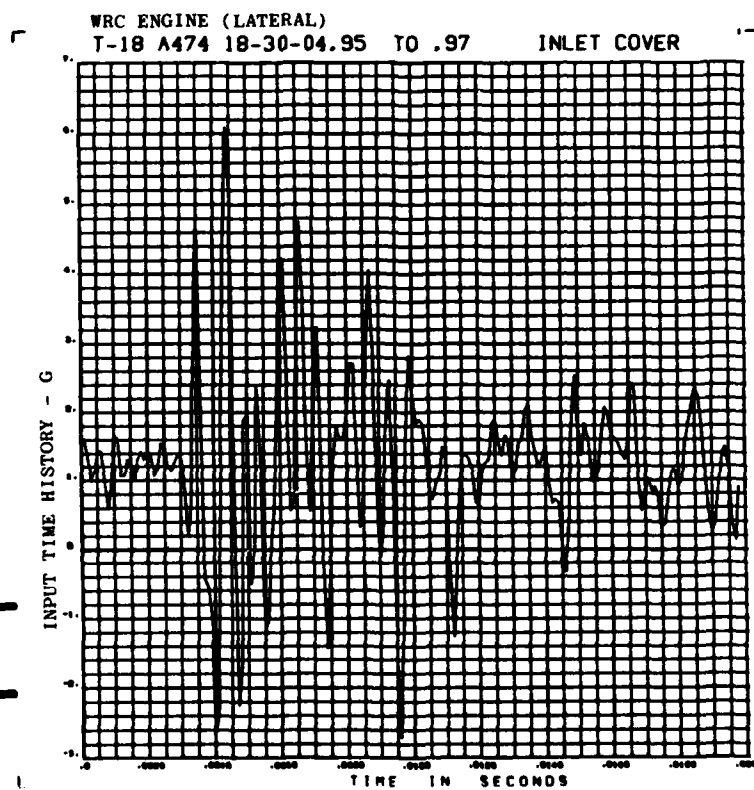


FIGURE 119

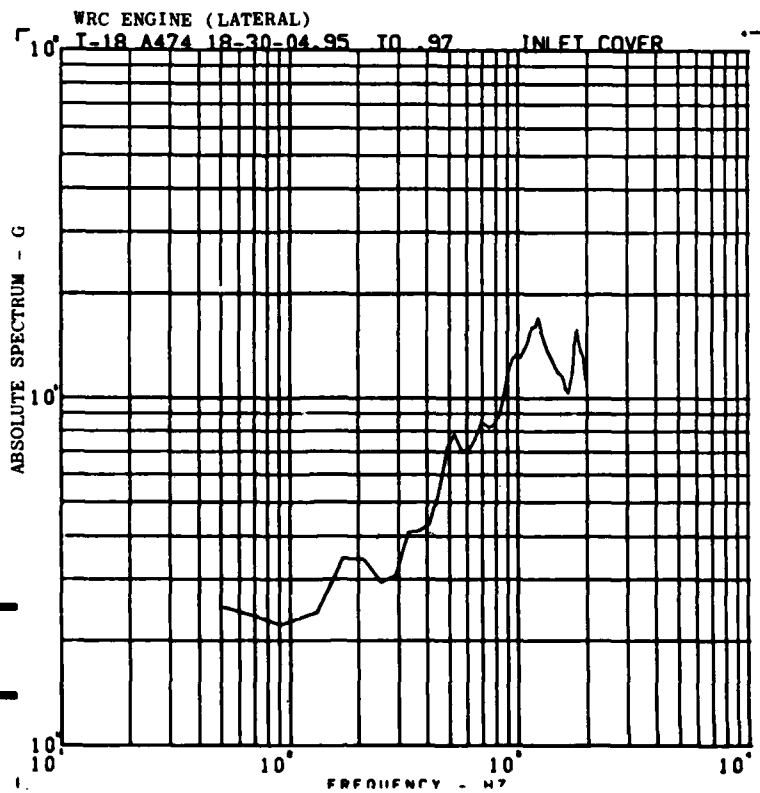


FIGURE 120

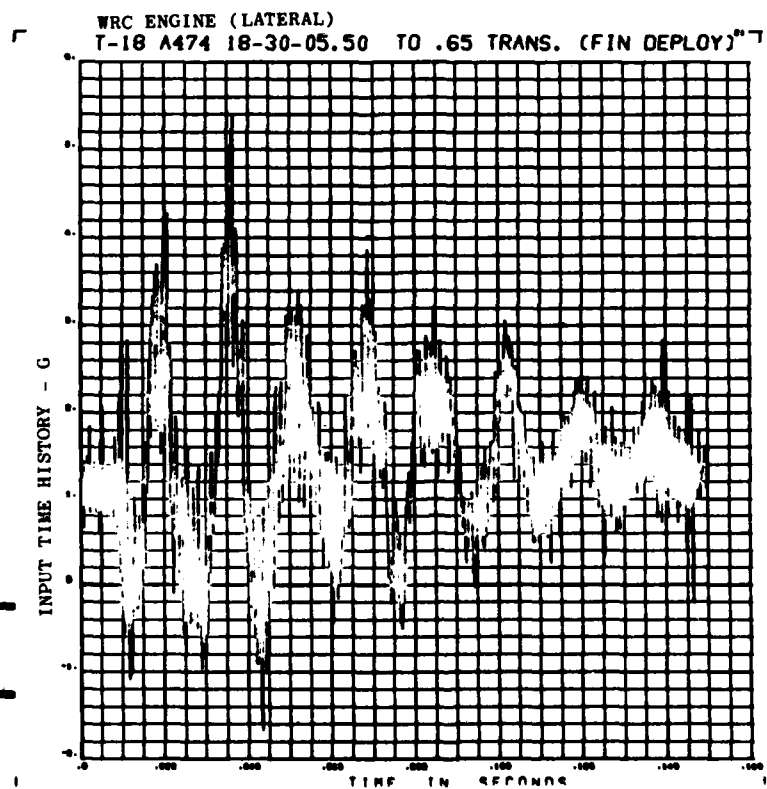


FIGURE 121

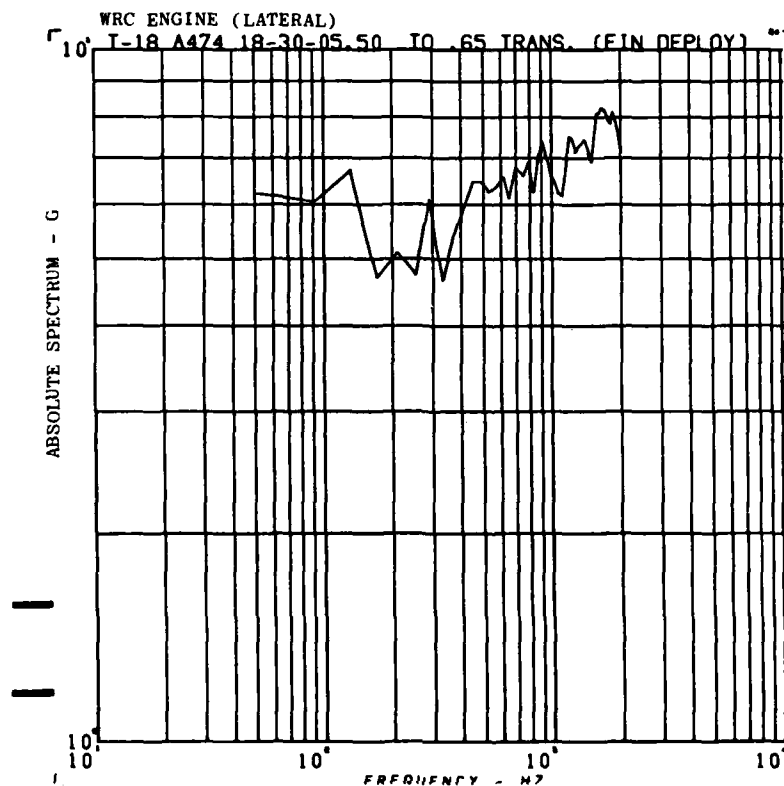


FIGURE 122

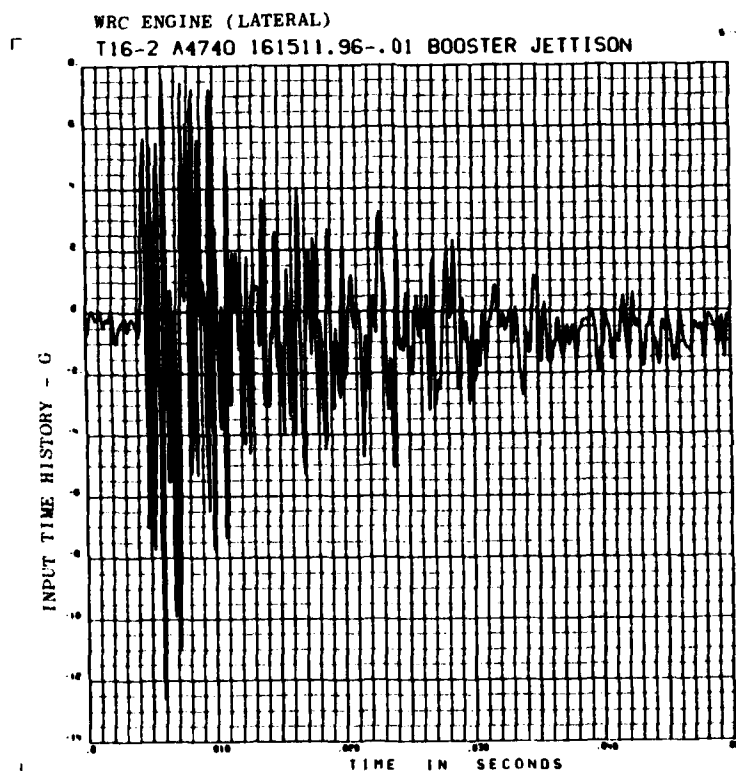


FIGURE 123

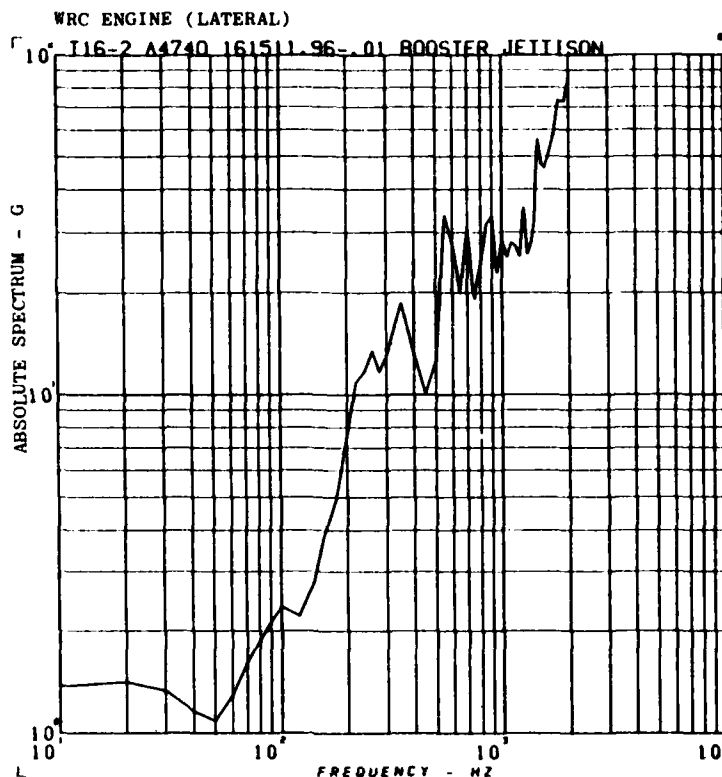


FIGURE 124

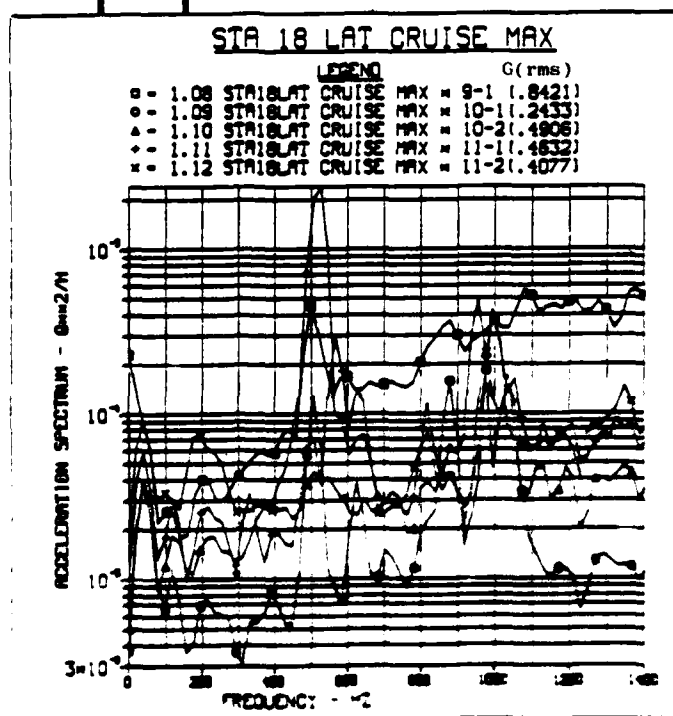


FIGURE 125

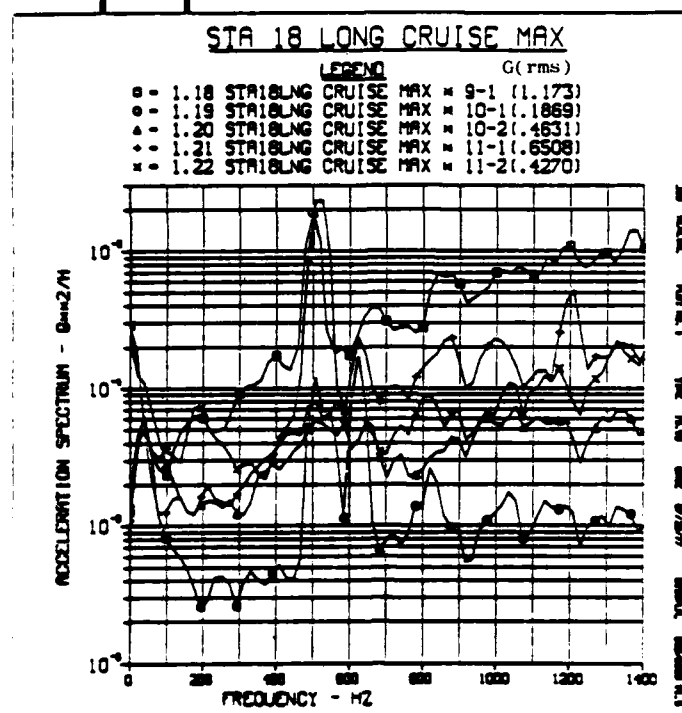


FIGURE 126

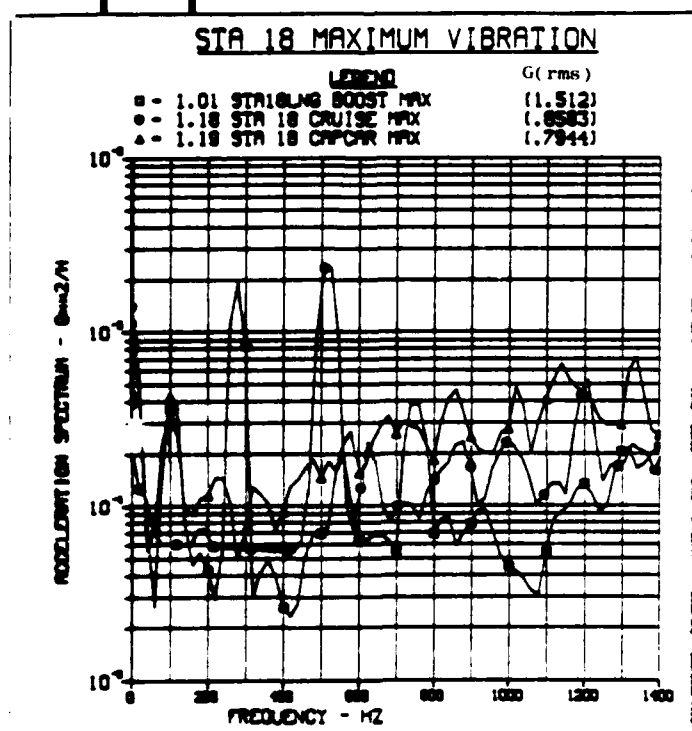


FIGURE 127

T12-3 OVERALL VIBRATION

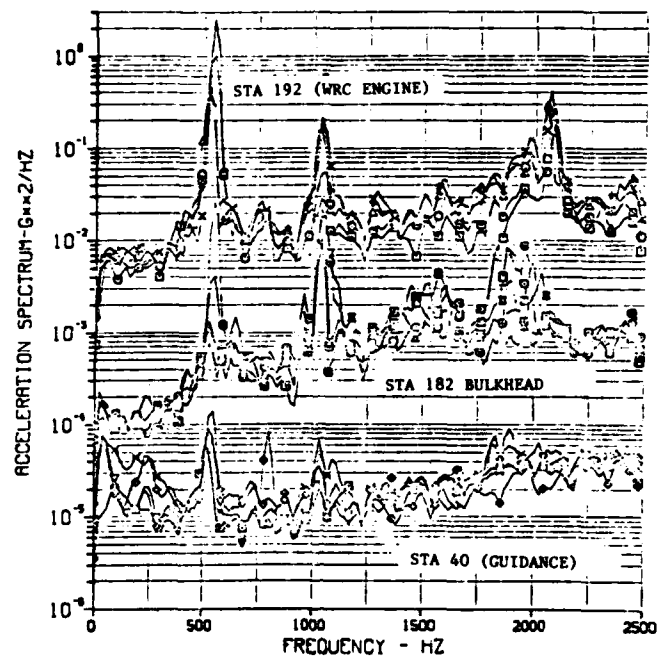


FIGURE 128

TEST PROGRAM TO DEVELOP VIBROACOUSTICS TEST CRITERIA
FOR THE GALILEO BUS

D.L. Kern/C.D. Hayes
JET PROPULSION LABORATORY
CALIFORNIA INSTITUTE OF TECHNOLOGY
PASADENA, CALIFORNIA

The Galileo spacecraft, to be launched on Shuttle/Wide Body Centaur, must be able to withstand random vibrations induced by the acoustic noise environment inside the Shuttle payload bay during liftoff and transonic/max Q events. In order to define random vibration test requirements for Galileo bus-mounted hardware, an extensive vibroacoustics test program was conducted on hardware available from the previous Voyager spacecraft development program. The Galileo test program consisted of acoustic tests on three configurations of the Voyager Dynamic Test Model bus and shaker random vibration tests on two flight-like bus equipment bay assemblies and one dummy equipment bay assembly. The primary goal of the acoustic tests was to define vibration levels at locations on the bus structure representative of inputs to bus equipment bay assemblies and to obtain response data on bus bay subassemblies for correlation with the vibration tests response data. The primary purpose of the vibration tests was to determine if the vibration tests excited subassembly responses at least as severely as the bus acoustic tests.

BACKGROUND

The Jet Propulsion Laboratory has been assigned by NASA the task to manage the Galileo program, an interplanetary spacecraft with a planned Jupiter orbit and probe deployment mission scheduled for launch via Shuttle/Wide Body Centaur in 1985. In support of this program, vibroacoustic test criteria have been developed for the spacecraft and assemblies. Due to the configuration similarities between Galileo and the Voyager spacecraft and the fact that the Galileo program is planning to use a significant amount of equipment inherited from the Voyager program, the initial assembly level random vibration test criteria was taken from the Voyager spacecraft program. A subsequent detailed analysis of the Voyager and Viking acoustic test data indicated that these test criteria were adequate, for the Shuttle payload bay liftoff acoustic environment, for all Galileo hardware except that mounted in the Galileo bus. For this bus mounted hardware, the adequacy was not established due to uncertainties in the test data. Therefore, in order to adequately define the random vibration

requirements for Galileo bus-mounted hardware, an extensive vibroacoustics test program was conducted on hardware which was available from the previous Voyager spacecraft development program. The test program consisted of acoustic tests on three configurations of the Voyager Dynamic Test Model (DTM) bus and shaker random vibration tests on two flight-like bus equipment bay assemblies and one dummy equipment bay assembly. The Voyager spacecraft DTM is shown in Figure 1 during Voyager program development acoustic tests.

ACOUSTIC TESTS DESCRIPTION

The Voyager DTM bus was selected as the test article for the acoustic tests because of its similarity to the Galileo bus. The two buses are nearly identical in configuration, except that the Galileo bus will have 8 equipment bays, whereas the Voyager DTM bus contains 10 bays. The bus outside diameters and the weights are similar (74 inches and 550 pounds for the Voyager bus and 63 inches and 500 pounds for Galileo). Figure 2 shows the Voyager DTM bus on



FIGURE 1. VOYAGER DTM SPACECRAFT ACOUSTIC TEST

its handling ring. Installation of electronic equipment in the bus bays is identical for the two spacecrafts. The electronic components are typically mounted in modules or on individual boards, which are referred to as subassemblies. All four edges of the subassemblies are attached by screws to the four sides of the bus bay. To install the subassemblies in a bus bay, they are attached by one edge to a handling fixture and the bus bay back shear plate is attached to the opposite edge of the subassemblies. The front shear plate of a bay is removed and the bay assembly is inserted in the bay. The back shear plate and the upper and lower edges of the subassemblies are then attached to the bus by screws from the outside of the bay, the handling fixture is removed, the front shear plate is replaced, and the front edges of the subassemblies are screwed down. Figure 3 shows an assembly mounted on the handling fixture, with back shear plate attached, ready to be installed in a bay of the Voyager DTM bus.

The primary goal of the acoustic tests was to define vibration levels at locations on the bus structure representative of inputs to bus equipment bay assemblies and to obtain response data on bus bay subassemblies for correlation with the vibration tests response data. In order to gain confidence that the measured vibration responses on the test specimen would actually represent responses measured on a full-up Galileo spacecraft, additional evaluations were made. These evaluations were to resolve apparent discrepancies in previous Voyager acoustic test data and to define and understand differences between the Voyager DTM and the Galileo spacecrafts which could affect the bus dynamic response characteristics. To resolve Voyager test data discrepancies, an evaluation and comparison of DTM and Proof Test Model (PTM) spacecraft configurations was conducted. The difference between these configurations is that the PTM has thermal blankets, flight equipment, and wire harnesses while the DTM has



FIGURE 2. VOYAGER DTM BUS ON HANDLING RING - ACOUSTIC TEST CONFIGURATION "C"

no blankets, dummy equipment, and no harnesses. The two major differences between Voyager and Galileo evaluated in the tests are that the Voyager DTM bus has a four point attachment to the supporting truss compared to an eight point attachment for the Galileo bus and that the Voyager DTM has a rigid 12 foot diameter epoxy graphite dish antenna, whereas the Galileo will have a 15 foot diameter metallic mesh dish antenna which will be folded up during launch. Also evaluated was response linearity with acoustic level since Galileo acoustic test requirements are 4dB higher overall than Voyager test levels.

Five acoustic test runs on three configurations of the Voyager DTM bus were conducted in the JPL 10,000 cubic foot reverberant acoustic chamber. The bus was supported in the chamber at either four or ten points on a handling ring. All three bus configurations utilized flight-like equipment, including wire harnessing, in six bays and dummy (mass mockup) equipment in the remaining four bays. Six microphones surrounding the test article were used to control the acoustic levels in the chamber and additional microphones monitored acoustic levels in the chamber and inside bus bays. Over one hundred accelerometers were used to monitor the



FIGURE 3. BAY ELECTRONICS ASSEMBLY READY TO BE INSTALLED IN THE VOYAGER DTM BUS

test article response during the acoustic tests. Slightly more than one half of these accelerometers were located internal to the bays on equipment and were intended primarily for correlation with the shaker vibration tests. The remainder of the accelerometers were mounted on the bus external structure or on the Voyager high gain antenna.

Acoustic test levels and durations were kept to the minimum required to achieve the test objectives since some of the test hardware was of flight quality and could be used by Galileo or future projects. Three acoustic test spectrums were run: Voyager qualification spectrum (143 dB overall), Galileo qualification spectrum (147 dB overall), and Galileo qualification spectrum minus 10 dB (137 dB overall). The Voyager qualification spectrum includes a 6 dB margin over maximum expected flight levels within the payload shroud of the Titan-Centaur launch vehicle. The Galileo qualification spectrum includes a 4 dB margin over maximum expected flight levels within the payload bay of the Space Shuttle. The Shuttle payload bay maximum expected flight levels assumed for Galileo are based on model and full scale acoustic tests conducted prior to the first STS flight and differ from acoustic levels specified by Johnson Space Center (JSC). The acoustic test spectrums are presented in Figure 4.

Table 1 summarizes the configurations and test spectrums employed for the acoustic test runs. Configuration A was intended to simulate the Voyager spacecraft DTM. The DTM bus was mounted by a four point attachment to the handling ring and the Voyager DTM high gain antenna dish and supporting structure was installed on top of the bus. Thermal blankets were not included. Figure 5 shows Configuration A in the acoustic chamber. Configuration B was intended to simulate the Galileo spacecraft. The Voyager DTM bus was mounted by a ten point attachment to the handling ring and mockup thermal blankets were installed. The mockup blankets consisted of a 2 mil thick outer layer of teflon and a 1 mil inner layer of teflon, enclosing 21 layers of 7 mil dacron net and 20 layers of 0.25 mil mylar in alternating layers. The surface density weight of the mockup blankets of .129 pounds per square foot matched the expected weight of the Galileo blankets. The blankets were tightly sewn together and totally enclosed the bus, with only minimum clearance around attachments to the handling ring. Since the Galileo high gain antenna dish is of a metallic mesh construction and thus is expected to have little effect on the bus vibration levels relative to the effect from the rigid Voyager antenna dish, no antenna was installed for configuration B. Configuration B is pictured in Figure 6. Configuration C, shown in Figure 2, was the same as Configuration B, except that the thermal blankets were removed. None of the acoustic test configurations included the booms and trusses (other than the antenna on Configuration A) attached to both the Voyager and the Galileo spacecraft buses.

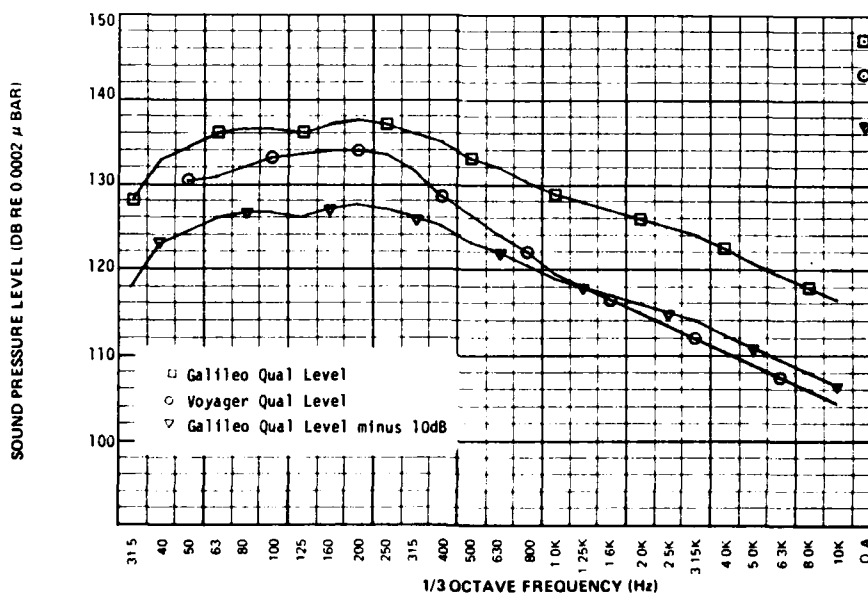


FIGURE 4. ACOUSTIC TEST SPECTRUMS

Run No.	Test Configuration	Test Spectrum	Overall Level
1	A (Voyager)	GLL (Qual -10 dB)	127 dB
2	A (Voyager)	Voyager (Qual)	143 dB
3	B (Galileo)	GLL (Qual -10 dB)	137 dB
4	B (Galileo)	GLL (Qual)	147 dB
5	C (VGR/GLL)	GLL (Qual -10 dB)	137 dB
GLL = Galileo VGR = Voyager			

TABLE 1. ACOUSTIC TEST RUNS



FIGURE 5. ACOUSTIC TEST CONFIGURATION "A" - VOYAGER DTM BUS AND HIGH GAIN ANTENNA ON HANDLING RING

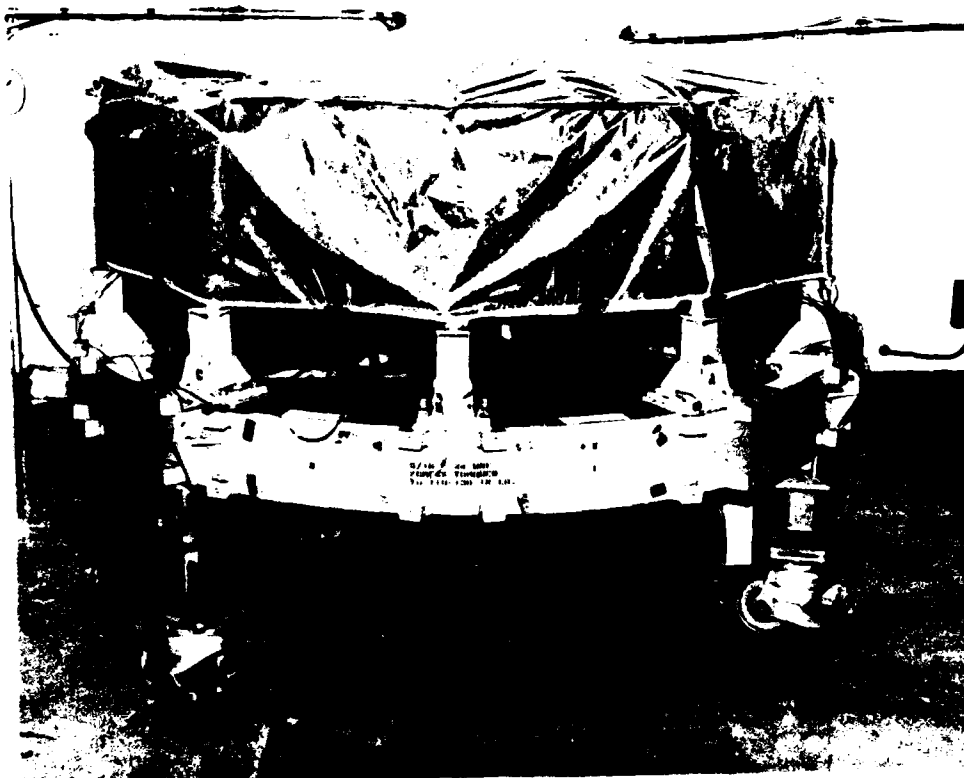


FIGURE 6. ACOUSTIC TEST CONFIGURATION "B" - VOYAGER DTM BUS WITH MOCK-UP
THERMAL BLANKETS ON HANDLING RING

VIBRATION TESTS DESCRIPTION

Random vibration tests were conducted on three of the bus bay assemblies in a special bay fixture. The primary purpose of the tests were to determine if the vibration tests excited subassembly responses at least as severely as the bus acoustic tests. The special bay fixture, which was also used for Voyager bus assembly level vibration qualification tests, is necessary since the bus assemblies are not self-contained; the bus bay structure provides the only support for the individual subassemblies. The configuration of the special bay fixture is similar to the bus bays, except that the fixture walls are stiffer and heavier to avoid excessive deflections across the fixture due to dynamic amplifications. The special bay fixture mounts on a rigid test fixture along the edges of both the front and back shear plates. Figure 7 shows a bus bay assembly undergoing vibration testing.

Two of the bus assemblies vibration tested were flight-like, including wire harnesses, although power was not on. One of the flight-like assemblies, shown in Figure 8, consisted only of modules. The modules are of various sizes and shapes and are machined from solid blocks of aluminum. The other flight-like assembly, shown in Figure 9, included both modules and boards. The boards are made of 0.25 inches thick honeycomb approximately 7 by 16.5 inches in dimension with 0.015 inches thick aluminum skin on either side. The third bus assembly vibration tested was a dummy (mass mockup). The dummy subassemblies consisted of flight-like boards with brass disks attached to simulate the mass of the components. The dummy assembly is shown in Figure 10. The special bay fixture was rigidly attached to an electrodynamic shaker and random vibration tests were conducted in three

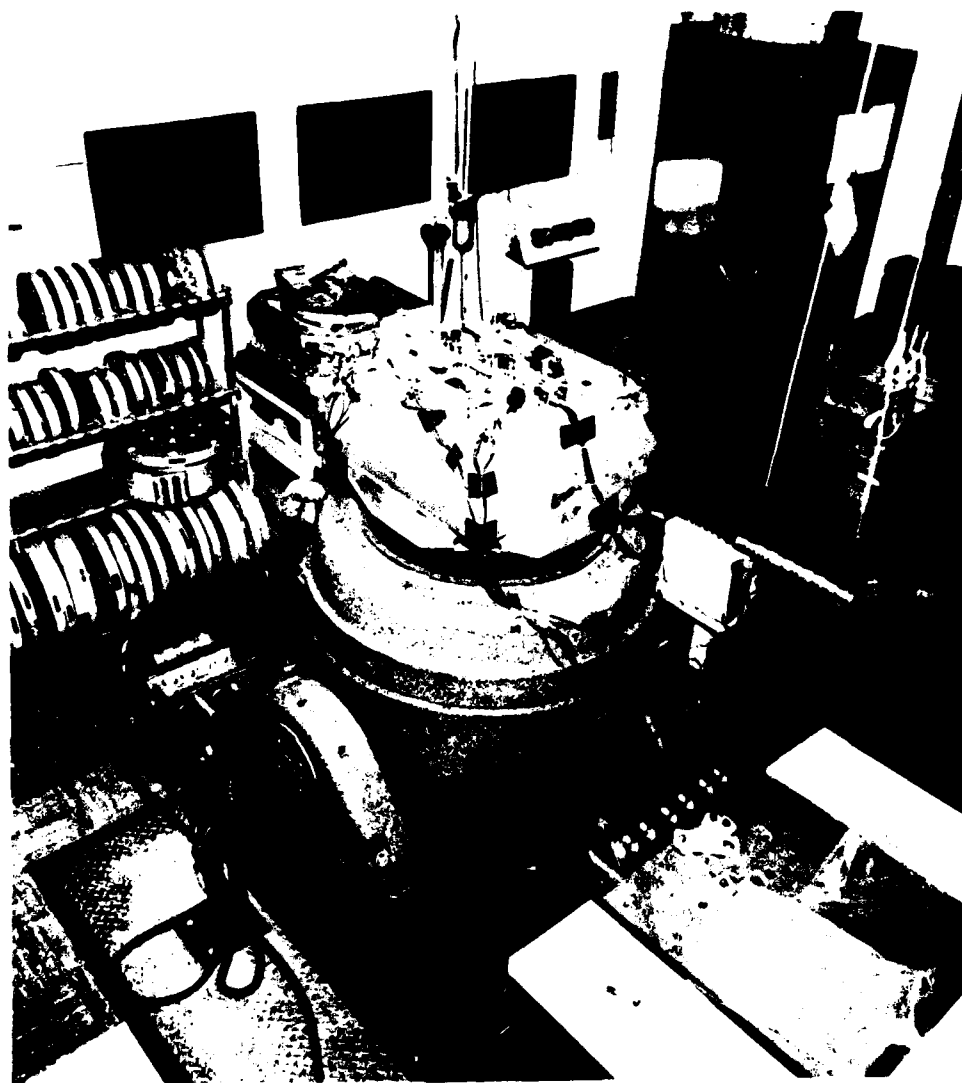


FIGURE 7. Bus Assembly Undergoing Vibration Testing

axes. The tests were controlled by averaging four accelerometers located at each of four corners on the rigid test fixture. The corners of the fixture are intended to represent the corners, or hard points, of the bus. The dummy bus bay assembly was vibrated at the initial Galileo bus assembly qualification levels and at 10 dB below qualification levels (qualification levels contain a 4dB margin over maximum expected flight environments). The two flight-

like assemblies, which are consigned for use in the Galileo program, were tested only at 10 dB below qualification levels to avoid potential damage. The random vibration test levels are shown in Table 2. Test times were limited to 30 seconds per run. Responses of the subassemblies were monitored with accelerometers at the same locations recorded during the bus acoustic tests.

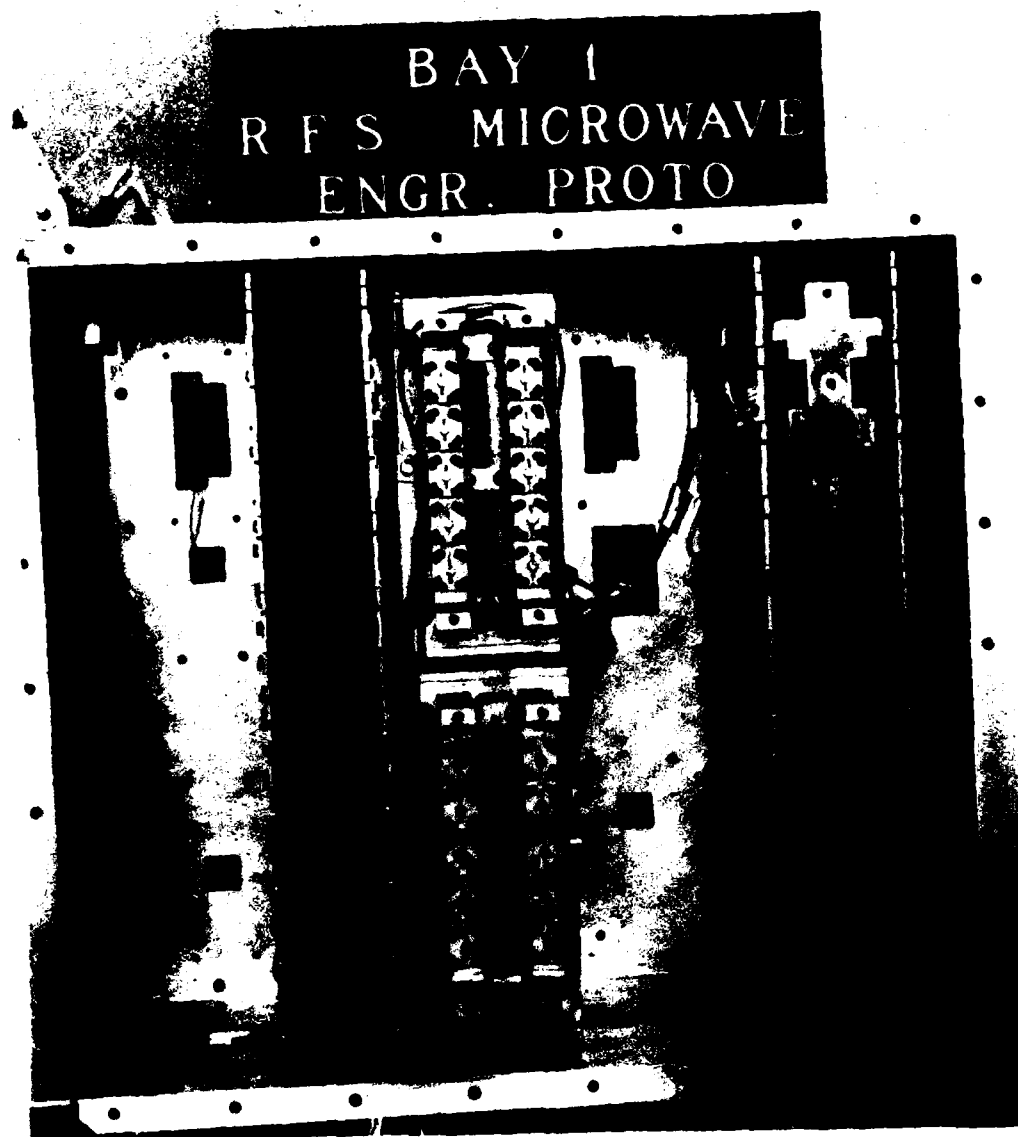


FIGURE 8. FLIGHT-LIKE BUS ASSEMBLY CONSISTING OF MODULES

DATA REDUCTION AND ANALYSIS

Microphone data from the tests were reduced to 1/3 octave band sound pressure levels from 31.5 to 10,000 Hz. The acoustic data were also reduced to pressure spectral density using 16 Hz bandwidths from 16 to 2000 Hz. Accelerometer data were reduced to acceleration spectral

density with 16 Hz bandwidths from 16 to 2000 Hz. The frequency domain vibration and acoustic data was then converted from analog to digital for evaluation using a statistical analysis and data display computer program. Data below 50 Hz was truncated due to a lack of reverberant chamber low frequency test capability.

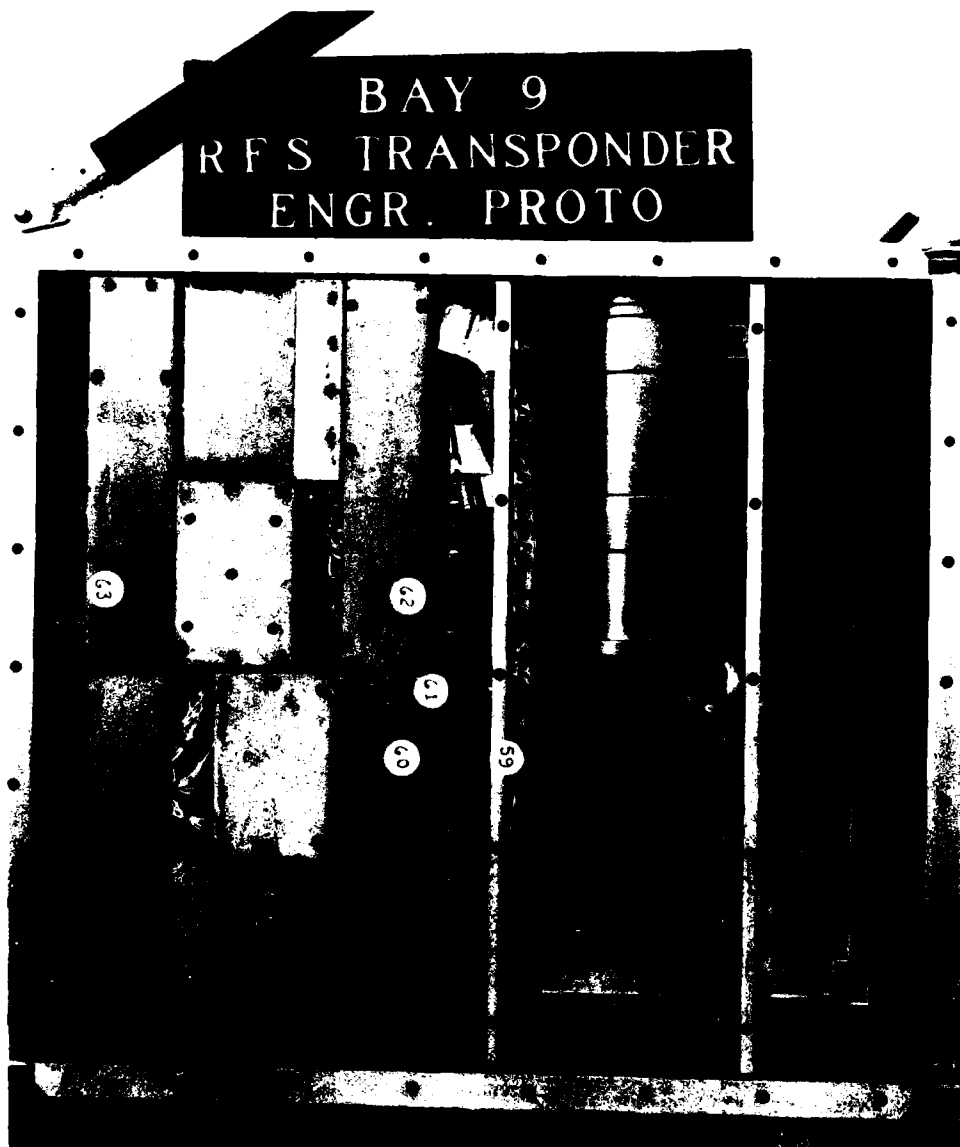


FIGURE 9. FLIGHT-LIKE BUS ASSEMBLY CONSISTING OF BOTH MODULES AND BOARDS

Vibration response data from both the acoustic and vibration tests were normalized to test input specifications to account for test control variances. Basically, two types of data analyses were performed. The first was averages of various groups of accelerometer data. Variances were also computed. This analysis serves to compare the statistical average levels of a group of response data to another group of data or to a specification, but does not provide information on the changes in distribution of responses from one test run to another. For comparisons of the responses for two test runs, an additional data analysis procedure was employed. The response data from one test run

was divided by the data from another test run on an accelerometer by accelerometer basis. The average and variances of the ratios of the two test runs were then computed for a group of accelerometers. This method of analysis provides some statistical information on the variations in response ratios with respect to location, but can possibly be misleading where the peak response frequencies shift between test runs. Also, knowledge of relative response magnitudes between frequency regions are lost with presentation of average response ratios. Both analysis methods were employed where considered appropriate.



FIGURE 10. DUMMY (MASS MOCK-UP) BUS ASSEMBLY CONSISTING OF BOARDS

ACOUSTIC TESTS RESULTS

The five acoustic test runs allowed various comparisons which provide a means of evaluating apparent discrepancies in past spacecraft acoustic test programs and which provide confidence in the validity of applying the test results to the real Galileo spacecraft. Evaluations made from the data were response linearity with acoustic level, effect of thermal blankets, differences between flight-like and dummy assemblies, effect of the antenna and the bus attachment configurations, and adequacy of the current Galileo bus assembly vibration test requirements. The results of these evaluations are discussed below.

Response Linearity

Vibration response linearity was evaluated from acoustic test Runs 3 and 4 (see Table 1). Since bus bay assembly shaker vibration tests on Voyager were controlled at the corners of the rigid test fixtures, only accelerometers on or near the corners, or hard points, of the bus were used for this evaluation. Runs 3 and 4 were identical in configuration, with a 10 dB difference in acoustic test levels. The response data for 32 accelerometers from Run 3 were scaled up 10 dB and the average and the variance were computed. The average and variance from Run 4 were also computed. The averages of the two runs are compared in Figure 11. In Figure 12 the average and variance of the ratios of responses for individual accelerometers are presented for Run 4 relative to Run 3 scaled up 10 dB. It can be seen from

Frequency (Hz)	Galileo Bus Assembly Qual Levels	Galileo Bus Assembly Qual Levels Minus 10 dB
25 - 100	+6 dB/octave	+6 dB/octave
100 - 250	0.1 G ² /Hz	0.01 G ² /Hz
250 - 500	-6 dB/octave	-6 dB/octave
500 - 2000	0.025 G ² /Hz	0.0025 G ² /Hz
OVERALL	8.3 Grms	2.6 Grms

TABLE 2. RANDOM VIBRATION TEST LEVELS

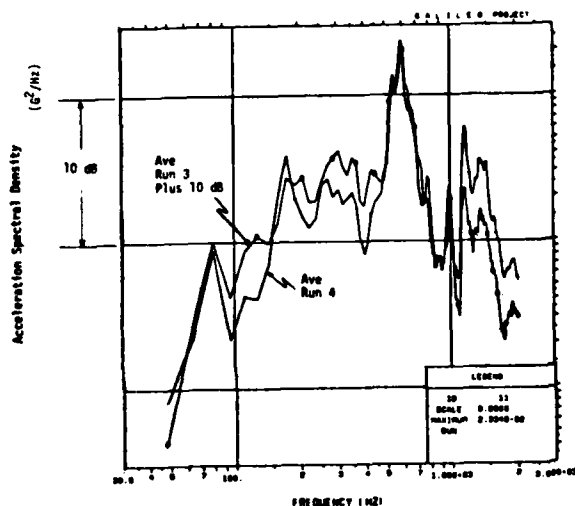


Figure 11. Response Linearity - Average of Run 4 Responses and Average of Run 3 Responses Plus 10 dB

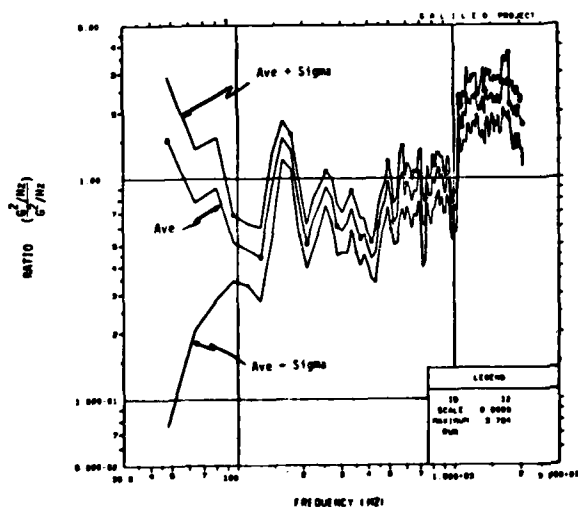


Figure 12. Response Linearity - Ratios of Run 4 Responses to Run 3 Responses Plus 10 dB

both Figures 11 and 12 that the bus response is linear with acoustic level within the range of the acoustic tests conducted. Structural nonlinearities would be expected to result in lower relative responses for the higher acoustic levels, but the variations in response for the two runs appear to be random.

Thermal Blankets Effect

The effect of thermal blankets on bus vibration response was evaluated by comparing Runs 3 and 5 (see Table 1). Acoustic test levels for these two runs were the same and the only difference in the configurations was that Run 5 had no blankets. The same analyses performed for the response linearity evaluation was also performed for Runs 3 and 5. Figure 13 shows the average of the corner accelerometer responses for Run 3 and for Run 5. Figure 14 presents the average and variance of the ratios of responses for individual accelerometers for Run 5 relative to Run 3. Both Figures 13 and 14 show that the responses for the two test runs are nearly identical, with only a very slight tendency for an increase in response at higher frequencies without blankets. Figure 15 shows the difference in the response means of the two runs computed from Figure 13 and the mean of the individual ratios from Figure 14 compared to the mass law theoretical effect of removing the blankets. The actual effect on response is negligible compared to the theoretical transmission loss due to the blanket.

Flight-like Versus Dummy Assemblies

Vibration responses for flight-like assemblies and for dummy (mass mockup) assemblies during spacecraft bus acoustic testing were compared for Run 4. Response data from measurements on board type subassemblies were used for this comparison due to the configuration similarity of the flight-like and dummy boards. Module subassemblies varied too greatly in configuration to allow a meaningful comparison. The construction of the dummy and flight-like boards are essentially identical, however, brass disks simulate the mass of components on the dummy boards, whereas the flight-like boards have real components, wiring, and wire harnesses and are coated with epoxy. For this comparison dummy and flight-like boards were chosen which have roughly similar mass distribution. Only data for accelerometers mounted perpendicular to the board surface and located towards the middle of the boards were used. Acoustic Run 4 vibration response data from 6 accelerometers on dummy boards were compared with 10 accelerometers on flight-like boards. Figure 16 shows the average of the responses on the dummy boards and on the flight-like boards. The data shows a slight trend for the dummy boards to respond higher than the flight-like boards, particularly at the peak first resonant frequencies, indicating more damping for the flight-like boards.

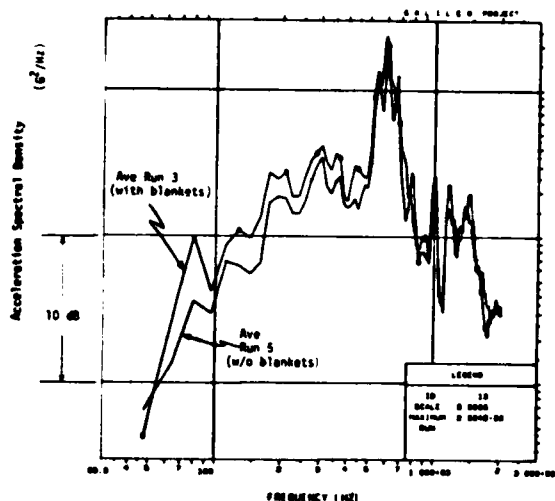


Figure 13. Thermal Blankets Effect - Average of Run 3 and Average of Run 5

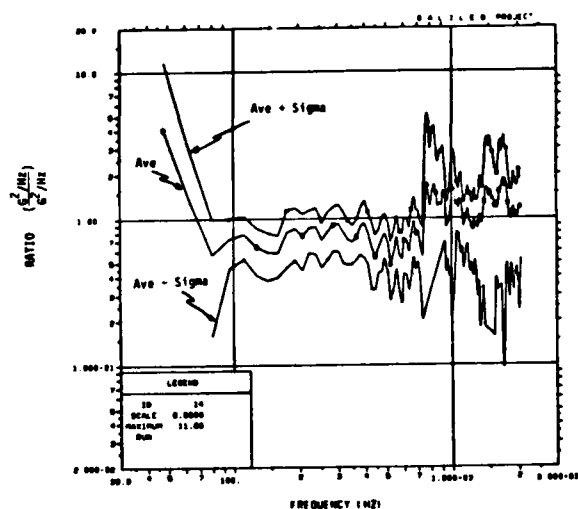


Figure 14. Thermal Blankets Effect - Ratios of Run 5 Responses to Run 3 Responses

Antenna and Bus Attachment Effects

The effect of the antenna and the four or ten point bus attachment configurations on bus vibration responses were not evaluated separately. However, an indication of the relative effects can be observed from the data. Figure 17 shows the average of all the responses on the top corners of the bus compared to the average on the bottom corners of the bus for Run 4. The test article configuration for Run 4 had no antenna and had a ten point bus attachment to

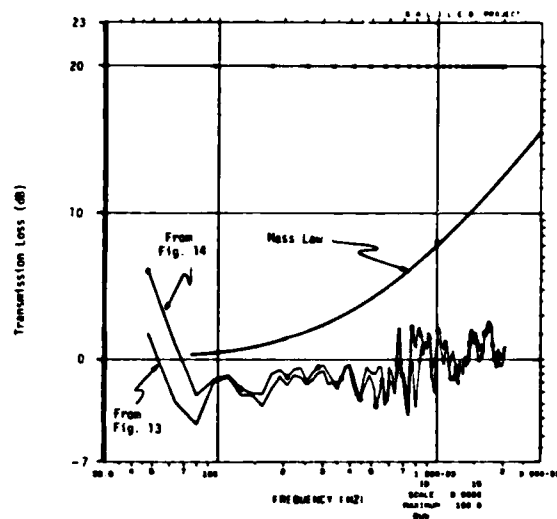


Figure 15. Transmission Loss Due to Thermal Blankets

the handling ring. It can be seen from the comparison of Figure 17 that the attachment to the handling ring has only a minor impact on the bus responses. The effect of the antenna may thus be determined from a comparison of Runs 1 and 5. Acoustic test Run 1 configuration had the antenna, a four point attachment between the bus and the handling ring, and no thermal blankets, while Run 5 configuration had no antenna, a ten point attachment, and no thermal blankets. Figure 18 compares the average of all bus corner responses for Runs 1 and 5. This comparison shows that the antenna has a very large effect on bus responses, particularly below about 200 Hz where responses are more than 20 dB higher with the antenna at some frequencies. In Figure 19 the average and variance of the ratios of responses for individual accelerometers are presented for Run 1 relative to Run 5. This figure shows the same results as Figure 18.

Vibration Test Requirements

Current Galileo bus assembly random vibration requirements are based on responses due to acoustic excitation at bus corners, or hard points. Figures 20, 21, and 22 show the average and average plus two sigma of the responses on or near the bus corners induced during acoustic test Run 4 for the Z axis (9 accelerometers), R axis (15 accelerometers), and T axis (10 accelerometers) respectively. The Z (vertical) axis is along the spacecraft centerline, the R axis is radial to the centerline and the T axis is perpendicular to both the Z and R axes, tangent to the bus front and back shear plates. The data shows that the corner responses are far below bus assembly test levels in the T axis and are generally lower in the Z and R axes except

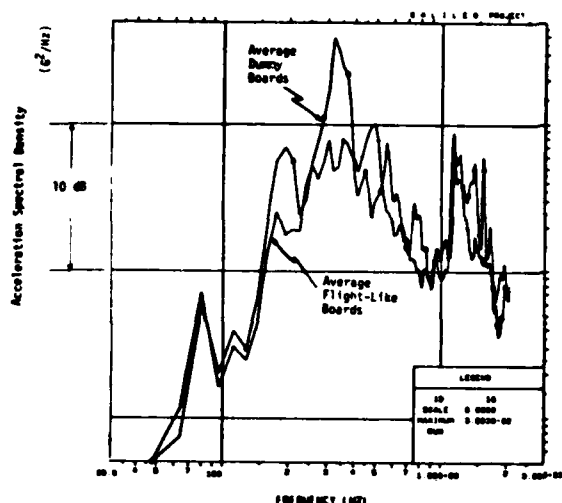


Figure 16. Flight-Like Versus Dummy Boards Response to Acoustic Test

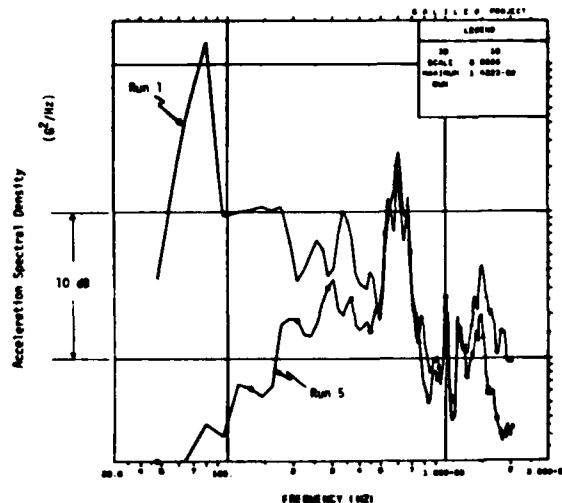


Figure 18. Voyager Antenna Effects - Average Response of Run 1 (with Antenna) and Average Response of Run 5 (w/o Antenna)

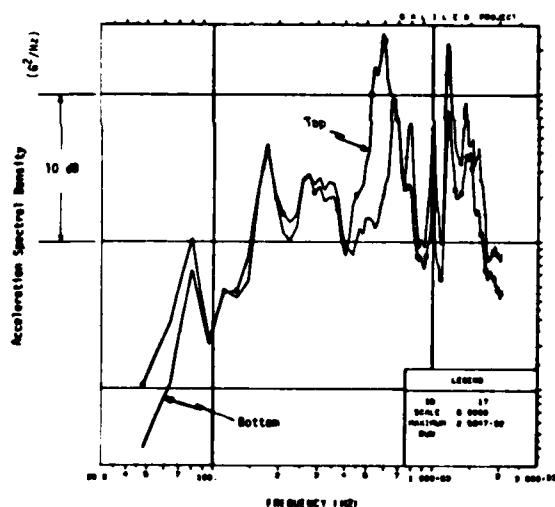


Figure 17. Average of the Responses on the Top Corners of the Bus Compared to the Average on the Bottom Corners of the Bus for Acoustic Test Run 4

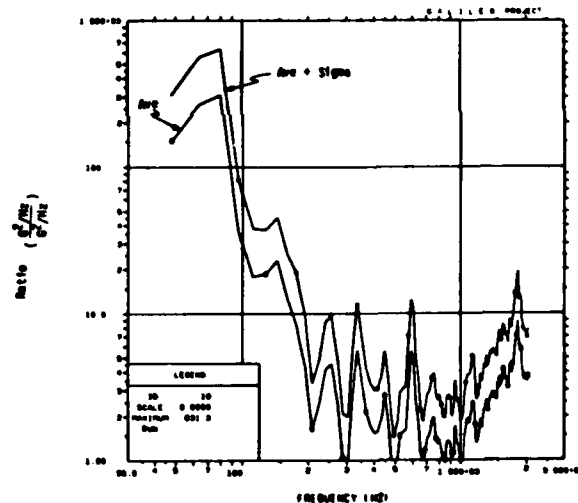


Figure 19. Voyager Antenna Effects - Ratios of Run 1 Responses to Run 5 Responses

for narrow spikes mostly in the 500 to 700 Hz range which slightly exceed test levels. Review of individual accelerometer data shows that the narrow spikes occur only at accelerometers located just off the corners (about 2 inches from the hard points).

It is reasonable to assume that the measured bus responses are generally representative of those

for a full up Galileo configuration spacecraft. The Voyager DTM bus has a high degree of structural similarity to the Galileo bus. However, the adequacy of the simulation of the bus attachments to the spacecraft trusses is questionable. Although the Galileo trusses supporting the bus are considerably stiffer than Voyager they are far more flexible than the handling ring. It is possible that the more flexible spacecraft trusses will increase low

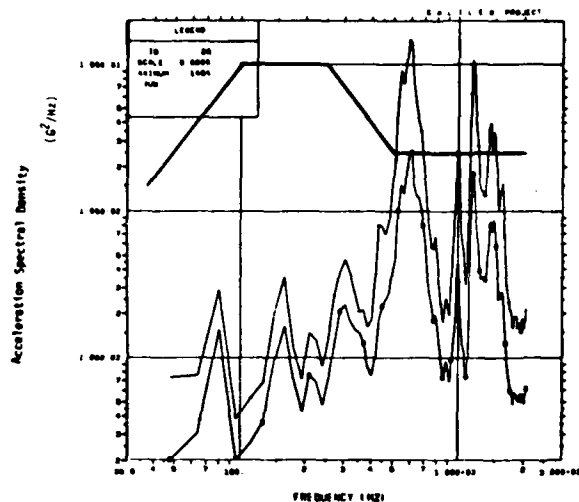


Figure 20. Average and Average Plus Two Sigma of the Responses on or Near Bus Corners During Acoustic Test Run 4 - Z Axis

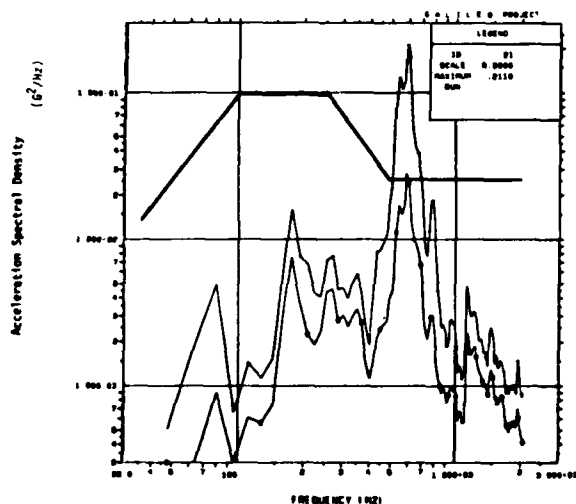


Figure 21. Average and Average Plus Two Sigma of the Responses on or Near Bus Corners During Acoustic Test Run 4 - R Axis

frequency responses below perhaps 100 Hz. However, above 100 Hz, the generally lower responses observed on the bus bottom corners may be increased when installed on the spacecraft trusses. The lack of appendages on the bus acoustic test configuration will also affect bus responses. The Galileo bus will support two RTG booms, a science boom, and the folded mesh dish antenna. None of these appendages will be nearly as effective an acoustic receptor as is

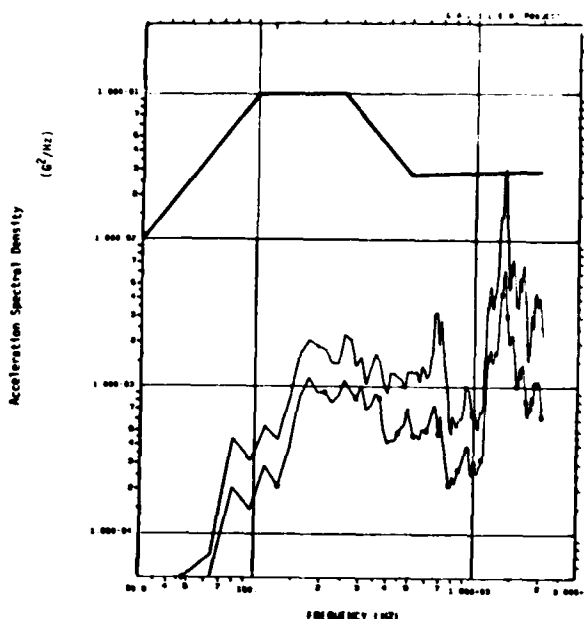


Figure 22. Average and Average Plus Two Sigma of the Responses on or Near Bus Corners During Acoustic Test Run 4 - T Axis

the Voyager high gain antenna, but they will probably increase bus levels some in the lower frequencies. In conclusion, it is believed that the Run 4 acoustic test results adequately represent Galileo spacecraft bus responses in the mid and high frequencies, but probably somewhat under represent below about 100 Hz.

Since the rigid vibration test fixture holds the special bay fixture along the edges of both the front and back shear plates, defining assembly vibration levels only by responses on or near bus corners is questionable. Figure 23 shows the average and average plus two sigma of responses from six accelerometers (4 in the Z axis and 2 in the R axis) on the edges of the shear plates near the bay centers. These responses exceed assembly test levels by a considerable amount in the 400 to 1500 Hz range.

Another problem in defining bus assembly random vibration test criteria is the special bay fixture required to support the subassemblies during test. Random vibration will be induced into the bus subassemblies during launch primarily by direct acoustic excitation of the bus shear plates. Yet the shaker vibration tests attempt to simulate the launch environment by inducing vibration through the rigidly held shear plate edges. The vibration levels on the special bay fixture shear plates induced by the shaker tests will not necessarily be similar to the shear plate vibration levels on the real bus induced by acoustics.

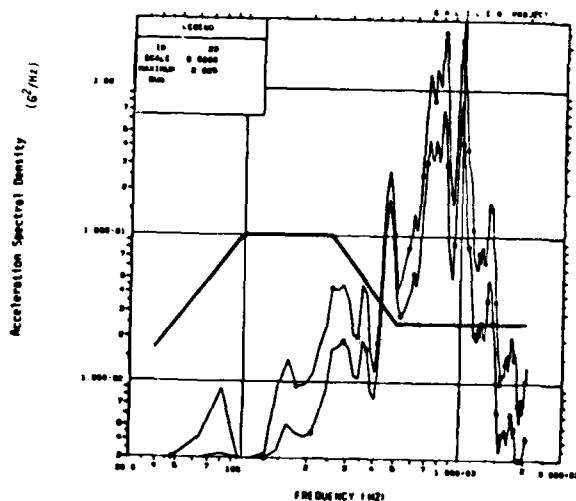


Figure 23. Average and Average Plus Two Sigma of the Responses on the Edges of the Shear Plates Near the Bay Centers During Acoustic Test Run 4 - Z and R Axes

In addition to the above difficulties in developing bus assembly vibration test criteria, the problems normally inherent in specifying conventional rigid fixture vibration tests are present. These are rigid fixture/assembly boundary conditions which do not simulate actual mounting impedance, coherent vibration input due to single axis testing with in-phase vibration at all attachment points as compared to normally incoherent vibroacoustic environments, and test control problems due to fixture resonances and the need for multi-control averaging. The bus assembly vibration tests discussed in the following section were intended to resolve these vibration criteria specification problems.

VIBRATION TESTS RESULTS

The shaker vibration tests on the three bus assemblies provided adequate subassembly response data for comparison with the bus acoustic tests. The three bays contained 26 accelerometers on subassemblies, 14 accelerometers in the T axis (perpendicular to the plane of the board-type subassemblies), 6 in the R axis, and 6 in the Z axis. The objective of the initial data analysis was to verify that current Galileo bus assembly vibration requirements are adequate. Subassembly responses from the vibration tests were compared with responses from the Run 4 bus acoustic test. For each accelerometer in the vibration tests, the response data for the three directions of shake were enveloped. The means of the three axes envelopes of the vibration test responses were then compared with the means of the responses from the acoustic test. This comparison, presented in Figure 24, shows that

the mean of the three directions envelope for the vibration test responses is generally an order of magnitude or more greater than the acoustic test responses. In order to further verify the adequacy of the Galileo test levels, response data for the acoustic and vibration tests were compared on an accelerometer by accelerometer basis. It was found that of the 26 accelerometer locations, the acoustic test

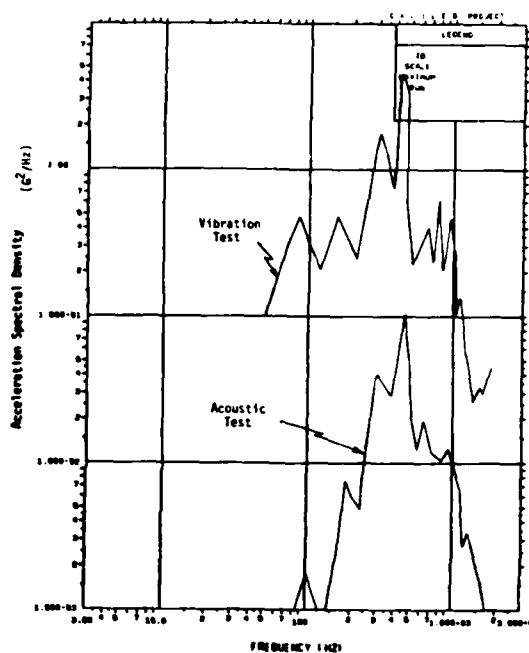


Figure 24. Subassembly Mean Envelope Response for the Three Vibration Tests Versus the Mean Response for the Acoustic Test Run 4

responses exceeded the three axes envelope of the vibration test responses at any 16 Hz frequency band at only five locations. The higher levels for the acoustic tests at these 5 locations were limited to only a few 16 Hz bandwidths in the higher frequencies, none of which corresponded to major subassembly resonances. It was concluded that the current vibration test levels are adequate, and in fact are quite conservative over most of the frequency range, particularly at major subassembly resonances.

Of more general interest than the adequacy of the Galileo test levels is the degree of conservatism inherent in specifying equipment rigid fixture vibration tests using input measurements from system acoustic tests. To determine this conservatism for Galileo bus assemblies, average transmissibilities were calculated for both the acoustic and the

vibration tests from two of the three bays vibration tested. The simplifying assumption was made that a subassembly response in a particular axis was induced by input vibration in that axis. For the acoustic tests, subassembly responses from Run 4 were divided by the average of the measurements on or near the bus corners (Figures 20, 21, and 22) in the axis of the particular subassembly response. Similar calculations were made for the vibration tests, dividing the subassembly responses by the average of the control accelerometer data in the appropriate axis. The acoustic and vibration tests transmissibilities were then statistically compared by two different methods. First, the average of the transmissibilities in each axis for the acoustic tests were compared with the average of the transmissibilities for the vibration tests in corresponding axes. These comparisons are shown in Figures 25, 26, and 27 for the Z, R, and T axes, respectively. For the second method, the transmissibilities for the vibration tests were divided by the transmissibilities for the acoustic tests on an accelerometer by accelerometer basis. The average and standard deviation of these ratios were then calculated for each axis and are shown in Figures 28, 29, and 30 for the Z, R, and T axes respectively. It can be seen in Figures 25 through 30 that in the low frequencies the transmissibilities are near unity for both the

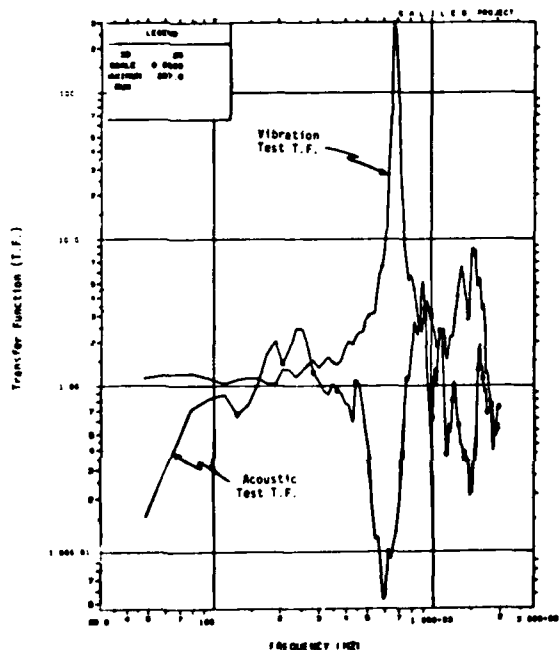


Figure 25. Z Axis Transfer Functions For Bays 1 & 9: Acoustic Test T.F. and Vibration Test T.F.

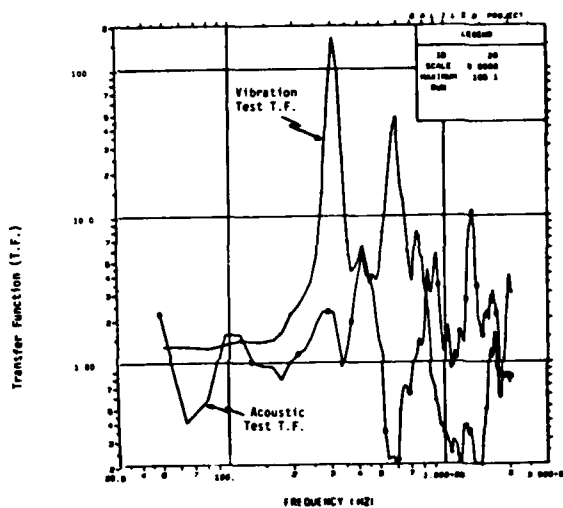


Figure 26. R Axis Transfer Functions For Bays 1 & 9: Acoustic Test T.F. and Vibration Test T.F.

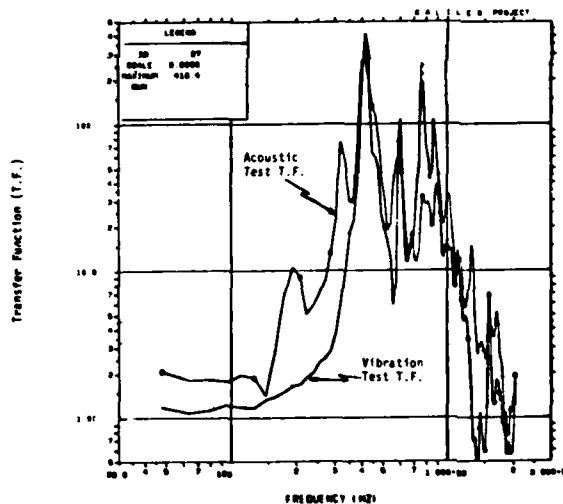


Figure 27. T Axis Transfer Functions For Bays 1 & 9: Acoustic Test T.F. and Vibration Test T.F.

vibration and the acoustic tests. About 300 Hz and above, where subassembly resonances exist, the vibration test transmissibilities are

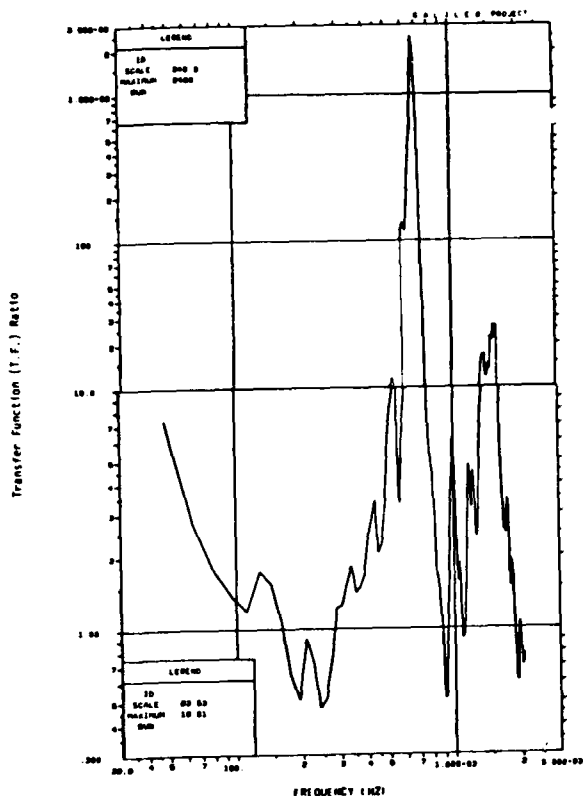


Figure 28. Ratio of Z Direction Transfer Functions: Vibration Test T.F./Acoustic Test T.F.

generally as much as 30 dB greater than the transmissibilities for the acoustic tests. However, the ratio of transmissibilities vary greatly; at some frequencies the acoustic test transmissibilities are considerably greater than the vibration test transmissibilities. It is evident from the data that the acoustic test responses cannot be meaningfully compared to the vibration test responses on an axis-by-axis basis.

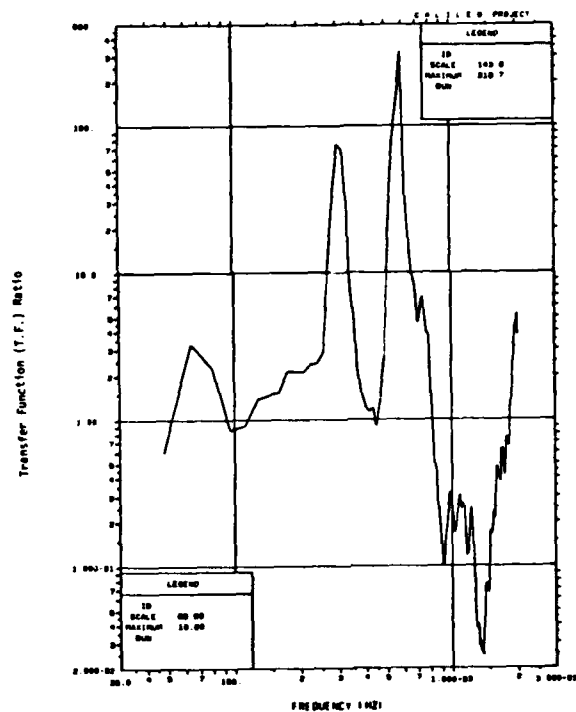


Figure 29. Ratio of R Direction Transfer Functions: Vibration Test T.F./Acoustic Test T.F.

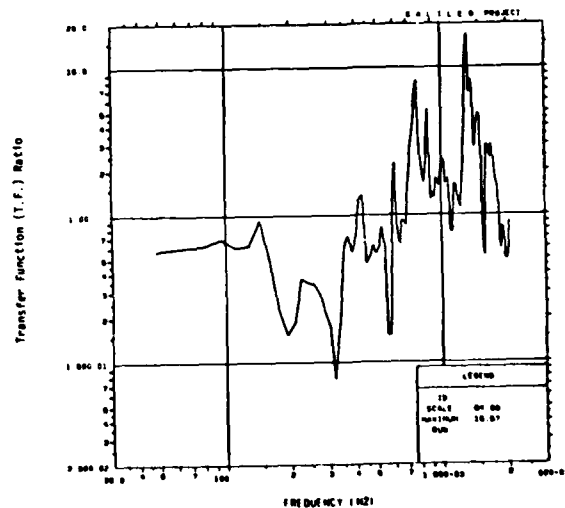


Figure 30. Ratio of T Direction Transfer Functions: Vibration Test T.F./Acoustic Test T.F.

SUMMARY AND CONCLUSIONS

A number of observations have been made on the results of the acoustic and vibration tests, some of which may be useful to others developing spacecraft vibroacoustic criteria, as well as to the Galileo Project. These observations are reviewed below.

1. Bus structural responses were linear within the range of the acoustic tests (137 dB to 147 dB overall).
2. The effect of thermal blankets on bus vibration response was negligible.
3. Dummy subassembly electronics boards (mass simulated components, no wiring or harnesses, and no epoxy coating) responded slightly higher to the acoustically induced vibration environment than did flight-like boards.
4. Installation of the high gain antenna on the bus increased bus responses more than 20 dB for some frequencies below about 200 Hz.
5. Bus responses at the bottom corners attached to the handling ring were generally slightly less than bus responses at the top corners.
6. Bus corner responses were generally within Galileo bus assembly vibration test requirements except for narrow band responses in the 500 to 700 Hz range. Installation of the bus on the spacecraft trusses instead of the handling ring and the installation of spacecraft appendages on the bus may increase bus responses. However, the effects of these factors are anticipated to be limited to lower frequencies where measured bus responses are about 10 dB below assembly test requirements.
7. Average subassembly responses to shaker assembly vibration tests were 10 to 20 dB higher than average subassembly responses to bus acoustic tests.
8. Transmissibilities for the vibration tests (subassembly responses to average control input) were as much as 30 dB higher than transmissibilities for the acoustic tests (subassembly responses to average bus corner responses) at subassembly resonances.

FURTHER INVESTIGATIONS

There are two areas related to the above described vibroacoustic test program which may warrant further investigation. The first is development of vibration test requirements for bus assemblies based on a comparison of subassembly responses during the bus acoustic and the assembly vibration tests. A conservative approach would have to be taken which provided high probability that the assembly vibration test excited at least as severe subassembly responses as did the bus acoustic test. However, the Galileo bus assembly designs are largely inherited from the Voyager program and have been proven to be capable of surviving current bus assembly vibration qualification test requirements. Also, current assembly random vibration flight acceptance test levels (4 dB below qualification levels) are near those levels commonly accepted as minimum vibration screening levels. Thus, little incentive exists at this time for lowering bus assembly vibration levels.

The other potential area for further investigation is the development of a vibroacoustic test fixture which better reproduces subassembly responses and which is also cost effective. Current Galileo bus assembly vibration testing is time consuming due to the need for three axis testing and the need to evaluate and mitigate the effects of unavoidable fixture resonances. A first approach would be to use the special bus bay assembly test fixture, or even the Voyager DTM bus, with the excitation provided by the reverberant acoustic chamber. Modifications to the fixture or bus bay may be necessary to increase the structure's modal density. Acoustic test level margins would be required to insure that the induced subassembly responses were at least as severe as induced by Galileo spacecraft acoustic tests.

This study program was carried out at the Jet Propulsion Laboratory, California Institute of Technology, under NASA contract NAS 7-100.

SLV-3 FLIGHT VIBRATION ENVIRONMENT

S.A. Palaniswami, G. Muthuraman, P. Balachandran
Aerospace Structures Division
Vikram Sarabhai Space Centre
Trivandrum, INDIA

The vibration test levels for SLV-3 was predicted based on empirical method. Second experimental flight of SLV-3 was instrumented at various locations to obtain actual vibration environment. Measurement scheme and data reduction are described. The various causes for the vibration are discussed in detail. The reduced levels from flight data are compared with predicted values.

INTRODUCTION

Indian Space Research Organisation designed and developed SLV-3 a four stage Satellite Launch Vehicle. Its second experimental flight SLV(E)-02 injected 36 Kg Rohini (RS1) Satellite in 300/900 KM orbit.

This experimental flight was instrumented with vibration packages at various locations to study the flight vibration environment.

The objectives of the study are :

- i) to reduce test levels from flight vibration data and update the predicted values which were earlier theoretically estimated using empirical prediction technique based on Barrett method.
- ii) to establish vibration loads for critical components.
- iii) to aid in flight failure analysis.

The vibration environment of SLV-3 from the second experimental flight is discussed in the following pages.

VIBRATION ENVIRONMENT

Launch Vehicle Systems undergo vibration during handling, transportation and flight. Of these flight vibration is the severest and critical for mission success. During flight, launch vehicle experiences vibration and shock as self imposed environment. Propulsion system - motor burning, exhaust jet noise and aerodynamic boundary layer noise are major agencies that create vibration. Vehicle experiences shocks at lift off, ignition and burn out of motors, separation of stages, heat shield ejection etc. To these shocks the vehicle structure responds as vibration transients which propagate from the point of disturbance to further end in addition to wave propagation. The vibration is thus function of structural characteristics, dynamic pressure, acoustic field, exhaust velocity and thrust perturbations.

PREDICTION OF VIBRATION ENVIRONMENT

The vibration test levels for sub-assemblies and components were earlier to the flight estimated using Barrett

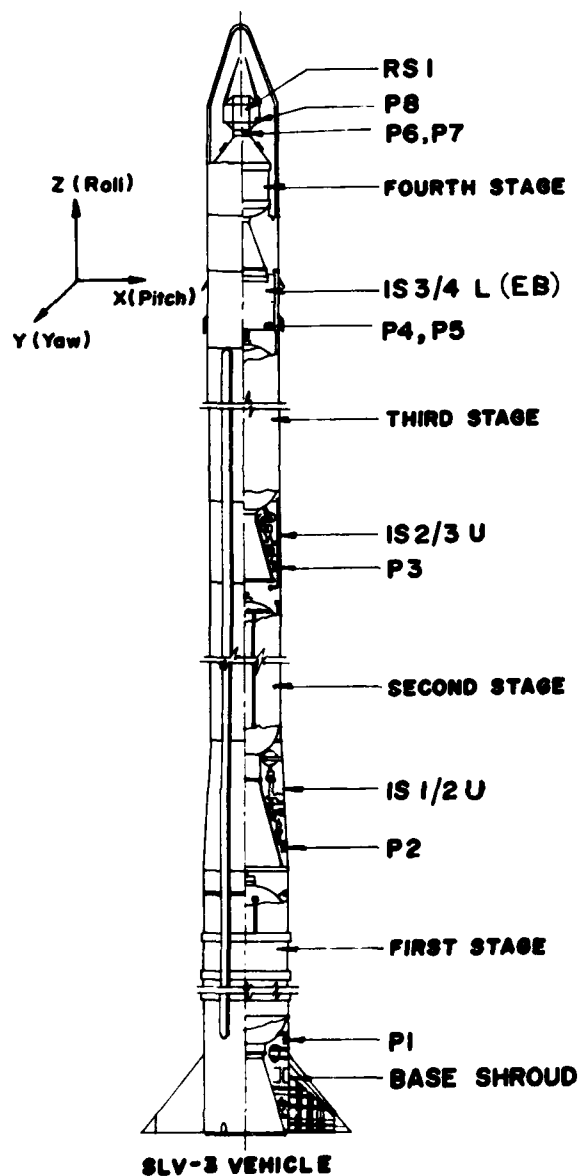


Fig. 1 - Location of Vibration pick-ups on SLV-3

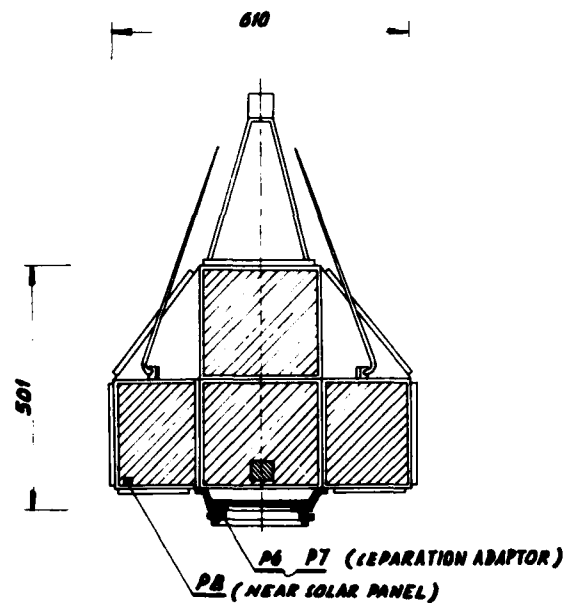


Fig. 2A - RS1

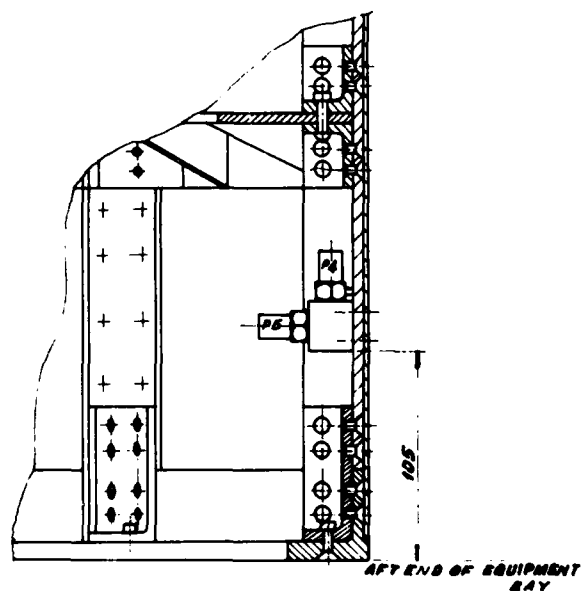


Fig. 2B - Typical mounting of pick-up

method (ref.1). This method involves scaling acoustic pressure, surface density of the structure, thrust and exhaust velocity of motor in the following manner.

$$A(f)_n = A(f)_r \left[\left(\frac{W}{A} \right)_r \left(\frac{A}{W} \right)_n \frac{P_n}{P_r} \right]^2 \quad -1$$

$$A(f)_n = A(f)_r \left[\frac{W_r}{W_n} \cdot \frac{T_n V_n}{T_r V_r} \right] \quad -2$$

where

$A(f)$ - Acceleration spectral density at frequency f ;

p - Rms acoustic pressure;

W
 A - Surface density of the structure

W - Weight of the structure

T - Thrust of the motor

V - Exhaust velocity of the motor

Subscripts n and r - new and reference vehicles

The test levels for various locations were estimated using equations (1) and (2) with proportionate weightage for acoustic and propulsion contributions depending upon those locations on the vehicle.

VIBRATION PACKAGE

The vibration pick up used in the flight is conventional piezoelectric type of accelerometer whose weight is 28 grams. The capacitive output is conditioned by airborne charge amplifier. The package is capable of operating in the stringent flight environments. The mounted resonance frequency is 19 KHz. The range of measurement is limited to 2000 Hz as the test requirement is 10-2000 Hz only. The package was developed for the specific purpose of acquiring vibration data on launch vehicles.

MEASUREMENT SCHEME

With limited telemetry channels available 8 measurement channels and 6 locations were identified for vibration response study. Out of 8 channels, 5 were located on the vehicle and 3 were on the satellite. Table 1 shows the scheme of measurement.

In the base shroud and in all interstages the pick-ups were mounted rigidly on to the longeron close to fore end/aft end ring to facilitate easy correlation with laboratory test response data. Two pick-ups were fixed on the separation adaptor of satellite. One pick-up was screwed on to the satellite structural frame very close to solar panel. Figure 1 shows the various locations of pick-ups P1 to P5 on the vehicle and Figure 2A the locations of P6 to P8 on the satellite and figure 2B the typical mounting of pick-up on to the structural member.

FLIGHT DATA ANALYSIS

The vibration data in all channels show considerable vibration levels during Stage I operation upto 72.8sec from lift off (Fig.3). The vibration levels in all channels slowly raise to maximum around T+40 seconds and fall down to minimum at around T+65 seconds. T+40 seconds corresponds to maximum dynamic pressure region. At forward end of vehicle the levels are considerable at time T+24 seconds which corresponds to transonic region (refer Figure 3).

As preprocessing procedure the signals were cleared by passing them through 2000 Hz low pass filters.

True Grms values are shown for all channels in figures 4 to 11. Power spectral density in 10-2000 Hz is obtained through real time analyser for 1 second sample time length. Exponential averaging during this 1 second data is adopted in the analysis. The response in 1 second sample time in q max region is self stationary while at other regions it is not strictly so. However the error introduced by exponential averaging in these regions is negligible as the

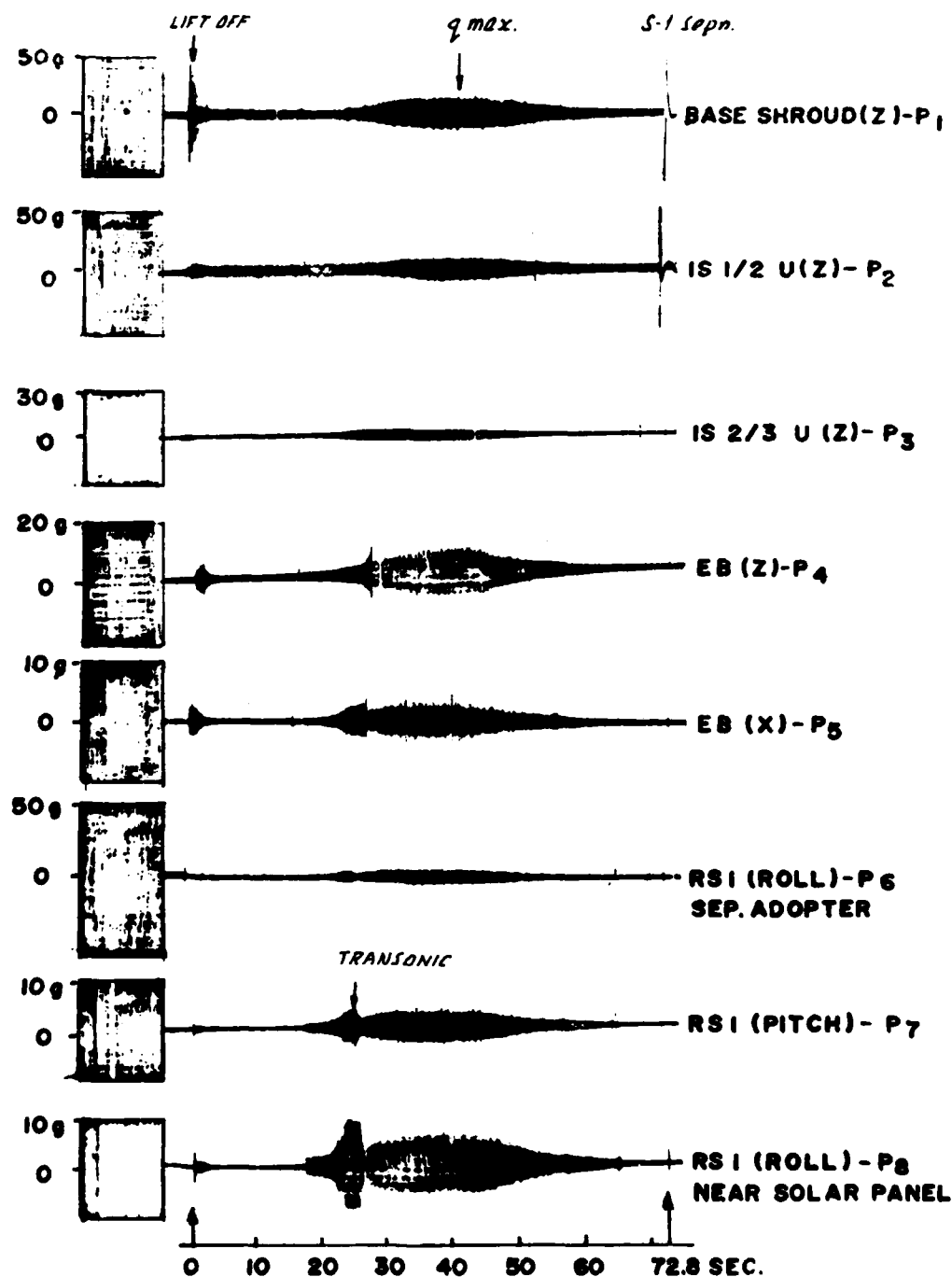
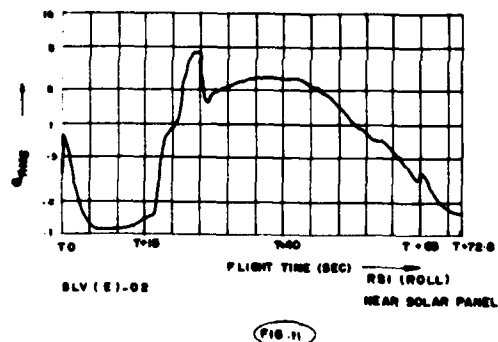
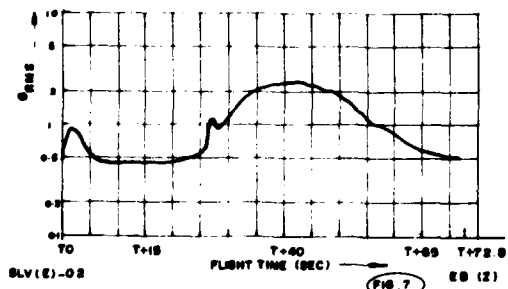
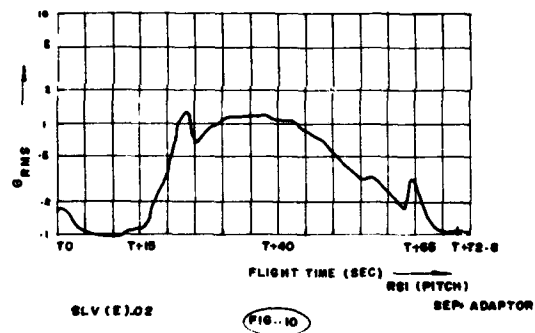
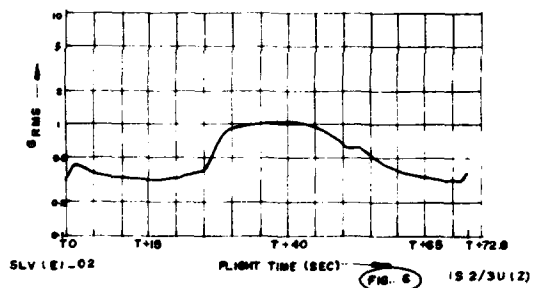
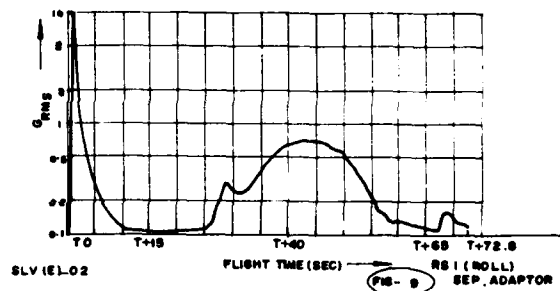
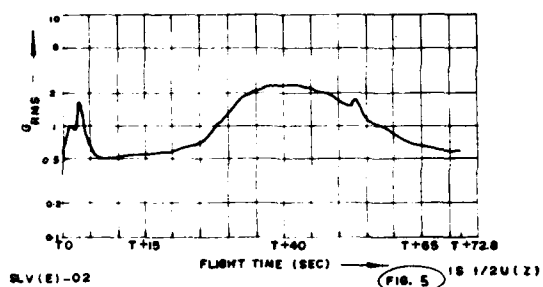
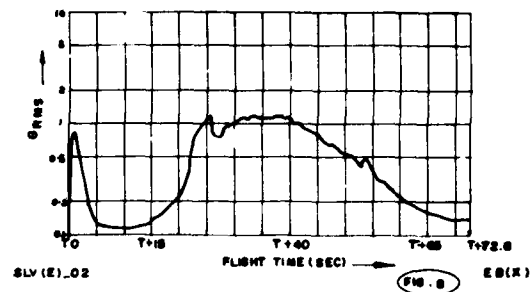
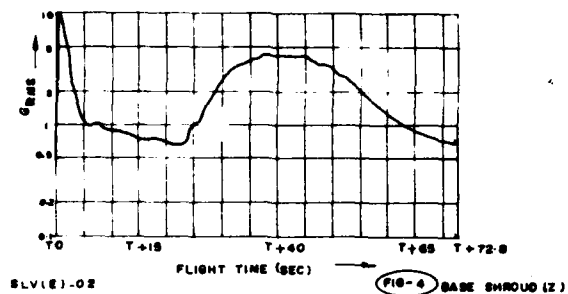


Fig. 3 - SLV(E)-02 Flight vibration responses upto Stage I separation



Figs 4-11 - Vibration levels upto stage I separation

TABLE 1
Measurement Scheme

LOCATION		Sens.Axis	Freq.Response (Hz)	Full Scale range (g)
No.	Description			
P1	Base Shroud	Roll (Z)	10 - 2000	± 50
P2	IS 1/2 U	Roll (Z)	10 - 2000	± 50
P3	IS 2/3 U	Roll (Z)	10 - 2000	± 30
P4	IS 3/4 L(EB)	Roll (Z)	10 - 2000	± 20
P5	IS 3/4 L(EB)	Pitch (X)	10 - 600	± 10
P6	Sat. Sep. adaptor	Roll (Z)	10 - 2000	± 50
P7	"	Pitch (X)	10 - 2000	± 10
P8	Satellite	Roll (Z)	10 - 2000	± 10

time length is small. The spectrum analysis at lift off, transonic and

TABLE 2

Grms Response at different Locations

Flight Region	P1	P2	P3	P4	P5	P6	P7	P8
q max	4.6	2.6	1.05	2.4	1.2	0.68	1.2	2.6
Transonic	1.0	0.7	0.40	1.1	1.2	0.3	1.3	4.5

q max regions is presented as psd plots in Figures 12 to 23. The Grms values at q max and transonic regions are tabulated in Table 2. Figures 24 and 25 indicate the level during stage II operation. The psd/Grms is very low during stage II and above stages operation as the dynamic pressure is very small after Stage I separation.

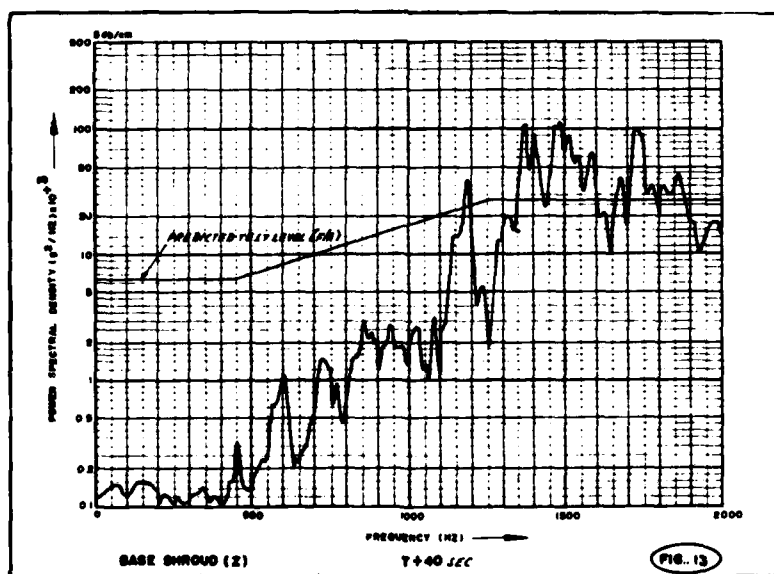
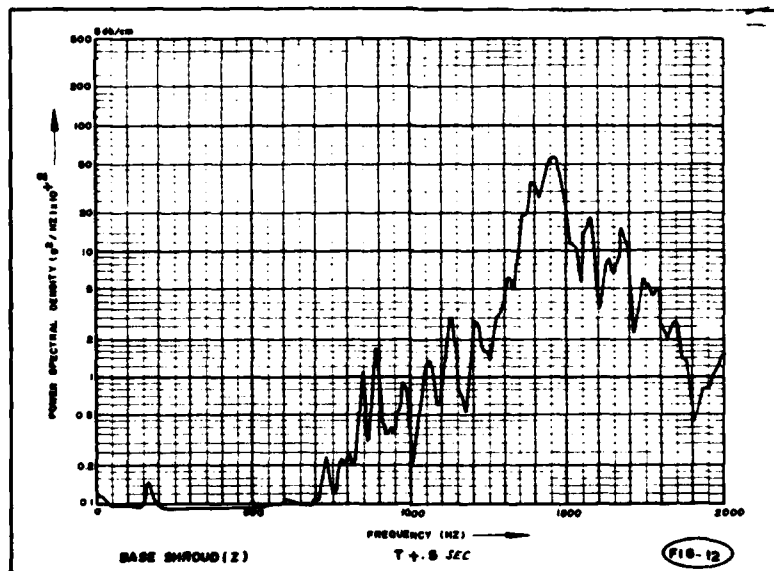
The data is edited suitably avoiding steady response for transient signal entry into the memory of shock response spectrum analyser. The shock response spectrum (SRS) is obtained

for transient events upto Stage II separation. Figures 26 to 33 are SRS for transient responses at Satellite location for damping ratio 2.5% (Q factor as 20).

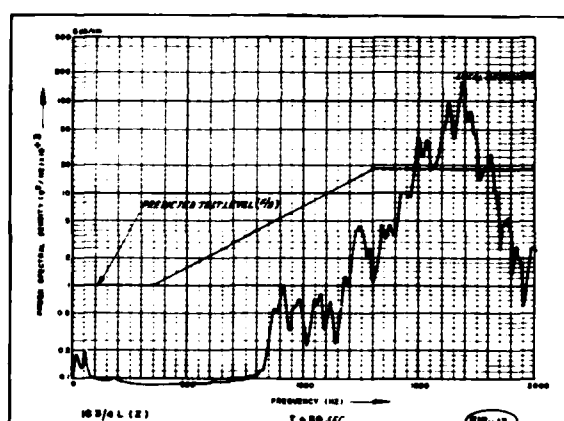
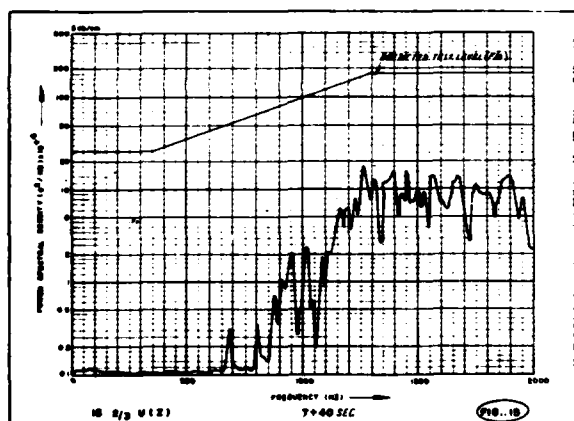
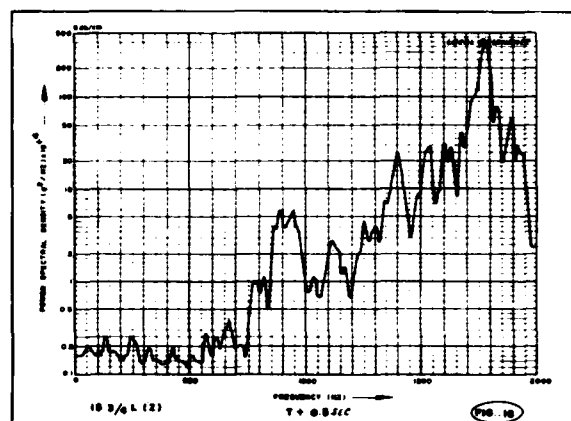
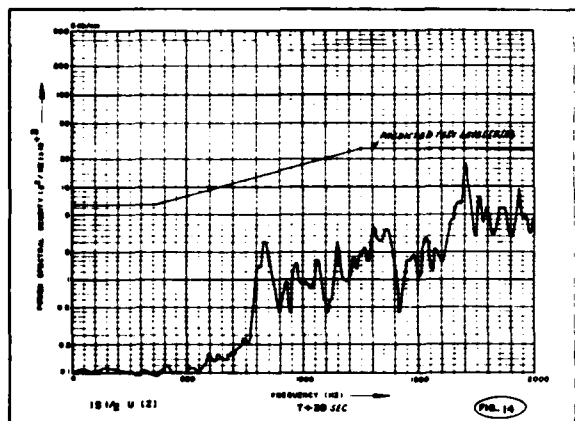
DISCUSSION

Rocket engines emit high velocity exhaust gases which mix with ambient air causing turbulent shear layers in the process. The pressure fluctuations of the turbulent shear layers are transmitted to the surroundings including the vehicle as acoustic noise. The distributed acoustic noise field over the vehicle surface causes structure to vibrate. This jet noise disturbance is maximum at lift off due to acoustic reflection from the ground and decreases as vehicle accelerates.

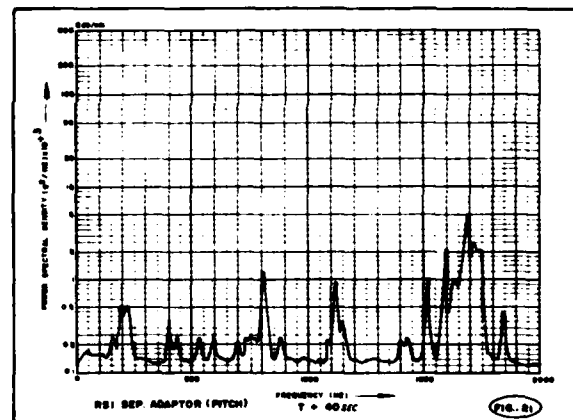
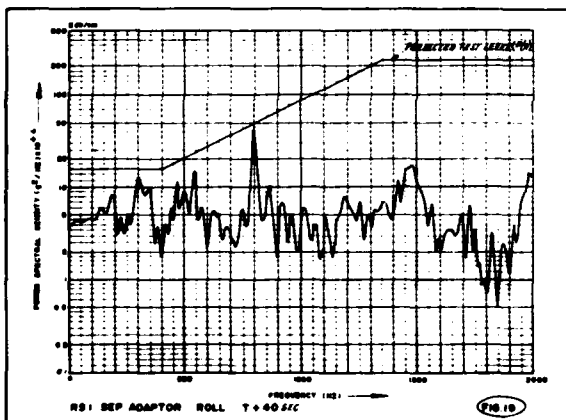
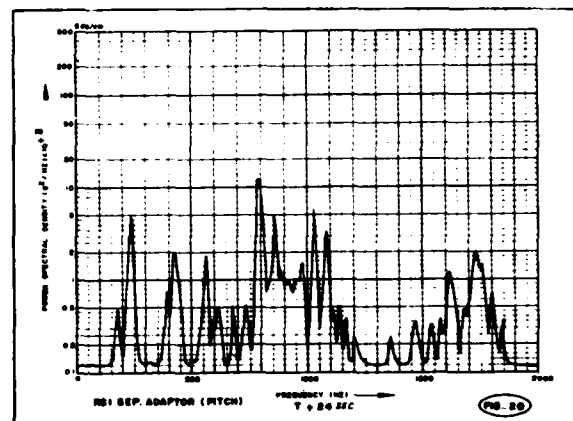
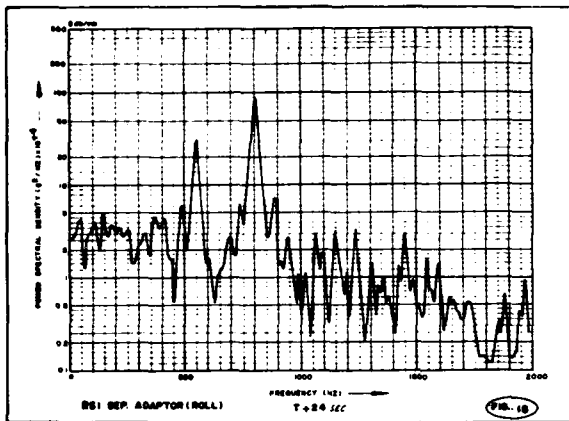
As the vehicle moves with increased velocity with time through atmosphere, the boundary layer on the vehicle is generally turbulent because of high Reynolds number. The resulting pressure fluctuation is applied over the vehicle surface and causes the structure to vibrate. As the vehicle cross sectional area changes from fore end to aft end, there may be shock waves occurring in the aerodynamic flow causing further increase in turbulence



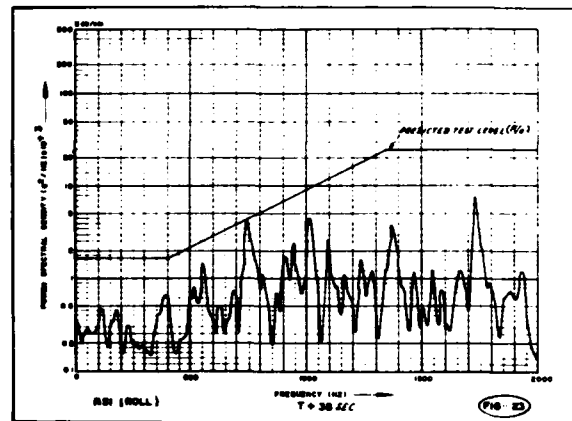
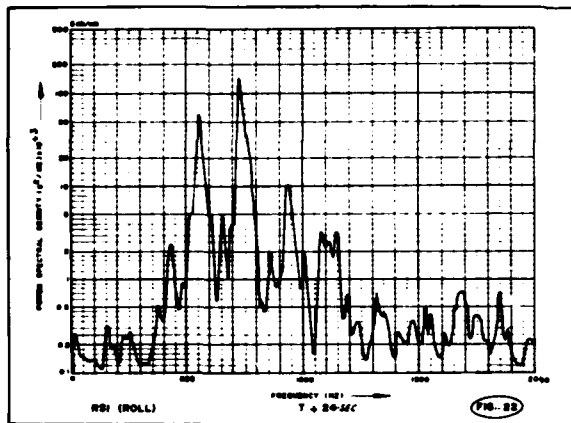
Figs 12 & 13 - Vibration spectrum for base shroud



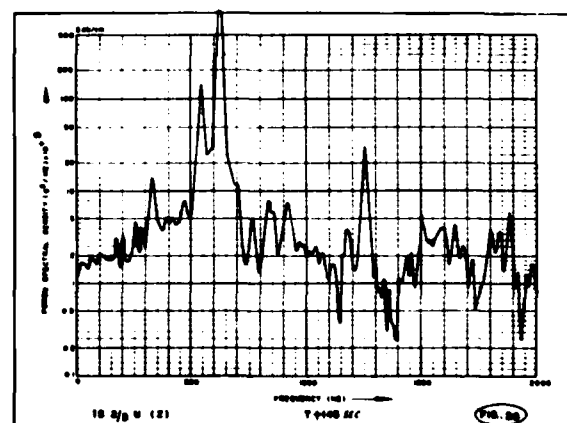
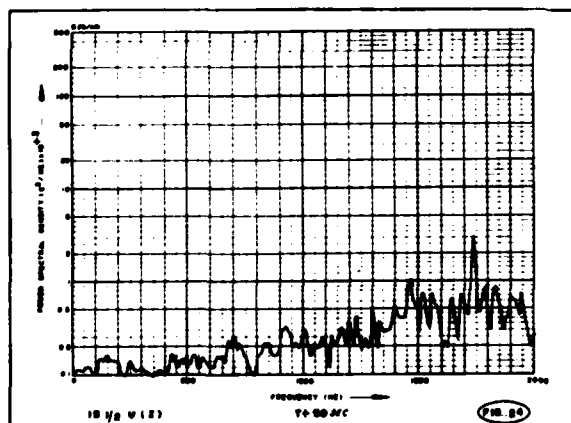
Figs 14-17 - Vibration spectrum for IS 1/2 U, IS 2/3 U and IS 3/4 L



Figs 18-21 - Vibration spectrum for RS1 at separation adaptor



Figs 22-23 - Vibration spectrum for RS1



Figs 24-25 - Vibration spectrum during Stage II operation

and fluctuating pressure. Possible flows separation will also add to it.

The structural vibration is also caused by random mixing of propellant gases inside the rocket engine combustion chamber. It generates fluctuating pressure on the engine wall. The vibration of the wall is transmitted throughout the vehicle but is often rapidly attenuated with distance from the source. This phenomenon exists throughout the flight until burn out.

Lift Off

In SLV(E)-02 flight lift off at T+180m.sec had caused high vibration level peak corresponding to full scale (50g) at base shroud. the vibration decayed very fast and its existence was less than 2.5 seconds. At all other locations the vibration level was much less than q max peak/transonic peak. The base shroud location being close to exhaust jet and ground, the acoustic reflection imparted high level of vibration. This jet noise power was maximum around 1500Hz (Refer Fig.12).

Transonic Region

In the transonic region the shock waves which have just formed at various locations are unstable and oscillate in their locations. During ascent phase, this transonic disturbance causes heavy vibration of the structure. Any protrusions like antenna will aid to the disturbance as local flow separations are created.

In SLV(E)-02 flight in the transonic region (T+24 to T+26 seconds) the vibration levels noticed were significant only at RS1 and Equipment Bay (EB) locations. Near nose cone expansion waves would have occurred and oscillated and thus creating excessive aerodynamic noise which caused higher level of vibration at RS1. The noise spectrum seems to be maximum in 500Hz to 1000Hz as seen in figures 18, 20 and 22. 576Hz and 728Hz components are distinctly seen in Figure 22 and they are identified from lab measurements as structural resonances.

At EB there were six numbers of antennas creating local flow separations. The vibration level was seen here also peaking in transonic region but the severity was less than that in RS1. No similar growth was in other locations.

q Max Region

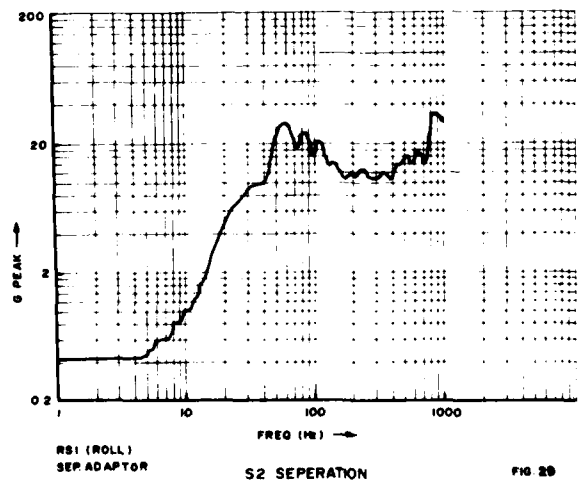
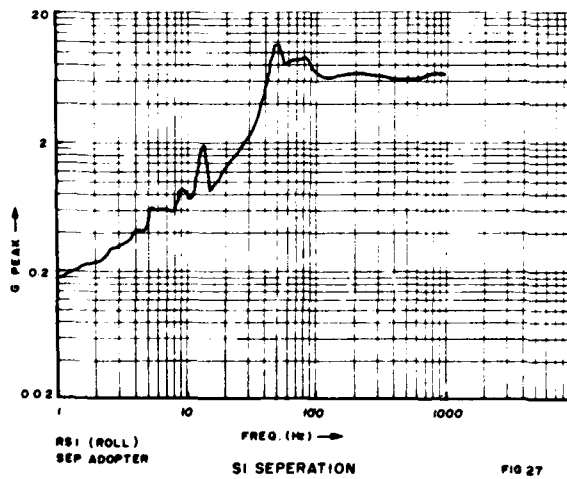
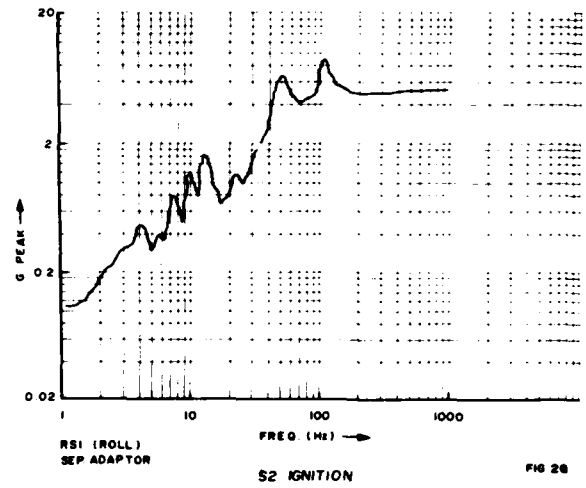
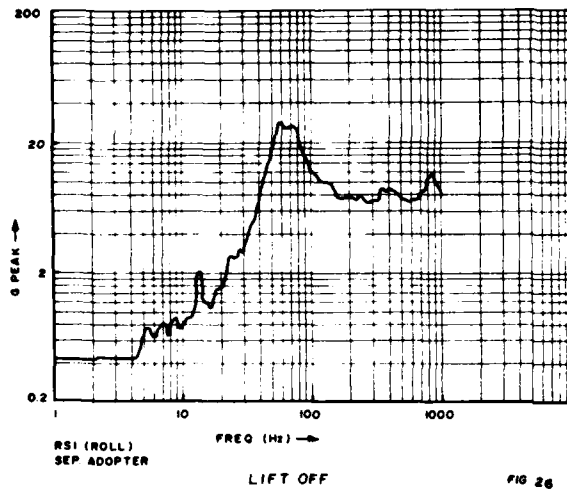
During supersonic flight the shock waves are generally stable as far as their locations are concerned. The fluctuating pressure field exhibits slow variation. The mechanically transmitted disturbance from the motor burning is more or less constant upto burn out. At q max region aerodynamic noise is the maximum.

In SLV(E)-02, fore end of vehicle experienced higher vibration levels due to increased aerodynamic noise. Aft end of SLV also experienced higher vibration levels due to the fact that a portion of jet noise travelled forward fore end through boundary layer and also increase in turbulence due to presence of fins. IS 2/3 location recorded minimum level as the location was aerodynamically very clean and hence less aerodynamic noise contribution to vibration.

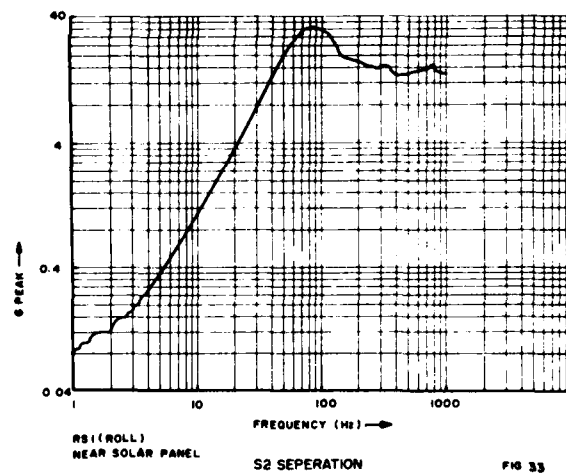
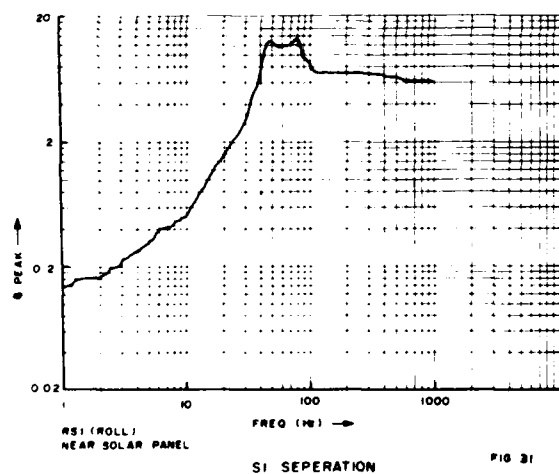
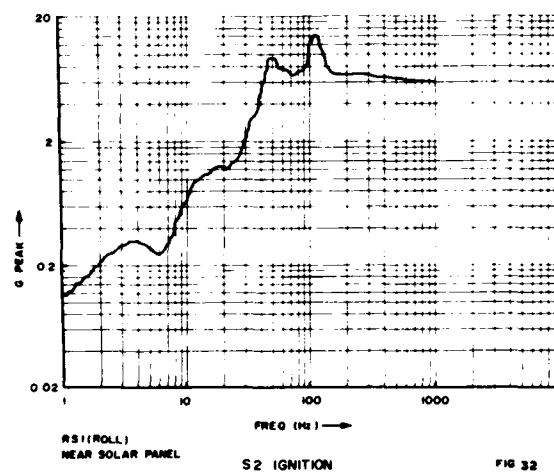
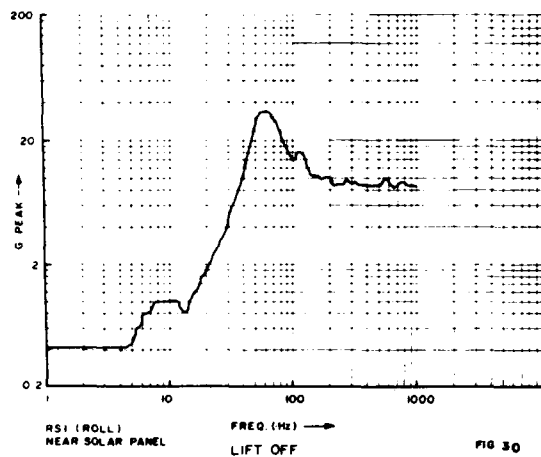
In the case of Satellite RS1, the vibration response in roll axis was found to be more severe at P8 than that at P6. The aerodynamic noise contribution at satellite (P8) is larger than that at Satellite separation adaptor (P6). Refer Figures 19 and 23. The mechanically transmitted vibration generally of low frequency was found to be more predominant at P6 than at P8. From the laboratory test the Grms response at P8 normalised over that of P6 is 1.29. From the flight data the normalised Grms response is calculated as 3.82. The increased figure is due to larger contribution of aerodynamic noise on heat shield nose to which RS1 is close by.

Transient Events

From the transient responses at fore end of vehicle (P6 and P8), it is seen that the shock loading due to lift off as well as separation are severe. At lift off the forcing function being reflected acoustic field induced high transient response at satellite locations. The shock induced by separation mechanism being pyrotechnique device is very high. S1 separation effect is less than that of S2 separation because of shock level attenuation with distance. The response induced is due to mechanical transmission as well as wave propagation.



Figs 26-29 - Shock Response spectrum for RS1 at separation adaptor



Figs 30-33 - Shock Response Spectrum for RS1

TABLE 3
Comparison of Shock Response Levels due to various Shocks

Events		(g peak)			
Location		Lift Off	S1 Separation	S2 Ignition	S2 Separation
P6	Max inst Acc.	6.4	3.6	3	9.5
	Max of SRS	30	11	6.5	28
P8	Max inst Acc.	6.9	3.7	3.4	10.4
	Max of SRS	34	13.2	14	34

CONCLUSION

The vibration environment of SLV-3 indicates that

- i) Vibration is predominant at fore end as well as aft end. The vibration transmitted through structure at location away from operating motor is very less.
- ii) Lift off vibration transient is severe only at base shroud corresponding to 100% of q max peak.
- iii) Transonic region imparts higher level of vibration only at fore end of the vehicle and lasts for very short duration. The pick-up P8 (full scale range $\pm 10g$) was saturated in transonic region.
- iv) Heat shield ejection or RCS activation does not seem to have induced any significant shocks.
- v) Separation shock responses are more severe than ignition shocks. At satellite location transient response due to lift off is equally critical.
- vi) The vibration level after Stage I separation is very low.

Reestimation of vibration test specifications are based on q max level as well as transonic response wherever it is applicable. The flight

vibration level is less than predicted test levels. The 95% envelopes of flight levels are lower bound to the earlier predicted values except at Base shroud. Table 4 illustrates Grms values of flight responses and prediction.

TABLE 4
Comparison of Predicted and Flight Grms values in 10Hz-2000Hz band

Location	Predicted Level Grms	Envelope of flight Response Grms
Base Shroud	6.4	6.99
IS 1/2 U	6.4	3.06
IS 2/3 U	4.8	1.26
IS 3/4L (EB)	4.6	3.69
RS1	5.4	2.96

Maximum vibration loads are experienced at transonic and q max regions as shown in Table 2. These data forms design input for critical elements like RGP, IMU, etc.

The vibration measurement indicates that throughout the flight, the health of the vehicle structure is good. No failure mode has been noticed.

REFERENCES

1. Robert E. Barrett, "Techniques for Predicting Localised Vibratory Environments of Rocket Vehicles" NASA TN D - 1836 Oct. 1963.
2. "General Environmental Test Specifications for Components and Sub-assemblies of SLV-3", VSSC, Nov. 1977.